FACULTAD DE CIENCIAS

# Effect of processing on the structure and properties of glasses and glass-ceramics for photonic applications

**Giulio Gorni**

Memoria para optar al grado de Doctor en Ciencias Físicas.

Directoras
Dr. María Jesús Pascual
Dr. María Yolanda Castro

Tutora
Prof. Luisa Bausá

Instituto de Cerámica y Vidrio

**Madrid, 2019**

Esta tesis doctoral ha sido realizada en el Departamento de Vidrios del Instituto de Cerámica y Vidrio (ICV-CSIC) y desarrollada en el marco de los proyectos MAT2013-48246-C2-1-P/2-P y MAT2017-87035-C2-1-P/-2-P(AEI/FEDER,UE).

La estancia en el "Laboratory of Optical Fibre Technology" de la Universidad de Bialystok (Polonia) ha sido financiada por el COST Action: MP1401.

El autor agradece al Consejo Superior de Investigaciones Científicas (CSIC) y a la dirección del Instituto de Cerámica y Vidrio por permitir la realización de esta tesis.

*Ai miei genitori*

*"Ci sono soltanto due possibili conclusioni: se il risultato conferma le ipotesi, allora hai appena fatto una misura; se il risultato è contrario alle ipotesi, allora hai fatto una scoperta".*

Enrico Fermi

**AGRADECIMIENTOS**

La primera vez que vine al Instituto de Cerámica y Vidrio fue a finales de 2013 para hacer mi TFM. Todavía me acuerdo cuando el Dr. Stefano Pelli estaba escribiendo a la Prof. Alicia Durán para organizar mi estancia en el ICV. Desde el primer contacto por email con Alicia tuve la impresión de encontrar una persona extremadamente dispuesta en aceptar a todos los que demostrasen ganas de trabajar y descubrir el mundo del vidrio. Esta impresión no era equivocada.

Las primeras personas que encontré en el ICV fueron la Dra. María Jesús Pascual y la Dra. Yolanda Castro que me siguieron a lo largo de los casi 8 meses que me quedé en el ICV.

Desde entonces han pasado más de 5 años y a día de hoy tengo esta tesis doctoral escrita.

Mis primeros agradecimientos son para la Prof. Alicia Durán y mis directoras de tesis, la Dra. María Jesús Pascual y la Dra. María Yolanda Castro. A todas ellas debo todo lo que he aprendido sobre los vidrios y vitrocéramicos en estos años de duro trabajo. Gracias por confiar en mí, contratándome a lo largo estos cuatro años de tesis. Gracias por haberme hecho viajar a muchos sitios y por haberme dado la posibilidad de asistir a escuelas especializadas y congresos internacionales. Gracias por haberme convertido en un científico.

A la Prof. Alicia Durán también debo un agradecimiento especial. Sin su perseverancia y su continuo apoyo hoy probablemente no tendría ni la mitad de los artículos publicados. Ya se lo agradecí de persona, pero me gustaría que quedase reflejado en esta tesis.

A mis directoras de tesis quiero agradecer sus esfuerzos en preparar, corregir y dar forma a esta tesis doctoral. ¡Creo que hemos hecho un gran trabajo! Gracias por haberme seguido constantemente en estos años. Nunca me he sentido solo. Gracias por vuestras sonrisas y buenas palabras en los momentos duros. Gracias por haberme enseñado a ser independiente, por dejarme responsabilidades como supervisar varios TFG y TFM y sobre todo, gracias por dejarme tomar la iniciativa.

Gracias también a la Prof. Luisa Bausá que ha sido mi tutora a lo largo de estos años. Gracias por su apoyo, por sus consejos, por evaluar mis actividades y por aclarar mis dudas. Luisa, gracias por haberme puesto en contacto con David y haberme hecho descubrir el EPR.

Un ringraziamento va al Dr. Stefano Pelli per avermi introdotto nel mondo dei vetri e vetroceramiche luminescenti e per avermi messo in contatto con questo

meraviglioso gruppo di ricerca. Grazie Stefano per i mesi passati all' IFAC facendo spettroscopia.

En esta tesis he tenido el placer de trabajar codo a codo con muchas personas. Cada una de ellas me ha dejado algo.

Muchas son las horas que he pasado en compañía del Dr. Jose J. Velázquez. A Jose quiero agradecerle su ayuda con la preparación de los materiales y la discusión de los resultados. Sin él parte de los resultados discutidos en esta tesis no habría sido posible. Además, su carcajada contagiosa y su optimismo han hecho sí que las duras horas de trabajo se convirtiesen en algo más llevadero. Jose, ¡a ver si ganamos el euromillón y nos mudamos a Las Canarias!

Un agradecimiento especial también es para la Prof. Rolindes Balda y el Prof. Joaquín Fernández. A ellos debo la caracterización óptica de los materiales de esta tesis. Sin su trabajo constante esta tesis estaría sin muchos de los resultados más relevantes. Gracias Rolindes y Joaquín por vuestra claridad y por los estudios tan detallados que habéis hecho de cada muestra. Ha sido un placer colaborar con vosotros y espero que podamos seguir haciéndolo en futuro.

La mayoría de los vidrios preparados en esta tesis no habría sido posible sin el apoyo de Juan Vargas y de Aritz Iglesias. Juntos hemos pasado muchas horas, pero tengo solo buenos recuerdos de momentos alegres. Con Juan aprendí a fundir los vidrios y todos los trucos del oficio. Juan, te deseo lo mejor y que disfrutes de tu merecida jubilación.

Con Aritz he tenido una buena relación de amistad. Compartí despacho con él durante mis primeros 8 meses en el ICV antes de empezar la tesis. Aritz fue quien me enseñó a moverme en el laboratorio de sol-gel. Su constante disponibilidad y soporte han sido de gran ayuda para esta tesis. Las noches en el sincrotrón midiendo muestras se han pasado más fácilmente con tu compañía. Aritz, espero que estés disfrutando de Tenerife, pero también espero que algún día puedas volver al ICV, hacen falta personas como tú en los centros de investigación.

Gracias a la Dra. Jadra Mosa por aclarar mis dudas sobre el sol-gel y por sus consejos sobre la preparación de las muestras.

También quiero dar las gracias al Dr. Glenn Mather por su ayuda con los refinamientos Rietveld y con el inglés.

En esta tesis he trabajado con distintos métodos de procesamiento, por la tanto he necesitado la ayuda de los técnicos del departamento. A Aritz Iglesia, Desirée Ruiz, Miguel Gómez, Eva Peiteado y Rosa Navidad quiero agradecerles por la organización del laboratorio, la gestión de los pedidos y sus ayudas que me han dado en estos años.

Con otros miembros del departamento de Vidrios no he trabajado directamente pero quería dar las gracias a todos por formar parte de un ambiente tan agradable y acogedor. Espero que en futuro nos sigamos viendo, sea trabajando en el ICV o en las cenas de Navidad!

I would like to thank Prof. Dominik Dorosz and Prof. Marcin Kochanowicz for the collaboration with the optical fibres. Thanks for giving me the opportunity to spend one month in the Laboratory of Optical Fibre Technology of the Bialystok University of Technology. Thanks for giving me the opportunity to prepare good optical fibres using our materials. I learnt the basics of fibre drawing and I hope to collaborate with you in the future.

A lo largo de esta tesis he podido ir tres veces al ESRF para hacer caracterizar las muestras. El haber descubierto el mundo de los sincrotrones ha sido una experiencia muy positiva y ha despertado mucha curiosidad en mí. Quería agradecer al Dr. Germán R. Castro, a la Dra. Aida Serrano y a la Dra. María Vila por su ayuda con las medidas y análisis de datos. Gracias por su amabilidad y disponibilidad en llevar a cabo de la mejor manera nuestros experimentos.

A Aida quiero agradecerle su constante ayuda con el análisis de datos y por enseñarme a manejar los programas. Gracias también por aclarar mis dudas sobre XAS.

Otro agradecimiento es para el Prof. David Bravo. Gracias a él he entrado en contacto con el EPR y he llevado a cabo estudios muy interesantes de los materiales. Además he podido aprender los aspectos básicos de esta técnica. David, gracias por tu tiempo y por tu claridad. Ha sido muy agradable pasar las tardes contigo haciendo medidas de EPR. Espero que podamos seguir colaborando en futuro.

En estos años pasados en el ICV he tenido la posibilidad de relacionarme y hablar con varios científicos. Quería darle las gracias al Dr. Fausto Rubio por su ayuda con las medidas de FTIR en el infrarrojo lejano. Sobre todo quería darle las gracias a él y a su grupo por regalarme un tubo de alúmina y el hilo Kanthal que he usado para preparar un horno de fibrado. También quería agradecer al Dr. Miguel Ángel Rodríguez por sus charlas científicas y sus consejos para la preparación del horno. Fausto, Miguel Ángel y Chus, gracias por animarme a construirlo.

Muchas veces trabajando en laboratorio se necesita un buen mantenimiento de los equipos. Las personas que hacen este trabajo pasan bastante desapercibidas pero sin ellos muchos de nuestros experimentos no se podrían llevar a cabo. Quería darles las gracias a Alberto, Dani y Victor por su ayuda con las reparaciones de los hornos. Gracias chicos, y también Jose Jiménez, por ayudarme a construir un horno para fibrar. Espero que pueda ser de ayuda para los que se quedan y los que vendrán.

También quería dar las gracias a Carlos Alonso, sin su habilidad e ingenio no habría tenido un molde para preparar las barritas de vidrio que he usado para preparar las fibras.

Las jornadas pasadas en el despacho, sea escribiendo artículos, preparando charlas o analizando datos no habrían sido tan llevaderas y tranquilas sin la buena compañía de las chicas del despacho: Laura, Sandra y Teresa. Gracias a ellas por ser tan amables, tranquilas y por ayudarme con el castellano.

Gracias a la Sociedad Española de Cerámica y Vidrio (SECV) y COST Action para financiar algunos viajes a congresos o estancias. Gracias a la SECV por elegirme como representante de España en el Student Speech Contest del ECerS 2017 de Budapest.

A lo largo de estos años he podido tener muchos momentos de diversión durante el café de la mañana y las comidas. Los momentos compartidos con María, Zoilo, Jose, Joaco, Laura, Ana, Miguel, Ángel, Macarena, Javi, Guille, David, Sandra, Javi, Begoña, Yoli, Jadra, Sara y Eva han servido para despejar la mente y pasar buenos ratos. Gracias a los momentos pasados a diario con ellos he aprendido mucho sobre el castellano y la cultura de España. Gracias a Begoña y Javi por habernos invitado varias veces a su casa, a las cañas en derecho o a copas en el Bienmesabe. Una vez en la Universidad un profesor dijo que las teorías científicas nacen delante de una cerveza….púes, ya deberíamos llevar unas cuantas!

Gracias a Zoilo y Jose por los buenos ratos pasados juntos comiendo o yendo de ruta. La próxima vez que vayamos de ruta nos pondremos los pantalones cortos. Zoilo, Jose, ya nos veremos en Madrid tomando una caña o comiendo una pasta *fatta a mano*. Gracias por vuestra amistad y por enseñarme el castellano callejero.

Por fin, quería dar las gracias a Paloma y Vicente por haberme tratado como un hijo.

Eccoci arrivati alla fine dei ringraziamenti.

Un enorme grazie va a María. Sono più di cinque anni passati insieme, tre vivendo sotto lo stesso tetto. Grazie per essere entrata a far parte della mia vita e per avermi fatto diventare una persona migliore. I viaggi ed i momenti passati con te sono così tanti che non basterebbero ore per descriverli tutti, comunque li conservo nel mio cuore. Grazie per essere una persona così buona. È anche grazie a te ed al tuo appoggio che questa tesi di dottorato sia stata scritta.

Un grazie speciale va ai miei genitori, Marcello e Gigliola. Grazie babbo e mamma per avermi fatto studiare ed aver sempre creduto in me. Dedico a voi questa tesi di

dottorato. Grazie per essermi stati sempre vicino anche se lontani. Immagino che avere un figlio lontano da casa ogni tanto generi nostalgia, però so anche che desiderate il meglio per me. Grazie per appoggiarmi in tutte le mie decisioni. Grazie per mandarmi i pacchetti con la cose buone che mi facevano sentire come a casa.

Grazie a mia sorella Arianna e a mio cognato Sauro per avermi fatto diventare zio della bellissima Camilla.

Espero haber mencionado, si no a todos, al menos a la mayoría!

Ciao!

**CONTENTS**

**ABBREVIATIONS**

| | |
|---|---|
| Melt-Quenching | MQ |
| Sol-Gel | SG |
| Nanocrystal | NC |
| Rare-Earth | RE |
| Tetraethyl Orthosilicate | TEOS |
| Triethoxy Methylsilane | MTES |
| Trifluoroacetic Acid | TFA |
| Differential Thermal Analysis | DTA |
| Thermo-Gravimetric Analysis | TGA |
| Coefficient of Thermal Expansion | CTE |
| X-Ray Diffraction | XRD |
| Grazing-Incidence X-Ray Diffraction | GI-XRD |
| Small Angle X-Ray Scattering | SAXS |
| X-Ray Fluorescence | XRF |
| X-Ray Absorption | XAS |
| X-Ray Absorption Near Edge Structure | XANES |
| Extended X-Ray Absorption Fine Structure | EXAFS |
| Energy-Dispersive X-ray spectroscopy | EDXS |
| Transmission Electron Microscopy | TEM |
| High Resolution Transmission Electron Microscopy | HRTEM |
| Scanning Transmission Electron Microscopy | STEM |
| Selected Area Electron Diffraction | SAED |
| Fourier Transform Infrared Spectroscopy | FTIR |
| Attenuated Total Reflection | ATR |
| Nuclear Magnetic Resonance | NMR |
| Electron Paramagnetic Resonance | EPR |
| Photoluminescence Emission | PL |
| Photoluminescence Excitation | PLE |
| Energy Transfer | ET |
| Up-Conversion | UC |
| Down-Conversion | DC |

**RESUMEN**

Los materiales ópticamente activos basados en vitrocerámicos transparentes dopados con tierras raras (TR) son considerados materiales muy prometedores para aplicaciones fotónicas. La incorporación de las TR en los nanocristales de fluoruro de baja energía fonónica mejora la emisión óptica y los procesos de transferencia de energía entre TR. La combinación de propiedades específicas de los cristales con los métodos de procesamiento del vidrio permite el desarrollo de nuevos materiales, como vitrocerámicos en forma de fibra óptica o película delgada. Sin embargo, la correlación entre el método de procesamiento, la estructura y las propiedades ópticas es un aspecto clave para una mejor comprensión y optimización de estos materiales.

Se han preparado materiales tanto por fusión como por sol-gel y se ha llevado a cabo una comparación con respecto a mecanismo de cristalización, estructura, incorporación de las TR en los nanocristales y propiedades ópticas.

Por fusión se han preparado vitrocerámicos de oxifluoruro transparentes a partir de composiciones de aluminosilicato. A partir del control de la composición del vidrio base se ha conseguido la cristalización nanocristales de $LaF_3$, α y β-$KLaF_4$, y soluciones sólidas de nanocristales de $NaLuF_4$, después del tratamiento térmico a $T_g$ + 20-100 °C. También se han preparado fibras ópticas vitrocerámicas con nanocristales de $LaF_3$ y $NaLuF_4$ mediante el proceso de fusión directa y el método de "varilla en tubo".

Por el método sol-gel se han obtenido, por primera vez, materiales con composiciones (100-x)$SiO_2$-x, con contenidos de hasta un 20% molar de fase activa x. Mediante el control de la síntesis y tras un tratamiento térmico entre 350 y 750 °C se han obtenido nanocristales de $LaF_3$, $GdF_3$ y $KLaF_4$ en una matriz vítrea de $SiO_2$.

El mecanismo de cristalización y la estructura de los materiales en masa, en forma de película delgada y como fibras se han estudiado exhaustivamente, comparando los resultados y estableciendo la diferencia según el método de procesamiento.

La cristalización de los materiales preparados por fusión se basa en un proceso controlado por difusión que puede comenzar o no a partir de zonas de separación de fase en el vidrio. El agotamiento de los elementos formadores de cristales induce un

cambio en la composición de la matriz vítrea, lo que provoca un crecimiento de los cristales auto limitado. El efecto de las TR sobre la cristalización también ha sido estudiado por análisis térmico diferencial y difracción de rayos X. Además, en el caso de cristales polimorfos, niveles específicos de dopaje favorecen la nucleación de ciertas fases.

Por otro lado, la cristalización de los materiales fabricados por sol-gel se produce mediante una reacción química seguida de la precipitación de los nanocristales. Mediante el proceso sol-gel se obtienen todas las fases polimorfas, aunque la fase más estable se convierte en la fase principal para tiempos largos de tratamiento térmico. En comparación con los materiales preparados por fusión, se han observado nanocristales homogéneamente distribuidos en la matriz vítrea después de tratamientos muy cortos.

La incorporación de las TR en los nanocristales de fluoruro se ha estudiado mediante absorción de rayos X y resonancia paramagnética electrónica. Tanto en el vidrio inicial como en el xerogel, se ha observado un entorno rico en flúor alrededor de las TR, lo que ha permitido elucidar el mecanismo de incorporación de las TR en los nanocristales.

También se ha cuantificado tanto la fracción cristalina, utilizando refinamiento Rietveld, como la concentración de TR en los nanocristales del fluoruro, demostrando cómo concentraciones bajas de dopante en todo el material (0,1% molar) producen concentraciones efectivas mucho más altas en los nanocristales. Además, se han observado diferencias relevantes para los materiales preparados por fusión y por sol-gel.

La caracterización óptica de los materiales dopados con TR ha mostrado la mejora de PL en los vitrocerómicos en comparación con los vidrios y xerogeles sin tratar. Los procesos de transferencia de energía más eficientes tienen lugar en los vitrocerámicos. Se han reproducido características ópticas similares a las de los monocristales tanto en los materiales masivos como en fibra preparados por sol-gel y por fusión respectivamente.

Se han obtenido por primera vez, espectros de fotoluminescencia en fibras ópticas vitrocerámicas similares a los de los monocristales de $LaF_3:Nd^{3+}$.

Sin embargo, para materiales obtenidos por sol-gel, se han observado diferencias notables en las medidas de fotoluminiscencia de materiales en masa y película delga y correlacionandose con las diferencias en la estructura.

**ABSTRACT**

Active optical materials based on transparent glass-ceramics doped with rare-earth (RE) ions are considered promising materials for photonic applications. The incorporation of RE ions in low phonon energy fluoride nanocrystals (NCs) enhances the optical emission along with the energy transfer processes between RE ions. The combination of specific crystal properties and glass processing methods allows novel materials to be developed, such as glass-ceramic optical fibres and thin films. However, the correlation between processing method, structure and optical properties is an essential step for a better understanding and optimisation of performance.

Materials have been prepared by melt quenching (MQ) and sol gel (SG), providing a comparison with respect to crystallisation mechanism, structure, dopant incorporation in the NCs and optical properties.

Transparent oxyfluoride glass-ceramics based on aluminosilicate compositions have been prepared by MQ. The crystallisation of $LaF_3$, α and β-$KLaF_4$, and a solid solution of $NaLuF_4$ NCs after heat treatment at $T_g$ +20-100 °C has been achieved by controlling the base glass composition. Glass-ceramic optical fibres with $LaF_3$ and $NaLuF_4$ NCs have also been prepared using direct melting process and the rod-in-tube method.

Sol-gel materials of compositions (100-x)$SiO_2$-x, with up to 20 mol % of active phase x, have been obtained for the first time. $LaF_3$, $GdF_3$ and $KLaF_4$ NCs have been precipitated by controlling the synthesis process and after heat treatment at 350-750 °C.

The crystallisation mechanism and structure of bulk materials, films and fibres have been extensively studied, comparing and establishing the differences according to the processing method.

The crystallisation of MQ materials is based on a diffusion-controlled process that may or may not start from initial phase-separation regions. The depletion of crystal formers induces a compositional change in the glass matrix causing a self-limited crystal growth. The effect of RE dopants on the crystallisation has also been studied by

DTA and XRD. Moreover, specific doping levels favour the nucleation of certain phases in polymorphous crystals.

In contrast, the crystallisation of sol-gel materials occurs *via* chemical reactions followed by crystal precipitation. In the case that all polymorphous phases are obtained, the principal phase is the most stable after long thermal treatments. NCs homogeneously distributed in the $SiO_2$ glass matrix are observed after fast heat treatment, compared to MQ materials.

The incorporation of RE dopants in the fluoride NCs has been studied using X-ray Absorption Spectroscopy (XAS) and Electron Paramagnetic Resonance Spectroscopy (EPR). The mechanism of RE incorporation in the NCs was elucidated from evidence of a fluorine-rich environment for RE ions in the initial glass and xerogel.

The quantification of crystal fraction, using Rietveld refinement, and RE-ion incorporation in the fluoride NCs have also been determined, demonstrating how low doping levels (0.1 mol%) produce much higher effective concentrations in the NCs. Relevant differences in the crystallised fraction have been observed for MQ and SG materials.

The optical characterisation of RE-doped materials showed the photoluminescence (PL) enhancement in the glass-ceramics compared to the untreated glass and xerogel samples. Stronger energy-transfer processes take place in the glass-ceramic. Crystal-like optical features have been reproduced in bulk and fibre materials prepared by SG and MQ, respectively.

PL spectra of $LaF_3:Nd^{3+}$ single crystals in glass-ceramic optical fibres have been obtained for the first time.

However, for SG materials, notable differences in the PL of bulk samples and thin films have been observed and correlated to the structure.

# *1. INTRODUCCIÓN GENERAL*

# 1. INTRODUCCIÓN GENERAL

## 1.1. Justificación de la temática

El vidrio es uno de los materiales más versátiles y sus aplicaciones van desde productos tradicionales hasta los dispositivos ópticos más avanzados. En el campo de la fotónica, considerada una tecnología clave para el siglo 21, los vidrios juegan un papel muy importante debido a su transparencia en una amplia gama del espectro electromagnético y por la variedad de métodos de procesamiento que permite preparar materiales para láser, recubrimientos nanométricos transparentes o fibras ópticas. Por otra parte, la transformación del vidrio en un material vitrocerámico a través de un proceso de cristalización controlada permite la mejora de muchas de las propiedades finales.

Los materiales ópticos activos basados en vitrocerámicos transparentes dopados con iones de TR han despertado un gran interés durante los últimos 20 años. La posibilidad de desarrollar ciertas fases nanocristalinas dopadas con TR embebidas en una matriz vítrea altamente estable ha demostrado el aumento de la emisión luminiscente y la posibilidad de obtener procesos ópticos nuevos o mejorados con respecto a los vidrios de partida. Además, la transparencia se puede mantener en el vitrocerámico mediante, entre otros, el control del tamaño de los nanocristales.

La preparación de vidrios de vitrocerámicos de oxifluoruro los cuales contienen nanocristales de fluoruro, conocidos por ser excelentes huéspedes de TR, ha sido el objeto de numerosos trabajos que se vienen desarrollando desde principios de los años 90 [1]. Las ventajas de estos materiales, con respecto a los vidrios y cristales de fluoruro, están relacionadas con la mayor estabilidad química y mecánica de los vidrios de óxidos y la posibilidad de cristalizar fases de fluoruro que no pueden ser preparadas de otro modo y/o conservadas a temperatura ambiente. Estos materiales han demostrado muy buenas propiedades fotónicas. La incorporación de las TR en los NCs de fluoruro da lugar a intensos fenómenos luminiscentes y procesos ópticos no lineales similares a los que se obtienen para mono-cristales de fluoruro. Además, los mismos métodos de procesamiento del vidrio pueden también ser aplicados a los

vitrocerámicos, permitiendo la preparación de nuevos dispositivos como fibras ópticas con núcleo vitrocerámico y películas delgadas.

El método de fusión es el proceso utilizado para producir vidrios y vitrocerámicos ópticos comerciales y es el método más utilizado para preparar vitrocerámicos de oxifluoruros. Sin embargo, este método presenta algunas limitaciones, por ejemplo, la dificultad de obtener materiales muy homogéneos a lo largo de la muestra, o la importante pérdida de flúor asociada a las altas temperaturas empleadas durante la fusión.

Por estas razones, el procesamiento sol-gel ha ganado cada vez más importancia para la preparación de materiales ópticos, especialmente en forma de película delgada para sistemas integrados o para aplicaciones en guía de onda. Este proceso químico permite obtener materiales mediante reacciones de hidrólisis y policondensación de precursores moleculares (típicamente a partir de alcóxidos metálicos). Se utilizan reactivos químicos muy puros y bajas temperaturas de sinterización, lo que permite obtener muestras más homogéneas y composiciones de oxifluoruro imposibles de preparar por el método de fusión.

La síntesis de vitrocerámicos de oxifluoruro utilizando el método sol-gel se remonta a finales de la década de los 90 [2–4], pero poca innovación, con respecto a síntesis y procesamiento, ha sido aportada durante los últimos 30 años. Las ventajas del método sol-gel no han sido plenamente explotadas y la mayoría de las publicaciones reportadas hasta la fecha se basan en síntesis muy parecidas. Por otra parte, el estudio de la relación entre procesamiento, estructura y propiedades ópticas es esencial para establecer el mejor método de procesamiento para una aplicación concreta. Dicho estudio se realiza en raras ocasiones y en la mayoría de los casos los trabajos de investigación se centran únicamente en la caracterización óptica. Además, un conocimiento profundo de la relación entre estructura y propiedades ópticas de los materiales preparados por diferentes rutas de procesamiento es fundamental para una mejor comprensión y optimización de los mismos.

## 1.2. Objetivos y aportación original

El objetivo principal de esta tesis es estudiar la relación entre el procesamiento, estructura y propiedades ópticas de vidrios y vitrocéramicos preparados utilizando los métodos de fusión y sol-gel para su uso en dispositivos ópticos.

Los objetivos específicos se resumen en tres puntos:

1. Preparación y caracterización de materiales vitrocerámicos dopados con TR, tanto en masa como en fibra, usando el método de fusión.

2. Preparación y caracterización de películas delgadas y materiales en masa dopados con TR, usando el método sol-gel.

3. Establecer la relación entre el procesamiento, la estructura atómica y las propiedades ópticas.

La elucidación del mecanismo de cristalización de los materiales vitrocerámicos desarrollados es clave para comprender las propiedades ópticas finales y se ha realizado en detalle en esta tesis. Otras cuestiones interesantes están relacionadas con la cuantificación de la fracción cristalizada dependiendo del método de procesamiento, y el estudio del mecanismo de incorporación de las TR en los nanocristales de fluoruro. El cambio del entorno cristalino alrededor de las TR es fundamental para la interpretación de las propiedades ópticas. Todos estos estudios se han abordado utilizando numerosas técnicas experimentales.

Como punto de partida para la preparación de vitrocerámicos dopados con varias TR y para obtener procesos ópticos tanto lineales como no lineales, se han empleado dos composiciones de vidrio, previamente estudiadas en otra tesis [5]. Una novedad notable es la preparación, por primera vez, de fibras ópticas con núcleo vitrocerámico conteniendo cristales de $LaF_3$ o $NaLuF_4$ y dopadas con $Nd^{3+}$ o $Er^{3+}$-$Yb^{3+}$. Se ha llevado a cabo un detallado estudio estructural y óptico, demostrando cómo ciertas propiedades se ven afectadas durante el proceso de fibrado. Aún más interesante son las propiedades ópticas de cristales de $LaF_3$ dopados con $Nd^{3+}$ que replican tanto en los

materiales en masa como en fibra. Se ha estudiado el efecto de los iones $Nd^{3+}$ sobre la cristalización de $LaF_3$ y $KLaF_4$, poniéndose de manifiesto cómo el nivel de dopaje puede alterar la fracción cristalina y/o las fases. La incorporación de dopantes en los nanocristales se ha estudiado por resonancia paramagnética electrónica, observándose cómo la difusión de TR en los nanocristales se ve afectada según el tipo de precursor. La combinación de varias técnicas experimentales ha permitido obtener una imagen clara del proceso de cristalización e incorporación de las TR, junto con una mejor comprensión de cómo ambos parámetros afectan a las propiedades ópticas.

Las principales novedades introducidas en esta tesis en relación al procesamiento sol-gel son la preparación de vitrocerámicos con un contenido de fase activa, $LaF_3$ y $GdF_3$, al menos doble con respeto a lo descrito hasta ahora en la literatura. La adición de un nuevo precursor al proceso de síntesis es también una gran novedad en este campo, que ha demostrado su eficacia para aumentar el espesor de las películas delgadas y la resistencia mecánica de las muestras masivas. La cristalización de $LaF_3$ en los materiales sol-gel ha sido descrita en detalle y en los materiales en masa se han medido espectros de emisión de cristales de $LaF_3$ dopados con $Nd^{3+}$. También se obtuvieron espectros de tipo cristalinos usando otros dopantes, lo que demuestra que la ruta sol-gel es una alternativa prometedora para la preparación de materiales ópticos novedosos. Varias técnicas estructurales, tales como la resonancia paramagnética electrónica, resonancia magnética nuclear y espectroscopía de absorción de rayos X, han aportado una información clara sobre el mecanismo de cristalización e incorporación de los dopantes. Estas técnicas no habían sido utilizadas antes para la caracterización de vitrocerámicos de oxifluoruros preparados por sol-gel. Comparando las propiedades estructurales y ópticas de películas delgadas y materiales en masa se ha observado que, para una misma fase cristalina, se obtienen diferentes tamaños de cristal y propiedades ópticas, lo que demuestra de nuevo el papel clave desempeñado por el método de procesamiento.

### 1.3. Trabajos compendiados

Los principales resultados obtenidos en esta tesis han sido descritos en 9 artículos científicos publicados en revistas científicas internacionales de alto prestigio. Sin embargo, este manuscrito se centra en 11 artículos científicos (9 de ellos publicados y 2 en preparación). Las publicaciones descritas en esta tesis se enumeran a continuación:

1. **Transparent glass-ceramics produced by sol-gel: a suitable alternative for photonic materials**

   G. Gorni, J.J. Velázquez, J. Mosa, R. Balda, J. Fernández, A. Durán, Y. Castro

   *Materials* 11, (2018) 212. doi:10.3390/ma11020204

2. **Transparent oxyfluoride nano-glass ceramics doped with $Pr^{3+}$ and $Pr^{3+}$-$Yb^{3+}$ for NIR emission.**

   G. Gorni, A. Cosci, S. Pelli, L. Pascual, A. Durán, M.J. Pascual.

   *Front. Mater*. (2017) 3:58. doi: 10.3389/fmats.2016.00058.

   Publicado en: W. Höland, J. Deubener, eds. (2017). Nucleation and Crystallization of Glasses and Glass-Ceramics. Lausanne: Frontiers Media. doi: 10.3389/978-2-88945-224-8

3. **Selective excitation in transparent oxyfluoride glass-ceramics doped with $Nd^{3+}$.**

   G. Gorni, J.J. Velázquez, G.C. Mather, A. Durán, G. Chen, M. Sundararajan, R. Balda, J. Fernández, M.J. Pascual.

   *J. Eur. Ceram. Soc.* 37 (2017) 1695-1706. *doi:10.1016/j.jeurceramsoc.2016.11.014*

4. **Effect of the heat treatment on the spectroscopic properties of $Er^{3+}$-$Yb^{3+}$-doped transparent oxyfluoride nano-glass-ceramics.**

   G. Gorni, R. Balda, J. Fernández, L. Pascual, A. Durán, M.J. Pascual.

   *J. Lumin*. 193 (2018) 51-60. doi:10.1016/j.jlumin.2017.05.063

5. **Effect of dopant precursors on the optical properties of rare-earths doped oxyfluoride glass-ceramics.**

   G. Gorni, A. Serrano, G.R. Castro, D. Bravo, R. Balda, J. Fernández, A. Durán, M.J. Pascual. *Borrador*

6. **Phase evolution of $KLaF_4$ nanocrystals and their effects on the photoluminescence of $Nd^{3+}$ doped transparent oxyfluoride glass-ceramics.**

   A. Cabral, R. Balda, J. Fernández, G. Gorni, J.J. Velázquez, L. Pascual, A. Durán, M.J. Pascual.

   *CrystEngComm.* 20 (2018) 5760–5771. doi:10.1039/C8CE00897C

7. **Oxyfluoride glass-ceramic fibers doped with $Nd^{3+}$: structural and optical characterization.**

   G. Gorni, R. Balda, J. Fernández, I. Iparraguirre, J.J. Velázquez, Y. Castro, L. Pascual, G. Chen, M. Sundararajan, M.J. Pascual, A. Durán.

   *CrystEngComm*. 19 (2017) 6620-6629. doi: 10.1039/C7CE01380A

8. **Crystallization mechanism in sol-gel oxyfluoride glass-ceramics.**

   G. Gorni, M.J. Pascual, A. Caballero, J.J. Velázquez, J. Mosa, Y. Castro, A. Durán.

   *J. Non-Cryst. Solids* 501 (2018) 145-152. doi:10.1016/j.jnoncrysol.2018.01.031

9. **$80SiO_2$-$20LaF_3$ oxyfluoride glass ceramic coatings doped with $Nd^{3+}$ for optical applications.**

   G. Gorni, R. Balda, J. Fernández, J.J. Velázquez, L. Pascual, J. Mosa, A. Durán, Y. Castro

   *Int. J. Appl. Glass Sci*. 9 (2018) 208-217. doi:10.1111/ijag.12338

10. **Transparent sol-gel oxyfluoride glass-ceramics with high crystalline fraction and study of RE incorporation.**

    G. Gorni, J.J. Velázquez, J. Mosa, G.C. Mather, M. Vila, A. Serrano, G R. Castro, D Bravo, R Balda, Fernández, A Durán, Y Castro. *Borrador.*

11. **Transparent $SiO_2$-$GdF_3$ sol-gel nano-glass ceramics for optical applications.**
J.J. Velázquez, J. Mosa, G. Gorni, R. Balda, J. Fernández, L. Pascual, A. Durán, Y. Castro.
*J. Sol-Gel Sci. Techn*ol. 89 (2019) 322-332. doi: 10.1007/s10971-018-4693-z

### 1.4. Estructura de la tesis

La tesis se divide en cinco partes. En la primera parte se ofrece una introducción general sobre los materiales sólidos dopados con TR para aplicaciones ópticas y fotónicas, indicando las diferencias más relevantes entre los materiales cristalinos y no cristalinos. Se ha prestado especial atención a los métodos de procesamiento de los vidrios y los vitrocerámicos, en particular a las composiciones de oxifluoruro transparentes preparadas por fusión y SG. Se describen brevemente los conceptos básicos de nucleación y cristalización junto con la explicación del fenómeno físico subyacente a la transparencia en los vitrocerámicos. También se presenta una revisión sobre las fibras vitrocerámicos de oxifluoruro junto con una revisión extendida sobre los vitrocerámicos de oxifluoruro preparados por SG. Esta primera parte termina con la explicación de las propiedades espectrales de las TR en sólidos, en el marco de la mecánica cuántica, junto con una descripción de los principales mecanismos de transferencia de energía.

La segunda sección describe los métodos experimentales utilizados en esta tesis: desde la preparación de los materiales hasta las caracterizaciones térmicas, estructurales y ópticas. Se proporciona una descripción resumida, pero con todos los detalles más importantes, para cada técnica experimental. De hecho, es difícil obtener una interpretación correcta y profunda de los resultados sin el conocimiento de los principios físicos básicos de cada técnica, especialmente cuando se comparan medidas obtenidas a partir de diferentes técnicas.

La tercera parte resume los principales resultados obtenidos en esta tesis que no se presentan necesariamente en orden cronológico de publicación.

Las conclusiones generales se describen en la cuarta parte y están escritas tanto en inglés como en español.

En la última parte, las publicaciones utilizadas para esta tesis se adjuntan siguiendo el orden secuencial utilizado en la parte de discusión.

# *2. GENERAL INTRODUCTION*

# 2. GENERAL INTRODUCTION

## 2.1. Motivation

Glass is one of the most versatile materials and its uses range from traditional glassware products to advanced optical materials. In the field of Photonics, considered a key-technology of the 21st century, glasses play a very crucial role for their transparency in a wide range of the electromagnetic spectrum and for the availability of processing methods that allows glass products to be shaped as bulk laser materials, transparent nanometric coatings or optical fibres. An improvement of certain glass properties is offered by the transformation of glass into glass-ceramics as a consequence of a controlled crystallisation process.

Active optical materials based on transparent glass-ceramics doped with RE ions have gained increasing interest during the last 20 years. The possibility to develop certain RE-doped NCs embedded in a highly stable glass matrix showed a great enhancement of the luminescence emission and the possibility to obtain new or improved optical processes with respect to glasses. Moreover, by controlling the NCs size, the transparency of an optical glass can be maintained.

A particular attention has been devoted to the preparation of oxide glasses containing fluoride NCs, known as excellent RE hosts. Such materials are known as oxyfluoride glass-ceramics and were developed since the 1990s [1]. The benefits of these materials, with respect to fluoride glasses and crystals, are associated with the higher chemical and mechanical stability of oxide glasses and the possibility to crystallise fluoride phases that cannot be otherwise prepared and/or preserved at room temperature. These materials have shown very good photonic properties. The incorporation of RE ions into fluoride NCs originates strong luminescence and nonlinear optical processes similar to those obtained for pure fluoride mono-crystals. Moreover, the same glass processing methods can also be applied to glass-ceramics, which permit the preparation of novel devices such as glass-ceramic optical fibres and thin films.

The classical MQ method is the process used to produce commercial optical glasses and glass-ceramics and it is still the most widely used method to prepare oxyfluoride glass-ceramics. However, this method has shown some limitations, for example the difficulty to obtain homogeneous materials with very small inhomogeneity throughout the sample, or the high temperatures involved during the melting of oxyfluoride compositions that cause relevant fluorine losses.

For these reasons, the SG process has acquired increasing importance for the preparation of optical glass materials, especially as thin films for integrated systems or waveguide applications. This chemical process is based on hydrolysis and polycondensation reactions of molecular precursors (typically a metal alkoxide). It uses very pure chemical reagents and low sintering temperatures, thus providing more homogeneous samples and oxyfluoride compositions impossible to be prepared through the melting process.

The preparation of oxyfluoride glass-ceramics using the SG process dates back to the end of the 90s [2–4] but poor innovation with respect to synthesis and processing has been provided during the last thirty years. The advantages of the SG process have not been fully exploited and most publications reported until now are based on very similar synthesis. Moreover, the knowledge of the relationship between processing, structure and optical properties is essential for the assessment of the best processing method for a specific application. Such a study is rarely done and in most cases, research papers are only focused on the optical characterisation. Hence a detailed study of the structure and optical properties of materials prepared by different processing routes is necessary to understand and optimise these materials.

### 2.2. Objectives and original contribution

The study of the effects of the processing method on the structural and optical properties is essential to optimise the processing and properties of novel optical materials. Therefore, the goal of this thesis is to study the relationship between *processing-structure-optical properties* of oxyfluoride glasses and glass-ceramics prepared using MQ and SG methods.

The main objectives of this thesis are summarised in three points:

1. Preparation and characterisation of RE-doped glass-ceramics in bulk and fibre form by MQ method.

2. Preparation and characterisation of RE-doped glass-ceramic thin films and bulk materials by SG method.

3. To establish the relationship between processing, atomic structure and optical properties.

The elucidation of the crystallisation mechanism for the glass-ceramic materials is a key-feature to understand the final optical properties and it is a crucial point faced in this thesis. Other interesting issues are related to quantify the obtained crystal fraction according to the processing method, and to study the mechanism of RE ions incorporation in the active fluoride NCs. The change of the environment around the RE ions after the crystallisation process is essential for the interpretation of the optical properties. Many efforts have been dedicated to this study using several experimental techniques.

Two glass compositions, previously studied in another thesis [5], have been used as starting point for the preparation of glass-ceramics doped with several RE ions to obtain linear and nonlinear optical processes. A remarkable novelty is the preparation, for the first time, of $LaF_3$ and $NaLuF_4$-glass-ceramic fibres doped with $Nd^{3+}$ and $Er^{3+}$-$Yb^{3+}$, respectively. A detailed structural and optical study was carried out demonstrating how certain properties are affected during the fibre drawing process. Even more interesting is that the optical properties of $LaF_3$:$Nd^{3+}$ bulk glass-ceramics are replicated in fibre form. The effect of $Nd^{3+}$ ions on the crystallisation of $LaF_3$ and $KLaF_4$ glass-ceramics has been described showing how the doping level can alter the crystal fraction and/or its phase. The incorporation of dopants, using different precursors, was studied by electron paramagnetic resonance, showing how the RE ions diffusion in the fluoride NCs changes. The combination of several experimental techniques has permitted a clear picture of the crystallisation process and RE dopants incorporation to

be obtained, together with a better understanding of how both parameters affect the optical properties.

The major novelties introduced in SG processing are the preparation of $LaF_3$ and $GdF_3$ glass-ceramics with an active phase content at least double than that reported so far. The addition of a new precursor to the synthesis process is also a great novelty in this field, demonstrating its effectiveness for increasing the thickness of films and the mechanical resistance of bulk samples. The crystallisation of $LaF_3$ in SG materials was also described in detail and $LaF_3:Nd^{3+}$ crystal spectra have also been measured for SG bulk glass-ceramics. Crystal-like optical features were also obtained using other dopants, demonstrating that the SG route offers a promising alternative for the preparation of novel optical materials. Several structural techniques such as EPR, NMR and XAS, have also given in this case a better and clearer picture about crystallisation mechanism and dopants incorporation. Such techniques have never been used for characterisation of SG oxyfluoride glass-ceramics. The comparison of structural and optical properties of thin films and bulk materials demonstrated that, for the same crystal phase, different crystal size and optical properties are obtained.

Thanks to the aforementioned results, a comparison between MQ and SG route has been made, demonstrating the key role played by the processing method. Summarizing, this thesis revealed how the crystallisation mechanism and RE ions incorporation are strongly affected by the selected route. The optical properties depend on composition, distribution of RE ions and processing method.

### 2.3. List of publications

The main results obtained in this thesis have been described in 9 scientific articles published in notorious international scientific journals. However, this manuscript is focused on 11 publications (9 already published and 2 in preparation). The publications discussed in this thesis are listed below:

1. **Transparent glass ceramics produced by sol-gel: a suitable alternative for photonic materials**

   G. Gorni, J.J. Velázquez, J. Mosa, R. Balda, J. Fernández, A. Durán, Y. Castro

*Materials* 11, (2018) 212. doi:10.3390/ma11020204

2. **Transparent oxyfluoride nano-glass ceramics doped with $Pr^{3+}$ and $Pr^{3+}$-$Yb^{3+}$ for NIR emission.**

   G. Gorni, A. Cosci, S. Pelli, L. Pascual, A. Durán, M.J. Pascual.

   *Front. Mater*. (2017) 3:58. doi: 10.3389/fmats.2016.00058 Published in: W. Höland, J. Deubener, eds. (2017). Nucleation and Crystallization of Glasses and Glass-Ceramics. Lausanne: Frontiers Media. doi: 10.3389/978-2-88945-224-8

3. **Selective excitation in transparent oxyfluoride glass-ceramics doped with $Nd^{3+}$.**

   G. Gorni, J.J. Velázquez, G.C. Mather, A. Durán, G. Chen, M. Sundararajan, R. Balda, J. Fernández, M.J. Pascual.

   *J. Eur. Ceram. Soc.* 37 (2017) 1695-1706. *doi:10.1016/j.jeurceramsoc.2016.11.014*

4. **Effect of the heat treatment on the spectroscopic properties of $Er^{3+}$-$Yb^{3+}$-doped transparent oxyfluoride nano-glass-ceramics.**

   G. Gorni, R. Balda, J. Fernández, L. Pascual, A. Durán, M.J. Pascual.

   *J. Lumin*. 193 (2018) 51-60. doi:10.1016/j.jlumin.2017.05.063

5. **Effect of dopant precursors on the optical properties of rare-earths doped oxyfluoride glass-ceramics.**

   G. Gorni, A. Serrano, G.R. Castro, D. Bravo, R. Balda, J. Fernández, A. Durán, M.J. Pascual. *Draft*

6. **Phase evolution of $KLaF_4$ nanocrystals and their effects on the photoluminescence of $Nd^{3+}$ doped transparent oxyfluoride glass-ceramics.**

   A. Cabral, R. Balda, J. Fernández, G. Gorni, J.J. Velázquez, L. Pascual, A. Durán, M.J. Pascual.

   *CrystEngComm.* 20 (2018) 5760–5771. doi:10.1039/C8CE00897C

7. **Oxyfluoride glass-ceramic fibers doped with $Nd^{3+}$: structural and optical characterization.**
   G. Gorni, R. Balda, J. Fernández, I. Iparraguirre, J.J. Velázquez, Y. Castro, L. Pascual, G. Chen, M. Sundararajan,, M.J. Pascual, A. Durán.
   *CrystEngComm*. 19 (2017) 6620-6629. doi: 10.1039/C7CE01380A

8. **Crystallization mechanism in sol-gel oxyfluoride glass-ceramics.**
   G. Gorni, M.J. Pascual, A. Caballero, J.J. Velázquez, J. Mosa, Y. Castro, A. Durán.
   *J. Non-Cryst. Solids* 501 (2018) 145-152. doi:10.1016/j.jnoncrysol.2018.01.031

9. **$80SiO_2$-$20LaF_3$ oxyfluoride glass ceramic coatings doped with $Nd^{3+}$ for optical applications.**
   G. Gorni, R. Balda, J. Fernández, J.J. Velázquez, L. Pascual, J. Mosa, A. Durán, Y. Castro
   *Int. J. Appl. Glass Sci*. 9 (2018) 208-217. doi:10.1111/ijag.12338

10. **Transparent sol-gel oxyfluoride glass-ceramics with high crystalline fraction and study of RE incorporation.**
    G. Gorni, J.J. Velázquez, J. Mosa, G.C. Mather, M. Vila, A. Serrano, G R. Castro, D Bravo, R Balda, Fernández, A Durán, Y Castro. *Draft*

11. **Transparent $SiO_2$-$GdF_3$ sol-gel nano-glass ceramics for optical applications.**
    J.J. Velázquez, J. Mosa, G. Gorni, R. Balda, J. Fernández, L. Pascual, A. Durán, Y. Castro.
    *J. Sol-Gel Sci. Techn*ol. 89 (2019) 322-332. doi: 10.1007/s10971-018-4693-z

### 2.4. Structure of the thesis

The thesis is divided into five parts. In the first part, a general introduction about RE-doped solid materials for optics and photonics is given, indicating the most relevant differences between crystalline and non-crystalline materials. Special attention has been paid to the glasses and glass-ceramics processing methods, in particular to transparent oxyfluoride compositions prepared by MQ and SG. The basic concepts of nucleation and crystallisation are briefly described along with the explanation of the

physical phenomenon underlying the transparency in glass-ceramics. A review about oxyfluoride glass-ceramic fibres is also presented together with an extended review about SG oxyfluoride glass-ceramics. This first part ends with the explanation of the spectral properties of RE ions in solids, in the framework of quantum mechanics, along with a description of the main energy transfer mechanisms.

The second section describes the experimental methods used in this thesis: including materials preparation, thermal, structural and optical characterisations. A brief description, but with all the most important details, is given for each experimental technique. In fact, it is hard to obtain a correct and deep interpretation of the results without the knowledge of the basics physical principles of each technique, especially when measurements of different techniques are compared.

The third part summarises the main results obtained in this thesis that are not necessarily presented according to the chronological order of the corresponding publications.

The general conclusions are described in the fourth part and are also written in Spanish.

In the last part, the publications used for this thesis are attached following the order of citation in the text

### 2.5. Optics and photonics: the key role of materials processing

Optics and photonics are fundamental technologies in modern life that provide us advanced devices as lasers, optical fibres, displays on our smartphones, medical diagnostics tools etc. [6]. Optics and photonic technologies have strongly increased across the globe over the past several years to such an extent that UNESCO declared 2015 the International Year of Light and Light-based technology [7].

Photonic technologies have brought a great boost towards innovation in several fields of science. Since 1960, 30% of Nobel Prize laureates have been photonics-related or strongly benefited from photonic technologies [8]. In 2014, Nature Photonics published an Editorial entitled "*Photonics dominates Nobel Prizes*" [9] describing the

awards for blue LEDs and super-resolution microscopy, thus highlighting the central role of this technology in the modern science.

Two inventions deserve a special mention in the field of optics and photonics: the laser and the optical fibres. The huge revolution brought by these two inventions, along with their potentiality and application in many fields, stimulated scientists all over the world to study and prepare new optical materials with higher efficiencies and/or new functionalities. A broad classification of optical materials is as passive and active components [10]. Passive components are generally used to split and combine signals, or alter them in various other ways. On the other side, optical active components, including optical sending and receiving modules, amplifiers, lasers etc., have received greater attention during the last decades.

In most cases, a central role is occupied by phosphor materials, i.e active materials that emit light under exposure to external stimulation, such as an electron beam, light at different wavelengths, electric field, etc. When a material emits light under optical excitation the term photoluminescence is used. Phosphor materials, also called *luminescent materials*, are widely applied and studied for laser applications, sensing, integration in photovoltaic devices, and more recently in biosensing, bioimaging or medical diagnosis [11–17]. The optical properties of these materials can drastically change depending on the processing parameters, and the correlation between the microstructure and the final optical properties has gained increasing attention. Such correlation allows a control at the micro/nano-scale, improving the luminescence emission and obtaining new or more intense physical phenomena.

In most optical active devices, a central role is occupied by RE ions that are globally recognised essential elements for technological applications especially in the field of luminescent materials. IUPAC defines the rare-earth elements (REEs) as a group of 17 chemically similar metallic elements including the 15 lanthanides, scandium and yttrium [18]. However, in the literature, the word REEs or RE is commonly used to indicate only the lanthanides, and this convention will be adopted in this thesis. The lanthanides are the elements with atomic number between 57 (lanthanum, La) and 71 (lutetium, Lu). The lanthanides all occur in nature, although

promethium, the rarest, only occurs in trace quantities in natural materials as it has no long-lived or stable isotopes [19]. The lanthanides form the largest chemically coherent group in the periodic table [20]. When these elements are in liquid or solid compounds their most stable oxidation state is 3+, consisting of partially filled inner 4f levels (with the exception of $La^{3+}$ that does not have any electron in f orbitals) screened by outer 5s and 5p orbitals and a majority of applications involve electronic transitions between states within a 4f configuration. A characteristic property of the 4f electrons is that they have localized states and exhibit weak (but observable) coupling to ligand electrons and lattice vibrations [21]. This allows the RE ions emission energies centred near the same values even in different hosts to be maintained, making them suitable for applications where certain wavelengths are required. However, even though there is a small interaction between 4f electrons and the surrounding medium, the luminescence of RE ions is sensitive to different surrounding media and it can be improved for example when the thermal vibrations (phonons) of the host are reduced, hence, it is suddenly understood the crucial role of the host material. Moreover, a suitable combination of RE ions and host material can provide nonlinear optical phenomena and convert the incident light in radiation with higher or lower frequency. The use of RE ions in telecom, lasers, lightening, etc. makes them indispensable nowadays. Some typical emission wavelengths are shown in Figure 2.1.

The optical properties of new or already existing materials can be improved, for example, by including NCs doped with RE ions in a certain host material. This kind of nanomaterials holds promise for bio-applications and photonic devices because they combine the unmatched advantages of RE ions properties with those arising from large surface-to-volume ratios and quantum confinement that are typical of nanomaterials [22]. Many studies consider nanoparticles doped with RE ions suspended in liquid phase or with phosphor powders. However, for many applications such as lasers, waveguides and optical fibres, lightening devices, etc., transparent solids and materials easy-to-handle are required.

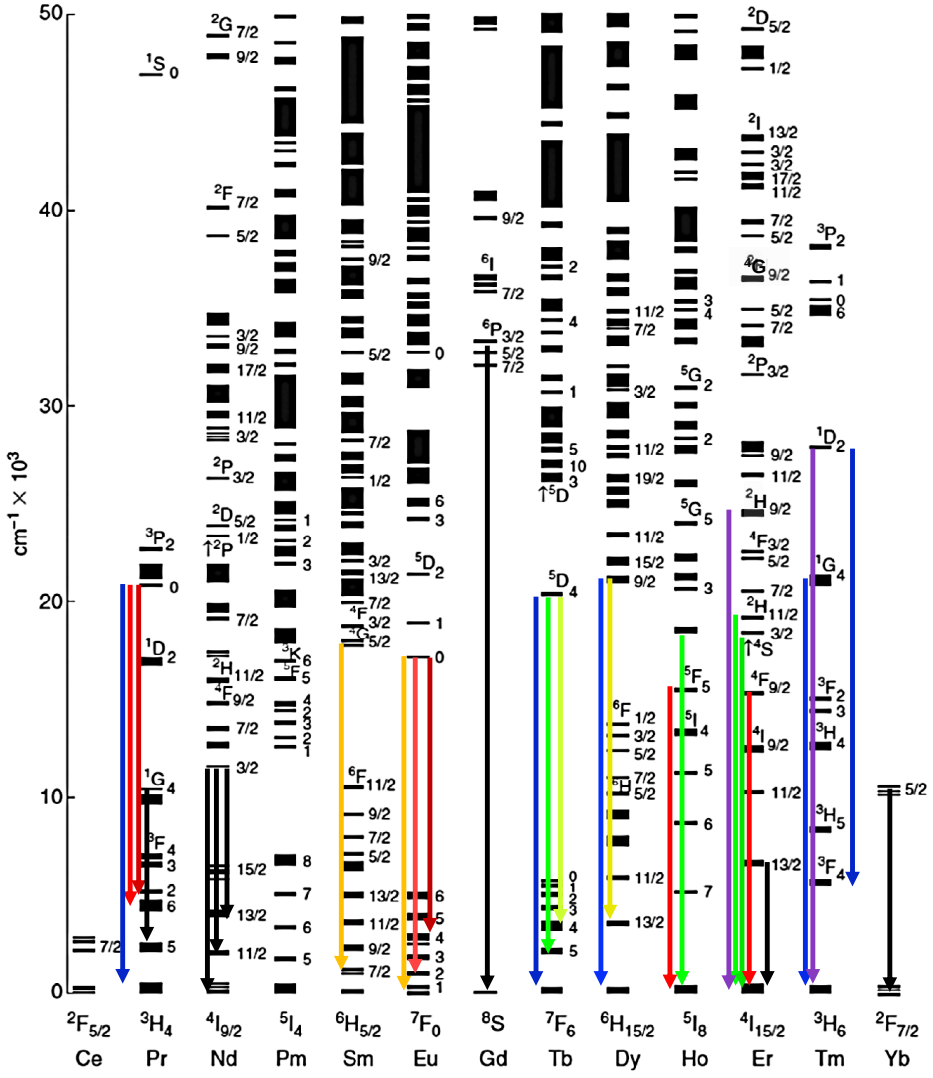


***Figure 2.1.*** *Energy levels of lanthanides, from $Ce^{3+}$ to $Yb^{3+}$, and some of the most interesting transitions for technological applications. The colour of the arrows indicates roughly the spectral region of the emission. UV and IR emission are in black. Adapted from [23].*

Different preparation methods such as single crystal growth, glass melting and ceramics processing have been employed for the production of RE-doped active solid materials. The predominance of certain materials with respect to others relies in the appropriate combination of properties and, synthesis and processing methods.

Single crystals have demonstrated better optical properties with respect to non-crystalline materials, for example the famous $Nd^{3+}$:YAG is maybe one of the most important lasers in the market [24]. RE-doped laser crystals often exhibit sharply defined lasing and pumping transitions because the RE ions occupy only one or few crystallographic sites. In addition, phonon frequencies of some crystal phases are much

lower than for other materials and this produces a notable increase in the luminescence efficiency. However, single crystals are quite expensive to be produced and time consuming. They need to be grown with a high optical quality and specific chemical composition for substituting host ions with active RE ions [25]. Moreover, only bulk samples are commonly produced, strongly reducing their applications to few devices, for example as bulk laser materials. The synthesis of polycrystalline materials has shown some advantages, such as the possibility of obtaining materials with good optical properties, similar to those of crystalline phases, using simpler processing routes. For example, $Y_2O_3$, considered as a promising host material for RE ions, can be obtained by a simple sintering process while this compound is hardly obtained by single crystal growth due to its high melting point, higher than 2400 °C [25]. In addition, polycrystalline materials have better thermo-mechanical properties than single crystals and the research of novel transparent ceramics has acquired the attention of many materials scientists.

Despite the good advantages of crystalline materials, in many applications (technological or not) a central role is occupied by non-crystalline materials, among which glasses are the most important [26]. Glass and glass-derived products are present everywhere: from the simplest and most common objects as windows or laboratory glassware, to high-tech products such as smartphone covering, TV and solar-cell panels, optical fibres etc. A unique feature of glass materials is the availability of processing methods to produce objects with size and shape ranging from optical fibres with micrometric diameter to giant flat glasses for architecture, as well as thin sheets for smart glass windows or transparent nanometric coatings, Figure 2.2. Contrary to crystals, the definition of "glass" has been changed and modified several times during the last 90 years [27] trying to include in the definition the main and most general features of the glassy or *vitreous state* [28]. The existence of the glass transition or transformation temperature, $T_g$, defines the vitreous state. Although some of glass properties can be expressed as a linear combination of the molar fractions of the components, the different atomic orderings of the network and the nature of the different elements give rise to nonlinear variations in certain transport properties (electrical, chemical, etc.). A technical and incomplete definition is "*Glass is an inorganic*

*product of fusion that has cooled to a rigid condition without crystallisation*" ASTM (C-162-92). Recently, an updated definition of "glass" has been given by Zanotto et al. [29]. Its simpler version is: "*Glass is a non-equilibrium, non-crystalline state of matter that appears solid on a short time scale but continuously relaxes towards the liquid state*".


***Figure 2.2.*** *Some technological applications of glasses prepared with different processing methods. Smart glass (top left), flat glass for building (top right), laser glass (bottom left), optical fibre for telecom (bottom centre) and hydrophobic or hydrophilic nano-coatings prepared by SG (bottom right).*

Glasses are essential materials for optics and photonics and it has been estimated that around 90% of optical components are made of glass [30]. Indeed, most of the optical lenses and optical fibres are made of glass. The application of glass technology to the preparation of optical active materials dates back to several decades ago and immediately demonstrated its potentiality. In 1960 Maiman invented the laser [31] (ruby laser) and just one year later, in 1961, Snitzer obtained the first $Nd^{3+}$ doped glass laser [32]. Few years later, taking advantage of the glass processing method, $Nd^{3+}$ glass fibre laser [33] and waveguide amplifiers [34] were obtained. In 1967, Deutschbein et al.[35] described $Nd^{3+}$ doped phosphate glasses and later SCHOTT produced the famous LG 750 laser glass [36]. In comparison to crystals, RE-doped glasses show much broader transitions and the local environment changes from site to site due to lack of long-range order. This multi-site distribution results in the broadening of the absorption spectra as well as in the laser emission and luminescence spectra. Many glass compositions are transparent over a wide spectral range, from Vis up to 3-5 μm and some compositions up to 11 μm [37]. In addition, most absorption and emission

bands are generally due to RE ions (or other elements) added to glasses and this convert them into suitable host materials for photonic applications. Moreover, glass compositions are not restricted by stoichiometric rules being possible to introduce slight or sometimes heavy modifications to tailor the desired optical or other physical properties. Bulk materials, optical fibres or thin films for waveguides have been studied extensively and their optical properties have been reported by many researchers during decades [20,38–40].

A further improvement of glass properties can be achieved by a controlled crystallisation to produce *glass-ceramics* [41–44]. The first applications were mostly related to increase the mechanical or thermal properties of glasses. Many papers were published describing the new properties of these materials along with a theoretical description of the crystallisation process. In particular, glass-ceramics have demonstrated to be a suitable choice for optical materials due to the possibility of combining the glass processing methods with the improved optical properties of certain crystal phases.

In the next section an introduction to glass-ceramics is given, with special focus on transparent oxyfluoride glass-ceramics produced by MQ and SG.

### 2.6. Glass-ceramics

In 1953, Donald Stookey produced for the first time a new type of material named *glass-ceramic* [45,46]. Today we know that such discovery was a fortuitous event because it was not Stookey's intention to heat treat an Ag containing lithium silicate glass up to 850 °C, quite above the glass transition temperature. But something just went wrong in the experiment and the next day this new opaque material was still solid and mechanically stronger than the initial glass [44]. The as prepared material contained $Li_2Si_2O_5$ crystals in the glass matrix grown thanks to Ag nuclei. Some years later, glass-ceramics based on aluminosilicate compositions were developed and commercialized as Corning Ware® for being used in cookery.

For many years, the term glass-ceramics was used to describe materials obtained by a controlled crystallisation of glasses and containing significant crystal fraction

(>50%). Some old definitions of glass-ceramics often included a lower limit of crystal fraction [47–49]. In fact, it is not obvious that a small fraction of crystals can improve some properties of a glass. But nowadays many interesting materials with improved properties have been prepared showing for example better luminescence or photo-refractive properties even though the crystal fraction is lower than 10 wt%. Moreover, new processing methods, as laser crystallisation, have emerged and used to produce glass-ceramics. To cover all possible glass-ceramics and take into account the variety of processing methods, several experts from the glass science community, most of them members of the TC07 "Crystallisation and glass-ceramics" of the International Commission on Glass (ICG), elaborated in 2018 an updated definition of glass-ceramic that is *processing-related* [50]. The fruitful discussion started during the "12$^{th}$ International Symposium on Crystallisation in Glasses and Liquids" that took place in Segovia and was organised by Spanish Ceramics and Glass Society (SECV) in collaboration with the Ceramics and Glass Institute (CSIC). According to this updated definition [50]:

*"Glass-ceramics are inorganic, non-metallic materials prepared by controlled crystallisation of glasses via different processing methods. They contain at least one type of functional crystalline phase and a residual glass. The volume fraction crystallized may vary from ppm to almost 100%".*

A key feature for the development of glass-ceramics with special properties is the possibility of obtaining different microstructures depending on chemical compositions, processing method and crystallisation process [44]. A controlled crystallisation process of glasses is an important factor for the development of glass-ceramics and without it, special properties could not be obtained. The development of crystals in a base glass generally takes place in two stages called nucleation and crystal growth. During nucleation, the formation of nuclei occurs and during the growth stage such nuclei develop into crystals [44]. In 1933, G. Tammann published a work about the glass state and introduced the concept of temperature dependence of nucleation and crystallisation of glasses [28]. According to Volmer' s definition, a nucleus is an entity that already belongs to the new phase but it is in unstable equilibrium with respect to

the supersaturated parent phase [44]. Thermodynamics and kinetics are hence fundamental to assess the formation ability of certain nuclei; in particular, as studied in detail by many researchers, the change in Gibbs free energy between the melt and the crystal is indicated as the thermodynamic driving force for the crystallisation process in glasses.

A distinction must be made between *homogeneous* and *heterogeneous nucleation* [44,50,51]. The term homogeneous refers to nucleation processes that occur in the absence of external active sites and a new phase is developed due to local fluctuations of density and kinetic energy. On the contrary, heterogeneous nucleation occurs in active sites, catalysing nucleation. These sites can be phase boundaries, special catalysts and foreign substrates, different from the parent phase. The change of Gibbs free energy during the glass-crystal transition can be expressed considering spherical particles of radius r [44]:

$$\Delta G = -\frac{4}{3}r^3\Delta G_v + 4\pi r^2\gamma + \Delta G_E \quad (2.1)$$

where the first negative term corresponds to the crystallisation energy release per unit volume ($\Delta G_v$) and the second positive one is due to the energy necessary to form a new surface, being $\gamma$ the interfacial energy. A further contribution related to elastic deformation ($\Delta G_E$) can be also taken into account; however, it will be omitted for the following reasoning. Due to the opposite effect of the volumetric term with respect to the superficial one, it is suddenly understood that a critical radius r* exists. For $r > r^*$ the Gibbs free energy variation is negative and the crystal grow proceeds while a smaller nucleus will dissolve because a positive variation of Gibbs free energy is produced.

$$r^* = -\frac{2\gamma}{\Delta G_v} \quad (2.2)$$

When $r=r^*$ the corresponding $\Delta G^*$ is expressed by:

$$\Delta G^* = -\frac{16\pi\gamma^3}{3(\Delta G_v)^2} \quad (2.3)$$

For heterogeneous nucleation the driving forces involved in the formation of a new phase are stronger than those required by the parent phase for its transformation into a crystal. In this case, $\Delta G_H^*$ can be expressed by $\Delta G^*$ with an angular factor $f(\theta)$ due to the contact angle ($\theta$) between a nucleus and the heterogeneous surface or catalyst:

$$\Delta G_H^* = \Delta G^* f(\theta) \tag{2.4}$$

$$f(\theta) = \frac{(2+\cos\theta)(1-\cos\theta)^2}{4} \tag{2.5}$$

The angular factor is always less than or equal to 1, hence heterogeneous nucleation leads to an effective reduction of free energy. In fact, there is no need to spend energy to create the surface. Therefore, surfaces that are readily wet by the liquid (defined by the contact angle), provide better nucleation sites.

Though only thermodynamic considerations have been made so far, the nucleation is also a kinetic process and the number of crystalline nuclei per unit volume and per unit time, called the nucleation rate I, can be expressed in this way [44]:

$$I = A \exp\left(\frac{\Delta G^* + \Delta G_d}{k_B T}\right) \tag{2.6}$$

where $\Delta G_d$ is the activation energy for the transport through the interface (diffusion barrier of the ions) and $\Delta G^*$ the change in the Gibbs free energy for the critical nucleus, A is a pre-exponential frequency factor, $k_B$ the Boltzmann's constant and T the absolute temperature. Once the nucleus has achieved the critical size r* (eq.2.2), the crystal growth can start and it is controlled by the extent to which material transport to the interface between the nucleus and the surrounding glass matrix is achieved. A general expression for the crystal growth rate is given by [44]:

$$U = aB \exp\left(-\frac{E_D}{k_B T}\right)\left[1 - \exp\left(-\frac{\Delta G}{k_B T}\right)\right] \tag{2.7}$$

a is the interatomic distance, B a frequency factor and $E_D$ and $\Delta G$ the kinetic (activation energy for diffusion) and thermodynamic barrier for crystal growth, respectively. I and U show maxima but they generally do not coincide and the maximum of I usually occurs at smaller temperatures than for U. In particular, for homogeneous nucleation,

the maximum nucleation temperature is slightly above the glass transition or transformation temperature, $T_g$, while for heterogeneous nucleation is lower [51]. If crystallisation occurs in a region where the crystal growth rate is high, and the nucleation rate is low, a relatively small number of large crystallites will be obtained. Instead, if crystallisation occurs where the nucleation rate is high and the crystal growth rate is low, numerous small crystallites are produced. This second condition is usually adopted for the preparation of conventional transparent glass-ceramics. Phase separation can be present or not and act as precursor for crystallisation. Phase separation is often encountered in oxyfluoride glass-ceramics as explained in detail in section 2.8.1.

## 2.7. Transparent glass-ceramics

An important achievement for the application of glass-ceramics in optics and photonics has been the development of transparent glass-ceramics. In 1959 Stookey reported that certain glasses, when crystallised by a simple heat treatment, form very fine-grained transparent materials [52]. In the mid of 1960s, Borrelli et al. [53,54] reported electro-optic activity of a microcrystalline ferroelectric niobate phase formed within a glass matrix after a controlled heat treatment. The author pointed out that to maintain the transparency, the crystal size had to be about one order of magnitude less than the wavelength of light. Moreover, the crystal size and the amount of the ferroelectric phase, which increase with temperature and time of heat treatment, control the dielectric constant of the material.

In 1969, Beall and Duke [52] published a paper giving a theoretical description of the transparency in glass-ceramics. Starting from fundamental physics theory about light scattering, the authors assumed spherical particles distributed in a homogenous medium and obtained a formula for the intensity of scattered light in a certain angular direction:

$$I(\theta) = I_0 \left(\frac{1+(\cos\theta)^2}{d^2}\right) \frac{8\pi^4 r^6}{\lambda^4} \left|\frac{M^2-1}{M^2+2}\right|^2 \quad (2.8)$$

where $I_0$ is the intensity of the incident beam, d is the distance from the scattering centre, r the radius of the particle, $\lambda$ the wavelength and M the ratio of the refractive

index of the particle to that of the surrounding medium. The authors concluded that glass-ceramics may transmit visible light if (1) the crystallites of all species are much smaller than the wavelength of visible light or (2) the optical anisotropy (birefringence) within the crystals and the difference of refractive index between crystals and glass matrix are very small.

Another interesting parameter to assess the transparency conditions is the turbidity (or attenuation due to scattering) [55]. There are two possible scenarios for particles much smaller than the wavelength of light: (1) independent particles widely separated (discrete particle approach); (2) particles more closely spaced with interparticle spacing no smaller than the particle radius (quasi-continuum model). For the first case, the turbidity, $\sigma_p$, is given by:

$$\sigma_p = \frac{32\pi^4}{3\lambda^4} NVa^3(n\Delta n)^2 \quad (2.9)$$

where $\lambda$ is the wavelength, N the particle number density, V is the particle volume, a the particle radius, n the refractive index of the crystal and $\Delta n$ the refractive index difference between crystal and matrix. Instead, for the second case (quasi-continuum model) the turbidity, $\sigma_c$, is described by the following equation:

$$\sigma_c = \frac{32 \times 10^{-3}\pi^4}{3^4}\left(a + \frac{W}{2}\right)^3 (n\Delta n)^2 \quad (2.10)$$

where W is the interparticle spacing. According to this equation, the transparency is still maintained for particle sizes ~ 30 nm and $\Delta n$ ~ 0.3. Such model was found to fit better the experimental turbidity values for transparent glass-ceramics than the model based on independent particles [55].

Based on this analysis, for non-isochemical systems (that is crystal phases having different chemical composition with respect to the glass matrix) [56–58], the crystal size generally must be in the nanometric range to preserve the transparency and avoid Rayleigh scattering, unless crystals and glass matrix have very similar refractive index. Moreover, in all the aforementioned works the authors outlined that a great advantage of glass-ceramics with respect to polycrystalline materials, formed by conventional ceramic processes, lies in the capacity and diversity of glass processing methods.

Therefore, glass-ceramics were considered as interesting materials because they combine the good physical properties of certain crystal phases with the glass processing methods.

Many crystalline phases for different applications were precipitated in glass matrices [44]. At the beginning, most of phases were oxide crystals containing Al or Si in addition to Mg or Zn, for example this is the case for β−quartz solid solutions, β-eucriptite, mullite, spinel, willemite, ghanite, forsterite etc.; but there are also other oxide phases with important optical or electrical applications as BBO, $SnO_2$, ZnO, $HfO_2$, $LiNbO_3$, $NaNbO_3$ etc., that acquired great interest.

A precise glass composition together with a controlled heat treatment is necessary to grow a specific crystal phase. Due to the great variety of crystal phases (oxides, fluorides etc.) studied during the last 60 years and taking into account that in many cases the glass-ceramic compositions for optical applications were centred on the system $SiO_2/Al_2O_3/M_2O/MO$ ($M_2$, M=alkaline and alkaline-earth metals), the preparation of transparent glass-ceramics coincided with the preparation of *nano-glass-ceramics* and in many papers both terms are used interchangeably.

The great revolution brought by the discovery of transparent glass-ceramics manifests itself in some outstanding products. For example, the famous ZERODUR® produced by Schott used for telescope mirrors due to its extremely low thermal expansion coefficient (CTE < 0.01-0.03 x $10^{-6}$ $K^{-1}$). ZERODUR® is an inorganic glass-ceramic in the system $Li_2O$-$Al_2O_3$-$SiO_2$ with 70 to 78% of β- quartz crystallites with size between 50-80 nm. The low thermal expansion is explained considering that crystals contract when they are subjected to heating, whereas the glass matrix itself expands. Several transparent glass-ceramics have been commercialized, see Figure 2.3, and more information can be found in the literature [41,44,59].

In the following section, a special attention is dedicated to a class of RE-doped transparent glass-ceramics containing fluoride crystals in aluminosilicate matrices (oxyfluoride glass-ceramics). These glass-ceramics are very attractive active optical materials and the objective of this thesis.

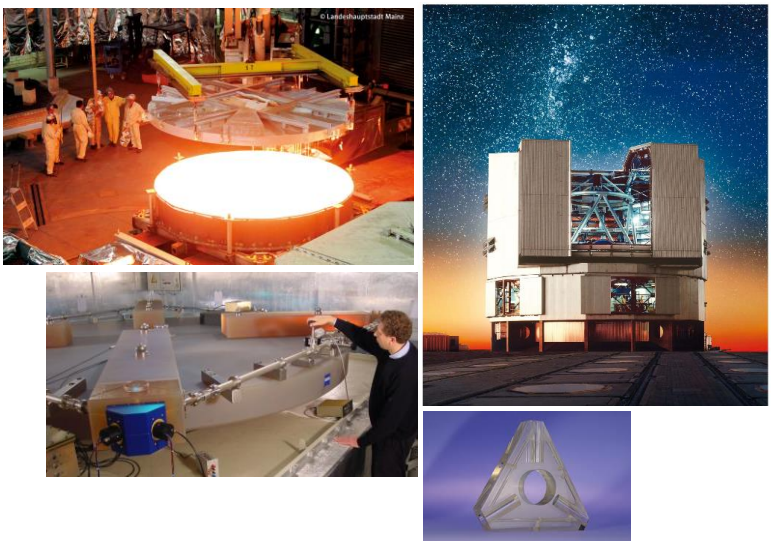

***Figure 2.3.*** *Applications based on ZERODUR® glass-ceramics. Preparation of mirror substrate (top left) for the Very-Large-Telescope (top right). Ring laser gyroscope for measuring Earth's rotation in the German Terrestrial Reference Station in Wettzell, Germany (bottom left) or for precise position measurement in aircrafts (bottom right).*

A summary of oxyfluoride glass-ceramics prepared by MQ is presented, followed by a review about SG materials. In fact, there is abundant literature about MQ materials summarised in review papers published recently. Therefore, only the most general features will be described, with special focus on glass-ceramic fibres, a very novel topic. Instead, a review paper about SG materials was recently published by our research group in 2018 and is attached as paper 1. This review describes the active oxyfluoride glass-ceramics prepared since the first works at the end of the 1990s and shows the improvements introduced by our research group with respect to synthesis, processing and structural characterisation of these materials.

## 2.8. Oxyfluoride glass-ceramics

Oxyfluoride nano-glass-ceramics are attractive materials for photonic applications, because they combine the very low phonon energy of fluoride NCs (300-450 $cm^{-1}$) and the high RE ions solubility in these phases, with the high chemical, mechanical and thermal stability of oxide glasses, especially the aluminosilicates.

Fluoride crystals have high electronegativity, small polarizability and weak covalency of the M-F bonds. When RE ions are embedded in fluoride phases they experience a small perturbation of the energy levels (few hundreds of $cm^{-1}$) and the overlapping of absorption and emission lines, which causes non-radiative losses by

cross-relaxation, is reduced in these weak crystal field materials [60]. Moreover, the probability of non-radiative transitions decrease exponentially with the number of phonons emitted. The low phonon energies of fluorides and the smaller crystal field splitting reduce the non-radiative decay rates and allow higher quantum efficiencies and better energy transfer processes to be reached. Finally, RE ions radiative lifetime is longer in fluoride crystals with respect to oxide crystals and glasses.

Fedorov et al. [61] summed up some advantages of oxyfluoride glass-ceramics with respect to other inorganic fluoride materials (crystals or glasses). A notable advantage is the possibility to stabilize metastable fluoride phases that cannot be otherwise prepared and/or preserved at room temperature. The oxide glass phase prevents NCs agglomeration and inhibits possible inactivation processes at the NCs surface (water adsorption etc.). Moreover, inorganic fluorides are hygroscopic, easily undergo pyrohydrolysis and in addition, fluoride glasses and their precursors are toxic and unstable.

The great interest towards these materials is reflected in the publications in 2012 [59] and 2015 [61,62] of three review papers about oxyfluoride glass-ceramics, each one containing around 300 references. In another review about transparent glass-ceramics, published in 2018 [63], oxyfluoride glass-ceramics were pointed out as promising materials for PL applications. Moreover, by typing "oxyfluoride" and "glass-ceramics" as keywords on Scopus, around 530 publications plus book chapters are found. It means an average of ~ 20 papers per year since the beginning of 1990s.

### 2.8.1. Melt-quenching as main processing method

MQ is the most common method for preparation of oxyfluoride glass-ceramics. It consists on melting a glass and then performing a control heat treatment to convert it into a glass-ceramic. In general, for MQ materials, the crystallisation process is performed at temperatures slightly higher than $T_g$ ($T_g$ + 20-100 °C) to ensure the growth of crystals with nanometric size.

The pioneering work of Wang and Ohwaki published in 1993 [1] demonstrated the possibility of obtaining transparent oxyfluoride glass-ceramics. The authors prepared

aluminosilicate glasses in which $Pb_xCd_{1-x}F_2$ crystals co-doped with $Yb^{3+}$ and $Er^{3+}$ ions were precipitated by a controlled heat treatment. The green up-conversion (UC) PL, due to the $^4S_{3/2}$-$^4I_{15}$ transition of $Er^{3+}$ ions, was 100 times stronger in the glass-ceramic than in the parent glass. This remarkable result was a clear proof of the advantages offered by the incorporation of RE ions in fluoride crystals. In 1995, P.A Tick et al. [64] reported the first transparent glass-ceramic doped with $Pr^{3+}$ for optical amplification at 1300 nm. In this paper, three fundamental issues were also outlined: (1) the fundamental role of the oxyfluoride parent glass composition; (2) the role of the NCs in reducing the concentration quenching of RE ions; (3) the reduction of non-radiative transitions due to low phonon energies of fluorides. For these reasons, many compositions have been studied in the last decades, with the purpose of obtaining different crystal phases and using different RE ions, singly or co-doped with other RE ions, to obtain enhanced linear and nonlinear optical processes [62].

A detailed description of most fluoride phases crystallised from aluminosilicate glasses is given in [61]. The authors also present a schematic "composition tree" for $SiO_2$-$Al_2O_3$ based-oxyfluoride glass-ceramics. The glass compositions can be quite complex and Fedorov [65,66] demonstrated that systems with 5-7 components have the highest possible stability. Some of the most studied active phases include $MF_2$ crystals such as $CaF_2$, $BaF_2$, $SrF_2$, $PbF_2$ or solid solutions; $MF_3$ crystals with $YF_3$ and $LaF_3$ being the most relevant; and other compositions based on ternary crystals ($M_1M_2F_4$) as $NaYF_4$, $NaGdF_4$, $NaLaF_4$, $KLaF_4$ etc.

Although glass compositions are not restricted by stoichiometry rules, there is a compositional range for oxyfluoride glasses that depends on the kind of fluoride phase and its content. A slight variation of known compositions is a good starting point to prepare new glass-ceramics, however, if $MF_x$ crystals are formed, by replacing M with chemically similar elements (M'), it is not ensured that $M'F_x$ crystals will be obtained. To predict whether a certain crystal phase will be formed after heat treatment of a new glass composition, it is a difficult task. In fact, thermal treatment of multicomponent glasses may result in the formation of different crystalline phases in the glass matrix [61]. Moreover, the addition of RE dopants can hinder the formation of certain crystal

phases that crystallise in the un-doped glass or promote the growth of one phase for polymorphous crystals [67,68].

The composition of $CaF_2$-glass-ceramics usually varies in the system $SiO_2$-$Al_2O_3$-CaO-$CaF_2$ with 65-80 mol% of ($SiO_2$+$Al_2O_3$) and 20-30 mol% $CaF_2$. In the case of $PbF_2$, or $Pb_xCd_{1-x}F_2$ solid solutions, most glass-ceramics are based on the initial Wang and Ohwaki's composition, or on its modifications, in the system $SiO_2$-$Al_2O_3$-$PbF_2$-$CdF_2$-$ZnF_2$ with 45-50 mol% ($SiO_2$ +$Al_2O_3$) and 20-30 mol% $PbF_2$ .

$LaF_3$ has been considered a promising host for its low phonon energy (350 $cm^{-1}$) [69–72] and good RE dopants solubility due to the same charge and similar sizes. $LaF_3$ has hexagonal symmetry and a tysonite structure with space group P-3cl [73–75]. One $La^{3+}$ ion is surrounded by eleven fluorine atoms in non-equivalent positions. Seven fluorine atoms are at the same distance (2.45 Å), two fluorine atoms are farther away (2.63 Å), and two at a greater distance (3.04 Å) [75,76]. Most of the results obtained in this thesis concern $LaF_3$ crystals.

$LaF_3$-glass-ceramics were obtained for the first time by Dejneka in 1995 using the $SiO_2$-$Al_2O_3$-$Na_2O$-$LaF_3$ system and the results published in 1998 [77,78]. Later, Sroda [79] gave an extensive description about the different role of single glass components for the crystallisation of $LaF_3$. $Al_2O_3$ is fundamental to increase the solubility of $LaF_3$ and $Na_2O$ addition is necessary to compensate the unbalanced charge of $[AlO_4]^-$ tetrahedral that otherwise is compensated by $La^{3+}$ ions making more difficult the crystallisation of $LaF_3$. But $Na^+$ can also form bonds with $SiO_2$ producing non-bridging oxygens. Therefore, the $LaF_3$ crystallisation ability depends on the $Na_2O/(SiO_2+Al_2O_3)$ ratio. A $LaF_3$ solubility limit was introduced as a function of $Al_2O_3$ and $Na_2O$ and defined by:

$$LaF_3 = ([Al_2O_3]-[Na_2O])/4. \quad (2.11)$$

If the $LaF_3$ amount is kept below such limit a transparent glass is obtained, on the contrary spontaneous crystallisation takes place. For typical compositions such limit is very low (1-3 mol%) and much higher $LaF_3$ contents (10-15 mol%) are generally added. As described by Dejneka [78], a transparent glass can be obtained by pouring it onto a

cold mould to inhibit crystallisation. Different $SiO_2/Al_2O$ ratios were also studied by Hemono et al. [80] for similar $LaF_3$ concentrations and it was concluded that $LaF_3$ crystallisation ability increases with the $SiO_2/Al_2O_3$ ratio. Moreover, higher $SiO_2$ contents allow improving the mechanical properties of these materials.

The most common compositions for $LaF_3$ glass-ceramics are in the system $SiO_2$-$Al_2O_3$-$Na_2O$-$LaF_3$ and have 65-75 mol% ($SiO_2$+$Al_2O_3$) and 10-15 mol% of $LaF_3$. Our research group developed the composition $55SiO_2$-$20Al_2O_3$-$15Al_2O_3$-$10LaF_3$ (55Si-10La) [80] that was extensively studied in a previous thesis focusing on its crystallisation mechanism [5,81]. This composition doped with RE ions has also been used in this thesis to correlate structure and optical properties. Moreover, it was also selected to prepare the first glass-ceramic fibres.

Other novel glass-ceramics are those in which ternary crystals $M_1M_2F_4$ are formed. Some of them are polymorphous and can assume more than one crystal structure, generally two. These crystal phases have shown excellent luminescent properties and the possibility to host RE ions in more than one crystallographic site [82,83]. For example, $NaYF_4$ was described as a promising UC host for $Er^{3+}$-$Yb^{3+}$ [84–89] with efficiency higher than $LaF_3$ [90]. Much less publications about $M_1M_2F_4$ glass-ceramics are encountered in the literature especially about the crystallisation mechanism of these glass-ceramics. Muñoz et al. [58] studied the crystallisation of $LaF_3$ and $NaLaF_4$ concluding that $NaLaF_4$ crystallisation is favoured with respect to $LaF_3$ for $SiO_2$ > 55 mol% and $Al_2O_3$ < 20 mol%. By replacing $Na_2O$ with $K_2O$, $KLaF_4$-glass-ceramics of molar composition $70SiO_2$-$7Al_2O_3$-$16K_2O$-$10LaF_3$ (70Si-7LaK) were prepared by our group demonstrating the possibility of obtaining cubic (α) and hexagonal (β) $KLaF_4$ crystals depending on the heat treatment [91]. The same glass composition has also been used in this thesis to study the effect of RE dopants on the crystallisation mechanism and luminescence properties. $KLaF_4$ crystals are very efficient RE-host especially the hexagonal phase which has a phonon energy ~ 262 $cm^{-1}$ [83,92].

The addition of high amount of fluoride active phases to oxide matrices would allow obtaining higher crystal fractions with consequent higher PL emissions due to the possibility of incorporating more RE ions and avoiding concentration quenching.

However, this is a real challenge for MQ-derived materials because: (1) very high melting temperatures are typically used (1400-1700 °C) causing relevant fluorine evaporation and (2) the addition of fluorine in most aluminosilicate compositions is limited due to spontaneous crystallisation. In fact, the addition of fluorine to oxide glasses causes a de-polymerisation of the network [93]. This process enhances the formation of phase separation regions due to liquid-liquid immiscibility of fluoride melts in oxide ones during the undercooling process.

The crystallisation mechanism of oxyfluoride glass-ceramics has been extensively studied by many authors [59,61,79–81,91,94–110]. It can start or not from initial phase separation of glasses. For many glass systems, it was observed that a liquid-liquid phase separation was already present in the as made glasses. The heat treatment promotes further phase separation and induces the crystallisation of the phase separated regions via diffusion. However, Rüssel [108] described a $SiO_2$-$Al_2O_3$-$K_2O$-$Na_2O$-CaO-$CaF_2$ glass where $CaF_2$ NCs grow without previous phase separation. A similar behaviour has been observed for the $KLaF_4$ crystallisation studied by our group [91]. No phase separation regions (or droplets) are observed in the as made glass, but after a proper heat treatment $KLaF_4$ NCs are formed by a diffusion-controlled process.

For non isochemical systems, each crystal nucleus is surrounded by a $SiO_2$-enriched layer depleted of the components of the forming crystal [5,96,105,106], see Figure 2.4.

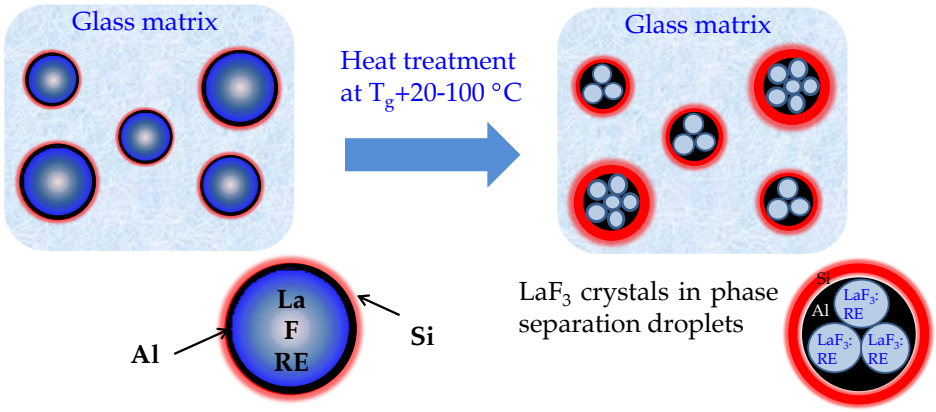


***Figure 2.4.*** *Simple scheme of the crystallisation mechanism in $LaF_3$-glass-ceramics. Initial phase-separation droplets promote the formation of NCs through a diffusion-controlled process.Adapted from [5, 95].*

For this reason, whether there is phase separation or not, the crystallisation process is always accompanied and limited by diffusion. As a consequence, for a fixed temperature the crystal size increases with the treatment time up to an asymptotic value. A similar behaviour occurs for the glass transition temperature due to the increase of viscosity caused by local changes of the glass matrix depleting of crystal formers (F, Alkaline etc).

The PL of oxyfluoride glass-ceramics have demonstrated much better luminescence or UC emission for $Nd^{3+}$, $Er^{3+}$, $Er^{3+}$-$Yb^{3+}$, $Tm^{3+}$-$Yb^{3+}$ etc. with respect to the precursor glasses [111–127]. Down-conversion processes were also studied demonstrating the possibility to convert UV-Vis photons into IR light using $Pr^{3+}$-$Yb^{3+}$, $Tb^{3+}$-$Yb^{3+}$ etc. [128–142]. Distinctive optical features of RE ions embedded in fluoride crystals are: more structured absorption and emission bands (Stark components) with respect to glasses, higher PL intensities, longer radiative lifetimes and better energy transfer mechanism.

Even though oxyfluoride glass-ceramics prepared by MQ have shown many potentialities as optical materials, there are still some fundamental points that need to be clarified. Some of them are related to obtaining a deeper comprehension of the glass formation regions and the prediction of the possible crystal phases that can be formed during crystallisation. Up to now, such studies have been carried out for specific phases and in many papers solid solutions are obtained due to the impossibility, or non-knowledge, of tailoring a glass composition to crystallise a specific phase. Other open questions are related to the quantification of crystal fractions and even more important, the quantification of the effective RE ions concentration in fluoride crystals. In fact, the luminescence properties of RE-doped materials are strongly dependent on the doping amount. Some authors claimed that RE ions do not enter at all in the crystal phase [143,144] while other asserted that most of RE ions get incorporated [100,145–147]. The effect of the dopants precursor on the final optical properties was studied only by few authors, observing differences when RE fluorides or oxides were used [148,149]. However, such researches did not receive much attention and today the use

of one type of precursor or another is considered irrelevant. Some of the aforementioned points have been treated and discussed in this thesis.

*2.8.1.1. Glass-ceramic fibres*

As stated in sections 2.6, glass-ceramics are prepared by typical glass processing methods. A great advantage of glass materials is that they can be drawn into fibres to prepare optical fibre lasers and amplifiers. In addition, several features such as small core size and long interaction length make optical fibres interesting for nonlinear optical processes.

A glass optical fibre is made of a glass core, in which the light travels, and a cladding material of refractive index lower than that of the core [150]. The most common method used today consists in the preparation of a *preform* made of core and cladding glasses that then is fibred [151]. $SiO_2$ preforms are produced by chemical vapour deposition but many multicomponent fibres (different composition of core and cladding) are prepared by the *rod-in-tube method* [151], i.e a core glass rod is placed into a tube made of cladding glass. An older method, still used for research purposes and to prepare commercial chalcogenide fibres, is the *double-crucible method* [151] in which two concentric crucibles host the core glass (in the inner crucible) and the cladding glass (in outer crucible).

The application of fibre drawing to obtain glass-ceramic fibres gained increasing interest in the last years and a review is presented below.

The first studies about transparent glass-ceramic fibres date back to the end of the 1990s when P.A. Tick, in a two-page paper [152], wondered if low-loss glass-ceramic optical fibres were possible. The author indicated four conditions to achieve this goal: (1) crystal size smaller than 15 nm; (2) interparticle spacing comparable with the crystal size; (3) narrow particle size distribution and (4) absence of clustering. Some years later, Tick et al. [153] drawn fibres with a core ~ 5 μm starting from a Wang and Ohwaki's modified composition in the system $SiO_2$-$Al_2O_3$-$PbF_2$-$CdF_2$-$YF_3$ and using the double crucible method. After the crystallisation process at 440-470 °C, a crystalline $YF_3$-$CdF_2$-$PbF_2$ solid solution with an average size ~ 6.5 nm was observed in the glass-

ceramic fibre. The authors concluded that low losses, ~ 1 dB/m or less, are possible in such systems in spite of a relatively large refractive index mismatch (0.06). In 2001, Samson et al. [154] described the first efficient glass-ceramic fibre laser doped with $Nd^{3+}$ using the same glass system and drawing process reported by Tick [153]. Similar slope efficiencies ~ 30% were obtained for glass and glass-ceramic, but the presence of NCs embedded within the core of the single-mode optical fibre allowed enhancing the fluorescence and gain spectrum, Figure 2.5.

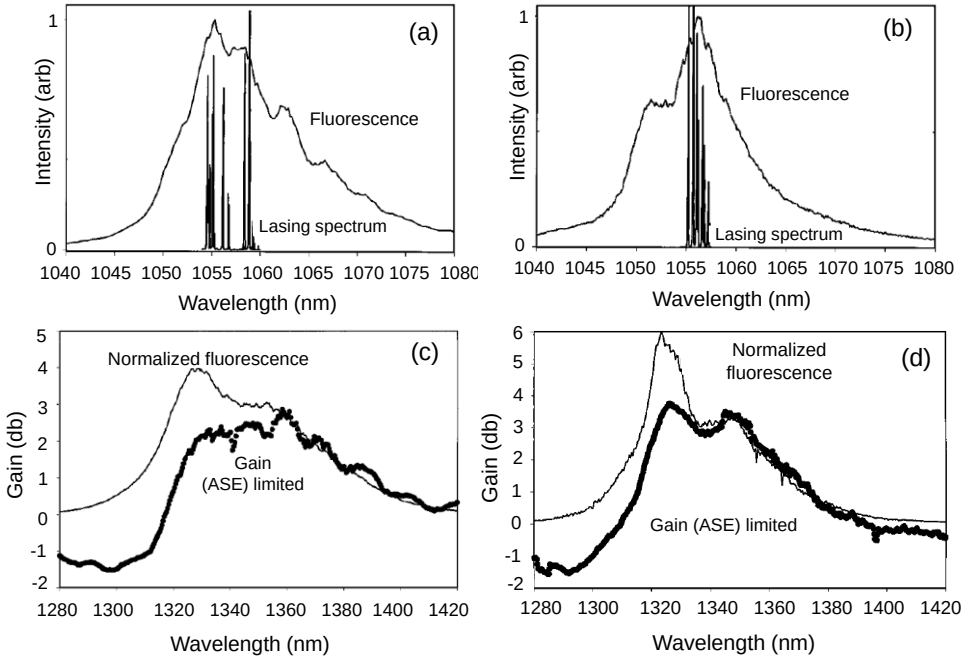


***Figure 2.5.*** *Fluorescence and lasing spectrum of the $^4F_{3/2}$-$^4I_{11/2}$ transition in (a) $Nd^{3+}$-doped glass fibre and (b) glass-ceramic fibre. Fluorescence and gain spectrum of the $^4F_{3/2}$-$^4I_{13/2}$ transition in (c) $Nd^{3+}$-doped glass fibre and (d) glass-ceramic fibre. ASE=amplified spontaneous emission* [154].

R. Lisiecki et al. [155] and Augustyn et al. [156] prepared glass-ceramic fibres using the glass composition $48SiO_2$-$11Al_2O_3$-$7Na_2O$-$10CaO$-$10PbO$-$11PbF_2$ (mol%) doped with $3ErF_3$ and co-doped with $1ErF_3$ and $3YbF_3$. The uncoated fibres were drawn at 720-740 °C from the rod glasses and then crystallised at 700 °C. $Pb_5Al_3F_{19}$, $Er_4F_2O_{11}Si_3$ and $Er_3FO_{10}Si_3$ crystalline phases were obtained with size below 10 nm. The incorporation of RE dopants in the crystal phases was indicated by a narrowing of the emission spectra and longer lifetimes of first excited state of $Er^{3+}$. The authors concluded that such materials may be considered as promising candidate for Erbium-Doped-Fibre-Amplifier (EDFA) operating within the telecommunication window. Cz.

Koepke et al. [157] prepared fibres with the same composition doped with 0.6$YbF_3$ and 0.2$ErF_3$ (mol%). The luminescence efficiency of the glass-ceramic fibre was two times higher with respect to the untreated fibre. A temperature dependence of $Er^{3+}$ luminescence at 1530 nm was observed by varying the temperature from 5 to 350 K. Such dependence was different for the glass-ceramic fibre and associated with a decrease of the phonon energy in the $Er^{3+}$ surrounding.

In 2012, M. Reben et al. [158] reported the preparation of $Nd^{3+}$-doped oxyfluoride glass ceramic optical fibre in the system $SiO_2$-$Al_2O_3$-ZnO-$Na_2O$-$SrF_2$ using the rod-in-tube method. $SrF_2$ NCs with size ~ 60 nm were observed after heat treatment at 635 °C. After excitation of $Nd^{3+}$ ions at 808 nm, only the $^4F_{3/2}$-$^4I_{11/2}$ emission was observed, whereas for the bulk glass-ceramic sample the three emissions $^4F_{3/2}$ - $^4I_{9/2}$, $^4F_{3/2}$ - $^4I_{11/2}$ and $^4F_{3/2}$ - $^4I_{15/2}$ were detected. Moreover, a red-shift of the $^4F_{3/2}$ - $^4I_{11/2}$ emission was observed changing from bulk (1060 nm) to fibre (1066 nm). The authors explained this result by an amplified spontaneous emission occurring in the fibre.

V.K. Khrishnaiah et al. [159] described the preparation and characterisation of $Yb^{3+}$-doped single-index glass-ceramic optical fibres produced by two methods: (1) by conventional drawing from a glass preform and, (2) by single crucible method (direct-melt process) followed by controlled heat-treatment. The glass system chosen by the authors, a variant of the initial Wang and Ohwaki's composition, was: 30$SiO_2$–15$Al_2O_3$–27$CdF_2$–22$PbF_2$–4$YF_3$–2$YbF_3$ (mol %). The authors observed that by using the second method, better quality glass-ceramics were obtained with NCs ~ 10 nm homogeneously distributed along the fibre. On the other hand, the preparation of glass-ceramic fibres by glass preform method did not allow a fine tailoring of the crystallisation process, size, shape and distribution of NCs. Higher $Yb^{3+}$ PL intensity and quantum yield (0.95) were obtained with respect to the untreated fibre (0.82).

Other authors, even though they focused their studies on bulk samples, outlined the possible applications of aluminosilicate oxyfluoride glass-ceramics for optical fibre applications. For example, V.K. Tikhomirov et al. [160] showed that $PbF_2$-containing glass-ceramics with composition 32$SiO_2$-9$AlO_{1.5}$-31.5$CdF_2$-18.5$PbF_2$-5.5$ZnF_2$ (mol%) doped with 3.5 mol% $ErF_3$ have potential applications in telecommunications. The

authors claimed the achievement of the largest wavelength divergence in the maximum of absorption (1505 nm) and emission (1544 nm) spectra of $Er^{3+}$ in developed glass-ceramics. Such result could be of benefit for reduction of noise in EDFA caused by overlap of emission and absorption bands at about 1.54 μm (i.e self-absorption). The same glass system was also used for single doping with 3.5 mol% of $Ho^{3+}$ and $Tm^{3+}$ [161]. The authors calculated the wavelength dependence of the net gain cross-section as a function of population inversion and obtained gain and laser/optical amplification parameters at about 2.0 and 1.8 μm for the $Ho^{3+}$ ($^5I_7$-$^5I_8$) and $Tm^{3+}$ ($^3H_6$-$^3F_4$) doped glass-ceramics, respectively. Moreover, due to crystallisation, the maximum gain cross section of $Ho^{3+}$ and $Tm^{3+}$-doped samples increased by 20% and 2.5%, respectively, and the obtained values were 1.5 and 2-3 times higher than those reported for fluoride glasses.

T. Suzuki et al. [162] studied glass-ceramics in the system $NaF$-$YF_3$-$Al_2O_3$-$SiO_2$ where $NaYF_4$ NCs, with size less than ~ 10 nm, were obtained after heat treatment at 580-620 °C. $Tb^{3+}$ and $Yb^{3+}$-co-doped glass and glass-ceramics showed green UC emission after excitation at 974 nm. However, the UC intensity was enhanced by the crystallisation process and the authors suggested the possible application of these materials as optical fibre amplifiers.

In 2013, J. Ballato and P. Dragic published a review paper on optical fibres entitled "*Rethinking Optical Fiber: New demands, Old Glasses*" [163], highlighting how in the last decades the "*the richness of the Periodic Table has largely been forgotten*" in favour of one material (silica $SiO_2$) into which only few components are added. The paper aimed to reassert the central role of glass science to meet future challenges for high-performance optical fibres. Special attention was paid to a new approach called "molten-core" or also "melt-in-tube" technique, thanks to which novel optical fibres have been prepared. This name comes from the fact that the cladding can be treated as a crucible in which the core is melted during the fibre drawing (1800-2000 °C) with the difference that the crucible is an integral part of the resulting fibre and serves to confine the molten core. A further advantage of this method relies in the extremely simplified experimental conditions: no matching of the core/cladding CTE and viscosity are

required. On the contrary, such matching condition plays a crucial role for fibre drawing using the common rod-in-tube method.

This idea was applied by J. Qiu and co-workers [63] for the preparation of transparent glass-ceramic fibres. In fact, special glass compositions, designed to be transformed into glass-ceramics, can lose transparency at typical drawing temperatures due to uncontrolled crystallisation. Instead, drawing the preform at really high temperatures allows to the core glass to be melted completely, avoiding crystallisation, while the cladding softens. Once glass fibres have been drawn, glass-ceramic fibres are simply obtained by a proper heat treatment. Transparent glass-ceramics containing oxide crystals were obtained for gallium-silicate [164] and aluminosilicate glasses [165,166].

Oxyfluoride glass-ceramics based on borosilicate compositions have been obtained recently using the melt-in-tube method [167,168]. In comparison to previous works, the authors substituted the $SiO_2$ cladding for a low temperature commercial borosilicate glass, thus permitting the drawing at 950 °C (melting temperature of core glasses). The authors observed an enhanced emission at 2.7 μm and longer lifetime of the $Er^{3+}$:$^4I_{11/2}$ - $^4I_{13/2}$ transition in $NaYF_4$-glass-ceramic fibres with respect to the precursor fibre [167]. The corresponding transmission losses at 1310 nm were 7.44 dB/m and 11.81 dB/m for glass and glass-ceramic fibres, respectively. By $Ho^{3+}$ co-doping, the emission region was extended from 2.6-2.82 μm up to 2.6-2.95 μm due to the effective energy transfer from $Er^{3+}$ to $Ho^{3+}$ ions embedded in $NaYF_4$ NCs [168], Figure 2.6.

The melt-in-tube technique applied to oxyfluoride glass-ceramics based on aluminosilicate compositions has not yet been reported. This could be related to the high melting temperatures of these glasses that would require the use of a $SiO_2$ cladding and a drawing temperature of at least 1800 °C, thereby causing extremely high fluorine losses.

Even though interesting progress have been made in the lasts years, a major obstacle for the commercialization of optical amplifiers based on glass-ceramic

materials is associated with the difficulties in the fabrication of fibres with minimal scattering loss and high luminescence efficiency [63].

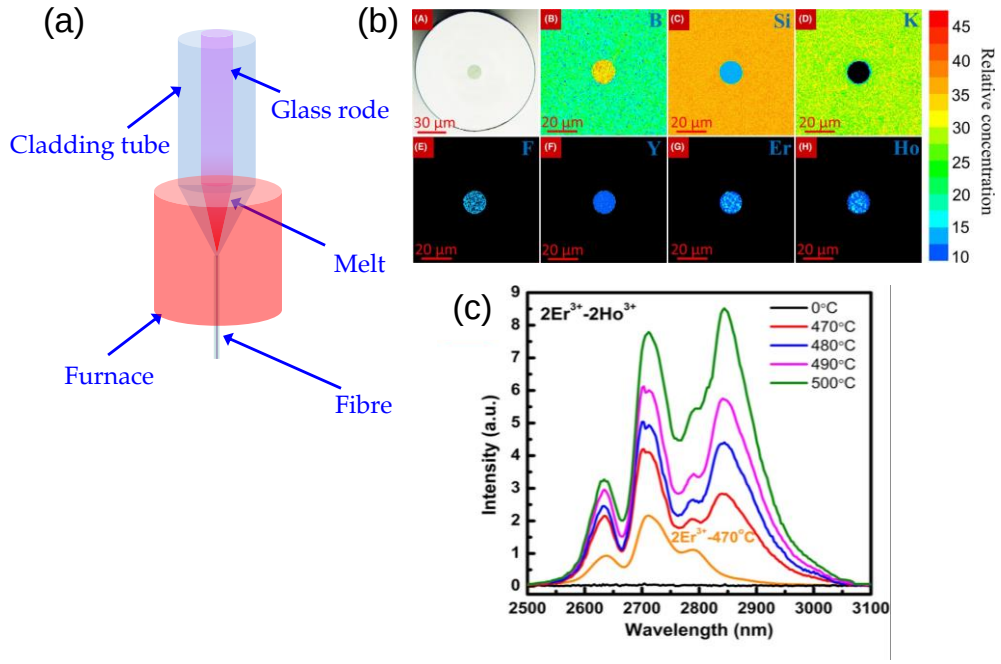


***Figure 2.6**. (a) Scheme of the melt-in-tube method. (b) Microscope picture and Electron-probe micro analysis (EPMA) for an oxyfluoride glass fibre described in* [168]. *(c) Mid-infrared (MIR) emission spectra under 980 nm excitation of $2Er^{3+}/2Ho^{3+}$-co-doped glass fibre and glass-ceramic fibres annealed at 470-500 °C for 5 h* [168].

### 2.8.2.Sol-gel as suitable alternative route

As described in the previous section, the usual method to prepare oxyfluoride glass-ceramics is glass MQ followed by controlled crystallisation. However, this procedure presents some drawbacks, most of them related to the high temperatures involved during the glass melting. In fact, high melting temperatures (1400-1700 °C) cause relevant fluorine loss (30–40%), limiting the final content of crystal phase that can be obtained and resulting in uncontrollable compositions with respect to fluorine and RE ions.

Furthermore, heat treatments, in general, are quite long (from 3 h up to 120 h) and thin films cannot be directly obtained, limiting the possibility of application in integrated devices.

Many researchers have tried different processing methods to overcome these limitations. In particular, the SG route has been recognized as a promising alternative

process to obtain transparent oxyfluoride glass-ceramics. In fact, SG is a handy, flexible, and quite cheap method to fabricate novel and innovative materials at temperatures much lower than those used for melting-derived materials. Such low temperatures allow a higher amount of fluoride NCs to be introduced with much better dispersion. Moreover, highly homogeneous materials can be obtained because SG is a chemical process using a bottom-up approach and no spontaneous crystallisation occurs at the typical synthesis temperatures (50-100 °C).

Another important feature of SG is the versatility of the processing method that allows thin films, powders, and bulk materials to be obtained. However, many few papers about SG oxyfluoride glass-ceramics are reported in the literature compared to materials prepared by MQ [61]. This is mostly associated with the requirement of the optimization of the synthesis method, and in many cases the starting precursor can also affect the final crystal phase. Most of the materials studied have a simple composition (mol%) that can be easily summarized with the formula:

$$(100 - x)SiO_2\text{-}x\ M_1F_2/M_1F_3/M_1M_2F_4/M_1M_2F_5 \quad (2.12)$$

where $M_1$ and $M_2$ are alkaline, alkaline-earth metals, or lanthanide elements, respectively.

SG synthesis typically involves the hydrolysis and polycondensation of metal salts or metal-organic precursors, such as tetraethyl orthosilicate (TEOS), in an alcoholic medium, to produce an amorphous network. The active phase and RE ions are prepared separately using acetates, nitrates, or chlorates as precursors and dissolved using a fluorine acid. The mixing of both solutions, followed by a controlled crystallisation, allows transparent oxyfluoride glass-ceramics to be obtained. In Figure 2.7 a schematic diagram of SG reactions is given.

Even though the SG method offers potential advantages to prepare oxyfluoride glass-ceramics, they have not been fully exploited. All the papers published to date describe the preparation of similar compositions containing nominal small crystal fractions (5-10 mol %) without estimating the real crystal content. Furthermore, in

many cases only slight changes are added to the already published compositions, the main modifications consisting of changing the dopants and/or their concentration.

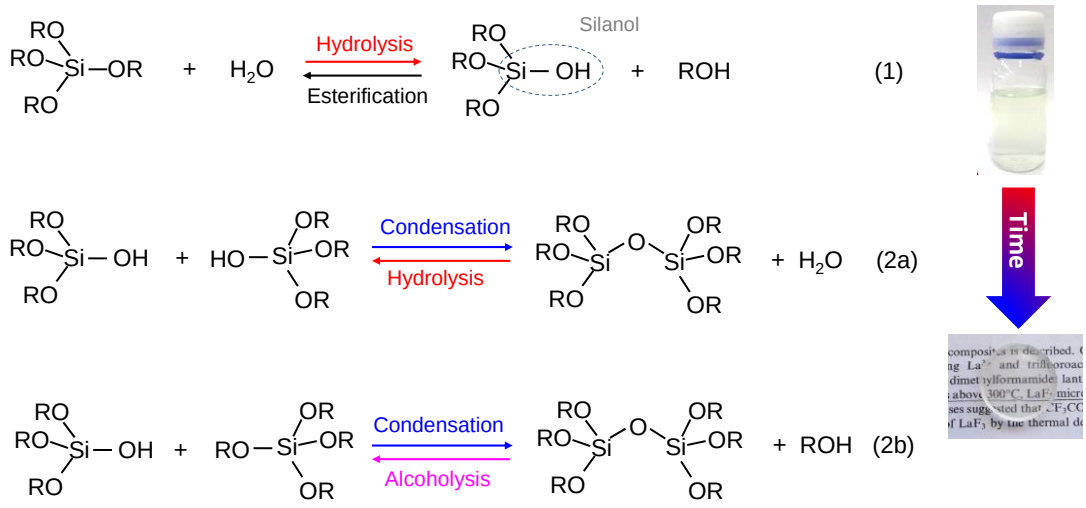


***Figure 2.7.*** *SG reactions. Adapted from* [169].

In the following sections, the most relevant results for several RE doped oxyfluoride glass-ceramics for photonics are briefly summarised. An extended version of this review can be consulted in paper 1.

$MgF_2$-based materials were the first fluorides produced by SG and the synthesis of $MgF_2$ introduced important novelties in the synthesis of oxyfluoride glass-ceramics. $SiO_2$-$MgF_2$ materials prepared by SG as bulk and thin films date back to 1996 [2] but it was in 1997 when Fujihara et al. [170] introduced the use of trifluoracetic acid (TFA) as fluorine source to produce $MgF_2$ thin films. Since this pioneering work, TFA was routinely used as fluorine source for the preparation of oxyfluoride materials using the SG method.

Other authors described the preparation of $Er^{3+}$-doped $SiO_2$-$PbF_2$ materials [171], and the UC emission using $Er^{3+}$-$Yb^{3+}$ [172]. Following the same synthesis and composition, Szpikowska-Sroka et al. prepared $Eu^{3+}$ and $Tb^{3+}$-doped materials and observed an increase of the PL in glass-ceramic samples compared to the untreated samples [173–175].

$90SiO_2$-$10SrF_2$ transparent glass-ceramics doped with 1 mol% of $Er^{3+}$ were prepared by Yu et al. [176] and no $Er^{3+}$ emission was detected unless for samples treated at 800 °C. The authors related this phenomenon with the presence of $OH^-$ groups that quenches the luminescence.

Zhou et al. prepared $95SiO_2$-$5CaF_2$ bulk samples doped with 1 mol % $Er^{3+}$. $CaF_2$ NCs of 20 nm were observed after heat treatment at 900 °C [177]. Instead, Georgescu et al. [178] prepared $89SiO_2$-$5CaF_2$-$5YbF_3$-$1ErF_3$ (mol %) glass-ceramics upon heat treatment at 800 °C. The optical characterisation showed the increase of UC emission changing from xerogel to glass-ceramic.

The first $95SiO_2$-$5BaF_2$ bulk materials doped with 0.5 and 1 mol% $Er^{3+}$ were reported in 2006 by Chen et al. [179]. $BaF_2$ NCs, 2-4 nm in size, crystallised after heat treatment at 300-700 °C. The PL emission was detected only for samples treated at 800 °C and both red and green UC emissions were observed upon 980 nm excitation. Secu et al. [180,181] prepared materials of the same compositions using $Pr^{3+}$, $Sm^{3+}$, $Eu^{3+}$, $Dy^{3+}$, and $Ho^{3+}$ as dopants. Better PL was obtained for the glass-ceramics, moreover, the $Eu^{3+}$ lifetime (at 620 nm), increased from 0.3 ms in the xerogel up to 4.7 ms in the glass-ceramic.

Fujihara et al. [182] obtained Eu-doped $90SiO_2$-$10BaMgF_4$ films with different porosity using N,N- dimethylformamide. $BaMgF_4$ NCs, 3 nm in size, were observed after heat treatment at 750 °C for 10 min. The reduction of $Eu^{3+}$ in $Eu^{2+}$ suggested the replacement of these ions for $Ba^{2+}$ ions in the fluoride NCs. The emission of $Eu^{2+}$ ions was much stronger for porous films due to higher photon confinement, producing an increase in the absorption process.

Another crystalline phase of great interest for photonics is $LaF_3$. Several papers about $LaF_3$ SG glass-ceramics were published since 1998, when Fuhijara et al. described the preparation of $LaF_3$ thin films on silica substrates [4]. The authors stated that it is not possible to prepared transparent materials with content of $LaF_3$ higher than 10 mol%.

On the other hand, Ribeiro et al. [183] prepared $90SiO_2$-$10LaF_3$/LaOF films in which $LaF_3$ and LaOF crystallised after heat treatment at 600 and 900 °C, respectively. The use of $Eu^{3+}$ as structural probe confirmed the change of symmetry around the ions after heat treatment at 500 and 600 °C, indicating the incorporation of $Eu^{3+}$ in the $LaF_3$ NCs. Thin films were used as planar waveguides at Vis and IR wavelengths, and losses ~1.8 dB/cm at 632.8 nm were obtained.

Biswas et al. [184] described the preparation of transparent $95SiO_2$-$5LaF_3$ glass-ceramics, doped with $Er^{3+}$ and $Yb^{3+}$, replacing TEOS with TMOS. Enhanced UC efficiency was observed in glass-ceramics due to the incorporation of RE ions in $LaF_3$ crystals. Other authors prepared materials with compositions $(100 - x)SiO_2$-$xLaF_3$ (x = 5 and 10 mol %), doped with (0.1-0.5) mol % of RE ions, following the Biswas's synthesis [185–190]. An interesting conclusion was that ~ 50% of $Er^{3+}$ ions are incorporated in $LaF_3$ NCs. Enhanced optical properties were observed in the glass-ceramics and the achievement of white light generation was possible by the combination of RE ions.

Méndez-Ramos et al. published results based on the $90SiO_2$-$10YF_3$ composition [191–193]. Efficient UC emission, along with intense emissions in the UV range, due to rare 4 and 5-infrared photon processes, were achieved when the samples were co-doped with $Yb^{3+}$-$Tm^{3+}$. Moreover, co-doping with $Ho^{3+}$ or $Er^{3+}$ produced the emission of white light.

$GdF_3$ is considered a promising host because $Gd^{3+}$ ions can act as sensitizer for other RE ions and favour some energy transfer processes [194]. Only a few papers about SG $GdF_3$ glass-ceramics have been published and with the nominal crystal phase content being less than 10 mol%. For example, Fuhijara et al. reported the synthesis of $90SiO_2$-$9GdF_3$ thin films doped with 1 mol % of $EuF_3$ [195] in which $GdF_3$ NCs, 5 nm in size, precipitated during heat treatment at 300 and 400 °C. Other authors studied the optical properties of $Eu^{3+}$-doped $SiO_2$-$GdF_3$ materials with a low content of active phase (3-6 mol%) and obtained stronger $Eu^{3+}$ emission in the glass-ceramics due to the incorporation of $Eu^{3+}$ in the $GdF_3$ NCs.

Complex fluoride structures, as $NaYF_4$, $KYF_4$ etc., have acquired great interest due to their good optical properties and the possibility to produce intense and efficient nonlinear optical processes.

$95SiO_2$-$5NaYF_4$ bulk materials doped with $0.1Er^{3+}$ and $0.3Yb^{3+}$ were reported in 2009 [196]. The red and green UC emission changed depending on the treatment temperature and pump power. The same composition was doped with $Eu^{3+}$, used as spectroscopic probe [197], and tri-doped with $Yb^{3+}$-$Ho^{3+}$-$Tm^{3+}$ [198] and $Yb^{3+}$-$Er^{3+}$-$Tm^{3+}$ [199] to obtain white light generation.

$LiYF_4$ is another promising host for RE ions. Secu et al. [200,201] prepared $(100 - x)SiO_2$-$xLiYF_4$ glass-ceramic powders doped with $Eu^{3+}$ and $Er^{3+}$-$Yb^{3+}$ obtaining stronger PL emission in the glass-ceramic samples with respect to crystalline $LiYF_4$ pellets doped with the same RE ions.

$SiO_2$-$BaYF_5$ materials doped with $Eu^{3+}$ and $Sm^3$ were produced using the SG method [202] and their luminescence compared to that of $BaYF_5$ NCs doped with $Eu^{3+}$ prepared by solvothermal method.

Some important novelties have been introduced with this thesis, the most important being: the incorporation of a new $SiO_2$ precursor in the synthesis, the preparation of bulk and films with a crystal fraction much higher than that reported so far and the study of both crystallisation mechanism and dopants incorporation in fluoride NCs. Some techniques such as XAS, EPR and NMR have been used to characterise these materials providing deeper insights about their structures, crystallisation and RE dopants incorporation in the NCs. Moreover, the crystallisation mechanism and dopants incorporation for materials prepared by MQ and SG have been compared.

### 2.9. Optical properties of RE ions and energy transfer mechanisms

RE ions are among the most important ions for technological applications in the field of optics and photonics. A brief introduction to these ions was given in section 2.5, indicating how many electronic transitions within 4f levels produce emission in the UV-Vis-NIR. However, a detailed explanation of the spectroscopic features of RE ions

is necessary to understand the optical properties described in this thesis. The origin of the energy levels of RE ions in solids, their possible optical transitions and the energy transfer mechanisms are explained by quantum-mechanics and are described in the next paragraphs.

### 2.9.1. Crystal field and Judd-Ofelt theory

The energy levels of the electrons in an isolated atom or in a certain compound are obtained by the Schröedinger equation:

$$H\psi = E\psi \tag{2.13}$$

where H is the Hamiltonian operator and $\psi$ the wave functions of the electrons. The Hamiltonian for a RE ion in a compound not subjected to any other external stimulation is given by [203]:

$$H = H_{FI} + H_{CF} \tag{2.14}$$

where $H_{FI}$ is the Hamiltonian for the free ion and $H_{CF}$, the *crystal field interaction*, takes into account the interaction of the ion with the surrounding medium (not necessarily a crystal). Limiting to the atomic Hamiltonian, without taking into account the spin Hamiltonian, $H_{FI}$ is mainly composed by three terms [203]:

$$H_{FI} = H_0 + H_{ee} + H_{SO} \tag{2.15}$$

where $H_0$ is the central field Hamiltonian including the interactions between the core and the valence electrons; $H_{ee}$ is the interaction between valence electrons and $H_{so}$ is the spin-orbit interaction, i.e the result of the interaction of the magnetic moment of the valence electrons with the magnetic field due to their orbital angular momentum. For some elements $H_{ee}$ is stronger than $H_{SO}$ and this condition is also considered applicable for RE ions, but some authors [204–206] pointed out that both terms should be considered simultaneously (*intermediate coupling scheme*) to obtain a better explanation of their spectra.

The situation for which $H_{SO}<H_{ee}$ is called Russell-Saunders or *LS-coupling* scheme and the order of magnitude for $H_0$, $H_{ee}$ and $H_{SO}$ is around 10 eV, 1 eV and $10^{-1}$-$10^{-2}$ eV,

respectively. If only $H_0$ is taken into account, the description of the system is too approximated and this Hamiltonian just gives the so-called *configuration energy*. By applying $H_{ee}$ as perturbation, the states with different values of L (total angular momentum) and S (total spin) get split and e*nergy terms* are obtained, the corresponding degeneracy being (2S+1)(2L+1). Finally, considering the $H_{SO}$ interaction, the degeneracy of terms with the same total angular momentum J (J=L+S) value is removed and we get *energy levels*. In LS coupling scheme the energy levels are indicated with the *term symbols* $^{(2S+1)}L_J$, using the letters S,P,D,F,G,H,I etc for L=0,1,2,3,4,5,6 etc. The quantum number J can take values from $J^{max}$=L+S to $J^{min}$=|L-S| by integer steps. Full shells and sub-shells contribute neither to total L nor to total S. Moreover, $H_{ee}$ and $H_{SO}$ applied to full or sub-shells just shift the energy levels all together without changing their order, hence to determine the ordering of energy levels only the outer valence electrons must be considered.

The ordering of the energy levels can be determined from theory but the calculations are complex. Fortunately, for the LS-coupling scheme, there are some rules which predict the ground state for various RE ions. These are known as Hund's rules which state [207]:

1. S is equal to its maximum value (consistent with the Pauli Exclusion Principle).

2. L is equal to its maximum value (consistent with rule 1).

3. For a less than half-filled shell, $J = J_{min} = |L-S|$, instead for more than half-filled shell, $J = J_{max} = L+S$.

For example, for $Pr^{3+}$ ions the electronic configuration is $[Xe]4f^2$ with two f electrons. The application of $H_{ee}$ gives the possible terms: $^1I$, $^3H$, $^1G$, $^3F$, $^1D$, $^3P$ and $^1S$. By applying rule 1, the possible ground terms are reduced to $^3H$, $^3F$ and $^3P$ and rule 2 indicates the $^3H$ term as the lowest energy level. Finally, by applying $H_{SO}$ the $^3H$ term gets slit in three possible energy levels: $^3H_4$, $^3H_5$ and $^3H_6$ and according to rule 3 the ground energy level of $Pr^{3+}$ is $^3H_4$, being $^3H_5$ and $^3H_6$ excited energy levels.

Only free RE ions have been considered up to now. The host has small influence on the energy levels of RE ions due to the shielding of 4f orbitals, and this situation corresponds to the *weak field approximation* for which $H_{CF}$ is treated as a small perturbation with respect to $H_{SO}$ and $H_{ee}$. This condition is considered applicable for both LS-coupling or for intermediate coupling [206]. The crystal field interaction can be expressed as an electrostatic interaction between the RE ion and the electric potential generated by the surrounding ions (ligands):

$$H_{CF} = -\sum_j e\, V_j \tag{2.16}$$

where -e is the electron charge and Vj is the potential generated by all ligands "in the position" of the electron j. Thanks to the Wignert-Eckart theorem [208,209] $H_{CF}$ can be expanded in a power series of equivalent operators, or Stevens operators $O_k^q$ [210], that transform as spherical harmonics. In this case, $H_{CF}$ becomes:

$$H_{CF} = -\sum_j e\, V_j = \sum_{k=0}^{\infty} \sum_{q=-k}^{k} B_k^q O_k^q \tag{2.17}$$

where $B_k^q$ are coefficients called *crystal field parameters*. Another interesting and useful way to express $H_{CF}$ is as sum of $H_{CF}$ (even) and $H_{CF}$ (odd), depending if they are proportional to even or odd powers of r, being r the radial distance from the RE ion under consideration [211].

Even though the sum runs on infinite elements, it is reduced to just few elements for symmetry reasons. Moreover, for f (l=3) electrons the maximum k is 6 and for different symmetries $H_{CF}$ is expressed by the following expressions [212] :

1. Cubic, octahedral or regular tetrahedral symmetry:

$$H_{CF} = B_4^0 O_4^0 + B_4^4 O_4^4 + B_6^0 O_6^0 + B_6^4 O_6^4 \tag{2.18a}$$

where $B_4^4 = 5B_4^0$ and $B_6^4 = -21B_6^0$

2. Tetragonal axial:

$$H_{CF} = B_2^0 O_2^0 + B_4^0 O_4^0 + B_4^4 O_4^4 + B_6^0 O_6^0 + B_6^4 O_6^4 + B_6^6 O_6^6 \tag{2.18b}$$

3. Trigonal axial symmetry:

$$H_{CF} = B_2^0 O_2^0 + B_4^0 O_4^0 + B_4^3 O_4^3 + B_6^0 O_6^0 + B_6^3 O_6^3 + B_6^6 O_6^6 \quad (2.18c)$$

4. Orthorhombic symmetry:

$$H_{CF} = B_2^0 O_2^0 + B_2^2 O_2^2 + B_4^0 O_4^0 + B_4^2 O_4^2 + B_4^4 O_4^4 + B_6^0 O_6^0 + B_6^2 O_6^2 + B_6^4 O_6^4 + B_6^6 O_6^6 \quad (2.18d)$$

5. Hexagonal symmetry:

$$H_{CF} = B_2^0 O_2^0 + B_4^0 O_4^0 + B_6^0 O_6^0 + B_6^6 O_6^6 \quad (2.18e)$$

The effect of $H_{CF}$ is to further split the energy levels with a certain J. How the levels split depends on the angular momentum and the point symmetry of the crystal (or the surrounding medium in general), instead the magnitude of the splitting depends on the particular host [213]. These new energy levels are called *Stark components* [209,211]. Figure 2.8 shows a schematic diagram for the different Hamiltonian contributions and its order of magnitude (1 $cm^{-1}$ ~ 1.2 × $10^{-4}$ eV).

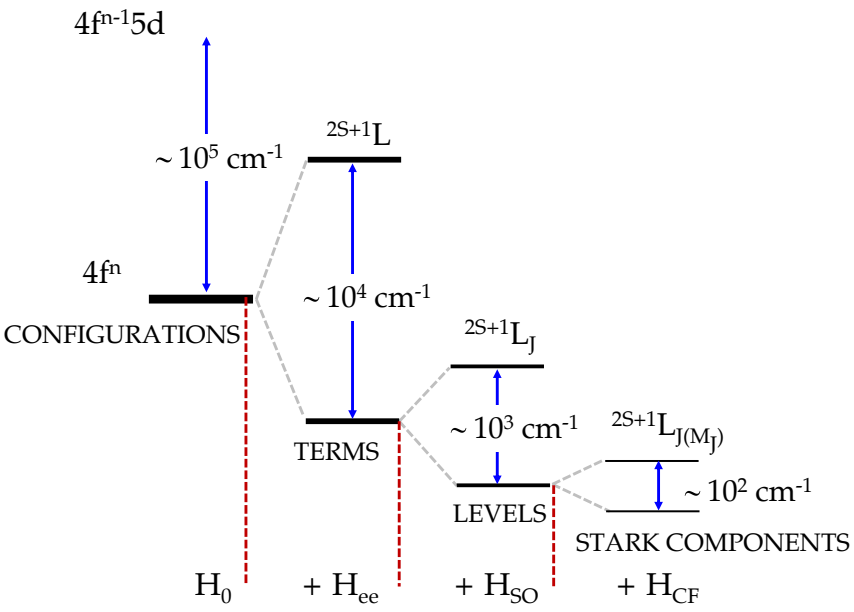


***Figure 2.8.*** *Schematic diagram and order of magnitude of the different interactions acting on a $4f^n$ configuration. Redrawn from* [211].

For example, we can observe in Figure 2.9 how the energy levels of $Nd^{3+}$ get modified when it is inside $LaF_3$ crystals. According to Carnall et al. [214], the coefficients $B_2^0$, $B_4^0$, $B_6^0$, $B_6^6$ for $Nd^{3+}$ in $LaF_3$ are 276, 1408, 1600 and 679 $cm^{-1}$,

respectively. In particular, Figure 2.10 shows in detail the Stark components for the $^4F_{3/2}$ and $^4I_{11/2}$ levels, responsible for the well-known $Nd^{3+}$ laser transitions.

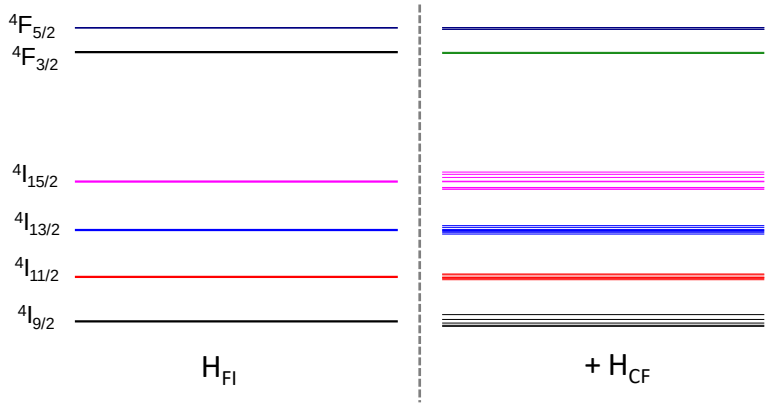


***Figure 2.9**. Effect of $LaF_3$ crystal field on the energy levels of $Nd^{3+}$. Data calculated from Carnall et al.* [214].

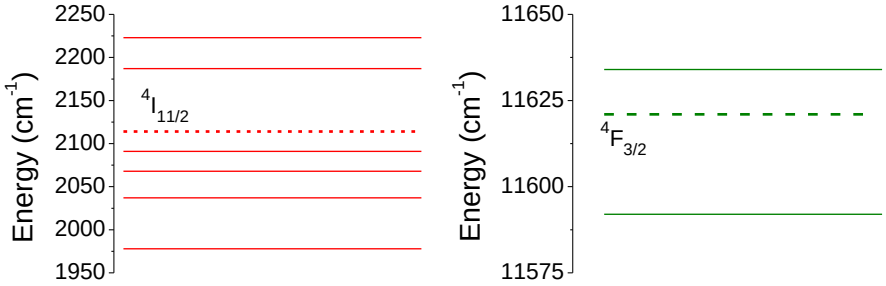


***Figure 2.10**. Detail of Stark components for the energy levels $^4I_{11/2}$ (left) and $^4F_{3/2}$ (right) of $Nd^{3+}$ in a $LaF_3$ crystal. The dashed lines indicate the energy levels in absence of crystal field.*

$H_{CF}$ described so far is the static part of the crystal field, however there is also the dynamic part that couples the electronic energy levels to vibrations [215]. In terms of luminescence, the dynamic component broadens emission lines into bands of varying widths and shapes. The Stark components of crystals are partially or well resolved at room temperature, depending on the phonon energy, and get sharper as the temperature is reduced. The Stark components for RE ions in glasses are not resolved because there is not point symmetry and ions placed in different sites of the glass matrix feel different crystal potential. For this reason, the optical spectra of RE ions in glasses are much broader than in crystals due to *inhomogeneous broadening*. Inhomogeneous line widths are essentially independent of temperature [215].

If we compare the energy levels of certain ions and the corresponding optical emission or absorption spectra, we can see that there are much less emission/absorption lines than energy levels. The absorption and emission of photons it is constrained by some selection rules that prohibit certain transitions. Such selection rules do not apply for example if thermal energy is given to the system. Selection rules for electromagnetic interaction takes into account the quantum numbers of the initial and final states, indicating whether a certain transition is allowed or forbidden.

The matter-radiation interaction Hamiltonian, in non-relativistic approximation, can be expressed as [216]:

$$H_{INT} = \sum_j \left[ -e\phi + \frac{1}{2m}\left(\mathbf{p_j} + e\mathbf{A}\right)^2 \right] \tag{2.19}$$

where $-e$ is the electron charge, m its mass, $\phi$ the scalar potential, $\mathbf{p}_j$ the momentum of the electron j and $\mathbf{A}$ the vector potential**.** Making a multipolar expansion, the following operators describe the interaction of the electromagnetic field with the electrons [209]:

$$\boldsymbol{\mu}_{ed} = -e\sum_j \mathbf{r}_j \tag{2.20}$$

$$\boldsymbol{\mu}_{md} = -\frac{e\hbar}{2mc}\sum_j\left(\mathbf{L}_j + 2\mathbf{S}_j\right) \tag{2.21}$$

$$\mathbf{Q}_{eq} = -\frac{1}{2}\sum_j(\mathbf{k}\cdot\mathbf{r}_j)\mathbf{r}_j \tag{2.22}$$

where c is the light speed, ħ is the reduced Planck constant and $\mathbf{k}$ the wave vector of the light wave. The operators $\boldsymbol{\mu}_{ed}$, $\boldsymbol{\mu}_{md}$ and $\mathbf{Q}_{eq}$ are the *electric dipole moment*, the *magnetic dipole moment* and the *electric quadrupole moment*, respectively. Both dipoles are first order interactions and the electric one is odd and the magnetic is even. The electric quadrupole is an even operator of second order (less strong interaction).

To determine if a certain transition occurs, the following matrix element between the initial and final state has to be calculated:

$$S(\alpha J, \alpha' J') = |\langle \alpha J|T^q|\alpha' J'\rangle|^2 \tag{2.23}$$

where $\alpha$ and $\alpha'$ include all the remaining good quantum numbers of the initial and final state and $T^q$ is a tensor operator, eqs. (2.20)-(2.22). The strength of a certain

transition is proportional to S($\alpha$ J,$\alpha$'J'), hence if this element is null the transition is forbidden, otherwise is allowed. A transition can be forbidden by a certain interaction mechanism (first order) but can be allowed by another one with different strength (second, third etc. orders). The *oscillator strength* is defined by:

$$f = \frac{8\pi^2 m\nu}{3he^2} S(J, J') \tag{2.24}$$

where ν is the frequency. If a transition is allowed, the coefficient of spontaneous emission can be calculated using the formula:

$$A_{JJ'} = \frac{4e^2\omega^3}{3\hbar c^3} n^3 \, S(\alpha J, \alpha' J') \tag{2.25}$$

where n is the refractive index of the medium and ω is the angular frequency (ω=2πν) of the J→J′ transition.

Laporte rule states that a dipole transition occurs if there is a parity change (Δl=±1), i.e., the initial and final states must have different parity. RE ions transitions between different electronic configurations, f→d, satisfies this condition. Moreover, for electrical dipole transitions $M(\alpha J, \alpha' J') \neq 0$ if $\Delta J = 0, \pm 1$.

Such transitions are much stronger than f → f transitions, the ones of interest for most photonic applications. In fact, intra-configuration transitions are forbidden to first order by electric dipole, but are allowed by *electric quadrupole*, *magnetic dipole* and *forced electric dipole* mechanisms. However, some authors showed that only the magnetic dipole and forced electric dipole mechanisms could account for the observed intensities [215]. However, not even the magnetic dipole mechanism can explain most of 4f-4f transitions in RE ions, because the selection rules are Δl=0 and ΔJ = 0,±1. For example, the $^4F_{3/2}$-$^4I_{11/2}$ transitions of $Nd^{3+}$ ions could occur neither by electric dipole nor by magnetic dipole mechanism. Moreover, the predicted strength of many transitions considered using a magnetic dipole interaction mechanism was quite smaller than the observed one.

An explanation of the possible mechanism underlying the electromagnetic transitions between 4f levels was given in 1962 by Judd [204] and Ofelt [205] that

treated the forced electric dipole mechanism in detail and, independently, reached an expression to describe the strength of transitions within 4f configuration. The Judd-Ofelt theory assumes that there is a certain mixing of wave functions of different parity. In particular, if there is not centre of inversion in the site occupied by the RE ions, the odd component of the crystal field $H_{CF}$(odd) is not null and mixes configurations with opposite parity [211].

Since $H_{CF}$ is a one-particle operator, the mixing can be: $4f^{n-1}nd$, $4f^{n-1}ng$ (for $n \geq 5$) and $n'd^{4d+1}4f^{n+1}$ ($d = 2$, $n' = 3$ and 4, corresponding to core excitations). In this case, the starting wave function is composed by the wave function of the total Hamiltonian ($H_{FI}$ +$H_{CF}$) plus a state with opposite parity which weight depends on $H_{CF}$(odd). For this new wave function J is not a good quantum number anymore and transition intensities between single Stark components can be calculated. However, if just the total integrated intensity between a J and J' level is desired, the following equation can be used to calculate electric dipole *line strength* [204,205,209,211]:

$$S_{ed} = \sum_{\lambda=2,4,6} \Omega_\lambda \left| \langle (4f^n) J \left| \mathbf{U}^\lambda \right| (4f^n)' J' \rangle \right|^2 \tag{2.26}$$

where $(4f^n)$ J and $(4f^n)$ 'J' are the wave function of the initial and final state in the case of intermediate coupling, $\mathbf{U}^\lambda$ is the irreducible tensor of the electric dipole operator and $\Omega_\lambda$ are the *Judd-Ofelt parameters*. The coefficient of spontaneous emission in this case becomes:

$$A_{JJ'} = \frac{4e^2\omega^3}{3\hbar c^3}\left[\frac{n(n^2+2)^2}{9} S_{ed} + n^3 S_{md}\right] \tag{2.27}$$

Other interesting parameters are the radiative lifetime $\tau_R$ and the branching ratio $\beta_{JJ'}$, defined by:

$$\frac{1}{\tau_R} = \sum_J A_{JJ'} \tag{2.28}$$

$$\beta_{JJ'} = \frac{A_{JJ'}}{\sum_J A_{JJ'}} \tag{2.29}$$

The Judd-Ofelt parameters give information about the chemical bonding of RE ions in solid host materials. For example, the parameter $\Omega_2$ is affected by covalent

bonding, while $\Omega_6$ is mostly related to the rigidity of the solid host in which the RE ions are situated [211].

To conclude this part, a mention to *hypersensitive transitions* is mandatory. They owe their name to the fact that they are exceptionally sensitive transitions and their intensity can vary strongly for different hosts [209]. In fact, when the electromagnetic radiation interacts with the matter, the oscillating electric field induces oscillating dipoles in the surrounding ligands with amplitude depending on the polarizability. This scheme is known as *dynamic coupling* [209,211]. As a consequence, the total electric field felt by RE ions has large electric gradients, thus promoting 4f-4f transitions with selection rules: $\Delta S=0$; $|\Delta L|\leq 2$; $|\Delta J|\leq 2$. These selection rules are the same as the ones for quadrupole transitions, but calculations have shown that their intensities are several orders of magnitude larger than the values expected for quadrupole transitions. Therefore, hypersensitive transitions are also called *pseudo-quadrupole transitions*. Once again, this interaction can be expressed in terms of $\mathbf{U}^{\lambda}$ operators and the hyperfine interactions are dominated by the $\mathbf{U}^2$ component. The intensity of a hypersensitive transition is vanishingly small when a RE ion occupies a pure centrosymmetric site and depends on the polarizability of ligands. Small departures from inversion site symmetry confer a relatively large intensity to hyperfine transitions while other 4f-4f transitions are virtually unchanged.

As example, the oscillator strength of the hyperfine transition $^4I_{9/2} \rightarrow {}^4G_{5/2}$ of $Nd^{3+}$ increases two orders of magnitude from $Nd^{3+}$ in $LaF_3$ to $NdI_3$ vapour [211]. Another interesting hypersensitive transition is the $^5D_0 \rightarrow {}^7F_2$ of $Eu^{3+}$, in particular, the ratio between this transition and the magnetic dipole transition $^5D_0 \rightarrow {}^7F_1$, called asymmetry ratio, gives a clear indication about the symmetry site of $Eu^{3+}$ ions [217].

### 2.9.2.Non-radiative de-excitation mechanisms

In the previous section, only reference to a radiative de-excitation mechanism was made, the radiative lifetime of a certain level being described by eq. 2.28. However, in many cases, a lower lifetime is obtained due to the interaction of RE ions with the vibrations of the host material. In fact, RE ions in solids can relax toward

lower energy levels by emitting phonons. The concept of phonon as a quantum of lattice vibration should be applied solely for crystals. In glasses, due to the absence of translational invariance, there is no a defined wave vector that can be associated to glass vibrations, anyway the term "glass phonons" is commonly accepted.

If the electronic levels are closely spaced (e.g., the Stark components of a multiplet), they can be bridged by one or two phonons and the transitions will occur rapidly [215]. The non-radiative decay rate, $W_{NR}$, is expressed by the following equation:

$$W_{NR} = Ce^{-\Delta E}[N(T) + 1]^p \quad (2.30)$$

where C and α are host-dependent parameters, ΔE is the energy gap between two levels, p is the number of phonons required to bridge that gap ($p = \Delta E/\hbar\omega_{ph}$) and N(T) is the occupation number for the effective phonon mode of angular frequency $\omega_{ph}$, described by the Bose-Einstein statistic [218]:

$$N(T) = \frac{1}{\exp\left(\frac{\hbar\omega_{ph}}{k_B T}\right)-1} \quad (2.31)$$

where $k_B$ is the Boltzmann constant. If the temperature is lowered, N(T) gets smaller and this corresponds to a reduction of thermal vibrations when a material is cooled down. Table 2.1 resumes C, α and $\hbar\omega_{ph}$ for some glasses and for $LaF_3$ crystals.

***Table 2.1.*** *Parameters describing the non-radiative relaxation of RE ions in some glass systems and in $LaF_3$ crystals. Adapted from* [215].

| Host | C ($s^{-1}$) | α ($10^{-3}$ cm) | ħω ($cm^{-1}$) |
|---|---|---|---|
| Borate | $2.9 \times 10^{12}$ | 3.8 | 1400 |
| Phosphate | $5.4 \times 10^{12}$ | 4.7 | 1200 |
| Silicate | $1.4 \times 10^{12}$ | 4.7 | 1100 |
| Germanate | $3.4 \times 10^{10}$ | 4.9 | 900 |
| Tellurite | $6.3 \times 10^{10}$ | 4.7 | 700 |
| $LaF_3$ crystal | $6.6 \times 10^{8}$ | 5.6 | 350 |

Non-radiative rates are generally much higher in glasses than in crystals of similar composition due to larger effective phonon frequencies (larger C) and stronger

electron-phonon coupling (smaller $\alpha$). If non-radiative processes are present, the lifetime is obtained by [215]:

$$\frac{1}{\tau} = A_{JJ'} + W_{NR} \quad (2.32)$$

The *homogenous broadening* of the emission bands is essentially caused by lifetime broadening. In fact, considering the Heisenberg energy uncertainty principle $\Delta E \Delta t \geq \hbar$, it is obtained that short living states are associated to broader spectra [215].

### 2.9.3. Energy transfer mechanisms

ET mechanisms are extremely important when RE ions concentration increases beyond a certain limit or when more than one kind of ions is present in the system. The ion directly excited is called *donor* or *sensitizer*, while the ion receiving this energy is called *activator* or *acceptor*.

The process can be a *radiative* or *non-radiative* ET (with or without the emission of photons) [215]. Radiative ET involves one ion emitting a photon that is reabsorbed by another ion. This process can cause modification of the band shape and produce longer lifetime, and this effect increases with the overlapping of absorption and emission bands of the ions.

On the other side, non-radiative ET between ions can also occur and such process is also responsible for the appearance of some interesting new optical phenomena. These interactions can be explained assuming a short-range *exchange interaction* (if there is overlap of wave functions of ions) or long-range electric interaction based on *multipolar* mechanisms [215]. According to Dexter [219], the possible mechanisms in order of decreasing strength are: the overlapping of the electric dipole fields of donor and acceptor, the overlapping of the dipole field of the donor with the quadrupole field of the acceptor, and exchange effects.

The rate of non-radiative ET between a donor (D) and an activator (A) can be expressed by [203,219]:

$$W_{DA} = \frac{2}{h} |\langle DA\ |H_{DA}|D'A'\rangle|^2 \int g_D(E) g_A(E) dE \quad (2.33)$$

where the integral gives the spectral overlap and the matrix element represents the interaction between the initial state $|DA\rangle$ and the final state $|D'A'\rangle$ due to the interaction Hamiltonian $H_{DA}$. The transfer rate $W_{DA}$ vanishes if there is not spectral overlap and the distance dependence resides in the interaction Hamiltonian. For example, for electric multipolar interaction the distance dependence is $R^{-n}$ (n=6, 8 or 10 for *electric dipole-electric dipole* interaction, for *electric dipole-electric quadrupole* interactions and for *electric quadrupole-electric quadrupole* interaction, respectively), being R the donor-activator distance [219]. This interaction has the classical counterpart based on ET between oscillating electric dipoles with distance dependence on $R^{-6}$ and $R^{-8}$. However, in this case no real photons are emitted. Instead, the exchange interaction is a quantum mechanical effect arising from the symmetry properties of the wave functions with respect to the exchange of spin and space coordinates of the electrons [219]. In fact, according to quantum mechanics, the initial electronic configuration of the donor can be exchanged with that of the acceptor without any multipolar mechanism. In this case, the distance dependence is exponential, since this interaction requires the overlap of the wave function for donor and acceptor.

Due to strong distance dependence of these interactions, Dexter concluded that the effect of "sensitization" can be extended to about $10^3$, $10^2$, and 30 lattice sites around each "sensitizer" for dipole-dipole, dipole-quadrupole and exchange interaction, respectively. An important point to keep in mind is that while multipolar interactions are constrained by selection rules depending on the levels involved and hence can vanish, the exchange interaction is not affected and it permits both allowed and forbidden transitions [219].

Another important point is that there are no restrictions about the number of steps involved for ET process. It can take the excitation energy far from the site where the absorption took place and this is known as *energy migration* [215]. This mechanism is useful for example in $Er^{3+}$-$Yb^{3+}$ co-doped materials, where $Yb^{3+}$ ions act as donors for $Er^{3+}$ ions. Quite higher $Yb^{3+}$ concentrations are commonly used with respect to $Er^{3+}$ to promote energy migration and reach $Yb^{3+}$ ions relatively close to $Er^{3+}$ ions such that ET can occur efficiently. However, when the concentration increases beyond a certain

value, the mean distance between the ions is reduced and there can be non-radiative losses before transferring the energy to the activator. Such phenomenon is called *concentration quenching* and the optical properties are strongly dependent on RE ions concentration [215]. Nevertheless, there is not an absolute value for concentration quenching: it depends on the host and the kind of ion.

When ET is present, there is an additional de-excitation mechanism and the lifetime is further reduced according to the following equation [215]:

$$\frac{1}{\tau} = A_{JJ'} + W_{NR} + W_{ET} \quad (2.34)$$

where $W_{ET}$ describes the ET rate.

Finally, ET processes require the absorption or emission of phonons for energy conservation when the transition energies for the ions involved are not resonant. The energy difference can be *provided by a phonon* if the initial state has lower energy, or *released to a phonon* in the opposite case [215].

*2.9.3.1. Up-Conversion*

UC has great interest for applications because it allows the conversion of excitation frequency to higher values. For example, IR radiation can be converted into Vis or UV depending on the energy levels of RE ions, the kind of host, and the number of steps involved in the process. This process is also known as Anti-Stokes process because it violates the well-known Stokes law for fluorescence light emitters which states that excitation photons are at a higher energy than emitted ones. Auzel made an extended review of the processes underlying the UC emission and the three main mechanisms are listed below [220].

1. *Excited State Absorption* (ESA). The excitation takes the form of successive absorption of pump photons by a single ground-state ion. Firstly, an ion is excited from the ground state G to an excited state $E_1$ and then, a second pump photon promotes the ion from $E_1$ to a higher excited state $E_2$. UC emission results in the radiative emission from $E_2$ to the ground state. This process can involve more than two excited states and the UC emission frequency can be increased further. To achieve

highly efficient ESA, a "ladder-like" arrangement of the energy levels is required, for example this is the case for $Er^{3+}$, $Ho^{3+}$ and $Tm^{3+}$ [221]. A scheme of this process is described in Figure 2.11a.

2. *Energy Transfer Up-Conversion* (ETU). This process involves two ions. A sensitizer, S, is first excited from the ground state to its metastable level, $E_S$, after absorbing a pump photon. Then S transfers its energy exciting the activator, A, to its upper state $E_1$, while S relaxes back to ground state $G_S$, Figure 2.11b. Then, A can be excited to $E_2$ by a second step ET and finally it decays radiatively to the ground state $G_A$ emitting UC emission. In this process, there is a strong influence on the RE ions concentration that affects the average distance. On the contrary, the ESA is not dependent on concentration involving one single ion. Anyway, the concentration cannot be increased too much because non-radiative losses can become important due to concentration quenching.

3. *Cooperative Up-Conversion* (CU). This is a process involving the interaction among three ions: two sensitizers S and one activator A. After irradiation with excitation photons, the two S ions can be excited to the excited state $E_s$. They simultaneously transfer their energy to A which is brought in the excited state $E_1$ and then A can decay radiatively to the ground state by UC emission, Figure 2.11c. The efficiency of this process is generally orders of magnitude lower than that of ESA or ETU, because it involves quasi-virtual levels, which are taken into account by quantum mechanics but at a higher order of perturbation hence with less probability.

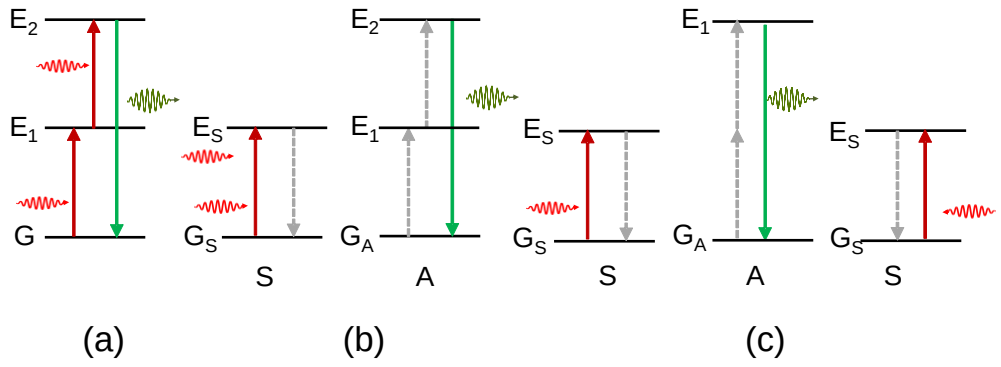


***Figure 2.11.*** *Up-Conversion processes: (a) Excited State Absorption (ESA), (b) Energy Transfer Up-Conversion (ETU), (c) Cooperative Up-Conversion (CU).*

The aforementioned processes can occur altogether but, as stated before, some processes are dominant with respect to others. An interesting feature of UC processes is that the emission intensity ($I_{UC}$) can be related to the incident, or pumping, intensity ($I_P$) by the following expression [222]:

$$I_{UC} \propto (I_P)^n \tag{2.35}$$

n being the number of photons involved in a certain UC process. By a logarithmic plot a straight line is obtained for each UC emission and the number of photons is obtained by the slope of the corresponding line.

*2.9.3.2. Down-Conversion*

The possibility to convert higher energy photons into ones with lower energy offers interesting applications. For example, one of the most interesting is related to increase the efficiency of photovoltaic solar cells by transforming UV photons into IR photons that are better absorbed by silicon solar cells [14].

The process can involve the production of one or more photons with lower energy. In the first case, the term Down-Shifting (DS) is used for the process that consists in the emission of one single photon of lower energy. The corresponding quantum efficiency is lower than one, due to nonradiative relaxations. Instead, the term DC or quantum-cutting (QC) is used to indicate the process in which more than one photon is emitted and the quantum efficiency can be higher than unity.

The first studies about the DC process were reported by Dexter in 1957, describing the possibility of "*photon-splitting*" that can produce quantum yields greater than unity [223]. As for the UC process, there are several possibilities to obtain DC emission, the most typical involving two RE ions, one acting as sensitizer (S) and the other as activator (A). However, there is also the possibility to split the incident photon into lower energy photons using only one kind of RE atom.

1. *DC with single ions*. This process was observed for $Pr^{3+}$ ions in $YF_3$ crystals [224]. The mechanism is schematically shown in Figure 2.12a, where the incident photon is converted into two lower energy photons.

2. *DC with ions pair*. This process was extensively described for $Pr^{3+}$-$Yb^{3+}$, $Pr^{3+}$ acting as sensitizer and $Yb^{3+}$ as activator. There are also other pairs used for DC as $Tb^{3+}$-$Yb^{3+}$ and $Tm^{3+}$-$Yb^{3+}$. One possibility is that S is excited by a high energy photon, then part of the energy is transferred to A and both ions emit, Figure 2.12b. Another very similar process involves the emission from S and ET to A that then emits, Figure 2.12c. There is also the possibility of two-ET from S to A followed by emission from A, Figure 2.12d and the last process involves the Cooperative ET (CET) from S to two A ions, Figure 2.12e.

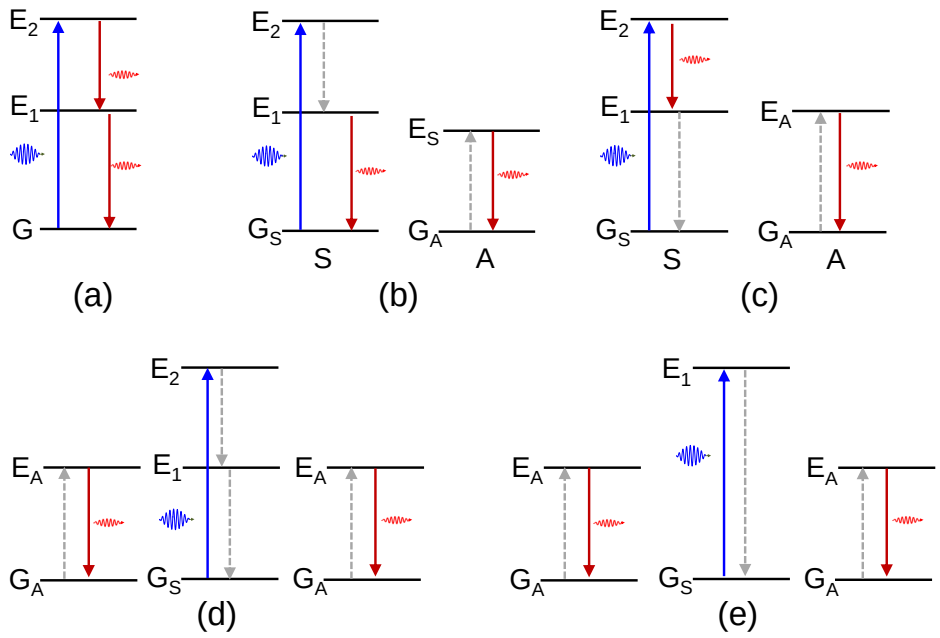


***Figure 2.12.*** *Down-Conversion processes (a) with single ion and (b)-(e) with ions pair.*

# *3. EXPERIMENTAL METHODS*

# 3. EXPERIMENTAL METHODS

In this section, a general overview of the synthesis and materials preparation is given together with the characterisation techniques used in this thesis. Materials characterisation was performed to evaluate the thermal, structural and optical properties and to correlate them with the different processing methods.

## 3.1. Materials preparation

### 3.1.1. Melt-quenching bulk materials and fibres

Glass compositions, listed in Table 3.1, were prepared by MQ method employing an electrical furnace in air atmosphere. The raw materials used were: $SiO_2$ (Saint-Gobain, 99.6%); $Al_2O_3$ (Panreac, 99.5 %), $Na_2CO_3$ (Panreac, > 99.5%), $K_2CO_3$ (Scharlab, 99.6%), $AlF_3$ (Alfa Aesar, 99.9%), NaF (Panreac, 99. 95%), $LaF_3$ (Alfa Aesar, 99.9%), $Lu_2O_3$ (Alfa Aesar 99.9%), $PrF_3$ (Alfa Aesar, 99.99%), $NdF_3$ (Alfa Aesar, 99.9%), $Nd_2O_3$ (Alfa Aesar, 99.99%), $ErF_3$ (Alfa Aesar, 99.99%), $Er_2O_3$ (Alfa Aesar, 99.99%) and $YbF_3$ (Alfa Aesar 99.99%). The $Al_2O_3$ powders were previously calcined at 800 °C during 12 h to remove $H_2O$.

Batches of 40-100 g of each composition were mechanically mixed for 60 min and then calcined at 1200-1300 °C during 1-2 h, using a Pt crucible covered with a cap, and then melted twice at 1550-1650 °C for 2 h. The melt was poured into a brass mould and the glass annealed at $T_g$+20-30 °C for 30 min.

Uncoated fibres of the 55Si10La composition doped with 0.1 and 2$NdF_3$ (mol%) were drawn using a prototype model, described in [225], a Pt crucible (with perforated bottom) heated by Joule effect, (see Figure 3.1a). Glass specimens were heated at 1100-1480 °C and fibres with different diameters (50-250 μm) were obtained by controlling the drawing speed. Thicker fibres (300-500 μm) were obtained using robber rolls rotating in opposite directions. A $SiO_2$ cladding was deposited on the glass-ceramic fibres using the SG method and following the synthesis described in the next section.

***Table 3.1.*** *Glass compositions used in this thesis.*

| | **55SLa10La** | | **70Si7LaK** | | **70Si6NaLu** | |
|---|---|---|---|---|---|---|
| **Components** | mol% | wt% | mol% | wt% | mol% | wt% |
| $SiO_2$ | 55 | 40.14 | 70 | 53.32 | 70 | 60.45 |
| $Al_2O_3$ | 20 | 24.77 | 7 | 9.27 | 5 | 7.33 |
| $Na_2O$ | 15 | 11.29 | | | 2 | 1.78 |
| $K_2O$ | | | 16 | 19.58 | | |
| $LaF_3$ | 10 | 23.80 | 7 | 17.82 | | |
| NaF | | | | | 18 | 10.86 |
| $AlF_3$ | | | | | 2 | 2.41 |
| $Lu_2O_3$ | | | | | 3 | 17.16 |

Optical fibres of the 70Si6NaLu composition doped with 0.5$ErF_3$ and 2$YbF_3$ (mol%) were prepared by the rod-in-tube method using the DURAN® glass as cladding material. Glass rods of 75 mm in length and with diameter of 10 mm were polished and placed in the DURAN® tubes obtained by drilling. The fibre drawing process was performed during a stage in the *Laboratory of Optical fibres Technology of the Bialystok University of Technology*. Fibres with core/cladding geometry of 1/2.5 and diameter of 150-250 μm were drawn at 1230 °C. A picture of the preform used for the drawing is shown in Figure 3.1b.

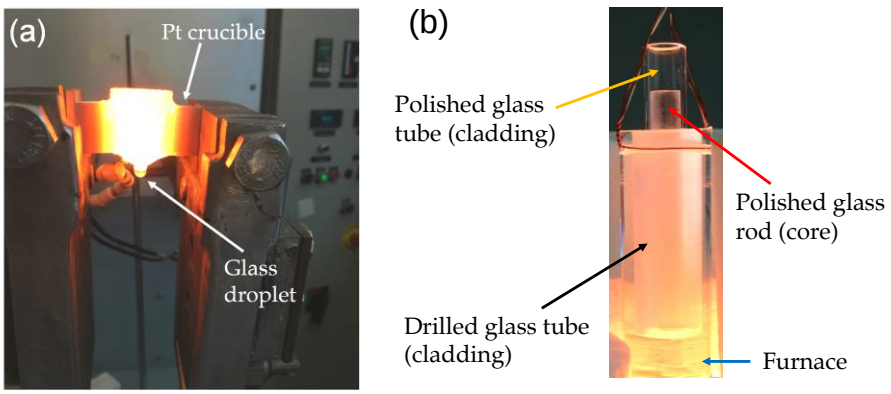


***Figure 3.1****. (a) System used for the preparation of uncoated fibres. (b) Preform used for fibres drawing with the rod-in-tube method.*

Glasses in bulk and fibre form were thermally treated at $T_g$+20-100 °C, using a heating rate of 10 °C/min, to obtain the corresponding glass-ceramics. The temperature

range used for crystallisation of different compositions goes approximately from 590 to 680 °C. Table 3.2 summarises all the doped-compositions studied in this thesis.

***Table 3.2.*** *Doped and co-doped compositions prepared as bulk materials and fibres (*). For singly doped-materials the dopant amounts are separated by a comma. For co-doped compositions different dopants are in the same column.*

| | **55SiLa10La**  | | **55SLa10La**  | | **55SiLa10La**  | | | **70Si7LaK**  | **70Si6NaLu**  |
|---|---|---|---|---|---|---|---|---|---|
| **Dopants** | mol% | | mol% | mol% | mol% | | | mol% | mol% |
| $PrF_3$ | 0.1 | 0.5 | | | | | | | |
| $NdF_3$ | | | 0.1*,0.2, 0.5,1, 2* | | | | | 0.1, 0.5, 1, 2 | |
| $Nd_2O_3$ | | | | 0.05, 0.5 | | | | | |
| $ErF_3$ | | | | | 0.1 | 0.5 | | | 0.5* |
| $Er_2O_3$ | | | | | | | 0.05 | | |
| $YbF_3$ | 0.5 | 1 | | | | 2, 4 | | | 2* |

3.1.2.Sol-gel bulk materials and thin films

Sols of compositions (100-x)$SiO_2$-x Active Phase, (x=10,20 mol%) were prepared by SG using the alkoxide route in acid conditions. High quality precursors were used: tetraethyorthosilicate (TEOS 98%, Sigma Aldrich ), Triethoxymethylsilane (MTES 98%, abcr), Lanthanum acetate (99.9 %, Sigma Aldrich), Gadolinium acetate (99.9% Alfa Aesar), Potassium acetate (99.0% Sigma Aldrich), Neodymium acetate (99.9% Alfa Aesar), Europium acetate (99.9% Sigma Aldrich), Erbium acetate (99.9% Alfa Aesar), trifluoracetic acid (TFA > 99%, Sigma Aldrich), absolute ethanol (99.9%, VWR), acetic acid (100%, Merck) andd hydrochloric acid (37%, abcr). The precursor molar ratios together with the different compositions are described in Table 3.3.

The synthesis was performed in two-steps: 1) a $SiO_2$ sol was prepared using TEOS or TEOS-MTES, ethanol and $H_2O$ 0.1M HCl to produce the hydrolysis; 2) an acetate dissolution containing all the active phase precursors and dopants, together with TFA and ethanol, was prepared and maintained at 40 °C for at least 2 h. A simple scheme for the SG synthesis is shown in Figure 3.2.

***Table 3.3.*** *Composition of the sols prepared in thesis together with the precursor molar ratios for thin films or bulk materials.*

| | $SiO_2$-$LaF_3$ Thin films | | $SiO_2$-$LaF_3$ Bulk | | $SiO_2$-$GdF_3$ Bulk | $SiO_2$-$KLaF_4$ Thin films |
|---|---|---|---|---|---|---|
| **$SiO_2$-Sol** | | | | | | |
| TEOS | 1 | 0.4 | 1 | 0.4 | 0.4 | 0.4 |
| MTES | | 0.6 | | 0.6 | 0.6 | 0.6 |
| Ethanol | 9.5 | 2.5 | 3 | 3 | 3 | 2.5 |
| $H_2O$ 0.1M HCl | 2 | 1 | 2 | 2 | 2 | 1 |
| $CH_3COOH$ (optional) | | 0.2 | | | 0.5 | 0.2 |
| **Acetate dissolution** | | | | | | |
| La(ac) | 1 | 1 | 1 | 1 | | |
| Ethanol | 5 | 5 | 8 | 8 | 8 | 5 |
| TFA | 5 | 5 | 5 | 5 | 5 | 5 |
| Gd(ac) | | | | | 1 | 1 |
| K(ac) | | | | | | 0.95 |

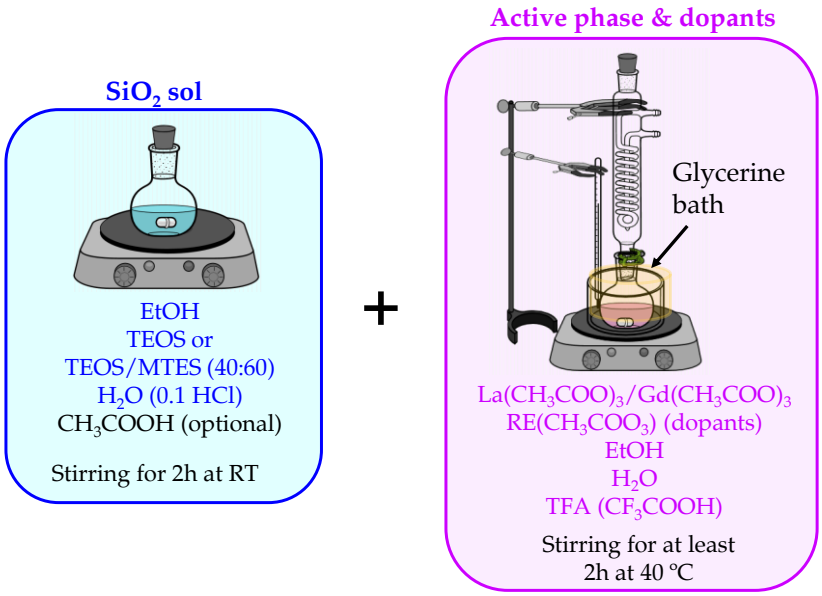


***Figure 3.2****. Scheme of the two-step synthesis used for the preparation of SG materials.*

The total $H_2O$ used in the synthesis of the sol was divided in two parts: one was added to the $SiO_2$ sol and the remaining to the acetate dissolution. Then, the corresponding acetates dissolution was added to the $SiO_2$ sol and stirred for at least 2 h to obtain the desired composition. The total $H_2O$:TEOS or $H_2O$:(TEOS+MTES) molar ratios (mol. %) was varied between 1.8-2.5 for thin films and 7.5-10 for bulk samples.

The doped-compositions are listed in Table 3.4, indicating if the synthesis was prepared using TEOS or TEOS-MTES.

Thin films were deposited by dip-coating onto Si and glass substrates using withdrawal rates in the range of 10-35 cm/min and then heated from 350 to 850 °C using a heating rate of 10 °C/min.

On the other hand, bulk samples, or self-supported layers were obtained by pouring 5-6 ml of the mix in a plastic container and dried at 50 °C for ten days or two weeks. Then, samples prepared with TEOS were sintered in the range 350-750 °C using a heating rate of 1 °C/min, while for TEOS/MTES samples the heating rate was increased to 10 °C/min and the maximum temperature used was 550 °C.

***Table 3.4.*** *(100-x)$SiO_2$-x active phase (x=10, 20 mol%) doped compositions used in this thesis. The headers indicated if the sol was prepared with TEOS or TEOS-MTES.*

| | **90-10/80-20 $SiO_2$-$LaF_3$ Thin films** | | **90-10/80-20 $SiO_2$-$LaF_3$ Bulk** | | **90-10/80-20 $SiO_2$-$GdF_3$ Bulk** |
|---|---|---|---|---|---|
| **Dopants** | TEOS | TEOS-MTES | TEOS | TEOS-MTES | TEOS-MTES |
| Nd(ac) | 0.5,2,3 | | 0.5, 3 | | |
| Eu(ac) | | | | | 0.5 |
| Er(ac) | | 0.5 | | 0.1, 0.5 | |

### 3.1.3.Sol-gel cladding for optical fibres prepared by melting

A $SiO_2$ sol was also prepared to cover the glass and glass-ceramic fibres of the 55Si10La composition described in the previous section. TEOS, MTES and a colloidal silica suspension (Ludox-AS 40, Sigma Aldrich, aqueous suspension 40 wt%, particle size 20 nm, pH 9) were mixed and concentrated nitric acid (65%, VWR) was added under vigorous stirring to induce hydrolysis and condensation reactions. This reaction is very exothermic and the sol needs to be kept in ice bath to control the reaction. Finally, absolute ethanol was added to obtain a $SiO_2$ concentration of 170 $gL^{-1}$. The final molar ratio of the silica sol was 1(TEOS + MTES):0.5Ludox:2.7EtOH. The fibres were coated and heated at 450 °C during 1 h.

### 3.2. Density

The density of liquid sol was obtained by weighting 1 ml of liquid in a precision balance.

The Archimedes method was used for bulk samples prepared by MQ. Firstly, the bulk sample was weighted in air (P), then the system (balance + sample) was tared and the sample placed in a liquid of known density ($\rho_L$) to obtain the buoyant force (A). During the measurements, the temperature of the liquid was measured with a thermometer. The density of the sample (ρ) was obtained by the formula:

$$\rho = \frac{P}{A}\rho_L \tag{3.1}$$

The ρ of glasses and glass-ceramics of the 55Si10La and 70Si7LaK compositions were measured using an analytical balance (A&D GR 200-EC) with sensibility of 0.0001 g. Distilled $H_2O$ was used as reference liquid and its density values at different temperature obtained from the Handbook of Chemistry and Physics [226]. Three measurements were performed for each sample to obtain a standard deviation.

### 3.3. Viscosity of the sols

The viscosity (η) is one of the most important parameters in the dip-coating process, since the thickness of the films is proportional to η, as described by the following equation [227]:

$$t = 0.94\frac{(\eta v)^{2/3}}{(\gamma_{LV})^{1/6}(\rho g)^{1/2}} \tag{3.2}$$

where $v$ is the withdrawal rate, ρ is the density, $\gamma_{LV}$ is the liquid-vapor surface tension and g the acceleration of gravity.

Furthermore, the hydrolysis and polycondensation reactions depend on several parameters such as: type of precursor, $H_2O$/alkoxide molar ratios, etc. and all affect to the viscosity [227,228]. To obtain homogenous coatings is necessary to control that the values of η remain between 2 and 5 mPa.s. On the other hand, the sol stability (variation of η with time) is important for all industrial applications.

The measurements of viscosity were performed, for the $SiO_2$-$LaF_3$ and $SiO_2$-$GdF_3$ sols aged at room temperature and at 5 °C during two months, using a vibro-viscometer SV-1A (A&D company). Calibrations were performed using distilled $H_2O$. Since the equipment measures directly the static viscosity, that is the product of density (ρ) and viscosity, the values of η were obtained by dividing the measured values for the density. Errors were calculated by standard deviation from three measurements.

### 3.4. X-Ray Fluorescence Spectroscopy

The knowledge of the chemical composition of the materials is an important factor to assess the loss of compounds after its preparations. XRF is one of the best analytical methods for this scope. When the electrons of the inner shells of atoms or ions are excited, the energy emitted by higher energy electrons that occupy lower energy levels is emitted in the form of X-Rays. Each atom or ion produces a *characteristic spectrum* that is detected with a spectrometer.

The measurements were performed on glasses of the 55Si10La and 70Si7LaK compositions using a Magic X 2400 (PANalytical) spectrometer. For the analysis, 0.3 g of sample were mixed with 5.5 g of lithium tetraborate ($Li_2B_4O_7$) and melted at 1100 °C to prepare the beads [229]. The quantification was performed using the IQ+ software (PANalytical).

### 3.5. Thermal characterisation

Thermal analysis corresponds to the group of techniques in which a physical property of a substance and/or its reaction products are measured as a function of temperature while the substance is subjected to a controlled temperature program. According to this definition such characterisation has to fulfil three conditions [230]:

1. It has to measure a physical quantity.
2. The measurement must be expressed - directly or indirectly - as a function of the temperature.

3. The measurement has to be performed using a controlled temperature program.

Thermal transformations change the materials altering one or more of its properties [231]. The change may be physical such as melting, crystalline transition or vaporisation, or chemical where reactions alter the chemical structure of the material. In the next sections, the most important techniques used for thermal characterisation are described.

### 3.5.1. Dilatometry

Thermodilatometry, or simply dilatometry, is a technique used to determine the coefficient of thermal expansion of a specimen from the relationship [232]:

$$\alpha = \frac{1}{l_0}\frac{dl}{dT} \tag{3.3}$$

where $\alpha$ is the CTE, $l_0$ is the initial length of the sample and dl/dT is the derivative of the change of length with temperature (i.e the slope of the line tangent to the curve). It is important to remark that the previous definition refers to a single temperature. However, for practical purposes, the most general definition is related to the *mean or average CTE* given by ASTM [232]:

$$\alpha_m = \frac{1}{l_0}\frac{l}{\Delta T} \tag{3.4}$$

Here, $\alpha_m$ is the slope of the straight line between two points on the curve representing the expansion over a particular temperature range from $T_1$ to $T_2$ ($\Delta T=T_2-T_1$). The SI unit of CTE quantity is $K^{-1}$ but in many cases the results are expressed in $°C^{-1}$. Most of glasses have a CTE in the range 0.5-20 $\times 10^{-6}$ $°C^{-1}$.

CTE, glass transition temperature ($T_g$) and dilatometric softening ($T_d$) points are essential parameters for the characterisation of glass materials and all can be obtained by dilatometry measurements. For glasses, the main effects on the CTE variation are associated with the thermal history and the chemical composition. Considering that the CTE of a glass is an additive physical quantity, it can be calculated by a weighted average of the CTEs of the single components (in mol%):

$$\alpha = \frac{\sum_i p_i \alpha_i}{100} \tag{3.5}$$

The corresponding $\alpha_i$ of some typical glass components can be consulted in [233].

One of the most used methods for thermal expansion measurement is the mechanical dilatometry based on the pushrod method in horizontal configuration. A typical configuration consists on a closed tube, in which the specimen is placed, in contact with the reference, and a rod runs down the axis of the tube when the sample expands. This configuration is sometimes called *differential dilatometer* [232].

In Figure 3.3 a typical dilatometric curve for a glass studied in this thesis is given. In the first part, the straight line from low temperature $T_1$ up to $T_2$ is due to the glass sample expansion. The linear region is where the glass still maintains its rigidity. After $T_2$ there is a slight deviation from linearity that becomes relevant from $T_i$ up to $T_f$ and corresponds to the glass transformation region being $T_i$ and $T_f$ the initial and final annealing points; the intersection of the tangents in $T_i$ and $T_f$ gives the $T_g$. The next linear region with bigger slope is due to the glass visco-plastic regime and the maximum of the curve gives the dilatometric softening point $T_d$.

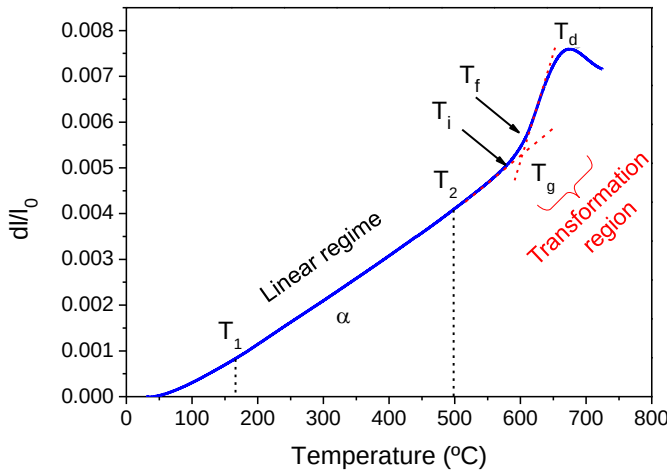


***Figure 3.3.*** *Dilatometric curve with the corresponding CTE, $T_g$ and $T_d$.*

Glass samples of the 55Si10La and 70Si7LaK compositions, with a length between 9-14 mm, were heated in the range 25-700 °C at a heating rate of 5 °C/min using a NETZSCH dilatometer. A calibration or correction curve is applied using $Al_2O_3$ as reference material to compensate the expansion of the measuring system. The detection

system stops the measurement at temperatures slightly higher than the dilatometric softening point $T_d$. The software used for data analysis is the NETZSCH Proteus® Software.

### 3.5.2. Differential Thermal Analysis and Thermogravimetric Analysis

Differential thermal analysis (DTA) is based on recording the temperature of a sample with respect to a thermally inert reference material when both are heated or cooled in a controlled atmosphere and following a specific heating programme, as for example a constant heating rate. The temperature difference between sample and reference due to the exothermic or endothermic processes is measured. Exothermic processes can be: crystallisation, oxidation, adsorption etc. and endothermic processes can be melting, phase transformation, dehydration, most of decomposition reactions etc. Similar to DTA is DSC (differential scanning calorimetry) where the instrument registers the heat released or absorbed by the sample with respect to a reference material [230].

In Figure 3.4 an example of DTA curve for a glass that undergoes crystallisation is given. The glass transition temperature ($T_g$), the beginning ($T_x$) and maximum ($T_p$) crystallisation temperatures, and the melting temperature ($T_m$) are shown. When more than one crystallisation peak is present, the terms primary, secondary etc. are used.

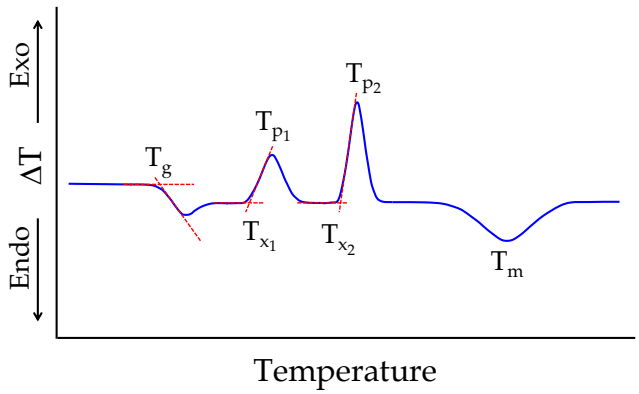


***Figure 3.4.*** *Example of DTA curve for a glass composition that presents two crystallization peaks.*

The measurement is affected by the instrument and the sample. The most relevant instrument factors are: the type of gas atmosphere and heating rate. A different

atmosphere can inhibit certain processes, for example oxidations are detected in air atmosphere but not in inert atmosphere.

The heating rate is a very important parameter in DTA and DSC which can be easily modified to obtain additional information. An increase of the heating rate generally shifts the position of $T_g$, $T_x$ and $T_p$ towards higher temperatures. As studied by Kissinger [234,235], the shifting of the peak with the heating rate provides information about the activation energy of a kinetic process. Furthermore, increasing the heating rate the peak area also increases when the temperature difference is plotted against temperature. Nevertheless, when the temperature difference is plotted against time the area does not change. The use of high heating rates (20-40 °C/min or higher) amplifies the DTA signal and small effects, that are not visible for standard heating rates (5-10 °C/min), can be detected. Thereby, recording DTA curves at different heating rates allows the crystallisation process of certain materials such as glass-ceramics to be estimated. A detailed theoretical description can be found in [236–243]. A schematic representation of the change of the crystallisation area with the heating rate (q) and the shifts towards higher temperature is schematically represented in Figure 3.5. The red dashed area is proportional to the sample amount that has crystallised at a fixed temperature T (black dashed line).

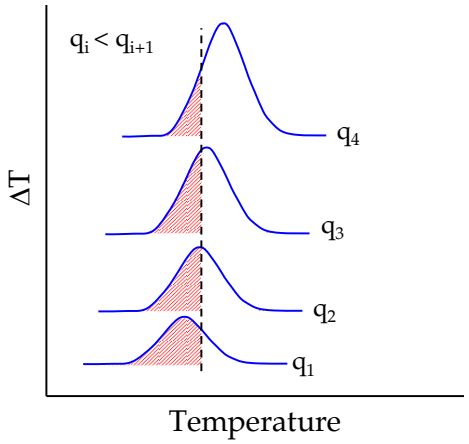


***Figure 3.5.*** *Schematic representation of the increase of the heating rate for a certain crystallisation process.*

Regarding the sample properties, mass, size and shape can strongly affect the measurement. Indeed, the signal area is proportional to the sample mass, whereas the form and size of the sample (powder, bulk specimens) affect the thermal conductivity.

Besides, the signal shape can be different for bulk (> 1 mm) or powder samples because some reactions or processes can be modified. For example, for powder samples, the crystallisation is enhanced when surface crystallisation is dominant.

Thermogravimetric analysis (TGA or TG) is another thermal analysis technique that determines the loss or gain of weight as a function of temperature. Such measurement provides additional information to study exothermic or endothermic processes for specific phenomena. Many instruments are prepared to detect simultaneously DTA/DSC and TGA to provide a better comprehension of the thermal processes involved. For example, during the glass transition process, which is an endothermic phenomenon, the sample mass is not affected, but during dehydration (endothermic process) there is a mass loss.

An example of TGA curve is given in Figure 3.6 where a first weight loss $\Delta w_1 \sim 20\%$ is followed by a bigger weight loss $\Delta w_2 \sim 55\%$.

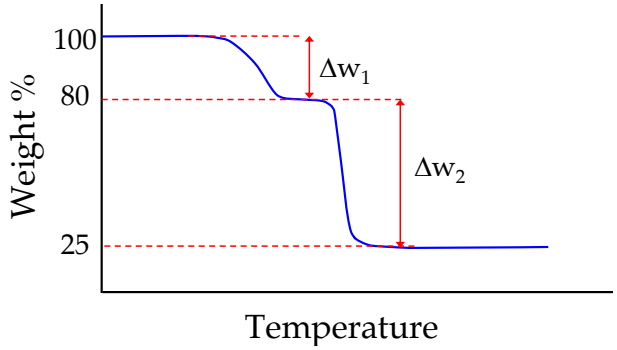


***Figure 3.6.*** *Example of a TGA measurement with two weight losses.*

Sometimes, the derivative of the TGA curve is calculated to extract further information. Moreover, the peak area of the derivative curve is proportional to the mass loss corresponding to certain phenomena. If a thermobalance is coupled to sample and reference, the TGA curve can be acquired together with the DTA/DSC measurement.

In this thesis, a SDT Q600 - TA Instruments was used to obtain simultaneously DTA and TG curves. This instrument uses alumina as reference material.

Parameters used for MQ materials

The measurements were performed on bulk specimens of 55Si10La composition with size of 1-1.25 mm using heating rates from 10 up to 60 °C/min. Fibre specimens with diameter of 200-250 μm were also analysed using heating rates up to 80 °C/min. All the measurements were performed in air using 20-30 mg of sample and varying the temperature from room temperature (RT) up to 1000 °C.

Parameters used for SG materials

Bulk specimens (gels) of $SiO_2$-$LaF_3$ and $SiO_2$-$GdF_3$ compositions were heated from RT up to 1250 °C using heating rates from 10 to 50 °C/min. Powder samples with particle size less than 60 μm were also analysed using the same conditions of bulk samples. In all cases, the curves were measured using 20-30 mg of sample in air and Ar atmosphere.

### 3.5.3. Hot-stage Microscopy

Hot-stage microscopy (HSM) is a technique used to measure the change of shape of a sample, normally powdered sample, when is heated. The sintering and flow behavior of glass powders can be monitored as a function of temperature. Sintering and flowing points correspond to specific viscosity values, as described in [244]. Typical viscosity points, corresponding to different processes, are shown in Table 3.5. This technique permits information of glass viscosity to be obtained using quite small sample amounts (< 1 g) and in a very fast way.

***Table 3.5**: Characteristic viscosity points obtained by HSM.*

| | **Shape** | **$\log \eta \pm \sigma$ (dPa.s)** |
|---|---|---|
| **Viscosity point** | | |
| First shrinkage |  | $8.9 \pm 0.3$ |
| Maximum shrinkage |  | $7.9 \pm 0.2$ |
| Softening point |  | $6.6 \pm 0.1$ |
| Half ball |  | $4.5 \pm 0.1$ |
| Flow point |  | $3.1 \pm 0.2$ |

In this thesis, the viscosity values of 55Si10La and 70Si6NaLu compositions were measured by an EM-201 picture analysis heating microscope (or optical dilatometer, Hessen Instrument). The instrument is equipped with an image analysis system and an electrical furnace with maximum temperature of 1600 °C. The software analyses the sample geometry during heating, and determines the percentage of decrease in height, width and area of the sample respect to its initial shape. The measurements were conducted in air at heating rates of 5 °C/min using powder glass samples (< 60 μm) and alumina supports.

### 3.6. Structural characterisation

The structural characterisation of materials gives information about the nature, (amorphous or crystalline for solids); the homogeneity at the micro/nanoscale, the kind of crystal phases and crystal sizes; the atomic bonds and the local atomic surroundings. All this information is necessary when certain properties (electrical, chemical, optical, etc.) of the material are determined by few atomic species, such as dopants, and their local surrounding.

Most structural characterisations in materials science are based on techniques that use or detect X-rays. These techniques give information about the atomic arrangement and local surrounding at the nanoscale. XRD provides information about periodic atomic structures (crystals). Instead, XAS allows the valence state of a certain ion and its local surrounding to be studied.

Another fundamental technique is TEM that produces electron micrographs at the micro/nanoscale. Sometimes TEM are coupled to EDXS spectrometers, making possible to study the chemical composition at the nanoscale.

The detection of mid or far infrared absorption provides information about molecular vibrations that are associated to specific bonds in a specific compound.

Finally, techniques based on magnetic spectroscopy of nuclei or electrons are very powerful tools for the detection of the local surrounding of specific ions.

Concluding, there is no one single technique that can simultaneously provide a complete description of the material structure; therefore, the combination of different techniques is indispensable when both global and local information are desired. In the next paragraphs, the most important techniques used in this thesis for structural characterisation are described.

### 3.6.1.X-Ray Diffraction

XRD is the most important technique to obtain information about crystal structure, as phase, lattice constants etc. Waves scattered by atoms placed in different atomic planes with distance d will be in phase, and hence they will interfere constructively, when the Bragg law is satisfied [245]:

$$2d \sin\theta = n\lambda \tag{3.6}$$

where θ is the incident angle (the angle between incident ray and the scatter plane), λ is the X-ray wavelength, d is the plane distance and n is an integer number, called the diffraction order, that is equal to the number of wavelengths in the path difference between diffracted X-rays. When such condition is satisfied, *diffraction maxima* or peaks are observed at different angles depending on the atomic distances. A schematic representation of the Bragg law is given in Figure 3.7.

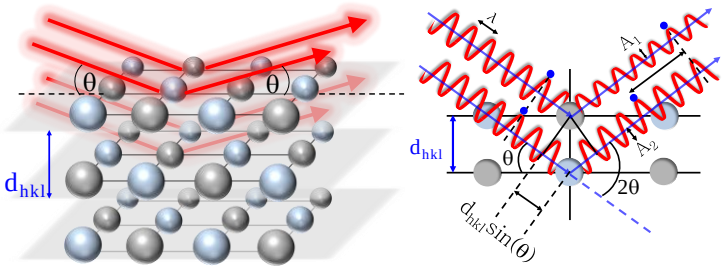


***Figure 3.7**. Sketch of Bragg law. Constructive interference is obtained when the phase difference of the scattered waves is an integer number of wavelengths. The blue point is a guide for the eye. In general, two different atoms scatter X-rays with different intensities ($A_1$ and $A_2$ are the corresponding amplitudes).*

For polycrystalline materials, the most common XRD technique consists in measuring the intensity of X-rays scattered as a function of the scattering angle (2θ) using a powder sample. A BRUKER D8 Advance powder diffractometer (θ-2θ

configuration) using the CuK$\alpha_1$=1.54056 Å radiation and equipped with a LYNXEYE-detector was used Figure 3.8. The identification of crystal phases was carried out using the DIFFRACplus EVA software which allows the diffractograms to be compared with standard XRD patterns (JCPDS or ICDD).

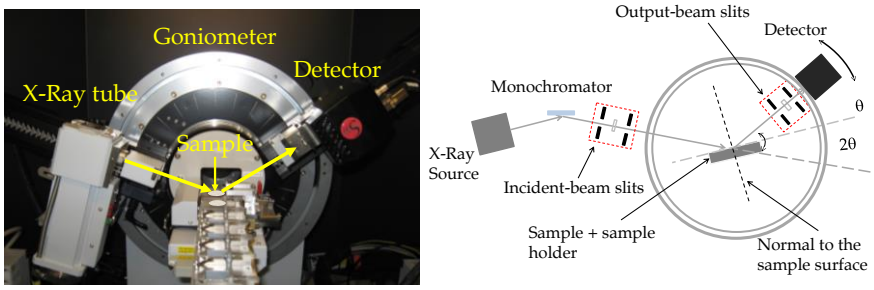


***Figure 3.8.*** *(Left) Picture of the Bruker D8 ADVANCED and (right) a simple scheme.*

The crystal size D was obtained by the Scherrer equation [246]:

$$D = \frac{0.94\lambda}{\cos\theta\sqrt{B_m^2 - B_i^2}} \tag{3.7}$$

where $\lambda$ is the X-ray wavelength, $\theta$ the Bragg angle of the diffraction peak, $B_m$ the full width at half maximum (FWHM) and $B_i$ is the instrumental broadening. $B_m$ and $\theta$ were obtained by a Pseudo-Voigt fit of the diffraction peaks.

Powder samples of glasses and glass-ceramics obtained by MQ (55Si10La, 70Si7Lak and 70Si6NaLu) and SG ($SiO_2$-$LaF_3$ and $SiO_2$-$GdF_3$) were milled to a particle size less than 60 μm and characterised by XRD. The angular range was 10-90 °, the step size 0.02-0.03 ° and the acquisition time varied between 1 and 3 s per step. When XRD experiments were performed using synchrotron radiation, the XRD patterns were acquired in similar angular ranges.

Rietveld refinement [247] was performed on 55Si10La and $SiO_2$-$LaF_3$ glass-ceramics to obtain information about crystal size, lattice parameters and crystal fraction. The quantification of the crystal fraction was performed by mixing a reference material (NaF) to the sample and using acetone to ensure good homogeneity. Then, the mix was dried at 60 °C. The real crystal fraction, $W_{phase}$, is obtained by the equation [56]:

$$W_{phase} = \frac{(W_{phase})_{RR} W_{std}}{(W_{std})_{RR}} \quad (3.8)$$

where $W_{std}$ is the real amount (wt%) of reference material, $(W_{std})_{RR}$ and $(W_{phase})_{RR}$ are the crystal fraction of standard and crystal phase obtained by the Rietveld refinement using the FullProf program [248].

Thin films of the $SiO_2$-$LaF_3$ composition, prepared by SG and deposited onto Si-wafer (111), were analysed in the angular range 10-70 ° using a Panalatycal X'per PRO working in grazing incidence (GI-XRD) configuration, incidence angle of 0.5 °. Some measurements were also performed using the GI-XRD of the BM25B-SpLine (ESRF).

### 3.6.2.Small Angle X-Ray Scattering

SAXS is an X-Ray technique that permits the structure of materials on a bigger scale to be studied. The basics of this technique are obtained considering the Bragg equation, eq. (3.6). The angle at which X-rays diffract varies inversely with the d spacing between atomic planes. Therefore, small spacing will produce signals at big angles. In crystals, the d-spacing is of the order of magnitude of the X-rays wavelength (0.5-5 Å), hence all the information scattered at very small angles (< 2 °) cannot be recorded by XRD. The scattered intensity measured in a SAXS depends on the size, form and electron density of such heterogeneities or particles [249].

SAXS can be applied to a large variety of samples in which heterogeneities should be studied. For example, in glass and glass-ceramic samples, phase separation and crystals can be observed by SAXS. If the electron density of one kind of heterogeneities is the most relevant, a "two-phase" approximation is postulated, considering an almost homogenous sample (phase 1) with scattering centres (phase 2). The scattering intensity increases with the electron density difference, called *contrast*.

A simple graphic relating the amplitude of the scattering vector (q) with the particle size (D) is given in Figure 3.9. For a certain angle (or scattering vector q), SAXS detects electron density fluctuations with sizes D~1/q, therefore, during a SAXS measurement the sample is analysed using variable "windows" with sizes inversely

proportional to q. Whenever an electron density contrast exists in a spatial region, a scattering signal at a corresponding q value will be produced.

Glass and glass-ceramic samples of the 55Si10La composition (bulk and fibres) were milled and pressed into pellets. The instrument used for the measurements is a commercial SAXSess, table-top system manufactured by Anton Paar, GmbH shown in Figure 3.10. A Cu $K\alpha_1$ line beam $\lambda$=1.54 Å (10 mm x 0.4 mm) was used and the scattered intensity, in the q range 0.01-0.1 Å, was recorded with an imaging plate. The 2D pattern was converted into 1D pattern and analysed with the Irena software to obtain the particle size distribution of phase separation droplets and crystals. The SAXS measurements of this thesis were performed in collaboration with Prof. Gang Chen from the Ohio University.

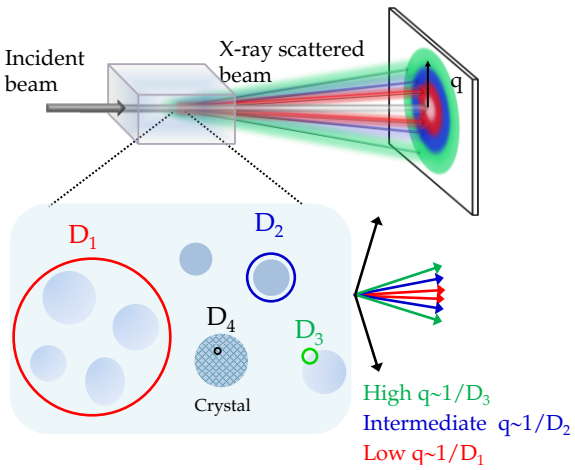


***Figure 3.9.*** *Sketch of SAXS experiment that can be thought as a way of looking at the material structure with "windows" of variable size D. If in a "window" of size D there are density fluctuations, the scattering is produced at q~1/D.*

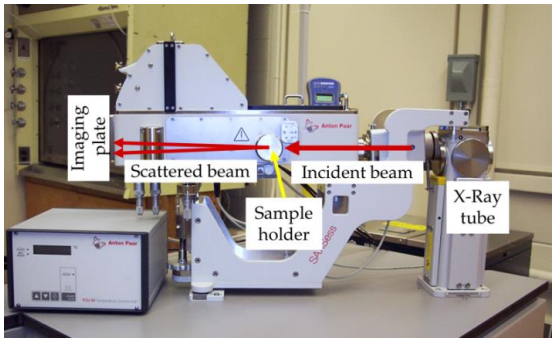


***Figure 3.10****. Instrument used for SAXS measurements (SAXSess, Anton Paar GmbH).*

### 3.6.3.X-Ray Absorption Spectroscopy

XAS provides information about the valence state of atomic specie and its local surrounding. When an incident X-rays beam interacts with matter, part of it is absorbed and other transmitted. The transmitted intensity, after passing a sample of thickness x and *linear attenuation coefficient* μ, is given by the Lambert-Beer law [250]:

$$I = I_0 e^{-\mu x} \tag{3.9}$$

Depending on the energy of the incident photon, electrons from inner K, L etc. shells can be excited to unoccupied levels. The absorption edges are labelled with the symbols given in Table 3.6 according to the inner electronic levels involved in the transitions.

***Table 3.6.*** *High energy edges and their corresponding core levels. Adapted from* [250].

| Edge | $M_V$ | $M_{IV}$ | $M_{III}$ | $M_{II}$ | $M_I$ | $L_{III}$ | $L_{II}$ | $L_I$ | K |
|---|---|---|---|---|---|---|---|---|---|
| Core level | $3d_{5/2}$ | $3d_{3/2}$ | $3p_{3/2}$ | $3p_{1/2}$ | 3s | $2p_{3/2}$ | $2p_{1/2}$ | 2s | 1s |

A typical XAS spectrum of an $Er^{3+}$ ion in a solid is given in Figure 3.11. Three main regions are observed: pre-edge, edge and post-edge [250]. The pre-edge is the part of the spectrum just below the edge and it is associated to dipole transitions between bound states, while the post-edge can extend up to ~ 1 keV above the edge and describes transitions to continuum states. The edge sets the onset energy for transitions to the continuum state and gives information about the ionic specie and its oxidation state. On the other side, the most relevant structural information is enclosed in the post edge that is commonly separated in two regions. The first region, XANES, extends for 30-50 eV above the edge; the second, EXAFS, that extends up to ~ 1 keV after the XANES region.

According to de Broglie relation, a wavelength $\lambda$ is associated to each particle depending on the particle momentum p and the Planck constant h:

$$\lambda = h/p \tag{3.10}$$

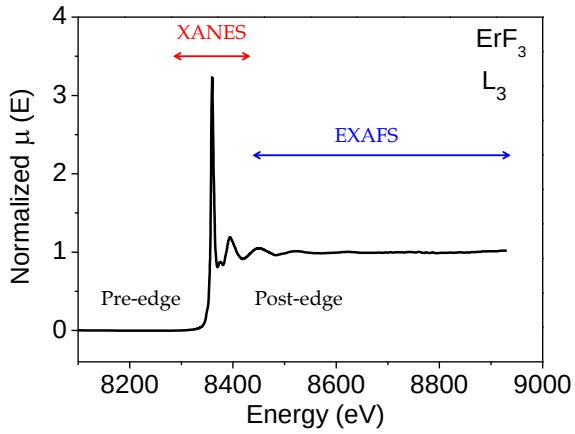


***Figure 3.11:*** *XAS spectrat the $L_3$ edge of $Er^{3+}$in $ErF_3$.*

In solids or condensed matter, atoms nearby can scatter the outgoing photoelectron. The final state of the photoelectron, calculated at the position of the absorber atom A, is described by a superposition of both waves. Such superposition can produce constructive interference corresponding with absorption maxima. If the outgoing and scattered waves are out of phase, destructive interference is produced and a local minimum in the absorption spectrum appears, Figure 3.12. The phase difference ($\Delta\phi$) depends on the distance travelled and the wave vector $k=2\pi/\lambda$, for this, the local structure around the atom determines the oscillatory behaviour of the post-edge region.

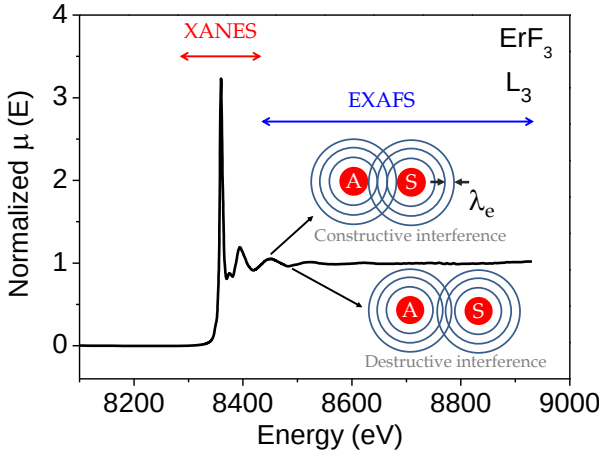


***Figure 3.12.*** *The outgoing photoelectron from the atom A is represented by a spherical wave with wavelength $\lambda_e$ that is scattered by an atom S. Depending on the scattering distance there can be constructive or destructive interference*

The EXAFS region can be analysed with accuracy using the following function [250]:

$$\chi(k) = \frac{\mu(k)-\mu_0(k)}{\mu_0(k)} \quad (3.11)$$

where $\mu$ is the X-ray absorption coefficient and $\mu_0$ is the absorption coefficient in absence of EXAFS effects (free atom) which cannot be directly measured. The $\chi(k)$ function is described as a smooth function to which oscillations superimpose to produce EXAFS spectra. The difference $\mu$-$\mu_0$ is divided by $\mu_0$ such that $\chi(k)$ describes an average structure around the absorbing species. By plotting $\chi(k)$, the EXAFS signal is composed of many oscillations which amplitude is proportional to the number of scattering atoms. The oscillation frequency is inversely proportional to the distance between absorbing and scattering centres, and the oscillations shape depends on the scattering atom [251].

The XANES region corresponds to energies slightly above the edge associated to longer photoelectron wavelengths, thus giving information of the structure at longer distances. XANES spectra are generally studied to obtain the oxidation state of an atom and its symmetry. The comparison with reference compounds allows a qualitative indication about site geometry and type of ligands to be obtained. Moreover, absorptions in the XANES region are usually more intense than for the EXAFS region and have better signal to noise ratio.

The experiments were performed at the synchrotron BM25A-Spline of the ESRF using the setup shown in Figure 3.13. Bulk samples were milled into powders and thin films were measured directly. Glass and glass-ceramic samples, prepared by MQ (55Si10La) and SG ($SiO_2$-$LaF_3$), doped with $Nd^{3+}$ and $Er^{3+}$ were measured as powders in fluorescence configuration ($I_f$) using a 13 element Si (Li) solid-state detector with the sample surface placed at an angle of 45 ° to the incident beam. The reference compounds, $NdF_3$, $Nd_2O$, $ErF_3$ and $Er_2O_3$, were mixed with cellulose and pressed to form a pellet and then measured in transmission mode. The incident ($I_0$) and transmitted intensity ($I_t$) were detected with two ionization chambers.

Data were analysed with the ATHENA and ARTEMIS software [252]. Measurements were performed at the $Nd^{3+}$-$L_2$ and $Er^{3+}$-$L_3$ edge. Edges were fitted using

an arctan as background and a Pseudo-Voigt function as edge peak. XANES spectra were further analysed by linear combinations of reference compounds spectra.

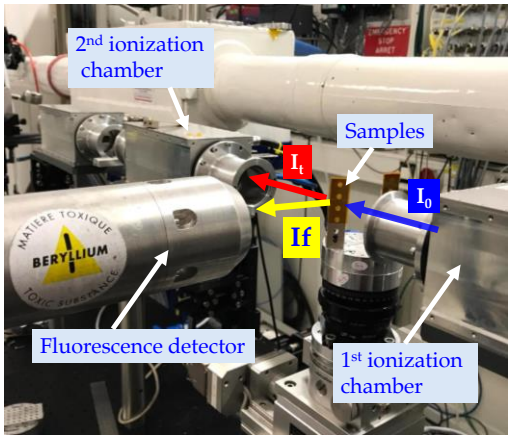


***Figure 3.13.*** *Setup of the BM25A-Spline (ESRF) used to measure XAS spectra in transmission and fluorescence configuration.*

### 3.6.4.High Resolution Transmission Electron Microscopy

TEM is an essential tool for the structural characterisation of nanomaterials because it allows images of a sample to a nanometric scale to be studied. XRD and SAXS techniques provide a global structural characterisation, while XAS describes the local structure around specific atoms. The results from these techniques give average structural information. However, TEM provides local structural information of a material on areas that can be less than 0.01 $\mu m^2$. Moreover, TEM is a very unique technique because it allows both diffraction patterns and images to be obtained, hence the information of both reciprocal space (diffraction) and real space (imaging) is accessible [253].

TEM enables both amplitude and phase contrast. Amplitude contrast is originated by different atomic masses, sample thickness and different diffraction intensities. The two basic ways of operation are the Bright-Field (BF) and Dark-Field (DF) modes.

HRTEM is based on phase contrast produced by the interference of transmitted and diffracted beams. In diffraction configuration, SAED patterns can be recorded, permitting the identification of the crystal phases. Modern HRTEM can also work in

STEM configuration. This configuration is especially useful for EDXS to study the chemical composition of a specific area of the sample.

Some glass and glass-ceramic samples were prepared by $Ar^+$ ion-binning. Firstly, plane parallel sheets were cut and then grinded and dimpled to a residual thickness of 15 μm. Then, ion-binning was performed with incident angle set to 8 °, potential difference to 5 kV and current to 5 mA. The milling time was varied between 10 and 14 h. However, such method is quite complex and several hours are necessary to prepare the samples. A simpler preparation method consists in milling the samples into fine powders and then dispersing in a solvent (ethanol or acetone). Few drops are deposited onto a carbon lacey on copper grid and dried to remove the solvent. In the case of thin films small powder amounts were obtained by scraping the films with a scalpel and then dispersing it in a solvent following the same process.

Glass and glass- ceramics obtained by MQ (55Si10La, 70Si7Lak and 70Si6NaLu) and SG ($SiO_2$-$LaF_3$ and $SiO_2$-$GdF_3$) were analysed using a JEOL 2100F TEM. The instrument works at 200 KV and has a point resolution of 0.19 nm. EDXS analysis was performed in STEM mode using an INCA x-sight (Oxford Instruments) detector and interfaced with the INCA Energy.

The micrographs obtained in this thesis were analysed with the Gatan Microscopy Suit Software. Plane distances of crystal phases are calculated and assigned to specific Miller indices by comparison with the JCPDS cards of the respective phases. The particle (crystalline or not) size distribution was obtained using a relatively high number of particles (100-300) and plotting histograms with a certain bin width. Such histograms are well fitted by one or more Gaussian curves for single and multimodal size distribution. Line scans were made along specific areas and data acquired up to obtain an acceptable signal to noise ratio. Only the elements present in the sample were considered for acquisition. Data were saved and analysed when the software did not reveal an appreciable drifting of the probe. A further image was taken after the measurement to check the scanned area that usually appears as a damaged area due to repetitive interactions with the electron probe. Results were considered reliable after checking that the scans were performed in the same area.

### 3.6.5.Fourier Transform Infrared Spectroscopy

Infrared (IR) spectroscopy is a versatile characterisation technique that provides information about the presence of certain molecules and atomic bonds in the material. Additionally, structural changes as a function of time or temperature can be studied.

The IR spectrum is commonly separated in three regions: near-IR (NIR), mid-IR (MIR) and far-IR (FIR). NIR ranges from 13000 to 4000 $cm^{-1}$ (~770-2500 nm) where most of overtone frequencies of OH, CH, or NH appear [254,255].

MIR goes from 4000 to 400 $cm^{-1}$ (2.5-25 μm) where most interesting vibrations of organic and inorganic materials appear, for this reason MIR is the most studied part for structural characterisation. Such region is further divided in four parts depending on the kind of bond associated to specific vibration frequencies. These parts are: the Y-H stretching region (4000-2500 $cm^{-1}$) e.g CH, OH; triple-bonds region (2500-2000 $cm^{-1}$), e.g C≡C, C≡N; the double-bond region (2000-1500 $cm^{-1}$), e.g C=O, C=C; and the "fingerprint region" (1500-500 $cm^{-1}$) where most of skeletal and bending vibrations are observed, e.g C-N, C-O.

The FIR region extends from 400 to 100 $cm^{-1}$ (25-100 μm) and crystal vibrations are usually observed (most vibrations of fluoride crystals occur in this region).

FTIR is the most used IR spectroscopy technique. FTIR spectrometers have a combination of mirrors and beam splitters as in a *Michelson interferometer* [254]. FTIR spectrometer can be used in several configurations: transmission, ATR, diffusive reflectance etc. In transmission measurements, liquid, thin films and powders can be measured. For powder samples, small amounts of sample (~ 2-5 mg) are mixed with KBr, or other IR transparent materials, to prepare a pellet. On the other side, KBr is highly hygroscopic and artefacts can be detected, especially $OH^-$ contaminations.

The ATR accessory is very useful because no further sample preparation is necessary and both powders and liquids can be measured directly. The sample is placed in contact with a high refractive index crystal (diamond/ZnSe). For powder samples, the contact with the crystal is ensured by a proper pressure arm.

In this thesis the Spectrum 100 FTIR of Perkin Elmer was used in transmission (thin films) and ATR configurations (powders) to measure glasses and glass-ceramics of the $SiO_2$-$LaF_3$ and $SiO_2$-$GdF_3$ compositions prepared by SG. The measurement range was 400-4000 $cm^{-1}$ in transmission mode and 650-4000 $cm^{-1}$ in ATR mode. The resolution was set to 4 $cm^{-1}$ and 4 scans were acquired for each measurement. To measure in transmission mode, 2-3 mg of sample were mixed to 250 mg of KBr to prepare pellets. Thin films were characterised in transmission mode depositing the coating on Si wafer (111) substrates. The software used for all FTIR measurements is the Spectrum software (Perkin Elmer). When the measurements were performed in ATR mode, the spectra of liquid or powder samples were properly corrected.

FTIR spectra of $SiO_2$-$LaF_3$ powders in the FIR region were collected in ATR configuration using the Nicolet 6700-Thermo Scientific. The range was set to 600-175 $cm^{-1}$ and the resolution to 4 $cm^{-1}$. Due to the lower S/N ratio, at least 128 scans were acquired for each measurement.

### 3.6.6. Electron Paramagnetic Resonance

EPR is a magnetic spectroscopy technique that provides identification of paramagnetic species and it is also very sensitive to their local surrounding [256,257]. Paramagnetism is due to the presence of unpaired electrons. Fortunately, most of RE ions are paramagnetic because they have incomplete 4f shells. Therefore, EPR is a powerful technique to characterise RE-doped glass-ceramics in which the local environment of these ions vary from amorphous (glass) to crystalline.

In EPR, the magnetic field is swept in a certain range and the transitions between Zeeman levels are induced by absorption of electromagnetic waves at fixed frequency. The resonance condition is [256]:

$$h\nu = g\mu_e B \tag{3.12}$$

where h is the Planck constant, $\nu$ the frequency, $\mu_e$ the Bohr magneton, B the magnetic field and g a constant that depends on the material. There is absorption whenever the

energy separation of Zeeman levels matches the photon energy. To obtain directly the g-values from the EPR a more convenient formula is:

$$g = \frac{714.477\ \nu(\mathrm{GHz})}{B(\mathrm{G})} \tag{3.13}$$

A sketch of the energy levels splitting for $Nd^{3+}$ in $LaF_3$ in presence of a variable magnetic field is shown in Figure 3.14.

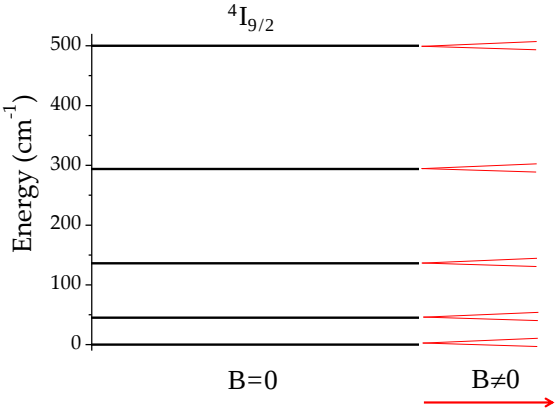


***Figure 3.14.*** *Sketch of the energy levels splitting for the $^4I_{9/2}$ multiplet of $Nd^{3+}$ in $LaF_3$ upon application of a variable magnetic field. The split (not in scale) depends on each level but it is shown equal for simplicity.*

In general, there are three *principal g values*, usually indicated as $g_x$, $g_y$ and $g_z$. Such values depend on the ions surrounding and satisfy one of the following conditions [256,257]:

$g_x=g_y=g_z$ (isotropic case) (3.14a)

$g_x=g_y$ ($g_\perp$)$\neq g_z$ ($g_{//}$) (axial symmetry), (3.14b)

$g_x\neq g_y\neq g_z$ (rhombic symmetry) (3.14c)

Polycrystalline materials are usually measured as powders and they produce typical EPR signals (derivative of absorption spectra) that for species with effective spin S'=1/2, as $Nd^{3+}$, $Er^{3+}$ and $Yb^{3+}$, are shown in Figure 3.15.

Bulk glass and glass-ceramic samples, prepared by MQ (55Si10La) and SG ($SiO_2$-$LaF_3$), and doped with $Nd^{3+}$ and $Er^{3+}$ were grounded to obtain powders and then rolled into Teflon tape. The EPR signals were detected in the 50-8000 G range using a Bruker ESP 300E spectrometer, shown in Figure 3.16, operating with a frequency of 9.47 GHz

and field modulation of 100 kHz. A cryostats was used to reduce the temperature to 5 K (liquid He). The power of the microwave frequency was set to avoid saturation effects and the background signal was acquired before the measurement. Simulations of EPR spectra were obtained using the EasySpin software [258]. These measurements were performed in collaboration with Prof. David Bravo from the Dep. de Física de Materiales de la Universidad Autónoma de Madrid (UAM).

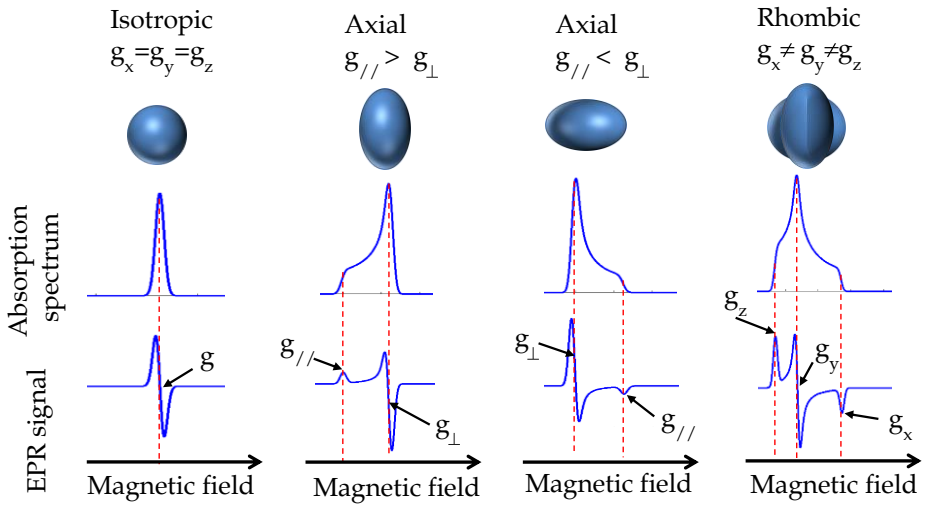


***Figure 3.15.*** *EPR absorption spectra and signals for powder samples containing one paramagnetic element with S'=1/2 placed in different symmetries. Data were simulated using the EasySpin software* [258].

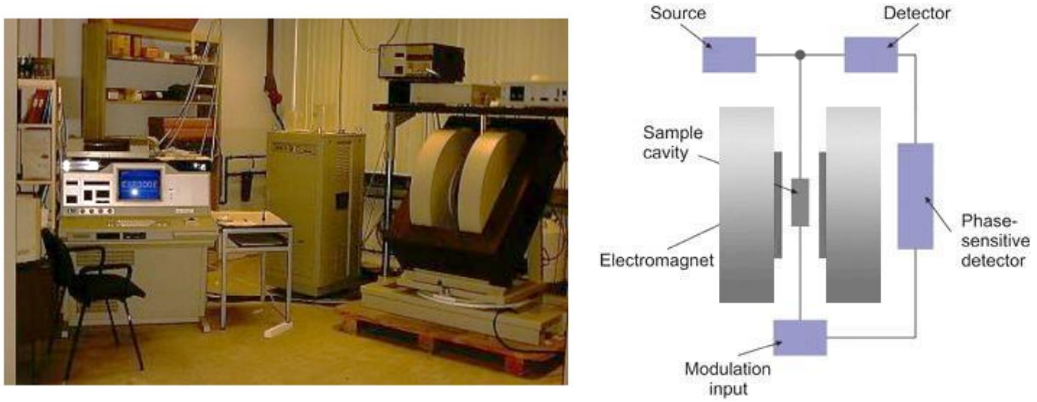


***Figure 3.16****. (Left) Picture and (right) sketch of the scheme of the EPR instrument used in this thesis.*

### 3.6.7. Nuclear Magnetic Resonance

NMR is similar to EPR but nuclei are perturbed instead of electrons. The physical principle of NMR consists in studying the transitions of nuclei between energy levels under the application of a magnetic field. Only nuclei with nuclear spin $I \neq 0$ can be studied. Some nuclei, such as $^{19}F$ and $^{29}Si$, are quite simple to be studied because they have $I=1/2$ and the main interaction is the dipole interaction. For nuclei with higher I such as $^{27}Al$ ($I=5/2$), other contributions, in addition to simple dipole interaction, are observed and their analysis is more complicated.

When a bare or isolated nucleus is subjected to a field of amplitude $B_0$, the energy required to induce transitions between two spin orientations is [259]:

$$\Delta E = \gamma h B_0 \tag{3.15}$$

where $\gamma$ is the gyromagnetic ratio and is a constant of the nucleus. Such transitions are produced by absorption of photons and the resonance frequency is called *Larmor frequency*.

However, the magnetic field which is felt by the nucleus, is affected by the shielding or deshielding of electrons and this effect causes a shift of the resonance frequency. For this reason, the resonance frequency of the sample, $\nu_x$, is measured with respect to the resonance frequency of reference compound, $\nu_{ref}$, and the *chemical shift* $\delta$ is defined as:

$$\delta = \frac{\nu_x - \nu_{ref}}{\nu_{ref}} \tag{3.16}$$

This physical quantity, generally expressed in ppm, gives all the information about the environment of the nuclei and it is independent on the external magnetic field $B_0$.

Such shielding effect is independent on the external magnetic field applied to the sample and it is anisotropic in solid samples. There are also other interactions such as dipole-dipole and quadrupole ($I>1/2$) that are also anisotropic. A typical configuration used in solid NMR is the so called magic-angle-spinning (MAS) in which the sample

spins at an angle of 54.7 ° respect to the direction of the magnetic field. This configuration allows anisotropic contributions to be removed, maintaining only the Zeeman interaction of specific nuclei in a magnetic field. By increasing the spinning speed, sharper absorption bands are observed [259].

In this thesis, an NMR spectrometer (Bruker AVANCE II) equipped with a 9.4 T magnet (400 MHz) and a 2.5 mm rotor spinning at 20 kHz was used to study $SiO_2$-$LaF_3$ samples prepared by SG. $^{19}F$ MAS/NMR was employed to study the change of the $^{19}F$ environment comparing gel and glass-ceramic materials. Small amounts of powder (with size <60 μm) were used and $LaF_3$ reference (99.9 %) was also measured for comparison.

## 3.7. Optical characterisation

The optical characterisation plays a fundamental role because the materials prepared in this thesis are aimed to be used as active devices for photonics. An extensive description of the optical properties of RE ions in solids was given in section 2.9. Some physical parameters such as the refractive index and thickness of thin films are necessary for certain applications as waveguides and optical fibres. However, the most important characterisation was performed by PL spectroscopy. A detailed analysis of the PL results provides information about the environment around the RE ions, the efficiency of the ET processes, the PL differences between glass and corresponding glass-ceramic, etc. All this information is useful to optimise the synthesis of the materials and/or the dopant amounts. Even more importantly, this characterisation completes the scope of this thesis that is intended to correlate the different processing methods with the structure and optical properties of RE-doped glasses and glass-ceramics. In the next sections, the optical techniques used in this thesis are described.

### 3.7.1.Spectroscopic Ellipsometry

Ellipsometry detects the light reflected from the sample surface. The key feature of ellipsometry is that it measures the change of polarized light after interaction with the sample. Ellipsometry measures two values: ψ and Δ, which represent the amplitude

ratio (ψ) and phase difference (Δ) between light waves known as p- and s-polarized light waves [260].

One of the most important applications of spectroscopic ellipsometry is the characterisation of thin films to obtain the refractive index and film thickness. The direct interpretation of the results is difficult therefore, mathematical models are necessary to obtain the physical parameters. A simple model to describe transparent glass-like films deposited on a substrate (glass, Si-wafer, etc.) is the Cauchy model, which relates the refractive index to the wavelength by this equation [260]:

$$n(\lambda) = A + \frac{B}{\lambda^2} + \frac{C}{\lambda^4} \tag{3.17}$$

where A, B, C are constants depending on the materials and λ is the wavelength.

The measurements were performed on SG thin films ($SiO_2$-$LaF_3$) and on melted glasses and glass-ceramics (55Si10La, 70Si7LaK, 70Si6NaLu) using a M2000U (J.A. Woollam Co., Inc.) ellipsometer. The spectral range was 250-1000 nm and the incidence angle was set to 50 and 60 °. The acquisition time was fixed to 10 s to increase the signal-to-noise ratio. Glass and glass-ceramic samples prepared by MQ were cut into plane parallel sheets and optically polished to a thickness of 2 mm. Thin films were fitted considering a Cauchy film deposited on glass or Si substrates (see Figure 3.17) and for bulk samples just a Cauchy dispersion relation was adopted. The data were analysed with the WVAVE32 or the EASE software. The results were considered reliable when the Mean-Squared-Error (MSE) has a value less than 15 (arb. units).

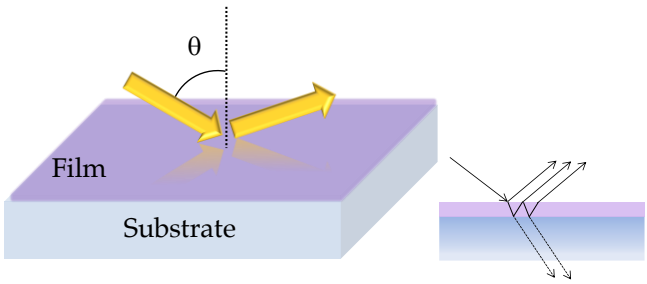


***Figure 3.17**. Model used to study thin films deposited on substrates.*

### 3.7.2. Absorption Spectroscopy

Absorption spectroscopy measures the absorption or radiation as a function of the wavelength. First of all, the transparency of glass and glass-ceramics can be evaluated; secondly, the absorption bands of RE ions, due to electronic excitations between the ground energy level and the excited levels (4f-4f) can be identified. Moreover, starting from absorption spectra, the Judd-Ofelt parameters (see section 2.9) are calculated and some relevant information about the RE ions environment are obtained [203].

If $I_{in}$ and $I_{out}$ are the incident and transmitted intensities, respectively, the transmittance T is given by:

$$T = \frac{I_{in}}{I_{out}} \tag{3.18}$$

The absorbance A is given by:

$$A = -\log_{10} T \tag{3.19}$$

The optical density (OD) is determined by normalizing A for the sample thickness d and the absorption coefficient $\alpha(cm^{-1})$ is:

$$\alpha(cm^{-1}) = \frac{OD}{\ln 10} \tag{3.20}$$

Glass and glass-ceramic samples prepared by MQ were cut into plane parallel sheets, optically polished to a thickness of 2 mm and then measured with a double-beam spectrophotometer Lambda 950 (Perkin-Elmer). The absorption spectra were acquired in the range 300-1700 nm depending on the RE dopants present in the sample using a step of 1 nm.

### 3.7.3. Photoluminescence Spectroscopy

PL spectroscopy measures the emitted light as a function of the incident wavelength. Two kinds of spectra, emission and excitation can be measured. In PL, the excitation wavelength is fixed and the emitted light intensity is recorded at different wavelengths by scanning the emission monochromator. In PLE spectra, the emission

monochromator is fixed at a specific wavelength while the excitation wavelength is scanned in a certain spectral range [203].

When RE ions occupy different positions in a material, different crystal fields act on them modifying slightly their energy levels. It is possible to study the different contributions by site-selective excitation and emission spectroscopy, and to obtain information about RE ions in amorphous and crystalline phases. The majority of optical characterisation described in this thesis was performed in collaboration with Prof. Rolindes Balda and Prof. Joaquín Fernández from the Bilbao University.

A scheme of the setup used for PL characterisation is shown in Figure 3.18a. Figure 3.18b shows a scheme of the setup used for lifetime measurements. Depending on the RE ions different excitation sources were used. All measurements were performed at RT but for site-selective PL and PLE experiments the samples were cooled down to 9 K using a continuous-flow cryostat.

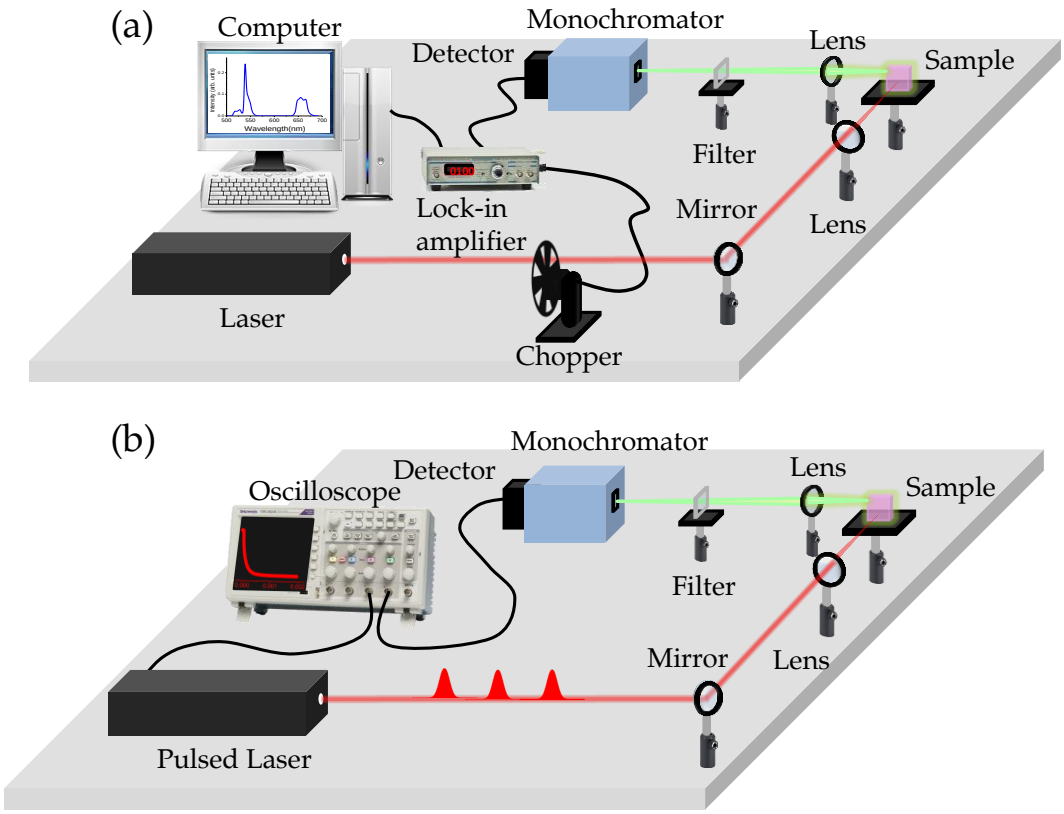


***Figure 3.18.*** *Sketch of the setup used for (a) PL and (b) lifetime measurements.*

For $Pr^{3+}$-$Yb^{3+}$ doped samples the excitation was performed using an InGaN led centred at 435 nm (Roithner) to excite $Pr^{3+}$ ions and with a fibre laser at 976 nm to excite $Yb^{3+}$ ions. The signal was analysed with a 0.32 m monochromator and detected with an S-20 photomultiplier (UV-Vis) or an InGaAs photodiode (IR) using a standard lock-in technique. For lifetime measurements, the InGaN led was modulated electronically (ITC4000-Thorlabs) and the signal acquired with a fast oscilloscope (Tektronix).

For the excitation of $Nd^{3+}$, $Er^{3+}$ and $Er^{3+}$-$Yb^{3+}$-doped samples a continuous wave (cw) Ti:sapphire ring laser (0.4 $cm^{-1}$ linewidth) was used. The fluorescence was analysed with a 0.25 m monochromator and the signal detected with an extended IR Hamamatsu H10330A-75 photomultiplier and amplified with a lock-in configuration. The visible emission was detected using a Hamamatsu R636 photomultiplier. $Er^{3+}$ ions were also excited using an Argon laser. Lifetime measurements were obtained by exciting the samples with a Ti:sapphire laser pumped by a pulsed frequency doubled Nd:YAG laser (9 ns pulse width) and data processed with a fast oscilloscope (Tektronix).

For $Gd^{3+}$ and $Eu^{3+}$-doped samples, the PL and PLE spectra were measured with a FS5 fluorescence spectrometer (Edinburg Instruments Ltd, UK) equipped with a 150 W Xenon lamp and the signal detected with a Hamamatsu R928 photomultiplier.

Tables 3.7 and 3.8 summarise the samples selected for optical characterisation.

***Table 3.7**. MQ materials used for the optical characterisation. The * symbol refers to fibre materials.*

| Composition | Dopants | Doping Level (mol%) | Thermal Treatment |
|---|---|---|---|
| **55Si10La** | $Pr^{3+}$<br>$Pr^{3+}$-$Yb^{3+}$ | 0.1,0.5<br>0.1-0.5,0.5-1 | GC 620°C-20, 40h<br>GC 660°C-20h |
| | $Nd^{3+}$ | 0.1*,0.2, 0.5, 1, 2* | GC 620°C-20, 40h<br>GC 660°C-20h<br>*GCF 640°C-40h |
| | $Er^{3+}$<br>$Er^{3+}$-$Yb^{3+}$ | 0.5<br>0.5-2; 0.5-4 | GC 620°C-20, 40h<br>GC 660°C-20h |
| **70Si7LaK** | $Nd^{3+}$ | 0.1, 0.5, 1, 2 | GC 590°C-150 h<br>GC 660°C-66 h |
| **70Si6NaLu** | $Er^{3+}$-$Yb^{3}$ | 0.5*-2* | *GCF 600°C-20h |

***Table 3.8**. SG samples used for the optical characterisation. The * symbol refers to thin films.*

| Composition | Dopants | Doping Level (mol%) | Thermal Treatment |
|---|---|---|---|
| **$90SiO_2$-$10LaF_3$**<br>**$80SiO_2$-$20LaF_3$**<br>**TEOS** | $Nd^{3+}$ | 0.5, 3<br>2*, 3* | GC bulk 650°C-3h<br>*GC film 350, 550, 650, 750 °C-3h |
| **$80SiO_2$-$20LaF_3$**<br>**TEOS-MTES** | $Er^{3+}$ | 0.5<br>0.1*,0.5* | GC bulk 550°C -1min, 1h<br>*GC film 550 °C-1 min,1h |
| **$90SiO_2$-$10GdF_3$**<br>**$80SiO_2$-$20GdF_3$**<br>**TEOS-MTES** | $Eu^{3+}$ | 0.5 | GC bulk 550° - 1 min |

# *4. OVERALL SUMMARY OF RESULTS AND DISCUSSION*

## 4. OVERALL SUMMARY OF RESULTS AND DISCUSSION

The first studies have been focused on the thermal properties of glasses and xerogels to evaluate their crystallisation mechanism and the effect of dopants addition. An extensive structural characterisation, using both global (XRD, SAXS) and local (XAS, HRTEM, EDXS, EPR) techniques, was used to correlate the processing method with the structure of the materials and the change of the dopants surrounding during the crystallisation process. A detailed optical characterisation, by means of steady state spectroscopy, site selective emission/excitation spectroscopy and lifetime measurement, gave a clear picture about the dopants incorporation and the effects of the crystal phase on linear and nonlinear optical processes. Some remarkable differences are observed with respect to crystallisation mechanism and dopants incorporation, depending on the processing method, showing how different processing methods can be used to design transparent glass-ceramics for promising applications.

Section 1 presents the results of MQ materials. The first results concern the 55Si10La composition, from which $LaF_3$ crystallises, doped with $Pr^{3+}$ and $Pr^{3+}$-$Yb^{3+}$ for DC, with $Er^{3+}$ and $Er^{3+}$-$Yb^{3+}$ for UC, and with $Nd^{3+}$ for laser applications. The effect of the initial dopant precursors (oxides or fluorides) on the incorporation of RE ions in $LaF_3$ crystals and the corresponding optical properties are also described. The effect of $Nd^{3+}$ ions on the structure and optical properties of 70Si7LaK glass-ceramics, where $KLaF_4$ crystallises, is also discussed. This section concludes with the results obtained for glass-ceramic fibres containing $LaF_3$ and $NaLuF_4$ crystals.

Section 2 describes the main achievements for SG materials. A relevant part is dedicated to explain the crystallisation mechanism of $SiO_2$-$LaF_3$ materials with special focus on the $80SiO_2$-$20LaF_3$ composition. Next, the results obtained for materials doped with $Nd^{3+}$and $Er^{3+}$ are described including XAS and EPR characterisations which have not been reported yet in the literature for this sort of materials. A comparison between $LaF_3$-glass-ceramics processed by melting and SG is carried out focusing on the crystallisation mechanism, dopants incorporation and optical properties. This section concludes with the optical results for the $80SiO_2$-$20GdF_3$ composition doped with $Eu^{3+}$ showing an efficient ET between $Gd^{3+}$ and $Eu^{3+}$ ions.

## 4.1. Section 1 – Melt-quenching materials

### 4.1.1. $LaF_3$– glass-ceramics

#### *4.1.1.1. Structure of $LaF_3$ glass-ceramics*

Transparent glasses of the 55Si10La composition doped with $Pr^{3+}$, $Pr^{3+}$-$Yb^{3+}$ (paper 2), $Nd^{3+}$ (paper 3), $Er^{3+}$ and $Er^{3+}$-$Yb^{3+}$ (paper 4) have been produced. The corresponding glass-ceramics maintained their transparency after the crystallisation process, always performed in the range $T_g$+20-100 °C. CTE, $T_g$, and $T_d$ were obtained by dilatometry. The $T_p$, the crystallisation stability parameter ($T_p$-$T_g$) and the crystallisation mechanism were also studied by DTA.

For all compositions the CTE is around 8.5-9.2 x $10^{-6}$ $°C^{-1}$ and the dilatometric softening point is in the range 660-670 °C. For a fixed dopant amount (0.5 mol%), the $T_g$ is slightly affected by the kind of dopant ($Pr^{3+}$, $Er^{3+}$, $Nd^{3+}$) while notable changes are observed by changing the doping amount. For example, on increasing the $Nd^{3+}$ concentration, $T_g$ varies almost linearly from 573 °C for the glass doped with $0.1NdF_3$ to 593 °C for the glass doped with $2NdF_3$ as described in paper 3. The stability parameter decreases with higher dopant content indicating a higher tendency to crystallise. This behaviour is well described for $Nd^{3+}$, $Er^{3+}$ and $Er^{3+}$-$Yb^{3+}$ doped samples (papers 3 and 4) showing how the stability parameter is reduced from ~ 100 °C to ~ 80 °C when increasing the doping level.

Quite broad crystallisation peaks are observed in DTA measurements and their intensity increases while the half-width decreases with the heating rate. This phenomenon is related with a phase-separation process. Phase separation is promoted by increasing the RE amount, leading to an increase of $T_g$. However, when high doping levels are used (> 2 mol %), the depolymerisation of the $SiO_2$ network increases and a slight decrease of $T_g$ is observed. This effect is observed for $Er^{3+}$ and $Er^{3+}$-$Yb^{3+}$ doped glasses described in paper 4.

The crystallisation mechanism was studied by non-isothermal crystallisation treating bulk samples at heating rates of 10-60 °C/min. The use of Kissinger and Ozawa's equation (described in papers 2 and 3) allowed the activation energy $E_a$, the

Avrami *n* parameter and the crystal growth dimensionality *m* parameter to be obtained. The activation energy is ~ 350 kJ/mol, and the *n* and *m* parameters are both equal to 1, Figure 4.1. This mechanism was associated to a diffusion-controlled process occurring in the volume of the material and starting from a constant number of nuclei. Phase separation is commonly encountered in oxyfluoride glass-ceramics due to fluoride melts immiscibility in oxide ones. However, this behaviour is not always observed, as it occurs for the 70Si7LaK composition described later (paper 6).

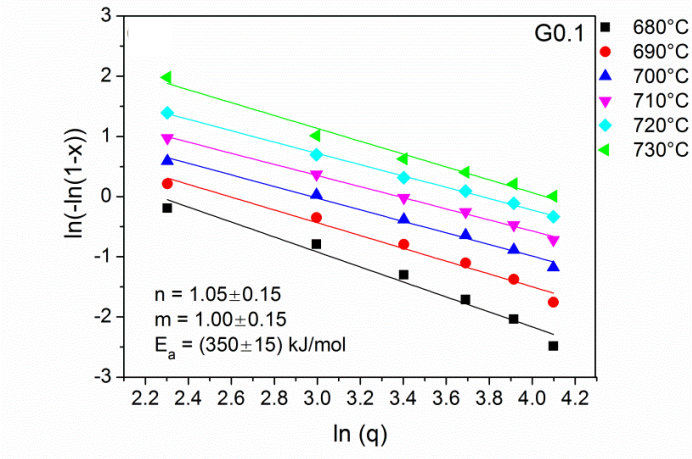


***Figure 4.1.*** *Ozawa plots for the 55Si10La glass doped with 0.1$NdF_3$ (mol%). The plots were obtained from DTA curves measured at heating rates of 10-60 °C/min. The temperatures used for the calculation of the area of the crystallisation peak are indicated on the right.*

An important result is that the dopants amount does not affect the crystallisation mechanism but affects the kinetic process. The crystallisation kinetics slows down when increasing the RE content. These results are confirmed by XRD. Only hexagonal $LaF_3$ NCs (JCPDS 00-032-0483) are present after heat treatment at 620-660 °C, and the evolution of the crystal size with the treatment time follows a characteristic behaviour according to the following empiric formula (paper 4):

$$\phi = \phi_0 + C\,(1 - e^{-t/t_s}) \qquad (4.1)$$

$\phi_0$ is the crystal size associated with small crystalline domains in the as made glass, and the second part describes an exponential growth with an asymptotic behaviour. The C parameter represents the growth rate in the linear region, instead $t_s$ is associated to the starting time for the occurrence of an inhibition phenomenon that limits further

crystal growth. The crystal size tends to grow linearly with the treatment time up to 3-5 h of thermal treatment but for longer times the crystal size stabilizes to a constant value. The $LaF_3$ crystal size in the asymptotic region varies between 8-14 nm at 620 °C.

For glasses doped with $Er^{3+}$ and $Er^{3+}$-$Yb^{3+}$, the C values slow down from 7.8 nm for glass-ceramics doped with $0.5Er^{3+}$ to 5.6 nm for those doped with $0.5Er^{3+}$-$2Yb^{3+}$ (paper 4) and the growth rate also decreases for $Nd^{3+}$-doped glass-ceramics, as described in paper 3.

Higher treatment temperatures allow bigger crystals to be grown but the same asymptotic behaviour is observed. In particular, higher treatment temperatures speed up the process and the asymptotic barrier is formed earlier. The growth rate decreases upon $Yb^{3+}$ addition for $Er^{3+}$-$Yb^{3+}$ doped samples (paper 4) and a similar behaviour is obtained for $Pr^{3+}$-$Yb^{3+}$ doped materials (paper 2).

As a result, a smaller crystal size is reached for heavier doped compositions. However, Rietveld refinement (paper 3), or the calculation of the area under XRD peaks (paper 4), have shown that the crystal fraction increases with the addition of dopants. The crystal fraction increases from 6 to almost 9 wt% when comparing 0.1 and $1NdF_3$-doped samples (paper 3). Therefore, it can be concluded that the dopants addition works like a nucleating agent promoting phase separation. A higher amount of crystals with smaller crystal size is obtained after the heat treatment. This phenomenon could be explained considering that heavier RE ions tend to form stronger bonds with fluorine. If such RE-F bonds are responsible for initial phase separation, then, heavier RE ions will provide a higher number of phase separated regions, acting as nuclei.

The plot of the crystal size as a function of the square root of time provides useful information for a diffusion-controlled crystal growth process, as shown in paper 6. It can be concluded that the process is dominated by diffusion when the crystal growth is approximately linear with the square root of the treatment time. This phenomenon occurs for crystal phases enriched in glass modifiers, or in ions different from network formers (Si and Al).

Further structural characterisation was performed by HRTEM and EDXS. Phase separation droplets are clearly visible in the 55Si10La glasses. The droplet size distribution was estimated by analysing 100-300 droplets to have statistically representative data that can be fitted by a single Gaussian centred in the range 20-45 nm, Figure 4.2a. In the $LaF_3$-glass-ceramics treated at 620 °C for 40 h the amorphous droplets are now composed of tiny $LaF_3$ crystals with a size less than 15 nm, in agreement with the values obtained by XRD, Figures 4.2b,c. The droplet size increases due to the development of crystals together with further phase separation. However, slightly sharper size distributions are observed for the glass-ceramic samples with respect to the precursor glasses (papers 3 and 4). For heat treatment at higher temperature, as 680 °C, even though the crystal size is still quite small (~ 25 nm), the droplets size becomes too big (~ 100 nm) and the glass-ceramics lost their transparency (paper 2). This is a typical feature of the 55Si10La composition in which several $LaF_3$ NCs grow in one phase separation droplet.

It is not possible to establish the composition and nature of crystals from HRTEM micrographs, but by a comparison with XRD results, it is concluded that only $LaF_3$ NCs are present in the glass-ceramic samples. FFT analysis provides a further proof of the kind of crystals showing typical $LaF_3$ planes distances. For example, the (111) and (113) lattice distances are determined (paper 3), being ~ 0.33 and 0.20 nm, respectively. The zone axis, through which individual crystals are observed, has also been determined by the corresponding digital diffraction pattern (DDP), as shown in paper 4.

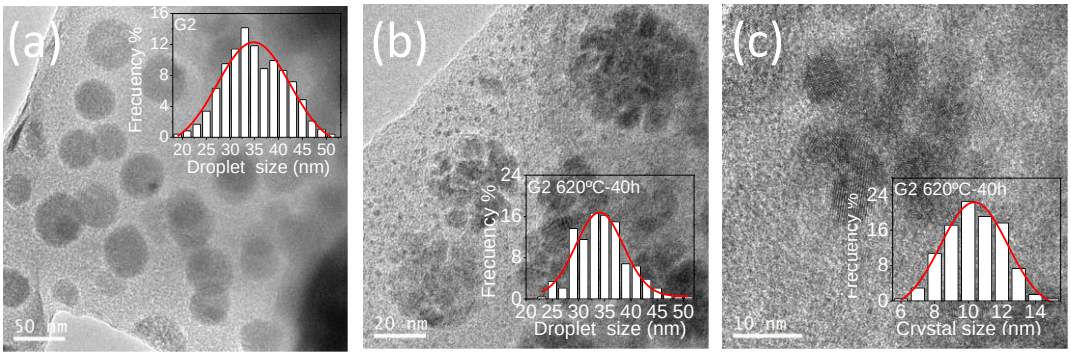


***Figure 4.2.*** *HRTEM of the 55i10La (a) glass and (b) glass-ceramic doped with 2$NdF_3$ (mol%) and treated at 620 ℃ for 40 h. (c) Detail of some crystals. The phase separation droplet size and crystal size distributions are also shown.*

Relevant information regarding the local chemical composition is obtained by EDXS analysis performed in phase separation droplets for the glasses and in the crystals for the glass-ceramics. In all cases, fluorine enrichment is observed. Even more interesting is the RE enrichment in these phase separation droplets, as observed for $Pr^{3+}$-$Yb^{3+}$ doped glass described in paper 2. La and F are the precursors of the crystal phase but the presence of other RE used as dopants is a very interesting result. It suggests that even in the as made glass the RE dopants are embedded in an amorphous fluorine-rich environment that is converted into a crystalline one after the crystallisation process. In the doped glass-ceramic samples, an enrichment of RE dopants into the crystals is observed, as discussed in papers 2, 3 and 4 and shown in Figure 4.3.

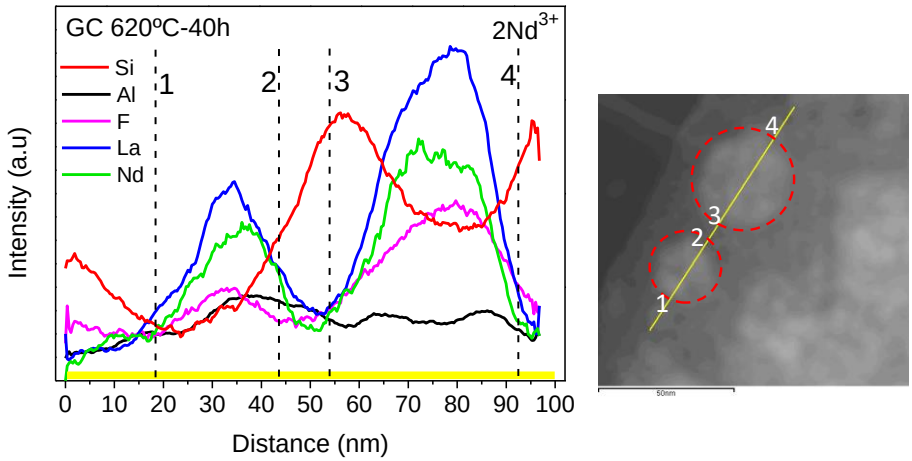


***Figure 4.3.*** *EDXS in STEM mode performed on two droplets of the 55Si10La glass-ceramic doped with 2 mol% $NdF_3$ and treated at 620 ºC for 40 h. The yellow line shown in the STEM image (right) is the scanning line. The numbers 1-2 and 3-4 delimitate the two droplets.*

Another interesting result is the observation of Si at the interface between the glass matrix and the crystals that are enclosed in initial phase separation droplets. Such Si enrichment is responsible for the decrease of the crystal growth rate with the treatment time and associated to the appearance of the asymptotic behaviour described earlier. In fact, when network modifiers diffuse and the crystals start to grow there is a local change of the glass composition that becomes depleted of such ions. Therefore, a relative higher Si concentration is reached at the droplet/matrix interface. Si acts as glass former and its increase causes a viscous barrier around the crystals that inhibits

crystal growth. Hence the crystal size maintains a constant value with the treatment time. Al is found at the interphase but relevant amounts are also observed between the crystals. Al acts as network former and Al–O bonds form an additional barrier of high viscosity. Its presence around the crystals can explain why several small NCs grow in the initial phase separation droplets instead of one single crystal. These results are in agreement with those described previously [5].

The use of SAXS to study glass and glass-ceramics offered an interesting global vision of these samples. SAXS is not sensitive to the amorphous or crystalline nature but only to electron density fluctuations. The SAXS results are difficult to be interpreted without further support from XRD and HRTEM, the latter providing information only of a small sample region (< 1 $\mu m^2$). However, the particle size distribution determined by SAXS for the glass and glass-ceramic of the 55Si10La composition doped with $Nd^{3+}$ and treated at 620 °C for 40 h (paper 3) show two main groups of particles, Figure 4.4. The first group, composed of particles below 10 nm, is associated with small phase separation droplets while the second group of particles (15- 60 nm) is associated with bigger phase separation droplets observed by HRTEM which distribution becomes narrower upon heat treatment. In the glass-ceramic samples, the scattering contribution from particles with a size ~ 10-15 nm can be also observed and it is associated to the formation of crystals. Such contribution is completely absent in the as made glass.

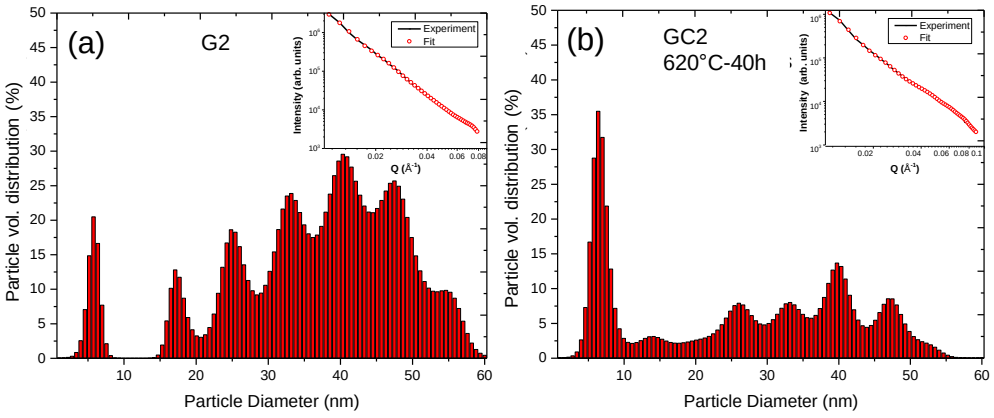


***Figure 4.4.*** *SAXS data (insets) and derived particle-volume distribution of the 55Si10La (a) glass and (b) glass-ceramic treated at 620 ℃ for 40 h. The samples are doped with 2$NdF_3$ (mol%).*

As observed from EDXS results, the RE dopants are already present in a fluorine-rich environment in the precursor glass. This fact has a crucial importance because the effective RE concentration in the fluoride NCs will determine the optical properties. Indeed, even though a nominal concentration is used (0.1-2 mol%) the effective concentration in the fluoride NCs is an essential parameter to be determined. Previous studies performed by our research group showed that there is a diffusion of $Tm^{3+}$ ions in $LaF_3$ NCs when the glass is converted into glass-ceramic [261]. $Tm^{3+}$ was introduced in the glass composition as $Tm_2O_3$. XAS studies, including both, XANES and the EXAFS regions, showed that the $Tm^{3+}$ environment changed from oxygen to fluorine and it was estimated that ~ 30% of $Tm^{3+}$ ions get incorporated in $LaF_3$ NCs after the heat treatment at 620 °C during 40 h. A rough estimation of the $Tm^{3+}$ incorporation was calculated taking into account the amount of crystal fraction.

In this thesis, the dopants have been mainly incorporated in the glass composition as fluorides $REF_3$. Some authors have prepared oxyfluoride glass-ceramics using different dopant precursors (fluorides, oxides etc.) and have performed some studies, including DTA/DSC and optical measurements, to observe whether there is a difference with respect to RE incorporation and optical properties [148,149]. The conclusion is that a more efficient incorporation of RE ions in the fluoride NCs is reached when fluoride precursors are used. Despite the aforementioned results, Fedorov et al. [61] stated in their review published in 2015 that there are no differences in using RE oxides or fluorides and both can be used, preferring the oxides for their lower cost.

In this thesis, all the compositions have been doped with fluoride precursors, as shown in Table 3.2 According to our observations, RE ions are already in a fluorine-rich environment in the as made glass but a diffusion from oxygen to fluorine surrounding was observed using $Tm_2O_3$ [261]. To further elucidate whether there is an effect on the RE incorporation using different precursors, glasses and glass-ceramics of the 55Si10La composition have also been prepared using oxide precursors. $Nd^{3+}$ and $Er^{3+}$ have been chosen as spectroscopic probes and the 55Si10La composition has been doped with 0.05-0.5$Nd_2O_3$, 0.1-1$NdF_3$, 0.1$ErF_3$ and 0.05 $Er_2O_3$ (mol%). The analysis was

mainly focused on local structural techniques as XAS and EPR. A different behaviour is observed when comparing $Nd^{3+}$ and $Er^{3+}$-doped samples. These results are extensively discussed in paper 5.

Pure $Nd_2O_3$ and $NdF_3$ reference compounds were also measured to compare the results (paper 4). XAS spectra for $0.5Nd_2O_3$ and $1NdF_3$ doped samples, performed at the $L_2$ edge, show clear differences in the XANES part of the spectrum (6730-6780 eV). Some typical features of the $NdF_3$ spectrum are better reproduced using $NdF_3$ as precursor.

The XAS spectra in the XANES and EXAFS regions for the samples doped with $0.05Nd_2O_3$ and $0.1NdF_3$ (mol%) were too noisy to obtain relevant information. However, great differences are observed in the white-line for these compositions. Once the measurements are normalized, the intensity of the white-line gives information about the occupation states for the 2p-5d transitions. As discussed by Choi [262], the covalence of the bond decreases and the absorption edge shifts slightly to higher energy changing from $RE_2O_3$ to $REF_3$. The intensity of the white-line is higher for the fluoride compound and it is even higher for a fluoride glass of similar composition.

Moreover, the intensity of the white-line changes remarkably suggesting a different environment for the $Nd^{3+}$ ions (paper 5). In the glass-ceramic samples, a strong decrease of the intensity of the white-line is observed for the $0.1NdF_3$-glass-ceramic while for the $0.05Nd_2O_3$-glass-ceramic the opposite occurs. After the heat treatment, part of $Nd^{3+}$ ions are embedded in $LaF_3$ NCs, hence the number of RE-F ionic bond increases. If an amorphous fluorine-rich environment prevails for the $0.1NdF_3$ glass, in the corresponding glass-ceramic such environment is pretty much ionic (crystalline) and the covalence decreases, causing a decrease of the white-line. Another interesting observation is that the intensity of the white-line for the $0.05Nd_2O_3$-glass-ceramic is higher than for the $0.1NdF_3$-glass-ceramic suggesting a less concentration of $Nd^{3+}$ in $LaF_3$ NCs.

To get more insights about the aforementioned results, EPR of $Nd_2O_3$ and $NdF_3$ doped samples was also performed. EPR is one of the best technique to study the local

environment of RE ions, especially those known as Kramer doublets ($Nd^{3+}$, $Er^{3+}$, $Dy^{3+}$, $Yb^{3+}$ etc.) [256]. $Nd^{3+}$ and $Er^{3+}$ ions have effective spin $S'$=1/2 and the typical EPR signal of $S'$=1/2 ions in powder form is given in Figure 3.15 of section 3.6.6. For rhombic or lower symmetry, as it is the case for $RE^{3+}$ in $LaF_3$ crystals, there are three principal g-values.

The EPR signals of the 0.1-1$NdF_3$ and 0.05-0.5$Nd_2O_3$-glass-ceramics treated at 620 °C during 40 h are shown in Figure 4.5. The resonance at ~2180 G, associated with $g_1$~3.1, is observed for both samples and it is assigned to one of the resonances of $Nd^{3+}$ in $LaF_3$ crystals [263,264]. However, the intensity of such resonance for the 0.1$NdF_3$ glass-ceramic is much higher than for the 0.05$Nd_2O_3$ glass-ceramic, indicating a much better incorporation of $Nd^{3+}$ ions in $LaF_3$ crystals when the $NdF_3$ precursor is used. The sharp resonance at ~1580 G, related to g ~ 4.27, is due to $Fe^{3+}$ ions [265], often encountered in silicate glasses and glass-ceramics prepared by MQ and due to $Fe^{3+}$ impurities present in $SiO_2$ precursor (sand). A detailed analysis allows another resonance at ~4830 G, associated with $g_2$ ~ 1.4, to be detected. Such resonance is not appreciable for the 0.05 $Nd_2O_3$ glass-ceramic and due to a lower $Nd^{3+}$ incorporation in the $LaF_3$ crystals.

Considering the 0.5$Nd_2O_3$ and 1$NdF_3$-glass-ceramic, a slightly different behaviour is observed. In both cases the presence of $Nd^{3+}$ in $LaF_3$ NCs is indicated by the resonance related to $g_1$ ~3.1. However, the resonance for 0.5$Nd_2O_3$-glass-ceramic is sharper than for the 1$NdF_3$-glass-ceramic, suggesting a lower $Nd^{3+}$ concentration in the $LaF_3$ NCs. Moreover, the second resonance associated with $g_2$ ~1.4 is better resolved for the 0.5$Nd_2O_3$-glass-ceramic and this indicates less spin-spin relaxations due to a lower effective concentration (paper 5).

Further studies were performed for the 1$NdF_3$-glass-ceramics prepared using heat treatment times of 3, 5, 20 and 40 h at 620 °C, to observe the incorporation of $Nd^{3+}$ ions with the treatment time, (paper 5). Increasing the treatment time from 3 to 40 h, the resonances of $Nd^{3+}$ in $LaF_3$ are better resolved and present less broadening, thus indicating a better crystallisation along with a higher fraction of $Nd^{3+}$ ions incorporated

in the $LaF_3$ NCs. The samples treated for 20 and 40 h show very similar results, also confirmed by PL (paper 3).

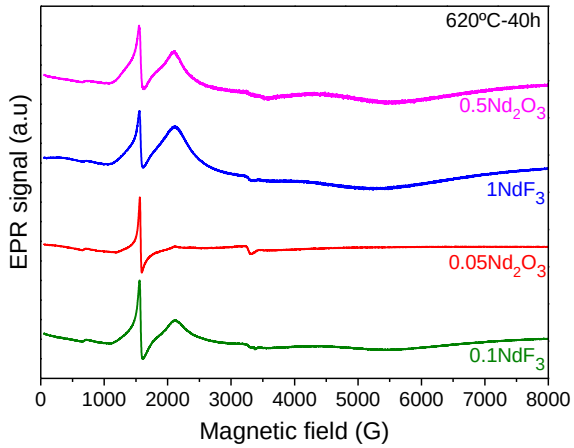


***Figure 4.5.*** *EPR signals for the 55Si10La glass-ceramics treated at 620 ℃ for 40 h and doped with 0.1 and 1$NdF_3$ (mol%) and with 0.05 and 0.5$Nd_2O_3$ (mol%).*

For the 0.1$ErF_3$ and 0.05$Er_2O_3$-doped glasses and glass-ceramics, there are practically no differences in XAS and EPR spectra, suggesting that $Er^{3+}$ ions are equally incorporated in $LaF_3$ independently on the precursor. XAS spectra, measured at the $L_3$-edge of $Er^{3+}$, indicate that the $Er^{3+}$ environment is mainly composed of fluorine ions, even in the precursor glass.

The results obtained so far show that using of oxide or fluoride precursors affect the final incorporation, but such effect depends on the amount and kind of dopant. A kind of "memory", as proposed by Mortier [148], seems retained by certain ions when used as different precursors. This behaviour could be related to the preservation, for $Nd^{3+}$ ions, of the first coordination sphere as in the starting precursor. In the case of $Er^{3+}$, the preference towards fluorine ions is dictated by its stronger field strength, the "memory" effect being less effective

The optical characterisation obtained for the 55Si10La composition doped with $Pr^{3+}$, $Pr^{3+}$-$Yb^{3+}$, $Er^{3+}$, $Er^{3+}$-$Yb^{3+}$ and $Nd^{3+}$ is discussed in the next section showing the remarkable effect of the crystal phase on the PL of the $RE^{3+}$ ions.

#### *4.1.1.2. Optical properties of RE-doped $LaF_3$ glass-ceramics*

In all cases, the 55Si10La compositions doped with several RE ions showed a clear evidence of the RE ions incorporation in $LaF_3$ NCs. Even more interestingly, such small crystals (8-14 nm) allow crystal-like optical features of single crystals (paper 3) to be reproduced. This result is extremely important because indicates that the RE ions get really incorporated in the interior of the NCs and few atomic planes are enough to screen them from the glass matrix. It is also worth noticing that part of the ions remains in the glass matrix or in amorphous phase separation droplets.

*Glasses and glass-ceramics doped with $Pr^{3+}$-$Yb^{3+}$*

The $Pr^{3+}$ ions were excited to the $^3P_2$ level by excitation at 435 nm (paper 2). By non-radiative decay the $^3P_0$ level was populated and the characteristic transitions of $Pr^{3+}$ ions were measured. Structure bands (Stark components) were observed for the glass-ceramic samples treated at 620 and 660 °C with respect to the precursor glasses, a clear indication of $Pr^{3+}$ incorporation in $LaF_3$ NCs. Quite intense transitions corresponding to the $^3P_1$-$^1G_4$ and $^1D_2$-$^3F_{3,4}$ emissions were observed for $Pr^{3+}$ doped samples, Figure 4.6a,b. However, such emissions become much less intense in the co-doped samples. Figure 4.6c,d. In addition, intense $Yb^{3+}$: $^2F_{5/2}$-$^2F_{7/2}$ emission at ~ 980 nm was recorded, indicating an ET from $Pr^{3+}$ to $Yb^{3+}$ ions.

The absence of any emission at 1300 nm means that the $^1G_4$-$^3H_5$ transition does not occur hence, the $^1G_4$ level is not populated. This conclusion is important to exclude the two-first order ET process between $Pr^{3+}$ and $Yb^{3+}$ ions and suggests that the cooperative ET (CET) is the main processes to transfer Vis light to IR light. Clear differences are observed between glass and glass-ceramics by studying the lifetime of the $^3P_0$ level, Figure 4.7. An ET ~ 60% is obtained for the glass-ceramic doped with $0.1Pr^{3+}$ and $0.5Yb^{3+}$ and treated at 620 °C during 40 h, the corresponding quantum efficiency being ~ 160%. An important remark is that longer treatment times or higher temperatures permit the ET efficiency to be increased. This phenomenon is associated to the increase of crystal size and fraction (higher temperature) and to a better diffusion of RE ions (longer treatment times).

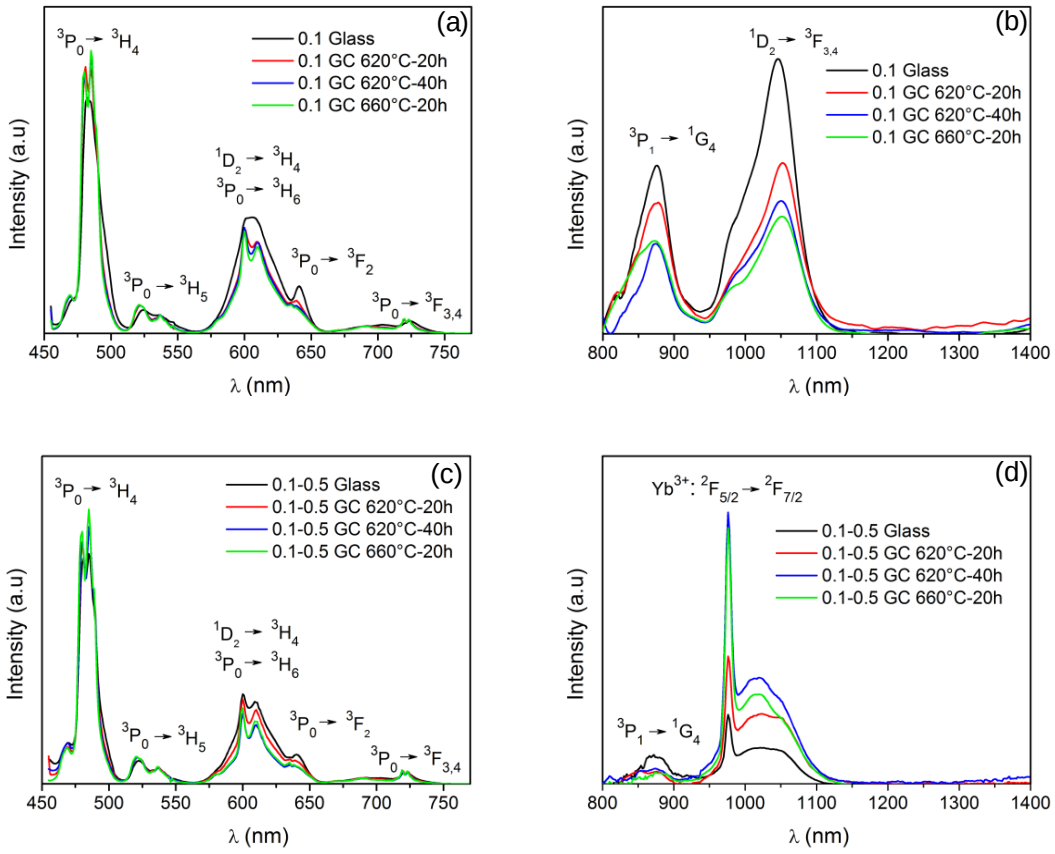


***Figure 4.6.*** *PL spectra of 55Si10La (a),(b) glasses and glass-ceramics doped with 0.1PrF₃ and (c),(d) co-doped with 0.5YbF₃.*

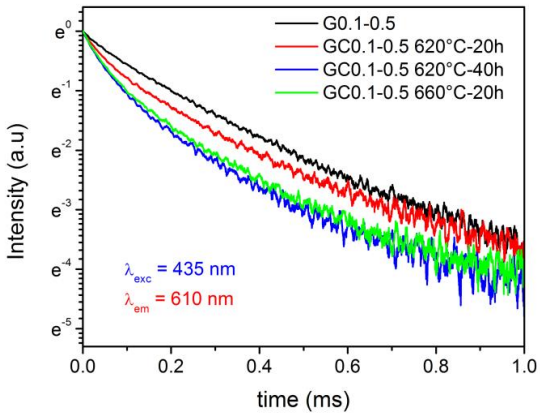


***Figure 4.7.*** *Lifetime of 55Si10La glass and glass-ceramics co-doped with 0.1PrF₃-0.5YbF₃ excited at 435 nm.*

*Glasses and glass-ceramics doped with $Nd^{3+}$*

For the 55Si10La composition doped with 0.1NdF₃ (paper 3) notable differences were observed in the PLE spectra of glass and glass-ceramics recording the luminescence at 1057 nm ($^4F_{3/2}$-$^4I_{11/2}$ transition). Sharp components are observed for the $^4I_{9/2}$-$^4F_{5/2}$ and $^4I_{9/2}$-$^4F_{3/2}$ transitions in the glass-ceramic samples. However, such features

almost disappear for higher doping levels, and selective PL and PLE spectra were measured for the glass-ceramics doped with 0.1$NdF_3$ treated at 620 °C for 40 h, (paper 3). By excitation at 802 nm, typical inhomogeneous broaden transitions are observed, typical of $Nd^{3+}$ in amorphous environment. Instead, by excitation at 786 nm a structured emission band was observed, in perfect agreement with that registered for $Nd^{3+}$:$LaF_3$ single crystals [267]. Therefore, two $Nd^{3+}$ environments are clearly observed in the glass-ceramic samples. To reduce the overlapping of amorphous and crystalline contribution, PL and PLE spectra were recorded lowering the temperature to 9 K, further confirming the previous results and showing a much better resolved PL spectrum, Figure 4.8.

Moreover, the splitting of the $^4I_{9/2}$-$^4F_{3/2}$ transition in two components was observed in PLE spectra, and, as shown in Figure 2.10 of section 2.9, this is in agreement with the presence of a well-defined crystal field. Increasing the doping level to 1$NdF_3$ the crystal-like features become less evident and both PL and PLE spectra of $Nd^{3+}$ in $LaF_3$ get broader.

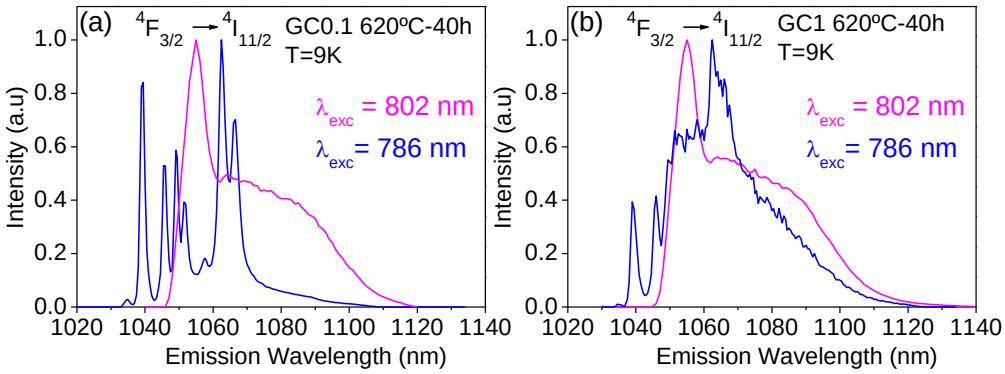


***Figure 4.8.*** *Low temperature (9 K) PL spectra obtained under excitation at 786 and 802 nm for glass-ceramics doped with (a) 0.1$NdF_3$ and (b) 1 $NdF_3$.*

The lifetime measured at 1057 nm (exc. 802 nm; $Nd^{3+}$ in glass) decreases from 336 to 233 μs comparing 0.1 and 2$NdF_3$ –doped samples, but the lifetime measured at 1039 nm (exc. 786 nm; $Nd^{3+}$ in $LaF_3$) shows a great quenching from 688 to 29 μs, Figure 4.9. The huge quenching found even for quite low nominal concentration (0.5 or 1$NdF_3$) is due to a much higher effective concentration in the $LaF_3$ NCs. This result is very important because it means that RE ions incorporated efficiently in the $LaF_3$

crystals. By using previous data about diffusion of $Tm^{3+}$ in $LaF_3$ for $Tm_2O_3$-doped glasses and glass-ceramics, it was concluded that for 0.1$NdF_3$–doped samples an effective concentration around 1.2 mol% should be produced in the $LaF_3$ NCs, and for doping with 1$NdF_3$ such value almost reaches 10 mol%. These values are around one order of magnitude higher than the nominal ones and concentration higher than 0.1$NdF_3$ causes a strong concentration quenching of the $Nd^{3+}$ emission. If the lifetimes are compared to those of $Nd^{3+}$:$LaF_3$ single crystals measured at the same temperature of 9 K and doped with different $Nd^{3+}$ amounts, even much higher effective concentrations are obtained [266]. For example, for the 0.1 mol% $NdF_3$ composition the effective concentration should be ~ 2 mol%, and ~ 50 mol% for the composition doped with 1 mol% $NdF_3$.

The results suggest that small amounts of dopant should be used, since the effective concentration of $Nd^{3+}$ is around one order of magnitude higher than the nominal one. These findings are also relevant for other dopants and serve as a guide to optimise the optical response of these active glass-ceramics.

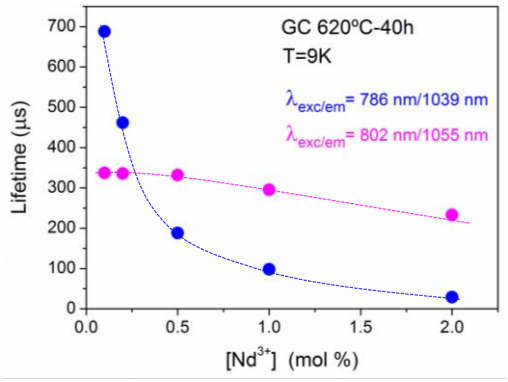


***Figure 4.9.*** *Low temperature (9 K) lifetime of 55Si10La glass-ceramics treated at 620 ℃ for 40 h and doped with 0.1-2$NdF_3$ (mol%). The blue points correspond to the lifetime of $Nd^{3+}$ ions in $LaF_3$ crystals, while the pink points correspond to the lifetime of $Nd^{3+}$ ions in amorphous environment. The dashed-lines are a guide for the eye.*

*Glasses and glass-ceramics doped with $Er^{3+}$-$Yb^{3+}$*

The IR, Vis and UC emissions were studied for the 55Si10La composition doped with 0.5$ErF_3$ and co-doped with 2 and 4$YbF_3$ (mol%), paper 4. An increase of the $^4I_{11/2}$-$^4I_{15/2}$ and $^4I_{13/2}$-$^4I_{15/2}$ ($Er^{3+}$) emissions was observed for excitation of $Er^{3+}$ ions at 800 nm

($^4I_{15/2}$-$^4I_{9/2}$) when glasses and glass-ceramics are compared. This behaviour is associated with a crystalline environment for the $Er^{3+}$ ions. A small ET from $Er^{3+}$ to $Yb^{3+}$ was also observed, indicated by the $^2F_{5/2}$-$^2F_{7/2}$ emission of $Yb^{3+}$ ions. By excitation at 980 nm, both the $^4I_{11/2}$ ($Er^{3+}$) and $^2F_{5/2}$ ($Yb^{3+}$) levels are excited and an effective ET from $Yb^{3+}$ to $Er^{3+}$ was observed, as demonstrated by the increase of the $^4I_{13/2}$-$^4I_{15/2}$ emission of $Er^{3+}$ in co-doped samples. Moreover, higher PL signals are obtained for the glass-ceramics indicating a lower phonon energy environment, further confirmed by the increase of the lifetime of the $^4I_{13/2}$ level of $Er^{3+}$ ions.

The green and red UC was studied exciting the $^4I_{11/2}$ ($Er^{3+}$) and $^2F_{5/2}$ ($Yb^{3+}$) levels at 980 nm. Higher UC emission was obtained for the co-doped samples and increasing the treatment temperature (paper 4). A remarkable observation is the much higher red to green ratio observed with respect to $Er^{3+}$ excitation at 488 nm. For example, for the $Er^{3+}$ singly doped samples this ratio increases from 0.05 to 0.5. A similar behaviour is observed for the co-doped compositions but the red to green ratio is highly dependent on the heat treatment, hence on the crystal size, Figure 4.10. The highest green UC emission is observed for the glass-ceramic co-doped with $2YbF_3$ treated for 20 h at 660 °C. These results indicate the possibility of colour tuning upon a proper crystallisation process. All the ET mechanisms, described in section 2.9, are extensively discussed in paper 4.

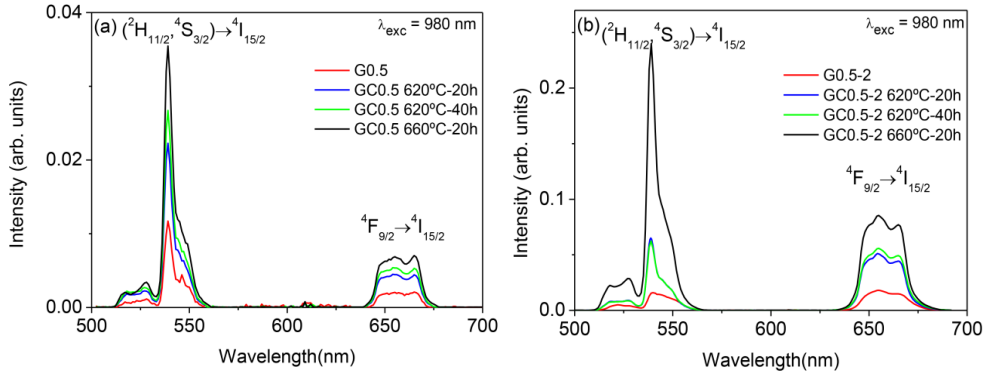


***Figure 4.10***. *Room temperature emission spectra obtained under excitation at 980 nm for the 55Si10La glassed and glass-ceramics doped with (a) 0.5$ErF_3$ and (b) co-doped with 0.5$ErF_3$-2$YbF_3$ (mol%).*

Finally, by studying the red and green intensity as a function of the pumping power (as described in section 2.8.3), a two photon mechanism for the UC was demonstrated (paper 4).

### 4.1.2. $KLaF_4$ glass-ceramics

During this thesis, another composition, called 70Si7LaK doped with $Nd^{3+}$ ions was also studied (paper 6). The interest of this composition relies on the possibility of growing $KLaF_4$ crystals, known as efficient host for RE ions. $KLaF_4$ crystals are polymorphic and possess two phases: cubic (α) and hexagonal (β). The hexagonal phase is more stable from a thermodynamic point of view and presents a very low phonon energy ~ 262 $cm^{-1}$ [83]. The use of $Nd^{3+}$ was dictated by the efficient replacement of $La^{3+}$ by $Nd^{3+}$, as previously described for the 55Si10La composition (paper 3). Moreover, $Nd^{3+}$, due to its few energy levels, allows out selective excitation PL experiments to be carried out. Transparent glasses were casted onto brass mould at room temperature and no spontaneous crystallisation was observed. The crystallisation and the optical properties of this composition were extensively described in paper 6, showing how the $Nd^{3+}$ content affects the phase evolution of $KLaF_4$ NCs.

Similar to 55Si10La composition, the addition of $Nd^{3+}$ increases the $T_g$ from 568 to 584 °C from $0.1NdF_3$ to $2NdF_3$-doped glasses. The increase of $T_g$ is related with a rise of viscosity at low temperature. A very interesting feature is the possibility to tune the kind of phase (α or β) by a specific doping level. For heat treatment at 590 °C (T slightly above $T_g$) the α phase crystallises in all samples and it is practically the only phase for all doping levels except for the glass-ceramic doped with $0.5NdF_3$.

The crystal size (in the asymptotic region) of the α phase ranges from 8-17 nm (590 °C) to 30 nm (660 °C), while for β phase the crystal size passes from 11 nm (590 °C) to 40 nm (660 °C), (paper 6). It is concluded that the two phases nucleates independently, being the $0.5NdF_3$-doped glass the best one to develop the β phase. The possibility of tailoring a specific crystal phase depending on the kind and amount of dopant along with a specific temperature-time programme has interesting perspectives for what concerns photonic applications.

Further structural characterisation of the 0.5$NdF_3$-glass-ceramic performed by HRTEM permitted both crystal phases to be identified, as shown in Figure 4.11. A bimodal crystal size distribution was measured, the size of α and β phase being in agreement with that obtained by XRD, (paper 6). No phase-separation regions were detected for this glass composition. A uniform glass matrix, without droplets homogenously dispersed, was observed.

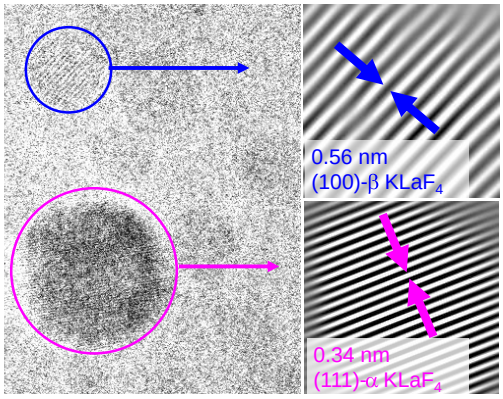


***Figure 4.11**. HRTEM micrograph of 70Si7LaK glass-ceramic doped with 0.5$NdF_3$ and treated 590 °C for 150 h. The lattice distances for α-$KLaF_4$ (cubic) and β-$KLaF_4$ (hexagonal) phases are also shown.*

A detailed optical characterisation showed the existence of $Nd^{3+}$ ions incorporated in both α and β phases, demonstrating how it is possible to isolate them. For example, clear differences are observed in the low temperature PLE spectra (emission at 1046 nm) for the glass-ceramic treated at 660 °C during 66 h and doped with 0.1 and 0.5$NdF_3$, Figure 4.12a. For the 0.1$NdF_3$-glass-ceramic, the $^4I_{9/2}$-$^4F_{5/2}$ band is composed of sharp peaks at 801 and 871 nm together with a broad band at 770-790 nm due to crystalline (α-$KLaF_4$) and amorphous environments, respectively. For the 0.5$NdF_3$-glass-ceramic a different PLE spectrum is obtained, where the same peak as for the 0.1$NdF_3$-glass-ceramic are observed in addition to a much more intense peak at 792 nm (β-$KLaF_4$). Moreover, the $^4I_{9/2}$-$^4F_{3/2}$ transition splits into two components in agreement with a well-defined crystal field with a lower symmetry than the cubic one. Further evidence was obtained from the PL spectra recorded at 9 K and exciting at 792 nm, Figure 4.12b. A glass-like emission of $Nd^{3+}$ ions was measured for the $^4I_{9/2}$-$^4F_{5/2}$ transition in the 0.1$NdF_3$- glass-ceramic. Instead, a structured band was obtained for the 0.5$NdF_3$-glass-ceramic, confirming that for the 792 nm excitation we mainly excite

$Nd^{3+}$ ions in β-$KLaF_4$. The lifetime for the 0.5$NdF_3$- glass-ceramic (emission at 1046 nm, excitation at 792 nm) is 440 μs and is described by a single exponential. More measurements and discussion for the 70Si7LaK composition are given in paper 6.

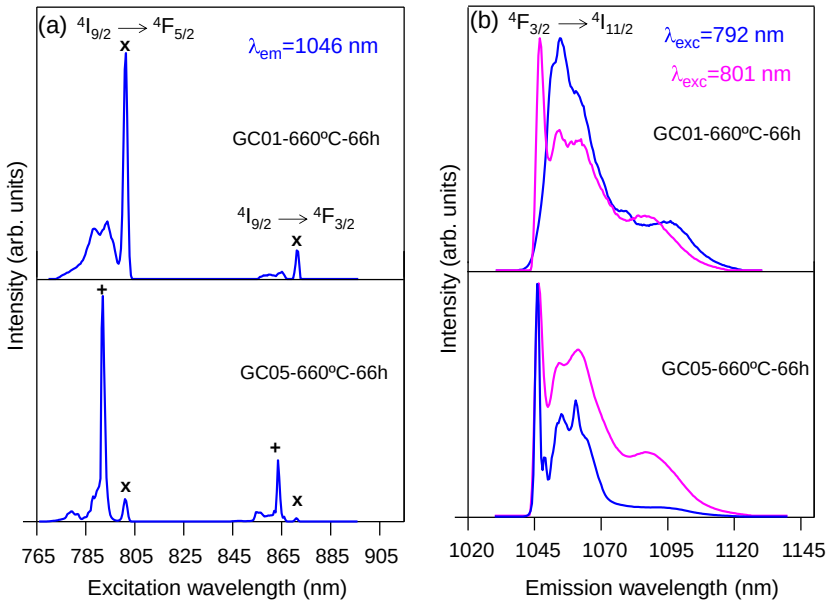


***Figure 4.12***. *Low temperature (9 K) (a) PLE and (b) PL spectra for 70Si7LaK glass-ceramics doped with 0.1 and 0.5$NdF_3$ (mol%) and treated at 660 ℃ for 66 h.*

### 4.1.3. Optical fibres

The processing methods offered by the MQ method have also been used to prepare optical fibres with a glass-ceramic core. These novel devices attracted great attention due to the possibility of growing high efficient fluoride NCs in optical fibres retaining the transparency of the untreated fibre. Moreover, longer interaction lengths (30-100 cm) can promote certain ET mechanism in nonlinear optical processes with respect to much smaller bulk lengths (1-5 mm).

A proper selection of the cladding glass is necessary to ensure a good and stable drawing process. Furthermore, the two glass compositions should have similar thermal properties (CTE, viscosity, $T_g$) in the temperature region used for drawing and crystallisation. For glass compositions that undergo crystallisation, the thermal stability parameter $\Delta T=T_p-T_g$ should be at least 200 °C to avoid spontaneous crystallisation during the drawing. This empirical requirement is very important for fibre drawing with the rod-in-tube method in which the cladding glass, acting as a

thermal barrier, prevents a fast heat loss. For direct-melting this condition can be relaxed, and glass compositions that have a stronger crystallisation tendency ($\Delta T<100$ °C) can also be drawn in transparent fibres avoiding spontaneous crystallisation. Another possibility is the use of quite high temperature cladding glasses and drawing the fibres in a temperature region in which the core glass is almost melted (similar to the melt-in-tube method). In this thesis both the direct-melting and the use of rod-in-tube method were used to prepare transparent fibres with a glass-ceramic core based on oxyfluoride compositions.

The effect of processing on the crystallisation and optical properties has also been discussed and related to that of the corresponding bulk samples. The first studies were performed on $Nd^{3+}$-doped fibres of the 55Si10La composition prepared by a direct-melting process (paper 7). Small glass pieces doped with 0.1 and 2$NdF_3$ were heated in a Pt crucible in the range 1150-1480 °C. Transparent uncoated fibres with diameters ranging from 50 to 500 μm were obtained and then crystallised. Very broad and weak crystallisation peaks in DTA curves indicate a lower crystallisation tendency with respect to the corresponding bulk samples (papers 3 and 7). A delay in crystallisation was clearly observed by XRD. No $LaF_3$ crystals were observed in the fibre unless for heat treatments at 620 °C for extremely long treatment times of 120 h, instead bulk samples crystallise at such temperature after 3-5 h. A slight increase of the temperature at 640 °C was sufficient to obtain $LaF_3$ crystals of ~10 nm and emission spectra similar to those of $LaF_3$:$Nd^{3+}$ crystals have been obtained, as described in paper 7.

Such delay of crystallisation was explained based on a lower phase separation produced during the drawing process. In fact, phase separation occurs during the cooling and the cooling rate increases in a drawing process with direct-melt. Therefore, more energy is necessary to promote phase separation and provoke crystallisation. However, by HRTEM, EDXS and SAXS, the same structure, as for bulk samples, was observed. Amorphous fibres were converted in glass-ceramic ones with the typical features of the 55Si10La compositions: NCs enclosed in initial phase separation droplets and enriched in $Nd^{3+}$ ions, Figure 4.13.

A $SiO_2$ viscous shell was formed around the crystals preventing further growth and the same crystallisation mechanism of bulk samples was observed. From the analysis of their structure, bulk and fibre samples cannot be distinguished. This result has a remarkable consequence for the preparation of photonic devices. In fact, if the optical properties of the bulk sample are known, those of the corresponding fibres can be guessed, thus permitting the optimization of dopants content and crystallisation process.

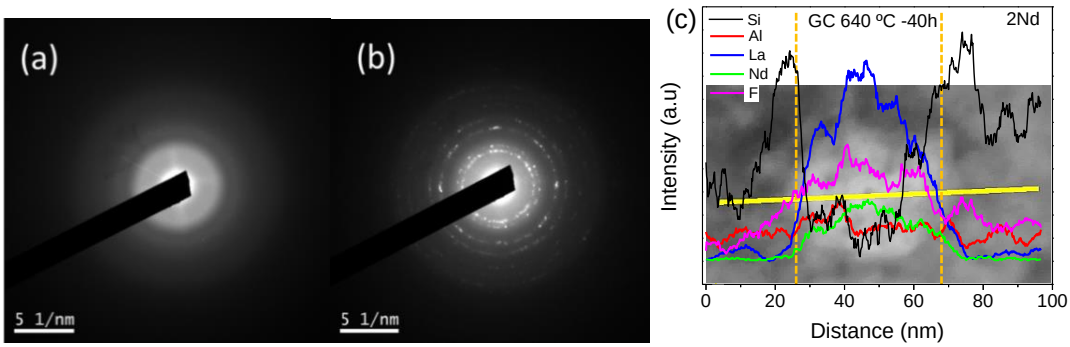


***Figure 4.13.*** *SAED of 55Si10La (a) fibre and (b) glass-ceramic fibre treated at 640 °C for 40 h and doped with 2$NdF_3$ (mol%). (c) EDXS in STEM mode of one droplets containing $LaF_3$ NCs.*

A SG cladding was made by dip-coating to cover a 30 cm glass-ceramic fibre using a silica sol, see section 3.1.3. Then, the coating was sintered at 450 °C for 1 h to obtain a dense 3 μm $SiO_2$ cladding (paper 7). The great novelty of this method is the absence of any thermal and mechanical requirement during the drawing. The cladding is deposited onto the glass-ceramic fibre and treated at temperature (450 °C) much less than the $T_g$ of the glass-ceramic core (~580 °C or higher). The problems of this method are: 1) the difficulty of covering quite larger fibres with a length longer than 50 cm; 2) the cladding thickness is limited to few μm, making difficult the preparation of different core/cladding geometries. On the other side, this method can be applied to a great variety of compositions.

Since very similar or indistinguishable nanostructures are observed for bulk samples and fibres prepared by direct melting method, similar optical properties are expected. In fact, it is the nanostructure around the $RE^{3+}$ ions that determines the

optical properties of these materials, and as shown for bulk samples, small NCs (10-15 nm) are able to reproduce optical features of mono-crystal samples, (paper 3).

For the untreated fibre, $Nd^{3+}$ excitation at 786 and 802 nm gives similar spectra corresponding to $Nd^{3+}$ in amorphous phase, Figure 4.14a. Instead, very different spectra were obtained for glass-ceramic fibres treated at 640 °C for 40 h and doped with $0.1NdF_3$, these spectra being similar to those obtained for the corresponding bulk samples, Figure 4.14b (compare with Figure 4.8). Therefore, even in these glass-ceramic fibres $Nd^{3+}$ ions are incorporated in both $LaF_3$ NCs and amorphous phase. Furthermore, the loss of typical crystal features is observed for the fibre doped with $2NdF_3$, indicating a high concentration quenching, in agreement with the results for bulk samples. The RT lifetime of the $0.1NdF_3$-glass-ceramic fibre treated at 640 °C measured at 1039 nm (exc. 786 nm) is 608 μs while at 1057 nm (exc. 802 nm) is 374 μs, (paper 7).

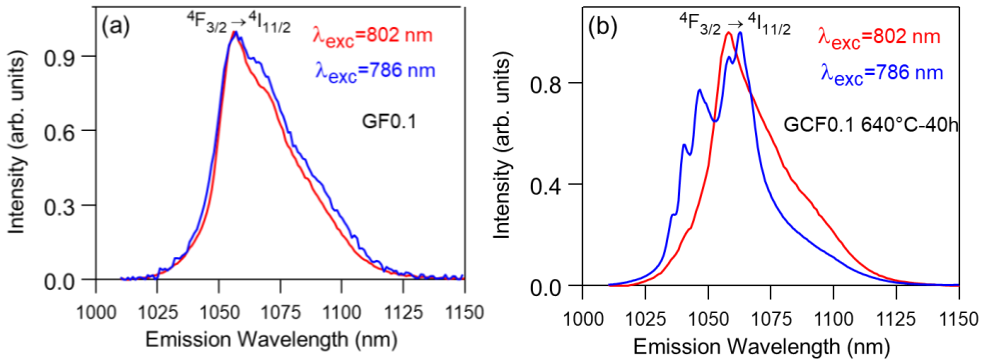


***Figure 4.14**. Room temperature emission spectra of 55Si10La (a) fibre and (b) glass-ceramic fibre treated at 640 °C for 40 h and doped with $0.1NdF_3$ (mol%).*

All the results discussed in the previous paragraphs confirm the great similarity of structure and optical properties for bulk and fibres prepared by direct melting, the main difference being a delay in the crystallisation process. Finally, even though interesting crystal-like optical features are obtained in glass-ceramic fibres, losses of 20 dB/m where obtained at 633 nm. Such value is quite high to obtain optical amplification.

The last paper described in this section concerns the preparation of glass-ceramic fibres based on $NaLuF_4$ solid solutions and doped with $Er^{3+}$-$Yb^{3+}$. The results for the

bulk samples, based on the 70Si6NaLu composition, are described elsewhere [127] and are not summarised in this section.

The $T_g$, CTE and refractive index are 525 °C, 7.4 ±0.5× $10^{-6}$ ($°C^{-1}$) and 1.49 at 588 nm, respectively. A study of the glass viscosity was performed with HSM (section 3.5.3). The viscosity of the 70Si6NaLu glass is ~ 4.1 dPa.s at 1000 °C. The DURAN® glass was selected as suitable cladding glass, with refractive index of 1.473 at 587.6 nm, due to the low refractive index of the 70Si6NaLu composition. An advantage of DURAN® glass is its quite high working point (4.1 dPa.s at 1260 °C) that permits fibre drawing up ~1250 °C, however this borosilicate glass has a quite low CTE (3.4±0.5 x$10^{-6}$ $°C^{-1}$) and $T_g$ (520 °C) with respect to the 70Si6NaLu composition.

Transparent and amorphous fibres with core/cladding geometry 100 μm/250 μm were drawn at 1230 °C using the rod-in-tube method (section 3.1.1). For lower drawing temperature (1100 °C) a white core was obtained due to excessive phase separation produced in the core fibres. Glass-ceramic fibres were obtained after treatment at 600 C during 10 and 20 h. This temperature is the typical crystallisation temperature of bulk sample and practically coincides with the dilatometric softening temperature of the DURAN® glass (~ 598 °C). For higher temperatures the cladding glass can be strongly deformed. XRD confirmed the absence of crystal phases in the as made fibres, while cubic solid solution of the type $NaLuF_4$ were obtained in the glass-ceramic core with an average size ~ 20 nm, Figure 4.15. As observed for the 55Si10La samples, the same heat treatment at 600 °C for 20 h performed on bulk samples produces much bigger fluoride crystals (~ 40 nm). However, this size is enough to obtain efficient UC processes using $Er^{3+}$ and $Yb^{3+}$ as dopants. HRTEM showed a wide crystal size distribution which value is in agreement with the XRD results. Such broad distribution can be related with the drawing process and the temperature gradient produced in the interior of the core glass rode. Moreover, few small crystals are already present in the fibre. During the crystallisation process new crystals grow and those already existing become bigger. Another interesting observation is the presence of elongated crystals not seen in the 55Si10La fibres.

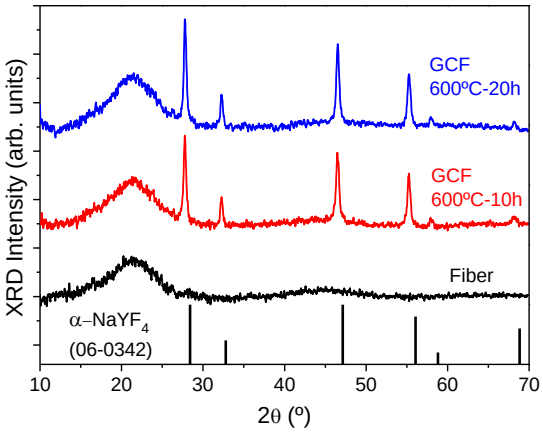


***Figure 4.15**. XRD of 70Si6NaLu fibre and glass-ceramic fibres treated at 600 °C during 10 and 20 h. The fibres are doped with 0.5ErF₃-2YbF₃ (mol%).*

The UC emission for $NaLuF_4$-glass-ceramic fibres, treated at 600 °C for 20 h, shows that similar spectra are obtained for glass-ceramic bulk [127] and fibre materials using similar excitation conditions, Figure 4.16a. This result confirms the incorporation of $Er^{3+}$ and $Yb^{3+}$ ions in the fluoride NCs. However, by an adequate focusing of the pumping power in the fibre, a different UC spectrum is obtained, the green UC emission becoming more important, Figure 4.16b.

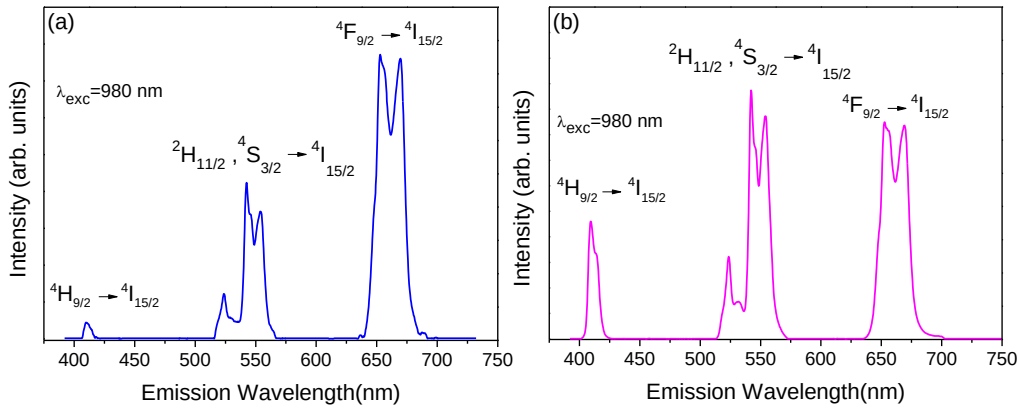


***Figure 4.16**. UC emission spectra for 0.5ErF₃-2YbF₃ doped 70Si6NaLu glass-ceramic fibres treated at 600 ℃ for 20 h exciting the system at 980 nm. The UC spectrum of (a) is obtained without focusing the excitation, while for (b) the excitation power was properfocused ly in the glass-ceramic fibre.*

## 4.2. Section 2- Sol-gel materials

### 4.2.1. $LaF_3$ glass-ceramics with TEOS

SG process was used for the preparation of novel compositions containing a higher active phase content. As described in the introduction, a common problem of oxyfluoride compositions prepared by melting is the high fluorine loss (30-40 wt%). Moreover, high fluoride contents in aluminosilicate compositions generally produce spontaneous crystallisation.

Great effort has been dedicated to study the crystallisation mechanism of bulk samples. Few authors studied the crystallisation mechanism of $SiO_2$-$MF_2$ phases using DTA and most of them considered that the crystallisation of fluorides in SG oxyfluoride glass-ceramics follows a diffusion-controlled process [171]. For a diffusion process some typical features are expected, as the increase of the crystal size with the heat treatment time and/or temperature and also the possibility to tailor certain phase controlling the crystallisation process. But the crystallisation mechanism of $80SiO_2$-$20LaF_3$ and similar compositions, studied in this thesis and extensively described in paper 8, is very different.

DTA curves of $SiO_2$-$MF_3$ xerogels present three different regions (papers 8 and): a first endothermic peak in the range 100-200 °C due to water and solvent removal; a sharp exothermic peak in the range 280-350 °C and a second exothermic peak in the range 450-600 °C, Figure 4.17a. The second exothermic peak disappears for heat treatment in Ar atmosphere hence it is associated to organic combustion. Instead, the first exothermic peak appears at the same temperature in both air and Ar atmospheres and it is associated to the crystallisation of fluoride crystals, Figure 4.17b. The peak is sharp comparing with several oxyfluoride compositions prepared by melting where the crystallisation peak is much broader (sometimes also difficult to be detected, papers 2 and 3). Moreover, a relevant weight loss (10-30 wt%) is also observed and associated with the crystallisation peak. All of these aspects indicate a fast process with mass release.

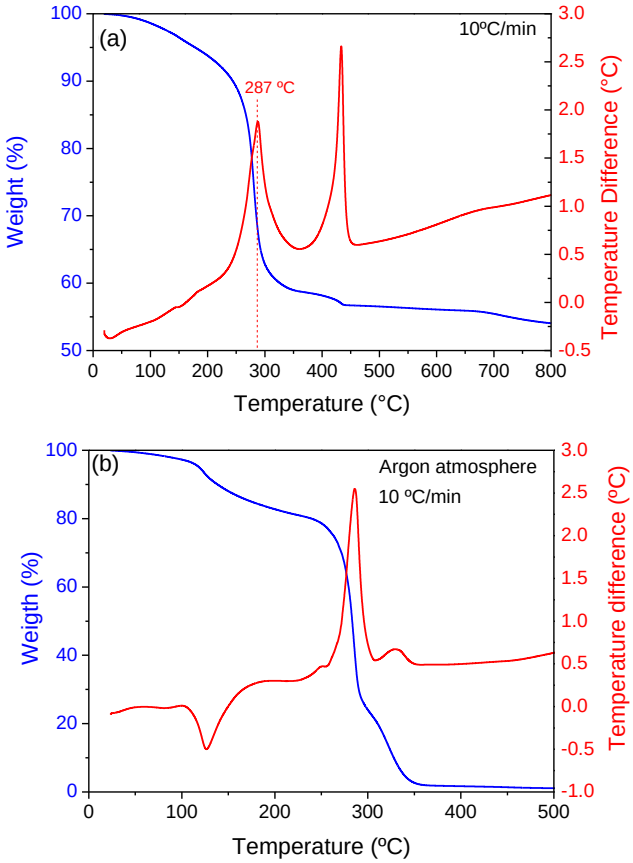


***Figure 4.17**. DTA (red) and TG (blue) curves for 80$SiO_2$-20$LaF_3$ sample measured in (a) air and (b) argon using a heating rate of 10 °C/min.*

Calculations performed using the Avrami's and Ozawa's equations indicate a similar crystallisation mechanism as for melted compositions, Figure 4.18.

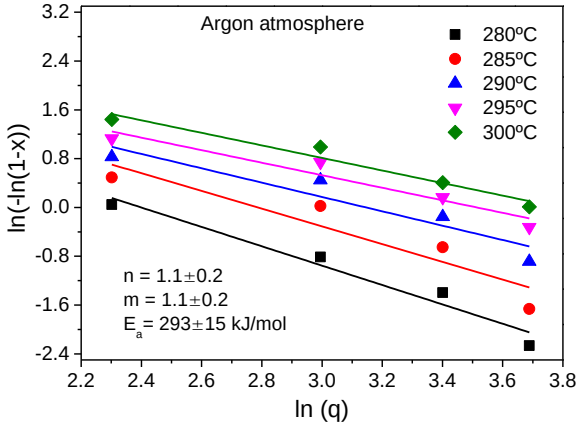


***Figure 4.18**. Ozawa plots for 80$SiO_2$-20$LaF_3$ bulk samples heated in Ar atmosphere with heating rates of 10-40 °C/min.*

However, remarkable differences are observed by studying the crystallisation kinetics by XRD. For example, fluoride NCs are already formed for heat treatment at 350, 450 and 550 °C during 1-5 minutes. Moreover, for $LaF_3$ NCs there is no crystal growth when increasing the treatment time and/or temperature up to ~ 800 °C. Even more surprisingly, the crystal size and crystalline fraction decrease for long treatment time, Figure 4.19a. A similar effect occurs if the sample is not quenched from the crystallisation temperature to RT, Figure 4.19b. These results are completely contradictory with a diffusion-controlled process. Furthermore, at high temperature it is considered that the precipitation of crystals is unstable.

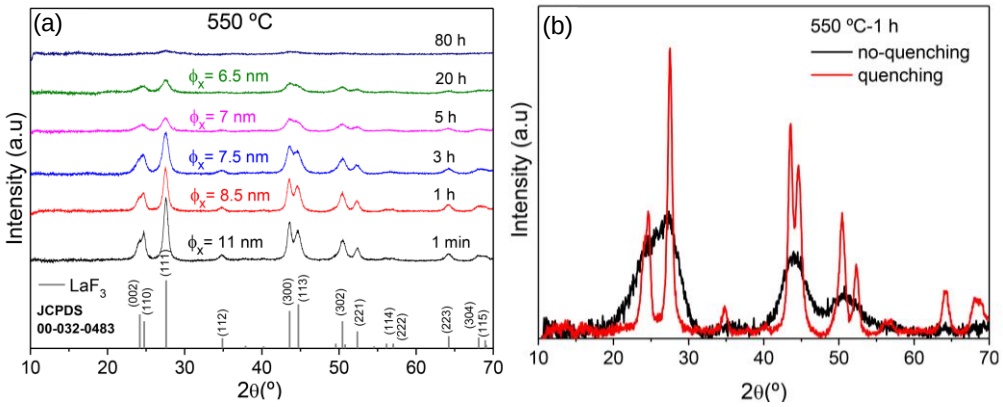


***Figure 4.19.*** *XRD of $80SiO_2$-$20LaF_3$ glass-ceramic bulk samples treated at 550 °C from 1 min up to 80 h. (b) Comparison between samples heat treated at 550 °C for 1 h and then quenched to room temperature (red) or cooled down in the furnace (black).*

characterisation of the fluorine environment in the xerogel and in the glass-ceramic sample was performed by $^{19}F$ MAS/NMR to understand the crystallisation mechanism, Figure 4.20. In the xerogel, only one single band at -76 ppm is observed indicating that fluorine ions are still coordinated to the TFA acid precursor. After the heat treatment at 550 °C for just 1 min, the fluorine environment has completely changed and it is practically like pure $LaF_3$ crystals with the three bands centred at -22, -18 and 26 ppm, respectively. Therefore, no bonds between fluorine ions and $SiO_2$ chains are observed, and from a thermodynamic point of view, the fluorides and the glass network evolve independently.

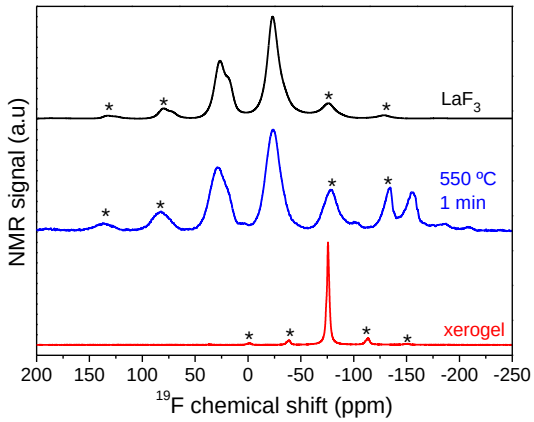


***Figure 4.20.*** *$^{19}F$ MAS/NMR of $80SiO_2$-$20LaF_3$ xerogel and glass-ceramic bulk treated at 550 °C for 1 min. The spectrum for the $LaF_3$ reference compound is also shown. The * symbol indicates spinning-side bands.*

Respect to the decrease of crystal size and fraction for long heating time, and considering that $LaF_3$ has one single stable phase at atmospheric pressure, the dissolution of $LaF_3$ crystals in the $SiO_2$ network was proposed, paper 8. A possible explanation is that for fast heat treatments (1 min or 1 h), cluster of crystals are formed that when the treatment time increases, the motion and separation in smaller crystals take place provoking the decrease of the crystal size. This argument was sustained by some authors [268]. On the contrary, the results described in paper 8 show that for 1 min of heat treatment, fluoride crystals homogenously distributed in the matrix are obtained (see also papers 10 and 11). Therefore, the formation of clusters is excluded.

All the aforementioned conclusions indicate that oxyfluoride glass-ceramics prepared by SG follow a completely different crystallisation process with respect to melted glasses. Moreover, the strong weight loss, associated with the crystallisation process of $LaF_3$, indicates a chemical decomposition of the starting precursors followed by crystal precipitation, as happens in the precipitation of salts in liquid phase. The driving force may be attributed to a supersaturation process [269].

Another important point that strongly affects the crystallisation process is the heating rate used for crystallisation. For fast heating rates, such as 10 °C/min, the crystallisation peak can be 4-5 times higher compared to measurements performed at 1 °C/min, paper 11. Anyway, in most cases a low heating rates was used to avoid the fracture tendency of bulk monoliths, also called self-supported layers. For examples,

bulk samples for optical characterisation prepared using TEOS were always treated at 1 °C/min to obtain crack-free samples.

It should be noted that one of the objectives of this thesis is the preparation of SG thin films for photonic applications. The best application of SG materials is as thin films because coatings can be deposited onto several substrates (glass, Si, metals etc), easy to handle, and big surfaces (10-20 $cm^2$) could be covered. For these reasons, thin film samples of $80SiO_2$-$20LaF_3$ composition doped with $Nd^{3+}$ were prepared for comparison with bulk samples and the results described in paper 8.

In the case of thin films, the stability studies of sols are important to ensure the maintenance of product, safety and efficacy. For this, the sol viscosity, described in section 3.3, was measured and a value of ~ 3 mPa.s was obtained. Such value is maintained for several weeks, demonstrating the good stability. For all the withdrawal rates used (maximum 35 cm/min) crack-free coatings were obtained using heating rates of 1 and 10 °C/min. All the results described below are referred to thin films prepared with TEOS and treated with a heating rate of 10 °C/min.

A maximum coating thickness of 600 nm was obtained for $80SiO_2$-$20LaF_3$ thin films prepared using TEOS as precursor and after heat treatment at 350 °C for 3 h, paper 9. The thickness decreases up to 325 nm when the heat treatment increases up to 850 °C. However, it is very difficult to study the crystallisation mechanism as well as to perform a detailed structural characterisation of thin films due to their low thickness For example, by GI-XRD a very broad diffraction peak was observed at ~ 27 ° for glass-ceramic films treated at 550 and 750 °C during 3 and 80 h, corresponding to more intense diffraction peak of $LaF_3$. Anyway, an estimation of the crystal size was impossible with such GI-XRD measurements. Furthermore, small $LaF_3$ NCs were observed by HRTEM only for heat treatment at 750 °C. However, since it is difficult to measure these sample by HRTEM, it is not excluded that also at lower temperatures, as 550 °C, $LaF_3$ crystals can be present. Small $LaF_3$ NCs with size of 4 nm were observed in bulk sample of the same composition, treated at 550 and 650 °C for 3 h, using XRD and HRTEM. The diffractogram of bulk samples treated at 650 °C for 3 h clearly shows $LaF_3$

diffraction peaks. Moreover, the crystal size obtained using the Scherrer equation is in agreement with that obtained from the HRTEM micrographs.

A first optical characterisation using $80SiO_2$-$20LaF_3$ thin films doped with 2 and $3Nd^{3+}$ (mol %) was performed to demonstrate the possibility of obtaining glass-ceramic films by SG, paper 9. A very low PL signal was obtained for the film treated at 150 °C (xerogel) but a notable increase of the PL was observed increasing the treatment temperature, Figure 4.21. However, the PL spectra show broad bands, typical of $Nd^{3+}$ ions in an amorphous environment. Even though the PL increases with the heat treatment, such behaviour is likely associated to a reduction of the $OH^-$ groups that is typical in SG materials. In fact, the high vibration frequency of $OH^-$ groups ($2^{nd}$ overtone band ~ 950 nm) can easily de-excite the $^4F_{3/2}$ energy level of $Nd^{3+}$ ions. FTIR spectra of thin films, measured in transmission, show a decrease of $OH^-$ groups when the temperature increases. Around 98% of $OH^-$ groups are eliminated for heat treatment at 850 °C. But such temperature it is quite high and other phases as LaOF can crystallise. For this reason, a compromise between treatment temperature and presence of $OH^-$ groups has to be reached hence the highest treatment temperature for thin films was fixed to 750 °C.

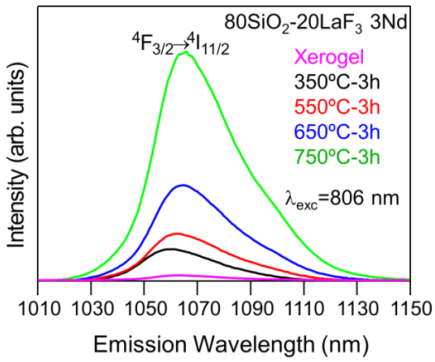


***Figure 4.21***. *Room temperature PL spectrum of $80SiO_2$-$20LaF_3$ xerogel and glass-ceramic thin films doped with $3Nd^{3+}$ and excited at 806 nm.*

Moreover, for all the treatment temperatures very low lifetimes, ~ 40 μs, were obtained at 1064 nm. Such low values could be associated or to an extremely high concentration of $Nd^{3+}$ in $LaF_3$ crystals or to the presence of high amounts of $OH^-$ groups. Another possibility is the presence of $Nd^{3+}$ at the interphase between crystals

and glass matrix that provokes a strong coupling of the crystals and glass network vibrations.

Compared to thin films, a completely different behaviour was obtained for $80SiO_2$-$20LaF_3$ bulk samples treated at 650 °C for 3 h. In this case, a clear indication of $Nd^{3+}$ incorporation in $LaF_3$ crystals was observed, paper 9. As described in paper 3, the emission of $Nd^{3+}$ ions in $LaF_3$ crystals is unambiguously distinguished from that of $Nd^{3+}$ ions in the glass matrix. In particular, for excitation at 786 nm the main emission is associated to $Nd^{3+}$ ions in $LaF_3$ crystals with well-resolved Stark components.

The emission spectrum of $80SiO_2$-$20LaF_3$ bulk sample treated at 650 °C for 3 h becomes much broader increasing the doping level from 0.5 to $3Nd^{3+}$ (mol%), as shown in Figure 4.22. A remarkable difference was observed between the bulk xerogel and the corresponding treated samples. In the xerogel, the excitation of $Nd^{3+}$ ions at 786 nm produces a spectrum associated with an amorphous surrounding, Figure 4.22. This is clearly related to the absence of $LaF_3$ crystals in the xerogel. Moreover, the PL intensity of the xerogel sample was ~ 100 times lower than for the corresponding bulk samples treated at 650 °C.

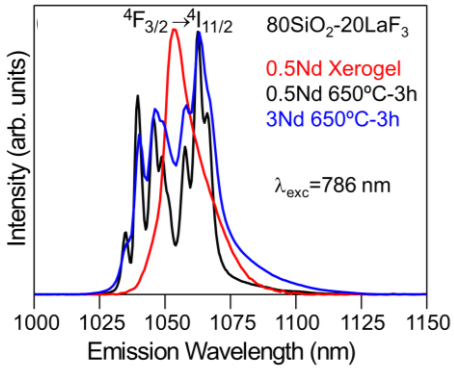


***Figure 4.22.*** *Room temperature PL spectra of $80SiO_2$-$20LaF_3$ xerogel and glass-ceramic bulk samples treated at 650 °C for 3 h, doped with 0.5 and $3Nd^{3+}$, under 786 nm excitation.*

Even though a clear indication of $Nd^{3+}$ in $LaF_3$ crystals was obtained for bulk samples, a lifetime of 147 μs was measured for the bulk sample doped with $0.5Nd^{3+}$ and treated at 650 °C during 3 h. The lifetime was strongly reduced to 18 μs for the samples doped with $3Nd^{3+}$. Such value indicates a strong concentration quenching and the high incorporation of $Nd^{3+}$ions in $LaF_3$ crystals.

In the case of $90SiO_2$-$10LaF_3$ composition doped with $Nd^{3+}$, a lower PL emission was obtained for both films and bulk samples treated in the same conditions. The lowest emission was also observed for $SiO_2$-$Nd^{3+}$ thin films (without $LaF_3$).

All these observations permit drawing important conclusions. 1) $Nd^{3+}$ ions are perfectly incorporated in $LaF_3$ crystals for bulk samples. 2) High concentration of dopants produces the emission quenching even for $Nd^{3+}$ concentration as low as $0.5Nd^{3+}$. Similar results were obtained for glass-ceramics prepared by MQ, where a strong luminescence quenching was observed above doping with $0.5Nd^{3+}$ (mol%), paper 3. For thin films, the behaviour is less clear and several factors play a decisive role as: $Nd^{3+}$ ions confined to the interphase crystal/matrix; much lower crystal size and fraction; and a high concentration of dopants. All these features can explain such broad PL and PLE bands, and the corresponding low lifetime values.

4.2.2. $LaF_3$ glass-ceramics with TEOS-MTES

With the aim of increasing the film thickness and the heating rate to study the crystallisation process, the synthesis was modified. A part of TEOS was substituted by MTES, an organic-inorganic precursor. In fact, as reported by Innocenzi et al. [270], using a TEOS:MTES molar ratio of 40:60, the film thickness could reach a maximum value of 2 μm. There are also other important advantages such as the reduction of $OH^-$ groups due to the hydrophobic nature of MTES [270,271], and the increase of the mechanical resistance of samples against cracking. The presence of $CH_3$ groups reduces the number of Si-O-Si bonds by replacing Si-OH for Si-$CH_3$ groups. The porosity and thickness increase, associated with a low matrix density and the relaxation of tensions trough pores. Thanks to this new precursor, it was possible to heat the bulk samples using a heating rate of 10 °C/min.

Interesting results were obtained for $80SiO_2$-$20LaF_3$ thin films and bulk samples doped with $Er^{3+}$ prepared with TEOS-MTES, paper 10. However, the difficulty of obtaining big crack-free bulk specimens, after crystallisation, is still one of the biggest problems to be faced.

Homogenous and crack-free film with thickness of ~ 1.4 μm was obtained after heat treatment at 550 °C for 1 h using a withdrawal rate of 35 °C/min. To understand better the structure of thin films, GI-XRD was performed at the Spline BM25B of the ESRF (λ=0.619 Å) on $80SiO_2$-$20LaF_3$ thin films doped with $0.5Er^{3+}$ and treated at 550 °C for 1 min. Quite broad diffraction peaks were observed around 10 and 11°. The first peak around 10 ° is the combination of the diffraction peaks from the (002) and (110) planes. The second and more intense peak at around 11 ° is due to diffraction from the (111) planes of $LaF_3$ crystals. For bulk samples of the same composition treated at 550 °C for 1 min, a better XRD pattern was observed and $LaF_3$ crystals were clearly identified. The crystal size was ~ 3 nm and 9 nm for thin film and bulk samples, respectively.

These results are also confirmed by HRTEM, where homogenously dispersed crystal are observed, even after fast heat treatment at 550 °C during 1 min, Figure 4.23. It is not possible to use higher temperature to heat treat samples prepared with MTES because the removal of $CH_3$ groups usually occurs between 550 and 600 °C producing the sample shrinkage and its cracking.

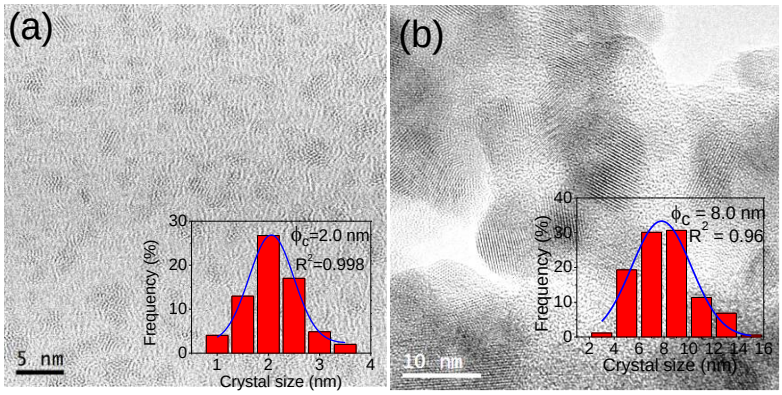


***Figure 4.23***. *HRTEM of $80SiO_2$-$20LaF_3$-0.5Er (a) thin film and (b) bulk sample treated at 550 °C for 1 min. The corresponding crystal size distributions are also shown.*

Another remarkable result is the possibility to quantify the crystal fraction using the Rietveld refinement. For $80SiO_2$-$20LaF_3$ bulk sample doped with $0.5Er^{3+}$ and treated at 550 °C for 1 min, a $LaF_3$ crystal fraction ~ 18wt% was obtained and shown in Figure 4.24, (paper 10). To our knowledge, this represents the highest crystal fraction reported in the literature for transparent oxyfluoride glass-ceramics prepared by SG.

This extremely interesting result demonstrates that by SG processing a much higher crystal fraction can be obtained with respect to glass-ceramics prepared by melting (paper 3).

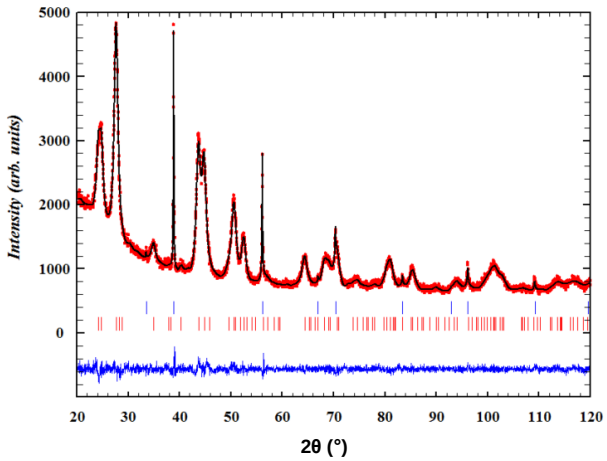


***Figure 4.24.*** *XRD pattern (black) and Rietveld refinement (red) for 80$SiO_2$-20$LaF_3$-0.5Er bulk sample treated at 550 °C for 1 min. The difference between the simulated and measured data is shown in blue.*

The study of the incorporation of $RE^{3+}$ ions and the change of their environment, when the xerogel is transformed into glass-ceramic, was also studied by XAS and EPR. The XAS results clearly demonstrate a fluorine-rich environment for both the xerogel and the glass-ceramic sample. However, a shrink of the first coordination shell suggests a change of the fluorine environment, from an amorphous to a crystalline one, after crystallisation. An estimation of $Er^{3+}$ ions environment in the glass-ceramic samples indicates that ~ 90% are in a fluorine-rich environment. If it is assumed that all fluorine is in the form of $LaF_3$, an $Er^{3+}$ effective concentration into the $LaF_3$ NCs around ~ 6.5 mol% is obtained. Such maximum theoretical value indicates that a great incorporation of $Er^{3+}$ ions occurs. This value should give an indication of the effective concentration even if other $RE^{3+}$ ions are used.

However, XAS is not sufficient to explain the incorporation of $RE^{+3}$ ions in $LaF_3$ crystals. For this reason, EPR measurements were performed on both xerogel and bulk samples doped with 0.1 and 0.5 $Er^{3+}$ (mol%) and treated at 550 °C during 1 min. For the xerogel sample a much broader EPR signal was observed in the range 500-1000 G, paper 10. Such broad band is clearly associated to an amorphous environment, similarly to that obtained for melted glasses (see paper 4 for comparison). In the case of

bulk samples, a remarkable observation is that practically all $Er^{3+}$ ions are found in $LaF_3$ crystals after the crystallisation process, Figure 4.25a. For the lowest $Er^{3+}$ concentration, the hyperfine structure due to $Er^{3+}$ isotopes with nuclear spin $I \neq 0$ is also resolved, Figure 4.25b. For $0.5Er^{3+}$-doped sample the hyperfine structure is broader and overlaps with the signal from $Er^{3+}$ ions with nuclear spin $I=0$. Therefore, it is concluded that for SG samples, most of RE ions are incorporated in the $LaF_3$ even after heat treatment during 1 min.

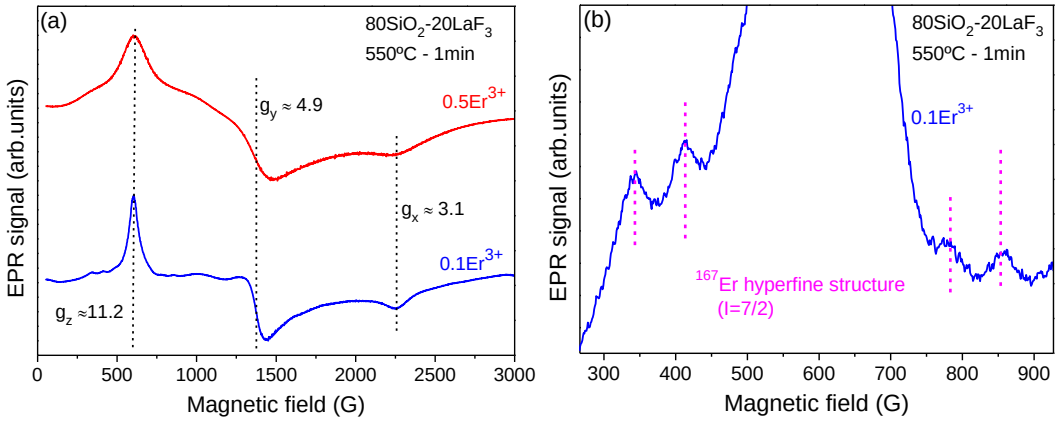


***Figure 4.25**. EPR signals for $80SiO_2$-$20LaF_3$ samples treated at 550 °C for 1 min and doped with 0.1 and $0.5Er^{3+}$. (b) Detail of the EPR signal with the hyperfine structure observed for the 0.1Er-doped sample.*

For $LaF_3$-glass-ceramics prepared by melting and doped with 0.1 and $0.5Er^{3+}$ (mol%) a noticeable amount of $Er^{3+}$ ions is still found in an amorphous environment after crystallisation, paper 5. Furthermore, the $RE^{3+}$ incorporation changes with time, as happens for diffusion processes.

These results are explained considering that in oxyfluoride xerogels, $La^{3+}$ and $RE^{3+}$ dopant ions are surrounding by TFA anions. Hence, an amorphous fluorine-rich environment is screening $La^{3+}$ and $RE^{3+}$ dopants (see $^{19}F$ NMR of Figure 4.20). After heat treatment, the chemical decomposition of the starting reagents causes the precipitation of $LaF_3$ NCs, and $RE^{3+}$ ions, used as dopants, get trapped in the fluoride NCs. Differently to melted glasses and glass-ceramics, the incorporation of $RE^{3+}$ ions happens during the crystallisation and evolves with time. This reasonable discussion permits explaining the $^{19}F$ NMR, XAS and EPR results described so far.

On the other hand, PL spectra of $80SiO_2$-$20LaF_3$ -$0.5Er^{3+}$ bulk and films were also studied. Sharp and well-defined Stark components were observed for the bulk sample treated at 550 °C for 1 min, confirming the presence of $Er^{3+}$ ions in $LaF_3$ NCs, Figure 4.26. For thin films the spectrum is much broader and similar to that of glasses. The small crystal size of $LaF_3$ NCs produced in thin films can explain this behaviour. In fact, important surface effects can provoke a strong coupling with the high phonons of the $SiO_2$-matrix.

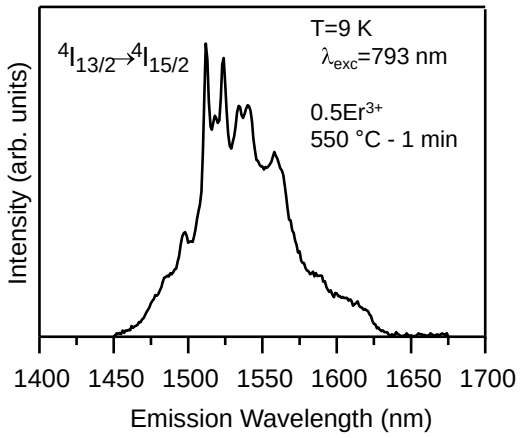


***Figure 4.26**. PL spectrum of $80SiO_2$-$20LaF_3$ glass-ceramic bulk sample doped with $0.5Er^{3+}$ and treated at 550 ℃ for 1 h.*

Summarising, the results suggest a completely different behaviour respect to crystallisation mechanism and RE incorporation for melted glasses.

To compare and confirm the results described so far, bulk samples with $SiO_2$-$GdF_3$ composition were prepared using TEOS-MTES and following the synthesis described for $SiO_2$-$LaF_3$ samples (table 3.3).

### 4.2.3. $GdF_3$ and $KLaF_4$ glass-ceramics with TEOS-MTES

$GdF_3$ and $KLaF_4$ are two interesting phases for photonic applications. In fact, $Gd^{3+}$ ions can act as sensitizer for $Eu^{3+}$, $Tb^{3+}$ or $Er^{3+}$, making this phase interesting for ET from UV to visible light [272,273]. On the other hand, $KLaF_4$ crystals have very low phonon energy, especially the hexagonal phase [83]. The possibility to prepare SG glass-ceramic materials with 20 mol% of these active phases is a really attractive opportunity to increase the optical efficiency of $RE^{3+}$-doped devices.

There is an important difference between $LaF_3$, $GdF_3$ and $KLaF_4$. $LaF_3$ has only one stable phase at atmospheric pressure [274], while $GdF_3$ and $KLaF_4$ exhibit two polymorphous structures. $GdF_3$ is found in hexagonal and orthorhombic phase, being the latter the most stable phase. Instead, $KLaF_4$ presents a cubic (less stable) and hexagonal phase (more stable). Moreover, $KLaF_4$ contains an alkaline ion that in glass matrices acts as network modifier.

Very similar DTA curves are observed for $90SiO_2$-$10GdF_3$ and $80SiO_2$-$20GdF_3$ compositions, with a crystallisation peak around 300 °C, paper 11. Similar DTA results are obtained for $90SiO_2$-$10KLaF_4$ and $80SiO_2$-$20KLaF_4$ compositions. In the case of $SiO_2$-$GdF_3$ compositions, both hexagonal (hexagonal $EuF_3$, JCPDS 00-032-0373) and orthorhombic (JCPDS 00-012-0788) phases were observed after heat treatment at 550 °C for 1 min, whereas XRD patterns of $SiO_2$-$KLaF_4$ samples, treated 350 °C for 1 min, show the crystallisation of $KLaF_4$ in cubic and hexagonal phases, being the cubic the main phase, Figure 4.27.

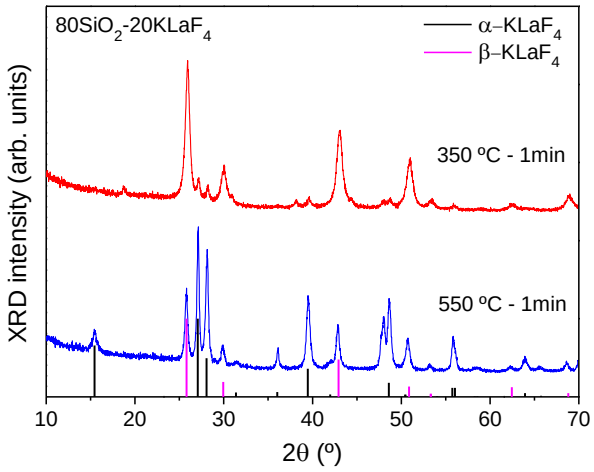


***Figure 4.27**. XRD patterns for $80SiO_2$-$20KLaF_4$ glass-ceramic bulk samples treated at 350 and 550 °C for 1 min. The XRD patterns for α and β-$KLaF_4$ phases are also shown.*

However, increasing the temperature to 550 °C, the main phase is the hexagonal one. The intensity of the diffraction maxima is similar for both thermal treatments, suggesting the transformation of the cubic phase to the hexagonal one which is the most stable phase. This behaviour is typical of precipitations occurring in liquid solutions, as described by some authors [269,275]. These results confirm again the idea of a crystallisation mechanism based on chemical decomposition and crystal

precipitation. Moreover, for polymorphic crystals a clear change of the crystal phase toward the most stable one is observed.

For $GdF_3$ crystals, hexagonal and orthorhombic phases are observed after heat treatment at 550 °C for 1 min up to 8 h. The crystal size of the hexagonal and orthorhombic phase is ~ 8 nm. No increase of the crystal size or crystalline fraction is observed when increasing the treatment time. The crystal dissolution with very long treatment time (> 8 h) is expected even for $GdF_3$ and $KLaF_4$, as happens for $LaF_3$ crystals. Therefore, all fluorides precipitated in $SiO_2$ matrices are not stable for long heat treatment times. This phenomenon is explained with the absence of bonds between the Si-O links and the fluorides.

The main results for $90SiO_2$-$10GdF_3$ and $80SiO_2$-$10GdF_3$ bulk samples doped with $0.5Eu^{3+}$ (mol%) are summarized in the next paragraphs because the $SiO_2$-$KLaF_4$ composition has only been partly studied in this thesis and further studies and tests are necessary.

One of the most relevant results for $SiO_2$-$GdF_3$ composition is given by the EDXS analysis of $GdF_3$ crystals precipitated after heat treatment at 550 °C during 1 min, Figure 4.28. A clear $Eu^{3+}$ ion enrichment is found in the crystals. As explained for the $LaF_3$ composition doped with $Er^{3+}$, the clear $RE^{3+}$ enrichment observed in $GdF_3$ crystals reinforces the idea of an incorporation mechanism of $RE^{3+}$ that occurs along with crystals precipitation. A detailed optical characterisation was performed for the $90SiO_2$-$10GdF_3$ and $80SiO_2$-$20GdF_3$ compositions and resumed below.

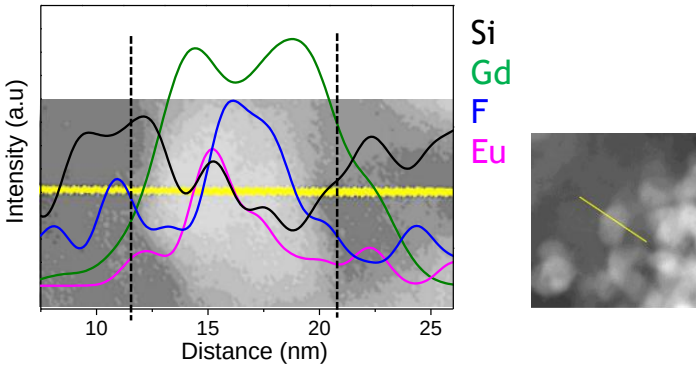


***Figure 4.28**. EDXS in STEM of $80SiO_2$-$20GdF_3$-0.5Eu bulk sample treated at 550 °C for 1 min. The yellow line is the scanning line.*

The use of $Eu^{3+}$ facilitates the study of the change of the environment thanks to the $^5D_0 \rightarrow {}^7F_2$ hypersensitive transition of $Eu^{3+}$ (see section 2.9). $Eu^{3+}$ ions were excited at 393 nm ($^7F_0$-$^5L_6$). The PL spectrum of the bulk xerogel sample shows quite broad $^5D_0$-$^7F_{0,1,2,3,4}$ emissions, typical of an amorphous environment, Figure 4.29. When $Gd^{3+}$ ions are excited at 273 nm ($^8S_{7/2}$-$^6I_J$), both $Gd^{3+}$ and $Eu^{3+}$ emissions are observed, indicating the occurrence of an ET process. However, the most intense signal is due to the $^6P_J$-$^8S_{7/2}$ emission of $Gd^{3+}$ ions, therefore such ET is not very efficient. Respect to bulk glass-ceramic samples treated at 550 °C during 1 min, the incorporation of $Eu^{3+}$ ions in the $GdF_3$ crystals is clearly observed. The $^5D_0$-$^7F_{0,1,2,3,4}$ emissions of $Eu^{3+}$ ions are now very sharp and structured in Stark components. Moreover, the $^6P_J$-$^8S_{7/2}$ emission of $Gd^{3+}$ is strongly reduced after excitation at 273 nm, indicating a more efficient ET between $Gd^{3+}$ and $Eu^{3+}$ ions in the glass-ceramic samples. The asymmetry ratio R, defined as $^5D_0$-$^7F_2$ /$^5D_0$-$^7F_1$ ratio, decreases from 2.77 for the xerogel to ~ 0.7 for the glass-ceramics. Similar values are obtained for $Eu^{3+}$ and $Gd^{3+}$ excitation at 393 and 273 nm, respectively. These results indicate that, after crystallisation, $Eu^{3+}$ ions pass from a non-centrosymmetric site (amorphous environment) to a centrosymmetric one ($GdF_3$ NCs).

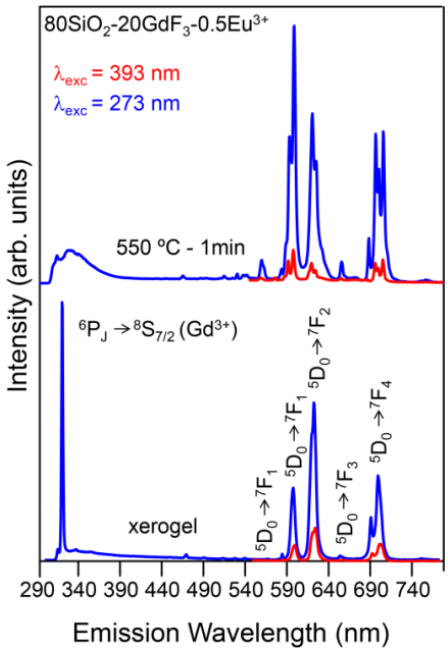


***Figure 4.29**. RT PL spectra for the 80SiO₂-20GdF₃-0.5Eu xerogel and glass-ceramic treated at 550 °C for 1 min under 393 and 273 nm excitation.*

The SG method has demonstrated to be an efficient route to obtain fluoride NCs. Doped and un-doped $GdF_3$ and $KLaF_4$ NCs dispersed in a $SiO_2$ matrix were efficiently obtained after fast heat treatment (1 min). Instead, the crystallisation of $GdF_3$ is much more complicated for melted compositions, and it has not been achieved in this thesis. Moreover, the crystallisation of hexagonal $KLaF_4$ in melted glasses was only obtained for specific doping levels.

Another advantage of the SG method is the possibility to add much higher active phase content, where most of $RE^{3+}$ ions could be incorporated in homogeneously dispersed crystals. After crystal precipitation, the fluorides are surrounded by the $SiO_2$ network inhibiting their diffusion and growth.

However, an important limitation, detected during this thesis, is the difficulty of increasing the crystal size or obtaining only a specific phase for polymorphous crystals. Alternative processing routes should be proposed. For example, the preparation of nanoparticles in liquid phase has been used by other authors [276]. No limitations to the crystal growth are imposed, because the crystallisation occurs in liquid phase and the ions mobility facilitate their diffusion and growth. Then, the nanoparticles can be added to a $SiO_2$ sol to prepare thin films and monoliths.

Moreover, another limitation of SG bulk samples is related to obtain large crack-free materials. The modification of the synthesis protocols and processing method is proposed to control the drying of xerogels using supercritical conditions in an autoclave.

In the next section the main conclusions obtained from this thesis are summarised.

# *CONCLUSIONS*

## CONCLUSIONS

*Materials preparation*

In this thesis, transparent glass-ceramics have been prepared by melt-quenching from three oxyfluoride glass compositions doped with $Pr^{3+}$-$Yb^{3+}$, $Nd^{3+}$ and $Er^{3+}$-$Yb^{3+}$.

$LaF_3$-glass-ceramic fibres have also been obtained using the direct-melting process with a single crucible. The glass-ceramic core was covered with 3 μm $SiO_2$ cladding prepared by sol-gel. The rod-in-tube method was applied for drawing $NaLuF_4$-optical fibre using commercial DURAN® glass for cladding.

Bulk and thin films containing up to 20 mol% of nominal active phase ($LaF_3$, $GdF_3$ and $KLaF_4$) were prepared by sol-gel from transparent and stable sols. Homogeneous and transparent films with good adhesion were obtained on different substrates (silica, soda-lime glass slide, Si-wafer and mica substrates).

By a partial replacement of TEOS with MTES precursor, thicker films of up to 1.4 μm were obtained using a withdrawal rate of 35 cm/min. Moreover, the mechanical resistance of bulk samples was increased due to the presence of $CH_3$ groups in the network, permitting thermal treatments at 10 °C/min to be used. The glass-ceramic samples were obtained after treatment at 350-750°C for short times.

$SiO_2$-$LaF_3$ and $SiO_2$-$GdF_3$ sol-gel glass-ceramics doped with $Nd^{3+}$, $Er^{3+}$ and $Eu^{3+}$ were successfully prepared, after controlling the synthesis process.

*Crystallisation and the effect of dopants*

The crystallisation mechanism of bulk and fibres prepared by melt-quenching is based on a diffusion-controlled process which starts from a constant number of nuclei.

For $LaF_3$-containing compositions, broad and weak crystallisation peaks were observed by differential thermal analysis. However, for other glass compositions, no relevant exothermic peaks were detected. Nevertheless, in all cases, the crystallisation of fluoride nanocrystals was achieved after thermal treatment.

The crystal size increases with treatment time at a fixed temperature until an asymptotic value in the range 8-40 nm is reached, the value of which depends on the glass composition and crystal phase.

Similar results were observed for the fibres but with a delay in crystallisation with respect to bulk samples of the same composition. This phenomenon was associated with the high cooling rate that the $LaF_3$-fibres suffered during the direct melting process.

However, for the fibres prepared with the rod-in-tube method, a shorter delay in crystallisation was observed due to the thermal screening produced by the cladding glass which reduces the cooling rate.

RE-dopants act as nucleating agents, promoting phase separation and leading to higher crystal fraction. The $LaF_3$ crystal fraction increased from 6% to almost 9 wt%, while the crystal size was reduced from 12 to 8 nm, when increasing the $NdF_3$ content from 0.1 to 1 mol%. Moreover, the crystallisation kinetics slows down with the addition of dopants. Similar results were obtained for $Er^{3+}$-$Yb^{3+}$-doped $LaF_3$-glass-ceramics when increasing the content of $Yb^{3+}$.

For $Nd^{3+}$-doped $KLaF_4$-glass-ceramics, the most significant phase obtained after crystallisation was α-$KLaF_4$. However, the addition of 0.5 mol% of $NdF_3$ also nucleates β-$KLaF_4$ phase. The nucleation of the β-phase is promoted for a specific doping level and the growth of α and β-phases occurs with independent kinetics.

The crystallisation of $LaF_3$, $GdF_3$ and $KLaF_4$ occurs in the range 290-300 °C for sol-gel bulk materials, according to the sharp exothermic peaks observed from DTA. Moreover, the crystallisation mechanism is very different from the diffusion-controlled process that occurs in glass-ceramics prepared by melting.

Neither the crystal size nor the fraction of $LaF_3$ increase when the heat treatment temperature and time increase; however, very fast heat treatments (1 min) at 350-550 °C are enough to precipitate the nanocrystals. Moreover, in contrast to melt-

quenching materials, crystal dissolution is observed for long treatment times, indicating the instability of fluorides at high temperatures.

The crystallisation mechanism of sol-gel glass-ceramics is based on a chemical decomposition followed by crystal precipitation, similar to the mechanism of crystal precipitation in the liquid phase. The proposed crystallisation mechanism has also been confirmed by $^{19}F$ NMR. No fluorine-silicon bonds are observed in the xerogel samples; instead, the coordination of fluorine ions with the TFA acid precursor is observed. The studies performed in this thesis indicate that RE dopants do not play a relevant role in the crystallisation process.

A crystal fraction of ~ 18 wt% was obtained for $80SiO_2$-$20LaF_3$ glass-ceramic bulk samples treated at 550 °C for 1 min, with crystal size ~ 10 nm. This fraction is the highest reported so far for $LaF_3$-glass-ceramics prepared by sol-gel.

For $SiO_2$-$LaF_3$ thin films, much broader XRD patterns were obtained, with a crystal size of 2-3 nm. The thinness and small crystal size (2-3 nm) of the films limited study of their crystallisation mechanism, so bulk samples were selected.

For polymorphous crystals, such as $GdF_3$ and $KLaF_4$, all the possible phases were observed even after a heat treatment of only 1 min. For $KLaF_4$-glass-ceramic, the α-phase is the main phase which precipitates at 350 °C after 1 min, but for treatment at 550°C the β-$KLaF_4$ is the main phase. A gradual transformation from the most unstable phase to the most stable one was observed with increasing temperature. A specific phase can be obtained by on controlling the heat treatment time or temperature.

*Nanostructure and dopant environment*

The typical nanostructure of $LaF_3$ and $NaLuF_4$-glass-ceramics prepared by melting is obtained by phase-separation droplets dispersed in the glass-matrix. For the $KLaF_4$-glass-ceramic, no phase separation is detected in the parent glass. The phase diagram of these three different compositions is the key to obtain a specific phase.

For $LaF_3$ glass-ceramics and $LaF_3$ glass-ceramic fibres, the initial size of amorphous phase-separation droplets increases after crystallisation and $LaF_3$ nanocrystals grow

inside them. However, for $NaLuF_4$-glass-ceramics, fluoride crystals develop from individual phase separation droplets in both bulk and fibre materials.

EDXS analysis of $LaF_3$ and $NaLuF_4$ demonstrated the enrichment of $SiO_2$ at the crystal/matrix interphase producing a viscous barrier and preventing further crystal growth after several hours of treatment. The difference arises from the $Al_2O_3$ content of the two compositions (55Si10La and 70Si6NaLu). For the $LaF_3$-composition, a much higher $Al_2O_3$ content (20 mol%) produces an additional viscous barrier surrounding the $LaF_3$ nanocrystals, preventing their growth in the form of single crystals. This process is responsible for the asymptotic behaviour of the crystal size.

The phase-separation droplets of the starting glass are already enriched in RE-dopants, which facilitates their incorporation in the fluoride nanocrystals during the crystallisation process. The presence of RE-ions in a fluorine rich-environment was also confirmed by XAS. However, part of the RE ions is still present in an amorphous environment even after heat treatment during 40 h, as confirmed by EPR measurements. A similar nanostructure was observed for glass-ceramic bulk and fibre materials.

Notable differences were observed by XAS and EPR when $Nd_2O_3$ or $NdF_3$ were used as raw materials for incorporation of $Nd^{3+}$ in the $LaF_3$ glass-ceramics. $NdF_3$ produces more efficient incorporation of $Nd^{3+}$ in the $LaF_3$ nanocrystals than $Nd_2O_3$. This behaviour was explained considering a "memory effect" of the first coordination sphere retained in the glass. The effective concentration of RE-ions in $LaF_3$ nanocrystals is at least ~ 10-15 times the nominal value.

Homogeneously distributed nanocrystals in a $SiO_2$ glass matrix were observed for sol-gel bulk and thin-film materials, after treatment at 550 °C for 1 min. XAS, EPR and EDXS showed that the RE incorporation in the fluoride nanocrystals occurs along with crystal precipitation. An amorphous fluorine-rich environment is already observed in the xerogel sample where the RE ions are screened by TFA anions. During the crystallisation process, the decomposition of fluorine-rich compounds cause the precipitation of fluoride crystals enriched with RE ions.

For low doping levels, such as 0.1 mol%, similar EPR signals were observed for RE ions in both glass-ceramics and single crystals, indicating the perfect incorporation of dopants in the fluoride nanocrystals. XAS analysis showed that around 90% of RE ions reside in the crystal phase after heat treatment.

*Optical properties*

The optical properties of glasses and glass-ceramics prepared by melting clearly demonstrated the incorporation of RE ions in the fluoride nanocrystals. Better energy transfer, up-conversion and down-conversion processes, along with much higher PL emission, were detected in the glass-ceramics compared to the glass.

For $Er^{3+}$-$Yb^{3+}$-doped $LaF_3$-glass-ceramics, a notable change of the red and green up-conversion emission with the crystal size was observed, allowing colour to be tuned with the heat treatment. A stronger green up-conversion was obtained when increasing the crystal size.

The spectral features of $LaF_3$:$Nd^{3+}$ single crystals were reproduced by a suitable selective excitation. For $Nd^{3+}$ doping levels higher than 0.5 mol% of $NdF_3$, a strong concentration quenching was observed, being the effective concentration at least 10 times the nominal value.

In this thesis, the first evidence of $LaF_3$:$Nd^{3+}$ emission in optical fibres has been obtained, with similar photoluminescence properties to the bulk samples. However, some improvements for the lasing or amplification process are still required, with the aim of reducing the propagation losses (16 dB/m).

For $Nd^{3+}$-doped $KLaF_4$-glass-ceramics, the emission was mainly attributed to the α-phase; however, on doping with 0.5 mol% of $NdF_3$, emissions from both α and β-phases were clearly observed.

For $Er^{3+}$-$Yb^{3+}$-doped $NaLuF_4$-glass-ceramic optical fibres, the up-conversion emission spectra were similar to those of the bulk samples but with a higher red up-conversion emission. However, the relative intensity of the red and green up-

conversion emissions changed when the excitation source was properly focused on the glass-ceramic fibre.

For $LaF_3$ and $GdF_3$ sol-gel glass-ceramic bulk samples, the incorporation of RE ions in the fluoride nanocrystals was unambiguously demonstrated due to the clear appearance of Stark components in emission and excitation spectra associated with fluoride crystals.

The spectral features of $LaF_3$:$Nd^{3+}$ single crystals have been reproduced in sol-gel bulk samples by selective excitation, confirming the incorporation of $Nd^{3+}$ in $LaF_3$ nanocrystals. The PL signal increased with the content of fluoride crystals, the concentration of which was ~ 100 times stronger compared to xerogel samples.

A stronger PL was also observed in $Eu^{3+}$-doped $GdF_3$ glass-ceramics along with a decrease of the asymmetry ratio $I(^5D_0\text{-}^7F_2)/I(^5D_0\text{-}^7F_1)$ of $Eu^{3+}$ ions after heat treatment at 550 °C for 1 min. These results clearly indicate a much better energy transfer process from $Gd^{3+}$ to $Eu^{3+}$ in $SiO_2$-$GdF_3$ glass-ceramic bulk samples due to the presence of $Eu^{3+}$ in $GdF_3$ nanocrystals.

For thin films, much broader spectral features were observed without clear evidence of RE-ion incorporation in fluoride nanocrystals. This result could be related to an extremely high effective concentration of RE ions in the fluoride nanocrystals, or to a strong coupling between the small fluoride nanocrystals and the glass matrix. However, the PL intensity increased with the treatment temperature, possibly associated with the reduction of $OH^-$ groups. Further studies are required to obtain glass-ceramic films with larger nanocrystals.

# *CONCLUSIONES*

## CONCLUSIONES

*Preparación de materiales*

En esta tesis se han obtenido vitrocerámicos transparentes a partir de la fusión de tres composiciones de vidrios de oxyfluoruro dopados con $Pr^{3+}$-$Yb^{3+}$, $Nd^{3+}$ y $Er^{3+}$-$Yb^{3+}$. A través de un tratamiento térmico de cristalización controlada, a una temperatura ligeramente superior a la $T_g$, se han obtenido vitrocerámicos con nanocristales de $LaF_3$ hexagonal, α y β-$KLaF_4$ o una solución sólida de nanocristales cúbicos del tipo $NaLuF_4$.

También se han obtenido fibras vitrocerámicas, conteniendo cristales de $LaF_3$, mediante el proceso de fusión directa usando un solo crisol. El núcleo vitrocerámico ha sido recubierto, a posteriori, con un revestimiento de $SiO_2$ de 3 μm preparado por el proceso sol-gel. El método de varilla en tubo se ha aplicado para obtener fibras ópticas con nanocristales de $NaLuF_4$ utilizando el vidrio comercial DURAN® para el revestimiento.

Mediante el método sol-gel se han preparado soles transparentes y estables a partir de los cuales se han obtenido películas delgadas y materiales en masa con un contenido de fase activa ($LaF_3$, $GdF_3$ y $KLaF_4$) hasta un 20% molar. Se ha observado una buena adherencia y homogeneidad de las películas delgadas sobre diferentes sustratos (sílice, portaobjetos de vidrio, silicio y mica).

Mediante una sustitución parcial de TEOS por MTES, se han obtenido películas delgadas con mayor espesor, hasta 1.4 μm, utilizando el método de inmersión y una velocidad de extracción de 35 cm/min. La incorporación de MTES ha permitido incrementar la resistencia mecánica de las muestras masivas debido a la presencia de los grupos $CH_3$ en la matriz y esto ha hecho posible usar tratamientos térmicos de 10 °C/min. Los vitrocerámicos se han obtenido después de tratamientos térmicos entre 350 y 750 ° C a tiempos cortos. Finalmente se han obtenido vitrocerámicos de composición $SiO_2$-$LaF_3$ y $SiO_2$-$GdF_3$ dopados con $Nd^{3+}$, $Er^{3+}$ y $Eu^{3+}$ después de la optimización del proceso de síntesis.

*Cristalización y efecto de los dopantes*

El mecanismo de cristalización de materiales en masa y fibras, preparadas por fusión, se basa en un proceso controlado por difusión que comienza a partir de un número constante de núcleos.

Mediante análisis térmico diferencial se han observado picos de cristalización anchos pero débiles para los vidrios que contienen $LaF_3$. Sin embargo, para otras composiciones no se han detectado picos exotérmicos de cristalización. De todos modos, para todas las composiciones, se ha conseguido la cristalización de nanocristales de fluoruro después de los tratamientos térmicos.

El tamaño de los cristales aumenta con el tiempo de tratamiento hasta alcanzar, para una temperatura fija, un valor asintótico entre 8 y 40 nm dependiendo de la composición del vidrio y de la fase cristalina.

Para las fibras de vidrio conteniendo $LaF_3$ se ha observado un comportamiento parecido pero con un retraso en la cristalización con respecto a las muestras en masa de la misma composición. Este fenómeno se ha asociado con la alta velocidad de enfriamiento a la que están sometidas las fibras durante el proceso de fibrado usando un solo crisol.

Para las fibras preparadas con el método de varilla en tubo, se ha observado un menor retraso de la cristalización debido al mayor apantallamiento térmico producido por el vidrio de revestimiento que reduce la velocidad de enfriamiento.

En el caso de los materiales preparados por fusión, los dopantes actúan como agentes de nucleación, promoviendo la separación de fases y produciendo una mayor fracción cristalina. La fracción cristalina de $LaF_3$ aumenta desde un 6% hasta casi un 9% en peso, mientras que el tamaño de los cristales se reduce de 12 a 8 nm, al aumentar el contenido de dopante $NdF_3$ de 0,1 a 1% molar. Además, la cinética de cristalización disminuye con la adición de dopantes. Se han obtenido resultados similares para los vitrocerámicos de $LaF_3$ dopados con $Er^{3+}$ -$Yb^{3+}$ al aumentar el contenido de $Yb^{3+}$.

Para los vitrocerámicos conteniendo nanocristales de $KLaF_4$ dopados con $Nd^{3+}$, la fase que se obtiene después de la cristalización ha sido α-$KLaF_4$. Sin embargo, para contenidos mayores de 0.5 % molar de $NdF_3$ se produce además una nucleación de la fase β-$KLaF_4$. Por lo tanto, la nucleación de la fase β se promueve para una cantidad de dopante específica y el crecimiento de las dos fases tiene lugar con una cinética de cristalización independiente.

Para materiales sol-gel en masa, se observa un pico exotérmico en el análisis térmico diferencial en el rango de 280-300 °C, asociado a la cristalización de $LaF_3$, $GdF_3$ y $KLaF_4$. Además, el mecanismo de cristalización es muy distinto al de un proceso controlado por difusión, típico de los vitrocerámicos preparados por fusión.

Tratamientos térmicos muy rápidos, 1 minuto a 350-550 °C, confirman la precipitación de los nanocristales. Sin embargo, a diferencia de los materiales preparados por fusión, el tamaño de cristal y la fracción cristalina de $LaF_3$ no aumentan al aumentar la temperatura y tiempo de tratamiento térmico. Para tratamientos térmicos largos se observa la disolución de los nanocristales, lo que pone de manifiesto la inestabilidad de los nanocristales de fluoruro a altas temperaturas en los materiales obtenidos por sol-gel.

El mecanismo de cristalización de los vitrocerámicos preparados por sol-gel se basa en una descomposición química seguida de una precipitación de los nanocristales, similar a lo que ocurre con la precipitación de cristales en fase líquida.

El mecanismo de cristalización también ha sido confirmado por resonancia magnética nuclear de $^{19}F$. De hecho, en el xerogel no se han observado enlaces entre flúor y silicio, sino que los iones de flúor están coordinados como en el ácido precursor, el TFA. Además, los estudios realizados en esta tesis indican que las TR usadas como dopantes no juegan un papel relevante en el proceso de cristalización.

Para el vitrocerámico en masa de composición $80SiO_2$-$20LaF_3$ tratado a 550 °C durante 1 min se han obtenidos cristales de $LaF_3$ de unos 10 nm y una fracción cristalina del 18% en peso. Este valor es el más alto reportado hasta la fecha para vitrocerámicos transparentes preparados por sol-gel.

Para las películas delgadas de la misma composición $SiO_2$-$LaF_3$, se han obtenido difractogramas mucho menos definidos y el tamaño de los nanocristales de $LaF_3$ es de unos 2-3 nm. El estudio del mecanismo de cristalización no se ha podido hacer utilizando las capas debido al bajo espesor de las mismas y al pequeño tamaño de los nanocristales.

En el caso de cristales polimorfos, como $GdF_3$ y $KLaF_4$, después de 1 minuto de tratamiento térmico se ha observado la cristalización de ambas fases cristalinas. Para los vitrocerámicos conteniendo $KLaF_4$, la fase α es la fase principal y precipita a partir de los 350 °C. Sin embargo, para tratamientos térmicos a 550 °C, la fase β llega a ser la mayoritaria frente a la α. Por lo tanto, se ha observado una transformación gradual de la fase menos estable (α) a la más estable termodinámicamente (β). Mediante el control del tiempo y / o la temperatura del tratamiento térmico se puede diseñar el vitrocerámico con la fase deseada.

*Nanoestructura y entorno de los dopantes*

La nano-estructura típica de los vitrocerámicos de $LaF_3$ y $NaLuF_4$ preparados por fusión está compuesta por pequeñas gotas de separación de fases dispersas en la matriz vítrea. Para los vitrocerámicos de $KLaF_4$, no se ha detectado separación de fases en el vidrio de partida. La clave para explicar las diferencias se halla en los diagramas de fase de estas tres composiciones distintas.

Para los vitrocerámicos y las fibras de $LaF_3$, el tamaño inicial de las gotas de separación de fases aumenta después de la cristalización y los nanocristales de $LaF_3$ crecen en su interior.

En los vitrocerámicos de $NaLuF_4$, tanto en los materiales en masa como en fibra, los nanocristales se desarrollan a partir de gotas de separación de fase individuales. La diferencia se debe al distinto contenido de $Al_2O_3$ de las dos composiciones (20% molar de $Al_2O_3$ para el 55Si10La y 5% molar de $Al_2O_3$ para el 70Si6NaLu).

El análisis por dispersión de energía de rayos X de los nanocristales de $LaF_3$ y $NaLuF_4$ ha indicado un enriquecimiento en $SiO_2$ en la interfase cristal/matriz después

de varias horas de tratamiento, produciendo una barrera viscosa que frena el crecimiento de los nanocristales. Este proceso es responsable del comportamiento asintótico del tamaño de los nanocristales en función del tiempo de tratamiento. Para la composición de $LaF_3$, un contenido de $Al_2O_3$ más alto (20% molar) produce una barrera viscosa adicional que rodea a los nanocristales de $LaF_3$, lo que impide su crecimiento en forma de un solo cristal.

Las gotas de separación de fase del vidrio de partida ya están enriquecidas en TR, lo que facilita su incorporación en los nanocristales de fluoruro durante la cristalización. La presencia de iones de TR en un ambiente rico en flúor también se ha confirmado por absorción de rayos X. Sin embargo, las medidas de resonancia paramagnética electrónica indican que parte de las TR se mantienen en un entorno amorfo después de tratamientos térmicos largos (40 h). Para las fibras se ha observado un comportamiento similar.

Las muestras conteniendo $LaF_3$ dopadas con $Nd^{3+}$, mostraron un comportamiento diferente dependiendo de la materia prima utilizada para la introducción de $Nd^{3+}$: $Nd_2O_3$ o $NdF_3$. Se observó una mayor incorporación de $Nd^{3+}$ en los nanocristales de $LaF_3$ cuando se usó $NdF_3$. Este comportamiento se explica considerando un "efecto memoria" por el cual las TR retienen la primera esfera de coordinación en el vidrio de partida. La concentración efectiva de TR en los nanocristales de $LaF_3$ es aproximadamente 10-15 veces el valor nominal.

Para materiales obtenidos por sol-gel, tanto en masa como en forma de película delgada y después de tratamientos térmicos a 550 °C durante 1 minuto se han observado nanocristales distribuidos homogéneamente en la matriz vítrea de $SiO_2$.

Las técnicas de absorción de rayos x, dispersión de energía de rayos x y resonancia paramagnética electrónica han confirmado la incorporación de TR en los nanocristales de fluoruro en el proceso de cristalización. De hecho, en el xerogel se observa un ambiente amorfo rico en flúor alrededor de las TR, que corresponde a las TR coordinadas y apantalladas con los aniones del ácido TFA. Las reacciones de

descomposición producen la precipitación de los fluoruros, atrapando a las TR en ellos y produciéndose la precipitación de nanocristales dopados.

Para niveles bajos de dopante, ~ 0,1% molar, la señal de resonancia paramagnética electrónica de las TR en los vitrocerámicos de $LaF_3$ es muy similar a la de los mono-cristales de $LaF_3$ dopados, indicando la buena incorporación de los dopantes en los nanocristales. Las medidas de absorción de rayos x han mostrado que alrededor del 90% de las TR se encuentra en la fase cristalina después del tratamiento térmico, confirmando los resultados de resonancia paramagnética electrónica.

*Propiedades ópticas*

Las propiedades ópticas de los vidrios y vitrocerámicos preparados por fusión han demostrado claramente la incorporación de las TR en los nanocristales de fluoruro. En los vitrocerámicos se han detectado procesos de transferencia de energía, upconversion y down-conversion más eficientes junto con una emisión de fotoluminiscencia mucho más intensa.

Para los vitrocerámicos de $LaF_3$ dopados con $Er^{3+}$-$Yb^{3+}$ se ha observado un cambio notable de la emisión verde y roja de upconversion con el tamaño de cristal, lo que permite tunear el color de le luz emitida en función del tratamiento térmico. En particular, se ha obtenido una emisión verde más intensa al aumentar el tamaño de los nanocristales.

Se han logrado reproducir mediante excitación selectiva las características espectrales de los mono-cristales de $LaF_3$: $Nd^{3+}$ Para niveles de dopante superiores a 0.5% molar de $NdF_3$, se ha observado una fuerte disminución de la fotoluminiscencia debido al "quenching" por concentración, siendo la concentración efectiva al menos 10 veces el valor nominal.

Para las fibras ópticas con nanocristales de $LaF_3$ se han obtenido resultados similares. Es la primera vez que se obtiene la emisión de $LaF_3$: $Nd^{3+}$ en fibras ópticas vitrocerámicas. Sin embargo, todavía se necesitan mejorar algunos aspectos para

conseguir reducir las pérdidas de propagación (16 dB / m) y poder utilizar estos dispositivos como amplificadores o láseres.

Para los vitrocerámicos de $KLaF_4$ dopados con $Nd^{3+}$, la emisión se ha relacionado principalmente con los iones $Nd^{3+}$ en cristales $\alpha$-$KLaF_4$, pero para un dopado con 0.5% molar de $NdF_3$ se ha observado claramente la emisión del $Nd^{3+}$ en ambas fases.

Para las fibras ópticas vitrocerámicas de $NaLuF_4$ dopadas con $Er^{3+}$-$Yb^{3+}$, se han obtenido espectros de emisión UC similares a los de las muestras masivas. Sin embargo, la intensidad relativa de las emisiones UC verde y roja, cambia cuando se focaliza la fuente de excitación en la fibra.

Para las muestras masivas preparadas por sol-gel conteniendo $LaF_3$ y $GdF_3$, se ha demostrado inequívocamente la incorporación de TR en los nanocristales de fluoruro debido a la clara aparición de las componentes Stark en los espectros tanto de emisión como de excitación.

A través de los experimentos de excitación selectiva de las muestras masivas preparadas por sol-gel, se han reproducido las características espectrales de los monocristales de $LaF_3$:$Nd^{3+}$, confirmando la incorporación de $Nd^{3+}$ en los nanocristales de $LaF_3$. La señal de fotoluminiscencia aumenta con el contenido de fase activa y es unas 100 veces más intensa en el vitrocéramico que en el xerogel.

También se ha detectado una fotoluminiscencia más intensa en los vitrocerámicos de $GdF_3$ dopados con $Eu^{3+}$ después de un tratamiento térmico a 550 °C durante 1 min. Además, se ha observado una disminución importante de la relación entre las emisiones $I(^5D_0$-$^7F_2)/I(^5D_0$-$^7F_1)$ de los iones $Eu^{3+}$. Estos resultados indican claramente un proceso de transferencia de energía de $Gd^{3+}$ a $Eu^{3+}$ mucho más eficaz en las muestras vitrocerámicas que en el xerogel debido a la presencia de $Eu^{3+}$ en los nanocristales de $GdF_3$.

En el caso de las películas delgadas se han observado espectros de PL mucho más anchos sin una clara evidencia de la presencia de las TR en los nanocristales de fluoruro. Este resultado estaría relacionado con una concentración efectiva de TR

extremadamente alta en los nanocristales o con un fuerte acoplamiento entre los fonones de los nanocristales con los de la matriz vítrea. Aunque se ha observado como la intensidad de fotoluminiscencia en las películas delgadas aumenta con la temperatura de tratamiento térmico, fenómeno posiblemente asociado con la reducción de los grupos $OH^-$. Sin embargo, es necesario realizar más estudios con el fin de películas delgadas vitrocerámicas con nanocristales de mayor tamaño.

# *REFERENCES*

## REFERENCES


[1] Y. Wang, J. Ohwaki, New transparent vitroceramics codoped with $Er^{3+}$ and $Yb^{3+}$ for efficient frequency upconversion, *Appl. Phys. Lett.* 63 (1993) 3268–3270. doi:10.1063/1.110170.

[2] A.A. Rywak, J.M. Burlitch, Sol-gel synthesis of nanocrystalline magnesium fluoride: Its use in the preparation of $MgF_2$ Films and $MgF_2$-$SiO_2$ composites, *Chem. Mater.* 8 (1996) 60–67. doi:10.1021/cm950109j.

[3] S. Fujihara, C. Mochizuki, T. Kimura, Formation of $LaF_3$ microcrystals in sol-gel silica, *J. Non-Cryst. Solids* 244 (1999) 267–274. doi:10.1016/S0022-3093(99)00009-5.

[4] S. Fujihara, M. Tada, T. Kimura, Sol-gel processing of $LaF_3$ thin films, *J. Ceram. Soc. JPN*. 106 (1998) 124–126. doi:10.2109/jcersj.106.124.

[5] A. de Pablos-Martín, *Vitrocerámicos transparentes del sistema $SiO_2$-$Al_2O_3$-$Na_2O$-$K_2O$-$LaF_3$/$YF_3$: Mecanismos de cristalización y propiedades ópticas*, Universidad Autónoma de Madrid, PhD Thesis, 2012.

[6] *Optics and photonics essential technologies for our nation*, The National Academies Press, Washington, DC, 2013. doi:10.17226/13491.

[7] http://www.light2015.org/Home.html, (2018).

[8] https://www.osa.org/en-us/100/osa100/items/osa_members_who_are_nobel_prize_winners/ (2018).

[9] Photonics dominates Nobel Prizes, *Nat. Photonics*. 8 (2014) 809. doi:10.1038/nphoton.2014.277.

[10] G.C. Righini, Passive integrated optical components, *J. Mod. Opt.* 35 (1988) 847–848. doi:10.1080/09500348814550981.

[11] C. Feldmann, T. Jüstel, C.R. Ronda, P.J. Schmidt, Inorganic luminescent materials: 100 Years of research and application, *Adv. Funct. Mater.* 13 (2003) 511–516. doi:10.1002/adfm.200301005.

[12] S. V. Eliseeva, J.C.G. Bünzli, Lanthanide luminescence for functional materials and bio-sciences, *Chem. Soc. Rev.* 39 (2010) 189–227. doi:10.1039/b905604c.

[13] J.C.G. Bünzli, Lanthanide luminescence for biomedical analyses and imaging, *Chem. Rev.* 110 (2010) 2729–2755. doi:10.1021/cr900362e.

[14] X. Huang, S. Han, W. Huang, X. Liu, Enhancing solar cell efficiency: the search for luminescent materials as spectral converters, *Chem. Soc. Rev.* 42 (2013) 173–201. doi:10.1039/c2cs35288e.

[15] N.C. George, K.A. Denault, R. Seshadri, Phosphors for solid-state white lighting, *Ann. Rev. Mater. Res.* 43 (2013) 481–501. doi:10.1146/annurev-matsci-073012-125702.

[16] X. Huang, Solid-state lighting: red phosphor converts white LEDs, *Nat. Photonics* 8 (2014) 748–749. doi:10.1038/nphoton.2014.221.

[17] H.U. Lee, S.Y. Park, S.C. Lee, S. Choi, S. Seo, H. Kim, J. Won, K. Choi, K.S. Kang, H.G. Park, H.S. Kim, H.R. An, K.H. Jeong, Y.C. Lee, J. Lee, Black bhosphorus (BP) nanodots for potential biomedical applications, *Small* 12 (2016) 214–219. doi:10.1002/smll.201502756.

[18] N.G. Connelly, T. Damhus, R.M. Hartshorn, A.T. Hutton, Eds., *Nomenclature of inorganic chemistry IUPAC Recommendations*, RSC Publishing, Cambridge, 2005.

[19] https://www.bgs.ac.uk/research/highlights/2010/rare_earth_elements.html

[20] G.C. Righini, M. Ferrari, Photoluminescence of rare-earth–doped glasses, *Riv. Nuovo Cimento* 28 (2006) 1–53. doi:10.1393/ncr/i2006-10010-8.

[21] G. Liu, J. Bernard, Eds., *Spectroscopic properties of rare earths in optical materials*, Springer, 2005.

[22] J. Zhou, J.L. Leaño, Z. Liu, D. Jin, K.L. Wong, R.S. Liu, J.C.G. Bünzli, Impact of lanthanide nanomaterials on photonic devices and smart applications, *Small* 14 (2018) 1801882. doi:10.1002/smll.201801882.

[23] J.C.G. Bünzli, S. V Eliseeva, Basics of lanthanide photophysics, in: P. Hänninen, H. Härmä, Eds., *Lanthanide luminescence*, Springer, Berlin, Heidelberg, 2011: pp. 1–45. doi:10.1007/4243_2010_3.

[24] http://www.scientificmaterials.com/products/nd-yag_yttrium_aluminum_garnet.php

[25] J. Lucas, P. Lucas, T. Le Mercier, A. Rollat, W. Davenport, Rare earth doped lasers and optical amplifiers, in: J. Lucas, P. Lucas, T. Le Mercier, A. Rollat, W. Davenport , Eds., *Rare earths science: technology, production and use*, Elsevier, Amsterdam, 2015, 319–332. doi:10.1016/B978-0-444-62735-3.00016-4.

[26] J.C. Mauro, E.D. Zanotto, Two centuries of glass research: historical trends, current status, and grand challenges for the Future, Int. *J. Appl. Glass Sci.* 5 (2014) 313–327. doi:10.1111/ijag.12087.

[27] B. Karmakar, Fundamentals of glass and glass Nanocomposites, in: B. Karmakar, K. Rademann, A.L. Stepanov, Eds., *Glass nanocomposites*, William Andrew Publishing, Boston, 2016, 3–53. doi:10.1016/B978-0-323-39309-6.00001-8.

[28] I.S. Gutzow, J.W.P. Schmelzer, The Vitreous State, 2nd Ed., Springer, 2013.

[29] E.D. Zanotto, J.C. Mauro, The glassy state of matter: its definition and ultimate fate, *J. Non-Cryst. Solids*. 471 (2017) 490–495. doi:10.1016/j.jnoncrysol.2017.05.019.

[30] R. DeCorby, Glasses for photonic integration, in: S. Kasap, P. Capper, Eds., Springer *Handbook of electronic and photonic materials*, Springer US, Boston, MA, 2007, 1041–1061. doi:10.1007/978-0-387-29185-7_43.

[31] T.H. Maiman, Stimulated Optical Radiation in Ruby, *Nature* 187 (1960) 493–494. doi:10.1038/scientificamerican0268-74.

[32] E. Snitzer, Optical maser action of $Nd^{3+}$ in a barium crown glass, *Phys. Rev. Lett.* 7 (1961) 444–446. doi:10.1103/PhysRevLett.7.444.

[33] C.J. Koester, E. Snitzer, Amplification in a fiber laser, *Appl. Opt.* 3 (1964) 1182–1186. doi:10.1364/AO.3.001182

[34] H. Yajima, S. Kawase, Y. Sekimoto, Amplification at 1.06 μm using a Nd: glass thin-film waveguide, *Appl. Phys. Lett.* 21 (1972) 407–409. doi:10.1063/1.1654432.

[35] O.K. Deutschbein, C.C. Pautrat, I.M. Svirchevsky, Les verres phosphates, nouveaux matériaux laser, *Rev. Phys. Appl.* 2 (1967) 29–37. doi:10.1051/rphysap:019670020102900.

[36] J.S. Hayden, Y.T. Hayden, J.H. Campbell, Effect of composition on the thermal, mechanical, and optical properties of phosphate laser glasses, *Proc. SPIE* 1277 (1990) 121–139. doi:10.1117/12.20590.

[37] Y. Ledemi, M. El-Amraoui, L. Calvez, X.-H. Zhang, B. Bureau, Y. Messaddeq, Colorless chalco-halide $Ga_2S_3$-$GeS_2$-CsCl glasses as new optical material, *Proc. SPIE* 8847 (2013) 884704–8. doi:10.1117/12.2024461.

[38] R. Balda, Ed., *Photonic glasses*, Research Signpost, 2006.

[39] F. Gan, L. Xu, Eds., *Photonic glasses*, World Scientific, 2006.

[40] M. Yamane, Y. Asahara, *Glasses for photonics*, Cambridge University Press, 2004.

[41] E.D. Zanotto, A Bright future for glass-ceramics, *Am. Ceram. Soc. Bull.* 89 (2010) 19–27.

[42] E.D. Zanotto, Glass crystallization research - A 36-year retrospective. Part II, methods of study and glass-ceramics, *Int. J. Appl. Glass Sci.* 4 (2013) 117–124. doi:10.1111/ijag.12024.

[43] M.J. Davis, E.D. Zanotto, Glass-ceramics and realization of the unobtainable: Property combinations that push the envelope, *MRS Bull.* 42 (2017) 195–199. doi:10.1557/mrs.2017.27.

[44] W. Höland, G.H. Beall, *Glass ceramic technology*, 2nd Ed., Wiley, 2012.

[45] S.D. Stookey, Chemical machining of photosensitive glass, *Ind. Eng. Chem.* 45 (1953) 115–118. doi:10.1021/ie50517a039.

[46] S. Stookey, History of the development of PYROCERAM, *Res. Manag.* 1 (1958) 155– 163. doi:10.1080/00345334.1958.11755484

[47] J.R. David, Ed., *ASM Materials Engineering Dictionary*, ASM International, 1992.

[48] M.C. Gonçalves, L.F. Santos, R.M. Almeida, Rare-earth-doped transparent glass ceramics, *Comptes Rendus Chim.* 5 (2002) 845–854. doi:10.1016/S1631-0748(02)01457-1.

[49] C.B. Carter, M.G. Norton, *Ceramic Materials*, 2nd Ed., Springer, 2013.

[50] J. Deubener, M. Allix, M.J. Davis, A. Durán, T. Höche, T. Honma, T. Komatsu, S. Krüger, I. Mitra, R. Müller, S. Nakane, M.J. Pascual, J.W.P. Schmelzer, E.D. Zanotto, S. Zhou, Updated definition of glass-ceramics, *J. Non-Cryst. Solids* 501 (2018) 3–10. doi:10.1016/j.jnoncrysol.2018.01.033.

[51] E.D. Zanotto, Glass Crystallization Research-A 36-Year Retrospective. Part I, fundamenal studies, *Int. J. Appl. Glass Sci.* 4 (2013) 105–116. doi:10.1111/ijag.12022.

[52] G.H. Beall, D.A. Duke, Transparent glass-ceramics, *J. Mater. Sci.* 4 (1969) 340–352. doi:10.1007/BF00550404.

[53] N.F. Borrelli, A. Herczog, R.D. Maurer, Electro-optic effect of ferroelectric microcrystals in a glass matrix, *Appl. Phys. Lett.* 7 (1965) 117–118. doi:10.1063/1.1754333.

[54] N.F. Borrelli, Electro-optic effect in transparent niobate glass-ceramic systems, *J. Appl. Phys.* 38 (1967) 4243–4247. doi:10.1063/1.1709111.

[55] G.H. Beall, L.R. Pinckney, Nanophase glass-ceramics, *J. Am. Ceram. Soc.* 1 (1999) 5–16. doi:10.1111/j.1151-2916.1999.tb01716.x

[56] A. De Pablos-Martín, G.C. Mather, F. Muñoz, S. Bhattacharyya, Th. Höche, J.R. Jinschek, T. Heil, A. Durán, M.J. Pascual, Design of oxy-fluoride glass-ceramics containing $NaLaF_4$ nano-crystals, *J. Non-Cryst. Solids* 356 (2010) 3071–3079. doi:10.1016/j.jnoncrysol.2010.04.057.

[57] K. Ritter, S. Gerlach, C. Rüssel, Photo induced surface near crystallization of a glass in the system $Na_2O/K_2O/CaO/Al_2O_3/SiO_2$, *J. Non-Cryst Solids* 356 (2010) 3090–3094. doi:10.1016/j.jnoncrysol.2010.04.056.

[58] F. Muñoz, A. De Pablos-Martín, N. Hémono, M.J. Pascual, A. Durán, L. Delevoye, L. Montagne, NMR investigation of the crystallization mechanism of $LaF_3$ and $NaLaF_4$ phases in aluminosilicate glasses, *J. Non-Cryst. Solids* 357 (2011) 1463–1468. doi:10.1016/j.jnoncrysol.2010.11.024.

[59] A. de Pablos-Martín, A. Durán, M.J. Pascual, Nanocrystallisation in oxyfluoride systems: mechanisms of crystallisation and photonic properties, *Int. Mater. Rev.* 57 (2012) 165–186. doi:10.1179/1743280411Y.0000000004.

[60] P. Hagenmuller, General Trends, in: P. Hagenmuller, Ed., *Inorganic solid fluorides. Chemistry and physics*, Academic Press, 1985, 1–16. doi:10.1016/B978-0-12-313370-0.50006-2.

[61] P.P. Fedorov, A.A. Luginina, A.I. Popov, Transparent oxyfluoride glass ceramics, *J. Fluor. Chem.* 172 (2015) 22–50. doi:10.1016/j.jfluchem.2015.01.009.

[62] A. de Pablos-Martín, M. Ferrari, M.J. Pascual, G.C. Righini, Glass-ceramics: a class of nanostructured materials for photonics, *Riv. Nuovo Cimento* 38 (2015) 311–369. doi:10.1393/ncr/i2015-10114-0.

[63] X. Liu, J. Zhou, S. Zhou, Y. Yue, J. Qiu, Transparent glass-ceramics functionalized by dispersed crystals, *Prog. Mater. Sci.* 97 (2018) 38–96. doi:10.1016/j.pmatsci.2018.02.006.

[64] P.A. Tick, N.F. Borrelli, L.K. Cornelius, M.A. Newhouse, Transparent glass ceramics for 1300 nm amplifier applications, *J. Appl. Phys.* 78 (1995) 6367–6374. doi:10.1063/1.360518.

[65] P.P. Fedorov, Glass formation criteria for fluoride systems, *Inorg. Mater.* 33 (1997) 1197–1205.

[66] P.P. Fedorov, Crystallochemical aspects of fluoride-glass formation, *Crystallogr. Rep.* 42 (1997) 1064–1075.

[67] H. Guo, H. Yu, X. Zhang, L. Chang, Z. Lan, Y. Li, L. Zhao, Doping concentration induced phase transition in $Eu^{3+}$-doped β-$PbF_2$ nano-particles, *Opt. Express.* 21 (2013) 24742-24752. doi:10.1364/OE.21.024742.

[68] Y. Li, L. Zhao, Y. Fu, Y. Shi, X. Zhang, H. Yu, Cubic to tetragonal phase transition of $Tm^{3+}$ doped nanocrystals in oxyfluoride glass ceramics, *AIP Adv.* 6 (2016) 25001-25007. doi:10.1063/1.4941442.

[69] H.H. Caspers, R.A. Buchanan, H.R. Marlin, Lattice vibrations of $LaF_3$, *J. Chem. Phys*. 41 (1964) 94–99. doi:10.1063/1.1725657.

[70] H.E. Rast, H.H. Caspers, S.A. Miller, R.A. Buchanan, Infrared dispersion and lattice Vibrations of $LaF_3$, *Phys. Rev*. 171 (1968) 1051–1057. doi:10.1103/PhysRev.171.1051

[71] M.J. Weber, Probabilities for radiative and nonradiative decay of $Er^{3+}$ in $LaF_3$, *Phys. Rev*. 157 (1967) 262–272. doi:10.1103/PhysRev.157.262.

[72] P.S. Peijzel, A. Meijerink, R.T. Wegh, M.F. Reid, G.W. Burdick, A complete $4f^n$ energy level diagram for all trivalent lanthanide ions, *J. Solid State Chem*. 178 (2005) 448–453. doi:10.1016/j.jssc.2004.07.046.

[73] D. Gregson, C.R.A. Catlow, A. V. Chadwick, G.H. Lander, A.N. Cormack, B.E.F. Fender, The Structure of $LaF_3$-a single-crystal neutron diffraction study at room temperature, *Acta Crystallogr. Sect. B*. 39 (1983) 687–691. doi:10.1107/S0108768183003249

[74] A. Zalkin, D.H. Templeton, Refinement of the trigonal crystal structure of lanthanum trifluoride with neutron diffraction data, *Acta Crystallogr. Sect. B*. 41 (1985) 91–93. doi:10.1107/S0108768185001689.

[75] A. Zalkin, D.H. Templeton, T.E. Hopkins, The atomic parameters in the lanthanum Trifluoride structure, *Inorg. Chem*. 5 (1966) 1466–1468. doi:10.1021/ic50042a047.

[76] B.L.C. Chamberland, The crystal chemistry of transition metal oxyfluorides, in: P. Hagenmuller, Ed., *Inorganic solid fluorides. Chemistry and physics*, Academic Press, 1985.

[77] M.J. Dejneka, Transparent oxyfluoride glass ceramics, *MRS Bull*. 23 (1998) 57–62. doi:10.1557/S0883769400031018.

[78] M.J. Dejneka, The luminescence and structure of novel transparent oxyfluoride glass-ceramics, *J. Non-Cryst. Solids* 239 (1998) 149–155. doi:10.1016/S0022-3093(98)00731-5.

[79] M. Środa, L. Stoch, Nanocrystallization of $LaF_3$ in oxyfluoride glass, *Opt. Appl*. 33 (2003) 161–166.

[80] N. Hémono, G. Pierre, F. Muñoz, A. de Pablos-Martín, M.J. Pascual, A. Durán, Processing of transparent glass-ceramics by nanocrystallisation of $LaF_3$, *J. Eur. Ceram. Soc*. 29 (2009) 2915–2920. doi:10.1016/j.jeurceramsoc.2009.05.013.

[81] A. de Pablos-Martín, N. Hémono, G.C. Mather, S. Bhattacharyya, T. Höche, H. Bornhöft, J. Deubener, F. Muñoz, A. Durán, M.J. Pascual, Crystallization kinetics of $LaF_3$ nanocrystals in an oxyfluoride glass, *J. Am. Ceram. Soc*. 94 (2011) 2420–2428. doi:10.1111/j.1551-2916.2011.04547.x.

[82] J. Dai, C. Yang, H. Zhang, H. Zhang, G. Feng, S. Zhou, Morphology control and enhancement of 1.5 mm emission in $Ca^{2+}/Ce^{3+}$ codoped $NaGdF_4:Yb^{3+},Er^{3+}$ submicrorods, *RSC Adv*. 7 (2017) 48238–48244. doi:10.1039/c7ra08254a.

[83] S. Ahmad, G.V. Prakash, R. Nagarajan, Hexagonally ordered $KLaF_4$ host: phase-controlled synthesis and luminescence studies, *Inorg. Chem*. 51 (2012) 12748−12754. doi:10.1021/ic301566e.

[84] G. Yi, H. Lu, S. Zhao, Y. Ge, W. Yang, Synthesis, characterization, and biological application of size-controlled nanocrystalline $NaYF_4$:Yb,Er infrared-to-visible up-conversion phosphors, *Nano Lett*. 4 (2004) 2191–2196. doi:10.1021/nl048680h.

[85] J.C. Boyer, F. Vetrone, L.A. Cuccia, J.A. Capobianco, Synthesis of colloidal upconverting $NaYF_4$ nanocrystals doped with $Er^{3+}$ , $Yb^{3+}$ and $Tm^{3+}$, $Yb^{3+}$ via thermal decomposition of lanthanide trifluoroacetate precursors, *J. Am. Chem. Soc*. 128 (2006) 7444–7445. doi:10.1021/ja061848b.

[86] J.C. Boyer, L. Cuccia, J.A. Capobianco, Synthesis of colloidal upconverting $NaYF_4$: $Er^{3+}/Yb^{3+}$ and $Tm^{3+}/Yb^{3+}$ monodisperse nanocrystals, *Nano Lett*. 7 (2007) 847–852. doi:10.1021/nl070235+.

[87] H. Schäfer, P. Ptacek, H. Eickmeier, M. Haase, Synthesis of hexagonal $Yb^{3+},Er^{3+}$ -doped $NaYF_4$ nanocrystals at low temperature, *Adv. Funct. Mater*. 19 (2009) 3091–3097. doi:10.1002/adfm.200900642.

[88] H. Ping, D. Chen, Y. Yu, Y. Wang, Judd-Ofelt analyses and luminescence of $Er^{3+}/Yb^{3+}$ co-doped transparent glass ceramics containing $NaYF_4$ nanocrystals, *J. Alloys Compd*. 490 (2010) 74–77. doi:10.1016/j.jallcom.2009.10.115.

[89] J.F. Suyver, A. Aebischer, D. Biner, P. Gerner, J. Grimm, S. Heer, K.W. Krämer, C. Reinhard, H.U. Güdel, Novel materials doped with trivalent lanthanides and transition metal ions showing near-infrared to visible photon upconversion, *Opt. Mater*. 27 (2005) 1111–1130. doi:10.1016/j.optmat.2004.10.021.

[90] T. Kano, H. Yamamoto, Y. Otomo, $NaLnF_4$: $Yb^{3+}$, $Er^{3+}$ (Ln: Y, Gd, La): efficient green-emitting infrared-excited phosphors, *J. Electrochem. Soc*. 119 (1972) 1561–1564. doi:10.1149/1.2404042.

[91] A. de Pablos-Martín, F. Muñoz, G.C. Mather, C. Patzig, S. Bhattacharyya, J.R. Jinschek, T. Höche, A. Durán, M.J. Pascual, $KLaF_4$ nanocrystallisation in oxyfluoride glass-ceramics, *CrystEngComm*. 15 (2013) 10323. doi:10.1039/c3ce41345d.

[92] S. Ahmad, S. Das, R. Nagarajan, G.V. Prakash, Optical properties of $Tb^{3+}$ doped $KLaF_4$ in cubic and hexagonal symmetries, *Opt. Mater*. 36 (2013) 396–401. doi:10.1016/j.optmat.2013.09.031.

[93] V.K. Tikhomirov, A.B. Seddon, M. Ferrari, M. Montagna, L.F. Santos, R.M. Almeida, On a qualitative model for the incorporation of fluoride nano-crystals within an oxide glass network in oxy-fluoride glass-ceramics, *J. Non-Cryst. Solids* 337 (2004) 191–195. doi:10.1016/j.jnoncrysol.2004.03.114.

[94] S. Bhattacharyya, C. Bocker, T. Heil, R. Jinschek, T. Höche, Rüssel, H. Kohl, H. Kohl, Experimental evidence of self-limited growth of nanocrystals in glass experimental evidence of self-limited growth of nanocrystals in glass, *Nano Lett*. 9 (2009) 2493–2496. doi:10.1021/nl901283r.

[95] S. Bhattacharyya, T. Höche, N. Hemono, M.J. Pascual, P.A. van Aken, Nano-crystallization in $LaF_3$-$Na_2O$-$Al_2O_3$-$SiO_2$ glass, *J. Cryst. Growth* 311 (2009) 4350–4355. doi:10.1016/j.jcrysgro.2009.07.027.

[96] C. Bocker, C. Rüssel, Transparent nano crystalline glass-ceramics by interface controlled crystallization, *Int. J. Appl. Glass Sci*. 181 (2013) 174–181. doi:10.1111/ijag.12033.

[97] C. Bocker, C. Rüssel, Self-organized nano-crystallisation of $BaF_2$ from $Na_2O/K_2O/BaF_2/Al2O_3/SiO_2$, *J. Eur. Ceram. Soc*. 29 (2009) 1221–1225. doi:10.1016/j.jeurceramsoc.2008.08.005.

[98] D. Chen, Y. Wang, Y. Yu, Z. Hu, Crystallization and fluorescence properties of $Nd^{3+}$-doped transparent oxyfluoride glass ceramics, *Mater. Sci. Eng. B* 123 (2005) 1–6. doi:10.1016/j.mseb.2005.06.008.

[99] D. Chen, Y. Wang, Y. Yu, E. Ma, Influence of $Yb^{3+}$ content on microstructure and fluorescence of oxyfluoride glass ceramics containing $LaF_3$ nano-crystals, *Mater. Chem. Phys*. 101 (2007) 464–469. doi:10.1016/j.matchemphys.2006.08.005.

[100] F. Goutaland, P. Jander, W.S. Brocklesby, G. Dai, Crystallisation effects on rare earth dopants in oxyfluoride glass ceramics, *Opt. Mater*. 22 (2003) 383–390. doi:10.1016/S0925-3467(02)00373-7.

[101] N. Hémono, G. Pierre, F. Muñoz, A. de Pablos-Martín, M.J. Pascual, A. Durán, Processing of transparent glass-ceramics by nanocrystallisation of $LaF_3$, *J. Eur. Ceram. Soc*. 29 (2009) 2915–2920. doi:10.1016/j.jeurceramsoc.2009.05.013.

[102] A. Herrmann, M. Tylkowski, C. Bocker, C. Rüssel, Cubic and hexagonal $NaGdF_4$ crystals precipitated from an aluminosilicate glass: preparation and luminescence properties, *Chem. Mater*. 25 (2013) 2878–2884. doi:10.1021/cm401454y.

[103] C. Lin, C. Rüssel, S. Dai, Chalcogenide glass-ceramics: functional design and crystallization mechanism, *Prog. Mater. Sci*. 93 (2018) 1–44. doi:10.1016/j.pmatsci.2017.11.001.

[104] F. Liu, Y. Wang, D. Chen, Y. Yu, Investigation on crystallization kinetics and microstructure of novel transparent glass ceramics containing Nd:$NaYF_4$ nano-crystals, *Mater. Sci. Eng. B* 136 (2007) 106–110. doi:10.1016/j.mseb.2006.09.012.

[105] M. Mortier, G. Patriarche, Structural characterisation of transparent oxyfluoride glass-ceramics, *J. Mater. Sci*. 35 (2000) 4849–4856. doi:10.1023/A:1017512232431

[106] V.S. Raghuwanshi, A. Hoell, C. Bocker, C. Rüssel, Experimental evidence of a diffusion barrier around $BaF_2$ nanocrystals in a silicate glass system by ASAXS, *CrystEngComm*. 14 (2012) 5215–5223. doi:10.1039/c2ce06544d.

[107] A. de Pablos-Martín, D. Ristic, A. Durán, M. Ferrari, M.J. Pascual, Crystallization and optical properties of $Tm^{3+}/Yb^{3+}$-co-doped $KLaF_4$ glass-ceramics, *CrystEngComm*. 19 (2017) 967–974. doi:10.1039/C6CE01845A.

[108] C. Rüssel, Nanocrystallization of $CaF_2$ from $Na_2O/K_2O/CaO/CaF_2/Al_2O_3/SiO_2$ glasses, *Chem. Mater*. (2005) 5843–5847. doi:10.1021/cm051430x.

[109] M. Środa, I. Wacławska, L. Stoch, M. Reben, DTA/DSC study of nanocrystallization in oxyfluoride glasses, *J. Therm. Anal. Calorim*. 77 (2004) 193–200. doi:10.1023/B:JTAN.0000033203.95251.d6.

[110] Y. Yu, D. Chen, Y. Cheng, Y. Wang, Z. Hu, F. Bao, Investigation on crystallization and influence of $Nd^{3+}$ doping of transparent oxyfluoride glass-ceramics, *J. Eur. Ceram. Soc*. 26 (2006) 2761–2767. doi:10.1016/j.jeurceramsoc.2005.05.002.

[111] S. Tanabe, H. Hayashi, T. Hanada, N. Onodera, Fluorescence properties of $Er^{3+}$ ions in glass ceramics containing $LaF_3$ nanocrystals, *Opt. Mater*. 19 (2002) 343–349. doi:10.1016/S0925-3467(01)00236-1.

[112] V. Lavin, I. Iparraguirre, J. Azkargorta, A. Mendioroz, J. González-Plata, R. Balda, J. Fernández, Stimulated and upconverted emissions of $Nd^{3+}$ in a transparent oxyfluoride glass-ceramic, *Opt. Mater*. 25 (2004) 201–208. doi:10.1016/S0925-3467(03)00270-2.

[113] M. Mattarelli, V.K. Tikhomirov, A.B. Seddon, M. Montagna, E. Moser, $Tm^{3+}$-activated transparent oxy-fluoride glass–ceramics : structural and spectroscopic properties, *J. Non-Cryst. Solids* 346 (2004) 354–358. doi:10.1016/j.jnoncrysol.2004.08.043.

[114] Z. Hu, E. Ma, Y. Wang, D. Chen, Fluorescence property investigations on $Er^{3+}$-doped oxyfluoride glass ceramics containing $LaF_3$ nanocrystals, *Mater. Chem. Phys*. 100 (2006) 308–312. doi:10.1016/j.matchemphys.2006.01.015.

[115] F. Liu, E. Ma, D. Chen, Y. Yu, Y. Wang, Tunable red-green upconversion luminescence in novel transparent glass ceramics containing Er: $NaYF_4$ nanocrystals, *J. Phys. Chem. B* 110 (2006) 20843–20846. doi:10.1021/jp063145m.

[116] D. Chen, Y. Wang, Y. Yu, E. Ma, F. Bao, Z. Hu, Y. Cheng, Influences of $Er^{3+}$ content on structure and upconversion emission of oxyfluoride glass ceramics containing $CaF_2$ nanocrystals, *Mater. Chem. Phys*. 95 (2006) 264–269. doi:10.1016/j.matchemphys.2005.06.017.

[117] F. Liu, Y. Wang, D. Chen, Y. Yu, E. Ma, L. Zhou, P. Huang, Upconversion emission of a novel glass ceramic containing $Er^{3+}$: $BaYF_5$ nano-crystals, *Mater. Lett*. 61 (2007) 5022–5025. doi:10.1016/j.matlet.2007.03.089.

[118] Z. Hu, Y. Wang, E. Ma, D. Chen, F. Bao, Microstructures and upconversion luminescence of $Er^{3+}$ doped and $Er^{3+}/Yb^{3+}$ co-doped oxyfluoride glass ceramics, *Mater. Chem. Phys*. 101 (2007) 234–237. doi:10.1016/j.matchemphys.2006.04.001.

[119] G. Lakshminarayana, J. Qiu, Photoluminescence of $Eu^{3+}$, $Tb^{3+}$ and $Tm^{3+}$-doped transparent $SiO_2$–$Al_2O_3$–LiF–$GdF_3$ glass ceramics, *J. Alloys Compd*. 476 (2009) 720–727. doi:10.1016/j.jallcom.2008.09.068.

[120] V.K. Tikhomirov, V.D. Rodríguez, J. Méndez-Ramos, J. del-Castillo, D. Kirilenko, G. Van Tendeloo, V.V. Moshchalkov, Optimizing Er/Yb ratio and content in Er–Yb co-doped glass-ceramics for enhancement of the up- and down-conversion luminescence, *Sol. Energ. Mater. Sol. C* 100 (2012) 209–215. doi:10.1016/j.solmat.2012.01.019.

[121] A. de Pablos-Martín, D. Ristic, S. Bhattacharyya, S. Bhattacharyya, Th. Höche, G.C. Mather, M.O. Ramírez, S. Soria, M. Ferrari, G.C. Righini, L.E. Bausá, A. Durán, M.J. Pascual, Effects of $Tm^{3+}$ additions on the crystallization of $LaF_3$ nanocrystals in oxyfluoride glasses: optical characterization and up-conversion, *J. Am. Ceram. Soc*. 96 (2013) 447-457. doi:10.1111/jace.12120.

[122] M. Yoo, J. Lee, H. Jeong, K. Lim, P. Babu, Enhancement of photoluminescence and upconversion in Er–Yb codoped nanocrystalline glass–ceramics, *Opt. Mater*. 35 (2013) 1922–1926. doi:10.1016/j.optmat.2012.12.020.

[123] Y. Wei, J. Li, J. Yang, X. Chi, H. Guo, Enhanced green upconversion in $Tb^{3+}$-$Yb^{3+}$ co- doped oxyfluoride glass ceramics containing $LaF_3$ nanocrystals, *J. Lumin*. 137 (2013) 70-72. doi:10.1016/j.jlumin.2012.11.017.

[124] M. Środa, K. Szlósarczyk, M. Rózanski, M. Sitarz, P. Jelen, Spectroscopy spectroscopic properties of transparent Er-doped oxyfluoride glass–ceramics with $GdF_3$, *Spectrochim. Acta A* 134 (2015) 631–637. doi:10.1016/j.saa.2014.06.066

[125] A. de Pablos-Martín, J. Méndez-Ramos, J. del-Castillo, A. Durán, V.D. Rodríguez, M.J. Pascual, Crystallization and up-conversion luminescence properties of $Er^{3+}/Yb^{3+}$-doped $NaYF_4$-based nano-glass-ceramics, *J. Eur. Ceram. Soc*. 35 (2015) 1831–1840. doi:10.1016/j.jeurceramsoc.2014.12.034.

[126] M.J. Pascual, C. Garrido, A. Durán, L. Pascual, A. de Pablos-Martín, J. Fernández, R. Balda, Optical properties of transparent glass–ceramics containing $Er^{3+}$-doped sodium lutetium fluoride nanocrystals, *Int. J. Appl. Glass Sci*. 40 (2016) 27–40. doi:10.1111/ijag.12177.

[127] J.J. Velázquez, R. Balda, J. Fernández, G. Gorni, G.C. Mather, L. Pascual, A. Durán, M.J. Pascual, Transparent glass-ceramics of sodium lutetium fluoride co-doped with erbium and ytterbium, *J. Non-Cryst. Solids* 501 (2018) 136–144. doi:10.1016/j.jnoncrysol.2017.12.051.

[128] G. Lakshminarayana, H. Yang, S. Ye, Y. Liu, J. Qiu, Cooperative downconversion luminescence in $Pr^{3+}/Yb^{3+}$:$SiO_2$–$Al_2O_3$–$BaF_2$–$GdF_3$ glasses, *J. Mater. Res*. 23 (2008) 3090–3095. doi:10.1557/JMR.2008.0372.

[129] S. Ye, B. Zhu, J. Luo, J. Chen, G. Lakshminarayana, J. Qiu, Enhanced cooperative quantum cutting in $Tm^{3+}$-$Yb^{3+}$ codoped glass ceramics containing $LaF_3$ nanocrystals, *Opt. Express* 16 (2008) 8989–8994. doi:10.1364/OE.16.008989

[130] S. Ye, B. Zhu, J. Chen, J. Luo, J.R. Qiu, Infrared quantum cutting in $Tb^{3+}$, $Yb^{3+}$ codoped transparent glass ceramics containing $CaF_2$ nanocrystals, *Appl. Phys. Lett*. 92 (2008) 2011–2014. doi:10.1063/1.2907496.

[131] D. Chen, Y. Yu, Y. Wang, P. Huang, F. Weng, Cooperative energy transfer up-conversion and quantum cutting down-conversion in $Yb^{3+}$: $TbF_3$ nanocrystals embedded glass ceramics, *J. Phys. Chem. C* 113 (2009) 6406–6410. doi: 10.1021/jp809995f

[132] Y. Katayama, S. Tanabe, Near infrared downconversion in $Pr^{3+}$-$Yb^{3+}$ codoped oxyfluoride glass ceramics, *Opt. Mater*. 33 (2010) 176–179. doi:10.1016/j.optmat.2010.07.016.

[133] Y. Xu, X. Zhang, S. Dai, B. Fan, H. Ma, J. Adam, J. Ren, G. Chen, Efficient near-infrared down-conversion in $Pr^{3+}$-$Yb^{3+}$ codoped glasses and glass ceramics containing $LaF_3$ nanocrystals, *J. Phys. Chem. C* 115 (2011) 13056–13062. doi:10.1021/jp201503v.

[134] D. Chen, Y. Wang, Y. Yu, P. Huang, F. Weng, Near-infrared quantum cutting in $Ho^{3+}/Yb^{3+}$ codoped nanostructured glass ceramic, *Opt. Lett*. 36 (2011) 876–878. doi:10.1364/OL.36.000876.

[135] K. Deng, X. Wei, X. Wang, Y. Chen, M. Yin, Near-infrared quantum cutting via resonant energy transfer from $Pr^{3+}$ to $Yb^{3+}$ in $LaF_3$, *Appl. Phys. B* 102 (2011) 555–558. doi:10.1007/s00340-011-4413-7.

[136] Q.J. Chen, W.J. Zhang, X.Y. Huang, G.P. Dong, M.Y. Peng, Q.Y. Zhang, Efficient down- and up-conversion of $Pr^{3+}$-$Yb^{3+}$ co-doped transparent oxyfluoride glass ceramics, *J. Alloys Compd*. 513 (2012) 139–144. doi:10.1016/j.jallcom.2011.10.007.

[137] Z. Pan, G. Sekar, R. Akrobetu, R. Mu, S.H. Morgan, Visible to near-infrared down-conversion luminescence in $Tb^{3+}$ and $Yb^{3+}$ co-doped lithium-lanthanum-aluminosilicate oxyfluoride glass and glass-ceramics, *J. Non-Cryst. Solids* 358 (2012) 1814–1817. doi:10.1016/j.jnoncrysol.2012.05.028.

[138] J. Zhou, Y. Teng, S. Zhou, J. Qiu, Quantum cutting in luminescent glasses and glass ceramics, *Int. J. Appl. Glass Sci*. 3 (2012) 299–308. doi:10.1111/ijag.12000.

[139] J. Zhou, Y. Teng, S. Ye, G. Lin, J. Qiu, A discussion on spectral modification from visible to near-infrared based on energy transfer for silicon solar cells, *Opt. Mater*. 34 (2012) 901–905. doi:10.1016/j.optmat.2011.12.002.

[140] Y. Katayama, S. Tanabe, Mechanism of quantum cutting in $Pr^{3+}$-$Yb^{3+}$ codoped oxyfluoride glass ceramics, *J. Lumin*. 134 (2013) 825–829. doi:10.1016/j.jlumin.2012.06.042.

[141] G. Xiang, J. Zhang, Z. Hao, X. Zhang, G. Pan, Y. Luo, S. Lü, H. Zhao, The energy transfer mechanism in $Pr^{3+}$ and $Yb^{3+}$ codoped β-$NaLuF_4$ nanocrystals, *Phys. Chem. Chem. Phys*. 16 (2014) 9289–9293. doi:10.1039/C4CP01184H.

[142] J.J. Velázquez, R. Balda, J. Fernández, G. Gorni, L. Pascual, G. Chen, M. Sundararajan, A. Durán, M.J. Pascual, Transparent oxy fluoride glass-ceramics with $NaGdF_4$ nanocrystals doped with $Pr^{3+}$ and $Pr^{3+}$-$Yb^{3+}$, *J. Lumin*. 193 (2018) 61–69. doi:10.1016/j.jlumin.2017.07.034.

[143] J. Pisarska, W. Ryba-Romanowski, G. Dominiak-Dzik, T. Goryczka, W.A. Pisarski, Near-infrared luminescence of rare earth ions in oxyfluoride lead borate glasses and transparent glass-ceramic materials, *Opt. Appl*. 38 (2008) 1–6.

[144] H. Yu, H. Guo, M. Zhang, Y. Liu, M. Liu, L. Zhao, Distribution of $Nd^{3+}$ ions in oxyfluoride glass ceramics, *Nanoscale Res. Lett*. 7 (2012) 1–7. doi:10.1186/1556-276X-7-275.

[145] M. Mortier, A. Bensalah, G. Dantelle, G. Patriarche, D. Vivien, Rare-earth doped oxyfluoride glass-ceramics and fluoride ceramics: synthesis and optical properties, *Opt. Mater*. 29 (2007) 1263–1270. doi:10.1016/j.optmat.2005.12.014.

[146] V.K. Tikhomirov, M. Mortier, P. Gredin, G. Patriarche, C. Görller-Walrand, V. V Moshchalkov, Preparation and up-conversion luminescence of 8 nm rare-earth doped fluoride nanoparticles, *Opt. Express* 16 (2008) 14544–9. doi:10.1364/OE.16.014544.

[147] D. Chen, Y. Yu, P. Huang, Y. Wang, Nanocrystallization of lanthanide trifluoride in an aluminosilicate glass matrix: dimorphism and rare earth partition, *CrystEngComm*. 11 (2009) 1686–1690. doi:10.1039/b904169a.

[148] M. Mortier, Nucleation and anionic environment of $Er^{3+}$ in a germanate glass, *J. Non-Cryst. Solids* 318 (2003) 56–62. doi:10.1016/S0022-3093(02)01856-2

[149] M. Abril, J. Méndez-Ramos, I.R. Martín, U.R. Rodríguez-Mendoza, V. Lavín, A. Delgado-Torres, V.D. Rodriguez, Optical properties of $Nd^{3+}$ ions in oxyfluoride glasses and glass ceramics comparing different preparation methods comparing different preparation methods, *J. Appl. Phys*. 95 (2004) 5271–5279. doi:10.1063/1.1707204.

[150] G.P. Agrawal, *Fiber-optic communication systems*, 4th Ed., Wiley, Hoboken, New Jersey, 2010.

[151] J. Ballato, H. Ebendorff-Heidepriem, J. Zhao, L. Petit, J. Troles, Glass and Process development for the next generation of optical fibers: A Review, *Fibers* 5 (2017) 1–25. doi:10.3390/fib5010011.

[152] P.A. Tick, Are low-loss glass–ceramic optical waveguides possible?, *Opt. Lett*. 23 (1998) 1904–1905. doi:10.1364/OL.23.001904.

[153] P.A. Tick, N.F. Borrelli, I.M. Reaney, The relationship between structure and transparency in glass-ceramic materials, *Opt. Mater*. 15 (2000) 81–91. doi:10.1016/S0925-3467(00)00017-3

[154] B.N. Samson, P.A. Tick, N.F. Borrelli, Efficient neodymium-doped glass-ceramic fiber laser and amplifier, *Opt. Lett*. 26 (2001) 145–147. doi:10.1364/OL.26.000145.

[155] R. Lisiecki, E. Augustyn, W. Ryba-romanowski, M. Zelechower, Er-doped and Er, Yb co-doped oxyfluoride glasses and glass–ceramics , structural and optical properties, *Opt. Mater*. 33 (2011) 1630–1637. doi:10.1016/j.optmat.2011.04.027.

[156] E. Augustyn, M. Zelechower, D. Stroz, J. Chraponski, The microstructure of erbium – ytterbium co-doped oxyfluoride glass–ceramic optical fibers, *Opt. Mater*. 34 (2012) 944–950. doi:10.1016/j.optmat.2011.04.037.

[157] C. Koepke, K. Wisniewski, M. Żelechower, E. Czerska, The role of phonons in the luminescence characteristics of SICLOF oxyfluoride glass and glass-ceramic fibers doped with $Er^{3+}/Yb^{3+}$, *J. Lumin*. 204 (2018) 278–283. doi:10.1016/j.jlumin.2018.08.035.

[158] M. Reben, D. Dorosz, J. Wasylak, B. Burtan, J. Jaglarz, J. Zontek, $Nd^{3+}$-Doped oxyfluoride glass ceramics optical fibre with $SrF_2$ nanocrystals, *Opt. Appl*. 42 (2012) 353–364. doi:10.5277/oa120213.

[159] K. V. Krishnaiah, Y. Ledemi, G. Cécile, E. Veron, X. Sauvage, S. Morency, E. Soares de Lima Filho, G. Nemova, M. Allix, Y. Messaddeq, R. Kashyap, Ytterbium-doped oxyfluoride nano-glass-ceramic fibers for laser cooling, *Opt. Mater. Express* 7 (2017) 104–113. doi:10.1364/OME.7.001980.

[160] V.K. Tikhomirov, D. Furniss, A.B. Seddon, I.M. Reaney, M. Beggiora, M. Ferrari, M. Montagna, R. Rolli, Fabrication and characterization of nanoscale, $Er^{3+}$-doped,

ultratransparent oxy-fluoride glass ceramics, *Appl. Phys. Lett*. 81 (2002) 1937–1939. doi:10.1063/1.1497196.

[161] V.K. Tikhomirov, J. Méndez-Ramos, V.D. Rodríguez, D. Furniss, A.B. Seddon, Gain cross-sections of transparent oxyfluoride glass-ceramics single-doped with $Ho^{3+}$ (at 2.0 μm) and with $Tm^{3+}$ (at 1.8 μm), *J. Alloys Compd*. 436 (2007) 216–220. doi:10.1016/j.jallcom.2006.07.008.

[162] T. Suzuki, S. Masaki, K. Mizuno, Y. Ohishi, Novel oxyfluoride glass and transparent glass-ceramics for fiber lasers and fiber amplifiers, *Proc. SPIE*. 7721 (2010) 77210T–1. doi:10.1117/12.854090.

[163] J. Ballato, P. Dragic, Rethinking optical fiber: new demands, old glasses, *J. Am. Ceram. Soc*. 96 (2013) 2675–2692. doi:10.1111/jace.12516.

[164] Z. Fang, S. Zheng, W. Peng, H. Zhang, Z. Ma, S. Zhou, D. Chen, J. Qiu, $Ni^{2+}$ doped glass ceramic fiber fabricated by melt-in-tube method and successive heat treatment, *Opt. Express* 23 (2015) 28258–28263. doi:10.1364/OE.23.028258.

[165] Z. Fang, S. Zheng, W. Peng, H. Zhang, S. Zhou, D. Chen, J. Qiu, Fabrication and characterization of glass-ceramic fiber-containing $Cr^{3+}$-doped $ZnAl_2O4$ nanocrystals, *J. Am. Ceram. Soc*. 98 (2015) 2772–2775. doi:10.1111/jace.13716.

[166] Z. Fang, X. Xiao, X. Wang, Z. Ma, E. Lewis, G. Farrell, P. Wang, J. Ren, H. Guo, J. Qiu, Glass-ceramic optical fiber containing $Ba_2TiSi_2O_8$ nanocrystals for frequency conversion of lasers, *Sci. Rep*. 7 (2017) 44456. doi:10.1038/srep44456.

[167] S. Kang, Z. Fang, X. Huang, Z. Chen, D. Yang, X. Xiao, J. Qiu, G. Dong, Precisely controllable fabrication of $Er^{3+}$-doped glass ceramic fibers: novel mid-infrared fiber laser materials, *J. Mater. Chem. C* 5 (2017) 4549–4556. doi:10.1039/c7tc00988g.

[168] S. Kang, H. Yu, T. Ouyang, Q. Chen, X. Huang, Z. Chen, J. Qiu, G. Dong, Novel $Er^{3+}$/$Ho^{3+}$-codoped glass-ceramic fibers for broadband tunable mid-infrared fiber lasers, *J. Am. Ceram. Soc*. 101 (2018) 3956–3967. doi:10.1111/jace.15692.

[169] Y. Liao, Y. Xu, Y. Chan, Semiconductor nanocrystals in sol–gel derived matrices, *Phys. Chem. Chem. Phys*. 15 (2013) 13694–13704. doi:10.1039/C3CP51351C.

[170] S. Fujihara, M. Tada, T. Kimura, Preparation and characterization of $MgF_2$ thin film by a trifluoroacetic acid method, *Thin Solid Films* 304 (1997) 252–255. doi:10.1016/S0040-6090(97)00156-9.

[171] W. Luo, Y. Wang, F. Bao, L. Zhou, X. Wang, Crystallization behavior of $PbF_2$-$SiO_2$ based bulk xerogels, *J. Non-Cryst. Solids* 347 (2004) 31–38. doi:10.1016/j.jnoncrysol.2004.09.020.

[172] J. del-Castillo, A.C. Yanes, J. Méndez-Ramos, V.K. Tikhomirov, V.D. Rodríguez, Structure and up-conversion luminescence in sol–gel derived $Er^{3+}$-$Yb^{3+}$ co-doped $SiO_2$:$PbF_2$ nano-glass–ceramics, *Opt. Mater*. 32 (2009) 104–107. doi:10.1016/j.optmat.2009.06.013.

[173] B. Szpikowska-Sroka, L. Zur, R. Czoik, T. Goryczka, A.S. Swinarew, M. Zadlo, W.A. Pisarski, Long-lived emission from $Eu^{3+}$:$PbF_2$ nanocrystals distributed into sol–gel silica glass, *J. Sol-Gel Sci. Technol*. 68 (2013) 278–283. doi:10.1007/s10971-013-3164-9.

[174] B. Szpikowska-Sroka, N. Pawlik, L. Zur, R. Czoik, T. Goryczka, W.A. Pisarski, Effect of fluoride ions on the optical properties of $Eu^{3+}$: $PbF_2$ nanocrystals embedded into sol-gel host materials, *Mater. Chem. Phys*. 174 (2016) 138–142. doi:10.1016/j.matchemphys.2016.02.060.

[175] B. Szpikowska-Sroka, N. Pawlik, T. Goryczka, E. Pietrasik, M. Bańczyk, W.A. Pisarski, Lead fluoride β-$PbF_2$ nanocrystals containing $Eu^{3+}$ and $Tb^{3+}$ ions embedded in sol-gel materials: Thermal, structural and optical investigations, *Ceram. Int*. 43 (2017) 8424–8432. doi:10.1016/j.ceramint.2017.03.192.

[176] Y. Yu, D. Chen, Y. Wang, W. Luo, Y. Zheng, Y. Cheng, L. Zhou, Structural evolution and its influence on luminescence of $SiO_2$–$SrF_2$–$ErF_3$ glass ceramics prepared by sol–gel method, *Mater. Chem. Phys*. 100 (2006) 241–245. doi:10.1016/j.matchemphys.2005.12.036.

[177] L. Zhou, D. Chen, W. Luo, Y. Wang, Y. Yu, F. Liu, Transparent glass ceramic containing $Er^{3+}$: $CaF_2$ nano-crystals prepared by sol–gel method, *Mater. Lett*. 61 (2007) 3988–3990. doi:10.1016/j.matlet.2007.01.001.

[178] S. Georgescu, A.M. Voiculescu, C. Matei, C.E. Secu, R.F. Negrea, M. Secu, Ultraviolet and visible up-conversion luminescence of $Er^{3+}$/$Yb^{3+}$ co-doped $CaF_2$ nanocrystals in sol–gel derived glass-ceramics, *J. Lumin*. 143 (2013) 150–156. doi:10.1016/j.jlumin.2013.04.002.

[179] D. Chen, Y. Wang, Y. Yu, E. Ma, L. Zhou, Microstructure and luminescence of transparent glass ceramic containing $Er^{3+}$: $BaF_2$ nano-crystals, *J. Solid State Chem*. 179 (2006) 532–537. doi:10.1016/j.jssc.2005.11.010.

[180] C.E. Secu, M. Secu, C. Ghica, L. Mihut, Rare-earth doped sol–gel derived oxyfluoride glass–ceramics: structural and optical characterization, *Opt. Mater*. 33 (2011) 1770–1774. doi:10.1016/j.optmat.2011.06.004.

[181] C.E. Secu, C. Bartha, S. Polosan, M. Secu, Thermally activated conversion of a silicate gel to an oxyfluoride glass ceramic: optical study using $Eu^{3+}$ probe ion, *J. Lumin*. 146 (2014) 539–543. doi:10.1016/j.jlumin.2013.10.013.

[182] S. Fujihara, S. Kitta, T. Kimura, Porous phosphor thin films of oxyfluoride $SiO_2$–$BaMgF_4$: $Eu^{2+}$ glass–ceramics prepared by sol–gel method, *Chem. Lett*. 32 (2003) 928–929. doi:10.1246/cl.2003.928.

[183] S.J.L. Ribeiro, C.C. Araújo, L. a. Bueno, R.R. Gonçalves, Y. Messaddeq, Sol-gel $Eu^{3+}$/$Tm^{3+}$ doped transparent glass-ceramic waveguides, *J. Non-Cryst. Solids* 348 (2004) 180–184. doi:10.1016/j.jnoncrysol.2004.08.164.

[184] A. Biswas, G.S. Maciel, C.S. Friend, P.N. Prasad, Upconversion properties of a transparent $Er^{3+}$-$Yb^{3+}$ co-doped $LaF_3$-$SiO_2$ glass-ceramics prepared by sol-gel method, *J. Non-Cryst. Solids* 316 (2003) 393–397. doi:10.1016/S0022-3093(02)01951-8.

[185] A.C. Yanes, J. del-Castillo, J. Méndez-ramos, V.D. Rodríguez, M.E. Torres, J. Arbiol, Luminescence and structural characterization of transparent nanostructured $Eu^{3+}$-doped $LaF_3$-$SiO_2$ glass–ceramics prepared by sol-gel method, *Opt. Mater*. 29 (2007) 999–1003. doi:10.1016/j.optmat.2006.02.021.

[186] J.J. Velázquez, A.C. Yanes, J. del-Castillo, J. Méndez-Ramos, V.D. Rodríguez, Optical properties of $Ho^{3+}$-$Yb^{3+}$ co-doped nanostructured $SiO_2$ -$LaF_3$ glass-ceramics prepared by sol-gel method, *Phys. Status Solidi* 204 (2007) 1762–1768. doi:10.1002/pssa.200675349.

[187] J. Méndez-Ramos, J.J. Velázquez, A. C. Yanes, J. del-Castillo, V.D. Rodriguez, Up-conversion in nanostructured $Yb^{3+}$-$Tm^{3+}$ co-doped sol-gel derived $SiO_2$-$LaF_3$ transparent glass-ceramics, *Phys. Status Solidi* 205 (2008) 330–334. doi:10.1002/pssa.200723296.

[188] A.C. Yanes, J.J. Velázquez, J. del-Castillo, J. Méndez-Ramos, V.D. Rodríguez, Colour tuneability and white light generation in $Yb^{3+}$–$Ho^{3+}$–$Tm^{3+}$ co-doped $SiO_2$–$LaF_3$ nano-glass-ceramics prepared by sol–gel method, *J. Sol-Gel Sci. Technol*. 51 (2009) 4–9. doi:10.1007/s10971-009-1924-3.

[189] J.J. Velázquez, V.D. Rodríguez, A.C. Yanes, J. del-Castillo, J. Méndez-Ramos, Increase in the $Tb^{3+}$ green emission in $SiO_2$-$LaF_3$ nano-glass-ceramics by codoping with $Dy^{3+}$ ions, *J. Appl. Phys*. 108 (2010) 113530–113536. doi:10.1063/1.3514552.

[190] J.J. Velázquez, V.D. Rodríguez, A.C. Yanes, J. Del Castillo, J. Méndez-Ramos, Photon down-shifting by energy transfer from $Sm^{3+}$ to $Eu^{3+}$ ions in sol-gel $SiO_2$-$LaF_3$ nano-glass-ceramics for photovoltaics, *Appl. Phys. B* 108 (2012) 577–583. doi:10.1007/s00340-012-4950-8.

[191] A. Santana-Alonso, J. Méndez-Ramos, A.C. Yanes, J. del-Castillo, V.D. Rodríguez, White light up-conversion in transparent sol–gel derived glass-ceramics containing $Yb^{3+}$–$Er^{3+}$–$Tm^{3+}$ triply-doped $YF_3$ nanocrystals, *Mater. Chem. Phys*. 124 (2010) 699–703. doi:10.1016/j.matchemphys.2010.07.038.

[192] A.C. Yanes, A. Santana-Alonso, J. Méndez-Ramos, J. del-Castillo, V.D. Rodríguez, Novel sol–gel nano-glass–ceramics comprising $Ln^{3+}$-Doped $YF_3$ nanocrystals: structure and high efficient UV up-conversion, *Adv. Funct. Mater*. 21 (2011) 3136–3142. doi:10.1002/adfm.201100146.

[193] J. Méndez-Ramos, A. Santana-Alonso, A.C. Yanes, J. del-Castillo, V.D. Rodríguez, Rare-earth doped $YF_3$ nanocrystals embedded in sol–gel silica glass matrix for white light generation, *J. Lumin*. 130 (2010) 2508–2511. doi:10.1016/j.jlumin.2010.08.027.

[194] D. Chen, Y. Wang, Y. Yu, P. Huang, Structure and optical spectroscopy of Eu-doped glass ceramics containing $GdF_3$ nanocrystals, *J. Phys. Chem. C* 112 (2008) 18943–18947. doi: 10.1021/jp808061x

[195] S. Fujihara, S. Koji, T. Kimura, Structure and optical properties of $(Gd,Eu)F_3$-nanocrystallized sol–gel silica films, *J. Mater. Chem*. 14 (2004) 1331–1335. doi:10.1039/B313784H

[196] A.C. Yanes, A. Santana-Alonso, J. Méndez-Ramos, J. del-Castillo, V.D. Rodríguez, $Yb^{3+}$-$Er^{3+}$ co-doped sol-gel transparent nano-glass-ceramics containing $NaYF_4$ nanocrystals for tuneable up-conversion phosphors, *J. Alloys Compd*. 480 (2009) 706–710. doi:10.1016/j.jallcom.2009.02.019.

[197] A. Santana-Alonso, A.C. Yanes, J. Méndez-Ramos, J. del-Castillo, V.D. Rodríguez, Sol-gel transparent nano-glass-ceramics containing $Eu^{3+}$-doped $NaYF_4$ nanocrystals, *J. Non-Cryst. Solids* 356 (2010) 933–936. doi:10.1016/j.jnoncrysol.2009.12.023.

[198] A. Santana-Alonso, J. Méndez-Ramos, A.C. Yanes, J. del-Castillo, V.D. Rodríguez, Up-conversion in sol-gel derived nano-glass-ceramics comprising $NaYF_4$ nano-crystals doped with $Yb^{3+}$, $Ho^{3+}$ and $Tm^{3+}$, *Opt. Mater*. 32 (2010) 903–908. doi:10.1016/j.optmat.2010.01.020.

[199] J. Méndez-Ramos, A.C. Yanes, A. Santana-Alonso, J. del-Castillo, V.D. Rodríguez, Colour tuneability in sol–gel nano-glass-ceramics comprising $Yb^{3+}$-$Er^{3+}$-$Tm^{3+}$ co-doped $NaYF_4$ nanocrystals, *J. Nanosci. Nanotechnol*. 10 (2010) 1273–1277. doi:10.1166/jnn.2010.1871.

[200] C.E. Secu, R.F. Negrea, M. Secu, $Eu^{3+}$ probe ion for rare-earth dopant site structure in sol–gel derived $LiYF_4$ oxyfluoride glass–ceramic, *Opt. Mater*. 35 (2013) 2456–2460. doi:10.1016/j.optmat.2013.06.053.

[201] M. Secu, C.E. Secu, Up-conversion luminescence of $Er^{3+}/Yb^{3+}$ co-doped $LiYF_4$ nanocrystals in sol-gel derived oxyfluoride glass-ceramics, *J. Non-Cryst. Solids* 426 (2015) 78–82. doi:10.1016/j.jnoncrysol.2015.07.010.

[202] J. del-Castillo, A.C. Yanes, S. Abe, P.F. Smet, Site selective spectroscopy in $BaYF_5$:$RE^{3+}$ (RE=Eu, Sm) nano-glass-ceramics, *J. Alloys Compd*. 635 (2015) 136–141. doi:10.1016/j.jallcom.2015.01.244.

[203] J.S. Garcia Solé, L. Bausá, D. Jaque, *An introduction to the optical spectroscopy of inorganic solids*, Wiley, 2005.

[204] B.R. Judd, Optical absorption intensities of rare-earth ions, *Phys. Rev*. 127 (1962) 750–761. doi:10.1103/PhysRev.127.750.

[205] G.S. Ofelt, Intensities of crystal spectra of rare-earth ions, *J. Chem. Phys*. 37 (1962) 511–520. doi:10.1063/1.1701366.

[206] H.H. Caspers, H.E. Rast, R.A. Buchanan, Intermediate coupling energy levels for $Nd^{3+}(4f^3)$ in $LaF_3$, *J. Chem. Phys*. 42 (1965) 3214–3217. doi:10.1063/1.1696401.

[207] W. Kutzelnigg, J.D. Morgan, Hund's rules, *Zeitschrift Für Phys. D Atoms, Mol. Clust*. 36 (1996) 197–214. doi:10.1007/BF01426405.

[208] K.T. Hecht, *Quantum mechanics*, Springer, New York, NY, 2000. doi:10.1007/978-1-4612-1272-0_32.

[209] B.M. Walsh, Judd-Ofelt theory: principles and practices, in: B. Di Bartolo, O. Forte, Eds., *Advances in spectroscopy for lasers and sensing*, Springer, Dordrecht, 2006: pp. 403–433.

[210] G. Herzberg, *Atomic spectra and atomic structure*, Dover Publications, 1952.

[211] O.L. Malta, L.D. Carlos, Intensities of 4f-4f transitions in glass materials, *Quim. Nova* 26 (2003) 889–895.

[212] V.S. Sastri, J.C.G. Bünzli, V.R. Rao, G.V.S. Rayudu, J.R. Perumareddi, Spectroscopy of lanthanide complexes, in: V.S. Sastri, J.C.G. Bünzli, V.R. Rao, G.V.S. Rayudu, J.R. Perumareddi, Eds., Modern aspects of rare earths and their complexes, Elsevier, 2003, 569–731. doi:10.1016/B978-044451010-5/50022-5.

[213] G.H. Dieke, *Spectra and energy levels of rare earth ions in crystals*, Interscience Publisher, 1968.

[214] W.T. Carnall, H. Crosswhite, H.M. Crosswhite, *Energy level structure and transition probabilities of the trivalent lanthanides in $LaF_3$*, Technical Report ANL-78-XX-95, Argonne National Laboratory, Argonne, IL, 1977.

[215] W.J. Miniscalco, Optical and Electronic Properties of Rare Earth Ions in Glasses, in: M.J.F. Digonnet, Ed., *Rare-earth-doped fiber lasers and amplifiers*, 2nd Ed., Marcel Dekker, 2001, 17–112.

[216] R. Loudon, *The quantum theory of light*, 3rd Ed., Oxford University Press, 2000.

[217] K. Binnemans, Interpretation of europium(III) spectra, *Coord. Chem. Rev*. 295 (2015) 1–45. doi:10.1016/j.ccr.2015.02.015.

[218] F. Schwabl, *Statistical mechanics*, 2nd Ed., Springer, 2006.

[219] D.L. Dexter, A Theory of sensitized luminescence in solids, *J. Chem. Phys*. 21 (1953) 836–850. doi:10.1063/1.1699044.

[220] F. Auzel, Upconversion and anti-stokes processes with f and d ions in solids, *Chem. Rev*. 104 (2004) 139–173. doi:10.1021/cr020357g.

[221] H. Dong, L.D. Sun, C.H. Yan, Energy transfer in lanthanide upconversion studies for extended optical applications, *Chem. Soc. Rev*. 44 (2015) 1608–1634. doi:10.1039/c4cs00188e.

[222] M. Pollnau, D.R. Gamelin, S.R. Lüthi, H.U. Güdel, M.P. Hehlen, Power dependence of upconversion luminescence in lanthanide and transition-metal-ion systems, *Phys. Rev. B* 61 (2000) 3337–3346. doi:10.1103/PhysRevB.61.3337.

[223] D.L. Dexter, Possibility of luminescent quantum yields greater than unity, *Phys. Rev*. 108 (1957) 630–633. doi:10.1103/PhysRev.108.630.

[224] J.L. Sommerdijk, A. Bril, A.W. de Jager, Two photon luminescence with ultraviolet excitation of trivalent praseodymium, *J. Lumin*. 8 (1974) 341–343.
doi: 0.1016/0022-2313(74)90006-4.

[225] A.D.E. Pablos, A. Duran, M. Nieto, Puesta a punto de un horno de fibrado de laboratorio para la obtención de fibra de vidrio, *Bol. Soc. Esp. Ceram. V*. 36 (1997) 517–523.

[226] R.C. Weast, Ed., *Handbook of chemistry and physics*, 66th Ed., CRR Press, Cleveland, 1985

[227] C.J. Brinker, G.W. Scherer, Film formation, in: *Sol-gel science. The physics and chemistry of sol-gel processing*, Academic Press, San Diego, 1990, 786–837.
doi:10.1016/B978-0-08-057103-4.50018-0.

[228] P. Innocenzi, *The sol to gel transition*, Springer, 2016. doi:10.1007/978-3-319-39718-4.

[229] M. Watanabe, Sample preparation for X-ray fluorescence analysis. Fusion bead method part 1 basic principles, *Rigaku J*. 31 (2015) 12–17.

[230] E. Sastre de Andrés, Análisis térmico, in: M. Faraldos, C. Goberna , Eds., *Técnicas de análisis y caracterizacion de Materiales*, 2nd Ed., Consejo Superior de Investigaciones Científicas, Madrid, 2011: pp. 651–697.

[231] S. Gaisford, V. Kett, P. Haines, *Principles of thermal analysis and calorimetry*, The Royal Society of Chemistry, 2016.

[232] J.M. Fernández Navarro, *El vidrio*, Consejo Superior de Investigaciones Científicas, Madrid, 2003.

[233] H. Scholze, *Glass. Nature, structure, and properties*, Springer, New York, 1991.

[234] H.E. Kissinger, Variation of peak temperature with heating rate in differential thermal analysis, *J. Res. Nat. Bur. Stand*. 57 (1956) 217–221. doi:10.6028/jres.057.026.

[235] H.E. Kissinger, Reaction kinetics in differential thermal analysis, *Anal. Chem*. 29 (1957) 1702–1706. doi:10.1021/ac60131a045.

[236] T. Ozawa, Kinetics of non-isothermal crystallization, *Polymer* 12 (1971) 150–158. doi:10.1016/0032-3861(71)90041-3.

[237] J.A. Augis, J.E. Bennett, Calculation of the Avrami parameters for heterogeneous solid state reactions using a modification of the Kissinger method, *J. Therm. Anal*. 13 (1978) 283–292. doi:10.1007/BF01912301.

[238] H.S. Chen, A method for evaluating viscosities of metallic glasses from the rates of thermal transformations, *J. Non-Cryst. Solids* 27 (1978) 257–263.
doi: /10.1016/0022-3093(78)90128-X.

[239] D.W. Henderson, Experimental analysis of non-isothermal transformations involving nucleation and growth, *J. Therm. Anal*. 15 (1979) 325–331. doi:10.1007/BF01903656.

[240] D.W. Henderson, Thermal analysis of non-isothermal crystallization kinetics in glass forming liquids, *J. Non-Cryst. Solids* 30 (1979) 301–315. doi:10.1016/0022-3093(79)90169-8.

[241] H. Yinnon, D.R. Uhlmann, Applications of thermoanalytical techniques to the study of crystallization kinetics in glass-forming liquids, part I: Theory, *J. Non-Cryst. Solids* 54 (1983) 253–275. doi:10.1016/0022-3093(83)90069-8.

[242] K. Matusita, T. Komatsu, R. Yokota, Kinetics of non-isothermal crystallization process and activation energy for crystal growth in amorphous materials, *J. Mater. Sci*. 19 (1984) 291–296. doi:10.1007/BF02403137.

[243] I.W. Donald, Crystallization kinetics of a lithium zinc silicate glass studied by DTA and DSC, *J. Non- Cryst. Solids* 345–346 (2004) 120–126.
doi:10.1016/j.jnoncrysol.2004.08.007.

[244] M.J. Pascual, L. Pascual, A. Durán, Determination of the viscosity- temperature curve for glasses on the basis of fixed viscosity points determined by hot stage microscopy, *Phys. Chem. Glass* 42 (2001) 61–66.

[245] B.D. Cullity, S.R. Stock, *Elements of X-ray diffraction*, 3rd Ed., Pearson, 2014.

[246] M. de Graef, M.E. McHenry, Structure of materials. *An introduction to crystallography, diffraction and symmetry*, 2nd Ed., Cambridge University Press, Cambridge, 2012.

[247] H.M. Rietveld, A profile refinement method for nuclear and magnetic structures, *J. Appl. Cryst*. 2 (1969) 65–71. doi:10.1107/S0021889869006558.

[248] J. Rodríguez-Carvajal, Recent advances in magnetic structure determination by neutron powder diffraction, *Phys. B Condens. Matter*. 192 (1993) 55–69. doi:10.1016/0921-4526(93)90108-I.

[249] S.A. Rice, Small angle scattering of X-rays. A. Guinier and G. Fournet. Translated by C. B. Wilson and with a bibliographical appendix by K. L. Yudowitch, *J. Polym. Sci*. 19 (1956) 594. doi:10.1002/pol.1956.120199326.

[250] P. Fornasini, Introduction to x-ray absorption spectroscopy, in: S. Mobilio, F. Boscherini, C. Meneghini, Eds., *Synchrotron Radiation. Basics, methods and applications*, Springer, 2015, 181–211.

[251] J.E. Penner-Hahn, X-ray absorption spectroscopy in coordination chemistry, Coord. Chem. Rev. 190–192 (1999) 1101–1123. doi:10.1016/S0010-8545(99)00160-5.

[252] B. Ravel, M. Newville, ATHENA, ARTEMIS, HEPHAESTUS: data analysis for X-ray absorption spectroscopy using IFEFFIT, *J. Synchrotron Radiat*. 12 (2005) 537–541. doi:10.1107/S0909049505012719.

[253] D.B. Williams, C.B. Carter, *Transmission electron microscopy. A textbook for materials Science*, 2nd Ed., Springer, 2009.

[254] B.C. Smith, *Fundamentals of Fourier transform infrared spectroscopy*, CRR Press, 2011.

[255] B. Stuart, *Infrared spectroscopy: fundamentals and applications*, Wiley, 2004.

[256] J.R. Weil, J.A. Bolton, *Electron paramagnetic resonance: elementary theory and practical applications*, 2nd Ed., Wiley, 2007.

[257] A. Lund, M. Shiotani, S. Shimada, *Principles and applications of ESR spectroscopy*, Springer, 2011.

[258] S. Stoll, A. Schweiger, EasySpin, a comprehensive software package for spectral simulation and analysis in EPR, *J. Magn. Reson*. 178 (2006) 42–55. doi:10.1016/j.jmr.2005.08.013.

[259] H. Eckert, Structural characterization of noncrystalline solids and glasses using solid state NMR, *Prog. Nucl. Magn. Reson. Spectrosc*. 24 (1992) 159–293. doi:10.1016/0079-6565(92)80001-V.

[260] H. Fujiwara, *Spectroscopic ellipsometry: principles and applications*, Wiley, 2007.

[261] A. de Pablos-Martín, M.A. García, A. Muñoz-Noval, G.R. Castro, A. Durán, M.J. Pascual, Analysis of the distribution of $Tm^{3+}$ ions in $LaF_3$ containing transparent glass-ceramics through X-ray absorption spectroscopy. *J. Non-Cryst. Solids*. 384 (2014) 83-87. 10.1016/j.jnoncrysol.2013.07.021.

[262] Y.G. Choi, Covalence of chemical bonds and white-line intensity of an $L_3$-edge X-ray absorption near-edge structure of rare earth elements embedded in glass, *Met. Mater. Int*. 15 (2009) 993–999. doi:10.1007/s12540-009-0993-8.

[263] J.M. Baker, R.S. Rubins, Electron spin resonance in two groups of lanthanon Salts, *Proc. Phys. Soc*. 1353 (1961) 1353–1360. doi:10.1088/0370-1328/78/6/338.

[264] M.B. Schulz, C.D. Jefries, Spin-lattice relaxation of rare-earth Ions in $LaF_3$, *Phys. Rev*. 149 (1966) 270–288. doi:10.1103/PhysRev.149.270.

[265] T. Castner, G.S. Newell, W.C. Holton, C.P. Slighter, Note on the paramagnetic resonance of iron in glass, *J. Chem. Phys*. 32 (1960) 668–673. doi:10.1063/1.1730779.

[266] J.Q. Hong, L.H. Zhang, P.X. Zhang, Y.Q. Wang, Y. Hang, Growth, optical characterization and evaluation of laser properties of Nd:$LaF_3$ crystal, *J. Alloys Compd*. 646 (2015) 706–709. doi:10.1016/j.jallcom.2015.05.172.

[267] Y.K. Voronko, T.G. Mamedov, V.V Osiko, A.M. Prokhorov, V.P. Sakun, I.A. Shcherbakov, Nature of non radiative excitation-energy relaxation in condensed media with high activator concentrations, *Sov. Phys. JETP* 44 (1977) 251–261.

[268] W. Luo, Y. Wang, Y. Cheng, F. Bao, L. Zhou, Crystallization and structural evolution of $YF_3$–$SiO_2$ xerogel, *Mater. Sci. Eng. B* 127 (2006) 218–223. doi:10.1016/j.mseb.2005.10.034.

[269] C. van Leeuwen, On the driving force for crystallization: the growth affinity, *J. Cryst. Growth*. 46 (1979) 91–95. doi:10.1016/0022-0248(79)90114-3.

[270] P. Innocenzi, M.O. Abdirashid, M. Guglielmi, Structure and properties of sol-gel coatings from methyltriethoxysilane and tetraethoxysilane, *J. Sol-Gel Sci. Technol*. 3 (1994) 47–55. doi:10.1007/BF00490148.

[271] Y. Ma, H.R. Lee, T. Tsuru, Study on preparation and hydrophobicity of MTES derived silica sol and gel, *Adv. Mater. Res*. 535–537 (2012) 2563–2566. doi:10.4028/www.scientific.net/AMR.535-537.2563.

[272] R. Wegh, H. Donker, A. Meijerink, R. Lamminmäki, J. Hölsä, Vacuum-ultraviolet spectroscopy and quantum cutting for $Gd^{3+}$ in $LiYF_4$, *Phys. Rev. B* 56 (1997) 13841–13848. doi:10.1103/PhysRevB.56.13841.

[273] K.D. Oskam, R.T. Wegh, H. Donker, E.V.D. van Loef, A. Meijerink, Downconversion: a new route to visible quantum cutting, *J. Alloys Compd*. 300–301 (2000) 421–425. doi:10.1016/S0925-8388(99)00755-0.

[274] W.A. Crichton, P. Bouvier, B. Winkler, A. Grzechnik, The structural behaviour of $LaF_3$ at high pressures, *Dalt. Trans*. 39 (2010) 4302–4311. doi:10.1039/b925817e.

[275] P.H. Karpinski, J.S. Wey, Precipitation processes, in: A.S. Myerson, Ed., *Handbook of industrial crystallization*, 2nd Ed., Butterworth-Heinemann,Woburn, 2002, 141–160. doi:10.1016/B978-075067012-8/50008-2.

[276] G. Ledoux, M.F. Joubert, S. Mishra, Upconversion phenomena in nanofluorides, in: A. Tressaud, K. R. Poeppelmeier, Eds., *Photonic and electronic properties of fluoride materials*, Elsevier, Boston, 2016:, 35–63. doi:10.1016/B978-0-12-801639-8.00003-9.

# *ANNEX*

# *PAPER 1*

**Transparent glass-ceramics produced by sol-gel: a suitable alternative for photonic materials.**

G. Gorni, J.J. Velázquez, J. Mosa, R. Balda, J. Fernández, A. Durán, Y. Castro

*Materials* **11**, (2018) 212. doi:10.3390/ma11020204

materials

MDPI

Article

# Transparent Glass-Ceramics Produced by Sol-Gel: A Suitable Alternative for Photonic Materials

**Giulio Gorni [1], Jose J. Velázquez [1], Jadra Mosa [1], Rolindes Balda [2,3], Joaquin Fernández [2,3], Alicia Durán [1,*] and Yolanda Castro [1,*]**

1 Instituto de Cerámica y Vidrio (CSIC), 28049 Madrid, Spain; ggorni@icv.csic.es (G.G.); josvel@icv.csic.es (J.J.V.); jmosa@icv.csic.es (J.M.)
2 Departamento de Física Aplicada I, Escuela Superior de Ingeniería, Universidad del País Vasco UPV/EHU, 48940 Bilbao, Spain; rolindes.balda@ehu.eus (R.B.); joaquin.fernandez@ehu.es (J.F.)
3 Centro de Física de Materiales UPV/EHU-CSIC, 20018 San Sebastian, Spain
* Correspondence: aduran@icv.csic.es (A.D.); castro@icv.csic.es (Y.C.)

Received: 11 January 2018; Accepted: 27 January 2018; Published: 30 January 2018

**Abstract:** Transparent glass-ceramics have shown interesting optical properties for several photonic applications. In particular, compositions based on oxide glass matrices with fluoride crystals embedded inside, known as oxyfluoride glass-ceramics, have gained increasing interest in the last few decades. Melt-quenching is still the most used method to prepare these materials but sol-gel has been indicated as a suitable alternative. Many papers have been published since the end of the 1990s, when these materials were prepared by sol-gel for the first time, thus a review of the achievements obtained so far is necessary. In the first part of this paper, a review of transparent sol-gel glass-ceramics is made focusing mainly on oxyfluoride compositions. Many interesting optical results have been obtained but very little innovation of synthesis and processing is found with respect to pioneering papers published 20 years ago. In the second part we describe the improvements in synthesis and processing obtained by the authors during the last five years. The main achievements are the preparation of oxyfluoride glass-ceramics with a much higher fluoride crystal fraction, at least double that reported up to now, and the first synthesis of $NaGdF_4$ glass-ceramics. Moreover, a new $SiO_2$ precursor was introduced in the synthesis, allowing for a reduction in the treatment temperature and favoring hydroxyl group removal. Interesting optical properties demonstrated the incorporation of dopant ions in the fluoride crystals, thus obtaining crystal-like spectra along with higher efficiencies with respect to xerogels, and hence demonstrating that these materials are a suitable alternative for photonic applications.

**Keywords:** sol-gel; oxyfluoride glass-ceramics; nanocrystal; optical properties

## 1. Introduction

Phosphor materials emit light under exposure to external stimulation, such as an electron beam, light at different wavelengths, voltage or electric field, etc. These materials are widely applied in light-emitting diodes, solar cells, sensing, catalysis, integration in photovoltaic devices, and more recently in biosensing, bioimaging, or medical diagnosis [1–6].

The optical properties of these materials can change drastically depending on the processing parameters. Thus, in the past two decades, interest in studying the synthesis and processing of nanophosphors to develop luminescent materials with high efficiency has increased. The properties of existing devices can be improved by including luminescent phosphors and/or nanocrystalline oxyfluorides doped with lanthanide ions ($Ln^{3+}$). $Ln^{3+}$ ions are commonly used as active ions because they show emissions in a wide spectral range, from UV to NIR, and their use in telecom, lasers, lightening, etc. makes them indispensable nowadays. Moreover, their most stable oxidation state is

3+, consisting of partially filled inner 4f levels screened by outer 5s and 5p orbitals. This allows for maintaining emission energies centered near the same values even in different hosts, making them suitable for applications where certain wavelengths are required. Several studies and applications deal with nanoparticles doped with $Ln^{3+}$ ions suspended in liquid phase or with phosphor powders. However, for many applications as laser materials, waveguides and optical fibers, lightening devices, etc., solid and easy-to-handle samples are required.

In particular, oxyfluoride nano-glass-ceramics (OxGCs) are attractive materials for photonic applications, because they combine the very low phonon energy of fluoride nanocrystals (NCs) (300–450 $cm^{-1}$) with the high chemical and mechanical stability of oxide glass matrices, especially alumino-silicate ones [7–9]. Moreover, such materials can be cast in several forms to obtain the desired device. However, to maintain the transparency and avoid Rayleigh scattering produced by the quite big difference of refractive index between the oxide glass matrix and fluoride crystals, precise control of the crystal size is mandatory. Hence, to obtain materials with high transparency in the UV-Vis range, NCs with a size lower than 40–50 nm are required.

The pioneering work about OxGCs, published in 1993 by Wang and Ohwaki [10], in which $Pb_xCd_{1-x}F_2$ fluoride NCs doped with $Er^{3+}$ and $Yb^{3+}$ ions were precipitated in a silica-aluminate glass matrix after a proper heat treatment, showed an increase in the Up-Conversion (UC) emission of GCs with respect to precursor glass. Since that paper, the number of publications about transparent GCs has grown exponentially. In the last few decades, many compositions have been studied with the aim of obtaining different crystal phases and using different $Ln^{3+}$ ions as dopants to obtain enhanced linear and nonlinear optical processes.

The usual method to prepare OxGCs is traditional glass melt-quenching (MQ). This method allows for obtaining several compositions; however, the most studied ones are those based on alumino-silicate matrices, even though there are also some studies of phosphate and fluoride GCs [11,12]. According to the definition of GCs [13], "*Glass-ceramics are ceramic materials formed through the controlled nucleation and crystallization of glass*". In general, for MQ materials, the crystallization process is performed at temperatures slightly higher than $T_g$ ($T_g$ + 20–100 °C) to ensure the growth of crystals with a nanometric size that permits maintaining transparency. Moreover, phase separation commonly acts as a precursor for crystallization and the typical crystallization mechanism is a diffusion-controlled process.

The MQ method presents some drawbacks, most of them related to the high temperatures involved during the glass melting. In fact, high melting temperatures (1400–1700 °C) cause relevant fluorine loss, up to 30–40%, thus limiting the final content of crystal phase that can be obtained and resulting in uncontrollable compositions with respect to fluorine and $Ln^{3+}$ ions. In addition, due to quite common phase separation of the precursor glass due to fluorine immiscibility in oxide glass matrices, it is a challenge to prepare high-quality samples for applications as laser devices or any other that requires high optical quality. Furthermore, heat treatments, in general, are quite long (from 3 h up to 120 h) and thin films cannot be directly obtained, thus limiting the possibility of application as integrated devices. Despite these disadvantages, the MQ method demonstrated the possibility of obtaining OxGCs as bulk materials with enhanced optical properties with respect to precursor glass, and in recent years, the preparation of novel OxGC optical fibers has also been achieved [14–17]. Therefore, MQ is still the most used processing method to obtain OxGCs and is also scalable to an industrial level. Indeed, transparent GC containing up to 75% of crystal fraction, with a crystal size below 40 nm, are extensively used in telescope mirrors [18].

To overcome previous limitations without giving up the field of OxGCs, many researchers tried different processing methods. In particular, the Sol-Gel (SG) route has been recognized and indicated as a promising alternative process to obtain transparent OxGCs. In fact, SG is a handy, flexible, and quite cheap method to fabricate novel and innovative materials at temperatures much lower than those used for MQ materials. Such low temperatures allow for introducing a higher amount of fluoride NCs with much better dispersion than in MQ compositions. Moreover, because SG is a chemical process using

a bottom-up approach, high homogeneity can be obtained with no phase separation detected in SG glasses or GCs.

Another important feature of SG is the versatility of the processing method that permits obtaining thin films, powders, and bulk materials. However, many fewer papers about SG OxGCs are reported in the literature compared to those describing materials prepared by MQ [8]. This is mostly associated with the requirement of the optimization of the synthesis method, and in many cases the starting precursor can also affect the final crystal phase. Most of the materials studied have a simple composition that can be easily summarized with the formula:

$$(100 - x)SiO_2\text{-}x\ M_1F_2/M_1F_3/M_1M_2F_4/M_1M_2F_5,$$

where $M_1$ and $M_2$ are alkaline, alkaline-earth metals, or lanthanide elements, respectively. More complex glass matrices, where $SiO_2$ is partly substituted with $Al_2O_3$, are also reported in the literature but are quite rare, and even more complex structures have also been prepared but for different applications as biomaterials [19].

SG synthesis typically involves the hydrolysis and polycondensation of metal salts or metal-organic precursors, such as tetraethyl orthosilicate (TEOS), in an alcoholic medium. The active phase and $Ln^{3+}$ ions are prepared separately using acetates, nitrates, or chlorates as precursors and dissolved using a fluorine acid. The mixing of both solutions, followed by a controlled crystallization, allows for obtaining transparent OxGCs.

Even though the SG method offers potential advantages, they have not been fully exploited, and all the papers published to date describe the preparation of similar compositions containing nominal small crystal fractions (5–10 mol %), with the real crystal content not being estimated. Furthermore, in many cases only slight changes are added to the already published compositions, the main modifications consisting of changing the dopants and/or their concentration.

In the following sections the most relevant results for several $Ln^{3+}$ doped OxGCs for optical applications studied to date and prepared by SG are summarized. The results are separated into two sections depending on the crystal phase. A third section regarding oxides and oxychlorides GCs has also been added, while in the last sections we will present the results and improvements introduced by our group in the last five years.

### *1.1. Alkaline-Earth Oxyfluoride Glass-Ceramics, $M_1F_2$ ($M_1$ = Mg, Pb, Sr, Ca, Ba), $M_1M_2F_4$ ($BaMgF_4$)*

Alkaline-earth fluoride GCs, with the formula $M_1F_2$ (M = Mg, Pb, Sr, Ca, Ba), are useful for photonic applications due to their high optical transparency in a wide spectral range, from (UV) ultraviolet to infrared (IR). $MgF_2$-based materials have been extensively studied for different applications, for example as protective coatings on glass optics due to their low chemical reactivity, low refractive index (1.38), and scratch- and weather-resistance. Even though this review is centered on materials with luminescence properties, $MgF_2$ materials deserve special attention because they have been among the first fluorides produced by SG. Even more interesting is that the synthesis of $MgF_2$ introduced important novelties in the synthesis of OxGCs.

One of the first works reported about $MgF_2$ NCs and $SiO_2$-$MgF_2$ materials prepared by SG as bulk and thin films dates back to 1996 [20]. $Mg(OCH_3)_2$ and HF were used as Mg and F sources, respectively, to obtain $MgF_2$ sol. $SiO_2$-$MgF_2$ sols were also prepared with ratios of (mol %) 20:80 and 40:60, using tetramethyl orthosilicate (TMOS) as the $SiO_2$ precursor. X-ray diffraction (XRD) showed that $MgF_2$ crystals precipitated in both sol and glass samples, but the crystal growth in $SiO_2$-$MgF_2$ samples was dramatically slowed (~15 nm) in comparison with that of pure $MgF_2$ samples (~115 nm). For $20SiO_2$:$80MgF_2$ samples, the crystal size maintained the same value. $MgF_2$ NCs have been obtained after treatment at different temperatures following the procedure described in [21]. In 1997 Fujihara et al. [22] reported on $MgF_2$ thin films using trifluoracetic acid (TFA) and $Mg(OC_2H_5)_2$ as a fluorine or magnesium precursor, respectively, with a molar ratio 1:2.6. The most important

innovation is the use of TFA as a fluorine precursor, together with an explanation of the fluoride NCs' formation. It was assumed that $Mg(OC_2H_5)_2$ complexes were formed in the xerogel and upon heat treatment, $Mg^{2+}$ ions react with thermally activated fluorine in $CF_3COO^-$ ions to form $MgF_2$ crystals. This decomposition reaction was accompanied by a huge weight loss, around 75%, as confirmed by Differential Thermal Analysis (DTA) (Figure 1). Some years later it was demonstrated that, thanks to the screening effect of $CF_3COO$ ions of TFA, metal cations with oxidation state 2+ or 3+ are prevented from being incorporated in the $SiO_2$ matrix, making possible subsequent fluoride NCs' precipitation upon heat treatment. Therefore, this work can be considered pioneering and a boost towards the preparation of OxGCs by SG.

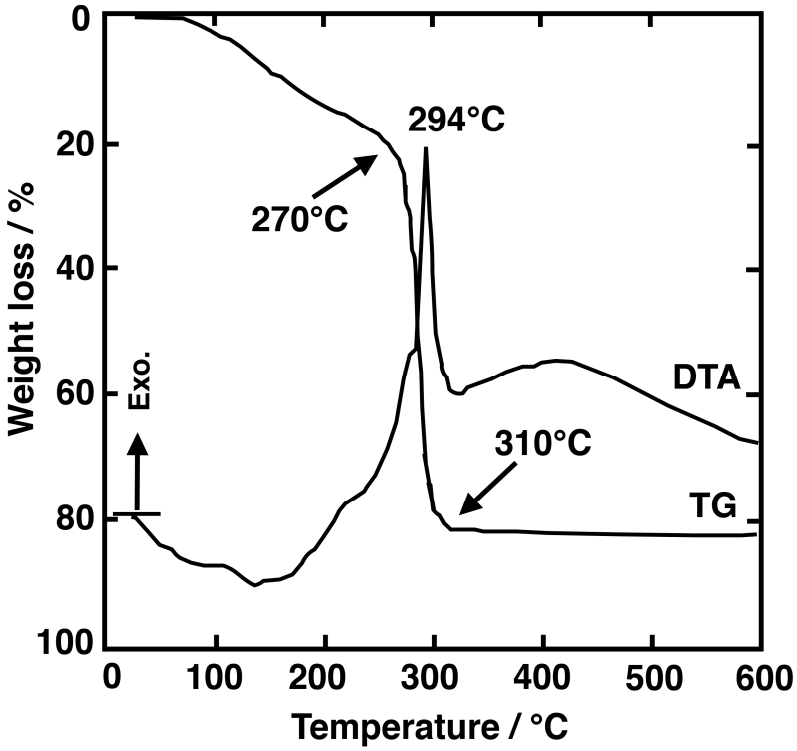


**Figure 1.** TGA/DTA curve of the $MgF_2$ gel obtained by drying the sol at 80 °C. Figure modified from Figure 4 of [22].

Another phase extensively studied is $PbF_2$. One of the first works associated with $SiO_2$-$PbF_2$ samples was reported in 2004 by Luo et al. [23]. Bulk materials of composition $90SiO_2$-$10PbF_2$ doped with $Er^{3+}$ were prepared using TEOS and TFA as the $SiO_2$ or fluorine precursor, respectively. The molar ratio of precursors $TEOS:CH_3CH_2OH:DMF:Pb(CH_3COO)_2:TFA:H_2O:HNO_3$ was 1:2:2:0.1:0.6:4:0.4. Upon heat treatment at 300 °C and 480 °C β-$PbF_2$ NCs precipitated in the glass matrix. $Er^{3+}$ ions seemed to be segregated at the surface of the crystallites and hindered the growth of $PbF_2$ NCs, thus delaying crystallization and reducing the crystal size from 20 to 9 nm. Other authors reported on UC measurements in bulk materials of the same composition doped with $0.1Er^{3+}$-$0.3Yb^{3+}$ [24]. A $TEOS:EtOH:H_2O:CH_3COOH$ ratio of 1:4:10:0.5 was used for the $SiO_2$ sol, while the ratio $Ln(CH_3COO)_3$:TFA was 1:4. UC bands showed well-resolved Stark components indicating the incorporation of $Ln^{3+}$ ions into $PbF_2$ crystals. Results for the same composition doped with $Tm^{3+}$-$Yb^{3+}$-$Er^{3+}$ and $Tm^{3+}$-$Yb^{3+}$-$Ho^{3+}$ were also reported [25]. In both cases, the color tunability of UC luminescence was obtained, allowing white UC generation. Following the same synthesis and composition of Luo et al. described before, Szpikowska-Sroka et al. published some papers about OxGCs with different dopants [26–28]. After heat treatment, $Eu^{3+}$ and $Tb^{3+}$ ions showed an increase in the emission spectra in GC samples with respect to the xerogels due to the incorporation of these ions

into the NCs. In fact, the asymmetry ratio, *R*, described as the ratio between the two visible emissions $I(^5D_0\text{-}^7F_2)/I(^5D_0\text{-}^7F_1)$ of $Eu^{3+}$, gives information about the nature of the environment surrounding the ion. Moreover, the effect of the TFA on the optical properties was also analyzed, showing the best result for a Pb/TFA ratio of 5 and corresponding to a crystal fraction of 3 wt %.

$90SiO_2\text{-}10SrF_2$ transparent GCs doped with $ErF_3$ (1 mol %) were prepared by Yu et al. in 2006 [29]. Samples treated at 300 °C already showed the precipitation of $SrF_2$ crystals with a size of 10 nm. The same crystal size is maintained for heat treatment up to 800 °C. However, upon excitation at 378 nm no $Er^{3+}$ emission was detected unless for samples treated at 800 °C. The authors attributed this phenomenon to the presence of –OH groups that quench the luminescence. Two years later, the same authors prepared transparent bulk samples of composition $90SiO_2\text{-}10SrF_2\text{-}0.5ErF_3$ and $97.5(90SiO_2\text{-}10SrF_2)\text{-}2.5Al_2O_3\text{-}0.5ErF_3$ (mol %) [30]. $Al_2O_3$ was added as the nitrate, with $Al^{3+}$ acting as a glass network former, replacing $Si^{4+}$. The introduction of $Al^{3+}$ to the $SiO_2$ network causes a decrease in non-bridging oxygens, hindering the crystallization of fluoride NCs. The $SiO_2\text{-}Al_2O_3$ glass matrix showed higher transparency in the UV region due to lower pore content and the final optical properties were better for this composition treated at 1000 °C. Very intense and visible UC luminescence was observed for GC based on $SiO_2\text{-}Al_2O_3$ matrix, as compared to the one with only $SiO_2$.

The first $SiO_2\text{-}CaF_2$ transparent GC prepared by SG was reported in 2007 by Zhou et al. [31]. $95SiO_2\text{-}5CaF_2$ bulk samples doped with 1 mol % $ErF_3$ were treated at 900 °C, allowing the precipitation of $CaF_2$ crystals of 20 nm in size, homogeneously distributed in the amorphous $SiO_2$ matrix. $Er^{3+}$ incorporation in the crystal phase was tested by Energy-Dispersive X-ray Spectroscopy (EDXS). Only Red UC emission was detected upon 980 nm excitation. Georgescu et al. prepared $89SiO_2\text{-}5CaF_2\text{-}5YbF_3\text{-}1ErF_3$ (mol %) GCs upon heat treatment at 800 °C [32]. A solid solution of $(Ca_{1-x}Ln_x)F_{2+x}$ crystals was observed by XRD, and both red–green and Violet-UV UC were observed when exciting the samples at 973 nm. The process was described as a two-photon and three-photon absorption process for visible and UV emissions, respectively, upon IR excitation. On the other hand, a different approach was used to prepare $95SiO_2\text{-}5CaF_2$ GCs [33]. $Er^{3+}$-doped $CaF_2$ crystals were previously synthesized by co-precipitation using $Er(NO_3)_3$, $Ca(NO_3)_2$, and ammonium bi-fluoride $NH_4HF_2$ as precursors. Then, NCs were mixed to $SiO_2$ sol, dried at 50 °C during one month and heat-treated to obtain bulk materials. The authors considered that conventional SG route does not allow control of the size and quantity of crystals as well as the $Ln^{3+}$ concentration into the NCs. The optical results showed that the UC emissions increased when passing from xerogels to GCs, the corresponding lifetimes of the $^4F_{9/2}\text{-}^4I_{15/2}$ emission being 1.3 μs and 1.7 ms, respectively. This effect was ascribed to the incorporation of $Er^{3+}$ into $CaF_2$ NCs with phonon energy around 460 $cm^{-1}$.

Another interesting host for $Ln^{3+}$ ions is $BaF_2$ due to its very low phonon energy, around 320 $cm^{-1}$. The first $SiO_2\text{-}BaF_2$ SG material was reported in 2006 by Chen et al. [34]. $95SiO_2\text{-}5BaF_2$ bulk materials were prepared and doped with 0.5 and 1 $Er^{3+}$ (mol %). $BaF_2$ crystals, 2–4 nm in size, precipitated in the glass matrix after heat treatment at 300 °C. Up to 700 °C, no relevant effects in the crystallization were observed. Over this temperature, the crystal grew up to 10 nm. However, treatment at higher temperature also caused the crystallization of the glass matrix in the form of cristobalite. The incorporation of $Er^{3+}$ ions into the NCs was revealed due to the shift of the XRD peaks toward higher angles in $Er^{3+}$-doped samples and by EDXS and Judd–Ofelt calculations. Photoluminescence (PL) emission was detected only for samples treated at 800 °C and green and red UC emissions were observed upon 980 nm excitation. The same composition and synthesis were used by Secu et al. when doping materials with $Pr^{3+}$, $Sm^{3+}$, $Eu^{3+}$, $Dy^{3+}$, and $Ho^{3+}$ [35,36]. Small $BaF_2$ crystals (~7 nm) were precipitated upon heat treatment at 800 °C for 1 h. No $Ln^{3+}$ emission was observed for xerogels except for $Eu^{3+}$, while for all the GCs typical 4f-4f transitions were observed showing the Stark splitting of the bands (Figure 2). Moreover, the typical $Eu^{3+}$ emissions in GCs indicated that these ions are effectively incorporated into NCs. The $Eu^{3+}$ lifetime, measured at 620 nm, increased from 0.3 to 4.7 ms passing from xerogel to GC.

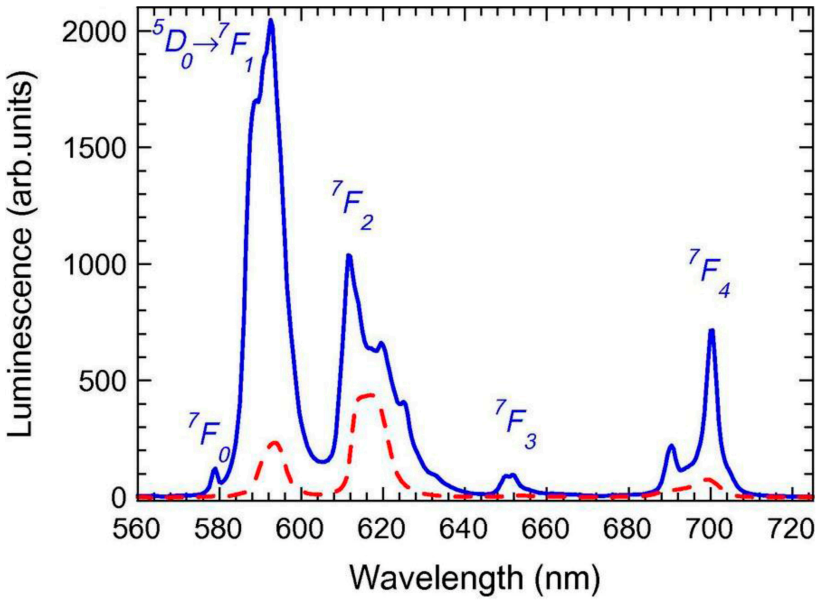


**Figure 2.** PL spectra recorded on $Eu^{3+}$-doped xerogel (dotted curve) and GC (solid curve) using λex. = 394 nm [35].

To conclude this first section, we mention the preparation of $90SiO_2$-$10BaMgF_4$ films doped with $Eu^{3+}$ prepared by Fujihara et al. [37]. Upon heat treatment at 750 °C for 10 min small $BaMgF_4$ NCs 3 nm in size, were observed by High-Resolution Transmission Electron Microscopy (HRTEM). By N,N-dimethylformamide (DMF) addition a porous film was obtained, while, without DMF the film was dense. DMF addition also favors crystallization, reducing stresses in films [38]. The corresponding PL measurements only showed $Eu^{2+}$ emission, meaning that $Eu^{2+}$ ions are effectively incorporated in the crystal phase, substituting $Ba^{2+}$ ions. Furthermore, $Eu^{2+}$ emission was much stronger for porous films due to higher photon confinement, producing an increase in the absorption process.

### *1.2. Lanthanides Oxyfluoride Glass-Ceramics, $M_1F_3$ ($M_1$ = La, Y, Gd) and $M_1M_2F_4$, $M_1M_2F_5$ ($M_1$ = Na, K, Li; $M_2$ = Gd, Y)*

#### 1.2.1. $M_1F_3$

Oxyfluoride GCs in which one element of the NCs former is a $Ln^{3+}$ ion are the most studied compositions. In fact, $Ln^{3+}$ ions are easily replaced by other ions used as dopants, due to their similar ionic radius and equal charge. Moreover, some ions as $Gd^{3+}$ are known to act as sensitizers for other ions as $Eu^{3+}$, $Tb^{3+,}$ and $Dy^{3+}$ [39–41], making possible energy transfer (ET) processes and thus making this NC phase attractive for several photonic applications.

Among all the lanthanide crystals, $LaF_3$ is the most studied. Several papers about $LaF_3$ OxGCs have been published since 1998, when Fuhijara et al. described the preparation of $LaF_3$ thin films on silica substrates [42]. In that work, the authors explained the importance of controlling the synthesis and heat treatment process to obtain high-purity $LaF_3$ NCs, avoiding the precipitation of other phases as LaOF. In the following years, the same authors worked extensively in the preparation of $SiO_2$–$LaF_3$ bulk samples, observing the crystallization of $LaF_3$ NCs with a size ranging from 10 to 30 nm [43]. They also studied the influence of TFA on the $LaF_3$ NCs' crystallization, proposing that such formation occurs by the following chemical reaction [44–46]:

$$La(CF_3COO)_3 \rightarrow LaF_3 + (CF_3CO)_2O + CO + CO_2.$$

However, the authors stated that it is not possible to raise the $LaF_3$ content beyond 10 mol % without losing transparency. Therefore, all the papers published after this work concentrated on

Fujihara's synthesis and composition, just changing the active phase. TMOS was partially or totally replaced by TEOS but the same stoichiometric ratios of $H_2O$ and TFA were used, bringing little innovation to the synthesis and processing of OxGC materials.

The preparation of transparent $Eu^{3+}$ doped $SiO_2$-$LaF_3$ and $SiO_2$-LaOF OxGC films, in which $Eu^{3+}$ ions were incorporated into the $LaF_3$ crystals, resulted in interesting PL emissions [47]. Results showed important differences depending on the sintering temperature and, therefore, on the crystals phase. On the other hand, Ribeiro et al. [48] prepared films with the same composition, finding that for heat treatment between 600 and 900 °C both $LaF_3$ and LaOF phases appeared. $Eu^{3+}$ ions emissions mainly from the $^5D_0$ excited state reflected the change in the environment of these ions. They used thin films as planar waveguides at Vis and IR wavelengths, reported losses ~1.8 dB/cm at 632.8 nm. However, the authors considered that the intensity of PL measurements depends on the nature of the crystal phase and the presence of –OH groups that are responsible for PL quenching. At such a high sintering temperature, –OH groups could be eliminated, but fluorine can be lost, producing a silica matrix rich of lanthanide ions and changing the emission spectra.

$LaF_3$ OxGC bulk materials were also prepared by other authors. Biswas et al. [49] described the preparation of transparent $95SiO_2$-$5LaF_3$ GC, after densification at 1000 °C, using TEOS instead of TMOS as the $SiO_2$ precursor and a TEOS:$H_2O$:$CH_3COOH$ molar ratio of 1:10:0.5. Optical results showed very good UC efficiency from the IR-to-UV region due to the $Yb^{3+}$–$Er^{3+}$ ET process, which is enhanced in GCs, suggesting the incorporation of $Er^{3+}$ ions in the low-phonon environment of $LaF_3$ NCs.

In order to optimize the optical properties, other authors have described the preparation of bulk GC materials with molar ratios $(100 - x)SiO_2$-$xLaF_3$ (x = 5 and 10 mol %), doped with (0.1–0.5) mol % of $Ln^{3+}$ ions and heat treated at temperature up to 1000 °C [50–55] following a similar synthesis to Biswas et al. Optical results showed that $Eu^{3+}$ ions could be selectively excited and, even more interesting, opened the way for the estimation of the percentage of ions that are incorporated in the NCs, concluding that at least 50% are effectively incorporated in $LaF_3$. Another paper [53] described the preparation of transparent $95SiO_2$-$5LaF_3$ bulk GC, co-doped and tri-doped with $Ln^{3+}$ ions. Good UC properties after excitation at ~980 nm were observed due to the interionic distance reduction between $Ln^{3+}$ ions, as a consequence of their incorporation into the NCs. Moreover, by increasing the pump power the emitting color was tuned, obtaining white light generation with potential applications in multicolor solid-state displays and optical integrated devices (Figure 3). The incorporation of a high amount of dopant ions, around 75%, in the precipitated $LaF_3$ NCs was also reported by Velázquez et al. [54] for $Tb^{3+}$-$Dy^{3+}$ co-doped GCs, showing enhanced UV absorption band and allowing a shift in such emission to the Vis range.

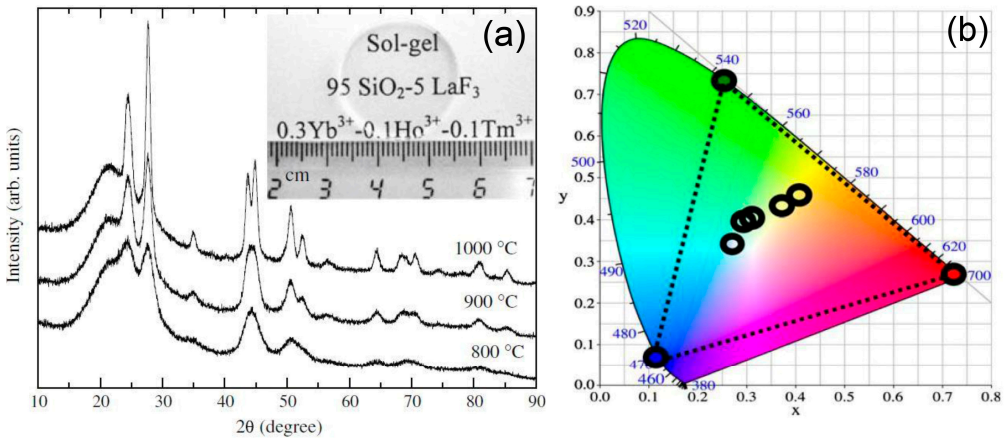


**Figure 3.** (**a**) XRD patterns of $95SiO_2$-$5LaF_3$ GCs at different temperatures and (**b**) CIR standard chromaticity showing the up-conversion emission for GCs co-doped with $0.3Yb^{3+}$, $0.1Ho^{3+}$ and 0.1 $Tm^{3+}$ [53].

Other oxyfluoride GCs with special interest for photonics are those containing $YF_3$ NCs. This crystal phase can act as a high quantum efficient host lattice for $Ln^{3+}$ ions. Since 1998, when Dejneka published one of the first works on $Eu^{3+}$-doped $YF_3$ OxGCs by the MQ method [56], many authors started preparing materials containing this crystal phase. However, it was necessary to wait until 2006 to find one of the first works related to SG bulk materials based on the composition $90SiO_2$-$10YF_3$ [57]. The authors precipitated $YF_3$ crystallites with sizes around 5 nm from the silica matrix when the xerogel was treated at 400 °C. According to the authors, NCs aggregated to form larger particles. By increasing the temperature to 600 °C, $YF_3$ NCs tended to separate without changing their size, finally resulting in a homogeneous distribution in the glass matrix. They proposed that the precipitation of these crystals in the glassy phase induces high stress in the local region, which was reduced when increasing the treatment temperature due to the separation of the NCs from the agglomerates. Méndez-Ramos and co-workers published results based on the same $90SiO_2$-$10YF_3$ composition [58–60]. In these works, using $Ln^{3+}$ as probe ions of the local environment, the authors found that a large fraction of optically active ions is efficiently embedded into the $YF_3$ NCs, 11 nm in size (Figure 4a). When the samples were co-doped with $Yb^{3+}$-$Tm^{3+}$, bright and efficient UC was achieved (Figure 4b), along with intense high-energy emissions in the UV range, due to rare 4- and 5-infrared photon processes. Moreover, co-doping with $Ho^{3+}$ or $Er^{3+}$ ions showed white light generation.

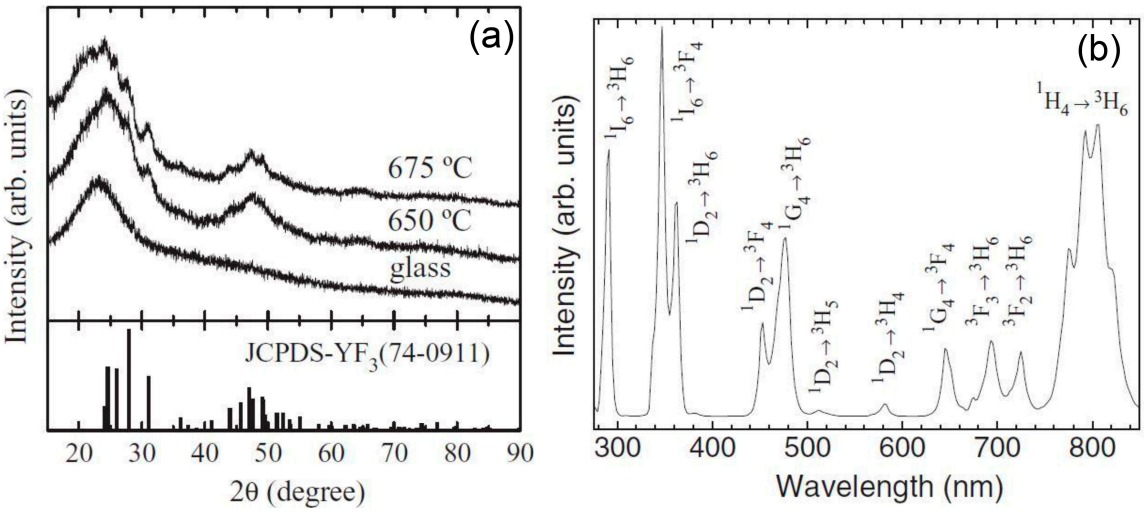


**Figure 4.** (**a**) XRD patterns of $90SiO_2$-$10YF_3$ $Ln^{3+}$-doped GCs heat treated at 650 and 675 °C together with the JCPDS-$YF_3$ and (**b**) Up-conversion emission spectrum of GCs co-doped with 1.5 $Yb^{3+}$ and 0.1 $Tm^{3+}$ heat-treated at 675 °C [60].

Differently to $LaF_3$ and $YF_3$, $GdF_3$ is considered a promising host because $Gd^{3+}$ ions can act as s sensitizer for other $Ln^{3+}$ ions and favor some ET processes [61], being suitable for application in Plasma Display Panels (PDPs) and mercury-free fluorescent lamps [62,63]. Only a few papers about SG $GdF_3$ OxGCs have been published, with the nominal crystal phase content being less than 10 mol %. Fuhijara et al. reported the synthesis of $90SiO_2$-$9GdF_3$ thin films doped with 1 mol % of $EuF_3$ [64]. Results confirmed that $GdF_3$ NCs, 5 nm in size, precipitated during heat treatment at 300 and 400 °C, Figure 5, but GdOF NCs appeared when the temperature was increased to 500 °C. More recently, Szpikowska-Sroka et al. studied the optical properties of $Eu^{3+}$-doped $SiO_2$-$GdF_3$ GCs, with a very low composition of active media, around 3–6 mol %, based on Fuhijara's synthesis [65–67]. The PL associated with $Eu^{3+}$ ions in $GdF_3$ phase was more efficient due to the low phonon energy of the crystal phase.

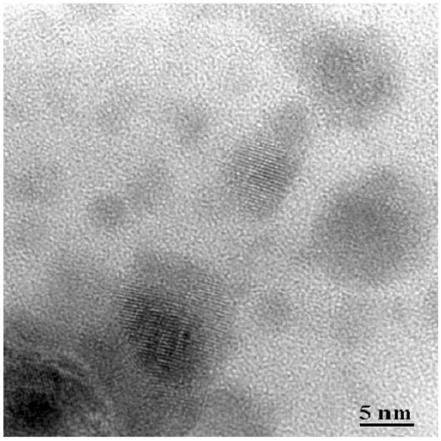


**Figure 5.** HRTEM image of $Eu^{3+}$ doped $SiO_2$-$GdF_3$ GC film heat = treated at 400 °C [64].

### 1.2.2. $M_1M_2F_4/F_5$

Complex fluoride structures became increasingly interesting in the last decade due to their good optical properties and capability of producing intense and efficient nonlinear optical processes as UC emission or other ET processes. In most cases phosphors were synthesized using SG, solvo-thermal, or co-precipitation methods and the final materials were used as powders. Other works concern the preparation of bulk materials and only few are about thin films.

Phosphors based on $NaYF_4$ crystals have been known since the 1970s for their excellent UC properties when doped with $Yb^{3+}$ and $Er^{3+}$. In particular, $NaYF_4$ phosphors' UC emission was found to be 4–5 times higher than that of $LaF_3$ crystals [68]. Kramer et al. proposed a route to synthesize only pure hexagonal $NaYF_4$ phosphors [69]. Moreover, transparent $NaYF_4$ OxGCs bulk materials have been obtained by the MQ method, showing interesting PL properties even more efficient than those of powder phosphors [70,71].

However, the first work on $NaYF_4$ OxGCs prepared by SG was published in 2009 by Yanes et al. [72]. $95SiO_2$–$5NaYF_4$ bulk materials doped with $0.1Er^{3+}$ and $0.3Yb^{3+}$ were obtained using acetates as precursor and the "Fujihara route". The ratio between red and green UC emission bands varied as a function of temperature of heat treatment and pump power resulting in color-tunable UC phosphors. The same authors also prepared $95SiO_2$–$5NaYF_4$ bulk materials doped with $0.1Eu^{3+}$ (mol %) [73]. $NaYF_4$ face-centered cubic NCs precipitated upon heat treatment between 550 and 650 °C, their size increasing from 5 to 10 nm with the treatment temperature. PL measurements demonstrated the incorporation of $Eu^{3+}$ into the NCs, due to changes of emission bands using a selective excitation, together with an increase in the lifetime. The authors also reported bright white light generation achieved in similar materials tri-doped with $Yb^{3+}$-$Ho^{3+}$-$Tm^{3+}$ [74] and $Yb^{3+}$-$Er^{3+}$-$Tm^{3+}$ [75].

To the best of our knowledge, no $KYF_4$ GC or composite materials prepared by MQ have been reported in the literature. The first GC was prepared by Mendez-Ramos et al. using the SG method and co-doping with $Yb^{3+}$-$Er^{3+}$-$Tm^{3+}$ [76]. The processing method was the same used by the authors for other phases such as $NaYF_4$, $LaF_3$, etc. K, Y, and $Ln^{3+}$ acetates were dissolved using ethanol, TFA, and water, while hydrolyzed TEOS were used as the $SiO_2$ precursor, employing the well-known TEOS:EtOH:$H_2O$:$CH_3COOH$ ratio 1:4:10:0.5. $KYF_4$ crystals, 14–20 nm in size, were observed treating $95SiO_2$-$5KYF_4$ bulk materials between 650 and 700 °C. Very well-resolved PL Stark components were observed for $Er^{3+}$ and $Tm^{3+}$ ions, indicating their incorporation into low-phonon $KYF_4$ crystals (Figure 6). UC was obtained upon $Yb^{3+}$ excitation at 980 nm and tunable emission was achieved depending on the dopant concentration and excitation power, allowing white light generation. The same composition was also studied by doping the system with other $Ln^{3+}$ ions [77–79]. In all cases, the incorporation of $Ln^{3+}$ ions into cubic $KYF_4$ crystals was proved by PL measurements that showed defined Stark components, a better DC and UC process, and an increased lifetime as compared

to emissions of $Ln^{3+}$ ions remaining in the glass matrix. The possibility of obtaining both UC and DC simultaneously had interesting applications for a photovoltaic silicon solar cell and white light-emitting diodes.

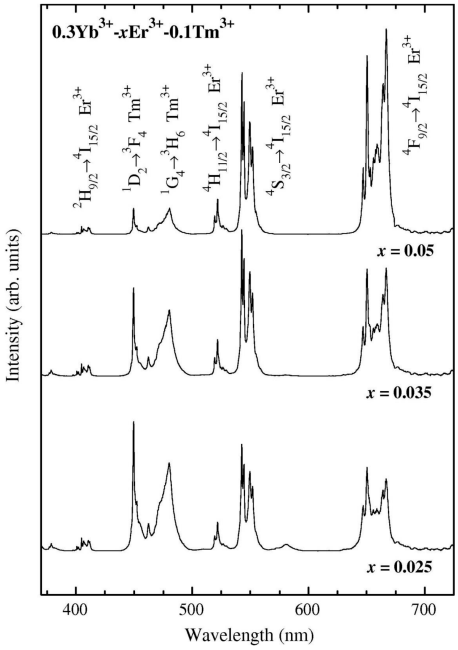


**Figure 6.** Up-conversion emission spectra of $95SiO_2$-$5KYF_4$ GCs co-doped with $Yb^{3+}$-$Er^{3+}$-$Tm^{3+}$ heat-treated at 700 °C [76].

Despite some works based on $LiYF_4$ OxGCs prepared by the MQ method appearing since 2009 [80], the first SG GCs containing $LiYF_4$ crystals dates back to 2013 with the works of Kawamura et al. [81] and Secu et al. [82]. In both cases the authors used Fujihara's synthesis, and Li and F were added in excess to avoid losses due to evaporation and guarantee $LiYF_4$ formation. In fact, a stoichiometric Y:Li ratio favored the crystallization of $YF_3$ instead of $LiYF_4$. Gel powders were then treated between 500 and 600 °C. Kawamura et al. obtained a mix of $LiYF_4$ and $YF_3$ phases when the Li:Y molar ratio was lower than 3, while only pure $LiYF_4$ phase was produced using this ratio. By EDXS analysis, $Nd^{3+}$ incorporation into the fluoride NCs was proven even though observable amounts of F, Nd, and Y were also detected in the glass matrix. UC spectra were obtained when exciting the samples at 800 nm, showing crystal-like behavior. The $Nd^{3+}$ lifetime in $LiYF_4$ was longer than in $YF_3$, suggesting a better $Nd^{3+}$ distribution for the former. The same authors prepared the same materials with only $LiYF_4$ crystals and treated the samples with HF to remove the $SiO_2$ matrix [83]. However, relevant amounts of O and Si were detected after HF treatment and PL measurements did not show a significant difference after and before the HF treatment, thus ensuring the presence of $Nd^{3+}$ ions in the fluoride NCs.

Secu et al. [82,84] prepared $(100 - x)SiO_2$-$xLiYF_4$ GC powders doped with $Eu^{3+}$ and $Er^{3+}$-$Yb^{3+}$ and compared the results for $LiYF_4$:$Eu^{3+}$ and $LiYF_4$:$Er^{3+}$-$Yb^{3+}$ crystal pellets. As compared to an untreated xerogel, $Eu^{3+}$-doped GC samples showed 7–8-fold stronger emission, a much longer lifetime of the $^5D_0$-$^7F_2$ red emission (613 nm), and better resolved bands due to the Stark splitting and reduced inhomogeneous broadening typical of amorphous environments. Crystal pellets and GCs showed similar PL spectra and lifetimes. For $Er^{3+}$-$Yb^{3+}$-doped samples, UC emission was detected in both GCs and crystal pellets. A saturation effect of the red UC emission was observed for GC samples, associated with the high $Ln^{3+}$ ions concentration, which caused a back-ET from $Er^{3+}$ to $Yb^{3+}$.

$BaYF_5$ and $BaGdF_5$ are other interesting crystal phases suitable for photonic applications. The first $95SiO_2$-$5BaYF_5$ GC obtained by SG was prepared recently using $Eu^{3+}$ and $Sm^{3+}$ as dopants [85]. After heat treatment at 750 °C cubic $BaYF_5$ NCs, 11 nm in size, were detected by HRTEM and XRD.

For comparison, $BaYF_5$ NCs were synthesized by the solvo-thermal method and dispersed in toluene. Similar PL features and lifetimes were obtained for the GC and the dispersed NCs. The same authors also prepared $95SiO_2$-$5BaGd_{(1-x)}RE_xF_5$ (x = 0 or 0.02 mol %, where RE = $Eu^{3+}$, $Sm^{3+}$, $Dy^{3+}$ and $Tb^{3+}$) GC [86]. After heat treatment at 650 °C, $BaGdF_5$ NCs, with a size around 10 nm, precipitated in the $SiO_2$ matrix (Figure 7). Upon $Gd^{3+}$ excitation at 272 nm or $Eu^{3+}$ direct excitation at 393 nm, very similar $Eu^{3+}$ emission spectra were obtained and the bands showed typical Stark components that were quite well resolved, thus confirming the incorporation of $Eu^{3+}$ in the $BaGdF_5$ NCs and the ET from $Gd^{3+}$ to $Eu^{3+}$.

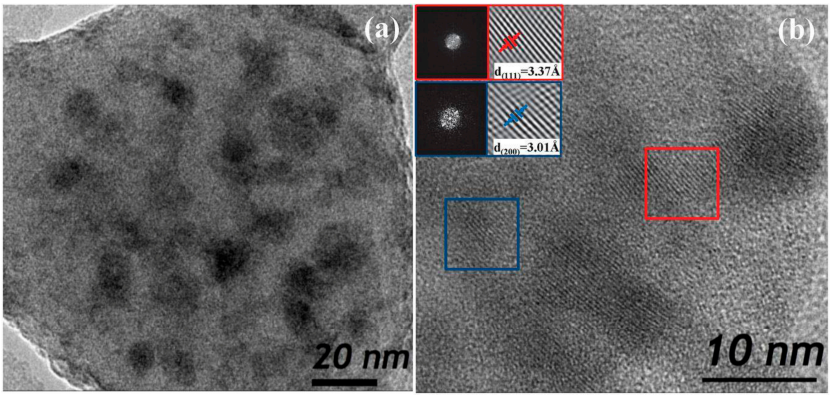


**Figure 7.** (**a**) TEM and (**b**) HRTEM images of $95SiO_2$-$5BaGd_{(1-x)}Eu_xF_5$. Inset show power spectrum (FFT pattern) and filtered higher-contrasted red and blue square nanoparticles [86].

### *1.3. Other Glass-Ceramics (Oxides and Oxyclorides)*

In this section we resume work concerning GCs based on different compositions containing oxide and oxychloride NCs. Oxide GCs have received great attention because some oxide phases present interesting properties. For example, it is worth citing $SnO_2$, which is a wide gap n-type semiconductor with strong UV absorption (energy gap ~3.6 eV at 300 K) and tunable emission spectra depending on the crystal size. In fact, $SnO_2$ is known to act as a Quantum Dot (QD) when the crystal size is smaller than or comparable to the Bohr radius, thus showing properties between bulk semiconductor and discrete molecules that have many applications in several technological fields. Significant blue-energy shift of the intrinsic absorption edge can be obtained by strong quantum confinement of excitons inside the QDs [87,88]. The incorporation of $SnO_2$ NCs in an $SiO_2$ glass matrix using SG dates back to 2002 with the works of Chiodini et al. [87] and Nogami et al. [89] Chiodini et al. reported on $98SiO_2$-$2SnO_2$ materials obtained by mixing TEOS and dibutyltin diacetate ($Sn(CH_2CH_2CH_2CH_3)_2(OOCCH_3)_2$) in ethanol and using a TEOS:$H_2O$ molar ratio of 1:8. The samples were heated from 450 to 1050 °C in an $O_2$ atmosphere and tetragonal $SnO_2$ NCs with a size of 1.5–2 nm were observed by HRTEM between 950 and 1050 °C. However, the NCs' size and distribution are strongly dependent on the atmosphere. NCs above 10 nm (clusters) were obtained for heat treatment at 1050 °C in reducing atmosphere. The near-UV absorption edge shifts to high energies by decreasing the synthesis temperature due to a decrease in the $SnO_2$ NCs' size. The author concluded that a possible application of these materials could be as all-optical switching devices. The authors also reported that an increase in the $SnO_2$ content up to 15 mol % produces negative photorefractivity, activated by UV-Vis light [90]. A refractive index change of −4 and −6, measured at 980 nm, was obtained after sample irradiation at 266 and 532 nm, respectively.

Nogami et al. prepared materials with compositions $(100 - x)SiO_2$-$xSnO_2$ (x = 1, 3 and 5 mol %) doped with 1 mol % of $Eu_2O_3$ [89]. They used TEOS as the $SiO_2$ precursor and $SnCl_2{\cdot}2H_2O$ together with $EuCl_3$ as $SnO_2$ and $Eu^{3+}$ precursors, respectively. After a gelation period at room temperature for two weeks, bulk samples were treated from 500 to 1000 °C to ensure the densification of the glass matrix and allow $SnO_2$ NCs' precipitation. For compositions containing 3 and 5 mol % of $SnO_2$, NCs with a size of 6.9 and 8.5 nm were obtained, while no NCs were observed for $99SiO_2$-$1SnO_2$

composition. Absorption measurements showed a blue shift of the band-tail with respect to $SnO_2$ bulk sample. Higher blue-shift and energy gap were obtained when decreasing the $SnO_2$ content, related to a smaller NCs size. PL showed that $Eu^{3+}$ emission intensity increases proportionally to the third power of $SnO_2$ concentration: $Eu^{3+}$ emission in a $95SiO_2$-$5SnO_2$ sample was 150 times higher than in $99SiO_2$–$1SnO_2$. PL excitation spectra revealed an ET process between $Eu^{3+}$ and $SnO_2$ NCs, thus indicating the incorporation of $Eu^{3+}$ in the crystal phase and making possible its emission upon $SnO_2$ excitation. Other authors studied $(100 - x)SiO_2$-$xSnO_2$ (x = 1–10 mol %) GCs doped with $Eu^{3+}$ and $Eu^{3+}$-$Tb^{3+}$ following Nogami's synthesis [91–93]. By increasing the $SnO_2$ content up to 10 mol % (NCs size ~5 nm), a low quantum confinement effect was observed. Hence, most research was performed on GCs containing 5 mol % of $SnO_2$ and the optical characterization showed that in strong confinement conditions the energy gap has a high dependence on the NCs' size. $Eu^{3+}$ ions incorporated in $SnO_2$ NCs were excited in the range 340–394 nm and, considering the variation of the band gap with the crystal size, the use of a certain excitation wavelength allowed for exciting only NCs with a defined crystal size, thus producing remarkable variation in the PL emission spectra. ET from $SnO_2$ NCs to $Tb^{3+}$ ions was observed in $Eu^{3+}$-$Tb^{3+}$-doped GCs. It was observed that the ET depends on the crystal size, being favored for the smallest NCs. A relevant drawback related to $SnO_2$ NCs is the low solubility of $Ln^{3+}$ limited to ~0.05%, the remaining ions being segregated at grain boundaries, probably in the form of $Ln_2Sn_2O_7$ crystals [94]. To overcome this limitation, Van Tran et al. [95,96] prepared $SiO_2$-$SnO_2$ GCs with a maximum nominal NCs concentration of 20 mol % to allow for higher $Ln^{3+}$ amount incorporation in $SnO_2$ NCs. The authors prepared $Er^{3+}$-doped materials and PL measurements showed that an increase in $SnO_2$ concentration promotes $Er^{3+}$ ions' incorporation in $SnO_2$ NCs.

Among $SiO_2$ glass matrices containing oxide NCs, those containing $ZrO_2$ crystals deserve special attention because $ZrO_2$ is a pretty cheap material, transparent over a wide range of wavelengths: from 300 nm to 8 μm, it has quite low phonon energy ~650 $cm^{-1}$ and a high refractive index. Such properties have been exploited to develop $Ln^{3+}$-activated planar waveguides at telecom wavelength [97,98]. $(100 - x)SiO_2$-$xZrO_2$ (x = 10–30 mol %) homogenous and crack-free thin films doped with $Er^{3+}$ were prepared following a synthesis route similar to $SnO_2$, using TEOS and $ZrOCl_2 \cdot 8H_2O$ as $SiO_2$ and $ZrO_2$ precursors, respectively. All waveguides showed the existence of one mode at 1550 nm with relatively low propagation losses; the refractive index increased from 1.492 to 1.609 for 10 and 30 mol % $ZrO_2$, respectively. Narrow $Er^{3+}$ emissions were observed in thin films with respect to glass materials, thus indicating $Er^{3+}$ incorporation in $ZrO_2$ NCs. Suhaimi et al. [99] prepared several $(100 - x)SiO_2$-$xZrO_2$ compositions (x = 30–70 mol %) doped with 0.58 mol % $Er^{3+}$. The refractive index at 1550 nm changed linearly from 1.6931 to 1.7334 by increasing $ZrO_2$ content. Much higher PL emission of $Er^{3+}$ at 568 nm was observed for films containing 70 mol % of $ZrO_2$, thus indicating that $ZrO_2$ facilitates $Er^{3+}$ to disperse homogeneously and the low phonon energy of the crystal phase reduces non-radiative losses. Other authors also studied $SiO_2$-$ZrO_2$ waveguides doped with $Er^{3+}$-$Yb^{3+}$ with $ZrO_2$ contents up to a maximum of 25 mol % [100]. Low roughness, a crack-free surface, and a high confinement coefficient were observed for all the compositions. $Er^{3+}$ NIR PL was enhanced when the waveguide was co-doped with $Yb^{3+}$, denoting an efficient ET between these ions. The authors considered the possibility of applying these materials as EDWA and WDM. Many GCs containing other oxide NCs have also been developed as waveguides [101–104].

To conclude this section, we mention the work of Secu et al. on oxychloride GCs [105]. $95SiO_2$-5LaOCl GCs doped with 1 mol % $Eu^{3+}$ were prepared following a similar synthesis to $LaF_3$ GCs but replacing TFA with trichloacetic acid ($CCl_3COOH$). LaOCl:$Er^{3+}$ pellets have also been prepared using a conventional solid state reaction between lanthanum oxide and ammonium chloride. DTA analysis showed that several exothermic peaks appear for measurements performed in air, but these peaks disappear completely for measurements in Ar. However, XRD confirmed the formation of LaOCl NCs, 20–60 nm in size, during heat treatment at 450–750 °C in air. For heat treatment in Ar, smaller crystal size and fraction were obtained. Judd–Ofelt analysis along with PL measurements

showed that, as the annealing temperature increases, a higher amount of $Eu^{3+}$ ions is incorporated in LaOCl NCs, thus producing a better resolved Stark component and a much longer lifetime with respect to xerogel. Similar results were obtained for LaOCl:$Eu^{3+}$ pellets, indicating the effective incorporation of $Eu^{3+}$ in this crystal phase.

### *1.4. Prospects and Perspectives*

In summary, most of the transparent SG OxGCs previously described are based on a unique synthesis developed by Fujihara et. al., using TMOS and/or TEOS as the $SiO_2$ precursor, TFA as the fluorine source, and with an upper limit of nominal crystal phase around 10 mol %. The real crystal fraction in GCs was never estimated by a reliable method as Rietveld refinement and the few works that reported such information only used optical results to estimate the crystal content. Furthermore, many papers describe materials with 5 mol % of nominal active phase, this being even less than that achievable by classical MQ and requiring an extremely long time for bulk sample preparation, from several weeks up to months. Moreover, quite high treatment temperatures, up to 1000 °C, are used to crystallize the fluoride NCs when the crystallization of fluorides detected by DTA occurs at around 300 °C. For all these reasons, research in the SG OxGCs field shows good and enhanced optical properties but no improvement of the synthesis, and no new processing methods have been reported in the literature since the first papers published 20 years ago.

In recent years, the GlaSS group of CSIC has been working on the optimization of the synthesis for significantly increasing the crystal content of SG OxGCs. In fact, it is worth noting that synthesis parameters such as molar ratios between precursors, temperature, and time of reaction are strictly dependent on the crystal phases and their content. Moreover, a unique synthesis, in general, is not suitable to obtain different compositions for the same crystal phase, and modifications of the synthesis are necessary to obtain novel materials. In addition, we partially replaced TEOS with methyltriethoxysilane (MTES) in the $SiO_2$ sol synthesis, reducing the sintering temperature to 550 °C and making it possible to obtain enhanced optical properties without a need for much higher treatment temperatures.

## 2. Experimental

### *2.1. Synthesis of $(100 - x)SiO_2$-$xLaF_3$*

Our research started with $LaF_3$ GC films prepared by dip-coating. The precursors used were TEOS, $H_2O$ (0.1 M HCl), EtOH, TFA, and $La(CH_3COO)_3$. Dopants were added as acetates. A first $SiO_2$ sol was prepared using a molar ratio 1TEOS:2$H_2O$ (0.1 HCl):9.5EtOH stirred for 2 h at room temperature. Separately, 1$La(CH_3COO)_3$:5EtOH:5TFA:4$H_2O$ were mixed and stirred for 2 h at 40 °C in a glycerine bath. By mixing different volumes of $SiO_2$ sol with the La solution, 90$SiO_2$-10$LaF_3$ and 80$SiO_2$-20$LaF_3$ compositions were obtained. To further increase the nominal $LaF_3$ concentration to 30 mol %, the La solution was modified, adding more TFA (7 mol %) to favor acetate dissolution. The last composition we obtained is 60$SiO_2$–40$LaF_3$ and in this case a further increase of TFA up to 10 mol % was necessary to obtain transparent thin films. Thin films were deposited by dip-coating on silica or Si substrates using a withdrawal rate of 20–45 cm/min. The thickness and refractive index of thin films were measured by a 2000 U ellipsometer (J.A. Woollam Co., Inc., Lincoln, NE, USA), using a Cauchy dispersion relation as a model.

Self-supported layers (or bulk-like samples) were also prepared with compositions 90$SiO_2$-10$LaF_3$ and 80$SiO_2$-20$LaF_3$ using the modified ratio of $SiO_2$ sol 1TEOS:7.5$H_2O$ (0.1 HCl):5EtOH while leaving unchanged the synthesis of La solution described before for thin films with the same composition. Samples were dried at 50 °C over two days and then the covering was removed, letting the solvent evaporate for seven days.

A further modification to obtain higher thickness of thin films and improve the mechanical resistance of self-supported layers was to partially replace TEOS with MTES in the ratio

40TEOS:60MTES [106]. A modification of the molar ratios was necessary for thin film preparation to obtain the highest film thickness along with good sol stability. In particular, for thin films the $SiO_2$ sol was prepared using 0.4TEOS:0.6MTES:1$H_2O$ (0.1 HCl):2.5EtOH:0.2$CH_3COOH$, while the La solution was left unchanged. For self-supported layers, the previous TEOS:$H_2O$ ratio was used, replacing TEOS with 0.4 TEOS + 0.6 MTES (mol %) to maintain the same ratio of $SiO_2$ precursor and $H_2O$, which is a crucial parameter for bulk-like samples.

### *2.2. Synthesis of (100 − x)$SiO_2$−x$GdF_3$/$NaGdF_4$*

90$SiO_2$-10$GdF_3$ and 80$SiO_2$-20$LaF_3$ self-supported layers were also obtained following the two-step process and using the aforementioned TEOS:MTES ratio for $SiO_2$ sol. In this case Gd solution, using Gd($CH_3COO$)$_3$ as precursor, was stirred for 24 h at 40 °C to obtain a homogeneous solution of the products, thus making possible the crystallization of $GdF_3$.

Finally, we prepared for the first time $SiO_2$-$NaGdF_4$ materials as self-supported layers and thin films. A $SiO_2$ sol was prepared using only TEOS as the $SiO_2$ precursor with the same ratios used for $SiO_2$-$LaF_3$ compositions. Then, Na($CH_3COO$), Gd($CH_3COO$)$_3$, EtOH, TFA, and $H_2O$ were mixed using similar ratios of TFA and EtOH and trying several Na:Gd ratios (1.125–0.80):1. The solution was stirred 24 h at 40 °C in a glycerin bath.

For all compositions, GCs were obtained after heat treatment at 550–750 °C from 1 min up to several hours using heating rates of 1–10 °C/min. In all cases, thermal quenching in air was performed to obtain good crystallization of the samples.

### *2.3. Thermal and Structural Characterization*

DTA was performed in air and argon (inert) atmosphere on small pieces of 1–1.25 mm in size, with heating rates 10–40 °C using SDT Q600 (TA Instruments, New Castle, DE, USA) equipment. Measurements were performed in the range 25–800 °C using 15–30 mg of sample.

High-resolution XRD patterns were collected in the range 6–27° at the synchrotron SpLine BM25B of the ESRF (European Synchrotron Radiation Facility, Grenoble, France) using a wavelength of 0.619 Å and a step size of 0.02°.

HRTEM was performed using a JEOL 2100 microscope (Akishima, Tokyo, Japan). Samples were prepared using lacey formvar carbon film that had a small amount of scratched sample deposited on them.

Fourier Transform Infra-Red (FTIR) spectra in the range 2000–600 $cm^{-1}$ were obtained, with a resolution of 4 $cm^{-1}$, using a Perkin Elmer Spectrum 100 instrument (Waltham, MA, USA).

$^{19}F$ magic-angle spinning nuclear magnetic resonance ($^{19}F$ MAS/NMR) spectra of xerogel and GCs were recorded using a NMR Spectrometer AVANCE II (BRUKER, Billerica, MA, USA) equipped with a 9.4 Tesla magnet (400 MHz) and a 2.5 mm rotor spinning at 20 kHz.

X-ray Absorption Spectroscopy (XAS) was measured at the SpLine BM25A of the ESRF collecting the spectra in fluorescence mode using a 13-element Si (Li) solid-state detector with the sample surface placed at an angle of 45° to the incident beam. Six scans were acquired to obtain an average spectrum. XAS data were processed using ATHENA software [107]. $Eu_2O_3$ and $EuF_3$ crystal powders were also measured as reference materials to compare their spectra with those of $Eu^{3+}$-doped xerogel and GC samples.

Photoluminescence measurements were recorded using a FS5 fluorescence spectrometer (Edinburgh Instruments Ltd., Livingston, UK) equipped with a 150 W Xenon lamp or Ti:sapphire ring laser (0.4 $cm^{-1}$ linewidth) in the 770–920 nm spectral range. The emission was detected by Hamamatsu H10330A-75 or Hamamatsu R928P photomultiplier (Hamamatsu City, Shizuoka, Japan).

Even though several compositions were prepared, most of the results shown in the next sections deal with 80$SiO_2$-20$LaF_3$/$GdF_3$/$NaGdF_4$ compositions, which have been studied in detail in recent years, all containing 20% of fluoride phases, at least double that reported by other authors.

## 3. Results and Discussion

### *3.1. Materials*

Transparent and crack-free GC thin films were obtained for all compositions, even for those containing 30 or 40 mol % of active phase. For single deposition at 30 cm/min and heat treatment at 550 °C for 1 h, thicknesses around 500 nm and 1 µm were obtained for TEOS and TEOS/MTES compositions, respectively. Higher thicknesses up to 900 nm and 1.7 µm were obtained for TEOS and TEOS/MTES, respectively, depositing two films or increasing the withdrawal rate. Hence, the addition of MTES in the $SiO_2$ sol allows a notable increase of the thickness, thus making this precursor attractive for application where a thin film of 1 µm or thicker is required. Transparent and high-quality films were obtained, as confirmed by a good agreement between ellipsometry measurements and fits.

Transparent and crack-free self-supported layers were also obtained after heat treatments. The addition of MTES allows increasing the heating rate up to 10 °C/min without the appearance of cracks.

### *3.2. Thermal and Structural Characterization*

#### 3.2.1. $SiO_2$–$LaF_3$

DTA measurements for (100 − x)$SiO_2$-x$LaF_3$ (x = 10–40 mol %) bulk samples obtained drying thin films sols are shown in Figure 8a. The curves show a first endothermic peak with a weight loss (not shown) associated with $H_2O$ and other solvent removal. Such an endothermic process is much more intense for a composition with a higher amount of La. This could be associated with the increasing water content passing from x = 10 to x = 40.

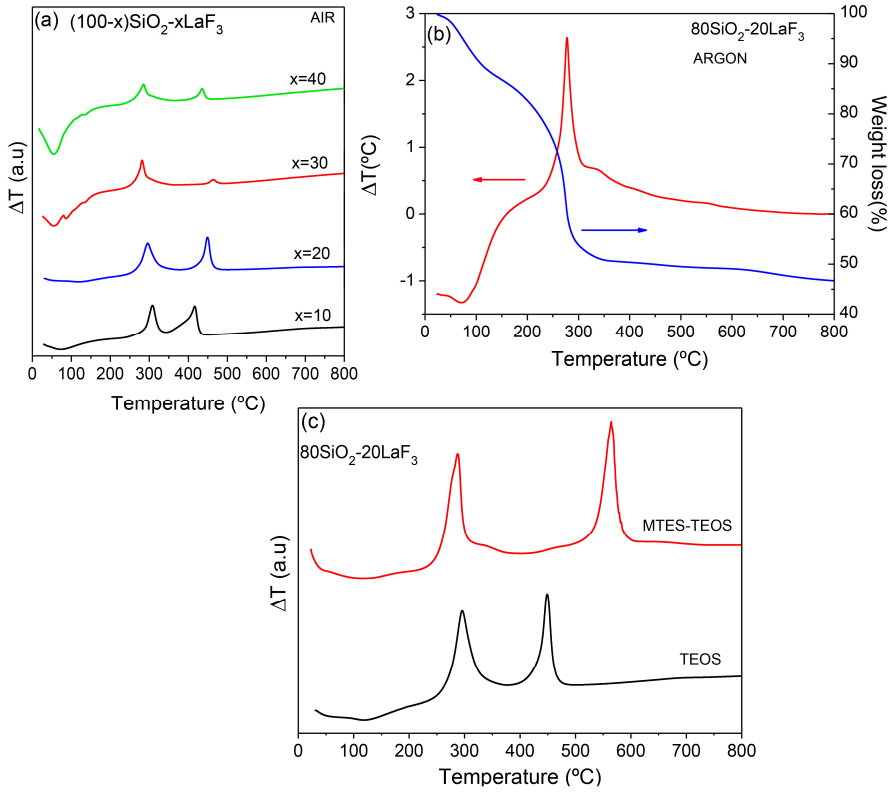


**Figure 8.** (**a**) DTA in air of (100 − x)$SiO_2$-x$LaF_3$ (x = 10–40 mol %) bulk samples prepared with TEOS; (**b**) DTA and TG in argon atmosphere of 80$SiO_2$-20$LaF_3$ bulk samples prepared with TEOS; (**c**) DTA in air of 80$SiO_2$-20$LaF_3$ bulk samples with TEOS and TEOS/MTES. All measurements were performed using a heating rate of 10 °C/min.

Then, a first exothermic peak appears around 300 °C, together with a big mass loss that increases passing from x = 10 to x = 40 mol %. The peak shifts towards lower temperatures when increasing the active phase content. As reported by other authors [43], such a peak is associated with the crystallization of $LaF_3$, favored by increasing the La content. Such crystallization takes place after a chemical decomposition with gas release, which is responsible for the notable weight loss. The intensity of the endothermic and exothermic peaks is affected by the sample amount used for the analysis, and therefore it cannot be compared quantitatively. The second exothermic peak in the range 400–500 °C is assigned to organic combustion and was not detected in an argon atmosphere (Figure 8b). The effect of the $SiO_2$ precursor on the DTA curve is shown in Figure 8c for $80SiO_2$-$20LaF_3$ samples prepared using TEOS and TEOS/MTES in the ratio 40:60 as $SiO_2$ precursor. The crystallization peak appears centered around the same value, near 300 °C, while the second exothermic peak is associated with organic combustion of different species. In fact, when MTES is used, $CH_3$ groups are introduced in the system and released around 550–600 °C. Such release is associated with a contraction of thin films and self-supported layers. Therefore, when MTES is used, treatment temperatures no higher than 550 °C should be used to avoid sample cracking. However, and concerning the crystallization mechanism, no relevant effects are introduced by the partial replacement of TEOS with MTES. The introduction of MTES improved the mechanical resistance during the treatment process and MTES bulk-like samples can be treated using a 10 °C/min heating rate instead of 1–2 °C/min, as is commonly used for samples prepared using only TEOS. Moreover, MTES addition facilitates –OH group removal [108], without requiring extremely high treatment temperatures (900–1000 °C).

The XRD of $80SiO_2$-$20LaF_3$ bulk sample prepared using TEOS/MTES and treated at 550 °C for 1 min is represented in Figure 9. Well-defined diffraction peaks are observed even for this fast treatment; the crystal size, estimated by Scherrer's equation, is around 8.5 nm. No relevant $SiO_2$ amorphous pattern is observed, different to the XRD results obtained by other authors [50–55,57], indicating a relevant increase of fluoride crystal fraction. Dopant incorporation, such as $Er^{3+}$, was confirmed by an appreciable shift of the diffraction peaks towards higher angles, associated with a shrinking of the unit cell due to the lower size of $Er^{3+}$ with respect to $La^{3+}$ [109]. By Rietveld refinement (not shown), we obtained a $LaF_3$ crystal fraction of 18 wt %, which is, to the best of our knowledge, the highest value of fluoride concentration ever reported in OxGCs. The crystallization mechanism of $LaF_3$ in SG OxGCs has been studied in a previous paper [91]. It was shown that the $LaF_3$ crystallization mechanism is very different to that for MQ GCs. In fact, for MQ GC a diffusion-controlled process is responsible for the crystallization of $LaF_3$ and many other fluoride phases; phase separation acts as a precursor for crystallization. On the contrary, $LaF_3$ crystallization in SG OxGCs is not a diffusion-controlled process but consists of a fast crystal precipitation taking place after a chemical decomposition. It was observed that $LaF_3$ NCs are not stable for heat treatment at crystallization or higher temperatures and amorphization was observed for a long treatment time (5–80 h) at 550 °C.

HRTEM micrographs of $80SiO_2$-$20LaF_3$ thin films and self-supported layers treated at 550 °C for 1 min are shown in Figure 10a,b, respectively. Very small $LaF_3$ NCs around 2–3 nm are observed in thin film samples, as confirmed by the crystal size distribution shown in the inset. For self-supported layers the crystal size is much bigger, around 8 nm, in agreement with the XRD results in Figure 3. In both cases homogeneously distributed NCs are observed, without the formation of clusters, even for such a fast heat treatment at 550 °C for 1 min.

NMR spectra of SG OxGCs are rarely encountered in the literature but the information that can be extracted is of relevant importance. In particular, $^{19}F$ NMR spectra allow for obtaining evidence about fluorine surrounding in the xerogel and how it changes after the crystallization process. Figure 11 shows $^{19}F$ MAS NMR of $80SiO_2$-$20LaF_3$ xerogel and GC treated at 550 °C for 1 min [110]. The spectrum of polycrystalline $LaF_3$ was also acquired for comparison. In the xerogel sample the fluorine surrounding is as in the precursor TFA acid and no bonding with Si is observed. After heat treatment at 550 °C for 1 min, the spectrum of the GC sample is practically the same as that

of the $LaF_3$ polycrystalline powders. This further indicates that a chemical reaction accompanied by fast crystal precipitation is responsible for the $LaF_3$ NCs' formation.

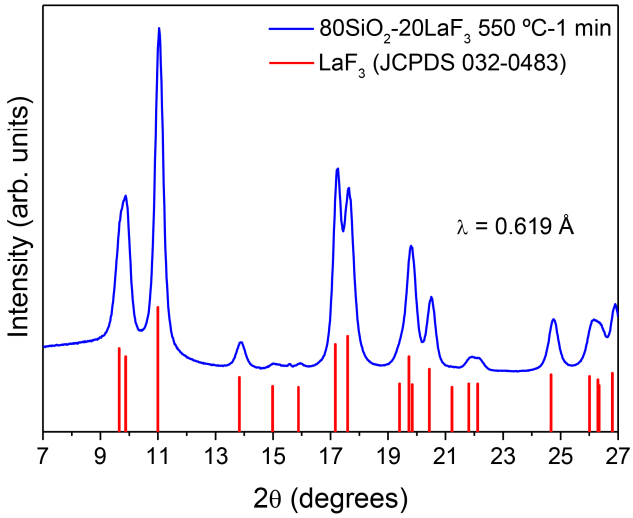


**Figure 9.** XRD of $80SiO_2$-$20LaF_3$ GC treated at 550 °C for 1 min performed at the synchrotron SpLine BM25B of the ESRF.

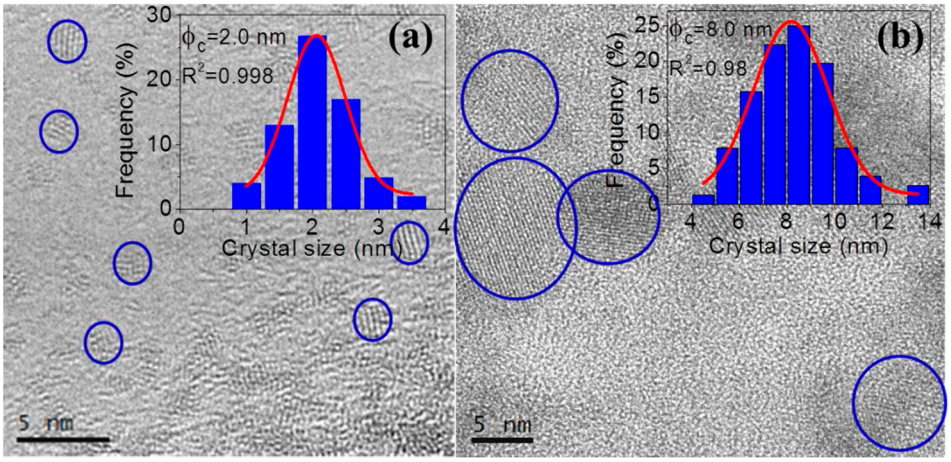


**Figure 10.** HRTEM of $80SiO_2$-$20LaF_3$ (**a**) thin film and (**b**) self-supported layer prepared using TEOS/MTES and treated at 550 °C for 1 min. The corresponding crystal size distributions are also shown.

These results are further confirmed by FTIR spectra of $80SiO_2$-$20LaF_3$ xerogel and GCs treated at 550 °C for 1 min and 1 h, as shown in Figure 12 [110]. In the xerogel, the bands centered at 1680 and 1650 $cm^{-1}$ are associated with H-O-H bending and C=O stretching vibrations, respectively. In the range 1500–1400 $cm^{-1}$ several absorption bands appear and are assigned to TFA, acetates, and/or derived ions [43]. A C-F stretching band is also identified between 1400 and 1000 $cm^{-1}$. All of these bands disappear in the GC sample, accompanied by $LaF_3$ NCs' precipitation. In the GC the bands in the range 1100–800 $cm^{-1}$ are associated with Si-O-Si asymmetric and symmetric stretching vibrations of [$SiO_4$] units. A small band at 1279 $cm^{-1}$, also present in the xerogel sample but much more intense, is assigned to C-O vibration and due to incompletely removed organic compounds. Such a band disappears over longer treatment times at 550 °C.

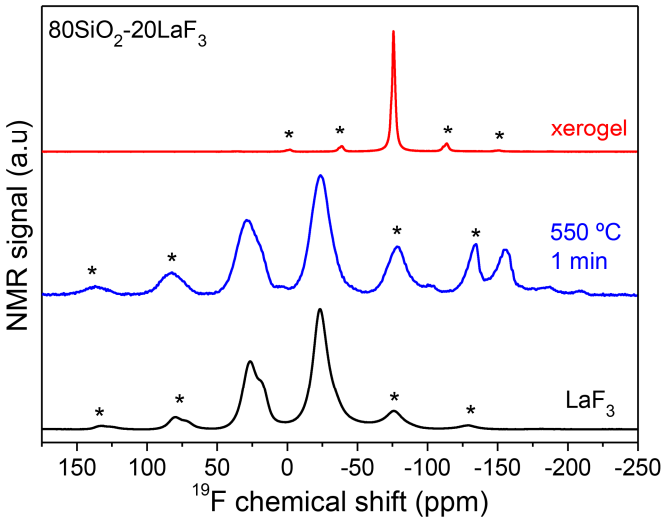


**Figure 11.** $^{19}F$ MAS-NMR spectra of $80SiO_2$-$20LaF_3$ xerogel and GC treated at 550 °C for 1 min. The spectrum of pure $LaF_3$ crystal powder is also given for comparison. Stars indicate spinning sidebands.

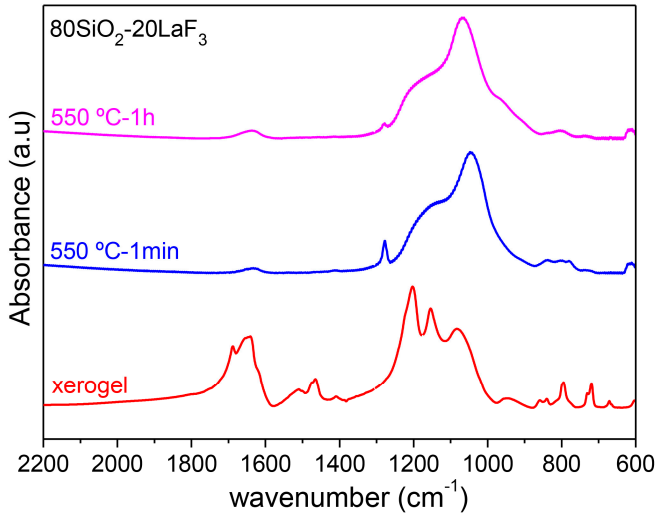


**Figure 12.** FTIR of $80SiO_2$-$20LaF_3$ xerogel and GC self-supported layer treated at 550 °C for 1 min and 1 h.

Photoluminescence (PL) measurements are of great importance in most papers about SG OxGCs; in particular, enhanced properties are obtained when dopants are embedded into the fluoride NCs with low phonon energy. As an example, low-temperature (9 K) PL emission and excitation spectra of $80SiO_2$-$20LaF_3$ xerogel and GC treated at 650 °C for 3 h and doped with 0.5 $Nd^{3+}$ are shown in Figure 13 [111]. Both the emission and excitation spectra of the xerogel show broad and less structured bands, indicating a predominant amorphous environment for $Nd^{3+}$ ions. Instead, for the GC sample sharp peaks and well-resolved Stark components are observed and associated with $Nd^{3+}$ emission in $LaF_3$ NCs. Similar features are observed for the excitation spectrum, where well-resolved peaks are observed for the $^4I_{9/2} \rightarrow {}^4F_{5/2}$ band; moreover, the $^4I_{9/2} \rightarrow {}^4F_{3/2}$ doublet narrows and splits into two main single components, as expected for a well-defined crystal field site. Therefore, $Nd^{3+}$ incorporation into $LaF_3$ NCs was unambiguously confirmed.

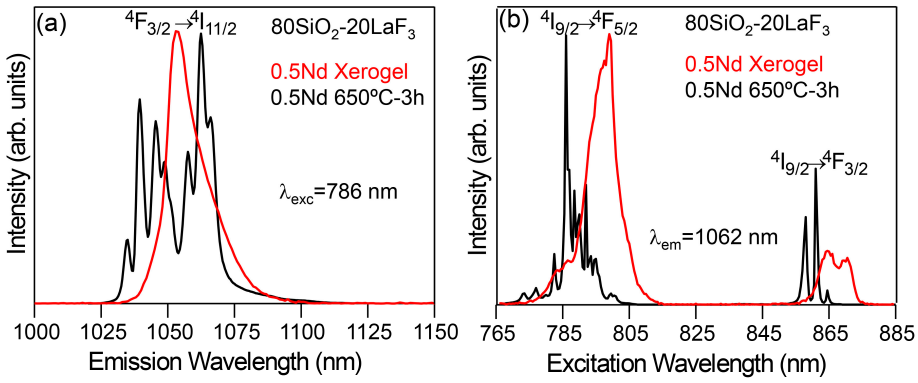


**Figure 13.** PL (**a**) emission and (**b**) excitation spectra of $80SiO_2$-$20LaF_3$ bulk xerogel and GC treated at 650 °C for 3 h. All spectra were recorded at 9 K.

### 3.2.2. $SiO_2$–$GdF_3$/$NaGdF_4$

Figure 14 shows DTA curves of the $90SiO_2$-$10NaGdF_4$ bulk-like sample. The weight loss between 70 and 200 °C, of less than 10%, is ascribed to solvent removal. Then, as usually occurs for SG oxyfluoride compositions, a strong and sharp exothermic peak appears around 300 °C along with a mass loss of 30%. Such an exothermic peak is associated with chemical decomposition with $NaGdF_4$ precipitation, similar to that described by other authors for other fluoride crystal phases [43,57,82]. Further weight loss for heat treatment in the range 400–600 °C can be associated with the combustion of organic compounds. The same sample measured in an argon atmosphere showed similar characteristics; therefore, the exothermic peak is associated with $NaGdF_4$ crystallization. Similar features are obtained for $SiO_2$-$GdF_3$ composition and described elsewhere [112].

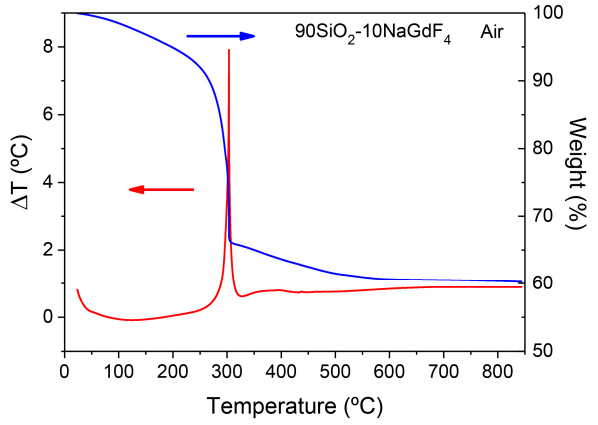


**Figure 14.** DTA (red) and TG (blue) curve of $90SiO_2$-$10NaGdF_4$ bulk sample acquired in air using a heating rate of 10 °C/min.

Diffractograms of (100 − x)$SiO_2$-x$GdF_3$ (x = 10 and 20 mol %) treated at 550 °C for 1 min are shown in Figure 15. As observed, both phases of $GdF_3$, orthorhombic and hexagonal, appear even for such fast heat treatment. It was shown that from $LaF_3$ to $EuF_3$, the hexagonal phase is preferred, while elements heavier than Gd are organized in orthorhombic structures [113]. Considering that Gd is right in the middle of a lanthanide series, it seems reasonable that a mixture of both phases appear. The relative intensity of hexagonal and orthorhombic structures is quite similar for all heat treatments, thus suggesting that there is no one preferential crystal structure but that both configurations coexist. Crystal size is around 8 and 9 nm for hexagonal and orthorhombic phases, respectively. Small changes in relative peak intensities can be associated with the deformation or preferential incorporation of $Eu^{3+}$ ions at certain crystallographic sites. Moreover, the fact that similar sizes are obtained for

both compositions suggests that NC formation is not related to the amount of the initial precursors, the mechanism being explained as fast crystal precipitation after a chemical reaction similar to that described by Fujihara for $LaF_3$ [43]. However, the final crystal fraction should be affected by the initial content as observed for $LaF_3$ compositions. Nevertheless, for $GdF_3$ crystallization a quite different scenario is observed with respect to $LaF_3$ crystallization, where an amorphization was observed over a long heat treatment time at 550 °C. In fact, no changes in the crystal size are observed for treatment times up to 8 h; the diffractograms of GCs treated for 1 min up to 8 h being practically the same. It seems that $GdF_3$ NCs are more stable against decomposition as opposed to $LaF_3$ ones. Further work is still necessary to clarify this point.

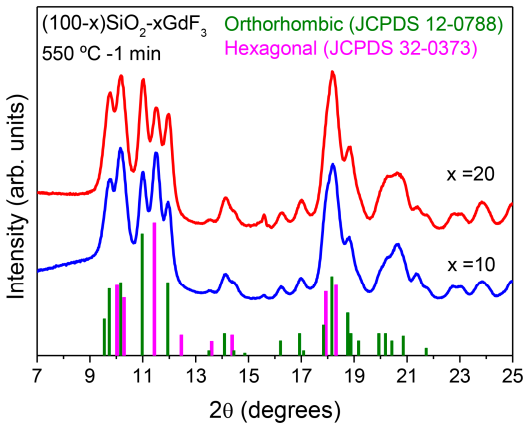


**Figure 15.** XRD of $(100 - x)SiO_2$-$xGdF_3$ (x = 10 and 20 mol %) GC treated at 550 °C for 1 min performed at the synchrotron SpLine BM25 of the ESRF.

It is also worth noting that $SiO_2$ precursors affect the final crystal phase and the crystal size. For example, for $80SiO_2$-$20GdF_3$ samples prepared using TEOS, only hexagonal crystals are detected but it was necessary to raise the temperature to 750 °C to obtain $GdF_3$ crystals. Instead, for TEOS/MTES samples, even for treatment temperature as low as 550 °C for 1 min, a good crystallization was obtained but in this case both a hexagonal and an orthorhombic phase appeared. Therefore, as was shown, the synthesis precursor and the different ratios between them can strongly affect the final crystal size, crystal fraction, and symmetry of the crystal phase. However, the influence of the $SiO_2$ precursors and the synthesis route on the crystallization tendency of the systems has not yet been totally elucidated.

XRD of $80SiO_2$-$20NaGdF_4$ are shown in Figure 16. This is the first time that $NaGdF_4$ crystals have been obtained in SG OxGCs. Diffractograms obtained for super-stoichiometric Na:Gd ratios caused the crystallization of silicates, along with $NaGdF_4$. Therefore, precise control of the Na:Gd ratio was necessary to avoid the formation of silicates during heat treatment and obtain only the precipitation of fluoride NCs. It is known that $Na^+$ acts as a network modifier, producing more open glass structures. In fact, $Na^+$ ions can break $SiO_4$ units, thus producing non-bridging oxygens with subsequent softening of the glass network. Hence, a sub-stoichiometric ratio Na:Gd 0.95:1 was necessary to ensure the complete reaction of Na with Gd, avoiding the presence of free $Na^+$ ions. As observed in Figure 16, both α and β-$NaGdF_4$ phases precipitated upon heat treatment at 600 °C for 1 h with a size of 4 and 13 nm, respectively. However, for longer heat treatments, up to 120 h, a relative decrease of the α phase, indicated by stars, is observed with respect to GC treated for only 1 h. Moreover, sharper peaks are observed after increasing the treatment time, thus indicating the formation of bigger crystals (more than 30 nm in size). Such behavior is quite different to that described for $LaF_3$, for which an increase of the treatment time increases neither the crystal size nor the crystal fraction. Therefore, it was suggested that $LaF_3$ crystals formation occurs as a fast precipitation when certain energy is given to the system, instead being a diffusion-limited process, as proposed by other authors. However, for $NaGdF_4$ OxGCs, a different crystallization mechanism occurs for polymorphous crystals;

in particular, the addition of alkaline earth elements could be responsible for the better crystallinity obtained by increasing the treatment time. In fact, the time-dependent diffusion of $Na^+$ ions could be relevant to achieve better crystallization.

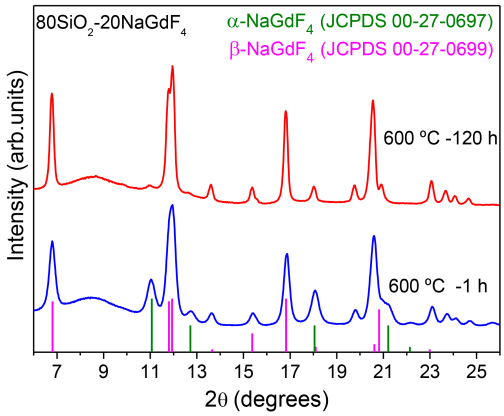


**Figure 16.** XRD of $80SiO_2$-$20NaGdF_4$ GC treated at 600 °C for 1 and 120 h. The measurements were performed at the synchrotron SpLine BM25 of the ESRF.

Bartha et al. [114] studied $NaYF_4$ phosphors and observed that for heat treatment at 300 °C, both cubic and hexagonal $NaYF_4$ micro crystals appeared. However, by increasing the treatment temperature to 400–600 °C, only a pure hexagonal $NaYF_4$ phase was observed. The authors explained such behavior as an autocatalytic process where the initial cubic $NaYF_4$ phase played a catalytic role, causing its fast self-accelerated crystallization. The energy resulting from the disintegration process of the initial $NaYF_4$ crystals contributed to the growth of hexagonal $NaYF_4$ phase. This mechanism could also explain the crystallization of $NaGdF_4$ NCs in OxGCs but further investigation has still to be done.

Figure 17 shows a micrograph of $80SiO_2$-$20GdF_3$ self-supported layer doped with 0.5 $Eu^{3+}$ treated at 550 °C for 1 min. As for $SiO_2$-$LaF_3$ GCs, homogeneously distributed NCs are observed and no agglomerates or clusters are observed, as suggested by other authors for $YF_3$ NCs [57]. By a detailed analysis of the microstructures, both hexagonal and orthorhombic crystals were detected according to JCPDS. EDXS of $Eu^{3+}$ doped $80SiO_2$-$20GdF_3$ GC treated at 550 °C for 1 min revealed that $Eu^{3+}$ ions are mostly concentrated into $GdF_3$ NCs. Therefore, dopant incorporation is very fast because even for a heat treatment as short as 1 min, most $Eu^{3+}$ ions are already embedded in the crystal phase. A better explanation of dopant incorporation is given later when the results about XAS will be discussed.

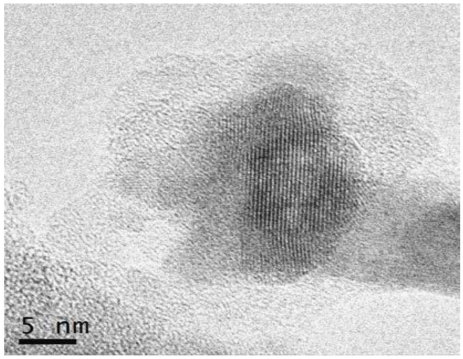


**Figure 17.** HRTEM of $80SiO_2$-$20GdF_3$ self-supported layer treated at 550 °C for 1 min.

FTIR spectra of $80SiO_2$-$20GdF_3$ xerogel and GC treated at 550 °C for 1 min are shown in Figure 18. Similar results are obtained with respect to the $80SiO_2$-$20LaF_3$ composition given in Figure 12. For the xerogel sample TFA and acetate vibration bands are still present but disappear after heat treatment

accompanied by $LaF_3$ crystallization. Similar features are obtained for $SiO_2$-$NaGdF_4$ compositions, thus indicating that a chemical reaction followed by NC precipitation is a common feature of all the studied compositions. However, differences in crystallization behavior are also observed by XRD and therefore the crystal growth can be dependent on crystal phase and synthesis conditions.

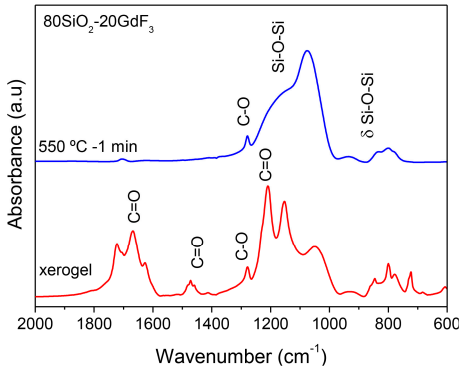


**Figure 18.** FTIR of $80SiO_2$-$20GdF_3$ xerogel and GC treated at 550 °C for 1 min.

The last results that are shown in this paper deal with XAS spectra of $80SiO_2$-$20GdF_3$ materials doped with $Eu^{3+}$. In particular, the spectra of the xerogel and GC sample are compared with the aim of gaining more insight into the $Eu^{3+}$ environment. Indeed, better optical efficiencies are obtained when dopants are embedded into the NCs and knowledge of the real dopants fraction incorporated into the NCs is crucial to improve and optimize the luminescence emission of these materials. Even though a certain nominal dopant concentration is used, the real concentration into the fluoride NCs is rarely estimated, the only results being extrapolated from optical measurements [54]. Moreover, to estimate the effective concentration into the NCs, even with 10–20% error, knowledge of the crystal fraction is necessary and such values are seldom or never reported for SG OxGCs. Last year our group started acquiring data to obtain this relevant information, but a lot of work has still to be done. However, some interesting conclusions can already be drawn from the results shown below. $Eu_2O_3$ and $EuF_3$ spectra are shown in Figure 19a, together with their derivate curves in Figure 19b. The maximum of the derivate curves is 6977.9 and 6979.5 eV, for $Eu_2O_3$ and $ErF_3$, respectively. A lower energy is associated with less electronegativity and a lower field strength of the $Ln^{3+}$ ion [115]. The uncertainty of the energy values is around 0.8 eV. Therefore, it can be confirmed that the two maxima are well separated from each other. Figure 20a,b show the results for a $80SiO_2$-$20GdF_3$ xerogel and GC samples treated at 550 °C for 1 min up to 8 h. In all cases, the absorption maximum is centered at ~6979 eV, practically the same value obtained for $EuF_3$ reference. Hence, even though by these measurements it is not possible to distinguish between a crystalline or amorphous environment, the crucial point is that a fluorine-rich environment is observed for all GCs and even for the xerogel sample. Such behavior could be explained considering that $Eu^{3+}$ ions are still coordinated to the surrounding TFA ions in the xerogel sample, and, after heat treatment, $GdF_3$ crystals precipitate together with $Eu^{3+}$ incorporation. These results are in agreement with $Eu^{3+}$-rich $GdF_3$ NCs observed by EDXS for $80SiO_2$-$20GdF_3$ GC treated at 550 °C for 1 min.

Previous calculations performed for $80SiO_2$-$20LaF_3$ samples doped with 0.5 $Er^{3+}$ showed that almost 91% of $Er^{3+}$ ions in GC samples are in a fluorine-rich environment, the effective concentration into the $LaF_3$ NCs thus being almost one order of magnitude higher than the nominal one. Similar results were obtained for MQ samples containing $LaF_3$ NCs and confirmed by PL results [116].

Finally, to conclude this section we show some optical results for $80SiO_2$-$20GdF_3$ self-supported layers doped with 0.5 $Eu^{3+}$. Photoluminescence measurements of GC treated at 550 °C for 1 min showed well-resolved structure together with a narrowing of the $Eu^{3+}$ with respect to the xerogel sample (Figure 21). Moreover, the *R* asymmetry ratio between the electric dipole transition ($^5D_0$-$^7F_2$) and the magnetic dipole transition ($^5D_0$-$^7F_1$) is reduced in GCs, thus indicating that $Eu^{3+}$ ions are

incorporated in the $GdF_3$ crystal phases. Moreover, the ET from $Gd^{3+}$ to $Eu^{3+}$ was observed in the GC sample and further supported by fluorescence decay lifetimes.

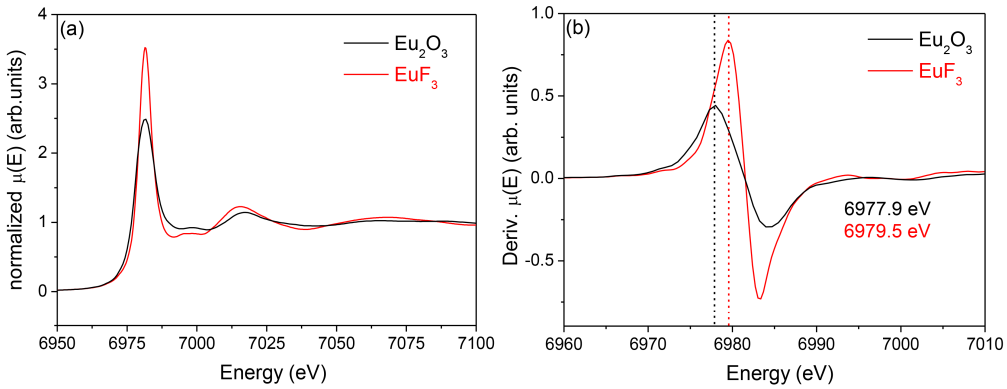


**Figure 19.** XAS (**a**) spectra and (**b**) derivate of $Eu_2O_3$ and $EuF_3$ reference samples. The values shown in (**b**) refer to the maximum of the derivate curves.

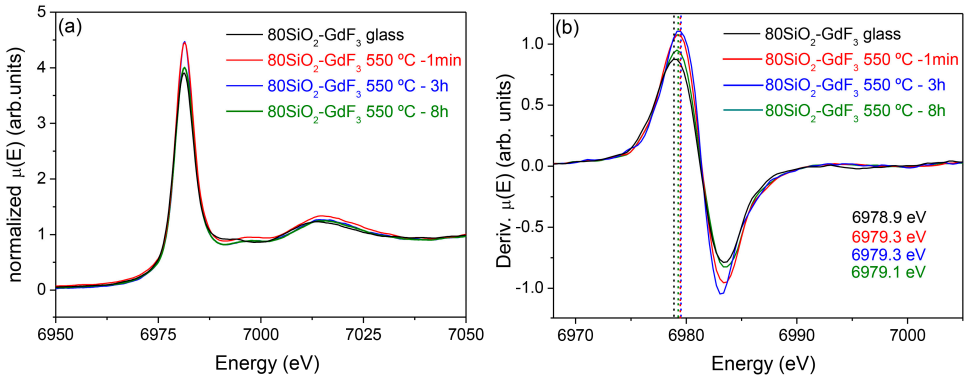


**Figure 20.** XAS (**a**) spectra and (**b**) derivate of $0.5Eu^{3+}$-doped $80SiO_2$-$20LaF_3$ xerogel and GC samples treated at 550 °C for 1 min up to 8 h. The values shown in (**b**) refer to the maximum of the derivate curves.

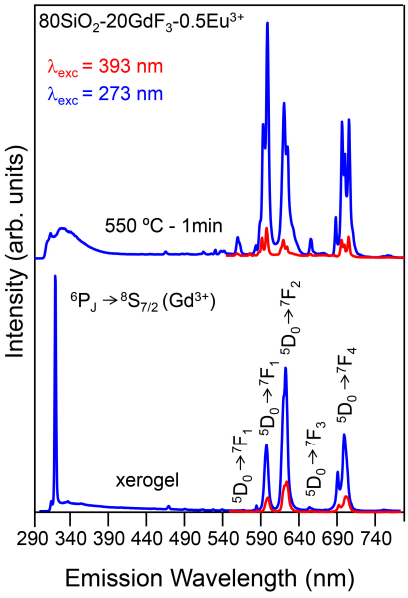


**Figure 21.** Emission spectra of $Eu^{3+}$ and $Gd^{3+}$ ions in xerogel (**bottom**) and GC (**top**) treated at 550 °C-1 min under excitation of $Eu^{3+}$ at 393 nm (red spectra) and of $Gd^{3+}$ at 273 nm (blue spectra).

## 4. Conclusions

Different research groups have studied the preparation of transparent GC materials using the MQ process and suitable control of the synthesis and heat treatment conditions. However, SG appears as a promising alternative to obtain innovative GCs with high fluorine content and high homogeneity at a lower temperature.

Most of the materials studied by SG are related with compositions $(100-x)SiO_2$-x $M_1F_2/M_1F_3/M_1M_2F_4/M_1M_2F_5$, containing a small nominal crystal fractions (x = 5–10 mol %), and are obtained using a similar synthesis procedure developed 20 years ago. Furthermore, the same $SiO_2$ precursor, TEOS or TMOS, is used in most works, and the precursor ratio rarely changes with respect to the first papers.

There is scarce information about the structural characterization of bulk and thin films; typical characterization is performed by means of XRD, HRTEM, and FTIR. However, most of the authors never calculated the real crystal fraction. Just one or two papers estimated the real active crystal content and concluded that for a nominal composition of 5 mol % of active phase, a 3 wt % of crystal phase is obtained after heat treatment. However, photoluminescence measurements of SG GCs showed very promising results. $Ln^{3+}$ incorporation in fluoride NCs was demonstrated by several authors and produced an improvement in the optical properties (linear or non-) due to the low phonon energy of the crystal hosts, thus opening the way to use SG materials for photonic applications.

On the other side, our group introduced an important modification to the SG synthesis of OxGCs. First of all, $LaF_3$- and $GdF_3$-based compositions with a much higher content of active phase (up to 40 mol %) have been prepared for the first time, together with $NaGdF_4$ OxGCs. Moreover, new precursors and deep synthesis modification were performed by partial replacement of TEOS with MTES.

A chemical reaction followed by fast crystal precipitation was indicated as responsible for the crystallization mechanism of fluoride NCs, as opposed to conventional diffusion-controlled processes. $LaF_3$ NCs were demonstrated to be unstable with aging at crystallization or higher temperatures for a long treatment time, while for $NaGdF_4$ an increase in the crystal size was observed when the treatment time increased. Therefore, the evolution and behavior of the NCs depend on the synthesis and the crystal phase.

Rietveld refinement confirmed that a crystal fraction ~18 wt % is obtained for $80SiO_2$-$20LaF_3$ GC treated at 550 °C for 1 min, such a value being the highest reported to date for SG OxGCs.

HRTEM showed that homogeneously distributed fluoride NCs precipitate in the $SiO_2$ glass matrix after fast heat treatment at 550 °C for 1 min using TEOS/MTES as $SiO_2$ precursors. Moreover, EDXS confirmed dopants' incorporation in the fluoride NCs even after fast heat treatment at 550 °C for 1 min, suggesting that dopant incorporation occurs along with NC precipitation. Such results were also confirmed by XAS measurements, revealing a fluorine-rich environment even in the xerogel sample.

Optical measurements unambiguously showed dopant incorporation in low-phonon-energy fluoride NCs. Well-resolved Stark components and crystal-like spectra were obtained for GC samples, resulting in much higher emission intensities and more efficient ET process with respect to xerogel samples.

Considering all the results published up to now and the benefits offered by the SG method, we think that transparent SG OxGCs materials can be considered of great interest and promising for several photonic applications, but improvement of synthesis and processing is still necessary. In this sense, we hope that this paper will be useful for researchers working in this field.

**Acknowledgments:** This work was supported by MINECO under projects MAT2013-48246-C2-1-P, MAT2013-48246-C2-2-P, and MAT2017-87035-C2-1-P/-2-P (AEI/FEDER, UE) and Basque Country Government IT-943-16 and PPG17/07. The authors are grateful for access to the Spanish Beamline (SpLine) at the ESRF facilities in Grenoble to perform experiments MA-3350 and 25-01-1014. Jose Joaquín Velázquez also acknowledges MINECO for Grant FPDI-2013-16895.

**Author Contributions:** G.G., J.J.V., J.M., R.B., J.F., A.D. and Y.C. conceived and designed the experiments; G.G., J.J.V., R.B. and J.F. performed the experiments; G.G., J.J.V., R.B., J.F., A.D., Y.C. analyzed the data; G.G., J.J.V., J.M., R.B. and J.F. contributed reagents/materials/analysis tools; G.G., J.J.V., J.M., R.B., J.F., A.D. and Y.C. wrote the paper.

**Conflicts of Interest:** The authors declare no conflict of interest.

## References


1. Feldmann, C.; Jüstel, T.; Ronda, C.R.; Schmidt, P.J. Inorganic luminescent materials: 100 years of research and application. *Adv. Funct. Mater.* **2003**, *13*, 511–516. [CrossRef]
2. George, N.C.; Denault, K.A.; Seshadri, R. Phosphors for solid-state white lightening. *Annu. Rev. Mater. Res.* **2013**, *43*, 481–501. [CrossRef]
3. Huang, X. Solid-state lighting: Red phosphor converts white LEDs. *Nat. Photonics* **2014**, *8*, 748–749. [CrossRef]
4. Huang, X.; Han, S.; Huang, W.; Liu, X. Enhancing solar cell efficiency: The search for luminescent materials as spectral converters. *Chem. Soc. Rev.* **2013**, *42*, 173–201. [CrossRef] [PubMed]
5. Eliseeva, S.V.; Bunzli, J.C.G. Lanthanide luminescence for functional materials and bio-sciences. *Chem. Soc. Rev.* **2010**, *39*, 189–227. [CrossRef] [PubMed]
6. Lee, H.U.; Park, S.Y.; Lee, S.C.; Choi, S.; Seo, S.; Kim, H.; Won, J.; Choi, K.; Kang, K.S.; Park, H.G.; et al. Black Phosphorus (BP) nanodots for potential biomedical applications. *Small* **2016**, *12*, 214–219. [CrossRef] [PubMed]
7. De Pablos-Martín, A.; Durán, A.; Pascual, M.J. Nanocrystallisation in oxyfluoride systems: Mechanisms of crystallisation and photonic properties. *Int. Mater. Rev.* **2012**, *57*, 165–186. [CrossRef]
8. Fedorov, P.P.; Luginina, A.A.; Popov, A.I. Transparent oxyfluoride glass ceramics. *J. Fluor. Chem.* **2015**, *172*, 22–50. [CrossRef]
9. De Pablos-Martín, A.; Ferrari, M.; Pascual, M.J.; Righini, G.C. Glass-ceramics: A class of nanostructured materials for photonics. *La Rivista del Nuovo Cimento* **2015**, *38*, 311–369. [CrossRef]
10. Wang, Y.; Ohwaki, J. New transparent vitroceramics codoped with $Er^{3+}$ and $Yb^{3+}$ for efficient frequency upconversion. *Appl. Phys. Lett.* **1993**, *63*, 3268–3270. [CrossRef]
11. Stevenson, A.J.; Serier-Brault, H.; Gredin, P.; Mortier, M. Fluoride materials for optical applications: Single crystals, ceramics, glasses, and glass–ceramics. *J. Fluor. Chem.* **2011**, *132*, 1165–1173. [CrossRef]
12. Lopez-Iscoa, P.; Salminen, T.; Hakkarainen, T.; Petit, L.; Janner, D.; Boetti, N.; Lastusaari, M.; Pugliese, D.; Paturi, P.; Milanese, D. Effect of partial crystallization on the structural and luminescence properties of $Er^{3+}$-doped phosphate glasses. *Materials* **2017**, *10*, 473. [CrossRef] [PubMed]
13. Höland, W.; Beall, G. *Glass-Ceramic Technology*, 3rd ed.; The American ceramic society: Westerville, OH, USA, 2002; pp. 15–18.
14. Augustyn, E.; Żelechower, M.; Stróż, D.; Chrapoński, J. The microstructure of erbium-ytterbium co-doped oxyfluoride glass-ceramic optical fibers. *Opt. Mater.* **2012**, *34*, 944–950. [CrossRef]
15. Reben, M.; Dorosz, D.; Wasylak, J.; Burtan-Gwizdala, B.; Jaglarz, J.; Zontek, J. $Nd^{3+}$-doped oxyfluoride glass ceramics optical fibre with $SrF_2$ nanocrystals. *Opt. Appl.* **2012**, *42*, 353–364. [CrossRef]
16. Krishnaiah, K.V.; Ledemi, Y.; Genevois, C.; Veron, E.; Sauvage, X.; Morency, S.; Soares de Lima Filho, E.; Nemova, G.; Allix, M.; Messaddeq, Y. Ytterbium-doped oxyfluoride nano-glass-ceramic fibers for laser cooling. *Opt. Mater. Express* **2017**, *7*, 1980–1994. [CrossRef]
17. Gorni, G.; Balda, R.; Fernández, J.; Ipparraguirre, I.; Velázquez, J.J.; Castro, Y.; Chen, G.; Sundararayan, M.; Pascual, M.J.; Durán, A. Oxyfluoride glass-ceramic fibers doped with $Nd^{3+}$: Structural and optical characterization. *CrystEngComm* **2017**, *19*, 6620–6629. [CrossRef]
18. Roberts, R.B.; Tainsh, R.J.; White, G.K. Thermal properties of Zerodur at low temperatures. *Cryogenics* **1982**, *22*, 566–568. [CrossRef]
19. Owens, G.J.; Singh, R.K.; Foroutan, F.; Alqaysi, M.; Han, C.M.; Mahapatra, C.; Kim, H.W.; Knowles, J.C. Sol-gel based materials for biomedical applications. *Prog. Mater. Sci.* **2016**, *77*, 1–79. [CrossRef]
20. Rywak, A.A.; Burlitch, J.M. Sol-gel synthesis of nanocrystalline magnesium fluoride: Its use in the preparation of $MgF_2$ films and $MgF_2$-$SiO_2$ composites. *Chem. Mater.* **1996**, *8*, 60–67. [CrossRef]

21. Rywak, A.A.; Burlitch, J.M. The crystal chemistry and thermal stability of sol-gel prepared fluoride-substituted talc. *Phys. Chem. Miner.* **1996**, *23*, 418–431. [CrossRef]
22. Fujihara, S.; Tada, M.; Kimura, T. Preparation and characterization of $MgF_2$ thin film by a trifluoroacetic acid method. *Thin Solid Films* **1997**, *304*, 252–255. [CrossRef]
23. Luo, W.; Wang, Y.; Bao, F.; Zhou, L.; Wang, X. Crystallization behavior of $PbF_2$-$SiO_2$ based bulk xerogels. *J. Non-Cryst. Solids* **2004**, *347*, 31–38. [CrossRef]
24. Del-Castillo, J.; Yanes, A.C.; Méndez-Ramos, J.; Tikhomirov, V.K.; Rodríguez, V.D. Structure and up-conversion luminescence in sol–gel derived $Er^{3+}$-$Yb^{3+}$ co-doped $SiO_2$:$PbF_2$ nano-glass-ceramics. *Opt. Mater.* **2009**, *32*, 104–107. [CrossRef]
25. Del-Castillo, J.; Yanes, A.C.; Méndez-Ramos, J.; Tikhomirov, V.K.; Moshchalkov, V.V.; Rodríguez, V.D. Sol-gel preparation and white up-conversion luminescence in rare-earth doped $PbF_2$ nanocrystals dissolved in silica glass. *J. Sol-Gel Sci. Technol.* **2010**, *53*, 509–514. [CrossRef]
26. Szpikowska-Sroka, B.; Zur, L.; Czoik, R.; Goryczka, T.; Swinarew, A.S.; Żadło, M.; Pisarski, W.A. Long-lived emission from $Eu^{3+}$:$PbF_2$ nanocrystals distributed into sol-gel silica glass. *J. Sol-Gel Sci. Technol.* **2013**, *68*, 278–283. [CrossRef]
27. Szpikowska-Sroka, B.; Pawlik, N.; Zur, L.; Czoik, R.; Goryczka, T.M.; Pisarski, W.A. Effect of fluoride ions on the optical properties of $Eu^{3+}$:$PbF_2$ nanocrystals embedded into sol-gel host materials. *Mater. Chem. Phys.* **2016**, *174*, 138–142. [CrossRef]
28. Szpikowska-Sroka, B.; Pawlik, N.; Goryczka, T.; Pietrasik, E.; Bańczyk, M.; Pisarski, W.A. Lead fluoride β-$PbF_2$ nanocrystals containing $Eu^{3+}$ and $Tb^{3+}$ ions embedded in sol-gel materials: Thermal, structural and optical investigations. *Ceram. Int.* **2017**, *43*, 8424–8432. [CrossRef]
29. Yu, Y.; Chen, D.; Wang, Y.; Luo, W.; Zheng, Y.; Cheng, Y.; Zhou, L. Structural evolution and its influence on luminescence of $SiO_2$-$SrF_2$-$ErF_3$ glass ceramics prepared by sol-gel method. *Mater. Chem. Phys.* **2006**, *100*, 241–245. [CrossRef]
30. Yu, Y.; Wang, Y.; Chen, D.; Liu, F. Efficient upconversion luminescence of $Er^{3+}$:$SrF_2$-$SiO_2$-$Al_2O_3$ sol-gel glass ceramics. *Ceram. Int.* **2008**, *34*, 2143–2146. [CrossRef]
31. Zhou, L.; Chen, D.; Luo, W.; Wang, Y.; Yu, Y.; Liu, F. Transparent glass ceramic containing $Er^{3+}$:$CaF_2$ nano-crystals prepared by sol-gel method. *Mater. Lett.* **2007**, *61*, 3988–3990. [CrossRef]
32. Georgescu, S.; Voiculescu, A.M.; Matei, C.; Secu, C.E.; Negre, R.F.; Secu, M. Ultraviolet and visible up-conversion luminescence of $Er^{3+}$/$Yb^{3+}$ co-doped $CaF_2$ nanocrystals in sol-gel derived glass-ceramics. *J. Lumin.* **2013**, *143*, 150–156. [CrossRef]
33. Jiang, Y.; Fan, J.; Jiang, B.; Mao, X.; Zhou, C.; Zhang, L. Structure and optical properties of transparent $Er^{3+}$-doped $CaF_2$-silica glass ceramic prepared by controllable sol-gel method. *Ceram. Int.* **2016**, *42*, 9571–9576. [CrossRef]
34. Chen, D.; Wang, Y.; Yu, Y.; Ma, E.; Zhou, L. Microstructure and luminescence of transparent glass ceramic containing $Er^{3+}$:$BaF_2$ nano-crystals. *J. Solid State Chem.* **2006**, *179*, 532–537. [CrossRef]
35. Secu, C.E.; Secu, M.; Ghica, C.; Mihut, L. Rare-earth doped sol-gel derived oxyfluoride glass-ceramics: Structural and optical characterization. *Opt. Mater.* **2011**, *33*, 1770–1774. [CrossRef]
36. Secu, C.E.; Bartha, C.; Polosan, S.; Secu, M. Thermally activated conversion of a silicate gel to an oxyfluoride glass ceramic: Optical study using $Eu^{3+}$ probe ion. *J. Lumin.* **2014**, *146*, 539–543. [CrossRef]
37. Fujihara, S.; Kitta, S.; Kimura, T. Porous Phosphor thin films of oxyfluoride $SiO_2$-$BaMgF_4$: $Eu^{2+}$ glass-ceramics prepared by sol-gel method. *Chem. Lett.* **2003**, *32*, 928–929. [CrossRef]
38. Kitta, S.; Fujihara, S.; Kimura, T. Porous $SiO_2$-$BaMgF_4$:Eu(II) glass-ceramic thin films and their strong blue photoluminescence. *J. Sol-Gel Sci. Technol.* **2004**, *32*, 263–266. [CrossRef]
39. Blasse, G.; van den Heuvel, G.P.M.; Van Dijk, T. Energy transfer from $Gd^{3+}$ to $Tb^{3+}$ and $Eu^{3+}$. *Chem. Phys. Lett.* **1979**, *62*, 600–602. [CrossRef]
40. Grzyb, T.; Runowski, M.; Lis, S. Facile synthesis, structural and spectroscopic properties of $GdF_3$:$Ce^{3+}$, $Ln^{3+}$ ($Ln^{3+}$ = $Sm^{3+}$, $Eu^{3+}$, $Tb^{3+}$, $Dy^{3+}$) nanocrystals with bright multicolor luminescence. *J. Lumin.* **2014**, *154*, 479–486. [CrossRef]
41. Pokhrel, M.; Mimun, L.C.; Yust, B.; Kumar, G.A.; Dhanale, A.; Tang, L.; Sardara, D.K. Stokes emission in $GdF_3$:$Nd^{3+}$ nanoparticles for bioimaging probes. *Nanoscale* **2014**, *6*, 1667–1674. [CrossRef] [PubMed]
42. Fujihara, S.; Tada, M.; Kimura, T. Sol-gel processing of $LaF_3$ thin films. *J. Ceram. Soc. JPN* **1998**, *106*, 124–126. [CrossRef]

43. Fujihara, S.; Tada, M.; Kimura, T. Formation of $LaF_3$ microcrystals in sol-gel silica. *J. Non-Cryst. Solids* **1999**, *244*, 267–274. [CrossRef]
44. Tada, M.; Fujihara, S.; Kimura, T. Sol-gel processing and characterization of alkaline earth and rare-earth fluoride thin films. *J. Mater. Res.* **1999**, *14*, 1610–1616. [CrossRef]
45. Fujihara, S.; Kato, T.; Kimura, T. Influence of solution composition on the formation of $SiO_2/LaF_3$ composites in the sol-gel process. *J. Mater. Sci.* **2000**, *35*, 2763–2767. [CrossRef]
46. Fujihara, S.; Tada, M.; Kimura, T. Controlling factors for the conversion of trifluoroacetate sols into thin metal fluoride coatings. *J. Sol-Gel Sci. Technol.* **2000**, *19*, 311–314. [CrossRef]
47. Fujihara, S.; Kato, T.; Kimura, T. Sol-gel synthesis of silica-based oxyfluoride glass-ceramic thin films: incorporation of $Eu^{3+}$ activators into crystallites. *J. Am. Ceram. Soc.* **2001**, *84*, 2716–2718. [CrossRef]
48. Ribeiro, S.J.L.; Araújo, C.C.; Bueno, L.A.; Gonçalves, R.R.; Messaddeq, Y. Sol-gel $Eu^{3+}/Tm^{3+}$ doped transparent glass-ceramic waveguides. *J. Non-Cryst. Solids* **2004**, *348*, 180–184. [CrossRef]
49. Biswas, A.; Maciel, G.S.; Friend, C.S.; Prasad, P.N. Upconversion properties of a transparent $Er^{3+}$-$Yb^{3+}$co-doped $LaF_3$-$SiO_2$ glass-ceramics prepared by sol-gel method. *J. Non-Cryst. Solids* **2003**, *316*, 393–397. [CrossRef]
50. Yanes, A.C.; del-Castillo, J.; Méndez-Ramos, J.; Rodríguez, V.D.; Torres, M.E.; Arbiol, J. Luminescence and structural characterization of transparent nanostructured $Eu^{3+}$-doped $LaF_3$-$SiO_2$ glass-ceramics prepared by sol-gel method. *Opt. Mater.* **2007**, *9*, 999–1003. [CrossRef]
51. Velázquez, J.J.; Yanes, A.C.; del Castillo, J.; Méndez-Ramos, J.; Rodríguez, V.D. Optical properties of $Ho^{3+}$-$Yb^{3+}$ co-doped nanostructured $SiO_2$-$LaF_3$ glass-ceramics prepared by sol-gel method. *Phys. Status Solidi A* **2007**, *204*, 1762–1768. [CrossRef]
52. Méndez-Ramos, J.; Velázquez, J.J.; Yanes, A.C.; del Castillo, J.; Rodríguez, V.D. Up-conversion in nanostructured $Yb^{3+}$-$Tm^{3+}$ co-doped sol-gel derived $SiO_2$-$LaF_3$ transparent glass-ceramics. *Phys. Status Solidi A* **2008**, *205*, 330–334. [CrossRef]
53. Yanes, A.C.; Velázquez, J.J.; del Castillo, J.; Méndez-Ramos, J.; Rodríguez, V.D. Colour tuneability and white light generation in $Yb^{3+}$-$Ho^{3+}$-$Tm^{3+}$ co-doped $SiO_2$-$LaF_3$ nano-glass-ceramics prepared by sol-gel method. *J. Sol-Gel Sci. Technol.* **2009**, *51*, 4–9. [CrossRef]
54. Velázquez, J.J.; Rodríguez, V.D.; Yanes, A.C.; del Castillo, J.; Méndez-Ramos, J. Increase in the $Tb^{3+}$ green emission in $SiO_2$-$LaF_3$ nano-glass-ceramics by codoping with $Dy^{3+}$ ions. *J. Appl. Phys.* **2010**, *108*, 113530–113536. [CrossRef]
55. Velázquez, J.J.; Rodríguez, V.D.; Yanes, A.C.; del Castillo, J.; Méndez-Ramos, J. Photon down-shifting by energy transfer from $Sm^{3+}$ to $Eu^{3+}$ ions in sol-gel $SiO_2$-$LaF_3$ nano-glass-ceramics for photovoltaics. *Appl. Phys. B* **2012**, *108*, 577–583. [CrossRef]
56. Dejneka, M.J. The luminescence and structure of novel transparent oxyfuoride glass-ceramics. *J. Non-Cryst. Solids* **1998**, *239*, 149–155. [CrossRef]
57. Luo, W.; Wang, Y.; Cheng, Y.; Bao, F.; Zhou, L. Crystallization and structural evolution of $YF_3$-$SiO_2$ xerogel. *Mater. Sci. Eng. B* **2006**, *127*, 218–223. [CrossRef]
58. Méndez-Ramos, J.; Santana-Alonso, A.; Yanes, A.C.; del Castillo, J.; Rodríguez, V.D. Rare-earth doped $YF_3$ nanocrystals embedded in sol-gel silica glass matrix for white light generation. *J. Lumin.* **2010**, *130*, 2508–2511. [CrossRef]
59. Santana-Alonso, A.; Méndez-Ramos, J.; Yanes, A.C.; del Castillo, J.; Rodríguez, V.D. White light up-conversion in transparent sol-gel derived glass-ceramics containing $Yb^{3+}$-$Er^{3+}$-$Tm^{3+}$ triply-doped $YF_3$ nanocrystals. *Mater. Chem. Phys.* **2010**, *124*, 699–703. [CrossRef]
60. Yanes, A.C.; Santana-Alonso, A.; Méndez-Ramos, J.; del Castillo, J.; Rodríguez, V.D. Novel sol-gel nano-glass-ceramics comprising $Ln^{3+}$-Doped $YF_3$ nanocrystals: structure and high efficient UV up-conversion. *Adv. Funct. Mater.* **2011**, *21*, 3136–3142. [CrossRef]
61. Chen, D.; Wang, Y.; Yu, Y.; Huang, P. Structure and optical spectroscopy of Eu-doped glass ceramics containing $GdF_3$ nanocrystals. *J. Phys. Chem. C* **2008**, *112*, 18943–18947. [CrossRef]
62. Shan, Z.; Chen, D.; Yu, Y.; Huang, P.; Lin, H.; Wang, Y. Luminescence in rare earth-doped transparent glass ceramics containing $GdF_3$ nanocrystals for lighting applications. *J. Mater. Sci.* **2010**, *45*, 2775–2779. [CrossRef]
63. Yin, W.; Zhao, L.; Zhou, L.; Gu, Z.; Liu, X.; Tian, G.; Jin, S.; Yan, L.; Ren, W.; Xing, G.; Zhao, Y. Enhanced red emission from $GdF_3$:$Yb^{3+}$, $Er^{3+}$ upconversion nanocrystals by $Li^+$ doping and their application for bioimaging. *Chem. Eur. J.* **2012**, *18*, 9239–9245. [CrossRef] [PubMed]

64. Fujihara, S.; Koji, S.; Kimura, T. Structure and optical properties of (Gd,Eu)$F_3$-nanocrystallized sol-gel silica films. *J. Mater. Chem.* **2004**, *14*, 1331–1335. [CrossRef]
65. Szpikowska-Sroka, B.; Zur, L.; Czoik, R.; Goryczka, T.; Żądło, M.; Pisarski, W.A. Ultraviolet-to-visible downconversion luminescence in solgel oxyfluoride glass ceramics containing $Eu^{3+}$:$GdF_3$ nanocrystals. *Opt. Lett.* **2014**, *39*, 3181–3184. [CrossRef] [PubMed]
66. Szpikowska-Sroka, B.; Pawlik, N.; Goryczka, T.; Pisarski, W.A. Influence of silicate sol-gel host matrices and catalyst agents on the luminescent properties of $Eu^{3+}$/$Gd^{3+}$ under different excitation wavelengths. *RSC Adv.* **2015**, *5*, 98773–98782. [CrossRef]
67. Pawlik, N.; Szpikowska-Sroka, B.; Sołtys, M.; Pisarski, W.A. Optical properties of silica sol-gel materials singly- and doubly-doped with $Eu^{3+}$and $Gd^{3+}$ ions. *J. Rare Earth* **2016**, *34*, 786–795. [CrossRef]
68. Kano, T.; Yamamoto, H.; Otomo, Y. $NaLnF_4$: $Yb^{3+}$, $Er^{3+}$ (Ln: Y, Gd, La): Efficient green-emitting infrared-excited phosphors. *J. Electrochem. Soc.* **1972**, *119*, 1561–1564. [CrossRef]
69. Krämer, K.W.; Biner, D.; Frei, G.; Güdel, H.U.; Hehlen, M.P.; Lüthi, S.R. Hexagonal sodium yttrium fluoride based green and blue emitting upconversion phosphors. *Chem. Mater.* **2004**, *16*, 1244–1251. [CrossRef]
70. Liu, F.; Ma, E.; Chen, D.; Yu, Y.; Wang, Y. Tunable red-green upconversion luminescence in novel transparent glass ceramics containing Er: $NaYF_4$ nanocrystals. *J. Phys. Chem. B* **2006**, *110*, 20843–20846. [CrossRef] [PubMed]
71. De Pablos-Martín, A.; Méndez-Ramos, J.; del Castillo, J.; Durán, A.; Rodríguez, V.D.; Pascual, M.J. Crystallization and up-conversion luminescence properties of $Er^{3+}$/$Yb^{3+}$-doped $NaYF_4$-based nano-glass-ceramics. *J. Eur. Ceram. Soc.* **2015**, *35*, 1831–1840. [CrossRef]
72. Yanes, A.C.; Santana-Alonso, A.; Méndez-Ramos, J.; del Castillo, J.; Rodríguez, V.D. $Yb^{3+}$-$Er^{3+}$ co-doped sol-gel transparent nano-glass-ceramics containing $NaYF_4$ nanocrystals for tuneable up-conversion phosphors. *J. Alloy. Compd.* **2009**, *480*, 706–710. [CrossRef]
73. Santana-Alonso, A.; Yanes, A.C.; Méndez-Ramos, J.; del Castillo, J.; Rodríguez, V.D. Sol-gel transparent nano-glass-ceramics containing $Eu^{3+}$-doped $NaYF_4$ nanocrystals. *J. Non-Cryst. Solids* **2010**, *356*, 933–936. [CrossRef]
74. Santana-Alonso, A.; Méndez-Ramos, J.; Yanes, A.C.; del Castillo, J.; Rodríguez, V.D. Up-conversion in sol-gel derived nano-glass-ceramics comprising $NaYF_4$ nano-crystals doped with $Yb^{3+}$, $Ho^{3+}$ and $Tm^{3+}$. *Opt. Mater.* **2010**, *32*, 903–908. [CrossRef]
75. Méndez-Ramos, J.; Yanes, A.C.; Santana-Alonso, A.; del Castillo, J.; Rodríguez, V.D. Colour tuneability in sol-gel nano-glass-ceramics comprising $Yb^{3+}$-$Er^{3+}$-$Tm^{3+}$ Co-Doped $NaYF_4$ nanocrystals. *J. Nanosci. Nanotechno.* **2010**, *10*, 1273–1277. [CrossRef]
76. Méndez-Ramos, J.; Yanes, A.C.; Santana-Alonso, A.; del Castillo, J. Highly efficient up-conversion and bright white light in RE co-doped $KYF_4$ nanocrystals in sol-gel silica matrix. *Chem. Phys. Lett.* **2013**, *555*, 196–201. [CrossRef]
77. Yanes, A.C.; Santana-Alonso, A.; Méndez-Ramos, J.; del Castillo, J. Structure and intense UV up-conversion emissions in $RE^{3+}$-doped sol-gel glass-ceramics containing $KYF_4$ nanocrystals. *Appl. Phys. B* **2013**, *113*, 589–596. [CrossRef]
78. Del Castillo, J.; Yanes, A.C.; Santana-Alonso, A.; Méndez-Ramos, J. Efficient dual-wavelength excitation of $Tb^{3+}$ emission in rare-earth doped $KYF_4$ cubic nanocrystals dispersed in silica sol-gel matrix. *Opt. Mater.* **2014**, *37*, 511–515. [CrossRef]
79. Yanes, A.C.; del Castillo, J. Enhanced emission via energy transfer in RE co-doped $SiO_2$-$KYF_4$ nano-glass-ceramics for white LEDs. *J. Alloy. Compd.* **2016**, *658*, 170–178. [CrossRef]
80. Deng, D.; Xu, S.; Zhao, S.; Li, C.; Wang, H.; Ju, H. Enhancement of upconversion luminescence in $Tm^{3+}$/$Er^{3+}$/$Yb^{3+}$-codoped glass ceramic containing $LiYF_4$ nanocrystals. *J. Lumin.* **2009**, *129*, 1266–1270. [CrossRef]
81. Kawamura, G.; Yoshimura, R.; Ota, K.; Oh, S.Y.; Hakiri, N.; Muto, H.; Hayakawa, T.; Matsuda, A. A unique approach to characterization of sol-gel-derived rare-earth-doped oxyfluoride glass-ceramics. *J. Am. Ceram. Soc.* **2013**, *96*, 476–480. [CrossRef]
82. Secu, C.E.; Negrea, R.F.; Secu, M. $Eu^{3+}$ probe ion for rare-earth dopant site structure in sol-gel derived $LiYF_4$ oxyfluoride glass-ceramic. *Opt. Mater.* **2013**, *35*, 2456–2460. [CrossRef]

83. Kawamura, G.; Yoshimura, R.; Ota, K.; Oh, S.Y.; Muto, H.; Hayakawa, T.; Matsuda, A. Extraction of $Nd^{3+}$-doped $LiYF_4$ phosphor from sol-gel-derived oxyfluoride glass ceramics by hydrofluoric acid treatment. *Opt. Mater.* **2013**, *45*, 1879–1881. [CrossRef]
84. Secu, M.; Secu, C.E. Up-conversion luminescence of $Er^{3+}/Yb^{3+}$ co-doped $LiYF_4$ nanocrystals in sol-gel derived oxyfluoride glass-ceramics. *J. Non-Cryst. Solids* **2015**, *426*, 78–82. [CrossRef]
85. Del Castillo, J.; Yanes, A.C.; Abe, S.; Smet, P.F. Site selective spectroscopy in $BaYF_5$:$RE^{3+}$ (RE = Eu, Sm) nano-glass-ceramics. *J. Alloy. Compd.* **2015**, *635*, 136–141. [CrossRef]
86. Del Castillo, J.; Yanes, A.C. Bright luminescence of $Gd^{3+}$ sensitized $RE^{3+}$-doped $SiO_2$-$BaGdF_5$ glass-ceramics for UV-LEDs colour conversion. *J. Alloy. Compd.* **2017**, *695*, 3736–3743. [CrossRef]
87. Chiodini, N.; Paleari, A.; DiMartino, D.; Spinolo, G. $SnO_2$ nanocrystals in $SiO_2$ : A wide-band-gap quantum-dot system. *Appl. Phys. Lett.* **2022**, *81*, 1702–1704. [CrossRef]
88. Du, J.; Zhao, R.; Xie, Y.; Li, J. Size-controlled synthesis of $SnO_2$ quantum dots and their gas-sensing performance. *Appl Surf. Sci.* **2015**, *346*, 256–262. [CrossRef]
89. Nogami, M.; Enomoto, T.; Hayakawa, T. Enhanced fluorescence of $Eu^{3+}$ induced by energy transfer from nanosized $SnO_2$ crystals in glass. *J. Lumin.* **2002**, *97*, 147–152. [CrossRef]
90. Chiodini, N.; Paleari, A.; Spinolo, G.; Crespi, P. Photorefractivity in $SiO_2$:$SnO_2$ glass-ceramics by visible light. *J. Non-Cryst. Solids* **2003**, *322*, 266–271. [CrossRef]
91. Yanes, A.C.; del Castillo, J.; Torres, M.; Peraza, J.; Rodríguez, V.D.; Méndez-Ramos, J. Nanocrystal-size selective spectroscopy in $SnO^2$: $Eu^{3+}$ semiconductor quantum dots. *Appl. Phys. Lett.* **2004**, *85*, 2343–2345. [CrossRef]
92. Del Castillo, J.; Rodríguez, V.D.; Yanes, A.C.; Méndez-Ramos, J.; Torres, M.E. Luminescent properties of transparent nanostructured $Eu^{3+}$ doped $SnO_2$–$SiO_2$ glass-ceramics prepared by the sol-gel method. *Nanotechnology* **2005**, *16*, S300–S303. [CrossRef]
93. Del Castillo, J.; Yanes, A.C.; Velázquez, J.J.; Méndez-Ramos, J.; Rodríguez, V.D. Luminescent properties of $Eu^{3+}$-$Tb^{3+}$-doped $SiO_2$-$SnO_2$-based nano-glass-ceramics prepared by sol-gel method. *J. Alloy. Compd.* **2009**, *473*, 571–575. [CrossRef]
94. Morais, E.A.; Ribeiro, S.J.L.; Scalvi, L.V.A.; Santilli, C.V.; Ruggiero, L.O.; Pulcinelli, S.H.; Messadeq, Y. Optical characteristics of $Er^{3+}$-$Yb^{3+}$ doped $SnO_2$ xerogels. *J. Alloy. Compd.* **2002**, *344*, 217–220. [CrossRef]
95. Van Tran, T.T.; Si Bui, T.; Turrell, S.; Capoen, B.; Roussel, P.; Bouazaoui, M.; Ferrari, M.; Cristini, O.; Kinowski, C. Controlled $SnO_2$ nanocrystal growth in $SiO_2$-$SnO_2$ glass-ceramic monoliths. *J. Raman Spectrosc.* **2012**, *43*, 869–875. [CrossRef]
96. Van Tran, T.T.; Turrell, S.; Capoen, B.; Le Van, H.; Ferrari, M.; Ristic, D.; Boussekey, L.; Kinowski, C. Environment segregation of $Er^{3+}$ emission in bulk sol-gel-derived $SiO_2$-$SnO_2$ glass ceramics. *J. Mater. Sci.* **2014**, *49*, 8226–8233. [CrossRef]
97. Gonçalves, R.R.; Messaddeq, Y.; Chiasera, A.; Jestin, Y.; Ferrari, M.; Ribeiro, S.J.L. Erbium-activated silica-zirconia planar waveguides prepared by sol-gel route. *Thin Solid Films* **2008**, *516*, 3094–3097. [CrossRef]
98. Gonçalves, R.R.; Guimarães, J.J.; Ferrari, J.L.; Maia, L.J.Q.; Ribeiro, S.J.L. Active planar waveguides based on sol-gel $Er^{3+}$-doped $SiO_2$-$ZrO_2$ for photonic applications: Morphological, structural and optical properties. *J. Non-Cryst. Solids* **2008**, *354*, 4846–4851. [CrossRef]
99. Suhaimi, N.F.M.; Rashid, S.N.M.; Junit, N.F.H.M.; Iznie Razakia, N.; Abd-Rahmana, M.K.; Ferrari, M. Effect of Zirconia in $Er^{3+}$-doped $SiO_2$-$ZrO_2$ for planar waveguide laser. In Proceedings of the 2012 IEEE 3rd International Conference on Photonics (ICP), Penang, Malaysia, 1–3 October 2012.
100. Dos Santos Cunha, C.; Ferrari, J.L.; de Oliveira, D.C.; Maia, L.J.Q.; Gomes, A.S.L.; Ribeiro, S.J.L.; Gonçalves, R.R. NIR luminescent $Er^{3+}/Yb^{3+}$ co-doped $SiO_2$-$ZrO_2$ nanostructured planar and channel waveguides: Optical and structural properties. *Mater. Chem. Phys.* **2012**, *136*, 120–129. [CrossRef]
101. Ribeiro, S.J.L.; Messaddeq, Y.; Gonçalves, R.R.; Ferrari, M.; Montagna, M.; Aegerter, M.A. Low optical loss planar waveguides prepared in an organic-inorganic hybrid system. *Appl. Phys. Lett.* **2000**, *77*, 3502–3504. [CrossRef]
102. Jestin, Y.; Armellini, C.; Chiappini, A.; Chiaser, A.; Ferrari, M.; Goyes, C.; Montagna, M.; Moser, E.; Nunzi Conti, G.; Pelli, S.; et al. Erbium activated $HfO_2$ based glass-ceramics waveguides for photonics. *J. Non-Cryst. Solids* **2007**, *353*, 494–497. [CrossRef]
103. Ferrari, J.L.; Lima, K.O.; Maia, L.J.Q.; Ribeiro, S.J.L.; Gonçalves, R.R. Structural and spectroscopic properties of luminescent $Er^{3+}$-Doped $SiO_2$-$Ta_2O_5$ nanocomposites. *J. Am. Ceram. Soc.* **2011**, *94*, 1230–1237. [CrossRef]

104. Aquino, F.T.; Ferrari, J.L.; Ribeiro, S.J.L.; Ferrier, A.; Goldner, P.; Gonçalves, R.R. Broadband NIR emission in novel sol-gel $Er^{3+}$-doped $SiO_2$-$Nb_2O_5$ glass ceramic planar waveguides for photonic applications. *Opt. Mater.* **2013**, *35*, 387–396. [CrossRef]
105. Secu, M.; Secu, C.E.; Bartha, C. Crystallization and luminescence properties of a new $Eu^{3+}$-doped LaOCl nano-glass-ceramic. *J. Eur. Ceram. Soc.* **2016**, *36*, 203–207. [CrossRef]
106. Innocenzi, P.; Abdirashid, M.O.; Guglielmi, M. Structure and properties of sol-gel coatings from methyltriethoxysilane and tetraethoxysilane. *J. Sol-Gel Sci. Technol.* **1994**, *3*, 47–55. [CrossRef]
107. Ravel, B.; Newville, M. ATHENA, ARTEMIS, HEPHAESTUS: Data analysis for X-ray absorption spectroscopy using IFEFFIT. *J. Synchrotron Radiat.* **2005**, *12*, 537–541. [CrossRef] [PubMed]
108. Ma, Y.; Lee, H.R.; Tsuru, T. Study on preparation and hydrophobicity of MTES derived silica sol and gel. *Adv. Mater. Res.* **2012**, *535–537*, 2563–2566. [CrossRef]
109. Jia, Y.Q. Crystal Radii and effective ionic radii of the rare earth ions. *J. Sol. State Chem.* **1991**, *95*, 184–187. [CrossRef]
110. Gorni, G.; Pascual, M.J.; Caballero, A.; Velázquez, J.J.; Mosa, J.; Castro, Y.; Durán, A. Crystallization mechanism in sol-gel oxyfluoride glass-ceramics. *J. Non-Cryst. Solids* **2018**, accepted.
111. Gorni, G.; Balda, R.; Ferández, J.; Velázquez, J.J.; Pascual, L.; Mosa, J.; Durán, A.; Castro, Y. $80SiO_2$-$20LaF_3$ oxyfluoride glass ceramic coatings doped with $Nd^{3+}$ for optical applications. *Int. J. Appl. Glass Sci.* **2017**, in press. [CrossRef]
112. Velázquez, J.J.; Mosa, J.; Gorni, G.; Balda, R.; Ferández, J.; Pascual, L.; Durán, A.; Castro, Y. Transparent $SiO_2$-$GdF_3$ sol-gel nano-glass ceramics for optical applications. *J. Sol-Gel Sci. Technol.* **2018**, under-review.
113. Chen, D.; Yu, Y.; Huang, P.; Wang, Y. Nanocrystallization of lanthanide trifluoride in an aluminosilicate glass matrix: Dimorphism and rare earth partition. *CrystEngComm* **2009**, *11*, 1686–1690. [CrossRef]
114. Bartha, C.; Secu, C.E.; Matei, E.; Secu, M. Crystallization kinetics mechanism investigation of sol-gel-derived $NaYF_4$:(Yb,Er) up-converting phosphors. *CrystEngComm* **2017**, *19*, 4992–5000. [CrossRef]
115. Agarwal, B.K.; Verma, L.P. A rule for chemical shifts of X-ray absorption edges. *J. Phys. C Solid State* **1970**, *3*, 535–537. [CrossRef]
116. Gorni, G.; Velázquez, J.J.; Mather, G.C.; Durán, A.; Chen, G.; Sundararaja, M.; Balda, R.; Ferández, J.; Pascual, M.J. Selective excitation in transparent oxyfluoride glass-ceramics doped with $Nd^{3+}$. *J. Eur. Ceram. Soc.* **2017**, *37*, 1695–1706. [CrossRef]


# *PAPER 2*

**Transparent oxyfluoride nano-glass ceramics doped with $Pr^{3+}$ and $Pr^{3+}$-$Yb^{3+}$ for NIR emission.**

G. Gorni, A. Cosci, S. Pelli, L. Pascual, A. Durán, M.J. Pascual.

*Front. Mater*. 3:58. doi: 10.3389/fmats.2016.00058. Published en: W. Höland, J. Deubener, eds. (2017). Nucleation and Crystallization of Glasses and Glass-Ceramics. Lausanne: Frontiers Media. doi: 10.3389/978-2-88945-224-8

frontiers in Materials

ORIGINAL RESEARCH
published: 03 January 2017
doi: 10.3389/fmats.2016.00058

# Transparent Oxyfluoride Nano-Glass Ceramics Doped with $Pr^{3+}$ and $Pr^{3+}$–$Yb^{3+}$ for NIR Emission

*Giulio Gorni[1], Alessandro Cosci[2,3], Stefano Pelli[2,3], Laura Pascual[4], Alicia Durán[1] and M. J. Pascual[1]**

[1] Instituto de Cerámica y Vidrio, Consejo Superior de Investigaciones Científicas (CSIC), Madrid, Spain, [2] Microdevices for Photonics Laboratory (MIP-LAB), Istituto di Fisica Applicata "Nello Carrara", Consiglio Nazionale delle Ricerche (CNR), Sesto Fiorentino, Italy, [3] Museo Storico della Fisica e Centro Studi e Ricerche Enrico Fermi, Roma, Italy, [4] Instituto de Catálisis y Petroleoquímica, Consejo Superior de Investigaciones Científicas (CSIC), Madrid, Spain

$Pr^{3+}$–$Yb^{3+}$ co-doped oxyfluoride glasses and glass-ceramics (GCs) containing $LaF_3$ nanocrystals have been prepared to obtain NIR emission of $Yb^{3+}$ ions upon $Pr^{3+}$ excitation in the blue region of the visible spectrum. Two different compositions have been tested: 0.1–0.5 Pr–Yb and 0.5–1 Pr–Yb, in addition to $Pr^{3+}$ singly doped samples. The crystallization mechanism of the nano-GCs was studied by differential thermal analysis revealing that it occurs from a constant number of nuclei, the crystal growth being limited by diffusion. High-resolution transmission microscopy demonstrated that phase separation acts as precursor for $LaF_3$ crystallization and a detailed analysis of the chemical composition (EDXS) revealed the enrichment in $RE^{3+}$ ions inside the initial phase separated droplets, from which the $LaF_3$ crystals are formed. The $RE^{3+}$ ions incorporation inside $LaF_3$ crystals was also proved by photoluminescence measurements showing Stark splitting of the $RE^{3+}$ ions energy levels in the glass-ceramic samples. Lifetime measurements showed the existence of a better energy transfer process between $Pr^{3+}$ and $Yb^{3+}$ ions in the GCs compared to the as made glass. The highest value of energy transfer efficiency is 59% and the highest theoretical quantum efficiency is 159%, obtained for GCs 0.1–0.5 Pr–Yb treated at 620°C for 40 h.

**Keywords: transparent, glass-ceramics, rare-earths, crystallization, down-conversion, solar energy**

OPEN ACCESS

***Edited by:***
*Joachim Deubener, Clausthal University of Technology, Germany*

***Reviewed by:***
*Paul M. Voyles, University of Wisconsin-Madison, USA*
*Chao Liu, Wuhan University of Technology, China*

****Correspondence:***
*Maria Jesús Pascual*
*mpascual@icv.csic.es*

***Specialty section:***
*This article was submitted to Glass Science, a section of the journal Frontiers in Materials*

***Received:*** *27 May 2016*
***Accepted:*** *14 December 2016*
***Published:*** *03 January 2017*

***Citation:***
*Gorni G, Cosci A, Pelli S, Pascual L, Durán A and Pascual MJ (2017) Transparent Oxyfluoride Nano-Glass Ceramics Doped with Pr3+ and Pr3+–Yb3+ for NIR Emission. Front. Mater. 3:58. doi: 10.3389/fmats.2016.00058*

## INTRODUCTION

Solar green energy is one of the emerging fields where rare earth (RE) ions are intensively used to improve silicon solar cells (SSCs) efficiency. In fact, the most important routes to reduce costs and promote the use of solar energy are: decrease refining and crystallization cost of silicon (the most widely used semiconductor), to use less silicon (thinner cells), developing thin films solar cells of less expensive materials (organic, polymeric) and/or improving SSCs efficiency.

Currently, many efforts are focused in the modification of the photovoltaic (PV) cells to make them more efficient. The main problem to improve PV energy conversion efficiency is associated with the spectral mismatch between the energy distribution of photons in the incident solar spectrum and the band-gap of silicon (Huang et al., 2013). Therefore, in the last years, solar down-converter materials doped with RE ions, able to convert the blue part of the solar spectrum to the range 980–1050 nm,

where silicon presents the best response, are becoming increasingly important (Trupe et al., 2002; Richards, 2006; van der Ende et al., 2009).

According to Abrams et al. (2011), a theoretical improvement of SSCs could be as high as 7% for an ideal lossless system; however, improvements (even though smaller than 7%) could be reached with a properly engineered solar converter layer.

Among the converter materials, glasses and glass-ceramics (GCs) for PV application are increasingly important thanks to their relatively easy production and engineering and their capability of hosting a great variety of RE ions in different concentrations.

Oxyfluoride nano-GCs containing luminescent RE ions have been extensively studied for their good mechanical and optical properties. Oxyfluoride nano-GCs are very attractive host materials, because they combine the very low phonon energy of fluoride nano-crystals environment, especially $LaF_3$ (<450 $cm^{-1}$). They are able to host $Ln^{3+}$ ions giving rise to high quantum efficiencies, with the high chemical and mechanical stability of a silicate glass matrix (de Pablos-Martín et al., 2012).

This paper describes the structural and optical properties of $LaF_3$ containing GCs doped with $Pr^{3+}$ and $Pr^{3+}$–$Yb^{3+}$ of composition $55SiO_2$–$20Al_2O_3$–$15Na_2O$–$10LaF_3$ (mol%) produced by melting-quenching (MQ). The properties of the un-doped glass system have been extensively studied elsewhere (Bhattacharyya et al., 2009; Hemono et al., 2009; de Pablos-Martín et al., 2011).

There are many published examples of different glass systems and crystalline phases studied for solar application with $Pr^{3+}$–$Yb^{3+}$. Indeed, we have chosen doping concentrations also relying on literature.

Chen et al. (2008) studied β-$YF_3$ containing GCs doped with 0.1 $Pr^{3+}$ and 0.1–1.5 $Yb^{3+}$ (mol %), obtaining the highest $Yb^{3+}$ emission for 1.0 $Yb^{3+}$ while for 1.5 $Yb^{3+}$ a quenching effect was observed. The corresponding energy transfer efficiency (ETE) and quantum efficiency (QE) were 90 and 190%, respectively.

Lakshminarayana and Qiu (2009) studied Pr–Yb down-conversion (DC) in oxyfluoride germanate glasses made by MQ and doped with 0.5 $Pr^{3+}$ and 2–30 $Yb^{3+}$ (mol %). The highest DC signal at 980 nm was measured for the 0.5 $Pr^{3+}$–4 $Yb^{3+}$ but the 0.5 $Pr^{3+}$–2 $Yb^{3+}$ produced almost as good results. $Pr^{3+}$ lifetimes at 608 nm were 9.5 and 4.9 μs and the ETE 35 and 66% for 2 and 4$Yb^{3+}$, respectively.

Chen et al. (2012) and Zhou et al. (2012) characterized oxyfluoride GCs containing $CaF_2$ nanocrystals. Chen et al. (2012) prepared materials with composition $45SiO_2$–$25Al_2O_3$–$10Na_2O$–$20CaF_2$–$0.1PrF_3$–$y YbF_3$ ($y = 0.1$–$1.0$) (mol%). The NIR emission suffered quenching for 1 $Yb^{3+}$ and the most intense signal was obtained for 0.5$Yb^{3+}$. The decay curve of $Pr^{3+}$:$^3P_0$–$^3H_6$ at 610 nm was measured and the lifetime for 0.5 $Yb^{3+}$ was 78 μs, and the ETE and QE were 53 and 153%, respectively. Zhou et al. (2012) studied the compositions $60SiO_2$–$20Al_2O_3$–$20CaF_2$:$0.4Pr^{3+}/x Yb^{3+}$ ($x = 0$, 1, 2, and 4) (mol%). For $Yb^{3+}$ concentrations higher than 1 mol% a quenching of $Yb^{3+}$ emission at 980 nm was measured and for 1 $Yb^{3+}$ the QE was 158%. The authors also tested a c-Si solar cell covered by the doped samples and measured a decrease compared with that covered by a host glass. Their conclusion was that a more efficient solar cell could be obtained by a proper ion doping concentration, an optimized sample thickness and the introduction of an antireflection film on the interface air-glass interface as well as the introduction of a waveguide structure on the DC layer to reduce emission losses.

Katayama studied the DC process of Pr–Yb in oxyfluoride glasses (Katayama and Tanabe, 2010a,b) and in $SrF_2$ GCs [Katayama and Tanabe, 2010a,b (p. 2); Katayama and Tanabe, 2013] with variable $Yb^{3+}$ concentration: 0.1 $Pr^{3+}$–$x Yb^{3+}$ ($x = 0$–2.9) obtaining the best DC emission for the highest $Yb^{3+}$ concentration. The ETE from the $Pr^{3+}$:$^3P_0$ to $Yb^{3+}$:$^2F_{5/2}$ increases from 42% for the glass to 75% for GCs, and the main ET process is a two-step process with $Yb^{3+}$ and $Pr^{3+}$ emission at 980 and 1300 nm, respectively. $Pr^{3+}$ emission at 1300 nm was more quenched, due to phonons, than in $SrF_2$-containing GCs.

Gao and Wondraczek (2013) obtained DC in boro-aluminosilicate glasses and $LaBO_3$ GCs doped with 1 $Pr^{3+}$–$x Yb^{3+}$ ($x = 0.1$–5). The best DC signal at 980 nm was obtained for 0.5 $Yb^{3+}$, the signal being quenched for higher concentrations, and the maximum value of the QE, obtained for 5 $Yb^{3+}$, was 183%.

Among all the studied materials there are a few examples regarding $LaF_3$-containing GCs doped with RE for DC produced by MQ, from which we point out the work of Xu et al. (2011) dealing with oxyfluoride GCs doped with $Pr^{3+}$–$Yb^{3+}$ of composition $40SiO_2$–$30Al_2O_3$–$18Na_2O$–$12LaF_3$ (mol%). However, in the work of Xu, the most relevant conclusions are as follows: (1) $Pr^{3+}$ ions are preferentially incorporated inside $LaF_3$ crystals, as shown by the increase of $Pr^{3+}$ emission at 600 nm in GCs compared to glass and (2) on the contrary $Yb^{3+}$ ions are not hosted inside $LaF_3$; therefore, the precipitation of $LaF_3$ crystals cannot improve the ET between $Pr^{3+}$ and $Yb^{3+}$.

Another study of $LaF_3$ crystals for DC emission is due to Deng et al. (2011) who studied crystalline powders of $LaF_3$ doped with $Pr^{3+}$–$Yb^{3+}$ prepared by co-precipitation method using $La^{3+}$, $Pr^{3+}$, and $Yb^{3+}$ as nitrates and $NH_4HF_2$ as fluorine source. For a fixed $Pr^{3+}$ concentration of 0.5 mol% several $Yb^{3+}$ concentrations were tested. With the increase of $Yb^{3+}$ concentration the visible emission from $Pr^{3+}$ weakens monotonically, while the NIR emission of $Yb^{3+}$ intensifies. However, a decrease of the $Yb^{3+}$ emission occurs for concentrations higher than 3%.

Xiang et al. (2014) studied $Pr^{3+}$–$Yb^{3+}$ doped β-$NaLuF_4$ hexagonal nanoplates with a size of 250 nm × 110 nm, synthesized by a solvo-thermal process. The ET from $Pr^{3+}$ ions to $Yb^{3+}$ ions occurs only by a two-step ET process when the $Yb^{3+}$ concentration is very low; however, increasing the $Yb^{3+}$ concentration, a cooperative ET process occurs for $Yb^{3+}$ concentration as high as 20 mol%.

Furthermore, there are many publications about spectroscopic characterization of RE ions doped materials for DC, but very few papers exist where a correlation between optical properties and material processing is made.

In this paper, glasses and GCs of composition $55SiO_2$–$20Al_2O_3$–$15Na_2O$–$10LaF_3$ (mol%) doped with 0.1 $Pr^{3+}$, 0.5 $Pr^{3+}$, 0.1–0.5 $Pr^{3+}$–$Yb^{3+}$, and 0.5–1 $Pr^{3+}$–$Yb^{3+}$ have been prepared. The structural properties of the materials have been studied by differential thermal analysis (DTA), X-ray diffraction (XRD), TEM and the optical properties by UV–VIS Absorption, photoluminescence (PL), and lifetime decay. The differences of the DC properties of the samples are described and the relationship of material processing with the optical properties is given.

# MATERIALS AND METHODS

## Glass Melting and Crystallization

Oxyfluoride glasses with composition $55SiO_2$–$20Al_2O_3$–$15Na_2O$–$10LaF_3$ (mol%) (55Si–10La) have been prepared by melting reagent grade $SiO_2$ sand (Saint-Gobain, Aviles, Spain, 99.6%), $Al_2O_3$ (Panreac), $Na_2CO_3$ (Sigma-Aldrich, >99.5%), $LaF_3$ (Alfa Aesar, 99.99%). $Pr^{3+}$ and $Yb^{3+}$ were added as fluorides (Alfa Aesar, 99.99%) in 0.1–0.5 and 0.5–1 concentrations (mol%). Samples doped with only $Pr^{3+}$ were also prepared for comparison of the optical properties. A more complete description of glass preparation was given in (de Pablos-Martín et al., 2011).

$Al_2O_3$ was previously annealed at 800°C for 12 h. Batch materials were weighed to obtain 100 g of glass, mixed for 1 h to ensure a good homogenization, put in a covered Pt crucible and annealed for 2 h at 1200°C. The Pt crucible was then placed in an elevator furnace for 1.5 h at 1650°C, the molten glasses were quenched in air onto a brass mold, fused again for 30 min to improve homogeneity and quenched onto a cold (−10°C) brass mold. The glasses were annealed at 600°C for 30 min for stress relaxation.

Glass-ceramics were obtained by heat treatment at 620°C for 1, 3, 5, 20, 40, and 80 h and at 660 and 680°C for 20 h. In all the cases, a heating rate of 10°C/min was used followed by quenching in air.

Heat treatments were performed on bulk specimens (size 1–1.25 mm).

## DTA and Crystallization Mechanism

Non-isothermal crystallization kinetics was studied by DTA/TG (SDT Q600—TA Instruments). Measurements have been performed on 20–30 mg of glass with particles size between 1 and 1.25 mm to reproduce bulk conditions. DTA scans were carried out with heating rates in the range 10–60°C/min.

The glass transition temperature $T_g$, crystallization activation energy $E_a$, and Avrami parameters ($n$, $m$) were calculated from DTA measurements.

The Avrami parameter $n$ allows assessing the crystallization process and was obtained employing the Ozawa equation (Ozawa, 1970):

$$\left(\frac{d\left[\ln\left[-\ln(1-x)\right]\right]}{d(\ln q)}\right)_T = -n, \tag{1}$$

where $x$ is the partial area of the crystallization peak calculated for a fixed temperature $T$ and $q$ is the heating rate. By using the Kissinger equation (Kissinger, 1956) the crystallization activation energy $E_a$ was obtained by

$$\ln\left(\frac{q}{T_p^2}\right) = -\frac{E_a}{RT_p} + C, \tag{2}$$

where $T_p$, $R$, and $C$ are the crystallization peak temperature, the gas constant and a constant, respectively. Finally, the $m$ parameter, representing the growth dimensionality, was obtained by the Matusita equation (Matusita and Sakka, 1980):

$$\ln\left(\frac{q^n}{T_p^2}\right) = -\frac{mE_a}{RT_p} + C'. \tag{3}$$

## X-Ray Diffraction

The heat-treated samples were milled and sieved (< 63 μm) and characterized by XRD with a Bruker D8 Advance diffractometer. Diffractograms were acquired in the rage $10 \leq 2\theta \leq 70°$ with a step size of 0.02° and 1 s acquisition for each step. Crystals size, $D$, was estimated using the Scherrer equation (Eq. 4), where $\lambda$ is the wavelength (1.54056 Å—$CuK\alpha_1$), $B_m$ the full width at half maximum of the $LaF_3$ peak (111) and θ its diffraction angle. The factor 0.94 corresponds to spherical crystals. Pseudo-Voigt function has been used to fit diffraction peak parameters. The instrumental broadening $B_i$ has been also taken into account using NaF powder properly milled and sieved (<63 μm):

$$D = \frac{0.94\lambda}{\cos\theta\sqrt{B_m^2 - B_i^2}}. \tag{4}$$

Crystalline growth can be described by the following equation:

$$r = Ut^p, \tag{5}$$

where $r$ is the crystal radius, $U$ the crystal growth rate, $t$ the time, and $p$ a growth exponent. The logarithmic form of Eq. 5 is commonly used:

$$\log(r) = \log(U) + p\log(t). \tag{6}$$

## High-Resolution Transmission Microscopy (HRTEM)

TEM samples of glasses and GCs were prepared by cutting slices, plane parallel grinding, dimpling to a residual thickness of 10–15 μm, and ion-beam thinning using $Ar^+$ ions. The angle of incidence was set to 8°, the beam energy to 5 kV, current to 5 mA, and milling time to 10–14 h. HRTEM including scanning transmission microscopy-high angle annular dark field and energy dispersive X-ray spectroscopy (EDXS) were performed with a JEOL 2100 field emission gun transmission electron microscope operating at 200 kV and providing a point resolution of 0.19 nm. The microscope was equipped with an energy dispersive X-ray spectrometer (EDXS—INCA x-sight, Oxford Instruments). EDXS analysis was performed in STEM mode, with a probe size of *ca*. 1 nm. In order to determine the particle distribution, we first assumed the particles to be spheres. No high contrast was obtained when working in the Scherzer focus, the shape of the particles was not well defined and difficult to measure. Thus, slightly under-focused TEM images were used to solve this problem. HAADF-STEM images were obtained where the particle shape was more distinguishable, and it is possible to measure the average diameter of the particles. By this method, only well-defined particles were measured which still resulted in a statistically well-representative data collection.

## Optical Properties

Bulk specimens were cut from the annealed glass and heat treated to obtain glass-ceramic materials. 0.1 Pr and 0.1–0.5 Pr–Yb glasses were treated at 620°C for 20 h and 40 h, and at 660°C for 20 h. 0.5 Pr and 0.5–1 Pr–Yb glasses were treated at 620°C for 40 h and 660°C for 20 h. All the samples have been

polished and optically characterized by UV–VIS absorption and PL spectroscopy.

UV–VIS spectra (Lambda 950—Perkin Elmer) were acquired between 300–2200 nm.

A photomultiplier tube (PMT) R6872 for UV–VIS and a Peltier cooled PbS for NIR detection were used as detectors.

A lock-in (5210-Princeton Research Instrument) configuration with an InGaN led at 435 nm (Roithner) as source for $Pr^{3+}$ excitation and a fiber laser at 976 nm to excite $Yb^{3+}$ ions was used to obtain PL spectra. A 2 × 2 $mm^2$ spot was produced with a lens focusing system and the samples were excited on the side edge to reduce re-absorption processes. Emission spectra were collected by an iHR-320 (Jobin-Yvon) spectrometer equipped with two gratings: 1200 g/mm blazed at 500 nm, and 600 g/mm blazed at 1000 nm. The detection system was calibrated using an incandescence lamp with known emission spectrum. A S-20 PMT and an InGaAs PD were used for UV–VIS and IR detection, respectively. Finally, all PL spectra were properly corrected for the instrument response.

Lifetime decay curves, upon excitation at 435 nm, were acquired with a fast oscilloscope (Tektronix), and the source was modulated electronically by a controller (ITC4000-Thorlabs).

For no single exponential decay, lifetimes were calculated using the following formula:

$$\tau_{avg} = \frac{\int_0^\infty t\, I(t)dt}{\int_0^\infty I(t)dt}. \quad (7)$$

The ETE and the QE were calculated using the following equations:

$$ETE = 1 - \frac{\tau_{Pr/Yb}}{\tau_{Pr}}, \quad (8)$$

$$QE = \eta_{Pr}(1 - ETE) + 2\eta_{Yb}ETE, \quad (9)$$

where $\tau_{Pr}$ and $\tau_{Pr/Yb}$ are the $Pr^{3+}$ lifetime, corresponding to the same excited state level, in doped and co-doped samples, while $\eta_{Pr}$ and $\eta_{Yb}$ are the $Pr^{3+}$ and $Yb^{3+}$ QEs.

# RESULTS AND DISCUSSION

## DTA and Crystallization Mechanism

Differential thermal analysis curves and the variation of glass transition temperature ($T_g$), crystallization starting temperature ($T_x$), and crystallization peak temperature ($T_p$), with the heating rate are given in **Figures 1A,B** for the samples doped with 0.1–0.5 Pr–Yb.

It was not possible to estimate $T_g$, $T_x$, $T_p$ from DTA curves performed at heating rate of 10°C/min due to very small endothermic peak ($T_g$) and exothermic peak ($T_x$, $T_p$) corresponding to $LaF_3$ crystallization. For 0.5–1 Pr–Yb doped glass the first values were obtained from a heating rate of 30°C/min.

The stability parameter, defined as $\Delta T = T_p - T_g$, is 114°C for both co-doped glasses for a heating rate of 10°C/min (calculated by extrapolation from the fits). The variation of $T_x$ and $T_p$ with the heating rate is faster than that of $T_g$, as confirmed by the slope parameter α in the equation $T = \alpha q$, summarized in **Table 1**. The calculated $T_g$ for a heating rate of 10°C/min are 570°C for 0.1–0.5 Pr–Yb and 585°C for 0.5–1 Pr–Yb. Higher $T_x$ and $T_p$

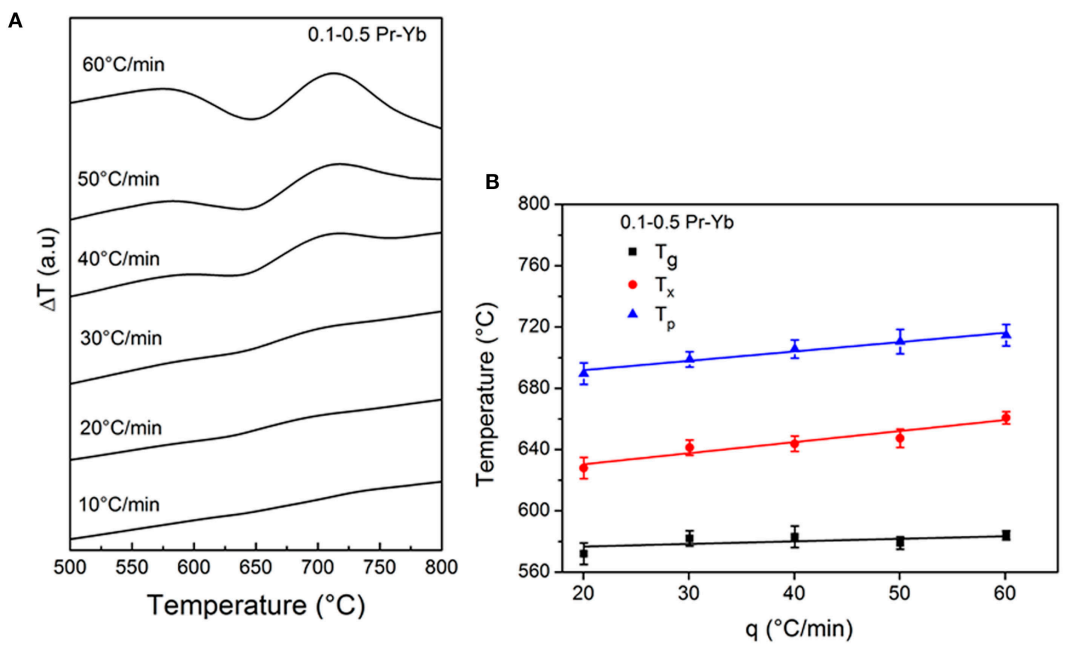


**FIGURE 1** | **(A)** Differential thermal analysis curves for 0.1–0.5 Pr–Yb glass performed at heating rates 10–60°C/min. **(B)** Variation of the glass transition temperature (square), crystallization starting temperature (circle), and $LaF_3$ crystallization peak temperature (triangle) with the heating rate.

values indicate a delay of the crystallization onset for materials with higher concentration of dopants.

By using Eq. 2, crystallization activation energies were calculated and their values are (329 ± 16) kJ/mol and (342 ± 18) kJ/mol for 0.1–0.5 Pr–Yb and 0.5–1 Pr–Yb, respectively. These results are similar to those obtained for the un-doped (de Pablos-Martín et al., 2011) and $Tm^{3+}$ doped glass (de Pablos-Martín et al., 2013), Avrami *n* parameter was calculated, using Eq. 1, from the slope of each line; a *n* mean value was obtained from the slope of the five lines represented in **Figures 2A,B** for 0.1–0.5 Pr–Yb and 0.5–1 Pr–Yb, respectively. By substituting the calculated crystallization activation energy into the Matusita equation (Eq. 3) and plotting the left side of Eq. 3 as a function of $E_a/RT_p$, the *m* parameter has been obtained from the slope of the lines represented in **Figures 2C,D**.

For 0.1–0.5 Pr–Yb, $n = 1.23 \pm 0.08$ and $m = 1.2 \pm 0.1$, while for 0.5–1 Pr–Yb $n = 0.86 \pm 0.08$ and $m = 0.84 \pm 0.08$. The two values of (*n, m*) for each composition are the same within uncertainties. The higher value obtained for the 0.1–0.5 Pr–Yb glass could be interpreted considering that the crystallization process is faster than for the 0.5–1 Pr–Yb glass. These parameters can be approximated to the nearest integer or semi-odd integer resulting in $n = 1$ and $m = 1$ for both materials. This means that the use of Kissinger equation is valid for the calculation of the crystallization activation energy and corresponds to a volumetric crystallization with crystal growth controlled by diffusion (Donald, 2004). The same (*n, m*) parameters were also obtained for the un-doped glass and for $Tm^{3+}$ doped glass (de Pablos-Martín et al., 2013), confirming that dopants do not affect the crystallization mechanism but may affect the crystallization kinetics and influence $LaF_3$ crystals size.

**TABLE 1 | Coefficients α (min) from the lines $T = \alpha$, *q* for the glass transition temperature ($T_g$), crystallization starting temperature ($T_x$), and crystallization peak temperature ($T_p$).**

| Glass | $\alpha_g$ | $\alpha_x$ | $\alpha_p$ |
|---|---|---|---|
| 55Si–10La 0.1–0.5 Pr–Yb | 0.17 ± 0.02 | 0.7 ± 0.1 | 0.61 ± 0.06 |
| 55Si–10La 0.5–1 Pr–Yb | 0.46 ± 0.07 | 0.7 ± 0.1 | 0.54 ± 0.06 |

## X-Ray Diffraction

X-ray diffraction measurements for GCs 0.1–0.5 Pr–Yb treated at 620°C for 1, 3, 5, 20, 40, and 80 h are given in **Figure 3A**, while diffractograms for heat treatment at 620, 660, and 680°C for 20 h are compared in **Figure 3B**. Very similar diffractograms have been obtained for GCs 0.5–1 Pr–Yb and are not represented.

In all the cases, $LaF_3$ was the only appearing crystalline phase confirmed by the reference (JCPDS 32-0483). All the distinguishable peaks of the diffraction pattern were labeled by Miller indexes. Crystals size was estimated using the generalized

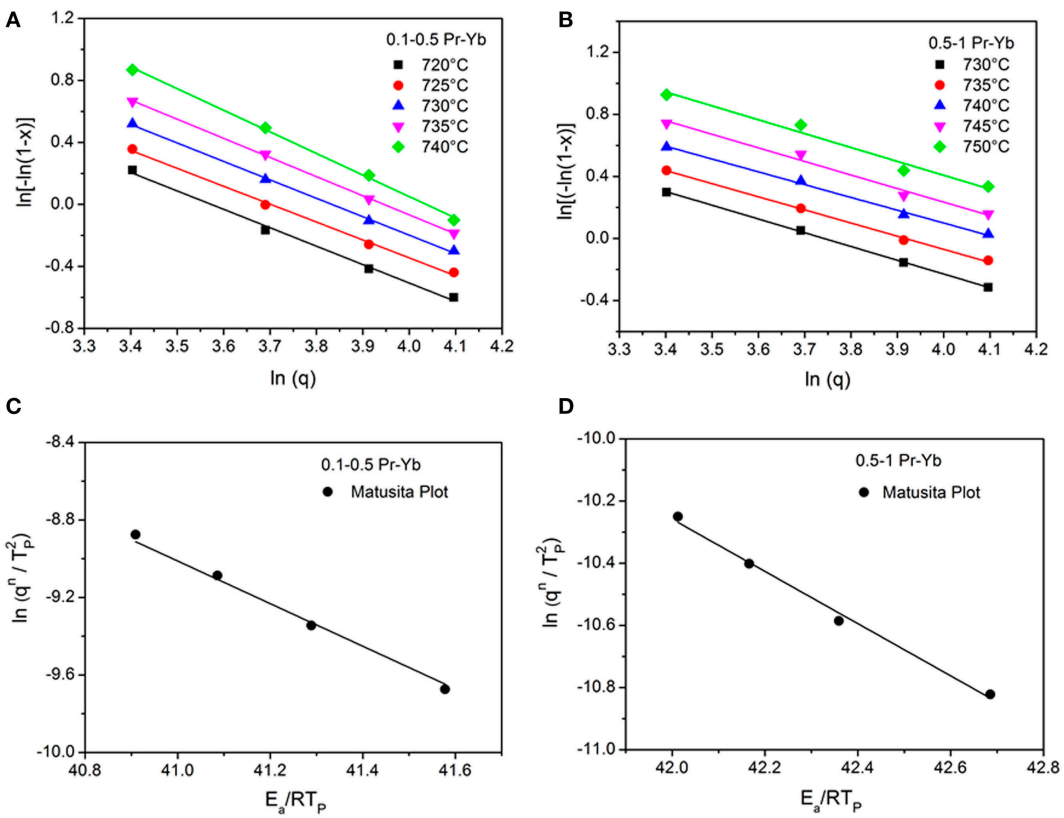


**FIGURE 2** | Ozawa plot for **(A)** 0.1–0.5 Pr–Yb and **(B)** 0.5–1 Pr–Yb doped glass. **(C)** Matusita plot for 0.1–0.5 Pr–Yb and **(D)** 0.5–1 Pr–Yb doped glass.

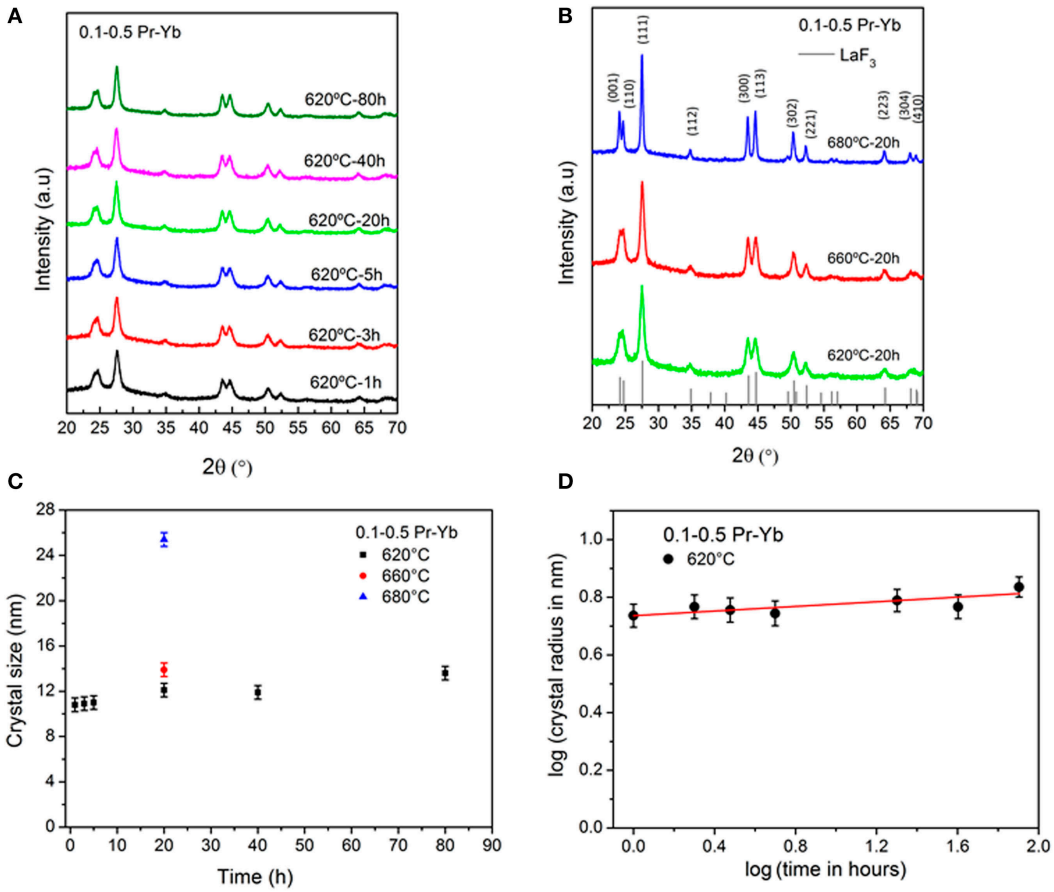


**FIGURE 3** | Diffractograms for glass-ceramics (GCs) 0.1–0.5 Pr–Yb treated at **(A)** 620°C for 1, 3, 5, 20, 40, and 80 h and at **(B)** 620, 660, and 680°C for 20 h. All diffractograms have been labeled by their Miller indices and the $LaF_3$ reference peaks are shown in the bottom. **(C)** Crystal size variation with the treatment time or temperature for GC 0.1–0.5 Pr–Yb treated at 620°C (square) during 1, 3, 5, 20, 40, 80 h, 660°C (circle) and 680°C (triangle) for 20 h. **(D)** Crystal growth *p* exponent for GCs treated at 620°C during 1, 3, 5, 20, 40, and 80 h.

Scherrer equation (Eq. 4), to take into account the instrumental broadening, applied to $LaF_3$ (111) peak ($2\theta \approx 27.5°$).

Crystal growth exponent $p$ has been estimated by Eq. 6. **Figure 3C** shows crystal size variation with treatment time, and **Figure 3D** shows the crystal growth exponent $p$ for GCs 0.1–0.5 Pr–Yb.

For GCs, 0.1–0.5 Pr–Yb crystals size at 620°C, shown in **Figure 3C**, is almost constant ≈12 nm for different treatment times, while treating the samples at different temperatures for the same time of 20 h, crystals size shows important changes. The increase of crystals size at higher temperature is indicated by the more intense diffraction peaks and by the narrowing of the peaks. At 660°C, crystals size is ≈14 nm and at 680°C ≈ 26 nm. As a consequence, for the heat treatment at 680°C, 20 h, the material partially lost its transparency due to quite bigger crystals. In fact, even though crystals are still quite small, the phase separation droplets containing several crystals inside have quite bigger sizes (as it will be shown in next section—Section "TEM"), ranging from an average value of 37 nm at 620°C up to ≈100 nm at 680°C. The GC starts to loose transparency at temperatures higher than 660°C. Moreover, temperatures higher than the glass softening temperature, ≈670°C, are not useful for practical purpose.

Glass-ceramics 0.5–1 Pr–Yb treated at 620°C, 1 h are almost amorphous and crystal size stabilizes to a constant value, around 11 nm, for treatments longer than 3 h. The onset of crystallization is delayed compared to GCs doped with 0.1–0.5 Pr–Yb, and this is associated with the higher activation energy (342 kJ/mol vs 329 kJ/mol). This is related to the nucleating effect of fluorides which promotes the production of smaller nuclei compared to what happens with lower fluoride content, according to which smaller nuclei should be favored. In fact, it is known that fluorine content in oxyfluoride glasses acts as a nucleating agent and suppresses crystal growth by increasing nuclei quantity (Chen et al., 2007; Bhattacharyya et al., 2009).

$Pr^{3+}$ singly doped samples showed very similar behavior and only $LaF_3$ crystals precipitate in the glass matrix, and the crystals size is similar to the one obtained for the co-doped samples.

The calculation of $p$ exponents was carried out using Eq. 6, starting from plots of crystals size for GCs treated at 620°C for 20 h. Data are plotted in **Figure 3D** for GCs 0.1–0.5 Pr–Yb. The crystal growth exponent at 620°C is $p = 0.040 \pm 0.005$, while for GCs 0.5–1 Pr–Yb the $p$ exponent is $p = 0.03 \pm 0.01$. The very small dependence of crystal growth on the time of heat treatment together with small values for crystal growth exponent $p$, indicates the presence of an inhibition phenomenon explained in detail in Bhattacharyya et al. (2009) and de Pablos-Martín et al. (2011, 2012). These previous studies showed that La and Si-enriched phase separation droplets are precipitated already during the preparation of the initial glass. Upon conversion of the glass into a nano-GCs by appropriate annealing, $LaF_3$ nano-crystals are formed within these droplets. Similar results have been obtained in this work as shown in Section "TEM."

## TEM

**Figure 4A** shows a TEM image of the 0.1–0.5 Pr–Yb glass. The starting glass presents phase separation with a narrow size distribution of the droplets between 15–40 nm and an average droplets size of 28 nm (**Figure 4B**). The majority of the droplets do not present any structure inside. However, in very few droplets, small crystalline domains of 5–7 nm in size have been also detected, but this incipient crystallinity in the base glass is not detectable by XRD. The chemical composition along 80 nm scanning line (**Figure 4C**) was measured by EDXS and represented in **Figure 4D**. The droplets are enriched in F, La, Pr and Yb, a clear evidence of RE incorporation inside the droplets. Furthermore, excess of Si and Al are relocated toward the periphery of the droplets, and the formation of a barrier enriched in glass formers prevent further crystal growth, during the crystallization process, due to the increase of viscosity.

**Figure 5A** shows an image of the GC 0.1–0.5 620°C, 20 h and bigger droplets, with average size ≈33 nm, were detected as compared to the untreated glass (**Figure 5B**). A feature of this glass system is the crystals formation inside the initial phase separation droplets, already enriched in crystals components in the as made glass. The size of the crystals inside each droplet is clearly observed in **Figure 5C**, and their size distribution is represented in **Figure 5D**. An average crystals size of 10 nm was obtained for this heat treatment, in agreement with the value obtained by XRD

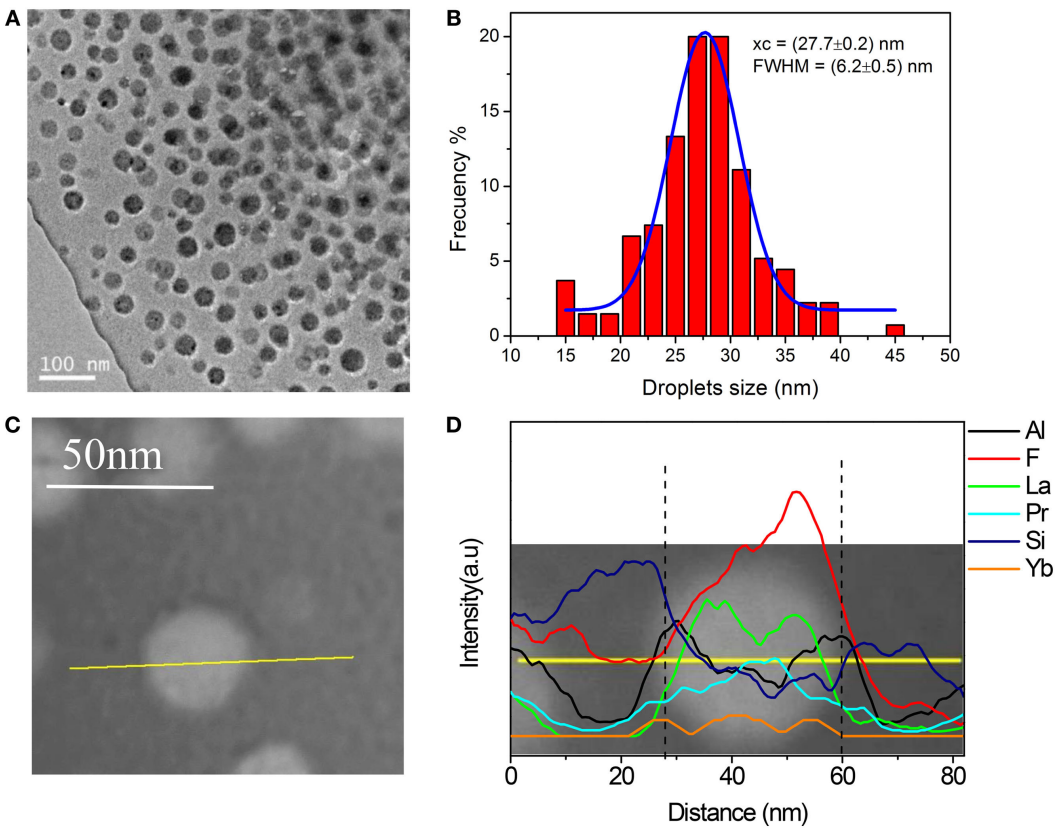


**FIGURE 4** | **(A)** TEM image of the 0.1–0.5 Pr–Yb glass showing phase separation droplets. **(B)** Droplet size distribution. **(C)** STEM image of the glass sample where the yellow line is the scanning line along which EDXS analysis was performed **(D)**.

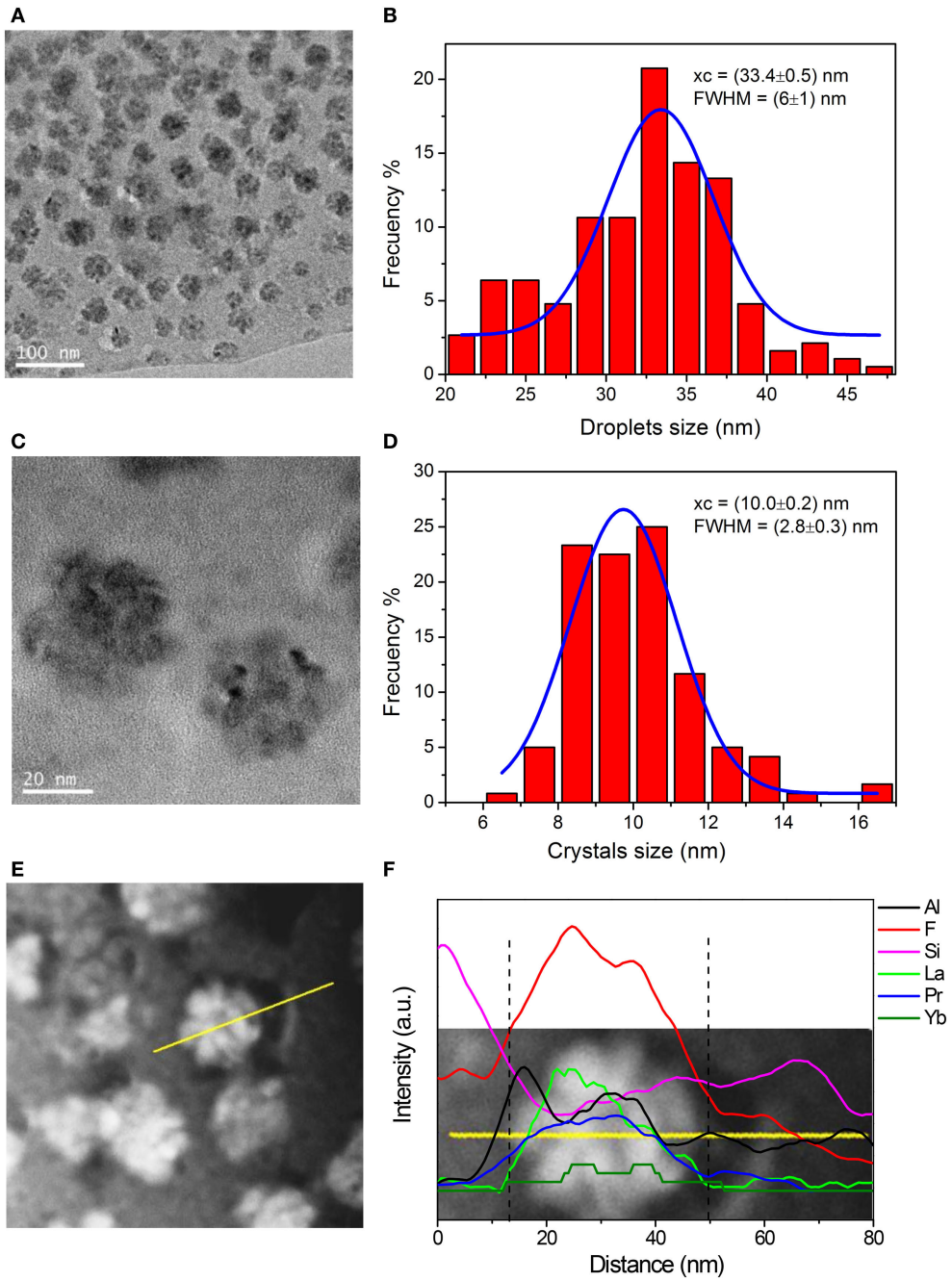


**FIGURE 5** | **(A)** TEM image of the glass-ceramic 0.1–0.5 Pr–Yb 620°C, 20 h and corresponding droplet size distribution **(B)**. **(C)** TEM image of two droplets and cystals size distribution inside the droplet **(D)**. **(E)** STEM image of the sample and EDXS analysis along the yellow line containing one droplet **(F)**.

measurements. **Figures 5E,F** show EDXS analysis of one single droplet. Al and Si are mostly confined in the interphase and tend to be smaller in correspondence of the maximum F, La, Pr, and Yb concentration, i.e., inside the droplet. Clear presence of RE ions inside the phase separation droplets and crystals is observed for glass and GCs. The detection of Yb is quite difficult, but its presence in the crystals is observed.

## Optical Properties

UV–VIS optical density for $Pr^{3+}$- and $Pr^{3+}$–$Yb^{3+}$-doped glasses and GCs are represented in **Figure 6**.

Glasses have lower absorbance compared to GCs that suffer Rayleigh scattering caused by density fluctuations due to the presence of nano-crystals inside the glass matrix. The strong UV absorption (Urbach tail) below 350 nm is due to electronic

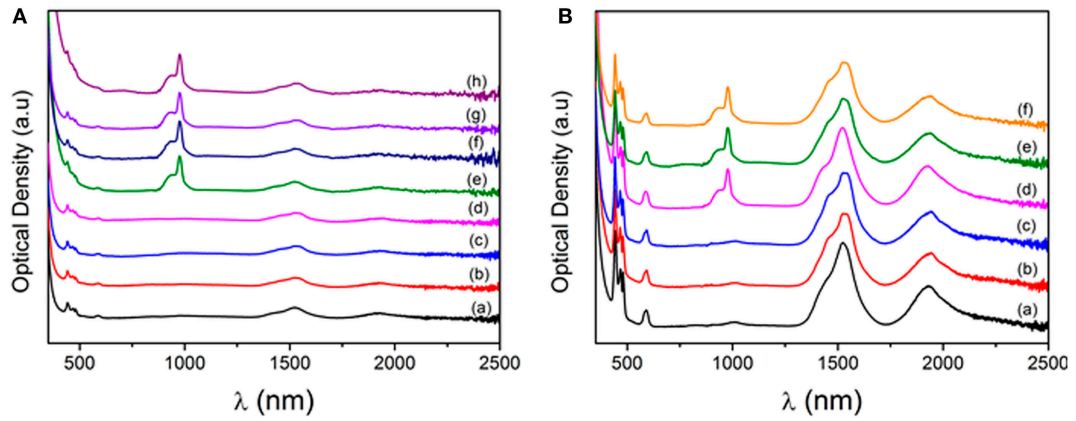


**FIGURE 6** | **(A)** Optical density for Glass 0.1 Pr (a), glass-ceramic (GC) 0.1 Pr 620°C, 20 h (b), GC 0.1 Pr 620°C, 40 h (c), GC 0.1 Pr 660°C, 20 h (d), Glass 0.1–0.5 Pr–Yb (e), GC 0.1–0.5 Pr–Yb 620°C, 20 h (f), GC 0.1–0.5 Pr–Yb 620°C, 40 h, and GC 0.1–0.5 Pr–Yb 660°C, 20 h (h). **(B)** Optical density for Glass 0.5 Pr (a), GC 0.5 Pr 620°C, 40 h (b), 0.5 Pr GC 660°C, 20 h (c), glass 0.5–1 Pr–Yb (d), GC 0.5–1 Pr–Yb 620°C, 40 h (e), and GC 0.5–1 Pr–Yb 660°C, 20 h (f).

transitions between the ligand (oxygen mainly) and the glass network former ion (silicon). In all materials the transitions between the 4f and 4f states corresponding to $Pr^{3+}$ and $Yb^{3+}$ ions are clearly visible. From the left, the following $Pr^{3+}$ transitions can be assigned: $^3H_0$–$^3P_{2,1,0}$ at 442, 466, and 480 nm, $^3H_4$–$^1D_2$ at 590 nm, $^3H_4$–$^3F_4$ at 1460 nm, $^3H_4$–$^3F_3$ at 1590, and $^3H_4$–$^3F_2$ at 1930 nm. The $Yb^{3+}$ transition $^2F_{7/2}$–$^2F_{5/2}$ is also observed at 980 nm. For 0.5 Pr and 0.5–1 Pr–Yb GCs (**Figure 6B**), a small underlying structure is observed for $Pr^{3+}$ absorption to the $^3F_3$ level, reflecting the different local field felt by $Pr^{3+}$ ions compared to glasses, a proof of $Pr^{3+}$ incorporation inside $LaF_3$ crystals that causes a narrowing of the band and the Stark components can be appreciated. However, clearer evidence of $RE^{3+}$ ions inside $LaF_3$ crystals appears in the PL spectra.

PL spectra for $Pr^{3+}$ doped and $Pr^{3+}$–$Yb^{3+}$ co-doped glasses and GCs are given in **Figure 7**. Excitation has been provided by an InGaN LED centered at 435 nm and $Pr^{3+}$ ions have been excited to the $^3P_2$ level. By non-radiative decay, the $^3P_0$ level is populated and $Pr^{3+}$ radiative emissions from this level to the three excited states $^3H_{4,5,6}$ and $^3F_{2,3,4}$ are clearly visible in the range 450–750 nm.

For samples singly doped with $Pr^{3+}$, the emission at 1.05 μm corresponding to the transition from $^1D_2$–$^3F_{3,4}$ levels is observed and the emission at 600 nm corresponding to the $^1D_2$–$^3H_4$ transition, in both doped and co-doped samples, overlaps with the $^3P_0$–$^3H_6$ emission band. The population of $^1D_2$ level is due to multi-phonon relaxation from the $^3P_0$ level, and this contribution is stronger in glass than in GCs, meaning the incorporation of $Pr^{3+}$ ions inside $LaF_3$ crystals, where phonons are much smaller.

However, in co-doped samples, the $^3P_0$ level is also quenched by the presence of $Yb^{3+}$ ions, producing a DC signal in the range 950–1150 nm, as a consequence of an ET process. The $Pr^{3+}$ transition $^1G_4$–$^3H_5$ at 1.3 μm is not observed in any samples, glass or GCs. Moreover, the $^3P_0$–$^1G_4$ transition at 950 is not osberved either.

For all samples, a more evident distinction in the $Pr^{3+}$ emission between glass and GCs is observed. Again, co-doped glasses present the lowest $Yb^{3+}$ DC signal at 976 nm while the $Pr^{3+}$ transition $^3P_0$–$^3H_6$ gets smaller passing from glass to GCs. Glass does not show sharp Stark splitting while a clear splitting of the $^3H_{5,6}$ and $^3F_4$ is visible in the GCs, a convincing proof that $Pr^{3+}$ ions are incorporated into $LaF_3$ crystals. However, $Yb^{3+}$ ions should be incorporated in $LaF_3$ crystals as well. In fact, a difference in the local environment between $Pr^{3+}$ and $Yb^{3+}$ does not seem favorable for ET processes. Additionally, DC emission gets stronger in GCs.

Xu et al. (2011) studied a 0.5–0.5 Pr–Yb doped oxyfluoride GCs containing $LaF_3$ crystals and found that the visible emission increases more than NIR emission passing from glass to GCs. Moreover, NIR emission of $Yb^{3+}$ ions did not increase monotonously with the heat treatment temperature or time. These results are in contradiction with ours. They concluded that $Yb^{3+}$ ions are not favored to be incorporated inside $LaF_3$ crystals, while we observed incorporation. TEM images (**Figure 5**), and particularly the elemental analysis with 1 nm resolution, showed an enrichment of $Yb^{3+}$ inside the droplets, while no significant $Yb^{3+}$ concentration was detected in the glass matrix.

While for 0.1–0.5 Pr–Yb doped samples the effect of the increase of temperature seems comparable to the increase of heat treatment time, for 0.5–1 Pr–Yb doped materials the increase of temperature produces the most evident improvement of $Yb^{3+}$ DC emission at 976 nm. This may be explained considering that a doping with 0.1–0.5 Pr–Yb produces a lower nuclei density, but bigger crystals are still possible by rising the annealing temperature (**Figure 3C**). In particular, bigger crystals can host more $RE^{3+}$ ions and a heat treatment at 620°C, 40 h thus produces an improvement of DC signal.

For 0.5–1 Pr–Yb, due to the quite higher fluoride content into the initial melt, the as made glass has a higher nuclei density thanks to the nucleating action of fluorine. The smaller initial

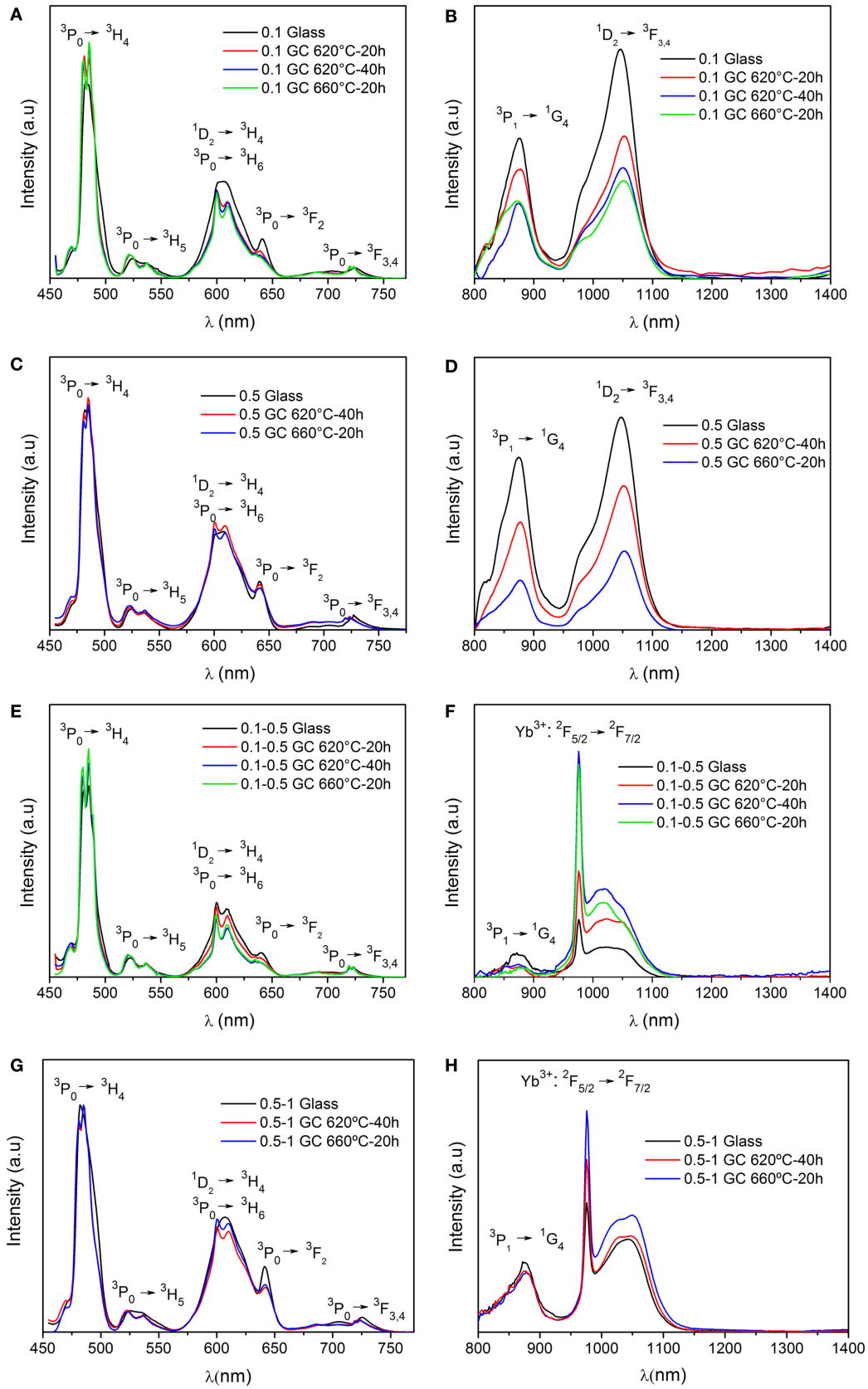


**FIGURE 7** | PL emission spectra for **(A,B)** 0.1 Pr, **(C,D)** 0.5 Pr, **(E,F)** 0.1–0.5 Pr–Yb, **(G,H)** 0.5–1 Pr–Yb doped samples. Excitation is at 435 nm.

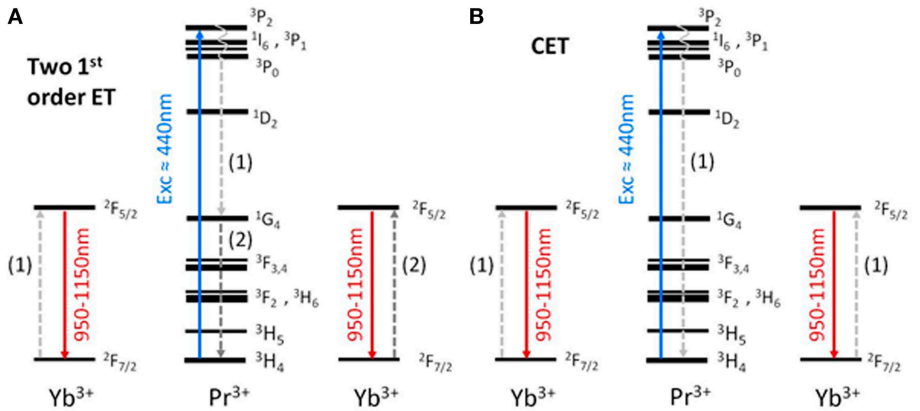


**FIGURE 8** | **(A)** Two first order energy transfer (ET) processes, the first being a cross relaxation. **(B)** Cooperative energy transfer between one $Pr^{3+}$ and two $Yb^{3+}$ ions.

nuclei make it more difficult to produce bigger crystals, due to the reduction of the effective cross-section to capture other crystal forming ions and to the presence of a diffusion barrier of higher viscosity around $LaF_3$ crystals that is formed earlier and which is expected to be thicker. In addition, in a glass doped with more $RE^{3+}$ ions, viscosity increases compared to un-doped glass (or to a less doped glass), at the temperatures of nano-glass ceramic formation ($T_g$ + 20–80°C) (de Pablos-Martín et al., 2013). As a consequence, $RE^{3+}$ ions diffusion inside crystals can require longer times, and therefore, the best improvement is obtained by rising the temperature until a decrease of viscosity starts to allow more $RE^{3+}$ ions diffusion inside the $LaF_3$ crystals but avoiding the growth of nanocrystals above 20 nm.

As suggested by van Wijngaarden et al. (2010), the cross relaxation scheme, **Figure 8A**, is the most common scheme for Pr–Yb DC. The two step ET process firstly allows $Yb^{3+}$ ions excitation to the $^2F_{5/2}$, and then $Pr^{3+}$ ions from the $^1G_4$ level transfer energy to $Yb^{3+}$ ions.

Xiang et al. (2014) found that, increasing $Yb^{3+}$ concentration to 10 mol%, cooperative energy transfer (CET) process, **Figure 8B**, becomes increasingly important and for very high concentration as 20 mol% CET process is the main ET process.

In this study, the absence of the emission at 1.3 μm ($^1G_4$–$^3H_5$) from $Pr^{3+}$ ions indicates that $^1G_4$ level is not populated or that this level is highly quenched in glass as well as in GCs. Considering that even for glass samples doped with only 0.1 mol% of $Pr^{3+}$ this emission is not observed, we are tempted to affirm that this transition hardly occurs in our samples. Furthermore, the $^3P_0$–$^1G_4$ transition at 950 nm is not observed in any sample and this is in agreement with the absence of population of the $^1G_4$ level and finally, it could be a proof of the fact that the CET from the $Pr^{3+}$ $^3P_0$ can be relevant for co-doped samples. Hence, it is possible to conclude that the ET between $Pr^{3+}$ to $Yb^{3+}$ ($^2F_{7/2}$–$^2F_{5/2}$) is improved in GCs respect to glass and CET could be quite relevant.

As suggested by Gao and Wondraczek (2013), the ET from the $^1G_4$ level of $Pr^{3+}$ to the $^2F_{5/2}$ level of $Yb^{3+}$ is rather unlikely because the $^1G_4$ level is almost 200 $cm^{-1}$ lower than the $Yb^{3+}$ $^2F_{5/2}$ level and an opposite back ET, from the $Yb^{3+}$ $^2F_{5/2}$ to the $Pr^{3+}$ $^1G_4$ level, should be favored. Considering that the ET from $^1G_4$ of $Pr^{3+}$ to the $^2F_{5/2}$ of $Yb^{3+}$ is not observed in our measurements, the back ET from $Yb^{3+}$ to $Pr^{3+}$ ions was also studied by direct excitation of $Yb^{3+}$ ions with a laser fiber at 976 nm. The corresponding PL measurements for GCs 0.1–0.5 Pr–Yb GC are given in **Figure 9**. The same results have been obtained for the GCs 0.5–1 Pr–Yb.

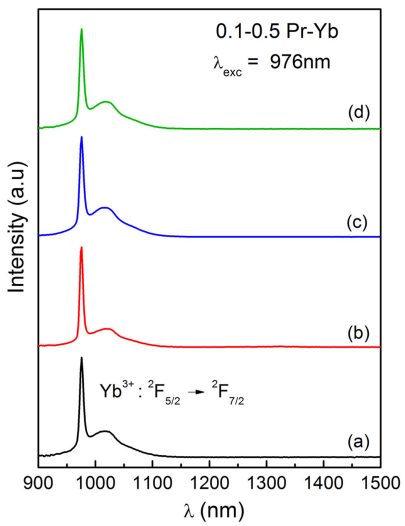


**FIGURE 9** | PL spectra upon Yb3+ direct excitation at 976 nm for the glass (a), glass-ceramics (GC) 620°C, 20 h (b), GC 620°C, 40 h (c), and GC 660°C, 20 h (d) for the 0.1–0.5 Pr–Yb composition.

As clearly observed, no $Pr^{3+}$ emission is present for direct excitation of $Yb^{3+}$ at 976 nm, meaning the absence of a back ET mechanism. Therefore, the first order ET from $^1G_4$ of $Pr^{3+}$ to $^2F_{5/2}$ of $Yb^{3+}$ is quite unlikely.

**Figure 10** shows $Pr^{3+}$ lifetime at 610 nm ($^3P_0$–$^3H_6$) for 0.1–0.5 Pr–Yb and 0.5–1 Pr–Yb co-doped samples, respectively. Lifetimes have been calculated by best fit and in all cases a bi-exponential fit has been necessary. Fast decays correspond to ET between neighbor ions while longer lifetimes give indication

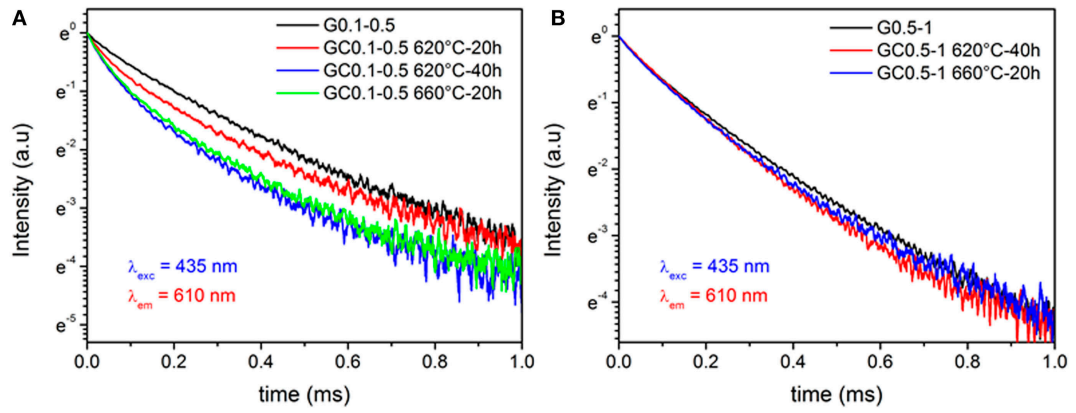


**FIGURE 10** | $Pr^{3+}$:$^3P_0$–$^3H_6$ transition lifetime at 610 nm upon 435 nm excitation, for **(A)** 0.1–0.5 Pr–Yb and **(B)** 0.5–1 Pr–Yb co-doped samples.

**TABLE 2 | $Pr^{3+}$ lifetime at 610 nm for co-doped and $Pr^{3+}$ singly doped (in parenthesis) glasses and glass-ceramics (GCs) with the corresponding energy transfer efficiency (ETE) and quantum efficiency (QE).**

| Sample | Lifetime (μs) | ETE (%) | QE (%) |
|---|---|---|---|
| G 0.1–0.5 | 240 (269) | 11 | 111 |
| GC 0.1–0.5 620°C, 20 h | 147 (271) | 46 | 146 |
| GC 0.1–0.5 620°C, 40 h | 123 (297) | 59 | 159 |
| GC 0.1–0.5 660°C, 20 h | 127 (290) | 56 | 156 |
| G 0.5–1 | 214 (235) | 9 | 109 |
| GC 0.5–1 620°C, 40 h | 165 (298) | 44 | 144 |
| GC 0.5–1 660°C, 20 h | 150 (277) | 46 | 146 |

about radiative emission lifetime, although there can be also not negligible contributions from ET over long distances (Katayama and Tanabe, 2013). Lifetime uncertainty is ≈ 5%. $Pr^{3+}$ emission in GCs has a more evident non-exponential profile. $Pr^{3+}$ decays in co-doped samples is faster than glass, and this is a further proof of a more efficient ET mechanism between $Pr^{3+}$ and $Yb^{3+}$ ions. For $Pr^{3+}$ singly doped samples, lifetime increases passing from glass to GCs and their values are summarized in **Table 2**.

ETE and QE of all co-doped samples have been calculated using Eqs 8 and 9. An estimation of the highest theoretical QE was obtained setting $\eta_{Pr}$ and $\eta_{Yb}$ in Eq. 9 equal to 1. The values are summarized in **Table 2**. ETE is quite smaller for glass than for GCs and for 0.1–0.5 Pr–Yb composition it is 11% for glass and almost 60% for GC 620°C, 40 h and the highest QE is 159%. For 0.5–1 Pr–Yb, the highest ETE value, obtained for GC 660°C, 20 h, is 46% and the highest QE is 146%. Therefore, the best results in terms of ETE and QE are obtained for the 0.1–0.5 Pr–Yb GC 620°C, 40 h, and this could be explained considering the higher ratio between $Pr^{3+}$ and $Yb^{3+}$ ions that should favor a more uniform $Yb^{3+}$ distribution around $Pr^{3+}$ increasing the probability of DC emission.

**Figure 11** shows $Yb^{3+}$ emission at 976 nm for both co-doped compositions. Near single exponential decay are observed for GCs samples, while non-radiative relaxation channels are more important for glasses. GCs lifetimes increase as compared to glasses and this is a further proof of $Yb^{3+}$ ions inside $LaF_3$ crystals. All $Yb^{3+}$ lifetimes are summarized in **Table 3**.

## CONCLUSION

Nano oxyfluoride GCs doped with 0.1 and 0.5 Pr and co-doped with 0.1–0.5 Pr–Yb and 0.5–1 Pr–Yb have been prepared with $LaF_3$ as only crystal phase. In all the cases, glasses and GCs treated at 620 and 660°C are perfectly transparent, due to the small crystal size (12–14 nm).

Crystallization kinetics showed that the crystal growth of $LaF_3$ starts from a constant number of nuclei already present in the as made glass and the process is controlled by diffusion. In particular, by increasing dopants concentration, the nuclei density increases but nuclei size gets smaller. Likewise, the increase of $T_g$ and $T_x$ for higher dopants concentrations causes a delay in the crystallization onset and limits $RE^{3+}$ ions diffusion due to higher viscosity.

Down-conversion emission of $Yb^{3+}$ was observed in the range 950–1,150 nm upon $Pr^{3+}$ excitation at 440 nm, and CET from the $^3P_0$ level of $Pr^{3+}$ could play relevant role in the ET process from $Pr^{3+}$ to $Yb^{3+}$.

$Pr^{3+}$ and $Yb^{3+}$ ions get incorporated inside $LaF_3$ crystals in GCs samples. This fact is strongly supported by the more evident Stark splitting of $Pr^{3+}$ emission spectra passing from glass to GCs, by the $Pr^{3+}$ lifetime decrease in GCs suggesting that a better ET occurs and by $Yb^{3+}$ lifetime increase in GCs indicating a decrease of non-radiative processes compared to glasses.

Glass-ceramics samples show better DC emission in the range 950–1150 nm compared to glasses and by a proper heat treatment it is possible to find the best combination to enhance $Yb^{3+}$ DC and suppress unwanted $Pr^{3+}$ emission. The highest ETE and QE were 59 and 159%, respectively, for GC 0.1–0.5 Pr–Yb 620°C, 40 h.

The results here described encourage continuing with further analysis of these materials as DC materials. In particular, different $RE^{3+}$ ions concentration combinations should be tested. The DC emission by $Yb^{3+}$ ions show the possibility of using this glass system in Photonics, even though further studies, regarding $RE^{3+}$ ions concentrations, materials thickness, etc., should be performed to optimize the best DC signal and the application of these materials.

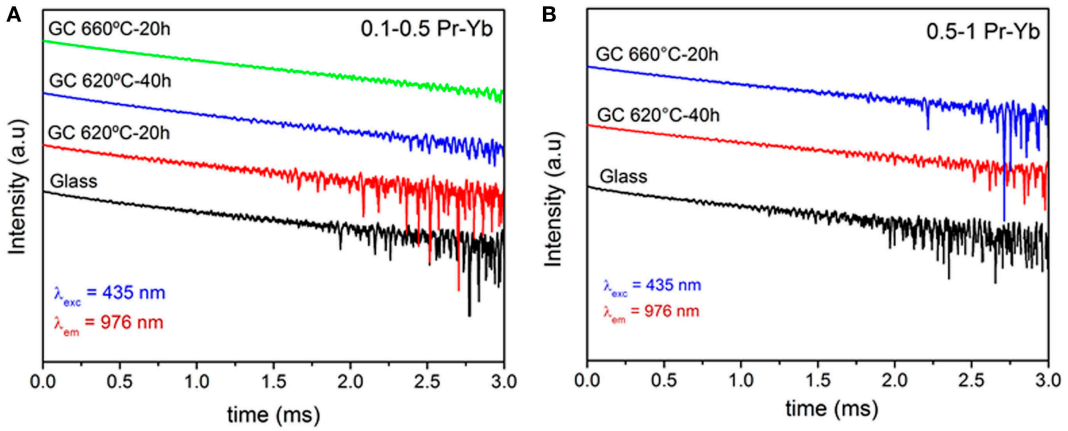


**FIGURE 11** | $Yb^{3+}$:$^2F_{5/2}$–$^2F_{7/2}$ transition lifetime at 976 nm upon 435 nm excitation, for **(A)** 0.1–0.5 Pr–Yb and **(B)** 0.5–1 Pr–Yb co-doped samples.

**TABLE 3 | $Yb^{3+}$: $^2F_{5/2}$–$^2F_{7/2}$ lifetime for all co-doped samples.**

| Sample | Lifetime (μs) |
|---|---|
| G 0.1–0.5 | 640 |
| GC 0.1–0.5 620°C, 20 h | 750 |
| GC 0.1–0.5 620°C, 40 h | 758 |
| GC 0.1–0.5 660°C, 20 h | 756 |
| G 0.5–1 | 630 |
| GC 0.5–1 620°C, 40 h | 700 |
| GC 0.5–1 660°C, 20 h | 705 |

## AUTHOR CONTRIBUTIONS

GG prepared the materials and studied their structural properties. He also measured lifetimes with SP. He contributed to the discussion of results and writing of the paper. AC contributed to the PL measurements. SP contributed to the management of the experiment and to the PL and lifetime measurements. LP performed HR-TEM characterization and analysis. AD and MP contributed to the structure and planning of the work, management of the experiments, work supervision and discussion, and writing of the paper.

## ACKNOWLEDGMENTS

The authors would like to thank Juan Vargas (technician at ICV-CSIC) for samples preparation.

## FUNDING

Financial support of the Spanish National Project MAT2013-48246-C2-1-P. GG wishes to acknowledge a grant given by the Tuscany region "Progetto Giovani Si" (Italy). AC wishes to acknowledge the financial support of the Ministero dell'Istruzione, dell'Università e della Ricerca (MIUR) through the Centro Fermi project "Premiale 2012 – Fisica e strumentazione per la salute dell'uomo."

## REFERENCES

Abrams, Z. R., Niv, A., and Zhang, X. (2011). Solar energy enhancement using down-converting particles: a rigorous approach. *J. Appl. Phys.* 109, 114905–114909. doi:10.1063/1.3592297

Bhattacharyya, S., Höche, T., Hemono, N., Pascual, M. J., and van Aken, P. A. (2009). Nano-crystallization in $LaF_3$-$Na_2O$-$Al_2O$-$SiO_2$ glass. *J. Cryst. Growth* 311, 4350–4355. doi:10.1016/j.jcrysgro.2009.07.027

Chen, D., Wang, Y., Yu, Y., Huang, P., and Weng, F. (2008). Near-infrared quantum cutting in transparent nanostructured glass-ceramics. *Opt. Lett.* 33, 1884–1886. doi:10.1364/OL.33.001884

Chen, D., Wang, Y., Yu, Y., and Ma, E. (2007). Influence of $Yb^{3+}$ content on microstructure and fluores-cence of oxyfluoride glass-ceramics containing $LaF_3$ nano-crystals. *Mater. Chem. Phys.* 101, 464–469. doi:10.1016/j.matchemphys.2006.08.005

Chen, Q. J., Zhang, W. J., Huang, X. Y., Dong, G. P., Peng, M. Y., and Zhang, Q. Y. (2012). Efficient down- and up-conversion of $Pr^{3+}$-$Yb^{3+}$ co-doped transparent oxyfluoride glass-ceramics. *J. Alloys Compd.* 513, 139–144. doi:10.1016/j.jallcom.2011.10.007

de Pablos-Martín, A., Durán, A., and Pascual, M. J. (2012). Nanocrystallisation in oxyfluoride systems: mechanisms of crystallisation and photonic properties. *Int. Mater. Rev.* 57, 165–186. doi:10.1179/1743280411Y.0000000004

de Pablos-Martín, A., Hemono, N., Mather, G. C., Bhattacharyya, S., Höche, T., Bornhöft, H., et al. (2011). Crystallization kinetics of $LaF_3$ nanocrystals in an oxyfluoride glass. *J. Am. Ceram. Soc.* 94, 2420–2428. doi:10.1111/j.1551-2916.2011.04547.x

de Pablos-Martín, A., Ristic, D., Bhattacharyya, S., Höche, T., Mather, G. C., Ramırez, M. O., et al. (2013). Effects of $Tm^{3+}$ additions on the crystallization of $LaF_3$ nanocrystals in oxyfluoride glasses: optical characterization and up-conversion. *J. Am. Ceram. Soc.* 96, 447–457. doi:10.1111/jace.12120

Deng, K., Wei, X., Wang, X., Chen, Y., and Yin, M. (2011). Near-infrared quantum cutting via resonant energy transfer from $Pr^{3+}$ to $Yb^{3+}$ in $LaF_3$. *Appl. Phys. B* 102, 555–558. doi:10.1007/s00340-011-4413-7

Donald, I. W. (2004). Crystallisation kinetics of a lithium zinc silicate glass studied by DTA and DSC. *J. Non Cryst. Solid* 345-346, 120–126. doi:10.1016/j.jnoncrysol.2004.08.007

Gao, G., and Wondraczek, L. (2013). Near-infrared down-conversion in $Pr^{3+}$/$Yb^{3+}$ co-doped boro-aluminosilicate glasses and $LaBO_3$ glass ceramics. *Opt. Mater. Express* 3, 633–644. doi:10.1364/OME.3.000633

Hemono, N., Pierre, G., Muñoz, F., de Pablos-Martín, A., Pascual, M. J., and Durán, A. (2009). Processing of transparent glass-ceramics by nano-crystallisation of $LaF_3$. *J. Eur. Ceram. Soc.* 29, 2915–2920. doi:10.1016/j.jeurceramsoc.2009.05.013

Huang, X., Han, S., Huang, W., and Liu, X. (2013). Enhancing solar cell efficiency: the search for luminescent materials as spectral converters. *Chem. Soc. Rev.* 42, 173–201. doi:10.1039/c2cs35288e

Katayama, Y., and Tanabe, S. (2010a). Near infrared down-conversion in $Pr^{3+}$–$Yb^{3+}$ codoped oxyfluoride glass ceramics. *Opt. Mater.* 33, 176–179. doi:10.1016/j.optmat.2010.07.016

Katayama, Y., and Tanabe, S. (2010b). Spectroscopy and 1 μm luminescence by visible quantum cutting in Pr3+-Yb3+ codoped glass. *Materials* 3, 2405–2411. doi:10.3390/ma3042405

Katayama, Y., and Tanabe, S. (2013). Mechanism of quantum cutting in $Pr^{3+}$–$Yb^{3+}$ codoped oxyfluoride glass ceramics. *J. Lumin.* 134, 825–829. doi:10.1016/j.jlumin.2012.06.042

Kissinger, H. E. (1956). Variation of peak temperature with heating rate in differential thermal analysis. *J. Res. Nat. Bur. Stand.* 57, 217–221. doi:10.6028/jres.057.026

Lakshminarayana, G., and Qiu, J. (2009). Near-infrared quantum cutting in $RE^{3+}/Yb^{3+}$ (RE = Pr, Tb, and Tm): $GeO_2$–$B_2O_3$–ZnO–$LaF_3$ glasses via down-conversion. *J. Alloys Compd.* 481, 582–589. doi:10.1016/j.jallcom.2009.03.034

Matusita, K., and Sakka, S. (1980). Kinetic study on crystallization of glass by differential thermal analysis – criterion on application of kissinger plot. *J. Non Cryst. Solid* 38, 741–746. doi:10.1016/0022-3093(80)90525-6

Ozawa, T. (1970). Kinetic analysis of derivative curves in thermal analysis. *J. Therm. Anal.* 2, 301–324. doi:10.1007/BF01911411

Richards, B. S. (2006). Luminescent layers for enhanced silicon solar cell performance: down-conversion. *Sol. Energy Mater. Sol. Cells* 90, 1189–1207. doi:10.1016/j.solmat.2005.07.001

Trupe, T., Green, M. A., and Wurfel, P. (2002). Improving solar cell efficiencies by down-conversion of high energy photons. *J. Appl. Phys.* 92, 1668–1674. doi:10.1063/1.1505677

van der Ende, B. M., Aarts, L., and Meijerink, A. (2009). Near-infrared quantum cutting for photovoltaics. *Adv. Mater.* 21, 3073–3077. doi:10.1002/adma.200802220

van Wijngaarden, J. T., Scheidelaar, S., Vlugt, T. J. H., Reid, M. F., and Meijerink, A. (2010). Energy transfer mechanism for down-conversion in the (Pr3+, Yb3+) Couple. *Phys. Rev. B* 81, 155112–155116. doi:10.1103/PhysRevB.81.155112

Xiang, G., Zhang, J., Hao, Z., Zhang, X., Pan, G., Luo, Y., et al. (2014). The energy transfer mechanism in $Pr^{3+}$ and $Yb^{3+}$ codoped β-$NaLuF_4$ nanocrystals. *Phys. Chem. Chem. Phys.* 16, 9289–9293. doi:10.1039/C4CP01184H

Xu, Y., Zhang, X., Dai, S., Fan, B., Ma, H., Adam, J.-L., et al. (2011). Efficient near-infrared down-conversion in Pr3+-Yb3+ codoped glasses and glass ceramics containing LaF3 nanocrystals. *J. Phys. Chem. C* 115, 13056–13062. doi:10.1021/jp201503v

Zhou, J., Tenga, Y., Ye, S., Linc, G., and Qiu, J. (2012). A discussion on spectral modification from visible to near-infrared based on energy transfer for silicon solar cells. *Opt. Mater.* 34, 901–905. doi:10.1016/j.optmat.2011.12.002

**Conflict of Interest Statement:** The authors declare that the research was conducted in the absence of any commercial or financial relationships that could be construed as a potential conflict of interest.

## *PAPER 3*

**Selective excitation in transparent oxyfluoride glass-ceramics doped with $Nd^{3+}$.**

G. Gorni, J.J. Velázquez, G.C. Mather, A. Durán, G. Chen, M. Sundararajan, R. Balda, J. Fernández, M.J. Pascual.

*J. Eur. Ceram. Soc.* **37** (2017) 1695-1706. *doi:10.1016/j.jeurceramsoc.2016.11.014*

Journal of the European Ceramic Society 37 (2017) 1695–1706

Contents lists available at www.sciencedirect.com

Journal of the European Ceramic Society

journal homepage: www.elsevier.com/locate/jeurceramsoc

Feature article

# Selective excitation in transparent oxyfluoride glass-ceramics doped with $Nd^{3+}$

G. Gorni[a], J.J. Velázquez[a], G.C. Mather[a], A. Durán[a], G. Chen[b], M. Sundararajan[b], R. Balda[c], J. Fernández[c], M.J. Pascual[a,*]

[a] Instituto de Cerámica y Vidrio (CSIC), C/Kelsen 5, 28049 Madrid, Spain
[b] Department of Physics and Astronomy, Ohio University, Athens, OH 45701, USA
[c] Applied Physic Department I, Superior School of Engineering, País Vasco University, Bilbao, Spain. Materials Physics Center CSIC-UPV/EHU, San Sebastian, Spain

ARTICLE INFO

*Article history:*
Received 27 September 2016
Received in revised form 3 November 2016
Accepted 6 November 2016
Available online 18 November 2016

*Keywords:*
Oxyfluoride
Transparent
Glass-ceramics
Neodimium
Laser emission

ABSTRACT

Transparent oxyfluoride nano-glass-ceramics have been prepared by melting-quenching and doped with five different $Nd^{3+}$ concentrations (0.1–2 mol%) to obtain the most efficient $^4F_{3/2} \rightarrow {}^4I_{11/2,13/2}$ emission. It was observed by differential thermal analysis (DTA) that the addition of $Nd^{3+}$ does not affect the crystallization mechanism which corresponds to a diffusion-controlled volumetric process that starts from a constant number of nuclei. Nevertheless, the presence of the dopant affects the kinetics due to the progressive increase of $T_g$ on increasing the $Nd^{3+}$ content. $LaF_3$ crystals with a size between 9 and 12 nm are obtained after heat treatments at $T_g$ + 20–80 °C as confirmed by X-ray diffraction (XRD) and high resolution transmission electron microscopy (HR-TEM). Energy dispersive X-ray (EDX) analysis shows the incorporation of $Nd^{3+}$ ions into the $LaF_3$ nano-crystals. Judd-Ofelt analysis from the absorption spectra further demonstrate the incorporation of $Nd^{3+}$ ions into the fluoride phase and the most relevant parameters such as radiative lifetime and stimulated emission cross-section are calculated. A detailed optical characterisation clearly shows that $Nd^{3+}$ ions in the glass-ceramics are incorporated in both crystalline and amorphous phases. Low temperature site-selective emission and excitation spectra, together with the different lifetime values of the $^4F_{3/2}$ state depending on the excitation and emission wavelengths, allow emission from $Nd^{3+}$ ions in the $LaF_3$ nanocrystals to be identified and correlated with the structural properties. As the $Nd^{3+}$ concentration is increased beyond 0.1 mol%, a stronger quenching of lifetime is observed for $Nd^{3+}$ ions residing in $LaF_3$ crystals than for those dispersed in the glass matrix. This strong concentration quenching is explained by the much higher concentration of $Nd^{3+}$ ions in the crystalline phase with respect to that in the glass matrix.



## 1. Introduction

The growing field of photonics demands the design of new rare-earth (RE)-based optical materials for their use in optical telecommunications, solid-state lasers, three-dimensional full-colour displays, solar cells, and other applications [1–5]. Oxyfluoride glass-ceramics are promising RE-hosting candidates due to their good processing and optical properties [6]. They combine the good chemical and mechanical stability of oxide-glass matrices with the excellent optical properties of low-phonon-energy fluoride nano-crystals.

Since 1993, when Wang and Ohwaki [7] obtained for the first time transparent oxyfluoride glass-ceramics containing $Pb_xCd_{1-x}F_2$ fluoride crystals doped with $Er^{3+}$ and $Yb^{3+}$ ions, the number of publications on transparent glass-ceramics has grown increasingly. Many compositions have been studied in recent years with the aim of obtaining different crystalline phases. Good review articles concerning oxyfluoride glass-ceramics have been published by A. de Pablos et al. [8] and Federov et al. [9].

* Corresponding author.
*E-mail address:* mpascual@icv.csic.es (M.J. Pascual).

http://dx.doi.org/10.1016/j.jeurceramsoc.2016.11.014
0955-2219/

A general glass system suitable for preparing glass-ceramics containing $LaF_3$ nano-crystals by the melt-quenching method is $SiO_2$-$Al_2O_3$-$Na_2O$-$LaF_3$. The percentage of $SiO_2$ generally varies between 40 and 65 mol%, with other components in the following ranges: $Al_2O_3$, 18–30 mol%; $Na_2O$, 10–20 mol%; and $LaF_3$ 10–15 mol%. A relevant parameter for assessing $LaF_3$ crystallization ability is the ratio $Na_2O/(SiO_2 + Al_2O_3)$ since La tends to compensate the electrical charge of the $[AlO_4]$ and $[SiO_4]$ tetrahedra only in oxygen bonds which are not saturated by $Na^+$ ions [10].

Many RE ions have been used to dope glass-ceramics with $LaF_3$ nano-crystals for different photonic applications. These include $Er^{3+}$ for telecommunications at 1.55 μm and for up-conversion (UC), $Pr^{3+}$ for telecommunications at 1.3 μm, $Tm^{3+}$ and $Tb^{3+}/Yb^{3+}$ for blue and green UC, $Tm^{3+}/Yb^{3+}$ for down-conversion (DC), and $Nd^{3+}$ and $Ho^{3+}/Tm^{3+}$ for infrared (IR) laser emission at 1.06 and 2 μm, respectively [11–20].

In this paper, an oxyfluoride glass with composition in mol% $55SiO_2$-$20Al_2O_3$-$154Na_2O$-$10LaF_3$ (55Si-10La) doped with several $Nd^{3+}$ concentrations (0.1–2 mol%) is investigated. The choice of this glass composition, previously developed in our research group [17,21] and [22], relies on the fact that very small $LaF_3$ crystals (~10 nm), one of the best fluoride hosts for RE ions, can precipitate in the glass matrix. As a consequence, very good transparency is still obtained upon the conversion of the glass into a glass-ceramic. Moreover, this glass system has a peculiar feature: phase separation acts as a precursor to crystallization, with several $LaF_3$ crystals tending to grow inside phase-separation droplets uniformly distributed throughout the glass matrix, thus impeding formation of clusters. In a previous work, $Tm^{3+}$-doped 55Si-10La glass-ceramics were studied by X-ray absorption near-edge structure XANES spectroscopy and extended X-ray absorption fine structure (EXAFS) spectroscopy with X-ray synchrotron radiation [23]. These techniques revealed that $Tm^{3+}$ incorporates preferentially into the $LaF_3$ nanocrystals by diffusion, the concentration of which increases with treatment time. For a thermal treatment of 10 h at 620 °C, the incorporation of $Tm^{3+}$ ions in the $LaF_3$ nanocrystals was about 17%, reaching 30% for 40 h of heat treatment.

Among the rare-earth ions, $Nd^{3+}$ has been recognized as one of the most efficient for solid-state lasers in crystals and glasses due to its intense $^4F_{3/2} \rightarrow {}^4I_{11/2}$ emission at around 1.06 μm [24]. Besides the interest of the $Nd^{3+}$ ion for infrared (IR) optical amplification, it can also be used as a probe for local ordering due to the close relation between its spectroscopic properties and the local structure and bonding at the ion site [24,25]. However, there are few works on the laser properties of $Nd^{3+}$ in transparent oxyfluoride glass-ceramics [26–36]. In some of these studies, the spectroscopic properties of $Nd^{3+}$-containing glass-ceramics differ very little from those of the precursor glasses, suggesting a more difficult incorporation of $Nd^{3+}$ ions into the crystalline phase compared to other RE ions. Pisarska et al. [28,29] did not find any difference in the fluorescence lifetime of the $^4F_{3/2}$ state in a heat-treated sample of an oxyfluoroborate glass, concluding that $Nd^{3+}$ ions are not incorporated in the crystalline phase. Yu et al. [19] studied $Nd^{3+}$-doped (0.5–3 mol%) glass-ceramics where $LaF_3$ precipitates with a crystal size between 10 and 15 nm. It was found that the most promising composition was that containing 0.5 mol% $Nd^{3+}$, in which glass-ceramics are more efficient than glasses. However, no deeper study of photoluminescence was performed.

In this work, the crystallisation mechanism and the structural and optical properties of $Nd^{3+}$-doped $LaF_3$ glass-ceramics are reported for their possible use as laser materials. In particular, the effect of $Nd^{3+}$ ions on the kinetics of crystallisation has been studied and the possibility to selectively separate the emission of $Nd^{3+}$ ions in the glass matrix from those embedded in $LaF_3$ nanocrystals is presented. Site-selective emission and excitation spectra together with the different lifetime values of the $^4F_{3/2}$ state depending on the excitation and emission wavelengths allows the emission of $Nd^{3+}$ ions in $LaF_3$ nanocrystals to be unambiguously identified [37–39].

## 2. Experimental

### 2.1. Materials and methods

Glasses of composition $55SiO_2$-$20Al_2O_3$-$15Na_2O$-$10LaF_3$ (55Si-10La) doped with 0.1, 0.2, 0.5, 1 and 2 $Nd^{3+}$ (in mol%) have been prepared by melting-quenching using as raw materials: $SiO_2$ sand (Saint-Gobain, 99.6%), $Al_2O_3$ (Panreac), $Na_2CO_3$ (Sigma Aldrich, >99.5 %), $LaF_3$ (Alfa Aesar, 99.9%) and $NdF_3$ (Alfa Aesar, 99.99%). The batches were calcined at 1200 °C for 2 h, melted at 1650 °C for 1.5 h and then quenched onto a brass mould. Glasses were melted again for 30 min and quenched onto a cold (−10 °C) brass mould. All the glasses were annealed at 600 °C for 30 min to eliminate residual stresses. From now on, glass samples will be labelled as G0.1, G0.2, G0.5, G1 and G2, for $Nd^{3+}$ concentrations of 0.1, 0.2, 0.5, 1, and 2 mol% respectively; corresponding glass-ceramics will be denoted as GCx.

Glass-ceramics samples were obtained by heat treatments of glass pieces at 620 °C for 1, 3, 5, 20, 40, 80 h and at 660 °C- 20 h, using a heating rate of 10 °C/min. Glass sheets (1 cm × 1 cm × 2 mm) were treated and then polished for optical characterization. One glass slab for each composition was not treated and used as reference glass to compare with the corresponding glass-ceramics.

### 2.2. Structural characterisation

Non-isothermal crystallisation kinetics were studied by DTA/TG (SDT Q600 – TA Instruments) using 20–30 mg of glass with particle size in the range 1–1.25 mm. DTA curves were obtained with heating rates in the range 10–60 °C/min. From these DTA data, the glass transition temperature $T_g$, Avrami $n$ parameter and crystal-growth dimensionality $m$ parameter were calculated from the Ozawa equation [40] and the Matusita equation [41] given by equations (1) and (2) respectively:

$$\left(\frac{d[\ln[-\ln(1-x)]]}{d(\ln q)}\right)_T = -n \tag{1}$$

$$\ln\left(\frac{q^n}{T_p^2}\right) = -\frac{mE_a}{RT_p} + Cost \tag{2}$$

In these relations, $x$ is the partial area of the crystallisation peak calculated for a fixed temperature $T$ and $q$ is the heating rate; $T_p$ and $R$ are the crystallisation peak temperature and the gas constant, respectively. The activation energy for crystallisation $E_a$ was calculated using the Kissinger equation [42]:

$$\ln\left(\frac{q}{T_p^2}\right) = -\frac{E_a}{RT_p} + Cost \tag{3}$$

The heat-treated specimens were milled, sieved (<63 μm) and characterised by XRD (Bruker D8 Advance diffractometer). XRD diffractograms were acquired in the range $10 \leq 2\theta \leq 70$, with a step-size of 0.02° and 1s acquisition time for each step. The crystal size was calculated using the Scherrer equation [43]:

$$D = \frac{0.94\lambda}{\cos\theta\sqrt{B_m^2 - B_i^2}} \tag{4}$$

where λ is the wavelength (1.54056 Å–CuK$\alpha_1$), $B_m$ the full width half maximum of the $LaF_3$ peak (111) and θ its diffraction angle. The factor 0.94 corresponds to spherical crystals. The pseudo-Voigt function was used to fit diffraction-peak parameters. The instrumental broadening $B_i$ has also been taken into account using milled and sieved NaF powder (<63 μm).

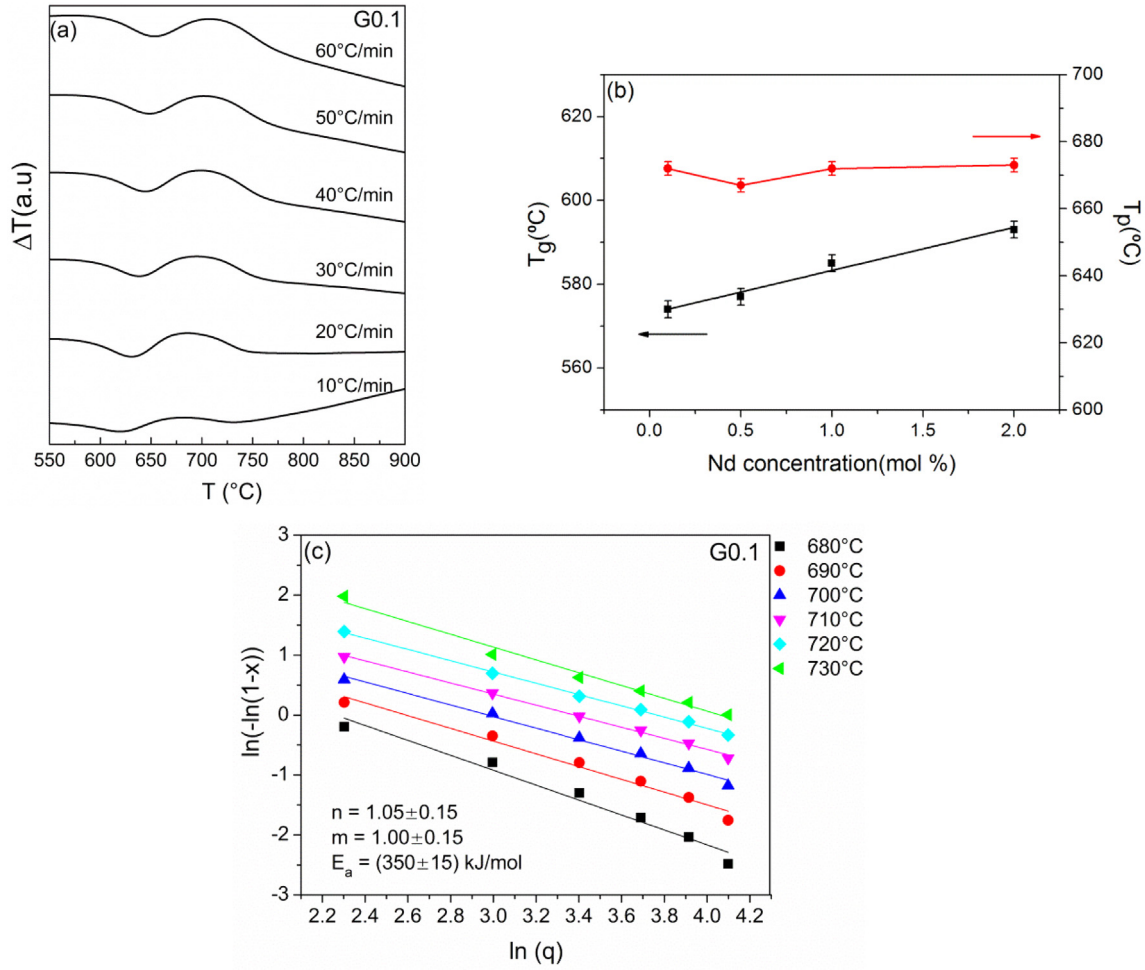


**Fig. 1.** (a) DTA curves at different heating rates of the G0.1 glass and (b) Tg variation with Nd concentration; (c) Ozawa plots.

The crystallised fraction of $LaF_3$ in the glass-ceramics obtained on a heat treatment at 620 °C for 40 h was estimated by quantitative Rietveld analysis employing a method that has been applied to similar compositions [17,22]. The glass was finely ground in an agate mortar, sieved through a 60 μm mesh then milled again with NaF (99.9%), which was used as internal standard in an appropriate quantity (5–6 wt%) to approximate the peak intensity of the nanocrystalline $LaF_3$. XRD powder data for Rietveld analysis were collected over the range $10° \leq 2\theta \leq 90°$ in a step-width of 0.0289° and a counting time of 4s per step employing a Bruker D8 high-resolution diffractometer equipped with a solid-state rapid LynxEye detector, and monochromatic Cu $K\alpha_1$ radiation. Rietveld refinement was performed with the Fullprof program using interpolation of background points to model the amorphous contribution to the pattern.

TEM samples of glasses and glass-ceramics were prepared using sieved powders of size <63 μm. High resolution electron microscopy (HR-TEM), including Scanning Transmission Electron Microscopy-High Angle Annular Dark Field (STEM-HAADF) were recorded on a JEOL 2100 field-emission gun transmission electron microscope operating at 200 kV with a point resolution of 0.19 nm. The microscope is equipped with an energy dispersive X-ray spectrometer (EDXS) (INCA x-sight, Oxford Instruments), which was operated in STEM mode, with a probe size of 1 nm.

Small-angle X-ray scattering (SAXS) measurements were performed using a commercial SAXS system (SAXSess, Anton Paar GmbH). The bulk samples were crushed into fine powders and then compressed into uniform thin pellets for the SAXS measurements. A Cu Kα line beam of 10 mm × 0.4 mm in size was incident on the samples, and the scattered X-rays were collected using an imaging plate in the q range of 0.01–0.1 $Å^{-1}$. The collected 2D patterns were converted into 1D patterns and treated using the line-beam profile. The 1D SAXS data were then analysed using the Irena software package [44] to obtain the particle-size distribution.

### 2.3. Optical characterisation

UV–vis absorption spectra of optical sheets were measured in the range 300–1000 nm using a Lamba 900-Perkin Elmer double-beam spectrophotometer.

Site-selective, steady-state emission and excitation spectra were recorded by exciting the samples with a continuous wave (cw) Ti:sapphire ring laser (0.4 $cm^{-1}$ linewidth) in the 770–920 nm spectral range. The fluorescence was analysed with a 0.25 m monochromator; the signal was detected by an extended IR Hamamatsu H10330A-75 photomultiplier and amplified by a standard lock-in technique. The sample temperature was varied between 10 and 300 K in a continuous-flow cryostat.

Lifetime measurements were obtained by exciting the samples with a Ti:sapphire laser pumped by a pulsed frequency-doubled Nd:YAG laser (9 ns pulse width), and detecting the emission with a Hamamatsu H10330A-75 photomultiplier. Data were processed by a Tektronix oscilloscope.

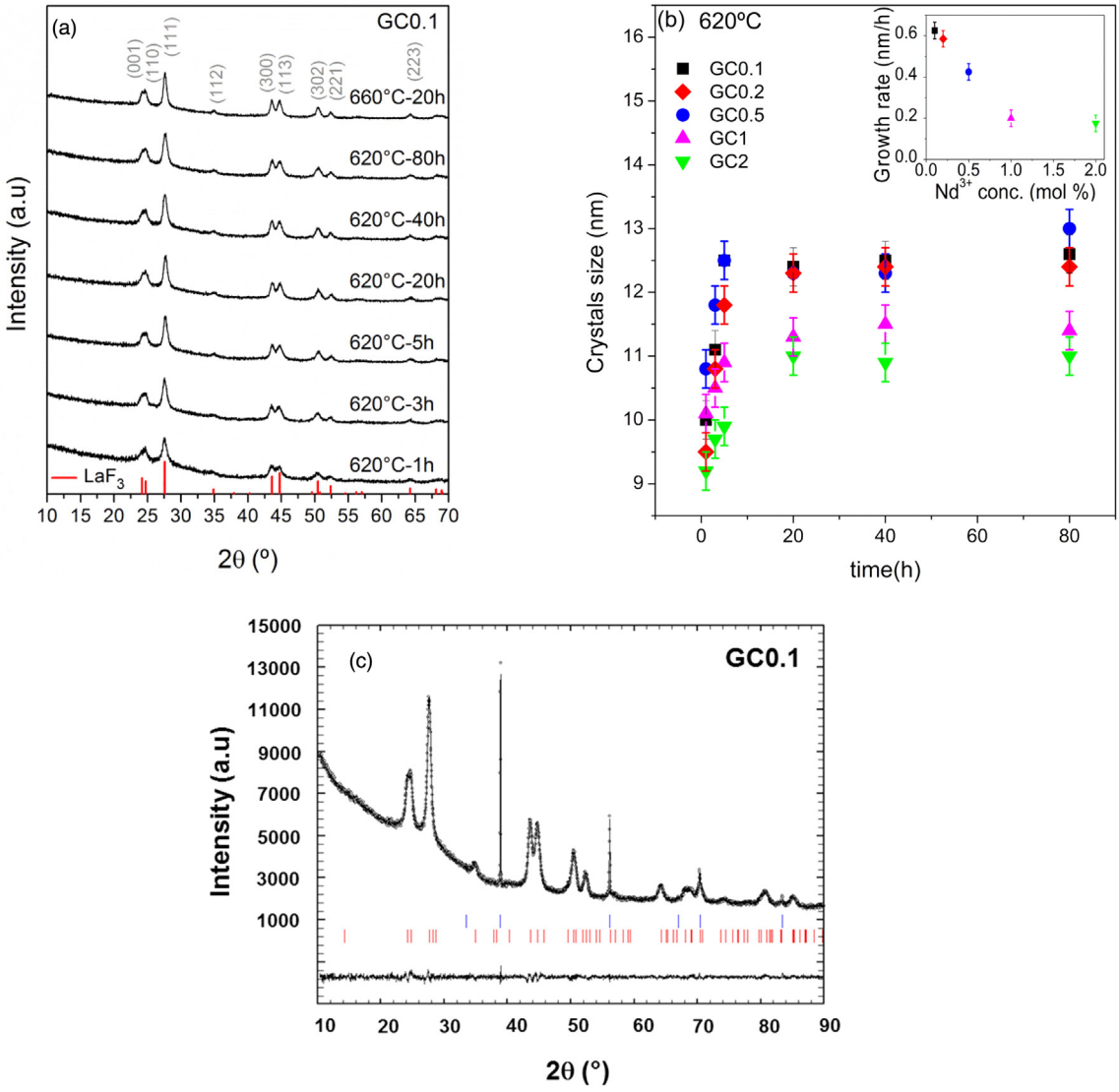


**Fig. 2.** (a) XRD diffractograms for GC0.1 treated at 620 °C for periods in the range 1–80 h and at 660 °C–20 h; (b) Crystals size for GC samples GC0.1, GC0.2, GC0.5, GC1 and GC2 treated at 620 °C and (inset) crystals growth rate in the range 1–5 h; (c) Observed and difference X-ray powder diffraction profiles of GC0.1 obtained at 620 °C during 40 h with 5 mol% NaF internal weight standard. The Bragg peaks of NaF and $LaF_3$ are indicated by top and bottom vertical bars, respectively. Refinement parameters $R_p = 1.53$; $R_{wp} = 2.0$; $\chi^2 = 1.44$ were obtained.

## 3. Results and discussion

### 3.1. Structural properties

Fig. 1a shows DTA curves for G0.1 for the heating rates 10–60 °C/min. The exothermic peak, $T_p$, at around 670 °C corresponds to the crystallisation of $LaF_3$ phase. Similar results were obtained for the undoped glass [22]. Fig. 1b shows the variation of $T_g$ and $T_p$ with $Nd^{3+}$ concentration for a heating rate of 10 °C/min, the same rate as used in all heat treatments. On increasing the $Nd^{3+}$ concentration, $T_g$ changes almost linearly from a value of 573 °C for the G0.1 sample to 593 °C for G2, while $T_p$ changes only a few degrees for increasing $Nd^{3+}$ contents. The crystallisation stability parameter, $\Delta T = T_p - T_g$, diminishes notably with higher $Nd^{3+}$ concentration, with G2 glasses showing a higher tendency to crystallise compared to the G0.1 glass. It appears, therefore, that $Nd^{3+}$ ions are acting as nucleating agent, and concomitantly increase the glass-matrix rigidity. This may be explained on considering that incorporation of RE ions usually increases glass viscosity in the high-viscosity regime, i.e for $T < T_g$ [17,45]. Additionally, RE incorporation could favour phase separation, which also leads to an increase in viscosity.

Fig. 1(c) shows the Ozawa plots of G0.1 for six different temperatures. For each plot, an $n$ value was obtained, and then a mean $n$ value was calculated and included in the figure together with the $m$ parameter. Similar $n$ and $m$ values, approximate to 1, were obtained for all compositions. These values correspond to a crystallisation process which starts from a constant number of nuclei and for which crystal growth is diffusion controlled [46]. The same behaviour was also observed for other oxyfluoride GCs [47], [48] and [49]. The addition of $Nd^{3+}$, even in quite varied concentrations, does not influence the crystallisation mechanism but affects the crystallisation kinetics. Moreover, the crystallisation activation energy, $E_a$, around 350 kJ/mol, is the same for all compositions and similar to that of the undoped glass [22].

Fig. 2(a) shows the XRD diffractograms of GC0.1 samples heat treated at 620 °C for 1, 3, 5, 20, 40 and 80 h and at 660 °C for 20 h. $LaF_3$ peaks (JCPDS 00-032-0483) are shown at the foot of the figure for reference. For all compositions, only $LaF_3$ crystals precipitate in the glass matrix; however, the crystal-growth kinetics slows down

as $Nd^{3+}$ content increases. Fig. 2b shows the crystal size of GCs at 620 °C for all the $Nd^{3+}$ concentrations; the crystal size for GCs at 660 °C is shown in the inset. On gradually increasing the $Nd^{3+}$ concentration, the crystal size decreases for treatments at 620 and 660 °C. On treatment at 620 °C, $LaF_3$ crystals grow from 10 nm to 12.5 nm during the first 5 h for the G0.1 glass, but grow less than 1 nm for G2. This may be explained on consideration of the higher $T_g$ of the G2 glass.

For heat treatment at 660 °C–20 h larger crystals are formed but a similar trend as observed for 620 °C is maintained. The inset of Fig. 2(b) shows the crystal growth rate for treatment at 620 °C in the range 1–5 h, since for times longer than 20 h the crystal size does not change with time. Crystal-growth rate decreases from GC0.1 to GC1, maintaining practically the same value for GC2.

Quantitative Rietveld refinements of the $LaF_3$ crystalline phase with NaF as internal standard were carried out for GCs obtained at the same thermal treatment of 620 °C during 40 h. The observed diffraction pattern and the difference between observed and calculated diffraction patterns for 0.1GC are shown in Fig. 2(c).

The following crystalline fractions (wt%) were determined with varying Nd content: 0.1GC (6.4), 0.5GC (9.9), 1GC (8.8), and 2GC (8.2). Although it is difficult to establish a clear tendency, it is apparent that an increase of the crystalline fraction takes place for Nd contents above 0.5 mol%, after which, the crystalline fraction tends to stabilise, or even slightly decrease, which is in good agreement with the smaller nanocrystals obtained with 1 and 2 mol% of Nd (Fig. 2(b)).

Fig. 3a and b show HR-TEM images of G2 glass at different magnifications. The inset of Fig. 3a indicates the size of the initial phase-separated droplets present in the glass; their mean size is $34.8 \pm 0.4$ nm, the FWHM is $18 \pm 2$ nm. No crystalline structure was observed. Fig. 3c and d show images of GC2 treated at 620 °C for 40 h. The amorphous phase-separated droplets in the glass samples formed several crystals inside. The droplet and crystal size distribution are given in the insets of Figs. 3c and d, respectively. The mean value of the droplets in the GC sample is $34.0 \pm 0.4$ nm, similar to that obtained for the glass, but the FWHM gets sharper giving a value of $10 \pm 1$ nm; the mean crystal size is centred at 10 nm, in agreement with the value obtained by XRD measurements for the GC2 620 °C–40 h sample.

Figs. 3e and f present crystal planes along the [111] and [113] directions calculated by FFT of some crystals shown in Fig. 3d, confirming the precipitation of $LaF_3$ crystals. The plane distances $d_{111}$ and $d_{113}$, which give the most intense peaks in the XRD diffractogram at 27.5° and 44.7° 2θ, are 0.33 nm and 0.20 nm, in good agreement with the values of 0.323 nm and 0.202 nm reported for $LaF_3$ in the JCPDS (00-032-0483) and the literature [50–52]. Fig. 3g presents the EDX curves across two adjacent droplets circled in red in Fig. 3h; the points 1–2 and 3–4 delimit the first and second droplet, respectively. The yellow line is the scanning line, also represented in Fig. 3g with the droplet size marked by vertical dashed grey lines. EDX analysis of Fig. 3g shows Si enrichment surrounding the phase-separated droplets, which leads to the formation of a barrier of higher viscosity around them.

The barrier formation appears to occur during the first 20 h of heat treatment since $LaF_3$ crystals grow during this time, and thereafter maintain their size. The incorporation of $Nd^{3+}$ inside the $LaF_3$ crystals is clearly visible from the EDX curves.

Fig. 4a and b show the particle volume distribution of G2 and GC2 samples (annealed at 620 °C for 40 h) as a function of particle diameter. The insets display the raw SAXS data and theoretical fit using the Irena program, from which the particle volume distribution was obtained. The particles can be classified into two distinctive size groups, group 1 below 10 nm and group 2 between 15 and 60 nm. The group 1 particles seen in both samples may be associated with

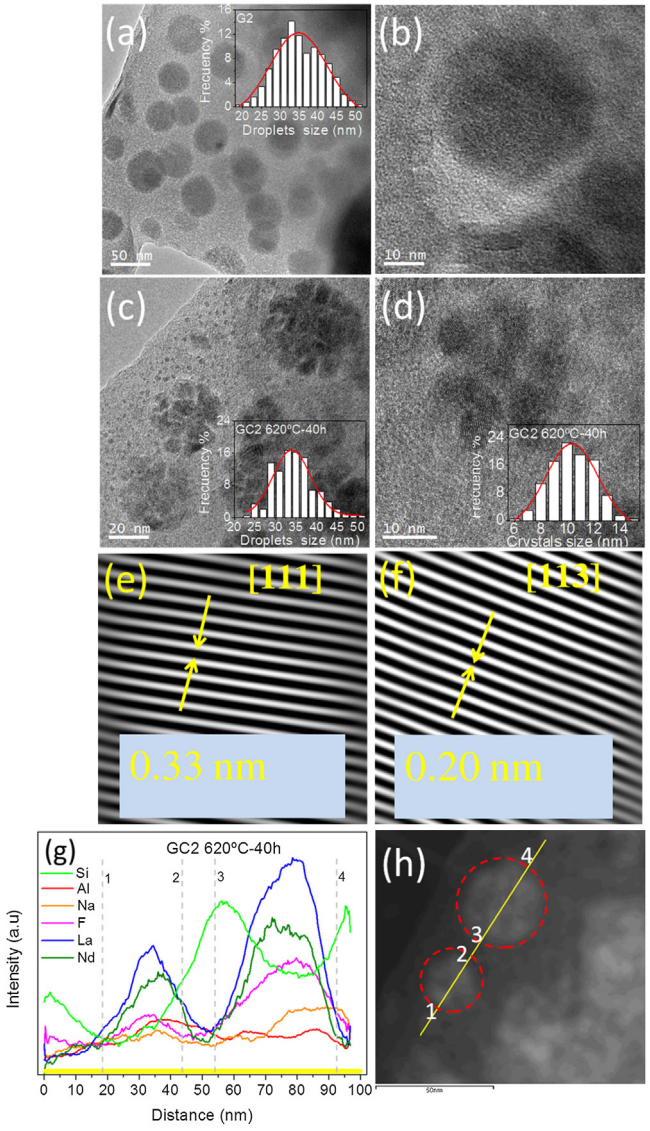


**Fig. 3.** (a) and (b) HR-TEM of G2 glass; (c) and (d) GC2 heat treated at 620 °C-40 h; (e) and (f) lattice planes of some crystals shown in (d); (g) EDX of the GC2 620 °C–40 h sample along 2 droplets containing several crystals (the yellow and light grey lines indicate the scanning line and droplet size, respectively); (h) STEM image of the droplets used for the EDX measurement where the yellow line is the same as that represented in (g). (For interpretation of the references to colour in this figure legend, the reader is referred to the web version of this article.)

very small initial phase-separated droplets which could not grow sufficiently to produce crystals. The group 2 particle size is, however, in very good agreement with the results obtained by TEM and is related with the scattering of phase-separated droplets. The calculated average diameters for these two groups of particles were 6 nm and 38 nm for the G2 sample, and 7 nm and 36 nm for the GC2 sample.

The SAXS results were roughly consistent with the TEM results reported in Fig. 3. The slightly larger average size (by about 2 nm) derived from the SAXS analysis compared to the TEM results could be due to the difference between particle-volume distribution (SAXS) and particle-number distribution (TEM), with the former having more weighting on the larger particles. One interesting feature is that the two groups of particles showed opposite growth behaviour upon thermal annealing: the group 1 particle-size distribution became broader while that of the group 2 particles became narrower after 40 h of annealing at 620 °C, which was consistent

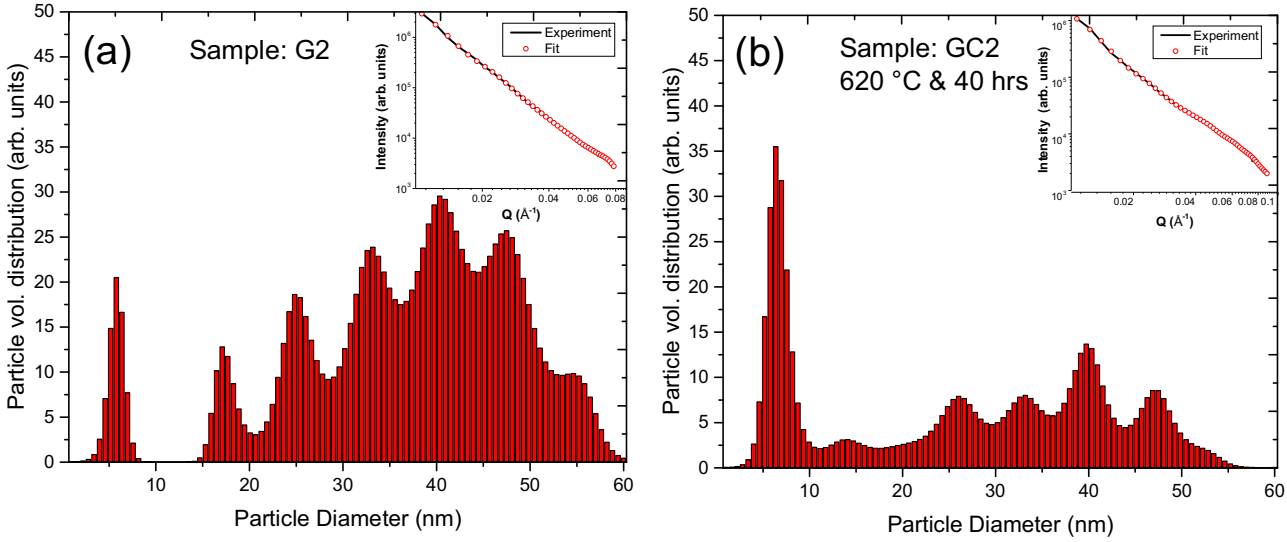


**Fig. 4.** SAXS data (insets) and derived particle-volume distribution of G2 (a) and GC2–620 °C treated for 40 hrs (b).

with the TEM observation. The thermal annealing also significantly enhanced the relative volume fraction of group 1 particles. New particles between 10 and 15 nm in diameter appeared in the GC2 sample after thermal annealing, which were probably related to the crystals as seen from the TEM and XRD results.

### 3.2. Absorption and emission properties

A further proof of $Nd^{3+}$ incorporation in the $LaF_3$ crystals comes from UV–vis absorption spectra in Fig. 5, in which GCs samples are compared with glasses. Figs. 5a and b show the absorption coefficient for the G0.1, G0.2, G0.5, G1 and G2 glasses and for the corresponding GC samples treated at 620 °C for 40 h. The bands observed in the spectra correspond to transitions from the fundamental level ($^4I_{9/2}$) to each of the excited levels of $Nd^{3+}$ ions. The glass samples present characteristic inhomogeneously-broadened absorption bands. However, in the case of the GC samples, the absorption bands are resolved better, indicating the incorporation of $Nd^{3+}$ ions in the $LaF_3$ nanocrystals precipitated during the heat treatments.

Fig. 5c presents the $^4I_{9/2}\rightarrow{}^4G_{5/2}$, $^2G_{7/2}$ absorption bands of G0.1 and G2 glasses, along with GC0.1 and GC2 glass-ceramics treated at 620 °C for 40 h, in greater detail. The absorption bands $^4I_{9/2}\rightarrow{}^4F_{7/2}$, $^4S_{3/2}$ and $^4I_{9/2}\rightarrow{}^4F_{5/2}$, $^2H_{9/2}$ in the GC samples are shown in the inset. Similar behaviour is also appreciable in the GC samples treated at 620 °C and 660 °C for 20 h. The $^4I_{9/2}\rightarrow{}^4G_{5/2}$ transition is well known to be a hypersensitive transition, exhibiting an electric quadrupole character which is strongly dependent on the ligand field. A clear change in the absorption band allows the Stark components in the GCs to be better resolved. The sharpening of the band in comparison to the initial glass indicates the presence of $Nd^{3+}$ ions inside the $LaF_3$ crystals. This is most clearly visible in the G0.1 sample, whereas on increasing the $Nd^{3+}$ content, the difference between glass and GCs is less apparent.

The absorption bands of the glass and GC samples doped with 2 mol% $Nd^{3+}$, together with the values of the refractive index and $Nd^{3+}$ concentration, have been used to determine the Judd-Ofelt parameters [53,54]. Using this theory, the calculated oscillator strengths can be expressed as a function of the reduced-matrix elements $\|U^t\|$ which are almost independent of the ion environment. To estimate the J-O parameters (Table 1), the values reported by Carnall et al. for $Nd^{3+}$ in $LaF_3$ [55] were employed. As is well known, the spectroscopic parameter $\Omega_2$ is related to the covalent nature of the chemical bonding between rare-earth ions and ligand ions [56]. As observed in Table 1, $\Omega_2$ decreases from $3.23\times10^{-20}$ in the glass sample to $2.82–2.89\times10^{-20}$ in the GC materials. That is, the heat treatment induces a reduction in the degree of covalence between $Nd^{3+}$ and its nearest neighbours. The decrease of $\Omega_2$ further confirms the incorporation of $Nd^{3+}$ ions into the precipitated nanocrystals. Moreover, the sum of the J-O parameters decreases for the GC samples due to the decreasing covalency of the bond between the $Nd^{3+}$ ion and surrounding anions in accordance with reported results [57].

**Table 1**
Judd-Ofelt parameters and r.m.s. deviation for precursor glass G2 and GC2.

| Sample | $\Omega_2$ (x$10^{-20}$) | $\Omega_4$ (x$10^{-20}$) | $\Omega_6$ (x$10^{-20}$) | r.m.s. |
|---|---|---|---|---|
| G2 | 3.23 | 6.23 | 5.03 | $5.35.10^{-7}$ |
| GC2–620 °C-20h | 2.85 | 5.57 | 4.37 | $5.25.10^{-7}$ |
| GC2–620 °C-40h | 2.82 | 5.48 | 4.31 | $5.16.10^{-7}$ |
| GC2–660 °C-20h | 2.89 | 5.45 | 4.17 | $5.35.10^{-7}$ |

The strength of the hypersensitive $^4I_{9/2}\rightarrow{}^4G_{5/2}$ transition, which is greatly affected by the environment of $Nd^{3+}$ ions, is dominated by the $\Omega_2$ parameter contribution, increasing with both the ligand polarisability and asymmetry of the surrounding environment [53,54]. The oscillator strength of this transition is reduced from $1796\times10^{-8}$ in the glass to $1609\times10^{-8}$, $1581\times10^{-8}$, and $1591\times10^{-8}$ in the GC 620 °C C-20 h, GC 620 °C-40 h, and GC 660 °C–20 h samples, respectively. This tendency confirms that the ligand field around the $Nd^{3+}$ ions changes as a consequence of the heat treatment and crystallisation process.

The spontaneous emission probabilities from the $^4F_{3/2}$ to $^4I_J$ states were calculated from the J-O parameters and used to obtain the radiative lifetimes.

The $^4F_{3/2}\rightarrow{}^4I_{11/2,13/2}$ steady-state fluorescence spectra were measured at room temperature for all samples by exciting with a Ti:sapphire laser at 802 nm in resonance with the $^4I_{9/2}\rightarrow{}^4F_{5/2}$,$^2H_{9/2}$ absorption band. Fig. 6 shows the emission for the samples doped with 2 mol% Nd. It can be seen that the emission is inhomogeneously broadened due to site-to-site variations in the local ligand field. The fluorescence band for the $^4F_{3/2}\rightarrow{}^4I_{11/2}$ emission was integrated and divided by the peak intensity to yield an effective linewidth [57]. From the measured effective linewidth and the spontaneous emission probability of the $^4F_{3/2}\rightarrow{}^4I_{11/2}$ laser transi-

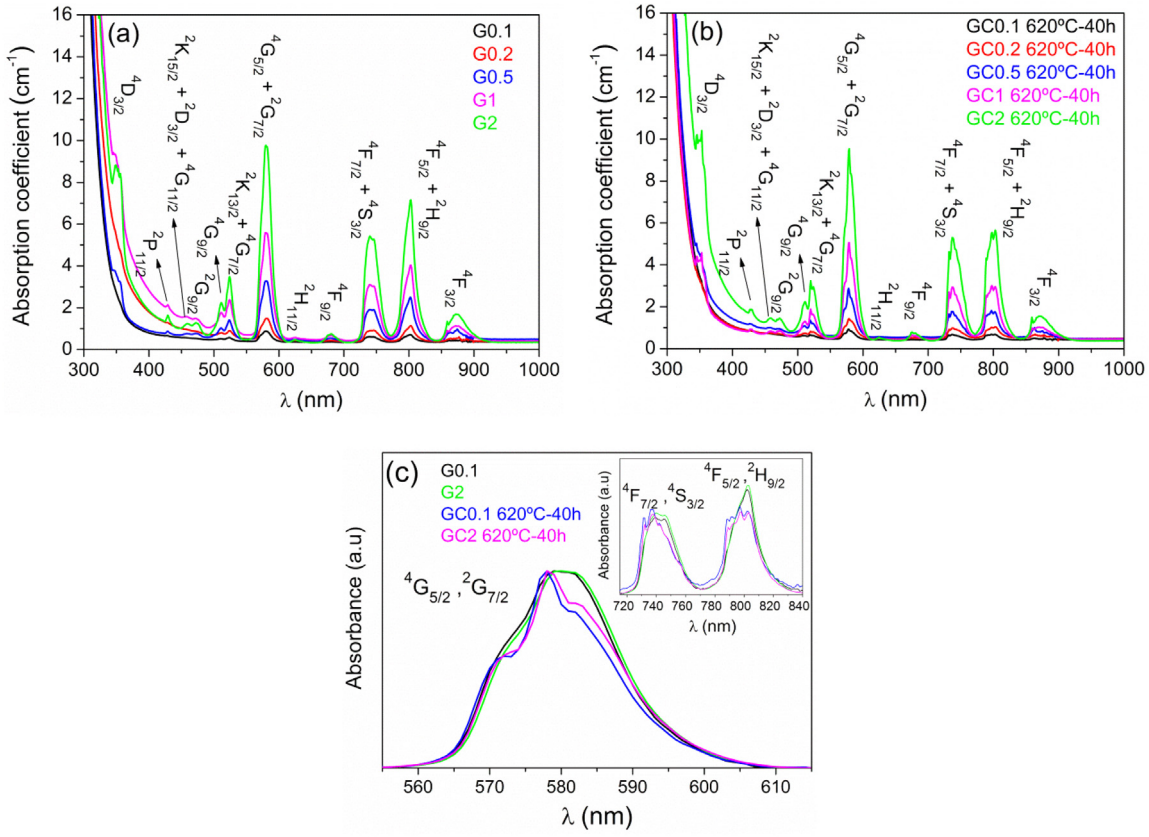


**Fig. 5.** (a) Absorption spectra of glasses G0.1, G0.5, G1, G2 and (b) GCs treated at 620 °C–40 h; (c) comparison of absorption transitions $^4I_{9/2} \rightarrow {}^4G_{5/2}, {}^2G_{7/2}$ and (inset) $^4I_{9/2} \rightarrow {}^4F_{7/2}$, $^4S_{3/2}$ and $^4I_{9/2} \rightarrow {}^4F_{5/2}$, $^2H_{9/2}$ in G0.1, G2, GC0.1 620 °C–40 h and GC2 620 °C-40 h.

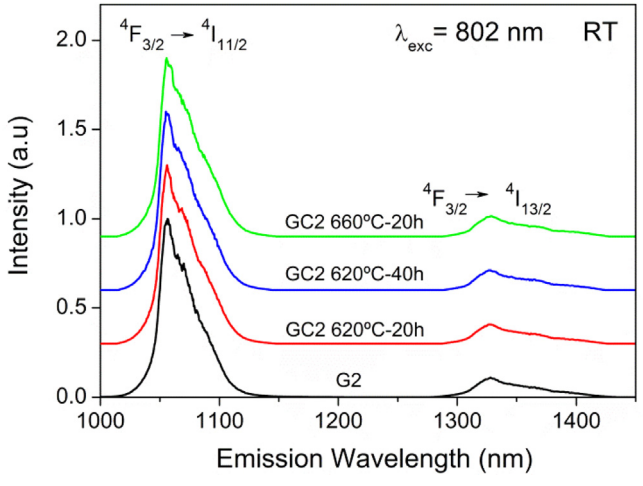


**Fig. 6.** Room-temperature emission spectra of the $^4F_{3/2} \rightarrow {}^4I_{11/2,13/2}$ transitions of $Nd^{3+}$ ions (2 mol%) obtained under excitation at 802 nm.

tion, calculated from the J-O parameters, the stimulated emission cross-section of this transition may be evaluated as [58]:

$$\sigma_p\left(\lambda_p\right) = \frac{\lambda_p^4}{8\pi c n^2 \Delta\lambda_{eff}} A\left[\left({}^4F_{3/2}\right);\left({}^4I_{11/2}\right)\right] \quad (5)$$

where $\lambda_p$ is the peak fluorescence wavelength, $n$ is the refractive index, $\Delta\lambda_{eff}$ is the effective linewidth of the $^4F_{3/2} \rightarrow {}^4I_{11/2}$ transition, and $A[({}^4F_{3/2});({}^4I_{11/2})]$ is the radiative transition probability for this transition.

**Table 2**
Room-temperature emission properties of G2 and GC2 samples.

| Sample | n | $\lambda_p$(nm) | $\Delta\lambda_{eff}$ (nm) | $\sigma_p$ (pm$^2$) | $\tau_R$ (μs) |
|---|---|---|---|---|---|
| G2 | 1.523 | 1057 | 35.95 | 2.8 | 345 |
| GC2–620 °C-20h | 1.525 | 1057 | 37.16 | 2.4 | 390 |
| GC2–620 °C-40h | 1.526 | 1057 | 37.60 | 2.3 | 395 |
| GC2–660 °C-20h | 1.526 | 1057 | 38.94 | 2.2 | 398 |

The stimulated emission cross-section for the $^4F_{3/2} \rightarrow {}^4I_{11/2}$ transition and other relevant parameters are presented in Table 2. The peak position remains unchanged for the GC samples and the effective linewidth slightly increases with the time of heat treatment. This behaviour, together with the lower radiative transition probability for the $^4F_{3/2} \rightarrow {}^4I_{11/2}$ emission for the crystallised samples, leads to smaller stimulated emission cross-sections for the GC samples, in the range of values found in silicate glasses (0.9–3.6 pm$^2$) [24].

The steady-state emission spectra exhibit similar spectral features for all concentrations and heat treatments. However, the excitation spectra of the GC samples doped with 0.1, 0.2, and 0.5 mol% performed in the spectral range 765–910 nm monitored at 1057 nm show a fine structure superimposed on the broad $^4I_{9/2} \rightarrow {}^4F_{5/2,3/2}$ bands of the glass, confirming the partial incorporation of $Nd^{3+}$ ions in the nanocrystals. In the samples doped with 1 and 2 mol%, $Nd^{3+}$ ions are responsible for the main contribution to the spectra in the amorphous environment. As an example, Fig. 7 shows the excitation spectra for the samples doped with 0.1 and 1 mol% where better resolved peaks are observed for the lower $Nd^{3+}$ concentration.

The decays of the $^4F_{3/2}$ state were obtained by exciting with a pulsed Ti:sapphire laser at 802 nm in the $^4I_{9/2} \rightarrow {}^4F_{5/2}$ absorption

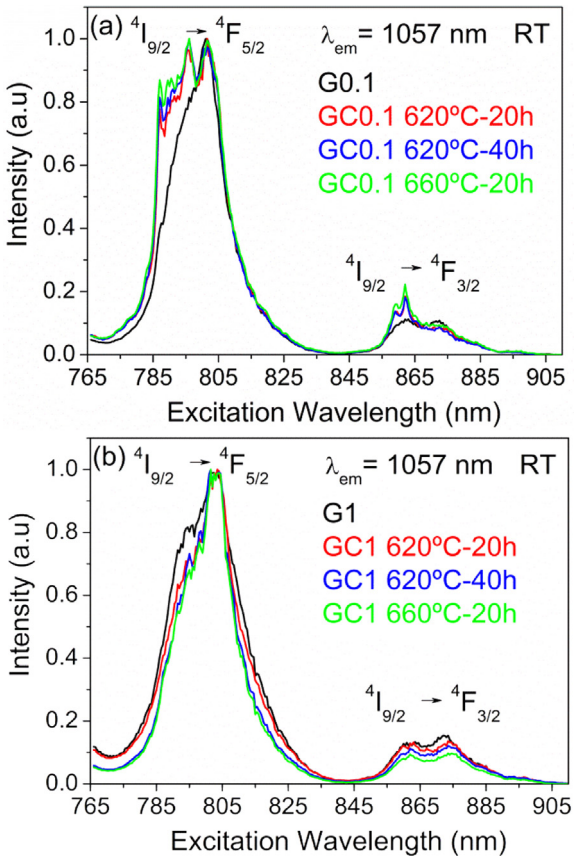


**Fig. 7.** Room temperature excitation spectra of the $^4I_{9/2} \rightarrow {}^4F_{5/2,3/2}$ transitions of $Nd^{3+}$ obtained by collecting the luminescence at 1057 nm for the samples doped with (a) 0.1 mol% $NdF_3$ and (b) 1% $NdF_3$.

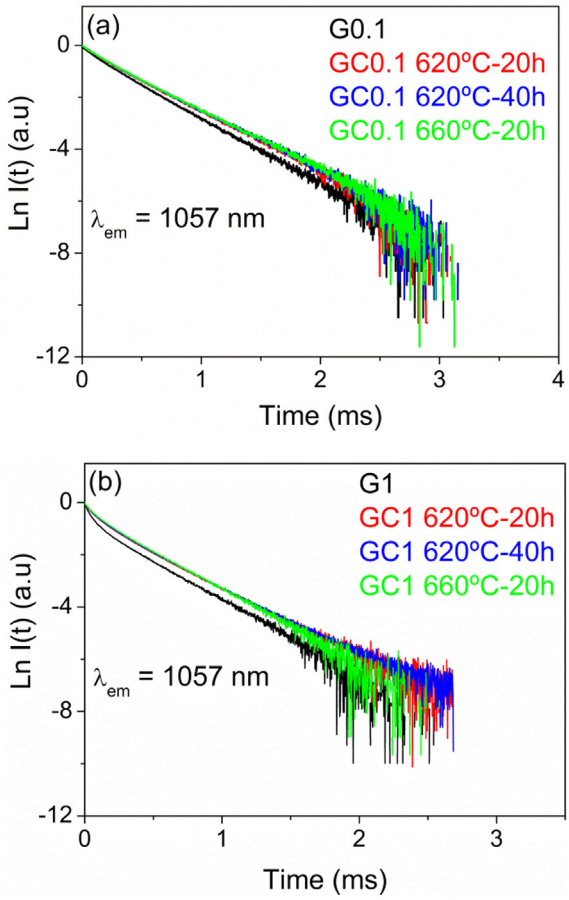


**Fig. 8.** Logarithmic plot of the room temperature experimental decays from the $^4F_{3/2}$ state for the samples doped with (a) 0.1 and (b) 1 mol% of $NdF_3$. The decays were obtained by exciting at $^4I_{9/2} \rightarrow {}^4F_{5/2}$ transition and monitored at 1057 nm.

**Table 3**
Experimental lifetimes of the $^4F_{3/2}$ level obtained under excitation at 802 nm by collecting the luminescence at 1057 nm as a function of $Nd^{3+}$ (mol%.) concentration and heat treatment. The radiative lifetime is shown in the last column.

| Sample | 0.1 | 0.2 | 0.5 | 1 | 2 | $\tau_R$ (μs) |
|---|---|---|---|---|---|---|
| Glass | 343 | 298 | 268 | 192 | 143 | 345 |
| GC 620 °C-20h | 382 | 350 | 308 | 251 | 187 | 390 |
| GC 620 °C-40h | 385 | 354 | 310 | 254 | 191 | 395 |
| GC 660 °C-20h | 388 | 360 | 315 | 254 | 197 | 398 |

band at 295 K. Fig. 8 shows the logarithmic plot of the experimental decays of the $^4F_{3/2}$ level for the samples doped with 0.1 and 1 mol% of $NdF_3$ at room temperature. The decays of the samples doped with 0.1 mol% may be described to a good approximation by a single exponential function, whereas the decays of the samples doped with 1 mol% deviate from a single exponential and the lifetime decreases.

Table 3 lists the lifetime values for all the samples. The lifetime values for the samples with concentrations higher than 0.1 mol% correspond to the average lifetime defined by:

$$\langle \tau \rangle = \frac{\int I(t)dt}{I_0} \quad (6)$$

where I(t) is the intensity at time t. According to these radiative lifetimes, the quantum efficiencies ($\eta = \tau_{exp}/\tau_R$) are around 99 and 41% for the glass samples doped with 0.1 and 2 mol%, respectively. This strong reduction of the quantum efficiency for increasing Nd concentration indicates the presence of non-radiative cross-relaxation processes such as ($^4F_{3/2}$, $^4I_{9/2}$)→ ($^4I_{15/2}$, $^4I_{15/2}$). The lifetime of the GC samples is longer than those of glass samples for all the concentrations, which suggests a fluoride environment for $Nd^{3+}$ ions according to their incorporation in the nanocrystals. The results are similar for the three heat treatments which indicate that after 20 h at 620 °C, the rare-earth ions are largely incorporated into a crystalline environment.

### 3.3. Site-selective spectroscopy

To obtain further information about the different environments for $Nd^{3+}$ ions in the glass-ceramics, emission spectra were performed by exciting at different wavelengths along the $^4I_{9/2} \rightarrow {}^4F_{5/2}$ absorption band. Fig. 9(a) shows the emission spectra obtained by exciting at 786 and 802 nm for the GC samples doped with 0.1 mol% of $Nd^{3+}$ treated at 620 °C-40 h. The figure reveals the strong difference between spectra of differing excitation wavelength, which indicates that $Nd^{3+}$ ions are in different crystal-field sites. The spectrum obtained at 786 nm shows a more resolved structure, indicating a crystalline environment for the $Nd^{3+}$ ions. In contrast, that obtained under excitation at 802 nm shows a more inhomogeneous broadened band similar to that of the glass sample. Moreover, the excitation spectra obtained by collecting the luminescence at 1039 and 1057 nm also reveal the presence of different environments for $Nd^{3+}$ ions. Fig. 9(b) shows the excitation spectra for the same sample doped with 0.1 mol% of $Nd^{3+}$. The spectrum monitored at 1039 nm presents narrower and well-resolved peaks corresponding to $Nd^{3+}$ ions in the nanocrystals. As concentration increases, the spectra become broader and less resolved.

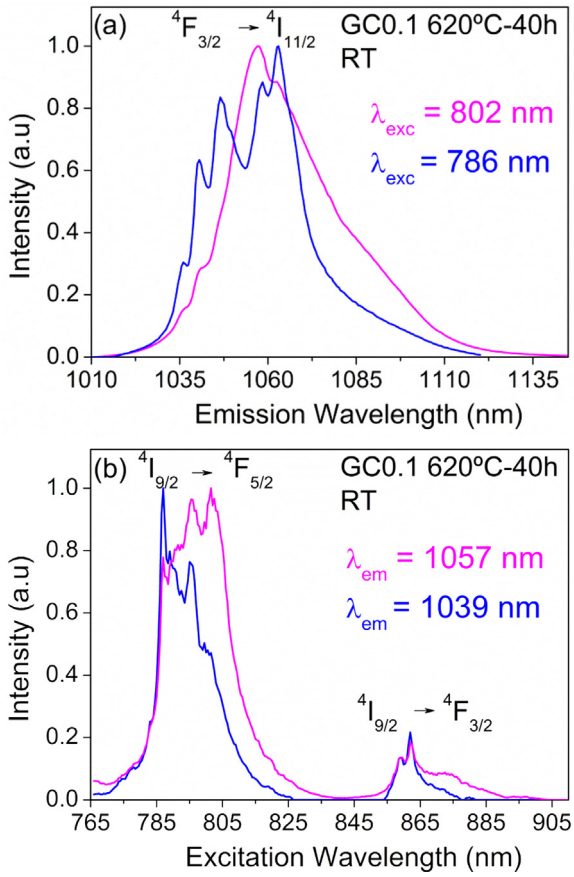


**Fig. 9.** (a) Room-temperature emission spectra obtained under excitation at 786 and 802 nm for GC0.1 620 °C-40 h; (b) excitation spectra obtained on collecting the luminescence at 1039 and 1057 nm for GC0.1 620 °C-40 h.

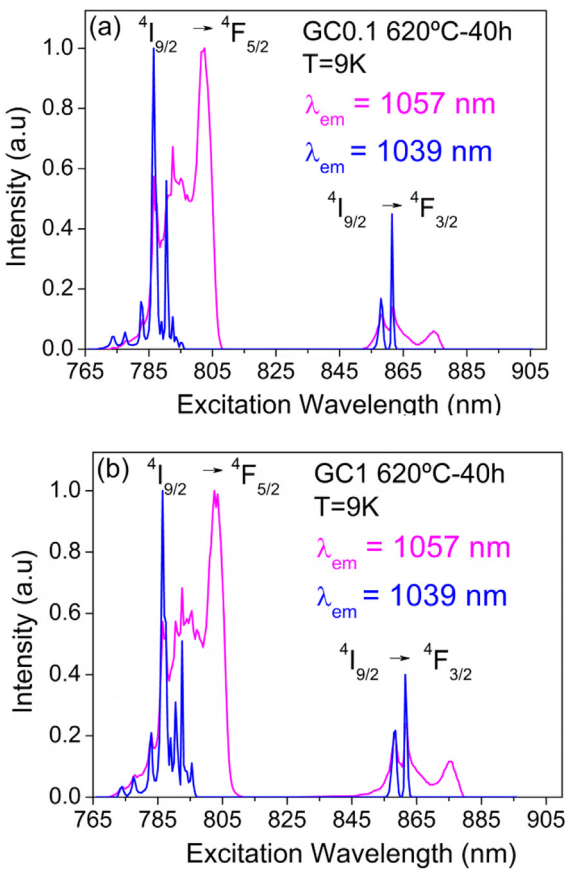


**Fig. 10.** Low-temperature excitation spectra obtained on collecting the luminescence at 1039 and 1057 nm for GC0.1 620 °C-24 h (a) and GC1 620 °C-40 h (b).

To clearly identify emission from $Nd^{3+}$ in the nanocrystals, the emission and excitation spectra were measured at low temperature, thereby minimising the overlapping of contributions from $Nd^{3+}$ in the crystalline and amorphous phases due to the lower thermal population of the higher energy Stark components of the ground and excited states. The low-temperature (9 K) excitation spectra are presented in Fig. 10 for the GC samples doped with 0.1 and 1 mol%. As observed in the spectra obtained at 1039 nm, the low-energy band corresponding to the $^4I_{9/2} \rightarrow {}^4F_{3/2}$ doublet narrows and divides into two single components, as expected for a well-defined crystal-field site. Moreover, the $^4I_{9/2} \rightarrow {}^4F_{5/2}$ band is composed of narrow and well-resolved peaks which indicate that the spectra obtained at 1039 nm correspond to $Nd^{3+}$ ions in the $LaF_3$ nanocrystals. Conversely, the spectra obtained at 1057 nm show broad bands similar to those found in the glass samples.

In order to confirm if the features shown by the excitation spectra monitored at 1039 nm can be unambiguously related to the $Nd^{3+}$ ions in the nanocrystals, site-selective steady-state emission spectra for the $^4F_{3/2} \rightarrow {}^4I_{11/2}$ transition were recorded by exciting at 786 and 802 nm. Fig. 11 shows the normalized emission spectra at 9 K obtained under excitation at 786 and 802 nm for the GC samples doped with 0.1 and 1 mol%, showing quite different emission spectra depending on the excitation wavelength. The spectrum obtained under excitation at 786 nm shows sharp peaks, one at 1039 nm which does not overlap with the emission spectrum obtained by exciting at 802 nm. In the latter, the sharp peaks disappear and the spectrum becomes broader and similar to that found in the glass sample. These results indicate that in the glass-ceramic samples excited at 786 nm, $Nd^{3+}$ ions mainly reside in the crystalline phase. As concentration increases, the emission from $Nd^{3+}$ ions in the nanocrystals decreases, and the spectra become broader with more poorly resolved peaks. Similar emission spectra are obtained by exciting the $^4I_{9/2} \rightarrow {}^4F_{3/2}$ band at 861.5 and 876 nm.

**Table 4**
Experimental lifetimes, at low temperature, of the $^4F_{3/2}$ level obtained under excitation at 790 and 802 nm collecting the luminescence at 1039 and 1057 nm, respectively.

| $NdF_3$ (mol%.) | $\lambda_{exc}$ = 786 nm | $\lambda_{exc}$ = 802 nm |
|---|---|---|
| | $\tau_{exp}$ (μs) | $\tau_{exp}$ (μs) |
| 0.1 | 688 | 336 |
| 0.2 | 462 | 337 |
| 0.5 | 188 | 332 |
| 1 | 98 | 295 |
| 2 | 29 | 233 |

Furthermore, the existence of different environments for the $Nd^{3+}$ ions in the $LaF_3$ nanocrystals is also reflected in the lifetimes of the $^4F_{3/2}$ state, the values of which should depend on the excitation and emission wavelengths. Lifetime measurements of the $^4F_{3/2}$ state were performed by exciting the samples at 786 and 802 nm, and collecting the luminescence at 1039 and 1057 nm, respectively (Fig. 12). Under excitation at 786 nm and collecting the luminescence at 1039 nm, the decay is a single exponential with a lifetime of 688 μs for the GC sample doped with 0.1%, whereas by exciting at 802 nm and collecting the luminescence at 1057 nm, the lifetime is 336 μs (Table 4). The longer lifetimes corresponds to the $Nd^{3+}$ ions incorporated in the nanocrystals. This lifetime is highly dependent on Nd concentration, decreasing to 98 μs for the GC samples doped with 1 mol%.

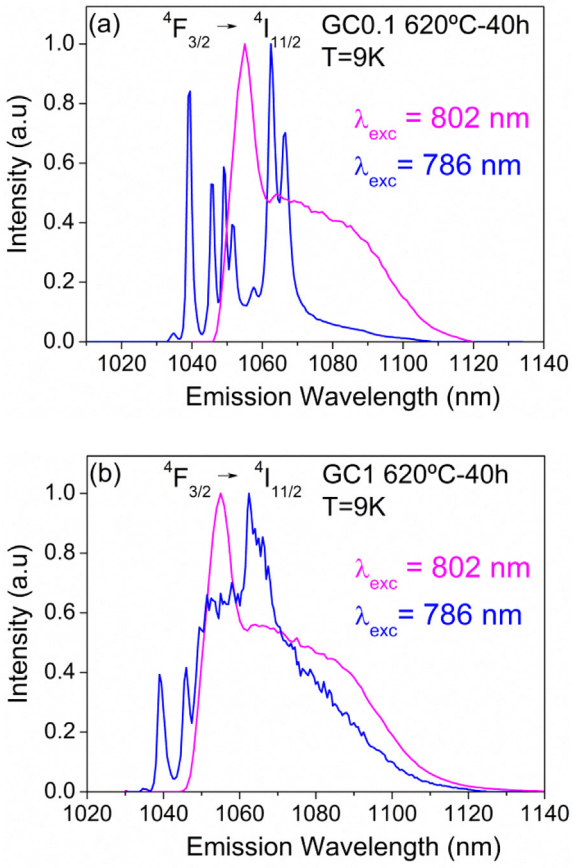


**Fig. 11.** Low temperature emission spectra obtained under excitation at 786 and 802 nm for GC0.1 620 °C-40 h (a) and GC1 620 °C-40 h (b).

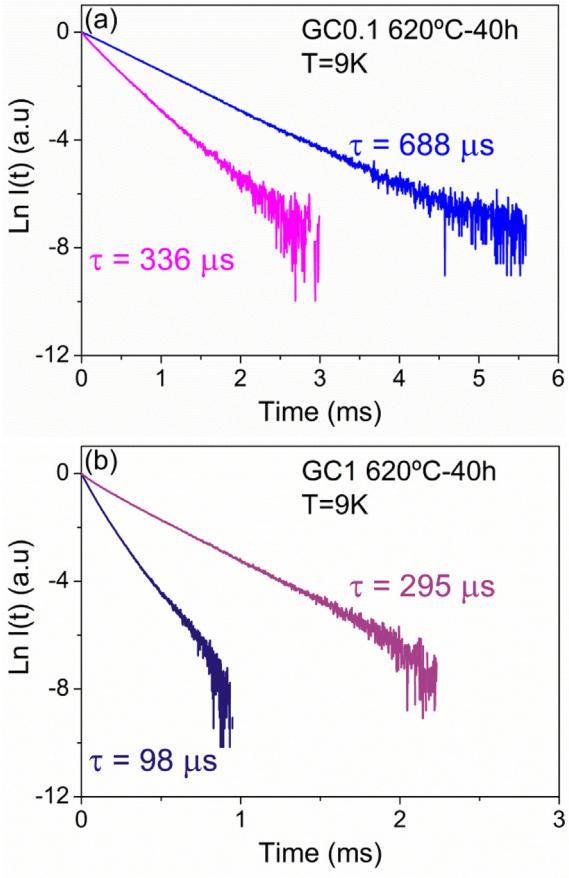


**Fig. 12.** Logarithmic plot of the experimental decays from the $^4F_{3/2}$ state obtained under excitation at 786 nm (blue lines) and 802 nm (pink lines) for GC0.1 620 °C-40h (a) and GC1 620 °C-40 h (b). (For interpretation of the references to colour in this figure legend, the reader is referred to the web version of this article.)

As observed, there is a strong quenching of the lifetimes of $Nd^{3+}$ in the $LaF_3$ nanocrystals, but much less so in the amorphous phase. This behaviour is likely explained from the considerable diffusion of $Nd^{3+}$ ions from the glass matrix to the $LaF_3$ nanocrystals, as confirmed in the same system doped with $Tm^{3+}$ studied by XANES [23]. In this previous work, the ionization energy $E_0$ of $Tm^{3+}$, calculated from the derivate function of the XANES spectra, increased during the crystallisation process, from the glass to the glass-ceramic. It was concluded; therefore, that part of the RE ions existed in a fluorine-rich environment, since the electronegativity of fluorine is higher than that of oxygen. Additionally, the decrease in FWHM of the $Tm^{3+}$ absorption-edge peak from the glass to the glass-ceramic indicated a higher symmetry and, correspondingly, crystallinity of the $Tm^{3+}$ environment in the glass-ceramics. Thus, an increase of the crystalline fraction with the heat treatment time at 620 °C, from 10 to 40 h, was concluded to occur simultaneously with the diffusion process, resulting in the incorporation of around 30% of $Tm^{3+}$ in the $LaF_3$ crystalline structure after 40 h. Starting from the crystalline fractions obtained by Rietveld refinement, the ratio of the concentration of $Tm^{3+}$ in the crystalline phase to that in the glass matrix was calculated (with an error of ~25%), to be approximately 12 for treatment times of 40 h.

In the present work, the same composition is used doping with $Nd^{3+}$. The GCs were obtained in similar conditions and the crystalline fractions calculated from Rietveld analysis are in close agreement with those obtained in the previous work [23]. In the present case, the crystalline fraction depends on the Nd content.

As discussed previously, for treatment times of 40 h, the diffusion process should be essentially complete, as indicated by the constant crystal size for treatments of 20 h and longer. If a silica-rich diffusion barrier is established, no further $Nd^{3+}$ diffusion will take place and so it is possible to consider that around 30% of the $Nd^{3+}$ ions will be in the crystalline phase. Using the same method followed in [23], the respective $Nd^{3+}$ contents in the amorphous and crystalline phases were calculated, with an error ~25%, and are shown in Table 5.

**Table 5**
Crystal fraction in wt% of glasses treated at 640 °C–40 h with different $Nd^{3+}$ concentrations (mol%.), along with the respective concentration of $Nd^{3+}$ in the glass matrix and $LaF_3$ nanocrystals NCs.

| Nd | wt% $LaF_3$ | Nd in glass | Nd in NCs |
|---|---|---|---|
| 0.1 | 6.4 | 0.076 | 1.2 |
| 1 | 8.8 | 0.65 | 8.58 |
| 2 | 8.2 | 1.3 | 17.16 |

The relative concentrations of $Nd^{3+}$ in the glass matrix and $LaF_3$ nanocrystals could explain the strong quenching of the $Nd^{3+}$ emission for $Nd^{3+}$ contents higher than 0.1%, whereas in the glass matrix no significant quenching is observed. Further work is in progress to confirm these calculations by measuring all the samples by XAS-XANES.

## 4. Conclusions

The crystallisation mechanism of transparent glass-ceramics in the system 55Si-10La doped with increasing $Nd^{3+}$ concentrations was confirmed as a diffusion-controlled process starting from a constant number of nuclei already present in the initial glass. The

addition of $Nd^{3+}$ increases the Tg of the glasses and appears to affect the crystallisation kinetics. As the $Nd^{3+}$ content increases, the crystallised fraction also increases indicating that $Nd^{3+}$ ions likely play a role as nucleating agent. Nevertheless, smaller crystals are obtained for the higher $Nd^{3+}$ content. TEM and SAXS techniques have provided complementary information about the size and distribution of phase separation droplets and nanocrystals in the base glass and their evolution in the corresponding glass-ceramics.

Preferential incorporation of $Nd^{3+}$ in the crystalline phase was confirmed by HR-TEM-EDX and several types of optical property measurement. These include splitting of the absorption and emission bands together with reduction of the $\Omega_2$ parameter in the glass-ceramic samples as compared to the glass samples, and site-selective spectroscopy obtained under excitation of the $^4I_{9/2} \rightarrow {}^4F_{3/2}/{}^4F_{5/2}$ transitions.

Low-temperature site-selective emission and excitation spectra together with different lifetime values of the $^4F_{3/2}$ state depending on the excitation and emission wavelengths allow emissions from $Nd^{3+}$ ions in the $LaF_3$ nanocrystals to be isolated and, in turn, correlation of the spectroscopic and structural properties. The optimum amount of dopant corresponds to 0.1 mol%; strong quenching of the lifetime of $Nd^{3+}$ in the $LaF_3$ nanocrystals occurs for higher concentrations.

## Acknowledgements

This work was supported by MINECO under Projects No. MAT2013-48246-C2-1-P and MAT2013-48246-C2-2-P and Basque Country Government IT-943-16. J.J. Velázquez also acknowledges MINECO under Grant FPDI-2013-16895. G.C. acknowledges the U.S. National Science Foundation for partial support under Grant # DMR-1507670. The authors wish to thank L. Pascual from ICP (CSIC) for her support in the TEM studies.

## References

[1] G. Blasse, B.C. Grabmaier, Luminescent Materials, Springer, New York, 1994.
[2] E. Downing, L. Hesselink, J. Ralston, R. Macfarlane, A three-color, solid-state, three-dimensional display, Science 273 (1996) 1185–1189, http://dx.doi.org/10.1126/science.273.5279.1185.
[3] E. Desurvire, Erbium-Doped Fiber Amplifiers: Principles and Applications, Wiley, New York, 1994.
[4] F. Wang, Y. Han, C.S. Lim, Y. Lu, J. Wang, J. Xu, H. Chen, C. Zhang, M. Hong, X. Liu, Simultaneous phase and size control of upconversion nanocrystals through lanthanide doping, Nature 463 (2010) 1061–1065, http://dx.doi.org/10.1038/nature08777.
[5] X. Huang, S. Han, W. Huang, X. Liu, Enhancing solar cell efficiency: the search for luminescent materials as spectral converters, Chem. Soc. Rev. 42 (2013) 173–201, http://dx.doi.org/10.1039/C2CS35288E.
[6] A. de Pablos-Martin, M. Ferrari, M.J. Pascual, G.C. Righini, Glass-ceramics: a class of nanostructured materials for photonics, Rivista del Nuovo Cimento 38 (2015) 311–369, http://dx.doi.org/10.1393/ncr/i2015-10114-0.
[7] Y. Wang, J. Ohwaki, New transparent vitroceramics codoped with $Er^{3+}$ and $Yb^{3+}$ for efficient frequency upconversion, Appl. Phys. Lett. 63 (1993) 3268–3270, http://dx.doi.org/10.1063/1.110170.
[8] A. de Pablos-Martín, A. Durán, M.J. Pascual, Nanocrystallisation in oxyfluoride systems: mechanisms of crystallisation and photonic properties, Int. Mater. Rev. 57 (2012) 165–186, http://dx.doi.org/10.1179/1743280411Y.0000000004.
[9] P.P. Fedorov, A.A. Luginina, A.I. Popov, Transparent oxyfluoride glass ceramics, J. Fluorine Chem. 172 (2015) 22–50, http://dx.doi.org/10.1016/j.jfluchem.2015.01.009.
[10] M. Sroda, I. Waclawska, L. Stoch, M. Reben, DTA/DSC study of nanocrystallization in oxyfluoride glasses, J. Therm. Anal. Calorim. 77 (2004) 193–200, http://dx.doi.org/10.1023/B:JTAN.0000033203.95251.d6.
[11] S. Tanabe, H. Hayashi, T. Hanada, N. Onodera, Fluorescence properties of $Er^{3+}$ ions in glass ceramics containing $LaF_3$ nanocrystals, Opt. Mater. 19 (2002) 343–349, http://dx.doi.org/10.1016/S0925-3467(01)00236-1.
[12] Z. Hu, E. Ma, Y. Wang, D. Chen, Fluorescence property investigations on $Er^{3+}$-doped oxyfluoride glass ceramics containing $LaF_3$ nanocrystals, Mater. Chem. Phys. 100 (2006) 308–312, http://dx.doi.org/10.1016/j.matchemphys.2006.01.015.
[13] E. Ma, Z. Hu, Y. Wang, F. Bao, J. Lumin, Influence of structural evolution on fluorescence properties of transparent glass ceramics containing $LaF_3$ nanocrystals, J. Lumin. 118 (2006) 131–138, http://dx.doi.org/10.1016/j.jlumin.2005.08.004.
[14] F. Goutaland, P. Jander, W.S. Brocklesby, G.J. Dai, Crystallisation effects on rare earth dopants in oxyfluoride glass ceramics, Opt. Mater. 22 (2003) 383–390, http://dx.doi.org/10.1016/S0925-3467(02)00373-7.
[15] A. Sarakovskis, J. Grube, G. Doke, M. Springis, Excited state absorption and energy-transfer mechanisms of up-conversion luminescence in $Er^{3+}$-doped oxyfluoride glass ceramics at different temperatures, J. Lumin. 130 (2010) 805–811, http://dx.doi.org/10.1016/j.jlumin.2009.11.037.
[16] J.J. Wei, J.W. Li, X.N. Chi Yang, H. Guo, Enhanced green upconversion in $Tb^{3+}$-$Yb^{3+}$ co-doped oxyfluoride glass ceramics containing $LaF_3$ nanocrystals, J. Lumin. 137 (2013) 70–72, http://dx.doi.org/10.1016/j.jlumin.2012.11.017.
[17] A. de Pablos-Martín, D. Ristic, S. Bhattacharyya, T. Höche, G.C. Mather, M.O. Ramírez, S. Soria, M. Ferrari, G.C. Righini, L.E. Bausá, A. Durán, M.J. Pascual, Effects of $Tm^{3+}$ additions on the crystallization of $LaF_3$ nanocrystals in oxyfluoride glasses: optical characterization and up-conversion, J. Am. Ceram. Soc. 96 (2013) 447–457, http://dx.doi.org/10.1111/jace.12120.
[18] S. Ye, B. Zhu, J. Luo, J. Chen, G. Lakshminarayana, J. Qiu, Enhanced cooperative quantum cutting in $Tm^{3+}$-$Yb^{3+}$ codoped glass ceramics containing $LaF_3$ nanocrystals, Opt. Express 16 (2008) 8989–8994, http://dx.doi.org/10.1364/OE.16.008989.
[19] Y. Yu, D. Chen, E. Ma, Y. Wang, Z. Hu, Spectroscopic properties of $Nd^{3+}$ doped transparent oxyfluoride glass ceramics, Spectrochim. Acta A 67 (2007) 709–713.
[20] W.J. Zhang, Q.J. Chen, Q.Y. Zhang, Z.H. Jiang, J. Non-Cryst. Solids 357 (2011) 2278–2281.
[21] N. Hémono, G. Pierre, F. Muñoz, A. de Pablos-Martín, M.J. Pascual, A. Durán, Processing of transparent glass-ceramics by nanocrystallisation of $LaF_3$, J. Eur. Ceram. Soc. 29 (2009) 2915–2920, http://dx.doi.org/10.1016/j.jeurceramsoc.2009.05.013.
[22] A. de Pablos-Martín, N. Hémono, G.C. Mather, S. Bhattacharyya, T. Höche, H. Bornhöft, J. Deubener, F. Muñoz, A. Durán, M.J. Pascual, Effects of $Tm^{3+}$ additions on the crystallization of $LaF_3$ nanocrystals in oxyfluoride glasses: optical characterization and up-conversion, J. Am. Ceram. Soc. 94 (2011) 2420–2428, http://dx.doi.org/10.1111/jace.12120.
[23] A. de Pablos-Martín, M.A. García, A. Muñoz-Noval, G.R. Castro, M.J. Pascual, A. Durán, Analysis of the distribution of $Tm^{3+}$ ions in $LaF_3$ containing transparent glass-ceramics through X-ray absorption spectroscopy, J. Non-Crystal. Solids 384 (2014) 83–87, http://dx.doi.org/10.1016/j.jnoncrysol.2013.07.021.
[24] M. J. Weber, Science and technology of laser glass, J. Non-Cryst. Solids 123 (1990) 208–222, http://dx.doi.org/10.1016/0022-3093(90)90786-L.
[25] R.R. Jacobs, M.J. Weber, Dependence of the $^4F_{3/2} \rightarrow {}^4I_{11/2}$ induced-emission cross section for $Nd^{3+}$ on glass composition, QE, IEEE J. Quantum Electron. QE-12 (1976) 102–111, http://dx.doi.org/10.1109/JQE.1976.1069101.
[26] V. Lavín, I. Iparraguirre, J. Azkargorta, A. Mendioroz, A. Gonzalez-Platas, R. Balda, J. Fernández, Opt. Mater. 25 (2) (2004) 201–208, http://dx.doi.org/10.1016/S0925-3467(03)00270-2.
[27] F. Lahoz, I.R. Martín, U.R. Rodríguez Mendoza, I. Iparraguirre, J. Azkargorta, A. Mendioroz, R. Balda, J. Fernández, V. Lavín, Rare earths in nanocrystalline glass ceramics, Opt. Mater. 27 (2005) 1762–1770, http://dx.doi.org/10.1016/j.optmat.2004.11.047.
[28] J. Pisarska, W. Ryba-Romanowski, G. Dominiak-Dzik, T. Goryczka, W.A. Pisarski, Nd-doped oxyfluoroborate glasses and glass-ceramics for NIR laser applications, J. Alloy Compd. 451 (2008) 223–225, http://dx.doi.org/10.1016/j.jallcom.2007.04.167.
[29] J. Pisarska, W. Ryba-Romanowski, G. Dominiak-Dzik, T. Goryczka, W.A. Pisarski, Near-infrared luminescence of rare earth ions in oxyfluoride lead borate glasses and transparent glass-ceramic materials, Opt Appl. 38 (2008) 211–216.
[30] M. Abril, J. Mendez-Ramos, I.R. Martin, U.R. Rodriguez-Mendoza, V. Lavin, A. Delgado-Torres, V.D. Rodriguez, P. Nunez, A.D. Lozano-Gorrin, Optical properties of $Nd^{3+}$ ions in oxyfluoride glasses and glass ceramics comparing different preparation methods, J. Appl Phys. 95 (2004) 5271–5279, http://dx.doi.org/10.1063/1.1707204.
[31] J. Mendez-Ramos, M. Abril, I.R. Martin, U.R. Rodriguez-Mendoza, V. Lavin, V.D. Rodriguez, P. Nunez, A.D. Lozano-Gorrin, Ultraviolet and visible upconversion luminescence in $Nd^{3+}$-doped oxyfluoride glasses and glass ceramics obtained by different preparation methods, J. Appl. Phys. 99 (2006) 113510, http://dx.doi.org/10.1063/1.2203395 (1-5).
[32] D. Chen, Y. Wang, Y. Yu, Z. Hu, Crystallization and fluorescence properties of $Nd^{3+}$-doped transparent oxyfluoride glass ceramics, Mater. Sci. Eng. B 123 (2005) 1–6, http://dx.doi.org/10.1016/j.mseb.2005.06.008.
[33] Y. Yu, D. Chen, Y. Cheng, Y.Y. Wang, Z. Hu, F. Bao, Investigation on crystallization and influence of $Nd^{3+}$ doping of transparent oxyfluoride glass-ceramics, J. Eur. Ceram. Soc. 26 (2006) 2761–2767, http://dx.doi.org/10.1016/j.jeurceramsoc.2005.05.002.
[34] F. Liu, Y. Wang, D. Chen, Y.L. Yu, Investigation on crystallization kinetics and microstructure of novel transparent glass ceramics containing Nd:$NaYF_4$ nano-crystals, Mater. Sci. Eng. B 136 (2007) 106–110, http://dx.doi.org/10.1016/j.mseb.2006.09.012.
[35] D. Chen, Y.S. Wang, E. Ma, Y. Yu, F. Liu, R.F. Li, Spectroscopic and stimulated emission characteristics of $Nd^{3+}$ in transparent glass ceramic embedding β-$YF_3$ nanocrystals, J. Appl. Phys. 102 (2007) 023504, http://dx.doi.org/10.1063/1.2753690 (1-6).

[36] B.N. Samson, P.A. Tick, N.F. Borrelli, Efficient neodymium-doped glass-ceramic fiber laser and amplifier, Opt. Lett. 26 (2001) 145–147, http://dx.doi.org/10.1364/OL.26.000145.
[37] M.V. Dmitruk, A.A. Kaminskii, Stimulated emission from $LaF^3$ $-Nd^{3+}$ crystal lasers, Soviet Physics JETP 26 (3) (1968) 531–534.
[38] H.H. Caspers, H.E. Rast, R.A. Buchanan, Intermediate coupling energy levels for $Nd^{3+}(^4f_3)$ in $LaF_3$, J. Chem. Phys. 42 (1965) 3214–3217, http://dx.doi.org/10.1063/1.1696401.
[39] J.Q. Hong, L.H. Zhang, P.X. Zhang, Y.Q. Wang, Y. Hang, Growth, optical characterization and evaluation of laser properties of Nd:$LaF_3$ crystal, J. Alloy Compd. 646 (2015) 706–709, http://dx.doi.org/10.1016/j.jallcom.2015.05.172.
[40] T. Ozawa, Kinetic analysis of derivative curves in thermal analysis, J. Thermal. Anal. 2 (1970) 301–324, http://dx.doi.org/10.1007/BF01911411.
[41] K. Matusita, S. Sakka, Kinetic study of crystallization of glass by differential thermal analysis criterion on application of Kissinger plot, J. Non- Cryst. Solids 38-39 (1980) 41–746, http://dx.doi.org/10.1016/0022-3093(80)90525-6.
[42] H.E. Kissinger, Variation of peak temperature with heating rate in differential thermal analysis, J. Res. Nat. Bur. Stand. 57 (1956) 217–221, http://dx.doi.org/10.6028/jres.057.026.
[43] B.D. Cullity, Elements of X-ray Diffraction, Addison-Wesley, Massachusetts, 1978.
[44] J. Ilavsky, P.R. Jemian, Irena: tool suite for modeling and analysis of small-angle scattering, J. Appl. Cryst. 42 (2009) 347–353, http://dx.doi.org/10.1107/S0021889809002222.
[45] M. Sroda, Effect of $Er_2O_3$ on thermal stability of oxyfluoride glass, J. Therm Anal Calorim. 97 (2009) 239–243, http://dx.doi.org/10.1007/s10973-009-0257-3.
[46] I.W. Donald, Crystallisation kinetics of a lithium zinc silicate glass studied by DTA and DSC, J. Non- Cryst. Solids 345-346 (2004) 120–126, http://dx.doi.org/10.1016/j.jnoncrysol.2004.08.007.
[47] Z. Hu, Y. Wang, F. Bao, W. Luo, Crystallization behavior and microstructure investigations on $LaF_3$ containing oxyfluoride glass ceramics, J. Non-Crystal. Solids 351 (2005) 722–728, http://dx.doi.org/10.1016/j.jnoncrysol.2005.01.075.
[48] A. de Pablos-Martín, F. Muñoz, G.C. Mather, C. Patzig, S. Bhattacharyya, J.R. Jinschek, T. Höche, A. Durán, M.J. Pascual, $KLaF_4$ nanocrystallisation in oxyfluoride glass-ceramics, Cryst. Eng. Comm. 15 (2013) 10323–10332, http://dx.doi.org/10.1039/C3CE41345D.
[49] P. Karmakar, A.K. Subudhi, K. Biswas, K. Annapurna, Crystallization kinetics analysis of $BaF_2$ and $BaGdF_5$ nanocrystals precipitated from oxyfluoride glass systems: a comparative study, Thermochim. Acta 610 (2015) 1–9, http://dx.doi.org/10.1016/j.tca.2015.04.019.
[50] A.C. Yanes, J. Del-Castillo, J. Méndez-Ramos, V.D. Rodríguez, M.E. Torres, J. Arbiol, Luminescence and structural characterization of transparent nanostructured $Eu^{3+}$-doped $LaF_3$–$SiO_2$ glass–ceramics prepared by sol–gel method, Opt. Mater. 29 (2007) 999–1003, http://dx.doi.org/10.1016/j.optmat.2006.02.021.
[51] N. Zhao, Wei Nie, Jun Mao, M. Yang, D. Wang, Y. Lin, Y. Fan, Z. Zhao, H. Wei, X. Ji, A general synthesis of high-quality inorganic nanocrystals via a two-phase method, Small 6 (22) (2010) 2558–2565, http://dx.doi.org/10.1002/smll.201001218.
[52] F. Li, C. Li, X. Liu, T. Bai, W. Dong, X. Zhang, Z. Shi, S. Feng, Microwave-assisted synthesis and up-down conversion luminescent properties of multicolor hydrophilic $LaF_3$:$Ln^{3+}$ nanocrystals, Dalton Trans. 42 (2013) 2015–2022, http://dx.doi.org/10.1039/C2DT32295A.
[53] B.R. Judd, Optical absorption intensities of rare-earth ions, Phys. Rev. 127 (1962) 750–761, http://dx.doi.org/10.1103/PhysRev.127.750.
[54] G.S. Ofelt, Intensities of crystal spectra of rare-earth Ions, J. Chem. Phys. 37 (1962) 511–520, http://dx.doi.org/10.1063/1.1701366.
[55] W.T. Carnall, H. Crosswhite, H.M. Crosswhite, Energy Level Structure and Transition Probabilities of the Trivalent Lanthanides in $LaF_3$, Argonne National Laboratory, Argonne, IL, 1977.
[56] S.F. Mason, R.D. Peacock, B. Stewart, Ligand-polarization contributions to the intensity of hypersensitive trivalent lanthanide transitions, Mol. Phys. 30 (1975) 1829–1841, http://dx.doi.org/10.1080/00268977500103321.
[57] P. Nachimuthu, R. Jagannathan, Judd-Ofelt parameters, hypersensitivity, and emission characteristics of $Ln^{3+}$ ($Nd^{3+}$, $Ho^{3+}$, and $Er^{3+}$) ions doped in PbO-$PbF_2$ glasses, J. Am. Soc. 82 (2) (2007) 387–392, http://dx.doi.org/10.1111/j.1551-2916.1999.tb20074.x.
[58] W.F. Krupke, Induced-emission cross sections in neodymium laser glasses, QE, IEEE J. of Quantum Electron. 10 (1974) 450–457, http://dx.doi.org/10.1109/JQE.1974.1068162.

# *PAPER 4*

**Effect of the heat treatment on the spectroscopic properties of $Er^{3+}$-$Yb^{3+}$-doped transparent oxyfluoride nano-glass-ceramics.**

G. Gorni, R. Balda, J. Fernández, L. Pascual, A. Durán, M.J. Pascual.

*J. Lumin*. **193** (2018) 51-60. doi:10.1016/j.jlumin.2017.05.063

Journal of Luminescence 193 (2018) 51–60

Contents lists available at ScienceDirect

Journal of Luminescence

journal homepage: www.elsevier.com/locate/jlumin

# Effect of the heat treatment on the spectroscopic properties of $Er^{3+}$-$Yb^{3+}$-doped transparent oxyfluoride nano-glass-ceramics

G. Gorni[a], R. Balda[b,c,*], J. Fernández[b,c], L. Pascual[d], A. Durán[a], M.J. Pascual[a]

[a] Instituto de Cerámica y Vidrio ICV-CSIC, Madrid, Spain
[b] Departamento de Física Aplicada I, Escuela Superior de Ingeniería, Universidad del País Vasco UPV/EHU, Bilbao, Spain
[c] Centro de Física de Materiales UPV/EHU-CSIC, San Sebastian, Spain
[d] Instituto de Catálisis y Petroleoquímica ICP-CSIC, Madrid, Spain

ARTICLE INFO

*Keywords:*
Glass ceramics
Oxyfluoride
$Er^{3+}/Yb^{3+}$ co-doping
Energy transfer
Upconversion

ABSTRACT

$Er^{3+}$-doped and $Er^{3+}$-$Yb^{3+}$-co-doped transparent oxyfluoride glass-ceramics (GCs) containing $LaF_3$ nano-crystals (NCs) have been prepared by the melting-quenching method and adequate thermal treatments. A detailed structural characterization, performed by X-ray diffraction (XRD) and high resolution transmission electron microscopy (HR-TEM), confirms the precipitation of $LaF_3$ NCs with a size in the 10–15 nm range. The crystal growth is fast in the very beginning, from a few min up to 3–5 h of treatment at 620 °C and then it slows down, up to 20 h. A $SiO_2$ enriched viscous barrier is formed around the NCs, thus preventing further crystal growth. The incorporation of $Er^{3+}$ and $Yb^{3+}$ ions into the NCs is proved by HR-TEM and energy dispersive X-ray spectroscopy (EDXS) analysis. Photoluminescence measurements have been performed upon visible and near infrared excitation. The energy transfer between $Yb^{3+}$ and $Er^{3+}$ ions is evidenced by the enhancement of the near infrared and Up-Conversion (UC) emissions of $Er^{3+}$ ions in the co-doped samples under 980 nm excitation. A moderate back transfer from $Er^{3+}$ to $Yb^{3+}$ ions has been also observed under near infrared excitation of $Er^{3+}$ ions at 800 nm. Upconverted green (($^2H_{11/2}$,$^4S_{3/2}$) → $^4I_{15/2}$) and red ($^4F_{9/2}$ → $^4I_{15/2}$) emissions were observed in all samples and attributed to a two photon process. The strong enhancement of the UC emission for the co-doped glass-ceramics samples further confirms the incorporation of the rare-earth ions in the $LaF_3$ NCs with a lower maximum phonon energy environment which reduces multi-phonon relaxation rates. Different red-to-green emission ratios are obtained depending on the heat treatment conditions for the glass-ceramic samples.

## 1. Introduction

Glass-ceramics have become increasingly important in the last decades because they combine the advantages of glass processing with the good properties of ceramic (or crystalline) materials, such as good mechanical, thermal and optical properties. Paying attention to optical materials for Vis-NIR application, transparent glass-ceramics are very attractive because they allow obtaining an active crystal phase in a glass matrix. In particular, oxide matrices in which low phonon energy (200–500 $cm^{-1}$) fluoride crystals precipitate, commonly known as oxyfluoride glass-ceramics (GCs), have been extensively studied [1–5]. From the pioneering work of Wang and Ohwaki in 1993 [6], concerning the efficient green and red Upconversion (UC) emission in $Er^{3+}$-$Yb^{3+}$ co-doped GCs containing $Pb_xCd_{1-x}F_2$ nano-crystals (NCs), many different fluoride crystal phases have been studied, showing the possibility of effectively improving the luminescence of rare-earth ions (REI) when they are embedded in fluoride NCs.

REI in their most stable oxidation state (3+) show a wide range of intra-band transitions (4f-4f), from UV to NIR, that are weakly affected by the ligand field due to the s an p orbital shielding, as compared for example to noble metals [7,8]. Their emission bands are roughly centred at the same energy in different host materials, glasses or crystals. This property converts them in the most important active ions for technological applications in the Vis-NIR range. Therefore, the continuous research for more efficient REI host materials has become the crucial point for the development of the new generation of optical materials. Even more interesting is the possibility of combining different REI to produce Down-Conversion (DC) and UC processes in which photons of smaller or higher energies are emitted upon absorption of incident photons [9]. Known examples are the DC processes in the $Pr^{3+}$-$Yb^{3+}$ doped materials [10–15] with applications in solar cells for blue to NIR light conversion, or the UC processes for $Er^{3+}$ and $Er^{3+}$-$Yb^{3+}$ ions with bio applications [16–24], where NIR light is used to analyse organic tissues, thanks to its deep penetration, and then

* Corresponding author at: Departamento de Física Aplicada I, Escuela Superior de Ingeniería, Universidad del País Vasco UPV/EHU, Bilbao, Spain.
*E-mail address:* rolindes.balda@ehu.eus (R. Balda).

http://dx.doi.org/10.1016/j.jlumin.2017.05.063
Received 26 April 2017; Received in revised form 19 May 2017; Accepted 23 May 2017
Available online 24 May 2017

converted into visible light. Further applications of UC materials can be found in the field of optical amplification and lasers [25–28].

Among different fluoride crystal phases, those containing REI such as $Gd^{3+}$ and $La^{3+}$ that show neither Vis nor NIR emission bands [29–31], offer the possibility of easily exchanging the REI of the host by those used as dopants due to their similar size and electronic configuration.

In a previous work performed by our group [32], describing $Nd^{3+}$ doped $LaF_3$ GCs, the $Nd^{3+}$ migration to the fluoride crystals was showed; using a selective excitation it was possible to select $Nd^{3+}$ ions embedded in the $LaF_3$ crystals, this leading to a highly improved luminescence efficiency and similar emission spectra to those obtained for pure $Nd^{3+}$ doped $LaF_3$ crystals. In this paper, both structural and optical results of bulk glasses and GCs containing $LaF_3$ crystals doped with $Er^{3+}$ and co-doped with $Yb^{3+}$ for NIR and UC emission are presented. There is abundant literature regarding $Er^{3+}$ and $Er^{3+}$-$Yb^{3+}$ doped $LaF_3$ materials, nevertheless, most of them refer to powders or nanoparticles dispersed in liquid phase [24,33–39] and only a very few are related to bulk or bulk-derived GCs [40–42]. The development of inorganic bulk materials with excellent luminescence properties and high ability to transmit light is useful for many optoelectronics applications such as solid state lasers, optical amplifiers, and sensors among others.

## 2. Experimental

### 2.1. Materials preparation

Glasses of composition $55SiO_2$-$20Al_2O_3$-$15Na_2O$-$10LaF_3$ (55Si-10La) doped with $0.5Er^{3+}$, $0.5Er^{3+}$-$2Yb^{3+}$ and $0.5Er^{3+}$-$4Yb^{3+}$ (mol %) have been prepared by the melting-quenching technique using as raw materials: $SiO_2$ (Saint-Gobin 99.6%), $Al_2O_3$ (Panreac), $Na_2CO_3$ (Sigma Aldrich, > 99.5%), $LaF_3$ (Alfa Aesar, 99.9%), $ErF_3$ (Alfa Aesar, 99.99%) and $YbF_3$ (Alfa Aesar, 99.99%). The batches were calcined at 1200 °C for 2 h, melted at 1650 °C for 1.5 h and then quenched onto a brass mould. The batches were melted again for 30 min and then quenched onto a cold brass mould to improve glass homogeneity. An annealing process at 600 °C for 30 min was performed on the as made glasses to eliminate residual stresses. In the following, glass samples will be labelled by G0.5, G0.5-2, G0.5-4 for $Er^{3+}$ and $Yb^{3+}$ concentrations equal to 0.5, 0.5-2 and 0.5-4, respectively, while corresponding glass-ceramics will be denoted with GC0.5, GC0.5-2 and GC0.5-4. Glass-ceramics samples have been obtained upon heat treatments of glass pieces at 620 °C-from 5 min up to 80 h and at 660 °C-20 h, using a heating rate of 10 °C/min in all cases. Glass sheets (1 cm × 1 cm × 2 mm) were treated at 620 °C-20 h and 40 h and at 660 °C-20 h and then polished for optical characterization. One glass sheet of each composition was polished but not heat treated. In this way it was possible to compare the as made glasses with the corresponding GCs, allowing to evaluate the influence of the treatment time/temperature (for a fixed temperature/time) onto the optical properties.

The density of samples was measured by the Archimedes's method using distilled water as liquid.

### 2.2. Thermal and dilatometric characterization

Small glass specimens (15 mm × 5 mm × 5 mm) were cut and analysed by dilatometry (Netzsch DIL 402 PC) using a heating rate of 5 °C/min. By a linear fit of the curve in the range 100–450 °C the dilatometric expansion coefficient α was obtained. The glass transition temperature ($T_g$) and the dilatometric softening point ($T_d$) were also obtained. Differential thermal analysis (SDT Q600 – TA Instruments) was performed on bulk specimens in the range 25–1000 °C using 20–30 mg of glass with particle size in the range 1–1.25 mm. DTA curves were obtained with heating rates of 10 °C/min.

### 2.3. Structural characterization

Bulk glass specimens were treated in the range 620–660 °C from 5 min up to 80 h to convert them into GC samples and then milled and sieved to a particle size lower than 60 μm and analysed by XRD (Bruker D8 Advance) in the range 10–70° with a step size of 0.02°. Peak fit was performed using the Pseudo-Voigt function and the crystal size was estimated using the Scherrer's equation:

$$D = \frac{0.94\lambda}{\cos\theta\sqrt{B_m^2 - B_i^2}} \quad (1)$$

where λ is the wavelength (1.54056 Å – CuKα$_1$), $B_m$ the full width half maximum of the $LaF_3$ peak (111) and θ its diffraction angle. The constant factor 0.94 is assumed considering spherical crystals. The instrumental broadening $B_i$ has been also taken into account.

High resolution transmission electron microscopy (HRTEM) data as well as scanning transmission electron microscopy-high angle annular dark field (STEM-HAADF) images and X-ray energy dispersive spectra (EDXS) were recorded on a JEOL TEM/STEM 2100F field emission gun transmission electron microscope operating at 200 kV and equipped with an EDXS spectrometer Oxford INCA X-sight system. XEDS analysis was performed in STEM mode. Small amounts of powders were dissolved in ethanol and then a drop was deposited onto a copper grid supporting a lacey carbon film.

### 2.4. Optical characterization

UV–Vis absorption spectra were collected in the range 300–1700 nm using a double beam spectrophotometer (Perkin Elmer LAMBA 950).

The steady-state emission measurements were made with a Ti-sapphire ring laser (0.4 $cm^{-1}$ linewidth) and an Argon laser as exciting light. The fluorescence was analysed with a 0.25 monochromator, and the signal was detected by an extended IR Hamamatsu H10330A-75 photomultiplier and finally amplified by a standard lock-in technique. Visible emission was detected by a Hamamatsu R636 photomultiplier. Lifetime measurements were obtained by exciting the samples with a Ti-sapphire laser pumped by a pulsed frequency doubled Nd:YAG laser (9 ns pulse width), and detecting the emission with Hamamatsu H10330A-75 photomultiplier. Data were processed by a Tektronix oscilloscope. All measurements were performed at room temperature.

## 3. Results and discussion

### 3.1. Glasses and GCs

Glasses and GCs perfectly transparent of all the compositions were successfully obtained after the thermal treatments. A little bluish color is observed for 0.5–4 glass and GC samples, related to light scattering produced by phase separation and crystallization due to higher dopants concentration. Anyway good transparency is still maintained, as shown in Section 3.4.1, with a slight increase in the absorption edge around 400 nm.

### 3.2. Thermal and dilatometric characterization

Dilatometric measurements showed that $Er^{3+}$ doped glass has $T_g$ around 596 °C (598 °C for the un-doped glass) while in co-doped samples $T_g$ diminishes down to 587 °C. This behaviour is likely associated to a higher fluorine content in the co-doped samples, this decreasing $T_g$. The dilatometric softening point $T_d$ diminishes from 670 °C to 656 °C when increasing $Yb^{3+}$ content, but the dilatometric expansion coefficient α is around 9.2 × $10^{-6}$ $m^{-1}$ for all the glasses, practically independent of $Yb^{3+}$ content. The transition and crystallization temperatures were determined by DTA analysis. The crystal-

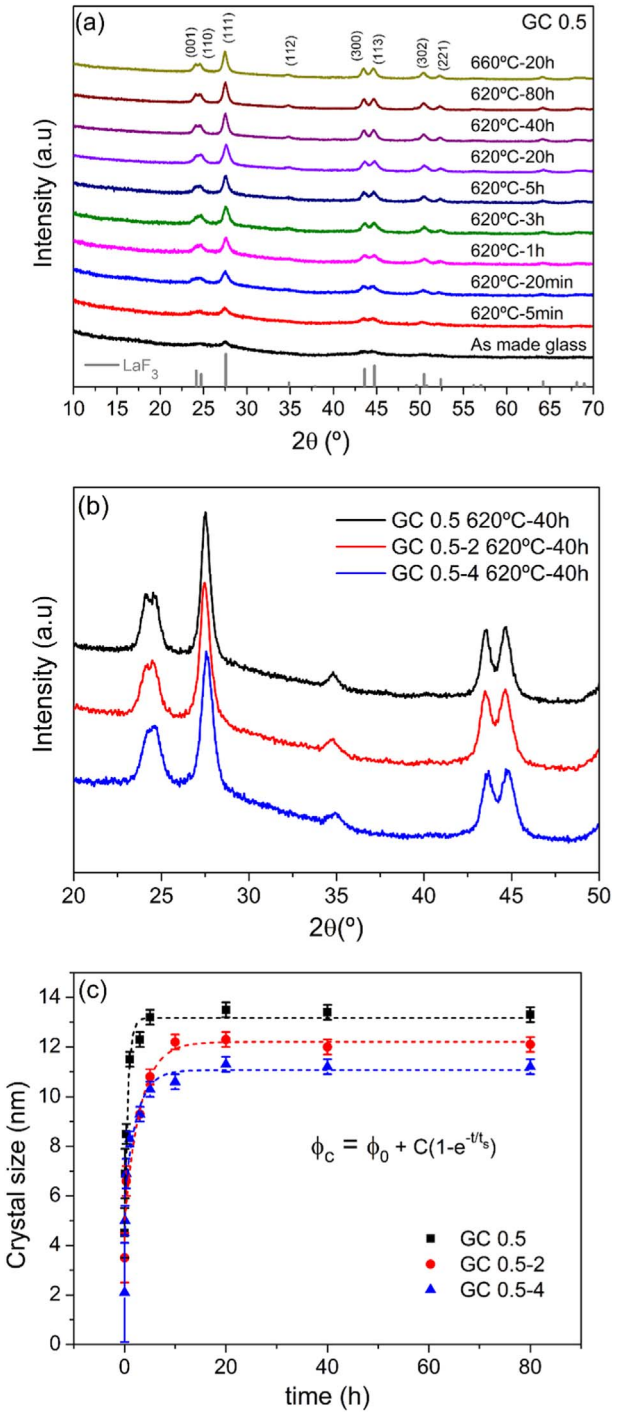


**Fig. 1.** (a) XRD diffractograms for glass and GCs samples doped with 0.5Er and treated at 620 °C during 5 min up to 80 h and treated at 660 °C-20 h. $LaF_3$ reference peaks are indicated (bottom). (b) XRD of GCs 620 °C-40 h for the three compositions. (c) Crystal size and fitting with the exponential asymptotic function of the initial glass and GCs treated at 620 °C from 5 min up to 80 h.

lization stability parameters $T_p$-$T_g$, where $T_p$ is the $LaF_3$ crystallization peak temperature, changes from 105 °C for the un-doped glass to 100 °C for $Er^{3+}$ single doped sample to 79 °C for co-doped ones. This indicates a higher crystallization tendency with the increase of dopant concentration. Similar results using $Nd^{3+}$ were deeply discussed in a previous work and support these conclusions [32]. In fact, it was observed that the stability parameter changed from 100 °C to 80 °C passing from 0.1 to 2 mol% of $Nd^{3+}$.

### 3.3. Structural characterization

#### 3.3.1. XRD and crystals size

Fig. 1(a) shows XRD of $Er^{3+}$ singly doped and $Er^{3+}$-$Yb^{3+}$ co-doped GC samples. It is confirmed that only $LaF_3$ precipitates in the glass matrix (JCPDS 00-032-0483). Diffractograms for heat treatment at 620 °C-40 h are compared for the three compositions 0.5, 0.5–2 and 0.5–4 in Fig. 1(b). It can be seen that passing from $Er^{3+}$ doped sample to co-doped ones the diffraction peaks become broader as a consequence of the smaller crystal size. In particular, less resolved diffraction doublets appear around 22° and the most intense peak at 27.5°, corresponding to $LaF_3$ (111) reflection, clearly showing an increase in the FWHM. Such broadening effects could be also associated to $LaF_3$ deformation as a consequence of the inclusion of doping ions ($Er^{3+}$ and $Yb^{3+}$) smaller than $La^{3+}$ ions in the crystals.

The variation of crystal size as a function of treatment time at 620 °C (Fig. 1(c)) indicates that crystal growth rate is almost linear at the very beginning, from 5 min up to 3–5 h, and then it stabilizes to a constant value due to formation of a viscous barrier around crystals. Crystal growth can be described by the following empirical law:

$$\phi_c = \phi_0 + C\left(1 - e^{-t/t_s}\right) \quad (2)$$

Here $\phi_0$ is the crystal size without thermal treatment, i.e corresponding to the small crystalline domains in the as made glass, the second part describing an exponential growth with asymptotic behaviour. $t_s$ could be associated to the starting time for the formation of a viscous barrier around the crystals. For $t$ much smaller than $t_s$ the crystal growth rate proceed linearly with the treatment time, but when $t$ approaches to $t_s$ the crystal growth rate suddenly decreases up to totally stop; further treatment time does not affect the crystal size.

A similar relation was proposed by Rüssel et al. [43] studying $CaF_2$ oxyfluoride GCs to describe the increase of $T_g$ that runs parallel with the increase of crystals quantity. They showed that $CaF_2$ crystals did not grow with the treatment time, but they considered a range of times from 10 up 80 h in the long time scale. Instead, we have extended the analysis to the very beginning of the crystal growth, just from 5 min up to 3 h of treatment.

Although the crystal size is not affected by increasing the treatment time (for long time of treatment), the crystal fraction can indeed increase. Furthermore, the increase of the treatment time influences the REI diffusion inside the fluoride NCs, as confirmed by studies about REI concentration incorporated in $LaF_3$ NCs [44]. After fitting, $C$ parameters equal to 7.8 nm, 7.1 nm and 5.6 nm are obtained for GC0.5, GC0.5-2 and GC0.5-4. This suggests that the crystal growth rate is delayed when increasing the $Yb^{3+}$ content. Moreover, the crystal size is influenced by the increase of co-dopants. In fact, as $Yb^{3+}$ content increases the crystals size corresponding to long heat treatment (> 20 h) stabilizes to a smaller value. The effect of $Yb^{3+}$ on the $LaF_3$ crystallization was studied in a previous work by Chen et al. [45] concluding that the smaller ionic radius of $Yb^{3+}$ causes a reduction in the lattice parameters with consequents deformations and tensions that justifies that the final crystals size decreases.

Increasing the treatment temperature up to 660 °C during 20 h, bigger crystals are formed which size increases up to 14–15 nm (not shown). However, for all compositions the crystal size is quite small, less than 50 nm, and therefore the optical transparency of all the GC samples is maintained. Heat treatments at temperatures higher than 660 °C were not useful for practical purpose due to the glass softening, as described in Section 3.1.

#### 3.3.2. Densities of glasses and GCs

Fig. 2 shows the density together with the crystallinity, calculated by the XRD peak area of (001), (110) and (111) diffraction peaks in the 2θ range 22–30°, of glass and GCs treated at 620 °C during 20 and 40 h. Errors bars are included in the symbols size. Co-doped glass and GCs

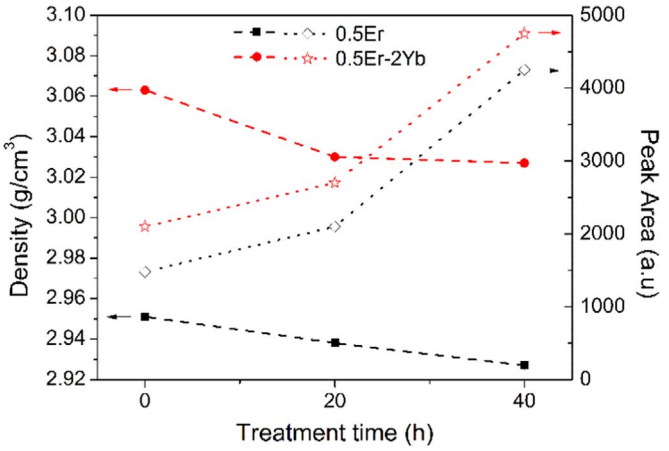


**Fig. 2.** Density (filled symbols) and XRD peak area (empty symbols) of initial glass and GCs treated at 620 °C during 20 and 40 h. The connexion lines are guides for the eye.

have higher density than $Er^{3+}$ singly doped samples due to co-doping with $Yb^{3+}$, heavier than $Er^{3+}$. However, for both compositions the density decreases with the increase of $LaF_3$ crystal fraction, passing from 2.95 g/cm$^3$ to 2.93 g/cm$^3$ for the 0.5 doped samples and from 3.06 g/cm$^3$ to 3.03 g/cm$^3$ for the 0.5-2 co-doped ones. Similar behaviour was observed for 0.5-4 samples, with densities higher than the other compositions. This phenomenon was also observed by Bocker et al. [46] and by Biswas et al. [47] studying GCs containing $BaF_2$ crystals. They concluded that the decrease in density can be attributed to an increase in the number of non-bridging oxygen in the glass matrix upon $BaF_2$ NCs formation followed by an expansion of overall glass network.

### 3.3.3. HRTEM

Microstructural characterization of glass and GC samples was performed by HRTEM and related STEM-HAADF along with EDXS analysis. Fig. 3 shows representative TEM micrographs of G0.5 (a) and G0.5-2 (b) glass samples with a clear formation of phase separation droplets. Particle size distribution of the droplets is also presented in the inset of Fig. 3, showing mean values of 26 nm and 30 nm, respectively.

In the case of the GC samples (Fig. 4(a) GC0.5 and (b) GC0.5-2), phase separation droplets are also observed for both samples, but some features must be highlighted. Firstly, the particle size distribution of the phase separation droplets was also determined (see the inset of Fig. 4(a) and (b)), and distributions can be fitted to a Gaussian in both samples with mean values of 41 nm and 30 nm and a FWHM of 17 nm and 10 nm, respectively. On the other side, NCs around 10 nm size develop inside the droplets, more evident in the case of the co-doped sample. The $LaF_3$ Tysonite type phase was identified from the interplanar distances measured in the HRTEM micrograph and in the DDP (Digital diffraction pattern) of one NC shown in Fig. 4(c) and (d).

Regarding the chemical composition of the droplets in the GC samples, several EDXS scan analyses were performed in STEM mode. The EDXS line scan spectra of two droplets of Fig. 5(a) and (b) indicate an enrichment of RE and fluorine inside the droplets, together with an increment of the Si concentration just at the interphase of the droplets. Thus, the local composition of the glass matrix is therefore affected by the phase separation and crystallization. As a consequence, the formation of a $SiO_2$ enriched shell that surrounds the droplets inhibits the crystal growth despite the thermal treatment, as it was previously observed [32,48]. Moreover, the presence of Al in the droplets could act as a second viscous barrier that allows the growth of several separate and independent crystals instead of one bigger crystal.

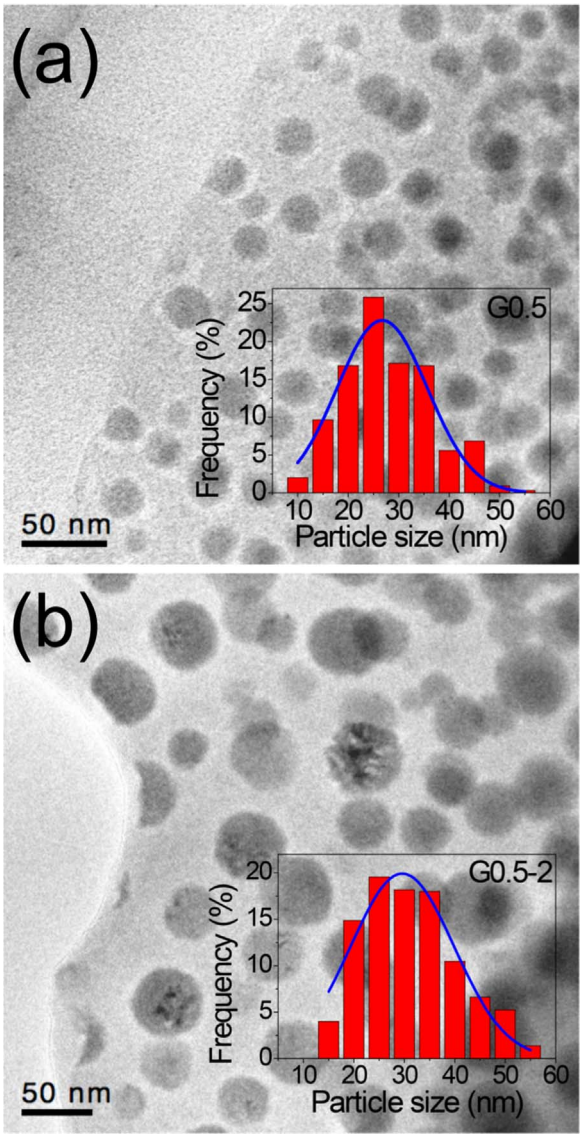


**Fig. 3.** TEM micrographs of (a) G0.5 and (b) G0.5-2 doped glass samples and its corresponding particle size distribution.

## 3.4. Optical characterization

### 3.4.1. UV–Vis–NIR absorption

UV–Vis absorption spectra for glass and GC 620 °C-40 h samples are shown in Fig. 6(a) and (b), respectively. All the bands are associated to the $RE^{3+}$ ions 4f–4f transitions from the ground state to the excited ones. From the left, the following $Er^{3+}$ ($^4I_{15/2}$) transitions can be associated: 377 nm ($^4G_{11/2}$), 406 nm ($^2H_{9/2}$), 450 nm ($^4F_{5/2}$), 487 nm ($^4F_{7/2}$), 520 nm ($^2H_{11/2}$), 541 nm ($^4S_{3/2}$), 651 nm ($^4F_{9/2}$), 797 nm ($^4I_{9/2}$), 976 nm ($^4I_{11/2}$) and 1530 nm ($^4I_{11/2}$). In $Yb^{3+}$ co-doped samples the strong absorption band of $Yb^{3+}$ ions at 980 nm ($^2F_{7/2}$-$^2F_{5/2}$) overlaps and hides the weak NIR transition of $Er^{3+}$ ions at 976 nm.

For 0.5-4 samples, the absorption edge is shifted to longer wavelengths. This is likely due to higher Rayleigh scattering, consequent to a more pronounced phase separation and crystallization tendency of this glass composition.

### 3.4.2. NIR luminescence

The NIR emission spectra of the $Er^{3+}$ and $Er^{3+}/Yb^{3+}$ co-doped samples have been obtained in the 900–1700 nm spectral range by exciting at different wavelengths in resonance with the $^4I_{9/2}$ ($Er^{3+}$) and $^4I_{11/2}$($Er^{3+}$)-$^2F_{5/2}$($Yb^{3+}$) levels. Fig. 7 shows the fluorescence spectra

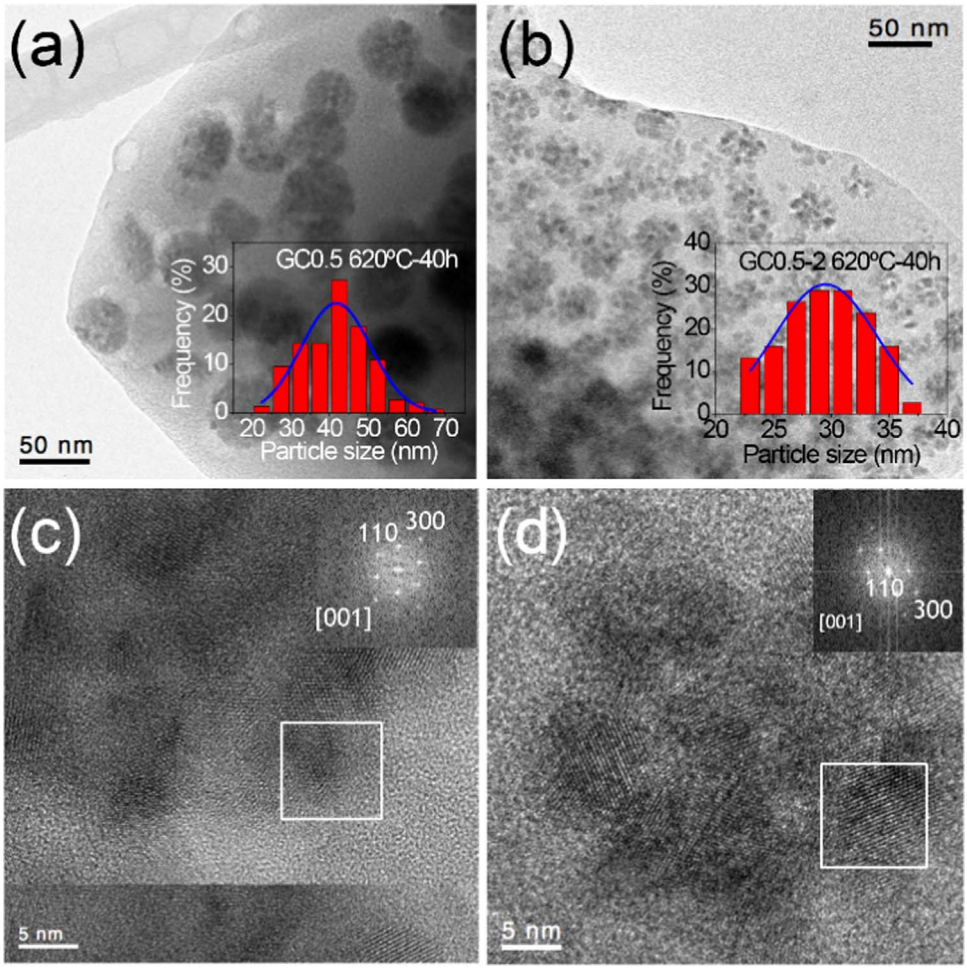


**Fig. 4.** TEM micrographs of (a) GC0.5 and (b) GC0.5-2 samples treated at 620 °C-40 h and its corresponding particle size distribution. (c) and (d) HRTEM of one droplet showing NCs and DDP of one $LaF_3$ crystallite along [001] zone axis.

for the $Er^{3+}$ single doped and $Yb^{3+}$ co-doped glass and GC samples obtained by exciting at 800 nm in resonance with the $^4I_{9/2}$ ($Er^{3+}$) level. After excitation of this level, the next lower levels are populated by multi-phonon relaxation. The spectra of the single doped samples show a weak emission corresponding to the $^4I_{11/2} \rightarrow {}^4I_{15/2}$ transition together with the $^4I_{13/2} \rightarrow {}^4I_{15/2}$ emission. The spectra of the GC samples show a better resolved structure for the $^4I_{11/2} \rightarrow {}^4I_{15/2}$ emission together with a significant increase of the $^4I_{11/2} \rightarrow {}^4I_{15/2}$ and $^4I_{13/2} \rightarrow {}^4I_{15/2}$ emission intensities which suggests the incorporation of $Er^{3+}$ in the NCs. In the case of the co-doped samples (Fig. 7(b) and (c)) the spectra show, in addition to the $Er^{3+}$ emissions, those corresponding to the $^2F_{5/2} \rightarrow {}^2F_{7/2}$ transition of $Yb^{3+}$. The presence of the $Yb^{3+}$ emission around 1000 nm indicates that an energy transfer from $Er^{3+}$ to $Yb^{3+}$ ions takes place.

Fig. 8 shows the emission spectra obtained for the same set of samples under 980 nm excitation allowing the simultaneous population of the $^4I_{11/2}$ ($Er^{3+}$) and $^2F_{5/2}$ ($Yb^{3+}$) levels. As observed, the peak position (~ 1530 nm) and linewidth (~ 62 nm) of the $^4I_{13/2} \rightarrow {}^4I_{15/2}$ ($Er^{3+}$) emission are similar for all samples but the fluorescence intensity increases after the heat treatment. Moreover, compared to the single doped sample, the addition of $Yb^{3+}$ leads to a further increase of the 1530 nm emission of $Er^{3+}$. As just observed in the absorption spectra, the introduction of $Yb^{3+}$ ions increases the optical absorption at 980 nm, which in turns increases the population of level $^4I_{11/2}$ due to the energy transfer from $Yb^{3+}$ to $Er^{3+}$, and consequently the emission from level $^4I_{13/2}$. The energy transfer from $Yb^{3+}$ to $Er^{3+}$ is also confirmed by the emission spectra obtained under 890 nm excitation where only $Yb^{3+}$ ions absorb.

The spectra in Fig. 9 show, in addition to the $Yb^{3+}$ emission, the $^4I_{13/2} \rightarrow {}^4I_{15/2}$ ($Er^{3+}$) band which confirms that an efficient $Yb^{3+} \rightarrow Er^{3+}$ energy transfer takes place.

The temporal evolution of the luminescence from $^4I_{13/2}$ level has been obtained for all samples under excitation at 800 nm. In all the cases, the experimental decays can be described, to a good approximation, by a single exponential function. The lifetime increases from 5.8 ms in the glass samples to 6.9 ms in the GCs treated at 660 °C-20 h and co-doped with 4 mol% of $YbF_3$ which suggests a fluorine environment for $Er^{3+}$ ions in the GC samples according with their incorporation in the NCs. As an example Fig. 10 shows the experimental decays for the single doped samples.

### 3.4.3. *Visible emissions under VIS and NIR excitations*

The visible emission spectra of $Er^{3+}$ ions in the 500–700 nm range have been obtained for all samples by exciting at 488 nm in resonance with the $^4I_{15/2} \rightarrow {}^4F_{7/2}$ transition. The excitation of the $^4F_{7/2}$ level is followed by non-radiative multi-phonon relaxation which populates the next lower levels. Fig. 11 shows the emission spectra for the single and co-doped samples. The spectra consist of three bands centred around 525, 540, and 660 nm corresponding to the $^2H_{11/2}, {}^4S_{3/2}, {}^4F_{9/2} \rightarrow {}^4I_{15/2}$ transitions, respectively. As observed, the main emission corresponds to the green one associated to the $(^2H_{11/2}, {}^4S_{3/2}) \rightarrow {}^4I_{15/2}$ thermalized transitions. The emission intensity increases significantly with the thermal treatments and the bands are better resolved in the GC samples in agreement with the incorporation of $Er^{3+}$ ions into the crystalline phase. It can be also observed that the ratio between the red (630–690 nm) and green (500–570 nm) emission intensities is very

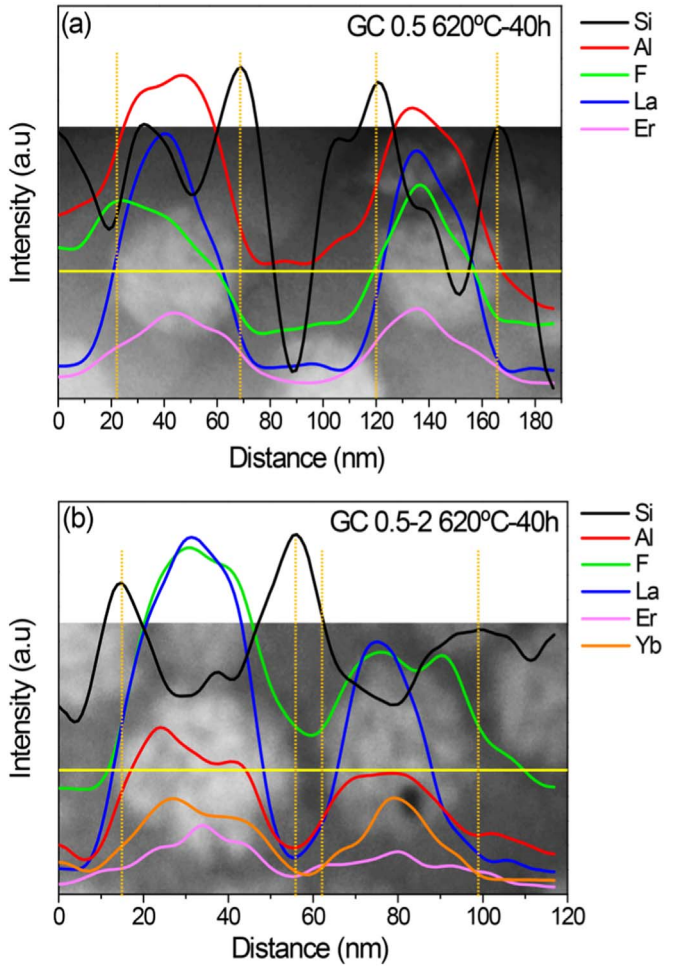


**Fig. 5.** STEM-HAADF image and EDXS line scan along 2 droplets in (a) GC0.5 and (b) GC0.5-2 samples treated at 620 °C-40 h.

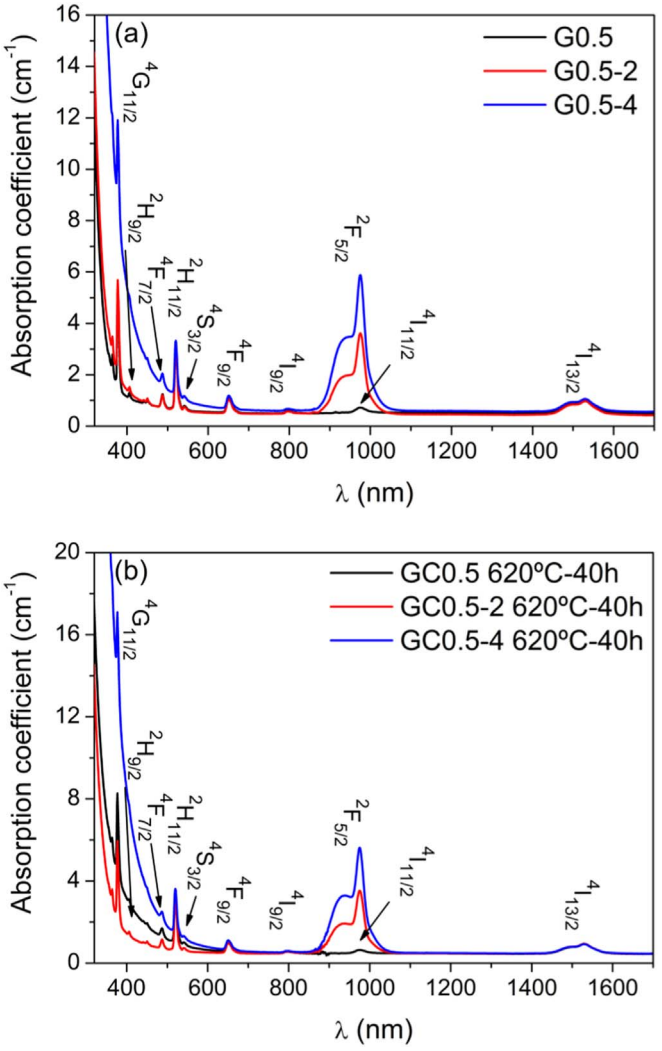


**Fig. 6.** UV–Vis–NIR absorption spectra for (a) glasses and (b) GCs 620 °C-40 h of all the three studied compositions.

small (≈ 0.05) and practically independent on the $Yb^{3+}$ co-doping and thermal treatment which indicates that the population of this level is due to multi-phonon relaxation from level $^4S_{3/2}$.

NIR-to-visible Upconverted luminescence has been observed by the naked eye under continuous wave excitation at 980 nm in resonance with the $^4I_{11/2}$ ($Er^{3+}$) and $^2F_{5/2}$ ($Yb^{3+}$) levels. As observed in Fig. 12 the UC emission spectra show the green ($^2H_{11/2}$,$^4S_{3/2}$) → $^4I_{15/2}$ and red $^4F_{9/2}$ → $^4I_{15/2}$ emissions as in the case of 488 nm excitation. The emission bands are better resolved and the intensity is higher in the heat-treated samples which confirms the incorporation of $Er^{3+}$ ions in the NCs with a lower phonon energy environment which reduces multi-phonon relaxation rates. In addition, the red-to-green emission ratio, which is 0.05 in the single doped samples under 488 nm excitation (Fig. 11(a)) increases to 0.5 under 980 nm (Fig. 12(a)) pumping wavelength suggesting the existence of additional mechanisms to populate $^4F_{9/2}$ ($Er^{3+}$) level.

The UC emission intensity is greatly enhanced by the presence of $Yb^{3+}$ ions (Fig. 12 (b),(c)), which suggests the existence of an effective $Yb^{3+}$ to $Er^{3+}$ energy transfer process. The most intense UC emission is observed for the co-doped GC0.5-2 sample treated at 660 °C-20 h. As in the case of the one photon emission, higher $Yb^{3+}$ concentration does not lead to an increase in the $Er^{3+}$ luminescence. This may be due to energy migration among $Yb^{3+}$ ions and/or to energy transfer to quencher centres [49,50]. Moreover, as can be observed in Fig. 12(b) and (c), the ratio between the red (from 630 to 690 nm) and green (from 500 to 570 nm) emissions, which is 0.5 in the single doped samples, increases to 1.6 (0.5Er-2Yb) and 1.5 (0.5Er-4Yb) for the co-doped samples treated at 620 °C-20 h, to 1.8 (0.5Er-2Yb) and 1.3 (0.5Er-4Yb) for the heat treatment at 620 °C-40 h and decreases down to 0.8 (0.5Er-2Yb) and 0.5 (0.5Er-4Yb) when these samples are treated at 660 °C-20 h. The higher red to green UC emission ratio in the co-doped samples treated at 620 °C compared to the samples treated at 660 °C could be related with the different crystal sizes of the NCs in the GC samples [51]. As mentioned in Section 3.3.1, the presence of $Yb^{3+}$ induces a reduction of the lattice parameters as well as of the size of the crystals. An increase of the treatment temperature up to 660 °C during 20 h, leads to the formation of bigger crystals and thus to a reduction of the red-to-green emission ratio. The decrease of the red-to-green emission ratio with increasing NCs size has been previously observed in other systems [51,52].

To determine the excitation mechanisms involved in the population of the $^4S_{3/2}$ and $^4F_{9/2}$ levels after 980 nm excitation, Upconverted green and red emission intensities at 540 and 660 nm were measured at different pumping powers. It is known that the UC emission intensity ($I_{up}$) depends on the incident pump power ($P_{pump}$) according to the relation $I_{up} \propto (P_{pump})^n$, where $n$ is the number of photons involved in the pumping mechanism. As an example, Fig. 13 shows the logarithmic plot of the Upconverted green and red emission intensities as a function of the pump power laser intensity for the co-doped sample with 2 mol% of $YbF_3$ treated at 660 °C-20 h. As can be seen the dependence is nearly quadratic with 1.89 and 1.85 slopes for the green and red emissions respectively which indicates that a two photon (TP) UC process populates levels $^4S_{3/2}$ and $^4F_{9/2}$.

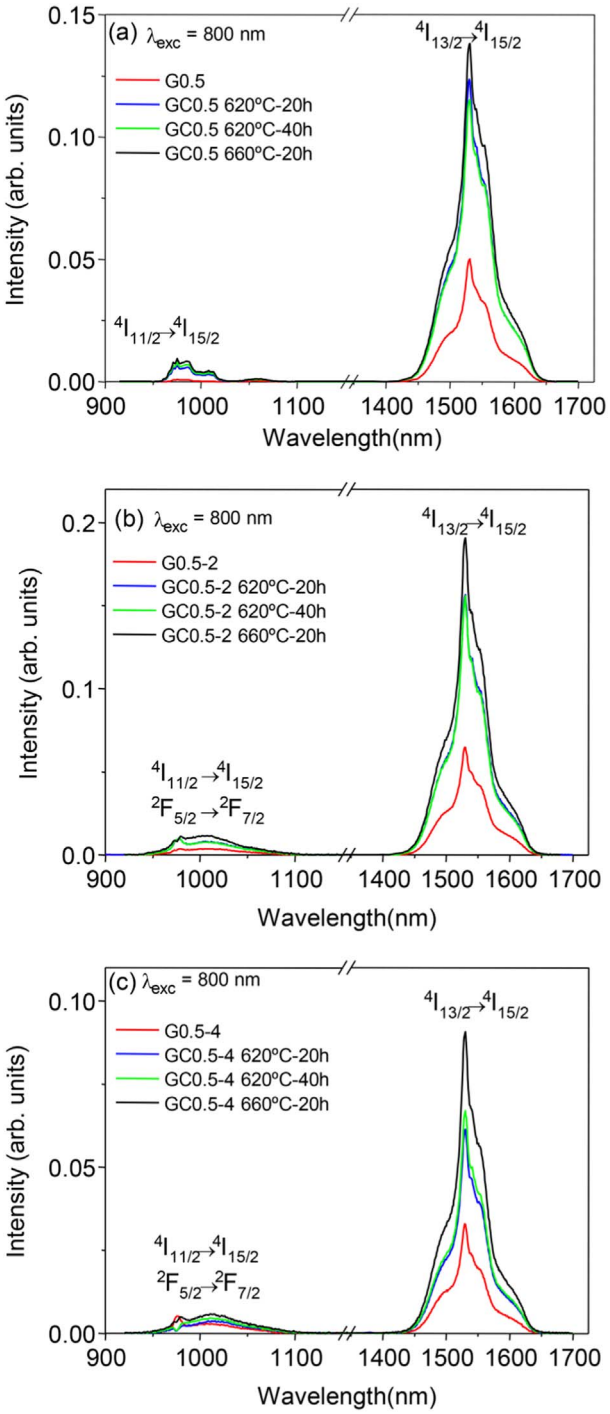


**Fig. 7.** Room temperature emission spectra of (a) 0.5% $Er^{3+}$ single doped glass and glass-ceramic samples, (b) 0.5% $Er^{3+}$-2%$Yb^{3+}$ and (c) 0.5% $Er^{3+}$-4%$Yb^{3+}$ co-doped glass and glass-ceramic samples obtained by exciting at 800 nm. The details of the different thermal treatments of the ceramic samples are also shown.

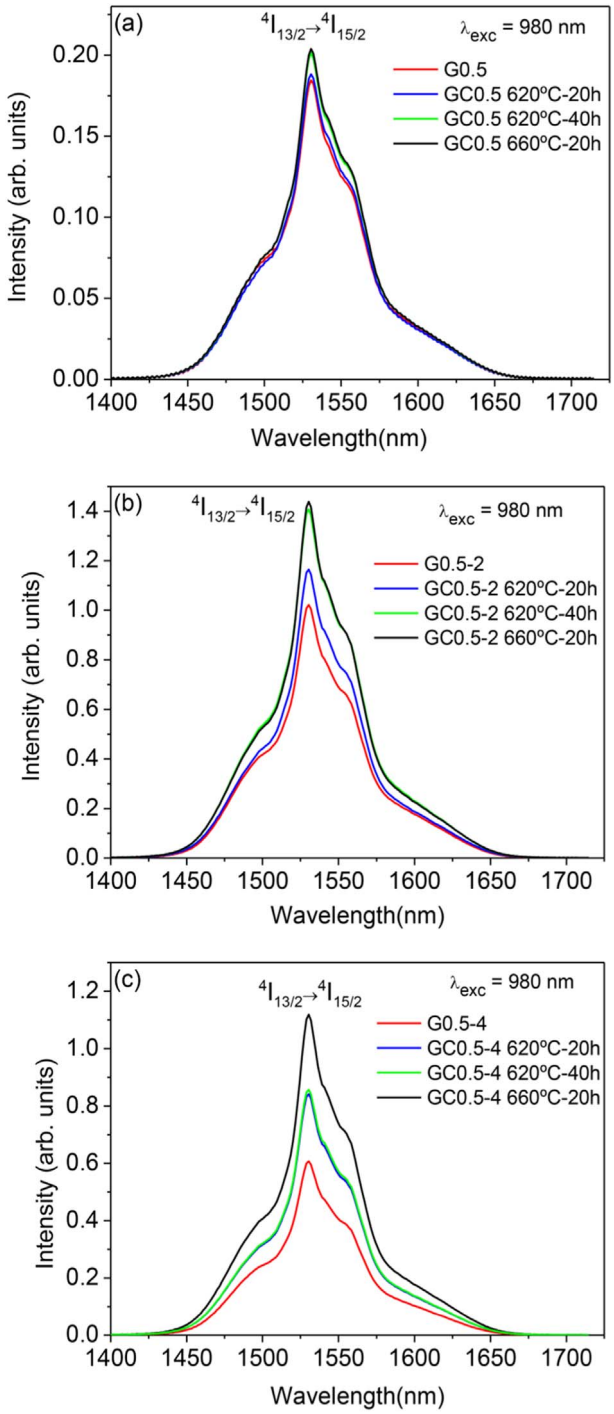


**Fig. 8.** Room temperature emission spectra of (a) 0.5% $Er^{3+}$ single doped glass and glass-ceramic samples, (b) 0.5% $Er^{3+}$-2%$Yb^{3+}$ and (c) 0.5% $Er^{3+}$-4%$Yb^{3+}$ co-doped glass and glass-ceramic samples obtained by exciting at 980 nm.

As it is well known under the 980 nm laser excitation, the $Er^{3+}$ ions are excited to the $^4I_{11/2}$ state by ground state absorption and by resonant energy transfer from the $Yb^{3+}$ ions through the ($^2F_{5/2} \rightarrow {}^2F_{7/2}$) ($Yb^{3+}$); ($^4I_{15/2} \rightarrow {}^4I_{11/2}$) ($Er^{3+}$) process (ET1) (See Fig. 14). Following this process, subsequent energy transfer from another $Yb^{3+}$ ion in the $^2F_{5/2}$ excited state can populate the $^4F_{7/2}$ state of $Er^{3+}$ ions (ET2). This process is dominant in the co-doped samples due to the larger absorption cross-section of the $^2F_{5/2}$ excited state of $Yb^{3+}$ compared with the $^4I_{11/2}$ excited state of $Er^{3+}$. The populated $^4F_{7/2}$ level may relax non-radiatively to the lower $^2H_{11/2}$ and $^4S_{3/2}$ levels, which produces the green emission.

In the single doped samples, the $Er^{3+}$ ions in the $^4I_{11/2}$ level can be excited to the $^4F_{7/2}$ state by excited state absorption (ESA) of a second infrared pump photon and/or by energy transfer Upconversion (ETU) process involving ($^4I_{11/2} \rightarrow {}^4I_{15/2}$) ($Er^{3+}$); ($^4I_{11/2} \rightarrow {}^4F_{7/2}$) ($Er^{3+}$) transitions. The population of the $^4I_{11/2}$ level increases with $Yb^{3+}$ co-doping as a result of the energy transfer from $Yb^{3+}$ ($^2F_{5/2}$) to $Er^{3+}$ ($^4I_{11/2}$). As a consequence, the probabilities of an ESA and/or ETU processes from the populated $^4I_{11/2}$ level are higher in the co-doped glasses than those in the $Er^{3+}$ single doped samples.

Concerning the red emission from level $^4F_{9/2}$, as mentioned before,

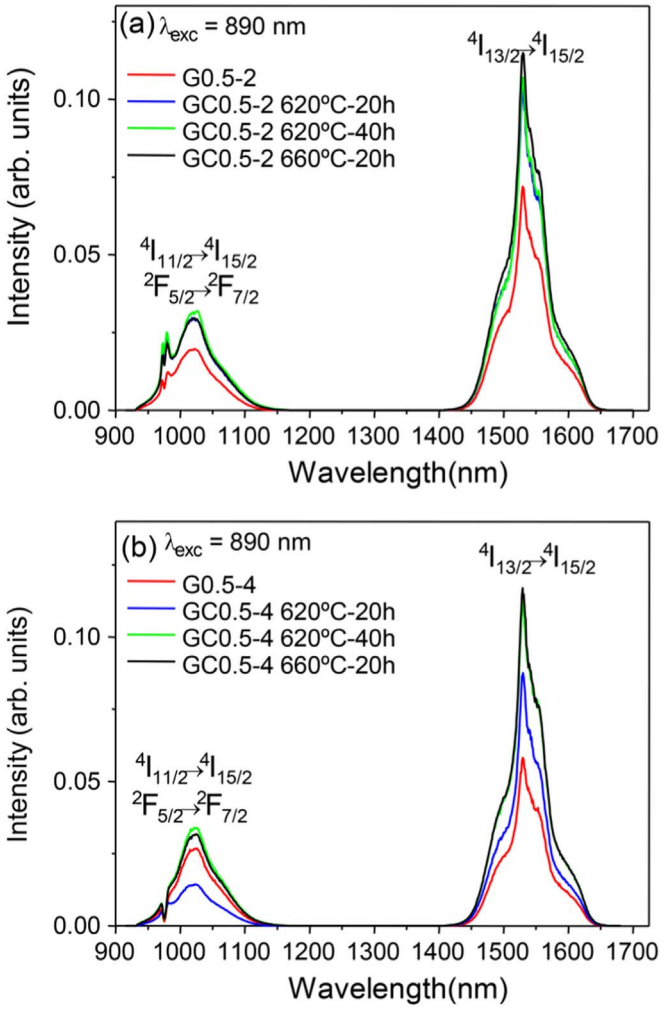


**Fig. 9.** Room temperature emission spectra of (a) 0.5-2 and (b) 0.5-4 co-doped glass and GCs samples obtained by exciting at 890 nm.

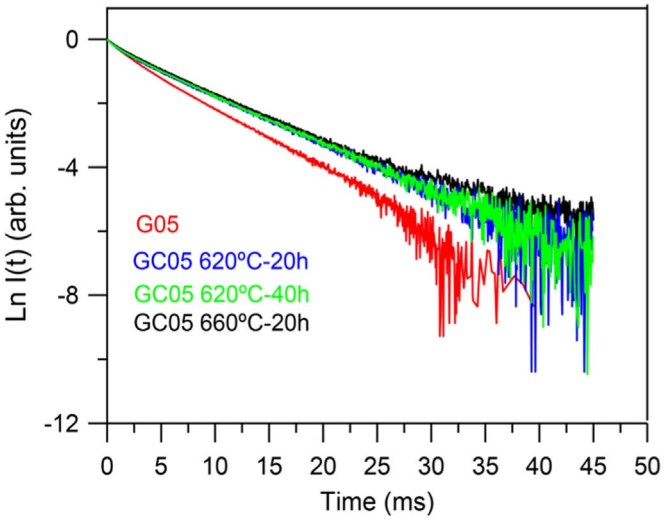


**Fig. 10.** Semilogarithmic plot of the fluorescence decays of the $^4I_{13/2}$ level of $Er^{3+}$ in the single doped samples.

under 488 nm excitation the population of this level is due to multi-phonon relaxation from level $^4S_{3/2}$ and is nearly independent on $Yb^{3+}$ concentration. However, this emission increases significantly for the co-doped samples under 980 nm excitation because $^4F_{9/2}$ level can be also

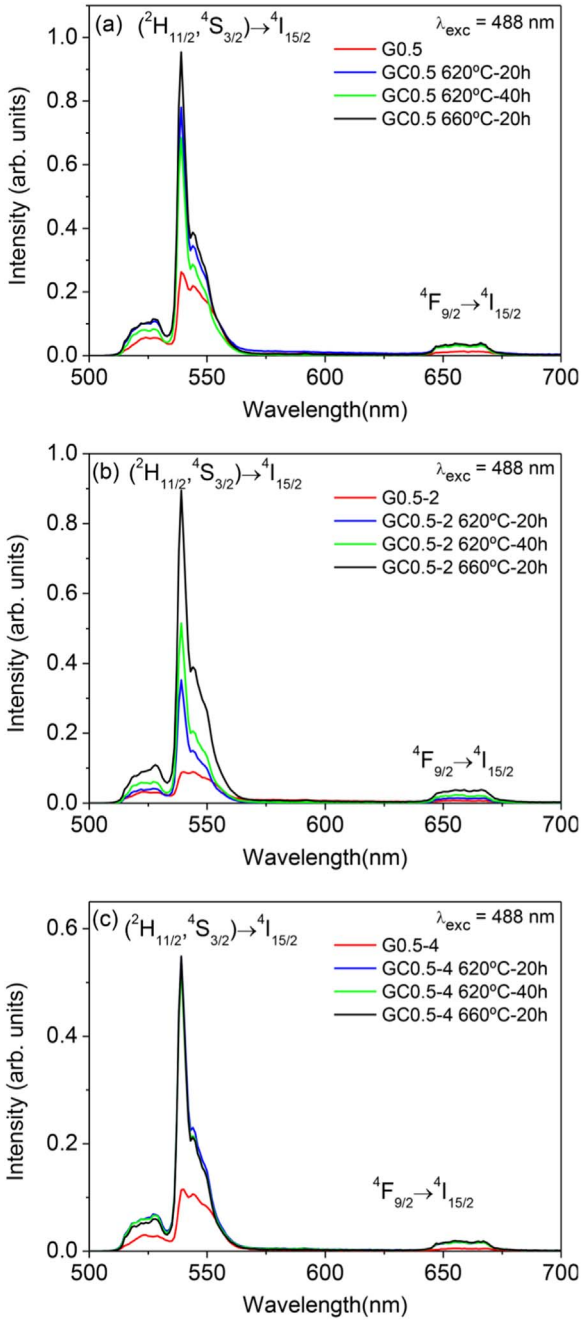


**Fig. 11.** Room temperature emission spectra obtained under excitation at 488 nm in the (a) 0.5% $Er^{3+}$ single doped glass and glass-ceramic samples, (b) 0.5% $Er^{3+}$-2%$Yb^{3+}$ and (c) 0.5% $Er^{3+}$-4%$Yb^{3+}$ co-doped glass and glass-ceramic samples.

populated by ESA from the $^4I_{13/2}$ level (populated non-radiatively from the $^4I_{11/2}$ level) and/or by energy transfer process described by ($^2F_{5/2} \rightarrow {}^2F_{7/2}$) ($Yb^{3+}$);($^4I_{13/2} \rightarrow {}^4F_{9/2}$) ($Er^{3+}$) (ET3) with an excess energy of around 1550 $cm^{-1}$. These processes can explain the enhancement of the red-to-green emission ratio in the co-doped samples.

## 4. Conclusions

Transparent oxyfluoride glass-ceramics doped with 0.5$Er^{3+}$ and co-doped with 2 and 4 $Yb^{3+}$ (mol%) have been successfully obtained. The precipitation of $LaF_3$ NCs was proved by XRD and HRTEM. The crystallization process starts from phase separation droplets already present in the glass, with further growth of NCs inside the droplets. The crystal growth is controlled by atoms diffusion and the crystal size is

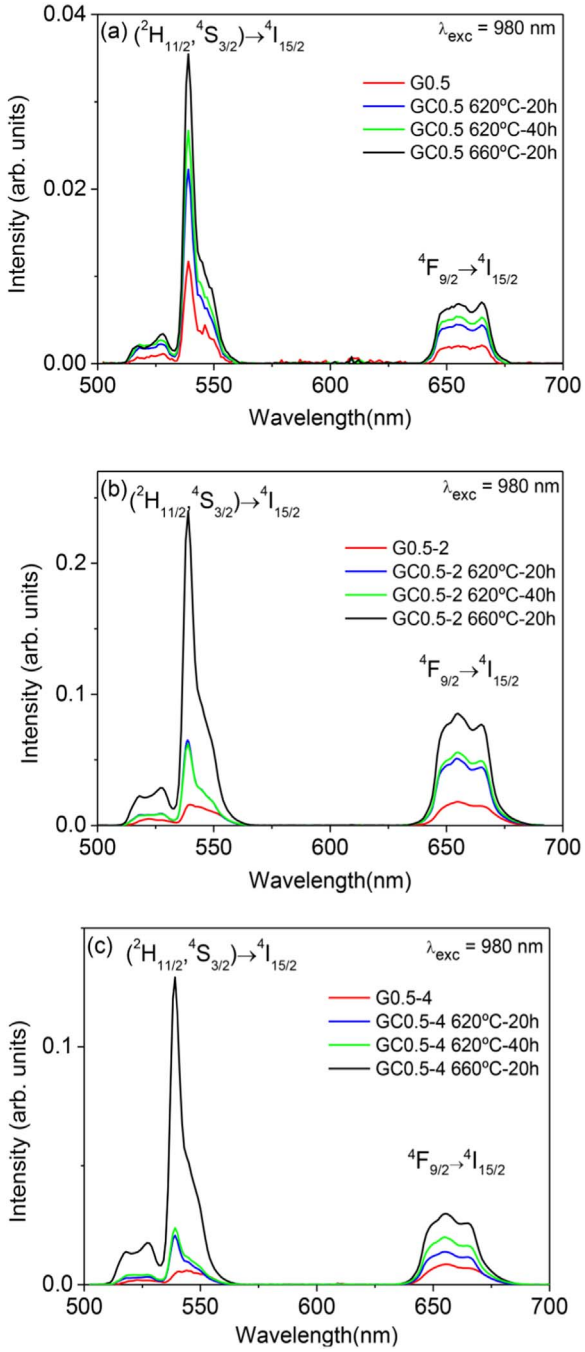


**Fig. 12.** Room temperature emission spectra obtained under excitation at 980 nm in the (a) 0.5% $Er^{3+}$ single doped glass and glass-ceramic samples, (b) 0.5% $Er^{3+}$-2%$Yb^{3+}$ and (c) 0.5% $Er^{3+}$-4%$Yb^{3+}$ co-doped glass and glass-ceramic samples.

limited by a $SiO_2$ barrier around the crystals that prevent further growth after 20 h of heat treatment at 620 °C. EDXS analysis clearly shows the REI incorporation in the fluoride NCs and the local change of the glass composition around the crystals.

The energy transfer between $Yb^{3+}$ and $Er^{3+}$ ions is evidenced by the enhancement of the NIR and UC emissions in the co-doped samples. A moderate back transfer from $Er^{3+}$ to $Yb^{3+}$ ions has also been observed under near infrared excitation of $Er^{3+}$ ions at 800 nm. Upconverted green emission due to the ($^2H_{11/2}$,$^4S_{3/2}$) → $^4I_{15/2}$ transitions together with a red emission corresponding to the $^4F_{9/2}$ → $^4I_{15/2}$ transition have been observed in all samples and attributed to a two photon process. An enhancement of the Upconverted emission is observed for the GC samples being most efficient for the 0.5-2 co-

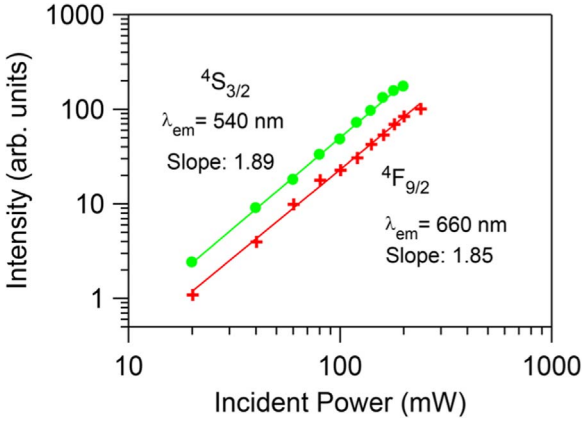


**Fig. 13.** Logarithmic plot of the integrated emission intensities of the upconversion from $^4S_{3/2}$, and $^4F_{9/2}$ levels as a function of the pump laser intensity obtained under excitation at 980 nm. Symbols correspond to the experimental data and solid lines are linear fits.

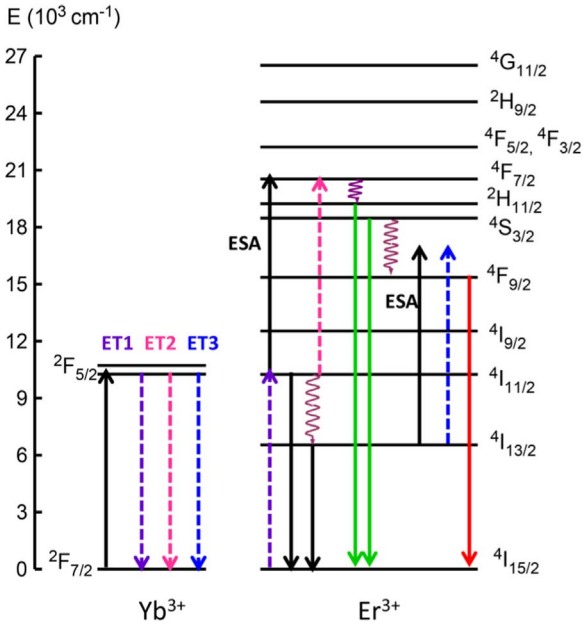


**Fig. 14.** Energy level diagram of $Er^{3+}$ and $Yb^{3+}$ ions and possible Upconversion mechanisms. Dashed lines corresponds to energy transfer processes.

doped sample treated at 660 °C-20 h. The obtained results thus furtherly confirm the incorporation of the REI in the $LaF_3$ NCs, and explain their higher emission efficiency due to the lower maximum phonon energy of the fluoride crystal lattice which reduces the multi-phonon relaxation rates. Depending on the heat treatment conditions a different red-to-green ratio in the UC emission is observed which opens the possibility to the preparation of GC materials with UC emission mostly centred towards green or red color.

## Acknowledgements

This work has been supported by the Spanish Government MINECO (Project MAT2013-48246-C2-1-P and MAT2013-48246-C2-2-P) and the Basque Country University (Project PPG17/07).

## References

[1] A. de Pablos-Martín, A. Durán, M.J. Pascual, Nanocrystallisation in oxyfluoride systems: mechanisms of crystallisation and photonic properties, Int. Mater. Rev. 57 (2012) 165–186, http://dx.doi.org/10.1179/1743280411Y.0000000004.

[2] A. de Pablos-Martin, M. Ferrari, M.J. Pascual, G.C. Righini, Glass-ceramics: a class of nanostructured materials for photonics, Riv. Nuovo Cim. 38 (2015) 311–369,

http://dx.doi.org/10.1393/ncr/i2015-10114-0.
[3] P.P. Fedorov, A.A. Luginina, A.I. Popov, Transparent oxyfluoride glass ceramics, J. Fluor. Chem. 172 (2015) 22–50, http://dx.doi.org/10.1016/j.jfluchem.2015.01.009.
[4] M. Mattarelli, M. Montagna, E. Moser, A. Chiasera, V. Tikhomirov, A.B. Seddon, S. Chaussedent, G. Nunzi Conti, S. Pelli, G.C. Righini, L. Zampedri, M. Ferrari, $Tm^{3+}$-activated transparent oxy-fluoride glass ceramics: structural and spectroscopic properties, J. Non-Cryst. Solids 345 & 346 (2004) 354–358, http://dx.doi.org/10.1016/j.jnoncrysol.2004.08.043.
[5] B. Boulard, O. Péron, Y. Jestin, M. Ferrari, C. Duverger-Arfuso, Fabrication and characterization of $Er^{3+}$-doped fluoride glass ceramics waveguides containing $LaF_3$ nano-crystals, J. Lumin. 129 (2009) 1637–1640, http://dx.doi.org/10.1016/j.jlumin.2009.01.031.
[6] Y. Wang, J. Ohwaki, New transparent vitroceramics co-doped with $Er^{3+}$and$Yb^{3+}$ for efficient frequency upconversion, Appl. Phys. Lett. 63 (1993) 3268–3270, http://dx.doi.org/10.1063/1.110170.
[7] W.J. Miniscalco, Optical and electronic properties of rare earth ions in glasses, in: M.J.F. Digonnet (Ed.), Rare-Earth-Doped Fiber Lasers and Amplifiers, 2nd ed., Marcel Dekker Inc, New York, 2001, pp. 18–130.
[8] G. Blasse, B.C. Grabmaier, Luminescent Materials, Springer, New York, 1994.
[9] F. Auzel, Upconversion and anti-Stokes processes with f and d Ions in solids, Chem. Rev. 104 (2004) 139–174, http://dx.doi.org/10.1021/cr020357g.
[10] Y. Xu, X. Zhang, S. Dai, B. Fan, H. Ma, J.-L. Adam, J. Ren, G. Chen, Efficient near-infrared down-conversion in $Pr^{3+}$-$Yb^{3+}$ co-doped glasses and glass ceramics containing $LaF_3$ nanocrystals, J. Phys. Chem. C 115 (2011) 13056–13062, http://dx.doi.org/10.1021/jp201503v.
[11] Q.J. Chen, W.J. Zhang, X.Y. Huang, G.P. Dong, M.Y. Peng, Q.Y. Zhang, Efficient down- and Upconversion of $Pr^{3+}$-$Yb^{3+}$ co-doped transparent oxyfluoride glass-ceramics, J. Alloy. Compd. 513 (2012) 139–144, http://dx.doi.org/10.1016/ j.jallcom.2011.10.007.
[12] J.T. van Wijngaarden, S. Scheidelaar, T.J.H. Vlugt, M.F. Reid, A. Meijerink, Energy transfer mechanism for down-conversion in the ($Pr^{3+}$, $Yb^{3+}$) couple, Phys. Rev. B 81 (2010) 155112–155116, http://dx.doi.org/10.1103/PhysRevB.81.155112.
[13] G. Gorni, A. Cosci, S. Pelli, L. Pascual, A. Durán, M.J. Pascual, Transparent oxyfluoride nano-glass ceramics doped with $Pr^{3+}$ and $Pr^{3+}$–$Yb^{3+}$ for NIR emission, Front. Mater. 3 (58) (2017) 1–14, http://dx.doi.org/10.3389/fmats.2016.00058.
[14] B. Dieudonné, B. Boulard, G. Alombert-Goget, A. Chiasera, Y. Gao, S. Kodjikian, M. Ferrari, Up- and down-conversion in $Yb^{3+}$-$Pr^{3+}$ co-doped fluoride glasses and glass ceramics, J. Non-Cryst. Solids 377 (2013) 105–109, http://dx.doi.org/10.1016/j.jnoncrysol.2012.12.025.
[15] O. Maalej, B. Boulard, B. Dieudonné, M. Ferrari, M. Dammak, M. Dammak, Downconversion in $Pr^{3+}$-$Yb^{3+}$ co-doped ZBLA fluoride glass, J. Lumin. 161 (2015) 198–201, http://dx.doi.org/10.1016/j.jlumin.2015.01.018.
[16] G. Yi, H. Lu, S. Zhao, Y. Ge, W. Yang, D. Chen, L.-H. Guo, Synthesis, characterization, and biological application of size-controlled nanocrystalline $NaYF_4$:Yb,Er infrared-to-visible Upconversion phosphors, Nano Lett. 4 (2004) 2191–2196, http://dx.doi.org/10.1021/nl048680h.
[17] Q. Liu, Y. Sun, T. Yang, W. Feng, C. Li, F. Li, Sub-10 nm hexagonal lanthanide-doped $NaLuF_4$ upconversion nanocrystals for sensitive bioimaging in vivo, J. Am. Chem. Soc. 133 (2011) 17122–17125, http://dx.doi.org/10.1021/ja207078s.
[18] M. Haase, H. Schäfer, Upconverting nanoparticles, Angew. Chem. Int. Ed. 50 (2011) 5808–5829.
[19] J. Zhou, Zg Liu, F. Li, Upconversion nanophosphors for small-animal imaging, Chem. Soc. Rev. 41 (2012) 1323–1349, http://dx.doi.org/10.1039/c1cs15187h.
[20] Y. Dai, P. Ma, Z. Cheng, X. Kang, X. Zhang, Z. Hou, C. Li, D. Yang, X. Zhai, J. Lin, Upconversion cell imaging and pH induced thermally controlled drug release from $NaYF_4$:$Yb^{3+}$/$Er^{3+}$@hydrogel core shell hybrid microspheres, ACS Nano 6 (2012) 3327–3338, http://dx.doi.org/10.1021/nn300303q.
[21] T. Yang, Y. Sun, Q. Liu, W. Feng, P. Yang, F. Li, Cubic sub-20 nm $NaLuF_4$-based upconversion nanophosphors for high-contrast bioimaging in different animal species, Biomaterials 33 (2012) 3733–3742, http://dx.doi.org/10.1016/j.biomaterials.2012.01.063.
[22] M. Wang, Y. Zhu, C. Mao, Synthesis of NIR-responsive $NaYF_4$:Yb,Er upconversion fluorescent nanoparticles using an optimized solvothermal method and their applications in enhanced development of latent fingerprints on various smooth substrates, Langmuir 31 (2015) 7084–7090, http://dx.doi.org/10.1021/acs.langmuir.5b01151.
[23] M. Alkahtani, A. Chen, J.J. Pedraza, J.M. González, D.Y. Parkinson, P.R. Hemmer, H. Liang, High resolution fluorescence bio-imaging upconversion nanoparticles in insects, Opt. Express 25 (2017) 1030–1039, http://dx.doi.org/10.1364/OE.25.001030.
[24] C. Altavilla, Upconverting Nanomaterials, CRC Press, New York, 2016.
[25] P. Xie, S.C. Rand, Visible cooperative upconversion laser in Er:$LiYF_4$, Opt. Lett. 17 (1992) 1198–1200, http://dx.doi.org/10.1364/OL.17.001198.
[26] P.E. Möbert, E.E. Heumann, E., G. Huber, B.H. Chai, Green $Er^{3+}$:$LiYF_4$, upconversion laser at 551 nm with $Yb^{3+}$ co-doping: a novel pumping scheme, Opt. Lett. 22 (1997) 151412–151414.
[27] H. Scheife, E. Heumann, B. Sebastian, Advances in Upconversion lasers based on $Er^{3+}$ and $Pr^{3+}$, Opt. Mater. 26 (2004) 365–374, http://dx.doi.org/10.1016/j.optmat.2003.10.010.
[28] R. Ye, C. Xu, X. Wang, J. Cui, Z. Zhou, Room-temperature near-infrared Upconversion lasing in single-crystal Er-Y chloride silicate nanowires, Sci. Rep. 6 (2016) 34407, http://dx.doi.org/10.1038/srep34407.
[29] G.H. Dieke, Spectra and Energy Levels of Rare Earth Ions in Crystals, Interscience Publishers, New York, 1968.
[30] W.T. Carnall, H. Crosswhite, H.M. Crosswhite, Energy Level Structure and Transition Probabilities of the Trivalent Lanthanides in $LaF_3$, Argonne National Laboratory, Argonne, IL, 1977.
[31] P.S. Peijzel, A. Meijerink, R.T. Wegh, M.F. Reid, G.W. Burdick, A complete 4f n energy level diagram for all trivalent lanthanide ions, J. Solid State Chem. 178 (2005) 448–453, http://dx.doi.org/10.1016/j.jssc.2004.07.046.
[32] G. Gorni, J.J. Velázquez, G.C. Mather, A. Durán, G. Chen, M. Sundararajan, R. Balda, J. Fernández, M.J. Pascual, Selective excitation in transparent oxyfluoride glass-ceramics doped with $Nd^{3+}$, J. Eur. Ceram. Soc. 37 (2017) 1695–1706, http://dx.doi.org/10.1016/j.jeurceramsoc.2016.11.014.
[33] J.W. Stouwdam, F.C.J.M. van Veggel, Near-infrared emission of redispersible $Er^{3+}$, $Nd^{3+}$, and $Ho^{3+}$ doped $LaF_3$ nanoparticles, Nano Lett. 2 (2002) 733–737, http://dx.doi.org/10.1021/nl025562q.
[34] G.-S. Yi, G.-M. Chow, Colloidal $LaF_3$:Yb,Er, $LaF_3$:Yb,Ho and $LaF_3$:Yb,Tm nanocrystals with multicolor upconversion fluorescence, J. Mater. Chem. 15 (2005) 4460–4464, http://dx.doi.org/10.1039/b508240d.
[35] J. Zhang, W. Qin, D. Zhao, Degejihu, J. Zhang, Y. Wang, C. Cao, Spectral variations and energy transfer processes on both $Er^{3+}$ ion concentration and excitation densities in $Yb^{3+}$–$Er^{3+}$ co-doped $LaF_3$ materials, J. Lumin. 122–123 (2007) 506–508, http://dx.doi.org/10.1016/j.jlumin.2006.01.220.
[36] J. Wang, J.H., D. Tang, X. Liu, Z. Zhen, Oleic acid (OA)-modified $LaF_3$:Er,Yb nanocrystals and their polymer hybrid materials for potential optical-amplification applications, J. Mater. Chem. 17 (2007) 1597, http://dx.doi.org/10.1039/B617754A.
[37] D. Zhang, C. Chen, F. Wang, D.M. Zhang, Optical gain and upconversion luminescence in $LaF_3$:Er, Yb nanoparticles-doped organic–inorganic hybrid materials waveguide amplifier, Appl. Phys. B 98 (2010) 791–795.
[38] Y. Yang, Y. Qu, J. Zhao, Q. Zeng, Y. Ran, Q. Zhang, X. Kong, H. Zhang, Fabrication of and drug delivery by an upconversion emission nanocomposite with monodisperse $LaF_3$:Yb,Er core/mesoporous silica shell structure, Eur. J. Inorg. Chem. (2010) 5195–5199 (DOI:0.1002/ejic.201000778).
[39] A.K. Singh, K. Kumar, A.C. Pandey, O. Parkash, S.B. Rai, D. Kumar, Photon avalanche upconversion and pump power studies in $LaF_3$:$Er^{3+}$/$Yb^{3+}$ phosphor, Appl. Phys. B 104 (2011) 1035–1041, http://dx.doi.org/10.1007/s00340-011-4673-2.
[40] Z. Chen, G. Wu, H. Jia, K. Sharafudeen, W. Dai, X. Zhang, S. Zeng, J. Liu, R. Wei, S. Lv, G. Dong, J. Qiu, Improved Upconversion luminescence from $Er^{3+}$:$LaF_3$ nanocrystals embedded in oxyfluoride glass ceramics via simultaneous triwavelength excitation, J. Phys. Chem. C 119 (2015) 24056–24061, http://dx.doi.org/10.1021/acs.jpcc.5b08103.
[41] A. Biswas, G.S. Maciel, C.S. Friend, P.N. Prasad, Upconversion properties of a transparent $Er^{3+}$-$Yb^{3+}$ co-doped $LaF_3$-$SiO_2$ glass-ceramics prepared by sol gel method, J. Non-Cryst. Solids 316 (2003) 393–397, http://dx.doi.org/10.1016/S0022-3093(02)01951-8.
[42] J. Huang, Y. Huang, T. Wu, Y. Huang, P. Zhang, High efficiency white luminescence in $Tm^{3+}$/$Er^{3+}$/$Yb^{3+}$ tri-doped oxyfluoride glass ceramic microsphere pumped by 976 nm laser, J. Lumin. 157 (2015) 215–219, http://dx.doi.org/10.1016/j.jlumin.2014.08.054.
[43] C. Rüssel, Nanocrystallization of $CaF_2$ from $Na_2O/K_2O/CaO/CaF_2/Al_2O_3/SiO_2$ glasses, Chem. Mater. 17 (2005) 5843–5847.
[44] A. de Pablos-Martín, M.A. García, A. Muñoz-Noval, G.R. Castro, M.J. Pascual, A. Durán, Analysis of the distribution of $Tm^{3+}$ ions in $LaF_3$ containing transparent glass-ceramics through X-ray absorption spectroscopy, J. Non-Cryst. Solids 384 (2014) 83–87, http://dx.doi.org/10.1016/j.jnoncrysol.2013.07.021.
[45] D. Chen, Y. Wang, Y. Yu, E. Ma, Influence of $Yb^{3+}$ content on microstructure and fluorescence of oxyfluoride glass ceramics containing $LaF_3$ nano-crystals, Mater. Chem. Phys. 101 (2007) 464–469, http://dx.doi.org/10.1016/j.matchemphys.2006.08.005.
[46] C. Bocker, C. Rüssel, Self-organized nano-crystallisation of $BaF_2$ from $Na_2O/K_2O/BaF_2/Al_2O_3/SiO_2$ glasses, J. Eur. Ceram. Soc. 29 (2009) 1221–1225, http://dx.doi.org/10.1016/j.jeurceramsoc.2008.08.005.
[47] K. Biswas, A.D. Sontakke, J. Ghosh, K. Annapurna, Enhanced blue emission from transparent oxyfluoride glass–ceramics containing $Pr^{3+}$:$BaF_2$ nanocrystals, J. Am. Ceram. Soc. 93 (2010) 1010–1017, http://dx.doi.org/10.1111/j.1551-2916.2009.03547.x.
[48] A. de Pablos-Martín, N. Hémono, G.C. Mather, S. Bhattacharyya, T. Höche, Hansjörg Bornhöft, J. Deubener, F. Muñoz, A. Durán, M.J. Pascual, Crystallization kinetics of $LaF_3$ nanocrystals in an oxyfluoride glass, J. Am. Ceram. Soc. 94 (2011) 2420–2428, http://dx.doi.org/10.1111/j.1551-2916.2011.04547.x.
[49] F. Auzel, G. Baldacchini, L. Laversenne, G. Boulon, Radiation trapping and self-quenching analysis in $Yb^{3+}$, $Er^{3+}$, and $Ho^{3+}$ doped $Y_2O_3$, Opt. Mater. 24 (2003) 103–109, http://dx.doi.org/10.1016/S0925-3467(03)00112-5.
[50] V.K. Tikhomirov, V.D. Rodríguez, J. Méndez-Ramos, J. delCastillo, D. Kirilenko, G. Van Tendeloo, V.V. Moshchalkov, Optimizing Er/Yb ratio and content in Er–Yb co-doped glass-ceramics for enhancement of the up-and down-conversion luminescence, Sol. Energ. Mater. Sol. C 100 (2012) 209–215, http://dx.doi.org/10.1016/j.solmat.2012.01.019.
[51] X. Bai, H. Song, G. Pan, Y. Lei, T. Wang, X. Ren, S. Lu, B. Dong, Q. Dai, L. Fan, Size-Dependent upconversion luminescence in $Er^{3+}$/$Yb^{3+}$-Co-doped nanocrystalline yttria: saturation and thermal effects, J. Phys. Chem. C 111 (2007) 13611–13617, http://dx.doi.org/10.1021/jp070122e.
[52] F. Vetrone, J.C. Boyer, J.A. Capobianco, A. Speghini, M. Bettinelli, Significance of $Yb^{3+}$ concentration on the upconversion mechanisms in co-doped $Y_2O_3$:$Er^{3+}$, $Yb^{3+}$ nanocrystals, J. Appl. Phys. 96 (2004) 661–667, http://dx.doi.org/10.1063/1.1739523.

# *PAPER 5*

**Effect of dopant precursors on the optical properties of rare-earths doped oxyfluoride glass-ceramics.**

G. Gorni, A. Serrano, G.R. Castro, D. Bravo, R. Balda, J. Fernández, A. Durán, M.J. Pascual.

*Draft*

# Effect of dopant precursors on the optical properties of rare-earths doped oxyfluoride glass-ceramics

G. Gorni*[1], A. Serrano[1,2], D. Bravo[3], G.R. Castro[2,4] R. Balda[5,6], J. Fernández[7], A. Durán[1], M.J. Pascual[1]

[1] *Instituto de Cerámica y Vidrio (CSIC), Spain*

[2] *SpLine, Spanish CRG Beamline - European Synchrotron Radiation Facility (ESRF), France*

[4] *Departamento de Física de Materiales, Universidad Autónoma de Madrid (UAM), Spain*

[4] *Instituto de Ciencia de Materiales de Madrid (CSIC), Spain*

[5] *Departamento Física Aplica I, Escuela Superior de Ingeniería, Universidad del País Vasco (UPV-EHU), Spain*

[6] *Centro de Física de Materiales, (UPV/EHU-CSIC), Spain*

[7] *Donostia International Physics Center DIPC, Spain*

ggorni@icv.csic.es

## 1. Introduction

The improvement of photoluminescence (PL) properties offered by the incorporation of small nano-crystals (NCs) doped with Rare-Earth (RE) ions in a glass matrix has been described since the 90's [1]. In the last 10 years, many papers were published related to glass-ceramics (GCs) functionalized by dispersed crystals doped with RE ions. A particular attention has been given to oxyfluoride GCs that combine the low phonon energy of fluoride crystals and high solubility of RE ions inside, with the good mechanical, thermal and chemical properties of oxide glasses, especially those based on aluminosilicate compositions. Since 2012, several review papers were published about transparent GCs, some related to oxyfluoride GCs, and another one including also oxide crystals [2–5].

The benefits of these materials reside mainly in the possibility of growing different crystal phases in oxide glass matrices thanks to a proper selection of the starting composition. However, no stoichiometric requirements are necessary and the same crystal phase can be obtained in different glass systems. Another great advantage of GCs with respect to other kind of materials is related with the availability of different processing methods: from classical melt-quenching (MQ) to sol-gel (SG), that allows the preparation of materials as bulk, films, powder or fibres. Most published works about oxyfluoride GCs concern bulk materials prepared by MQ [3] doped with RE ions, however, a review paper about SG oxyfluoride GCs was also published recently [6]. Moreover, the preparation of optical fibres with GC core has emerged as an interesting field and several works were published since 2015. An enhancement of linear and nonlinear optical processes was observed in GCs with respect to the precursor glasses due to the

successful incorporation of RE ions inside the active crystal phase [7-21]. The possibility of obtaining crystal-like optical properties in bulk, films and fibres clearly demonstrated a great enhancement of PL intensity and lifetime with respect to the untreated glass.

A fundamental point to take into account during the processing is the amount of RE ions added to the system. In fact, the dopants content will strongly affect the final PL properties and the knowledge of the effective incorporation of RE ions inside the NCs is hardly or never estimated. It is well known that for some ions, as $Nd^{3+}$, in glasses and also in $LaF_3$ crystals, there is a limit around ~ 1 mol% to prevent concentration quenching [22–24]. However, in oxyfluoride GCs such limit was demonstrated to be strongly reduced to ~ 0.1 mol% due to the high concentration of RE ions in fluoride NCs [25]. This behaviour is explained considering the small crystal fraction of oxyfluoride GCs produced by MQ, that hardly reaches 10 wt%, along with the high diffusion of RE ions into the fluoride NCs, thus producing a great enhancement of the effective concentration in the NCs.

If the initial dopant precursor can affect the final optical properties is another unsolved problem when considering the quantification of RE ions incorporation in NCs. From a theoretical point of view there should not be any effect because the initial precursor is dissolved during the melting process and the use of dopant as oxides, chlorides, fluorides etc. should produce the same effect. In 2003, M. Mortier [26] studied the nucleation of $PbF_2$ crystallites in a germanate glass ($GeO_2$–PbO–$PbF_2$) doped with different erbium oxide and halides using DTA analysis. The author concluded that [26]: "*a memory of the way of introduction of the rare earth ions is kept after melting of the initial polycrystalline powders*" and *"most probably, the surrounding anions are preserved through the melting process as verified with our thermal analysis*". In 2004, M. Abril et al. [27] studied oxyfluoride glasses and GCs doped with $NdF_3$, $Nd_2O_3$ and a $Nd^{3+}$ doping solution. The optical results indicated that GCs doped with $NdF_3$ presented the best values for spectroscopic parameters as the stimulated cross section of the $^4F_{3/2}$-$^4I_{11/2}$ laser transition. In fact, it was observed that $Nd^{3+}$ incorporation in fluoride crystals is higher when $NdF_3$ is used (~86 %) whereas for $Nd_2O_3$-doped sample a smaller concentration was found. However, despite the aforementioned results, Fedorov et al. [3] stated in their review published in 2015 that there are no differences in using RE oxides or fluorides and both can be used, preferring the oxides for their lower cost, less toxicity and hygroscopicity. The RE ions inner polyhedral coordination will be the same using RE fluorides instead of the oxides.

For these reasons, the combination of local structural techniques is necessary for a better understanding of RE-doped glasses and glass-ceramics. For example, X-Ray Absorption Spectroscopy (XAS) is a powerful technique to characterize the short-range order of glassy materials [28] but it is not commonly used to study oxyfluoride glass-ceramics and the RE ions surrounding.

In this study, we analyse a glass composition, named 55Si10La in which $LaF_3$ NCs are formed after a proper crystallisation process, doped with $Nd^{3+}$ and $Er^{3+}$ used as oxides and fluorides. The environment surrounding the ions in glass and GCs has been examined with XAS and the incorporation of the ions in $LaF_3$ was studied by Electron Paramagnetic Resonance (EPR) and site-selective photoluminescence (PL).

## 2. Experimental

### *2.1 Materials preparation*

Glasses of composition (mol%) $55SiO_2$-$20Al_2O_3$-$15Na_2O$-$10LaF_3$ with $0.1NdF_3$-$2NdF_3$, $0.05Nd_2O_3$, $0.5Nd_2O_3$, 0.1-$0.5ErF_3$ and $0.05Er_2O_3$ were prepared by MQ using: $SiO_2$ (Saint-Gobin 99.6%), $Al_2O_3$ (Panreac), $Na_2CO_3$ (Sigma Aldrich,>99.5%), $LaF_3$ (Alfa Aesar, 99.9%), $NdF_3$ (Alfa Aesar, 99.99%), $Nd_2O_3$ (Alfa Aesar 99.99%), $ErF_3$ (Alfa Aesar, 99.99%) and $Er_2O_3$ (Alfa Aesar, 99.99%) as raw materials. The samples will be labelled G/GC-x$NdF_3$/$Nd_2O_3$ or G/GC-$ErF_3$/$Er_2O_3$ to indicate glasses or GC doped with x mol% of $NdF_3$/$Nd_2O_3$ or with $ErF_3$/$Er_2O_3$. The experimental procedure is fully explained elsewhere [12,25]. GCs were treated at 620 ºC for 3, 5, 20 and 40 h to crystallise $LaF_3$. Optical sheets 1 cm x 1 cm x 2 mm were polished for optical characterisation.

### *2.2 X-Ray Absorption Spectroscopy*

X-Ray Absorption Spectroscopy (XAS) was performed to evaluate the RE ions surrounding. The samples were characterized at the Nd $L_2$ and Er $L_3$-edge at the SpLine-CRG BM25 beamline at the ESRF. A different edge has been used for $Nd^{3+}$ and $Er^{3+}$ because the $L_3$ edge of $Nd^{3+}$ partially overlaps with the fluorescence signal of $La^{3+}$.

XAS measurements of powdered samples were collected at RT in fluorescence mode using a 13 element Si (Li) solid-state detector with the sample surface placed at an angle of 45° to the incident beam, with the final spectra representing an average of 4 scans. The XAS data were processed using the ATHENA software [29]. $NdF_3$, $Nd_2O_3$, $ErF_3$ and $Er_2O_3$ standards were measured in fluorescence mode as well as in transmission mode using an ionization chamber.

### *2.3 Electron Paramagnetic Resonance*

Electron Paramagnetic Resonance (EPR) spectra were recorded by a Bruker ESP 300E spectrometer working in the X-band with field modulation of 100 kHz. The temperature of the sample was controlled with a continuous-flow helium cryostat (Oxford InstrumentsESR900). The values of the resonance magnetic fields and microwave frequencies were measured with a NMR Gauss-meter (Bruker ESP 300E) and a frequency-meter (Hewlett-Packard5342A), respectively. Small amount of powders (~ 0.8 g) were enrolled in Teflon tape and placed in a sample holder.

*2.4 Photoluminescence and lifetime*

Site-selective steady-state emission and excitation spectra were recorded by exciting the samples with a continuous wave (cw) Ti:sapphire ring laser (0.4 $cm^{-1}$ linewidth) in the 770–920 nm spectral range. The fluorescence was analyzed with a 0.25 m monochromator, and the signal was detected by an extended IR Hamamatsu H10330A-75 photomultiplier and finally amplified by a standard lock-in technique. Measurements were performed at 9 K by using a continuous flow cryostat.

Lifetime measurements were obtained by exciting the samples with a Ti-sapphire laser pumped by a pulsed frequency-doubled Nd:YAG laser (9 ns pulse width), and detecting the emission with Hamamatsu H10330A-75 photomultiplier. Data were processed by a Tektronix oscilloscope.

## 3. Results and discussion

Transparent glasses and GCs were obtained after the melting process and controlled heat treatment at 620 °C for 3-40 h.

*3.1 XAS*

X-ray absorption near edge structure (XANES) spectra of $NdF_3$ and $Nd_2O_3$ references at $L_2$-edge are shown in Figure 1a together with their first derivative spectra, inset of Figure 1a. Some differences in the absorption signal are revealed depending on the coordination of $Nd^{3+}$ ions. For example, the corresponding maxima of the first derivatives are obtained at ~ 6723 and 6722 eV for $NdF_3$ and $Nd_2O_3$, respectively. The shift of RE ions absorption edge towards higher photon energy is affected by the ligand ions, being the shift towards higher energy for RE fluorides than for oxides [30,31] However, the energy shift of the absorption edge observed for $NdF_3$ and $Nd_2O_3$ references is very slight. Most relevant differences are found in the XANES range 6730-6840 eV. $Nd_2O_3$ presents resonances at ~ 6738, 6757 and 6802 eV whereas for $NdF_3$ resonances are shifted towards higher values: 6743, 6758 and 6804 eV. Another feature of $NdF_3$ is the presence of a “valley” at ~ 6735 eV whereas $Nd_2O_3$ presents a resonance almost at this energy.

XAS spectra of glasses (G) and GCs doped with $1NdF_3$ and $0.5Nd_2O_3$ are given in Figure 1b. The XANES region reveals some differences when oxides or fluorides are used as precursor. For G-$1NdF_3$ the resonance at 6738 eV, corresponding to $Nd_2O_3$, is not observed, instead a “valley” is appreciated and similar to the one of $NdF_3$ reference. The other resonances at higher energy are broader but are centred at the same values that for $NdF_3$ For GC-$1NdF_3$ the “valley”

at 6735 eV is much better defined and the other resonances are narrower than for the glass and more similar to those of $NdF_3$. This result indicates that even though the initial $Nd^{3+}$ surrounding in the glass is mostly rich in fluorine, a change around $Nd^{3+}$ ions occurs as a consequence of the crystallisation process thus producing less broadened resonances and a spectrum very similar to that of $NdF_3$ for the GCs.

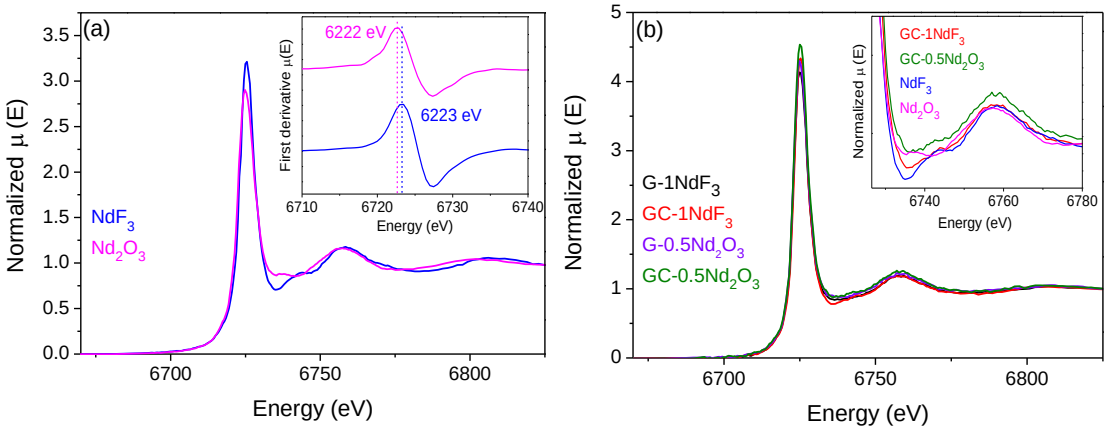


Figure 1. (a) XAS spectra and (inset) first derivative curves of $NdF_3$ and $Nd_2O_3$ reference compound. (b) XANES spectra and (inset) detail of the XANES region for glasses and GCs doped with $1NdF_3$ and $0.5Nd_2O_3$.

The absorption spectrum of G-$0.5Nd_2O_3$ sample, represented in Figure 1b, shows neither the $Nd_2O_3$ resonance at 6738 eV nor the "valley" at 6735 eV associated to $NdF_3$. The other resonances in the absorption response of G-$0.5Nd_2O_3$ are more similar to $NdF_3$ than to $Nd_2O_3$ but in the first part of the XANES region the G-$0.5Nd_2O_3$ spectrum is more similar to $Nd_2O_3$. For GC-$0.5Nd_2O_3$ the 'valley at 6735 eV becomes more visible and also the first resonance (shoulder) and the second one become more similar to those of $NdF_3$, suggesting a progressive transformation around $Nd^{3+}$ ions during the crystallisation process. However, with respect to the GC-$1NdF_3$ sample, the XANES spectrum changes towards that of $NdF_3$ but there are still remarkable differences when $Nd_2O_3$ is used as precursor; such differences are smaller when $NdF_3$ is used as dopant precursor.

The whiteline of the four samples and the references was fitted using a Pseudo-Voigt function after removal of the edge continuum jump described by an arctan function. The values of the full-width at half maximum (FWHM) and the intensity were free parameters in the fitting and are summarized in Table 1.

A slight decrease of the FWHM is observed in the GC compared to the glass, which is associated with a more ordered environment due to RE ions inside $LaF_3$ NCs. A similar behaviour was obtained by de Pablos et al. in a previous study of $Tm^{3+}$ doped $LaF_3$-GCs [32]. The whiteline intensity varies slightly for glasses and GCs. It increases in the GC for both oxide and fluoride precursors. According to Y.C. Choi [33], when RE ions are in oxygens

environment, the whiteline intensity decreases and get broader due to a higher covalence nature of the RE-O bond with respect to RE-F one (as we noted in the XANES scans of $NdF_3$ and $Nd_2O_3$ references). Such phenomenon causes a less hybridization of the valence orbitals for fluoride compounds and hence increases the local density of states (LDOS) of 5d levels. The whiteline intensity is also affected by the RE ions concentration. Choi [33] suggested that the study of whiteline intensities of RE-doped glasses could be useful to define the solubility limit of these ions in glass systems before preventing clusters and concentration quenching. In fact, the author observed that for different fluoride glasses doped with 0.3, 0.5 and 1 mol% of $Ho^{3+}$ the same whiteline intensity was obtained, meaning that no clusters were formed. However, for higher concentrations a cluster formation is possible and the whiteline intensity decreases due to overlaps of d orbitals causing a decrease of LDOS. Therefore, in our case the change of the whiteline intensity could be explained considering that in the glasses there is still part of $Nd^{3+}$ ions surrounded by oxygen ions but after the heat treatment the amount of $Nd^{3+}$ ions inside the $LaF_3$ crystals increases. In addition, the highest intensity is obtained for the GC-0.5$Nd_2O_3$ suggesting that a smaller effective concentration is expected in this GC with respect to GC-1$NdF_3$, hence indicating less $Nd^{3+}$ ions in $LaF_3$ crystals when the oxide precursor is used.

The analysis of the XANES region for the samples doped with 0.1$NdF_3$ and 0.05$Nd_2O_3$ is quite difficult due to the poor signal/noise ratio induced by the low concentration of absorbing atoms. However, it is still possible to draw some conclusions based on the whiteline intensities that for these concentrations are strongly affected when comparing glass and GC, Figure 2 and Table 1. As stated before, if RE ions in glasses are homogenously distributed the whiteline intensity should not be altered. A large difference is observed in the intensities for G-0.1$NdF_3$ and G-0.05$N_2O_3$, indicating a different environment for the $Nd^{3+}$ ions. Based on the different intensity of RE-O and RE-F bonds, the local $Nd^{3+}$ environment in glass, when $Nd_2O_3$ is used as precursor, is still dominated oxygens ions, producing smaller whiteline intensity. On the contrary, a much stronger whiteline is obtained for G-0.1$NdF_3$, suggesting a fluorine-rich environment. Moreover, comparing G-0.1$NdF_3$ and G-1$NdF_3$ the white-line reduces by ~ 40% whereas from G-0.05$Nd_2O_3$ to G-0.5$Nd_2O_3$ the change is ~30%. This result indicates that higher clustering of $Nd^{3+}$ ions is obtained for $NdF_3$ doped glasses than for $Nd_2O_3$-doped ones. For what concerns the GC samples, a strong decrease of the whiteline intensity is observed for the GC-0.1$NdF_3$ while for the GC-0.05$Nd_2O_3$ the opposite occurs. This result cannot be explained by the different environment of the RE ions and the explanation could be found in the following reasoning. After the heat treatment part of $Nd^{3+}$ ions are embedded in $LaF_3$ NCs, hence the number of RE-F ionic bond increases. Choi [33] observed that the whiteline intensities of the glasses are all stronger than their crystalline counterpart. If for G-0.1$NdF_3$ an amorphous fluorine-rich environment prevails, in GC-0.1$NdF_3$ such environment is pretty much ionic (crystalline) and the covalence decreases, causing a decrease of the whiteline signal. Instead, the

transformation of G-0.05$Nd_2O_3$ to GC-0.05$Nd_2O_3$ produces higher whiteline intensity, meaning that $Nd^{3+}$ ions gradually pass from an oxygen-like environment to a fluorine-rich one. Once again the whiteline intensity of GC-0.05$Nd_2O_3$ is higher than that of GC-0.1$NdF_3$ suggesting lower amount of $Nd^{3+}$ ions incorporated in $LaF_3$ NCs.

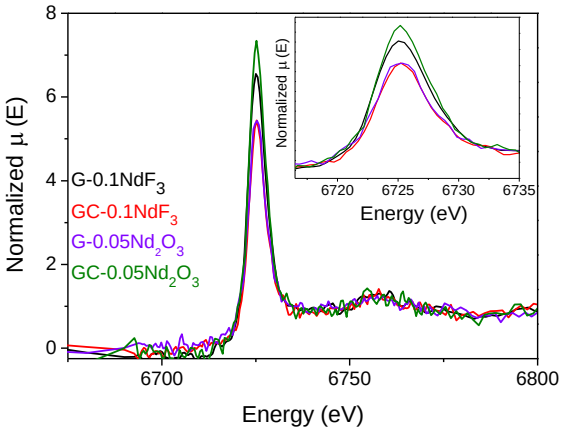


Figure 2. XANES spectra for glasses and GCs doped with 0.1$NdF_3$ and 0.05$Nd_2O_3$.

Table 1. FWHM of the whiteline for the G and GCs shown in Figures 1 and 2.

| Sample | FWHM (eV) | Whiteline intensity |
|---|---|---|
| G-1$NdF_3$ | 5.4 | 23.0 |
| GC-1$NdF_3$ | 5.1 | 23.6 |
| G-05$Nd_2O_3$ | 5.4 | 24.2 |
| GC-05$Nd_2O_3$ | 5.2 | 25.1 |
| G-0.1$NdF_3$ | 5.4 | 37 |
| GC-0.1$NdF_3$ | 5.1 | 30 |
| G-005$Nd_2O_3$ | 5.2 | 34 |
| GC-005$Nd_2O_3$ | 5.2 | 41 |
| $NdF_3$ | 5.5 | 19.3 |
| $Nd_2O_3$ | 6.1 | 18.3 |

Figure 3a shows the XANES spectra at the $L_3$-edge and their first derivatives (inset) of $ErF_3$ and $Er_2O_3$ references. The position at the absorption edge calculated as the maximum of the first derivative spectrum, is ~8357 eV and 8359 eV for $Er_2O_3$ and $ErF_3$, respectively. In this case, a broader and less intense white line is also observed for the oxide reference, confirming our results obtained for the $Nd^{3+}$ absorption edge and those published by Y.C. Choi [33]. The XANES region presents clear differences between the two precursors. $Er_2O_3$ shows two resonances at ~ 8378 and 8396 eV, instead they appear at ~ 8375 and 8394 eV for $ErF_3$.

Figure 3b shows the XANES spectra of glasses and GC prepared with $Er_2O_3$ and $ErF_3$ precursors. In all cases the XANES response is more similar to that of $ErF_3$ reference

compound, hence suggesting a fluorine-rich environment for all $Er^{3+}$-doped samples. No relevant variations of whiteline intensity and width are observed for these samples. Differently to what happens to $Nd^{3+}$-doped samples, the use of oxide or fluoride compounds does not produce significant environment differences around the $Er^{3+}$ absorbing atoms.

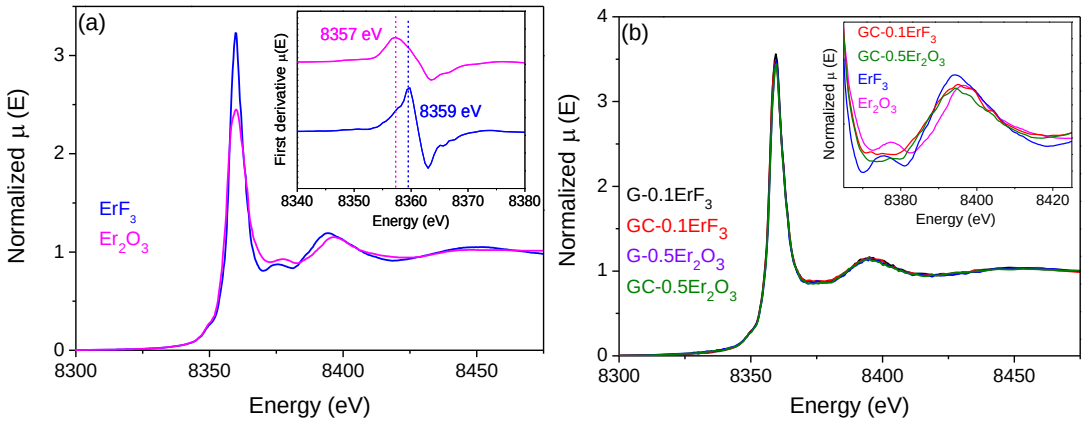


Figure 3. (a) XAS spectra and (inset) first derivative curves of $ErF_3$ and $Er_2O_3$ reference compound. (b) XANES spectra and (inset) detail of the XANES region for glasses and GCs doped with $0.1ErF_3$ and $0.05Er_2O_3$.

*3.3 EPR*

EPR measurements of $Nd^{3+}$ and $Er^{3+}$-doped samples have been carried out to obtain a direct evidence of the incorporation of these ions in $LaF_3$ NCs. Their spectrum is only observed at liquid He temperatures, so that only their lowest Kramers doublet is populated. Therefore, the spectrum of $Nd^{3+}$ and $Er^{3+}$ can be described by a Spin Hamiltonian with effective spin $S'=1/2$ and would only show one resonance line for each magnetic field orientation. Moreover, powders are composed of randomly distributed crystals hence the principal axes of the g-matrix have all possible orientations relative to the direction of the magnetic field. Therefore, in the case of $LaF_3$ phase (rhombic symmetry) the first derivative EPR spectrum only shows three lines appearing at three different principal g-values $g_1$, $g_2$ and $g_3$. These values have been previously reported for $Nd^{3+}$ and $Er^{3+}$-doped $LaF_3$ single crystals [34,35]. Figures 4a and 4b show the EPR signals of $NdF_3$-doped glasses and GCs with different $Nd^{3+}$ concentrations. The sharp signal at ~ 1587 G, corresponding to a g=4.27±.0.01, is associated to $Fe^{3+}$ impurities due to $SiO_2$ precursor [36,37]. This signal is also observed in other glass and GC samples prepared by other authors [38-41]. The other resonance at ~ 3263 G is related to the background and to the g-line of $Fe^{3+}$ impurities. This signal is also visible at room temperature (RT), hence it is excluded that can be related to RE ions. Increasing the $Nd^{3+}$ content a broad signal overlaps with the $Fe^{3+}$ signal and considering the absence of crystalline phases, such signal is associated to $Nd^{3+}$ in the amorphous glass matrix. Such signal also broadens remarkably increasing the $Nd^{3+}$ content and for quite high concentrations such as 1 and 2 mol% it smears in a range of

approx. 2000 G. Such behaviour is typical of glasses where broad resonances are observed due to site-to-site different environment and for high concentration the fast spin-spin relaxation broadens the resonance. Similar results were obtained by Dantelle et al. [38] for $Yb^{3+}$ doped glasses. The GC samples show interesting features, the appearance of new resonances at ~ 2130 and 4919 G corresponding to $g_1$=3.17±0.01 and $g_2$=1.37±0.02 (Figure 4b). Such values are in perfect agreement with those reported for $LaF_3$ single crystals [34,35]. The $g_3$ resonance is not observed and both $g_1$ and $g_2$-lines become broader increasing the $Nd^{3+}$ content due to stronger spin-spin relaxation process. Similar results were obtained by U. Rocha et al. [42] studying $LaF_3$ nanoparticles (NPs) doped with different amount of $Nd^{3+}$. Only for low concentration such as 0.2 mol% the three g resonances were observed together with the hyperfine structure of $g_1$-line. However, in our case, the effective concentration of $Nd^{3+}$ in $LaF_3$ crystals is much higher than the nominal one as reported in a previous paper [25]. It was found an effective concentration in $LaF_3$ NCs of ~ 1 mol% for GC-0.1$NdF_3$, one order of magnitude higher than the nominal value.

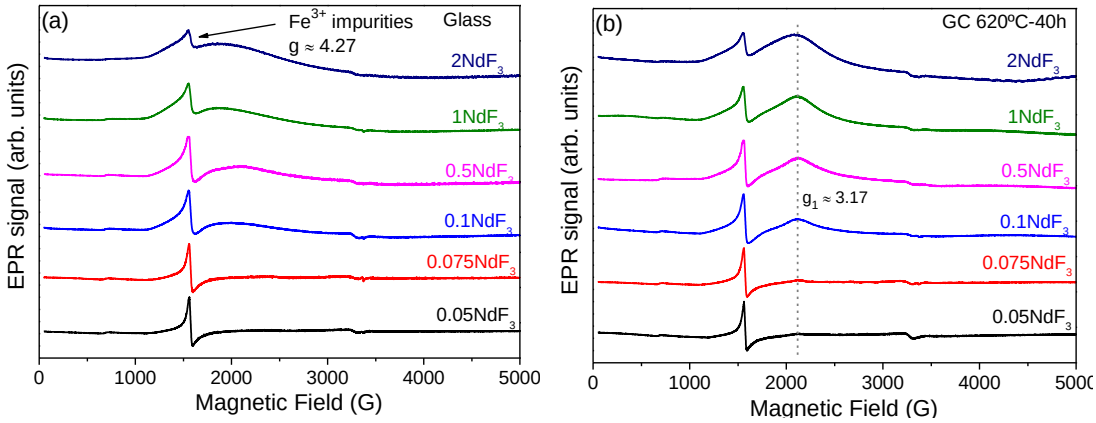


Figure 4. EPR signals of (a) glasses and (b) glass-ceramics doped with 0.05-2$NdF_3$.

Another interesting result is obtained comparing four GCs doped with 1$NdF_3$ and heat treated at 620 ºC for 3, 5, 20 and 40 h. The corresponding EPR signals are shown in Figure 5. A careful analysis of the samples treated for 3 and 40 h shows that width of $g_1$-line reduces increasing the treatment time and this is associated to a better crystallised sample as indicated by the intensity of the diffraction patterns and the increase of the crystal size [12,25] . Furthermore, for the GC treated 40 h the $g_2$-line is also visible further confirming the increase of the $LaF_3$ NCs and a better incorporation of $Nd^{3+}$ ions inside them. The samples treated for 5 and 20 h follow a similar trend.

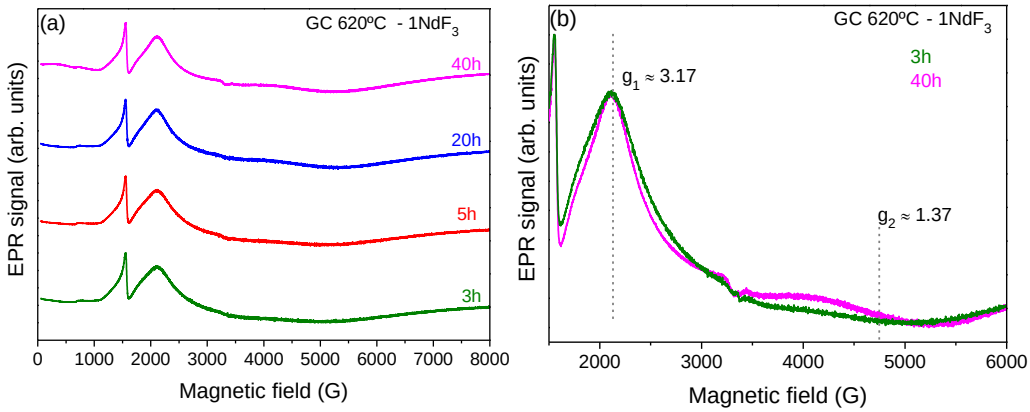


Figure 5. EPR signals of GCs doped with $1NdF_3$ and treated at 620 °C during 3, 5, 20 and 40 h. (b) Detail of EPR signals for GCs treated at 620 °C during 3 and 40 h.

Figure 6 compares the EPR signals of GC-$0.1NdF_3$, GC-$1NdF_3$, GC-$0.05Nd_2O_3$ and GC-$05Nd_2O_3$. Remarkable difference is suddenly observed for the less concentrated samples. While the $Nd^{3+}$ incorporation is clearly demonstrated for the GC-$01NdF_3$ by the visible $g_1$ and $g_2$-lines, only the $g_1$-line is observed for the GC-$0.05Nd_2O_3$, its intensity being very small. Such difference is not so strong for the GC-$1NdF_3$ and GC-$0.5Nd_2O_3$ but the intensity of the $g_1$-line associated to $NdF_3$-doped GC is stronger and also broader with respect to $Nd_2O_3$-doped GC. All these results are in agreement with those found by XAS and shown in Figures 1b. There is a noticeable difference in both XAS and EPR spectra for low $Nd^{3+}$ concentrations. Both techniques indicate that, after the heat treatment, when $Nd_2O_3$ is used as precursor less $Nd^{3+}$ ions are incorporated in $LaF_3$ NCs. This could be explained considering the oxygen shell still surrounding $Nd^{3+}$ ions in glass sample that inhibits or delay their incorporation in $LaF_3$ NCs. When $Nd^{3+}$ concentration increases the XAS differences are still visible but the effects are weakened by the very high $Nd^{3+}$ effective concentration in $LaF_3$ [25]. Nevertheless, similar conclusions are obtained once again and confirm that when $Nd_2O_3$ is used as dopant less $Nd^{3+}$ ions get incorporated in $LaF_3$ crystal phase.

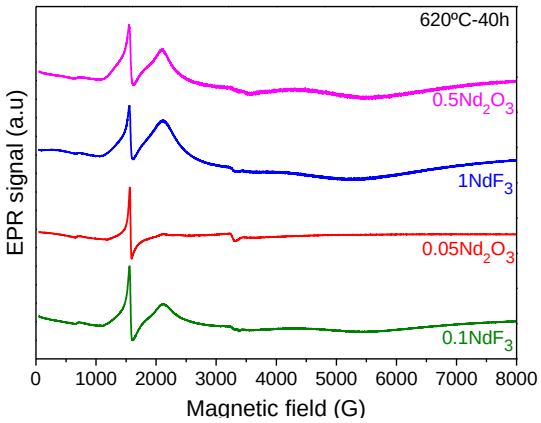


Figure 6. EPR signals of GCs dope with 0.1 and $1NdF_3$ and 0.05 and $0.5Nd_2O_3$.

EPR signals of $ErF_3$-doped samples are given in Figure 7. A sharp signal at 2130 G associated to $Fe^{3+}$ impurities is also observed in this sample. A quite broad resonance appears at low field, corresponding to a g ~ 12, is associated to $Er^{3+}$ ions in a fluorine-rich environment. In fact, for the sample doped with $0.5ErF_3$ there is a small tip superimposed to the quite broad band corresponding to $g_1 \sim 11.3\pm0.1$ in agreement with the one of $Er^{3+}$ in $LaF_3$ single crystals [34,35] and in $Er^{3+}$doped NPs [43]. For the higher doped sample the $Er^{3+}$ signal increases and the other two resonances corresponding to $g_2 \sim 4.9\pm0.2$ and $g_3 \sim 3.1\pm0.2$ are observed and unambiguously attributed to $Er^{3+}$ in $LaF_3$ NCs. The presence of small traces of $LaF_3$ NCs for $0.5ErF_3$ doped samples was also noticed in a previous work [12]. The fact that even in the starting glass there are some NCs suggest the high nucleating agent effect of $Er^{3+}$ ions in this system. In the GC samples, the $Er^{3+}$ resonances become well resolved for both dopant concentrations, being sharper for the less concentrated sample. A careful look at the $g_1$-line of the GC-$0.1ErF_3$ reveals a weak peak (left hand side) and two weak shoulders (right hand side) associated to the hyperfine structure of $^{167}Er$ ions with a nuclear spin $I$=7/2 whose abundance is around 22%. These weak resonances are not observed for the higher doped sample. These results indicate the further incorporation of $Er^{3+}$ ions in $LaF_3$ NCs after the crystallisation process, the effective concentration for the $0.5ErF_3$-doped sample being quite higher. It is worth noticing that the broader signal at low field is still present for the GC samples but it is reduced in intensity with respect to glass samples. This indicates that there is still an important amount of $Er^{3+}$ ions outside the $LaF_3$ NCs.

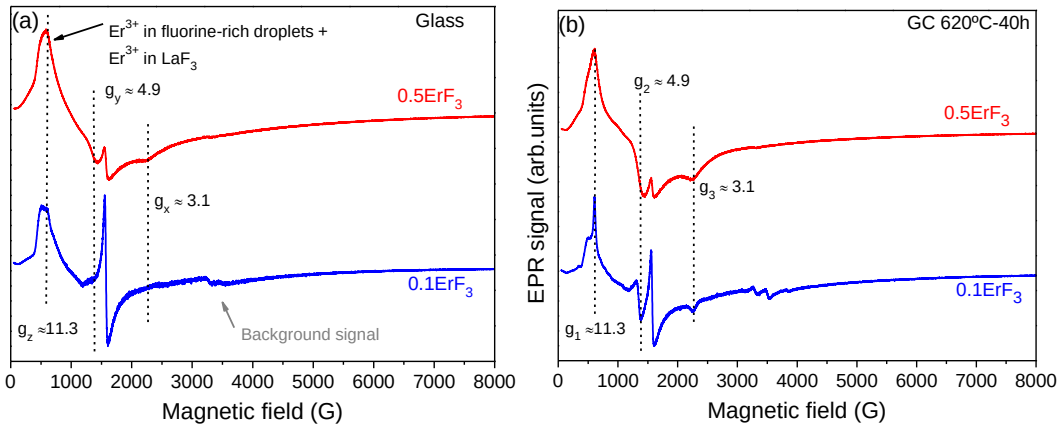


Figure 7. EPR signals of (a) glasses and (b) GCs doped with 0.1 and 0.5$ErF_3$.

The EPR signals of glasses and GCs doped with $ErF_3$ and $Er_2O_3$ are given in Figure 8. Very similar features are obtained for G-0.1$ErF_3$ and G-0.05$Nd_2O_3$ and for the oxide-doped sample there are also tiny perceivable resonances associated to $Er^{3+}$ in $LaF_3$ NCs. After the crystallisation process, sharp resonances appear for both samples indicating the progressive incorporation of $Er^{3+}$ ions in $LaF_3$ NCs. Anyway, there are no remarkable differences in using $Er_2O_3$ or $ErF_3$ for $Er^{3+}$-doped samples, thus confirming the previous results of XANES.

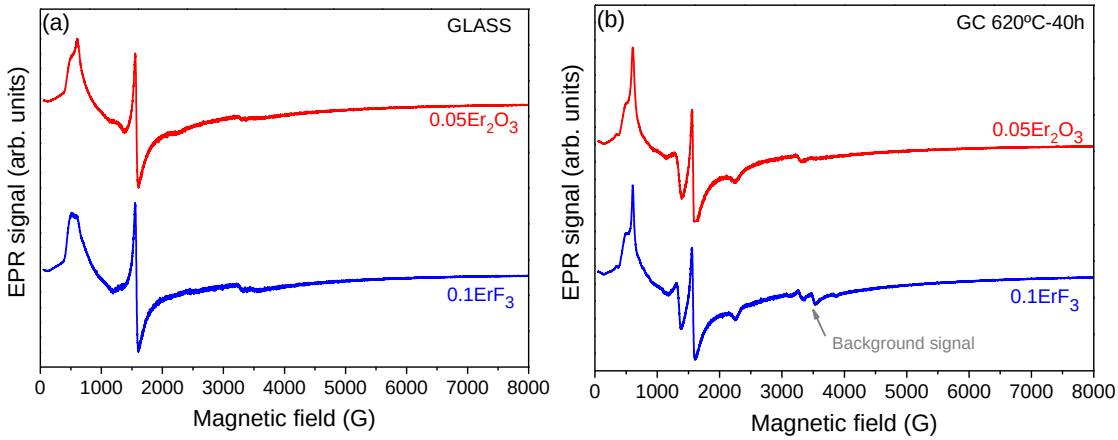


Figure 8. EPR signals of (a) glasses and (b) GCs doped with 0.1$ErF_3$ and 0.05$Er_2O_3$.

*3.4 PL and lifetime*

The previous results concerning $Nd^{3+}$ incorporation on the NCs are confirmed by site-selective laser spectroscopy and lifetime measurements. As we have mentioned before, in a previous work, some of the authors obtained the $Nd^{3+}$ emission in $LaF_3$ NCs in GC samples heat treated at 620 ºC-40 h doped with different $NdF_3$ concentrations by selective excitation at 786 nm in the $^4F_{5/2}$ level. It was found that at this excitation wavelength, the contribution to the emission spectrum corresponds to $Nd^{3+}$ ions incorporated in the $LaF_3$ NCs whereas by exciting at 802 nm,

a broad band similar to the one of the glass sample is observed corresponding to the emission of $Nd^{3+}$ in an amorphous environment. The relative contribution of both emissions in the crystalline and amorphous phase was strongly affected by $Nd^{3+}$ concentration.

At low concentration ($0.1NdF_3$), the most efficient emission corresponds to $Nd^{3+}$ ions in the NCs whereas the emission from the amorphous phase dominates at higher concentrations ($1NdF_3$), due to the strong concentration quenching of $Nd^{3+}$ in the NCs.

To analyse the effect of $Nd_2O_3$ doping on the luminescence of $Nd^{3+}$ in the NCs, we have obtained the low temperature (T=9K) emission spectra under the same experimental conditions to compare the results with those found in $NdF_3$ doped GC.

As an example, Figures 9a and 9b show the low temperature emission spectra corresponding to the $^4F_{3/2} \rightarrow {}^4I_{11/2}$ laser transitions of the GC sample heat treated at 620 ºC-40 h obtained under excitation at 786 and 802 nm, the wavelengths at which is possible to separate the contribution to the emission from $Nd^{3+}$ ions in the NCs and in the amorphous phase. As can be seen, in both cases, the relative contribution of $Nd^{3+}$ emission in the NCs, obtained by exciting at 786 nm, is higher than the one corresponding to the amorphous phase (802 nm excitation), however, the sample doped with 0.05% $Nd_2O_2$ shows a slightly lower contribution from $Nd^{3+}$ in the crystalline phase compared to the amorphous one.

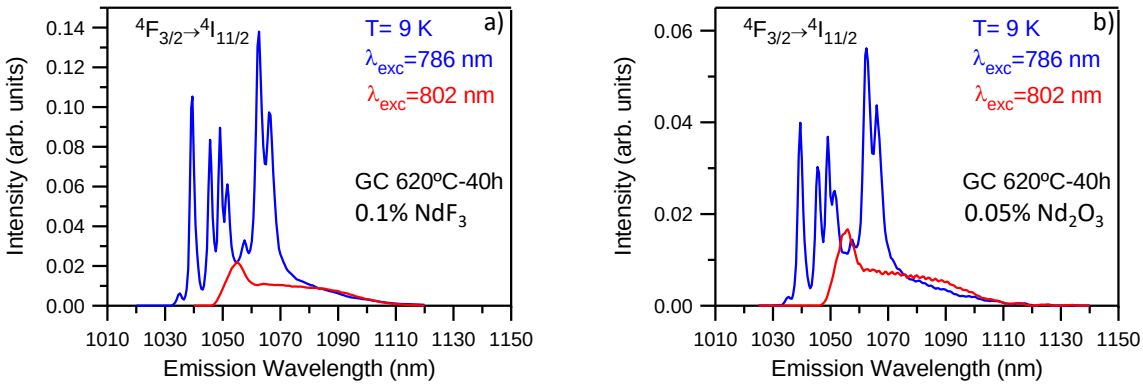


Figure 9. Low temperature (9K) emission spectra obtained under excitation at 786 nm (blue line) and 802 nm (red line) for the GC sample doped with (a) $0.1NdF_3$ and (b) $0.05Nd_2O_3$.

Figure 10a and 10b show the emission spectra recorded at 9 K under 786 and 802 nm excitation for the samples doped with $1NdF_3$ and $0.5Nd_2O_3$. At this concentration, for the sample doped with $NdF_3$ (Figure 11a), the emission from $Nd^{3+}$ in the amorphous phase is nearly twice the one of $Nd^{3+}$ in $LaF_3$ NCs due to concentration quenching. Moreover, the spectrum becomes broader and with less resolved peaks. In the case of the GC sample doped with $0.5Nd_2O_3$, both emissions from $Nd^{3+}$ ions in the crystalline and amorphous phases are similar with a more resolved spectrum under 786 nm excitation than in the case of $NdF_3$ doping. These results

indicate a lower concentration quenching of the $Nd^{3+}$ emission in the NCs for the GC samples doped with $Nd_2O_3$ according with a less $Nd^{3+}$ incorporated in $LaF_3$ NCs.

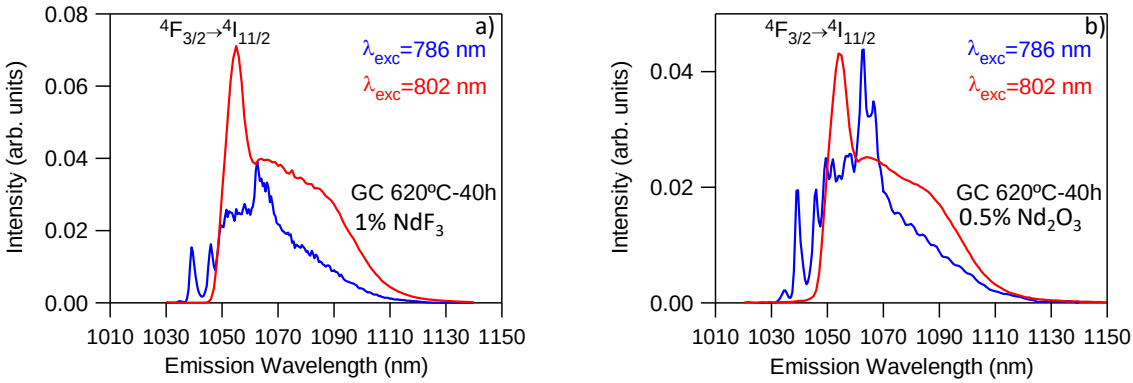


Figure 10. Low temperature (9K) emission spectra obtained under excitation at 786 nm (blue line) and 802 nm (red line) for the GC sample doped with (a) $1NdF_3$ and (b) $0.5Nd_2O_3$.

The lifetime values of $Nd^{3+}$ ions in the NCs are also affected by concentration quenching decreasing from 688 µs for the sample doped with 0.1 mol% $NdF_3$ to 98 µs for the one doped with $1NdF_3$. The lifetime values corresponding to the $Nd^{3+}$ ions incorporated in the NCs have been obtained at 9 K by exciting at 786 nm collecting the luminescence at 1039 nm. Figure 11a displays the decays for the GC samples doped with $0.1NdF_3$ and $0.05Nd_2O_3$. As can be seen, the decays can be described by a single exponential function and the lifetime values are 688 µs and 635 µs, respectively. As concentration increases, there is decrease of the lifetimes due to concentration quenching however this quenching is reduced in the case of the sample with $0.5Nd_2O_3$ compared with the $1NdF_3$ doped GC sample. As shown in Figure 11b, the decay for the GC sample doped with $0.5Nd_2O_3$ is nearly single exponential with a lifetime of 163 µs whereas the decay for the GC sample doped with $1NdF_3$ is not single exponential with a lifetime of 98 µs. The longer lifetime in the case of the sample doped with $0.5Nd_2O_3$ suggests that in this sample the effective concentration is lower than in the case of the one doped with $1NdF_3$ and less $Nd^{3+}$ ions are incorporated in the NCs in agreement with the results obtained from XANES and EPR.

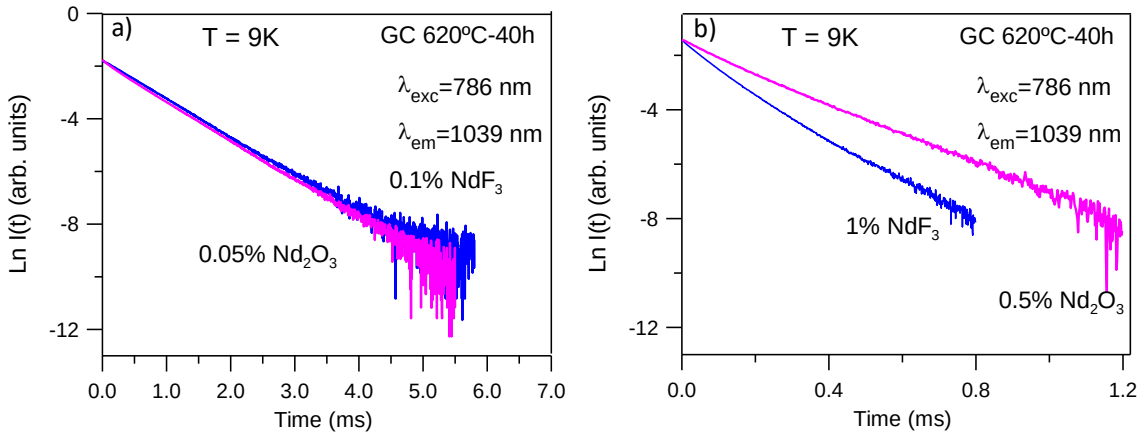


Figure 11. Semilogarithmic plot of the experimental decays from the $^4F_{3/2}$ state obtained under excitation at 786 nm collecting the luminescence at 1039 nm (a) for the GC samples doped with (a) $0.1NdF_3$ (blue line) and $0.05Nd_2O_3$ (pink line) and (b) $1NdF_3$ (blue line) and $0.5Nd_2O_3$ (pink line).

In the case of $ErF_3$ and $Er_2O_3$ the fluorescence decay curves from $^4I_{13/2}$ level for both samples have been obtained by pumping level $^4I_{9/2}$ at 801 nm collecting the luminescence at 1540 nm at the maximum of the $^4I_{13/2} \rightarrow {}^4I_{15/2}$ emission. For both samples a similar lifetime of around 6.5 ms was obtained with no significant differences in the experimental decays. This result is in agreement with those obtained from XANES and EPR.

## 4. Conclusions

Transparent oxyfluoride glass-ceramics with $LaF_3$ NCs, doped with $Nd^{3+}$ and $Er^{3+}$ using oxide and fluoride precursors, were prepared by MQ and controlled crystallisation. The local environment of the RE ions was studied using XAS, EPR and PL. Clear differences in XAS and EPR spectra were observed for $Nd^{3+}$-doped samples indicating a lower incorporation of $Nd^{3+}$ in the $LaF_3$ NCs when the oxide precursor is used. PL measurements confirmed this result. The lifetime of $Nd^{3+}$ in the $LaF_3$ NCs increased from 635 (using $Nd_2O_3$) to 688 μs (using $NdF_3$) for low doping level (0.1 mol% $Nd^{3+}$). Instead, the lifetime decreased from 163 to 98 μs for higher doping level (1 mol% $Nd^{3+}$), showing a stronger concentration quenching when $NdF_3$ is used. For $Er^{3+}$-doped samples (0.1 mol% $Er^{3+}$) very similar XAS, EPR, PL spectra and lifetimes were observed, indicating that a similar incorporation of $Er^{3+}$ in the $LaF_3$ NCs is obtained using oxide or fluoride precursors. Therefore, the effect of the dopant precursor on the incorporation of the RE ions depends on both nature of RE ion and its content.

**Acknowledgments**

This work was supported by MINECO under projects MAT2013-48246-C2-1-P/-2-P and MAT2017-87035-C2-1-P/-2-P (AEI/FEDER, UE), and Basque Country University PPG17/07 and GIU17/014. We acknowledge The European Synchrotron (ESRF), MINECO, and CSIC for provision of synchrotron radiation facilities in using the BM25-SpLine beamline. We also thank the BM25-SpLine staff for the technical support beyond their duties. This presentation is a part of dissemination activities of project FunGlass. This project has received funding from the European Union´s Horizon 2020 research and innovation program under grant agreement No 739566. A.S. acknowledges the financial support from the Comunidad de Madrid for an "Atracción de Talento Investigador" contract (No. 2017-t2/IND5395). D.B acknowledges "Ministerio de Ciencia e Innovación" for the project MAT2016-75362-C3-1-R.

**REFERENCES**

[1] Y. Wang, J. Ohwaki, New transparent vitroceramics codoped with $Er^{3+}$ and$Yb^{3+}$ for efficient frequency upconversion, Appl. Phys. Lett. 63 (1993) 3268–3270. doi:10.1063/1.110170.

[2] A. de Pablos-Martín, A. Durán, M.J. Pascual, Nanocrystallisation in oxyfluoride systems: mechanisms of crystallisation and photonic properties, Int. Mater. Rev. 57 (2012) 165–186. doi:10.1179/1743280411Y.0000000004.

[3] P.P. Fedorov, A.A. Luginina, A.I. Popov, Transparent oxyfluoride glass ceramics, J. Fluor. Chem. 172 (2015) 22–50. doi:10.1016/j.jfluchem.2015.01.009.

[4] X. Liu, J. Zhou, S. Zhou, Y. Yue, J. Qiu, Transparent glass-ceramics functionalized by dispersed crystals, Prog. Mater. Sci. 97 (2018) 38–96. doi:10.1016/j.pmatsci.2018.02.006.

[5] A. de Pablos-Martín, M. Ferrari, M.J. Pascual, G.C. Righini, Glass-ceramics: A class of nanostructured materials for photonics, Riv. Nuovo Cimento. 38 (2015) 311–369. doi:10.1393/ncr/i2015-10114-0.

[6] G. Gorni, J.J. Velázquez, J. Mosa, R. Balda, J. Fernández, A. Durán, Y. Castro, Transparent Glass-Ceramics Produced by Sol-Gel : A Suitable Alternative for Photonic Materials, Materials 11 (2018) 212. doi:10.3390/ma11020212.

[7] S. Tanabe, H. Hayashi, T. Hanada, N. Onodera, Fluorescence properties of $Er^{3+}$ ions in glass ceramics containing $LaF_3$ nanocrystals, Opt. Mater. 19 (2002) 343–349. doi:10.1016/S0925-3467(01)00236-1.

[8] M. Mattarelli, V.K. Tikhomirov, A.B. Seddon, M. Montagna, E. Moser, $Tm^{3+}$-activated transparent oxy-fluoride glass–ceramics : structural and spectroscopic properties, J. Non-Cryst. Solids 346 (2004) 354–358. doi:10.1016/j.jnoncrysol.2004.08.043.

[9] V. Lavin, I. Iparraguirre, J. Azkargorta, A. Mendioroz, J. González-Plata, R. Balda, J. Fernández, Stimulated and upconverted emissions of $Nd^{3+}$ in a transparent oxyfluoride glass-ceramic, Opt. Mater 25 (2004) 201–208. doi:10.1016/S0925-3467(03)00270-2.

[10] V.K. Tikhomirov, V.D. Rodríguez, J. Méndez-Ramos, J. Del-Castillo, D. Kirilenko, G. Van Tendeloo, V.V. Moshchalkov, Optimizing Er/Yb ratio and content in Er–Yb co-doped glass-ceramics for enhancement of the up- and down-conversion luminescence, Sol. Energy Mater. Sol. C. 100 (2012) 209–215. doi:10.1016/j.solmat.2012.01.019.

[11] Y. Wei, J. Li, J. Yang, X. Chi, H. Guo, Enhanced green upconversion in $Tb^{3+}$-$Yb^{3+}$ co-doped oxyfluoride glass ceramics containing $LaF_3$ nanocrystals, J. Lumin. 137 (2013) 70–72. doi:10.1016/j.jlumin.2012.11.017.

[12] G. Gorni, R. Balda, J. Fernández, L. Pascual, A. Durán, M.J. Pascual, Effect of the heat treatment on the spectroscopic properties of $Er^{3}$-$Yb^{3+}$-doped transparent oxy fluoride nano-glass-ceramics, J. Lumin. 193 (2018) 51–60. doi:10.1016/j.jlumin.2017.05.063.

[13] J.J. Velázquez, R. Balda, J. Fernández, G. Gorni, G.C. Mather, L. Pascual, A. Durán, M.J. Pascual, Transparent glass-ceramics of sodium lutetium fluoride co-doped with erbium and ytterbium, J. Non-Cryst. Solids 501 (2018) 136–144. doi:10.1016/j.jnoncrysol.2017.12.051.

[14] Z. Chen, G. Wu, H. Jia, K. Sharafudeen, W. Dai, X. Zhang, S. Zeng, J. Liu, R. Wei, S. Lv, G. Dong, J. Qiu, Improved Up-Conversion Luminescence from $Er^{3+}$: $LaF_3$ Nanocrystals Embedded in Oxy fluoride Glass Ceramics via Simultaneous Triwavelength Excitation, J. Phys. Chem. C. 119 (2015) 24056– 24061. doi:10.1021/acs.jpcc.5b08103.

[15] V.K. Tikhomirov, D. Furniss, A.B. Seddon, I.M. Reaney, M. Beggiora, M. Ferrari, M. Montagna, R. Rolli, Fabrication and characterization of nanoscale, $Er^{3+}$-doped, ultratransparent oxy-fluoride glass ceramics, Appl. Phys. Lett. 8 (2002) 1937-1939. doi:10.1063/1.1497196.

[16] Z. Fang, S. Zheng, W. Peng, H. Zhang, S. Zhou, D. Chen, J. Qiu, Fabrication and Characterization of Glass-Ceramic Fiber-Containing $Cr^{3+}$-Doped $ZnAl_2O_4$ Nanocrystals, J. Am. Ceram. Soc. 98 (2015) 2772–2775. doi:10.1111/jace.13716.

[17] Z. Fang, X. Xiao, X. Wang, Z. Ma, E. Lewis, G. Farrell, P. Wang, J. Ren, H. Guo, J. Qiu, Glass-ceramic optical fiber containing $Ba_2TiSi_2O_8$ nanocrystals for frequency conversion of lasers, Sci. Rep. 7 (2017) 44456. doi:10.1038/srep44456.

[18] C. Koepke, K. Wisniewski, M. Żelechower, E. Czerska, The role of phonons in the luminescence characteristics of SICLOF oxyfluoride glass and glass-ceramic fibers doped with $Er^{3+}/Yb^{3+}$, J. Lumin. 204 (2018) 278–283. doi:10.1016/j.jlumin.2018.08.035.

[19] K.V. Rishnaiah, Y.Ledemi, C. Genevois, E.Veron, X. Sauvage, S. Morency, E.S, de Lima Filho, G. Nemova, M. Allix, Y. Messaddeq, R. Kashyap, Ytterbium-doped oxyfluoride nano-glass-ceramic fibers for laser cooling, Opt. Mater.Exp. 7(2017) 104–113.

[20] G. Gorni, R. Balda, J. Fernández, I. Iparraguirre, J.J Velázquez, Y. Castro, L. Pascual, G. Chen, M. Sundararajan, M.J. Pascual, A. Durám, Oxyfluoride glass–ceramic fibers doped with $Nd^{3+}$: structural and optical characterization, CrystEngComm. 19 (2017) 6620–6629.doi:10.1039/C7CE01380A.

[21] B.N. Samson, P.A. Tick, N.F. Borrelli, Efficient neodymium-doped glass-ceramic fiber laser and amplifier, Opt. Lett. 26 (2001) 145–147. doi:10.1364/OL.26.000145.

[22] C.K. Asawa, M. Robinson, Temperature-Dependent Concentration Quenching of Fluorescence by Cross Relaxation of $Nd^{3+}$ in $LaF_3$, Phys. Rev. 141 (1966) 251–258. doi:10.1103/PhysRev.141.251.

[23] R. Balda, J. Fernandez, A. Mendioroz, J.L. Adams, B. Boulard, Temperature-dependent concentration quenching of $Nd^{3+}$ fluorescence in fluoride glasses, J.Phys. Condens. Matter. 6 (1994) 913–924. doi:10.1088/0953-8984/6/4/011.

[24] A.D. Sontakke, K. Biswas, A.K. Mandal, K. Annapurna, Concentration quenched luminescence and energy transfer analysis of $Nd^{3+}$ ion doped Ba-Al-metaphosphate laser glasses, Appl. Phys. B. 101 (2010) 235–244. doi:10.1007/s00340-010-4010-1.

[25] G. Gorni, J.J. Velázquez, G.C. Mather, A. Durán, G. Chen, M. Sundararajan, R. Balda, J. Fernández, M.J. Pascual, Selective excitation in transparent oxyfluoride glass-ceramics doped with $Nd^{3+}$, J. Eur. Ceram. Soc. 37 (2017) 1695–1706. doi:10.1016/j.jeurceramsoc.2016.11.014.

[26] M. Mortier, Nucleation and anionic environment of $Er^{3+}$ in a germanate glass, J. Non-Cryst. Solids 318 (2003) 56–62.

[27] M. Abril, J. Méndez-Ramos, I.R. Martín, U.R. Rodríguez-Mendoza, V. Lavín, A. Delgado-Torres, V.D. Rodriguez, Optical properties of $Nd^{3+}$ ions in oxyfluoride glasses and glass ceramics comparing different preparation methods comparing different preparation methods, J. Appl. Phys. 95 (2004) 5271–5279. doi:10.1063/1.1707204.

[28] V.R. Mastelaro, E.D. Zanotto, X-ray Absorption Fine Structure (XAFS) studies of oxide glasses-A 45-year overview, Materials 11 (2018) 212. doi:10.3390/ma11020204.

[29] B. Ravel, M. Newville, ATHENA, ARTEMIS, HEPHAESTUS: data analysis for X-ray absorption spectroscopy using IFEFFIT, J. Synchrotron Radiat. 12 (2005) 537–541. doi:10.1107/S0909049505012719.

[30] A.I. Figueroa, G. van der Laan, S.E. Harrison, G. Cibin, T. Hesjedal, Oxidation Effects in Rare Earth Doped Topological Insulator Thin Films, Sci. Rep. 6 (2016) 22935.doi:10.1038/srep22935.

[31] B.K. Agarwal, L.P. Verma, A rule for chemical shifts of X-ray absorption edges, J. Phys. C Solid State Phys. 3 (1970) 535–537. doi:10.1088/0022-3719/3/3/007.

[32] A. De Pablos-Martín, M. A. García, A. Muñoz-Noval, G.R. Castro, M.J. Pascual, A. Durán, Analysis of the distribution of $Tm^{3+}$ ions in $LaF_3$ containing transparent glass-ceramics through X-ray absorption spectroscopy, J. Non-Cryst. Solids 384 (2014) 83–87. doi:10.1016/j.jnoncrysol.2013.07.021.

[33] Y.G. Choi, Covalence of chemical bonds and white-line intensity of an $L_3$-edge X-ray absorption near-edge structure of rare earth elements embedded in glass, Met. Mater. Int. 15 (2009) 993–999. doi:10.1007/s12540-009-0993-8.

[34] J.M. Baker, R.S. Rubins, Electron Spin Resonance in Two Groups of Lanthanon Salts, Proc. Phys. Soc. 1353 (1961) 1353–1360. doi:10.1088/0370-1328/78/6/338.

[35] M.B. Schulz, C.D. Jefries, Spin-Lattice Relaxation of Rare-Earth Ions in $LaF_3$, Phys. Rev. 149 (1966) 270–288. doi:10.1103/PhysRev.149.270.

[36] T. Castner, G.S. Newell, W.C. Holton, C.P. Slighter, Note on the paramagnetic resonance of iron in glass, J. Chem. Phys. 32 (1960) 668–673. doi:10.1063/1.1730779.

[37] C.M. Brodbeck, Investigations of g-value correlations associated with the g =4.3 ESR signal of $Fe^{3+}$ in glass, J. Non-Cryst. Solids 40 (1980) 305–313. doi:10.1016/0022-3093(80)90108-8.

[38] G. Dantelle, M. Mortier, P. Goldner, D. Vivien, EPR and optical study of $Yb^{3+}$- doped β-$PbF_2$ single crystals and nanocrystals of glass-ceramics, J. Phys.Condens. Matter. 18 (2006) 7905–7922. doi:10.1088/0953-8984/18/34/005.

[39] V. Mehta, D. Gourier, A. Mansingh, A.L. Dawar, EPR of $Nd^{3+}$ ions in phosphate and borate glasses, Solid State Commun. 109 (1999) 513–517. doi:10.1016/S0038-1098(98)00598-5.

[40] B. V Padlyak, R. Lisiecki, T.B. Padlyak, V.T. Adamiv, Spectroscopy of $Nd^{3+}$ luminescence centres in $Li_2B_4O_7$: Nd, $LiCaBO_3$: Nd, and $CaB_4O_7$: Nd glasses, J. Lumin. 198 (2018) 183–192. doi:10.1016/j.jlumin.2018.02.046.

[41] B. V Padlyak, R. Lisiecki, W. Ryba-romanowski, Spectroscopy of the Er-doped lithium tetraborate glasses, Opt. Mater. 54 (2016) 126–133. doi:10.1016/j.optmat.2016.02.025.

[42] U. Rocha, C. Jacinto, K. Upendra, F.J. López, D. Bravo, J. García, D. Jaque, Real-time deep-tissue thermal sensing with sub-degree resolution by thermally improved $Nd^{3+}$: $LaF_3$ multifunctional nanoparticles, J. Lumin. 175 (2016) 149–157. doi:10.1016/j.jlumin.2016.02.034.

[43] E.C. Ximendes, U. Rocha, C. Jacinto, K.U. Kumar, D. Bravo, F.J. López, E.M. Rodríguez, J. García-solé, D. Jaque, Self-monitored photothermal nanoparticles based on core–shell engineering, Nanoscale. 8 (2016) 3057–3066. doi:10.1039/c5nr08904b.

# *PAPER 6*

**Phase evolution of $KLaF_4$ NCs and their effects on the photoluminescence of $Nd^{3+}$ doped transparent oxyfluoride glass-ceramics.**

A. Cabral, R. Balda, J. Fernández, G. Gorni, J.J. Velázquez, L. Pascual, A. Durán, M.J. Pascual.

*CrystEngComm.* **20** (2018) 5760–5771. doi:10.1039/C8CE00897C

CrystEngComm

PAPER

View Article Online
View Journal | View Issue



Cite this: *CrystEngComm*, 2018, **20**, 5760

# Phase evolution of $KLaF_4$ nanocrystals and their effects on the photoluminescence of $Nd^{3+}$ doped transparent oxyfluoride glass-ceramics

A. A. Cabral, [a] R. Balda, [bc] J. Fernández,[bc] G. Gorni, [d] J. J. Velázquez, [d] L. Pascual, [e] A. Durán [d] and M. J. Pascual *[d]

Received 30th May 2018,
Accepted 13th August 2018

DOI: 10.1039/c8ce00897c

rsc.li/crystengcomm

Transparent oxyfluoride glass-ceramics (GCs) were prepared starting from the glass composition $70SiO_2$–$7Al_2O_3$–$16K_2O$–$7LaF_3$ (mol%) doped with four different $Nd^{3+}$ concentrations (0.1–2 mol%). The glass-ceramics were prepared by heat treatment above the corresponding glass transition temperatures ($T_g$ + 10–100 °C). Depending on the $Nd^{3+}$ concentration, cubic (α-phase) and hexagonal (β-phase) $KLaF_4$ nanocrystals (NCs) precipitated from the starting glass. By X-ray diffraction (XRD) and high resolution transmission electron microscopy (HR-TEM), the crystallization of the cubic structure was observed for all compositions, while β-$KLaF_4$ nanocrystals were mostly detected for the glass-ceramic samples doped with 0.5 mol% $NdF_3$. This noteworthy result is confirmed by site-selective laser spectroscopy. The presence of α-$KLaF_4$ and β-$KLaF_4$ crystalline phases is unambiguously identified from the emission and excitation spectra and lifetime measurements of the $^4F_{3/2}$ state of $Nd^{3+}$ ions. The spectroscopic results confirm those obtained with XRD and HR-TEM techniques: α-$KLaF_4$ NCs are found to be present for all $NdF_3$ concentrations whereas β-$KLaF_4$ NCs are predominant in the glass-ceramic samples doped with 0.5 mol%.

## 1. Introduction

The development of transparent glass-ceramic materials with NCs homogeneously distributed in a glass matrix is highly desirable in the photonic applications field. They combine the efficient incorporation of active rare-earth (RE) ions into low phonon energy fluoride crystals and the good thermal stability and high mechanical and chemical properties of an aluminosilicate glass matrix; therefore they are potential candidates for numerous optical applications.[1–6]

Rigorous control of the nucleation and crystal growth processes is required. In principle, these GCs are prepared from non-isochemical systems, where the chemical composition of the residual glass changes during the crystallization process, and the corresponding crystal growth rates vary with heat treatment time. Nevertheless, there are two scenarios: (i) if NCs are enriched in network glass formers, the crystal growth rate increases; (ii) if a phase is enriched in network modifiers, a diffusion barrier is formed and a decreasing crystal growth rate is obtained. This latter effect leads to self-organized crystallization processes, as demonstrated for $Na_2O/K_2O/CaO/CaF_2/Al_2O_3/SiO_2$[7] and $Na_2O/K_2O/BaF_2/Al_2O_3/SiO_2$ GCs.[8,9]

Concerning $Na_2O$–$Al_2O_3$–$SiO_2$–$LaF_3$ glass systems and based on the crystal chemical nature of the elements, Sroda *et al.*[10] pointed out that the production of transparent oxyfluoride GCs obtained through the precipitation of $LaF_3$ crystals in the glass network is highly dependent on the $Na_2O/(SiO_2 + Al_2O_3)$ ratio. In fact, $LaF_3$ nanocrystallization was confirmed in some un-doped silicate glasses with nominal compositions $40SiO_2$–$30Al_2O_3$–$18Na_2O$–$12LaF_3$ (mol%)[11,12] and $55SiO_2$–$20Al_2O_3$–$15Na_2O$–$10LaF_3$ (mol%),[13] hereafter called 55Si-10La. When this latter composition was doped with $Tm^{3+}$, the largest $LaF_3$ NCs were obtained as compared to the un-doped composition, and the dopant affected the crystal growth velocity, but did not influence the crystallization mechanism.[14,15] Recently, Gorni *et al.*[16] prepared transparent 55Si-10La GCs doped with several $Nd^{3+}$ concentrations and concluded that the crystallization mechanism was controlled by diffusion with a fixed number of nuclei, which did not change with the addition of $Nd^{3+}$. Moreover, they were able, upon selective excitation, to reproduce the optical properties of pure $LaF_3$ crystals doped with $Nd^{3+}$, thus obtaining a notable increase of luminescence efficiency. They also

[a] *Departamento de Física, Instituto Federal do Maranhão – IFMA, 65030-001, São Luis, MA, Brazil*
[b] *Departamento de Física Aplicada I, Escuela Superior de Ingeniería, Universidad del País Vasco UPV-EHU, Bilbao, Spain*
[c] *Centro de Física de Materiales UPV/EHU-CSIC, San Sebastian, Spain*
[d] *Instituto de Cerámica y Vidrio (ICV-CSIC), C/Kelsen 5, 28049 Madrid, Spain. E-mail: mpascual@icv.csic.es*
[e] *Instituto de Catálisis y Petroleoquímica (ICP-CSIC), C/Marie Curie 2, 28049 Madrid, Spain*

prepared optical fibers of the same composition and obtained similar results.[17]

On the other hand, $NaLaF_4$ NCs with a size ≈20 nm enclosed in a $SiO_2$ enriched barrier have been detected in a mixed alkali glass composition $70SiO_2$–$7Al_2O_3$–$8Na_2O$–$8K_2O$–$7LaF_3$ (mol%) (70Si-7La).[18] When this glass composition was doped with $Tm^{3+}$, the size of these NCs was nearly constant around 14 nm, with a delayed crystallization process.[19]

Another oxyfluoride glass composition with peculiar crystallization characteristics is $70SiO_2$–$7Al_2O_3$–$16K_2O$–$7LaF_3$ (mol%), hereafter called 70Si-7LaK. In comparison with the mixed alkali glass $70SiO_2$–$7Al_2O_3$–$8Na_2O$–$8K_2O$–$7LaF_3$ (mol%), the 70Si-7LaK glass exhibits higher viscosity and lower kinetic fragility.[20] In addition, depending on the chosen temperature of heat-treatment, for the first time α-$KLaF_4$ and β-$KLaF_4$ NCs were achieved, which had cubic and hexagonal structures, respectively. Nevertheless, the crystallization process was drastically modified when the 70Si-7LaK glass was co-doped with 0.2 mol% $Tm_2O_3$ and 0.5 mol% $YbF_3$, and β-$KLaF_4$ NCs were not detected, even after heat-treatment at 580 °C for 150 h.[21] The relevance of this finding is strongly related to better fluorescence and higher up-conversion properties of the β crystalline phase, as previously demonstrated for other glass systems, where cubic and hexagonal $Na(Y,Gd)F_4$ crystals precipitate.[22–27] In particular, $NaYF_4$ is known to be one of the most efficient hosts of rare earth (RE) ions for near-infrared to visible up-conversion emission and has been investigated for its use in bio-imaging and tissue detection.[28,29] The phase exists in high temperature cubic and low-temperature hexagonal polymorphs.[30] A phonon energy of 262 $cm^{-1}$ has been reported for hexagonal $KLaF_4$.[31] Tyagi *et al.*[32] suggested that the advantageous lower phonon energy of $KLaF_4$ in comparison with $NaYF_4$ (360 $cm^{-1}$) arises from the greater radius of the alkali-metal ion, whereas the greater size of the La ions in $KLaF_4$ as compared with that of the Y ions in $NaYF_4$ imparts higher stability.[33]

Some papers have been published concerning the optical properties of the $KLaF_4$ crystalline phase. In particular, cubic $KLaF_4$ crystals present interesting optical properties when doped with high contents of $Eu^{3+}$ ions, resulting in a strong red color and longer lifetimes after excitation with different wavelengths.[34] These results make $KLaF_4$ a promising material for white light LEDs and other display applications. On the other hand, S. Ahmad *et al.*[35] showed that cubic and hexagonal $KLaF_4$ crystals can be efficient green emitters when doped with various concentrations of $Tb^{3+}$ ions, resulting in a color tuning from bluish-green to green as the ion concentration changes. All of these results suggest its potential use as a light emitting phosphor for LEDs, mercury-free lamps and plasma display panels or biological applications when this phase is co-doped with $Yb^{3+}$ ions by means of an up-conversion process.

Therefore, continuing the research to find a way to precipitate β-$KLaF_4$ NCs (phonon energy around 262 $cm^{-1}$), this paper aims to investigate the crystallization process of the 70Si-7LaK glass samples doped with different amounts of $Nd^{3+}$ and analyze its influence on the crystallization behavior and on the optical properties. $Nd^{3+}$ has an intense $^4F_{3/2} \rightarrow {}^4I_{11/2}$ emission at around 1.06 μm,[36] a well-known wavelength for laser applications. Moreover, it can also be used as a probe allowing the local structure of the ion to be related to the spectroscopic properties.[37]

## 2. Experimental section

### 2.1. Material preparation

Glass samples of composition $70SiO_2$–$7Al_2O_3$–$16K_2O$–$7LaF_3$ (70Si7LaK) doped with 0.1, 0.5, 1 and 2 $NdF_3$ (in mol%), hereinafter called G01; G05; G1 and G2, respectively, were prepared by melting–quenching using the following reagent grade raw materials: $SiO_2$ (Saint Gobain, 99.6%), $Al_2O_3$ (Panreac, 99.5%), $K_2CO_3$ (Scharlab 99.6%), $LaF_3$ (Alfa Aesar, 99.9%), and $NdF_3$ (Alfa Aesar, 99.9%) in an electric furnace. After mixing the reagents, the batches were homogenized in a Turbula mixer for 1 h, calcined in a covered platinum crucible at 1300 °C for 1 h and then melted at 1550 °C for 1 h. The melting process was carried out twice in order to improve homogenization. Further, the liquid was quickly quenched in air onto a brass mold and then annealed above the glass transition temperature ($T_g$) to avoid residual thermal stress. The chemical composition of the glass samples was analyzed by X-ray fluorescence spectroscopy (XRF) using a PANalytical spectrometer. All oxides were determined employing the melting method with $Li_2B_4O_7$, whereas elemental fluorine analysis was performed on pressed pellets of powdered glass (63 μm, 8 g) in order to avoid fluorine volatilization.

GCs of each composition were obtained by heat treatment of bulk glass samples at 590 °C and 660 °C from 1 to 342 h. Depending on the $Nd^{3+}$ concentration, the corresponding GCs will be denoted as GC*x*.

### 2.2. Thermal and structural characterization

Glass samples with dimensions of 9 × 7 × 5 mm were prepared for each composition to determine $T_g$ by dilatometry. The samples were heated in air at a heating rate of 5 K $min^{-1}$ using a Netzsch Gerätebau dilatometer, model 402 EP; the estimated error of $T_g$ was ±1 °C.

After heat treatment at 590 °C and 660 °C for different times, the glass-ceramic samples were milled, sieved (<63 μm) and characterized by XRD using an X-ray diffractometer D8 ADVANCE (Bruker) equipped with a Lynx Eye detector. The patterns were collected with a step size of 0.017° and a fixed counting time of 1.63 s per step, using monochromatic Cu-$K_\alpha$ radiation (1.5406 Å) over the angular range $10 \leq 2\theta \leq 60°$. The size of the NCs was estimated by the Scherrer equation (eqn (1)) using diffraction peaks at $2\theta \approx 43°$ and $2\theta \approx 38°$, which corresponded to the cubic (α-$KLaF_4$) and hexagonal (β-$KLaF_4$) phases, respectively:

$$D = \frac{G\lambda}{\cos\theta\sqrt{B_m^{\,2} - B_i^{\,2}}} \quad (1)$$

where $D$ is the crystal size, $G$ is a constant whose value is 0.94 (spherical crystals), $B_m$ is the full width at half maximum of the peak, and $\theta$ is the Bragg angle. The errors were calculated by peak fitting (pseudo-Voigt function) and in accordance with error theory. The instrumental broadening $B_i$ was calculated using NaF as a reference (<63 μm).

The crystalline phases were indexed using the ICDS database (Inorganic Crystal Structure Database).

### 2.3. Transmission electron microscopy

Samples for HR-TEM of the base glass and the corresponding GCs were prepared from sieved powders of size <63 μm dispersed in ethanol. The micrographs were recorded using a JEOL 2100 field-emission gun transmission electron microscope operating at 200 kV with a point resolution of 0.19 nm. Micrograph analysis was performed using Gatan Digital Micrograph software.

### 2.4. Optical characterization

Plano-parallel sheets (1 × 1 $cm^2$ size and 2 mm thickness) of the parent glass and the corresponding GC samples obtained at 590 °C for 24 and 150 h and at 660 °C for 66 and 150 h were prepared and polished for the optical characterization.

Site-selective steady-state emission and excitation spectra were recorded by exciting the samples with a continuous wave (cw) Ti:sapphire ring laser (0.4 $cm^{-1}$ linewidth) in the spectral range of 770–920 nm. The fluorescence was analyzed with a 0.25 m monochromator, and the signal was detected using an extended IR Hamamatsu H10330A-75 photomultiplier and finally amplified by a standard lock-in technique. The sample temperature was varied between 10 and 300 K in a continuous flow cryostat.

Lifetime measurements were obtained by exciting the samples with a Ti-sapphire laser pumped using a pulsed, frequency-doubled Nd:YAG laser (9 ns pulse width) and detecting the emission with the Hamamatsu H10330A-75 photomultiplier. Data were processed using a Tektronix oscilloscope.

## 3. Results and discussion

### 3.1. Chemical analysis and dilatometry

Transparent glass samples for each composition were obtained. The corresponding XRD patterns did not reveal the presence of any crystalline phase. Table 1 presents the nominal and analyzed compositions of each glass. From these results, the fluorine loss is estimated and given in the last line of the table. The fluorine loss varies between 28 and 40 wt%. The chemical analysis of the other elements shows values roughly in agreement with the nominal ones. Such large fluorine loss is quite typical in these compositions due to the high melting temperatures involved.

Fig. 1 shows the increasing tendency of $T_g$ with the $Nd^{3+}$ content. The $T_g$ value of the un-doped glass is 552 ± 2 °C.[20] As can be observed, $T_g$ increases from 568 °C to 584 °C, which is in agreement with previous results obtained by Gorni *et al.*[16] Consequently, the glass network becomes more rigid as the $NdF_3$ increases and the viscosity increases as suggested by Sroda[10] and de Pablos-Martín.[20]

### 3.2. X-ray diffraction (XRD)

Fig. 2(a–d) show the XRD diffractograms of the GC01 and GC05 samples heat treated at 590 °C for 1 h up to 150 h and at 660 °C for 1 to 192 h. From Fig. 2(a and b), it is observed that α-$KLaF_4$ peaks (JCPDS 00-075-2020) appear at both temperatures and are denoted by "x". Nevertheless, small traces of β-$KLaF_4$ NCs (JCPDS 00-075-1927) were also detected for GC01 heat treated at 660 °C for times longer than 144 h. The diffractograms of GC1 and GC2 compositions are similar to GC01, so they are not presented here. For GC05, cubic (α-$KLaF_4$) and hexagonal (β-$KLaF_4$) NCs precipitated at both treatment temperatures, Fig. 2(c and d).

Fig. 2 demonstrates that the diffraction peaks obtained for each composition become narrower and more intense as the temperature and time of heat treatment increase, respectively, thus indicating an increase of both crystal size and fraction.

Fig. 3 shows the crystal size of α-$KLaF_4$ and β-$KLaF_4$ crystals after heat treatments at 590 °C and 660 °C.

The crystal size increases with time for each $Nd^{3+}$ concentration at both temperatures but tends to stabilize after a certain time, which agrees with the un-doped and co-doped GCs.[20,21] Nevertheless, β-$KLaF_4$ NCs were detected by standard XRD only for GC05 at these temperatures.

The average crystal size changes with $Nd^{3+}$ concentration and varies from ≈8 nm for GC01 to ≈17 nm for GC05 (α-$KLaF_4$) at 590 °C, while the un-doped[20] and Tm–Yb co-doped[21] GCs have crystals with a mean size of ≈9 nm and 5.5 nm, respectively. In addition, α-$KLaF_4$ NCs were not detected

Table 1 Nominal and analyzed chemical compositions (in mol%) of each glass

| Glass components | G01 | | G05 | | G1 | | G2 | |
|---|---|---|---|---|---|---|---|---|
| | Nominal | Analyzed | Nominal | Analyzed | Nominal | Analyzed | Nominal | Analyzed |
| $SiO_2$ | 69.93 | 70.8 | 69.65 | 70.0 | 69.30 | 71.5 | 68.60 | 69.6 |
| $K_2O$ | 15.98 | 15.9 | 15.92 | 16.2 | 15.84 | 15.4 | 15.68 | 15.4 |
| $Al_2O_3$ | 6.99 | 7.1 | 6.97 | 7.3 | 6.93 | 7.4 | 6.86 | 7.1 |
| $LaF_3$ | 6.99 | 6.2 | 6.97 | 6.1 | 6.93 | 5.0 | 6.86 | 6.4 |
| $NdF_3$ | 0.10 | 0.06 | 0.50 | 0.3 | 1.00 | 0.7 | 2.00 | 1.5 |
| F | 21.27 | 18.8 | 22.41 | 19.2 | 23.79 | 17.1 | 26.58 | 23.7 |
| F loss (wt%) | | 28 | | 32 | | 40 | | 34 |

 

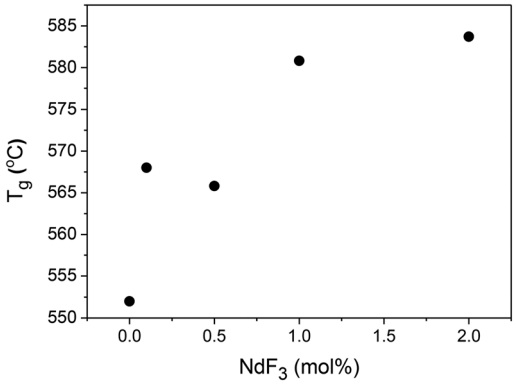


**Fig. 1** $T_g$ evolution with $NdF_3$ content (mol%). The $T_g$ of the undoped glass is also shown for comparison.

for GC01 after periods of time less than 15 h at this treatment temperature. Additionally, β-$KLaF_4$ NCs were detected only for GC05 for times longer than 15 h, which indicated that hexagonal nanocrystals need longer growth times.

Even when taking into account GCs with similar compositions, one should remember that the crystal size is highly temperature dependent. In this case, the treatment temperature used (590 °C) is higher than the one used to monitor the crystal growth of un-doped and Tm–Yb co-doped glasses (580 °C).[20,21] However, Fig. 3a shows that only GC01 presents a crystal size comparable to un-doped glass, which could be attributed to their very similar viscosity temperature dependence. For both temperatures, the crystal growth rate is very slow.

As the temperature increases, β-$KLaF_4$ NCs are detected in GC05 from shorter times of heat treatment at 660 °C, and they are larger than the cubic ones. Nevertheless, the crystal growth rates of α-$KLaF_4$ and β-$KLaF_4$ NCs at 590 °C as well as at 660 °C are strictly different, which means that their corresponding growth kinetics is independent. This result sheds a different light on the crystallization of the 70Si-7LaK composition. Hence, in comparison with previous work,[20,21] it could be stated that both crystalline phases coexist even at lower temperatures, coming probably from the residual fluorine in the glassy matrix, and it is not then clear if a polymorphic transformation of one phase to the other occurs.

Nevertheless, at least one question needs a more convincing answer: why do the β-$KLaF_4$ nanocrystals precipitate only for GC05?

High resolution XRD patterns were collected at the BM25 SpLine of the ESRF in Grenoble using 20 keV energy (corresponding to a wavelength of 0.619 Å) in order to obtain more insight and to overcome the detection limit of typical XRD instruments. Diffractograms were acquired in the range of 5–25° (corresponding to the range of 10–60° using standard $CuK\alpha_1$ radiation) using a step size of 0.02°. GC01 and GC05 heat treated at 590 °C for 150 h were measured and the corresponding diffractograms are shown in Fig. 4.

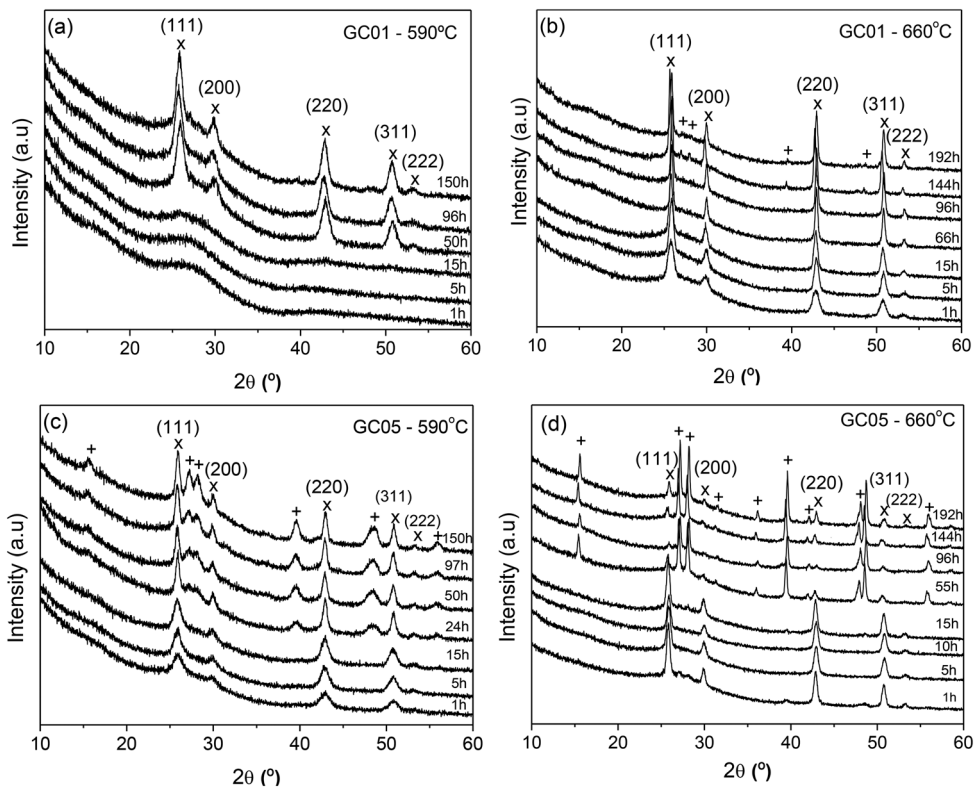


**Fig. 2** XRD patterns of the GC01 and GC05 samples heat-treated at different temperatures and times: (a) GC01 – 590 °C; (b) GC01 – 660 °C; (c) GC05 – 590 °C; and (d) GC05 – 660 °C. (x): α-$KLaF_4$ and (+): β-$KLaF_4$.

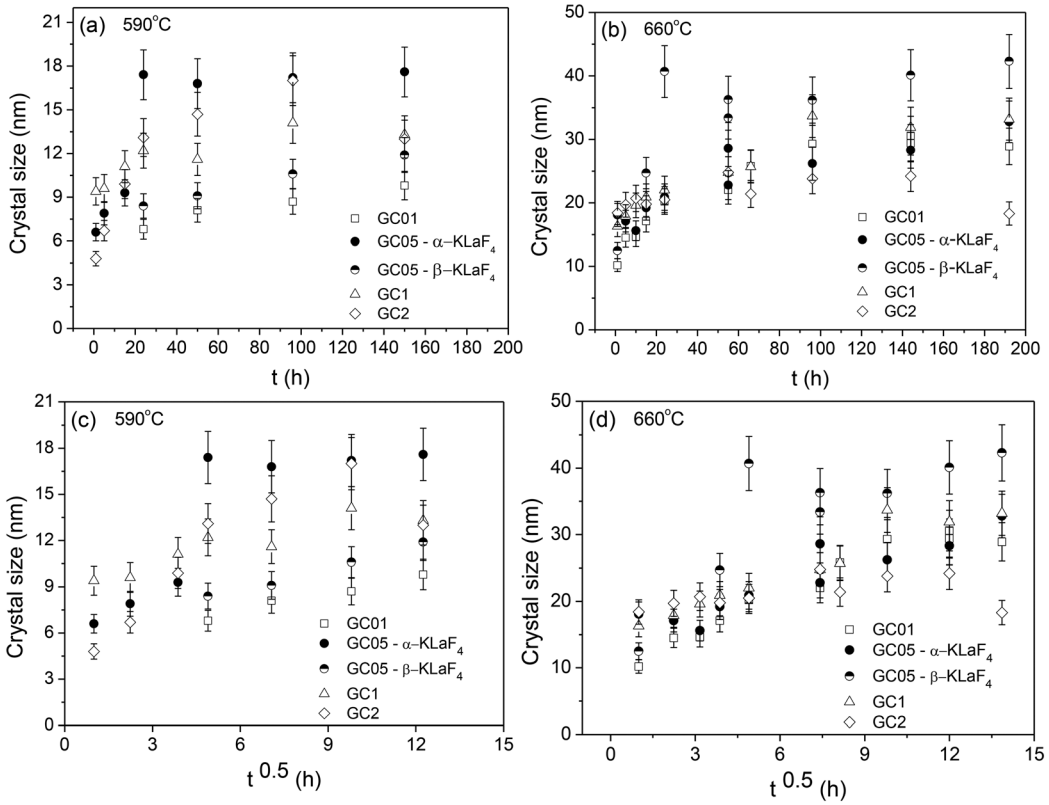


**Fig. 3** Crystal size (nm) as a function of time ($t$) after heat treatment at (a) 590 °C and (b) 660 °C, and crystal size (nm) as a function of $t^{0.5}$ after heat treatment at (c) 590 °C and (d) 660 °C.

Fig. 4(b) confirms the precipitation of cubic and hexagonal $KLaF_4$ NCs for GC05, where the corresponding patterns have relative intensities similar to the one given in Fig. 2c. In addition, the size of α-$KLaF_4$ and β- $KLaF_4$ NCs is estimated to be ~20 nm and 11 nm, respectively, which is in excellent agreement with the results shown in Fig. 3(a).

On the other hand, both $KLaF_4$ phases were detected for GC01 treated at 590 °C for 150 h (Fig. 4(a)), with sizes being ~9 and 11 nm for α and β-$KLaF_4$ crystals, respectively. Thus, the size of α-$KLaF_4$ NCs is in agreement with that given in Fig. 3. Nevertheless, the crystallization of the cubic phase is favored, since the β-$KLaF_4$ phase has a lower crystalline fraction than the cubic one.

Therefore, one can conclude that the hexagonal NCs are not a unique feature of the GC05 samples. Perhaps, these crystals also precipitate in GC1 and GC2 samples, even though they can be affected by the dopant concentration and the kind of dopant, such as $Tm^{3+}$ and $Yb^{3+}$, where β-$KLaF_4$ NCs are not detected.[21] In both cases, high-resolution XRD is a powerful technique that can clear these questions.

Taking into account that α-$KLaF_4$ and β-$KLaF_4$ NCs of GC05 precipitate with distinct crystal growth rates and they are also identified by high-resolution XRD at 590 °C for GC01, this could be an argument to conclude that the crystallization of the hexagonal phase did not come from the cubic one.

Comparing Fig. 2 and 4, it is observed that the intensity of the diffraction peaks increases even for times longer than 100 h, while the size of the NCs remains almost constant. Therefore, one can infer the formation of a viscous layer enriched in silica around the crystals, which hinders further crystal growth,[18] and the crystallization takes place from a fixed number of nuclei, as previously demonstrated for other oxyfluoride systems.[13,16]

Assuming a fixed number of nuclei, the crystallization is controlled by the interface or diffusion,[38] and it can be distinguished by the dependence of the crystal size on the time. In the former, the crystal dimensions should increase linearly with time, while for the diffusion-controlled growth, they should increase with the square root of time (=$t^{0.5}$). Then, the crystal size *vs.* $t^{0.5}$ curves (Fig. 3c and d) of all GCs tend to be linearly dependent, which confirms that the diffusion governs the crystal growth of these glass samples.

### 3.3. HR-TEM

The HR-TEM images of the base glass samples indicate that there are no signs of phase separation in the initial glass as previously observed in the undoped glass composition.[20]

Fig. 5(a and b) present the bright field micrographs of GC01 treated at 590 °C for 150 h. Only α-$KLaF_4$ crystals were detected by HR-TEM, with the fraction of β-$KLaF_4$ crystals being very low and therefore hard to detect (see Fig. 4(a) for comparison). The size of α-$KLaF_4$ NCs, around 9 nm, is in good agreement with the XRD results. Fig. 5b shows the HR-

 

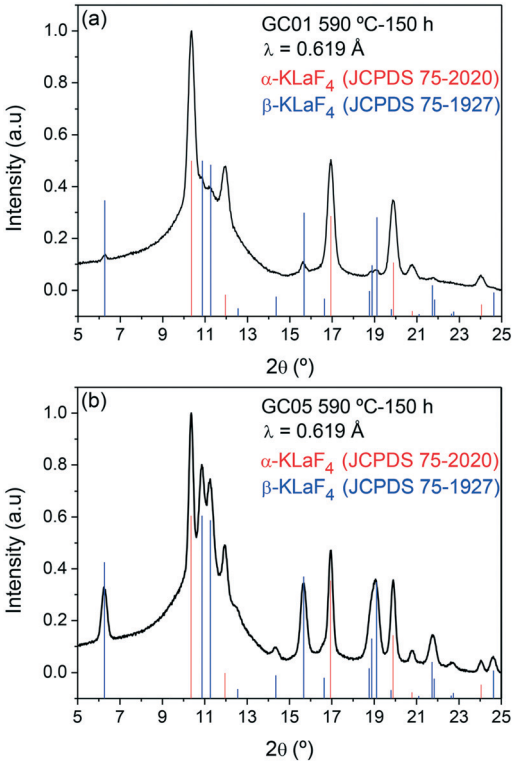


Fig. 4 XRD patterns of (a) GC01 and (b) GC05 treated at 590 °C-150 h performed at the BM25-SpLine of the ESRF. JCPDS reference patterns of α and β-$KLaF_4$ crystals are also given.

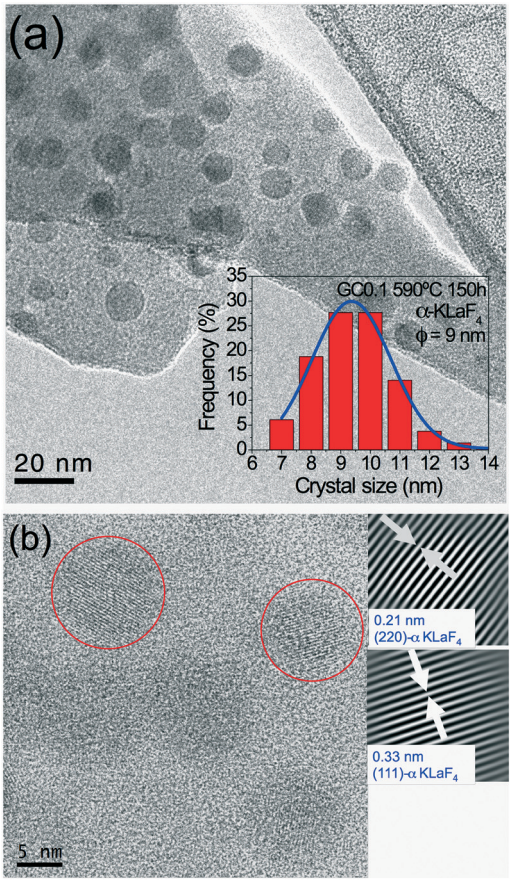


Fig. 5 (a) HRTEM micrograph of GC01 treated at 590 °C-150 h with the α-$KLaF_4$ crystal size distribution. (b) HRTEM micrograph showing five α-$KLaF_4$ crystals. For two of them (encircled in red) the plane distances were obtained by FFT (fast Fourier transform) and their corresponding filtered images are also shown.

TEM micrograph with the corresponding filtered images of two crystals where lattice planes can be seen. The lattice distance values of 0.21 nm and 0.33 nm are in good agreement with the (220) and (111) planes of the α-$KLaF_4$ crystals, corresponding to the two highest diffraction peaks that appear around 43 and 26°, respectively (see Fig. 2(a and b)).

Fig. 6(a and b) show the micrographs of GC05 treated at 590 °C-150 h. Particle size distributions were obtained by measuring close to 300 particles from different areas. The histogram displays two different maxima, which means that the particle size is not homogeneous. This is indicative of the coexistence of the α and β phases which also have different crystal sizes as has been also obtained by XRD. To corroborate this feature, the size distribution was well fitted to a two Gaussian peak curve. From the fit, two mean values at $X_{c1}$ = 8.9 nm and $X_{c2}$ = 18.1 nm and standard deviation widths of 4.6 and 4.4 nm, respectively, were obtained. From the crystal size determined from the XRD data of Fig. 3a, we can conclude that the former mean value of Gaussian 1 is attributable to the β phase and the latter (Gaussian 2) to the α phase. Additionally, using fast Fourier transform, the lattice distances of both phases were estimated to be 0.56 nm for the (100) planes of the β phase and 0.34 nm for the (111) planes of the α phase (Fig. 6b).

The HR-TEM micrographs of the GC05 glass-ceramic sample heat treated at 660 °C for 144 h in which XRD showed bigger β-$KLaF_4$ crystals (near 40 nm) were also obtained (Fig. 7a and b). The electron diffraction pattern (Fig. 7b) indicates a clear mixture of the α and β phases. The β crystals are very unstable under the electron beam. The structure degrades as observed in the diffuse streaking appearing in the FFT. Despite that, the image offers a confirmation of the presence of β-$KLaF_4$ crystals in the GC05 material where a crystal oriented along the [101] zone axis is presented.

The increasing concentration of RE dopants has been demonstrated to have an influence on the phase evolution in oxyfluoride glass-ceramics and on fluoride and double fluoride NCs. These are some of the related papers found in the literature:

H. Guo *et al.*[39] previously studied how the doping concentration induced phase transition in $Eu^{3+}$-doped β-$PbF_2$ nanoparticles from oxyfluoride glass $(50-x)SiO_2$–$40PbF_2$–$10CdF_2$–$xEu_2O_3$ (mole fraction $x$ = 0.05, 0.1, 0.5, 1.5). $Ln^{3+}$ ions are substituted for $Pb^{2+}$ sites and the doping concentration induces a site symmetry distortion from Oh to D4h. By PL and XRD studies, they concluded that the structure of low-doped nanoparticles is cubic $PbEuF_9$. With the increase of doping concentration, the cubic $Pb_3EuF_9$ transforms to tetragonal $PbEuF_5$. Given the fact that the number of substituting $Eu^{3+}$

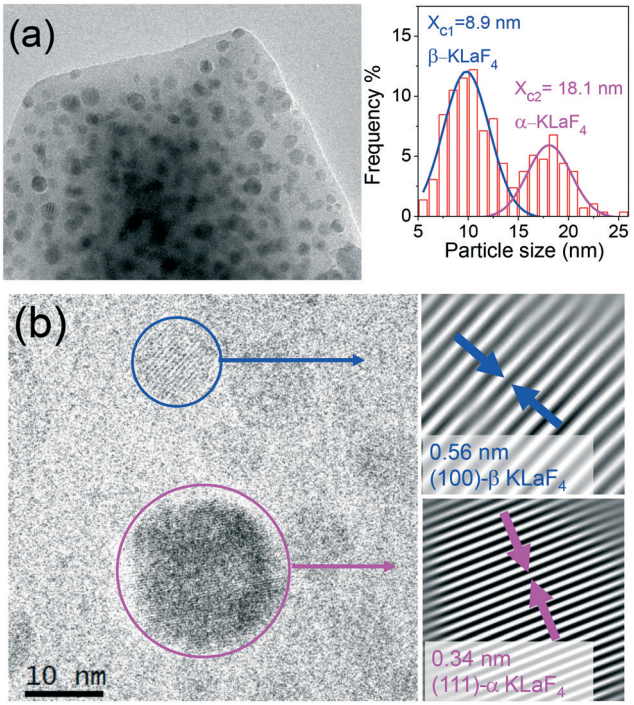


**Fig. 6** (a) HR-TEM micrographs of GC05 heat-treated at 590 °C-150 h. The crystal size distributions of α and β phases are also given in the top and bottom right images. (b) Details of α and β crystals with their corresponding plane distances.

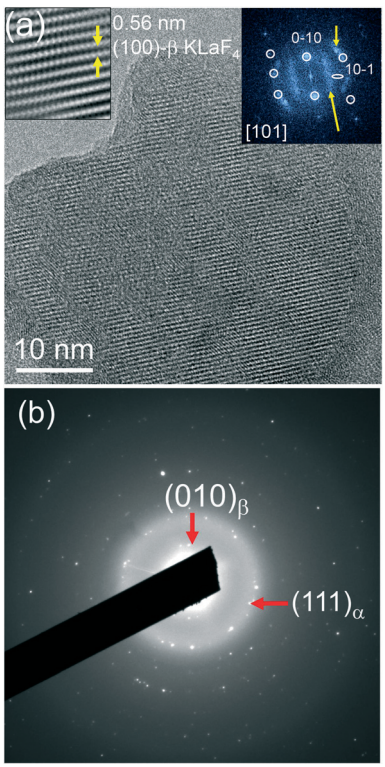


**Fig. 7** (a) HR-TEM micrographs of a β-$KLaF_4$ crystal in GC05 heat-treated at 660 °C-144 h. (b) Electron diffraction pattern of the same sample showing the presence of both α and β crystals.

ions in a single cubic cell increases with doping concentration, the structure of NCs changes from β to tetragonal, coexisting both phases for 0.05 GC. The same has been observed by Y. Li *et al.*[40] from $Tm^{3+}$ nanocrystals using the same base glass composition.

Liu *et al.* have demonstrated rational tunability of the size and phase of $NaYF_4$ NCs by doping with RE ions to change the crystal growth rate.[41] However, there have been few systematic theoretical and experimental studies focusing on how RE ion doping can modify the shape and phase of NCs.[42] X. Wang *et al.*[43] studied the size and shape modifications, phase transition, and enhanced luminescence of fluoride NCs induced by doping using in this case a novel soft chemistry route. These changes were proved to originate from the surface charge redistribution of the crystal nuclei induced by inner electron charge transfer between dopant ions and lattice cations.

In our study, we claim that the controlled crystallization of the two phases takes place firstly as an effect of the thermal treatment. In the undoped glass, the precipitation of the α phase takes place at lower temperatures (around 580 °C), and at higher temperatures (up to 660 °C at which the GCs remain transparent) the precipitation of the β phase is also promoted and the two phases coexist. From the obtained results, we conclude that there is no polymorphic transformation from the α phase to the β phase during the thermal treatment when the doping concentration increases. However, these two phases nucleate independently with very different crystal growth rates.

The Nd added acts as a nucleant since it favors the crystallization process as a whole but the concentration of 0.5 Nd seems to be the optimum one to favour the nucleation of the β phase that becomes even the main phase for GC05 treated at 660 °C.

### 3.4. Optical characterization: site-selective laser spectroscopy

As we have seen in the previous sections, β-$KLaF_4$ nanocrystals precipitate mostly in GC05. This noteworthy result is also confirmed by site-selective laser spectroscopy. This section presents the spectroscopic results for the glass and GC samples doped with 0.1, 0.5, and 1 mol% $NdF_3$ heat treated at 590 °C-24 h, 590 °C-150 h, 660 °C-66 h and 660 °C-150 h.

The $^4F_{3/2} \rightarrow {}^4I_{11/2}$ steady-state fluorescence spectra were measured at room temperature for the glass and GC samples by exciting with a Ti-sapphire laser at 804 nm in resonance with the $^4I_{9/2} \rightarrow {}^4F_{5/2}, {}^2H_{9/2}$ absorption band. Fig. 8(a) shows the emission for the glass and GC01. As can be seen, the emission is inhomogeneously broadened due to site-to-site variations in the local ligand field. The peak position (~1054 nm) and effective linewidth (~33 nm), calculated from the integrated fluorescence band divided by the peak intensity, do not change significantly in the GC samples compared to the glass sample. Similar emission spectra are observed for all $NdF_3$ concentrations at this excitation wavelength. However, in the heat treated samples the excitation spectra obtained in

 

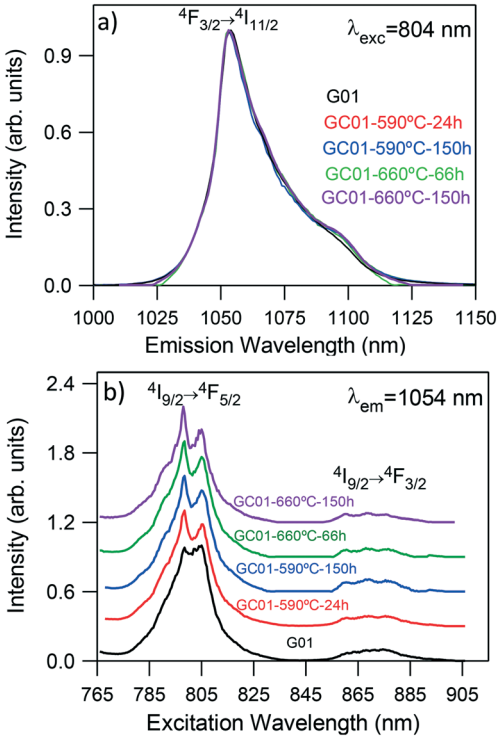


**Fig. 8** (a) Room temperature normalized emission spectra obtained under excitation at 804 nm for the G01 sample treated at 590 °C-24 h, 590 °C-150 h, 660 °C-66 h, and 660 °C-150 h. (b) Excitation spectra obtained by collecting the luminescence at 1054 nm for the G01 sample treated at 590 °C-24 h, 590 °C-150 h, 660 °C-66 h, and 660 °C-150 h.

the 765–905 nm spectral range monitored at 1054 nm show a better resolved structure for the $^4I_{9/2} \rightarrow {}^4F_{5/2,3/2}$ bands with respect to glass, which suggests the partial incorporation of $Nd^{3+}$ ions in the NCs. As an example, Fig. 8(b) displays the excitation spectra of the glass and GC01 samples treated at 590 °C-24 h, 590 °C-150 h, 660 °C-66 h, and 660 °C-150 h. As can be seen, the sample treated at 660 °C-150 h shows a more resolved structure. A similar behavior is observed for the samples doped with 1 mol% (not shown). However, the excitation spectra of the GC05 shows, in addition to the observed features of the $^4I_{9/2} \rightarrow {}^4F_{5/2,3/2}$ bands, sharp peaks at around 792 and 864 nm that do not appear in the GC01 and GC1 samples and can be related to the presence of the β-$KLaF_4$ nanocrystals (see Fig. 9). These new peaks are more intense for the GC sample treated at 660 °C-66 h and decrease for the treatment during 150 h.

To determine if these additional peaks correspond to a different type of atomic environment of $Nd^{3+}$ ions in these GCs, emission spectra have been obtained by exciting at different wavelengths along the $^4I_{9/2} \rightarrow {}^4F_{5/2}$ absorption band. For comparison, Fig. 10 shows the normalized emission spectra obtained by exciting at 792 and 804 nm for the GC01 and GC05 samples treated at 660 °C-66 h. The spectra of the GC01 sample present inhomogeneous broadened bands similar to the ones of the glass sample for both excitation wavelengths, whereas the emission spectrum of the GC05 sample,

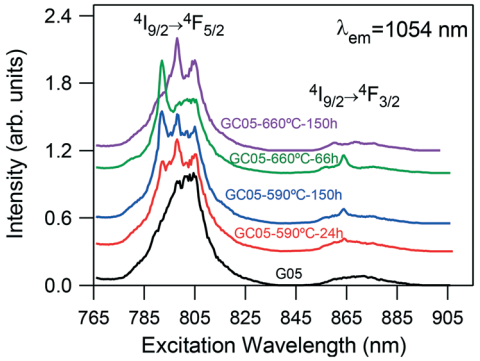


**Fig. 9** Excitation spectra of the glass and GC05 samples treated at 590 °C-24 h, 590 °C-150 h, 660 °C-66 h, and 660 °C-150 h obtained by collecting the luminescence at 1054 nm.

obtained under excitation at 792 nm, narrows and shows a more resolved structure which exhibits a new peak around 1046 nm.

To better identify the emission from the $Nd^{3+}$ in the NCs, the emission and excitation spectra have been measured at low temperature to minimize the overlapping of the contributions from $Nd^{3+}$ in the crystalline and amorphous phases due to the thermal population of the higher energy Stark components of the ground and excited states.

The low temperature (9 K) excitation spectra have been obtained at different emission wavelengths along the $^4F_{3/2} \rightarrow {}^4I_{11/2}$ laser transition. Fig. 11 shows the excitation spectra for the GC01 and GC05 samples heat treated at 660 °C-66 h

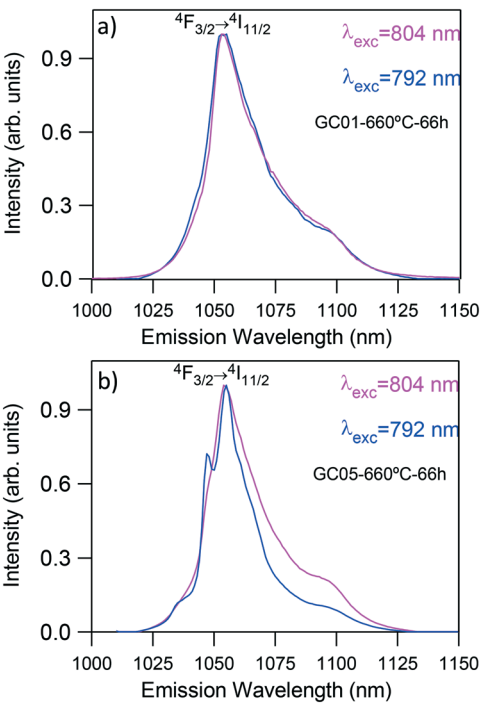


**Fig. 10** Room temperature emission spectra obtained under excitation at 792 and 804 nm for the (a) GC01 and (b) GC05 samples heat treated at 660 °C-66 h.

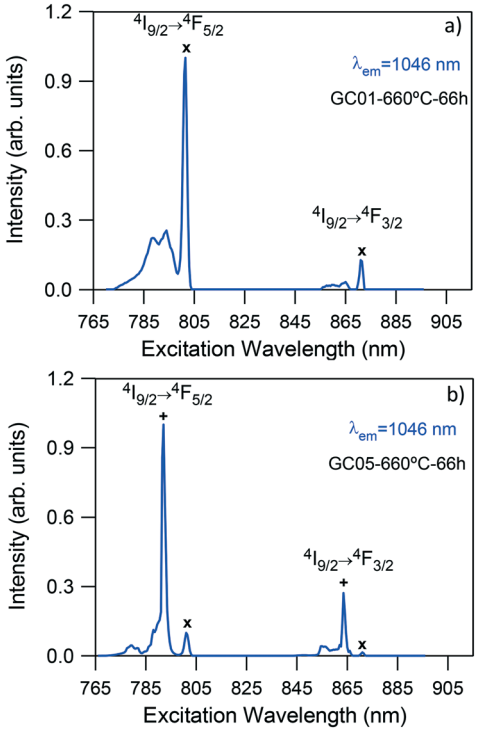


**Fig. 11** Low temperature excitation spectra obtained by collecting the luminescence at 1046 nm for the (a) GC01 and (b) GC05 samples treated at 660 °C-66 h. Peak labels correspond to (x) α-$KLaF_4$ and (+) β-$KLaF_4$ crystalline phases.

obtained by collecting the luminescence at 1046 nm (the wavelength corresponding to the additional peak that appears in the room temperature emission spectrum of the GC05 under excitation at 792 nm). The figure depicts how the spectra change depending on the $NdF_3$ concentration, which indicates that $Nd^{3+}$ ions are in different crystal field sites. As observed in the spectrum obtained by collecting the luminescence at 1046 nm for GC01 (Fig. 11(a)), the $^4I_{9/2} \rightarrow {}^4F_{5/2}$ band is composed of a sharp peak at 801 nm in addition to a broad component which indicates the presence of crystalline and amorphous environments for $Nd^{3+}$ ions. Moreover, the $^4I_{9/2} \rightarrow {}^4F_{3/2}$ transition presents a broad component together with an isolated narrow peak at around 871 nm, which suggest that $Nd^{3+}$ ions are in a crystalline environment. The same behavior is observed for the heat treatment at 590 °C-150 h and 660 °C-150 h for GC01. However, the excitation spectrum of the sample doped with 0.5 mol% shows a different behavior. As can be seen in Fig. 11(b), the spectrum obtained by collecting the luminescence at 1046 nm shows, for the $^4I_{9/2} \rightarrow {}^4F_{5/2}$ transition, sharp and well resolved peaks with the most intense one located at 792 nm together with a much less intense peak at 801 nm also observed in the sample doped with 0.1 mol%, which indicates different crystalline environments for $Nd^{3+}$ ions. The band corresponding to the $^4I_{9/2} \rightarrow {}^4F_{3/2}$ transition narrows into two components with the low energy main peak at around 863.5 nm as expected for one well defined crystal field site of symmetry lower than cubic. This band also shows a very weak peak at 871 nm, the one observed in GC01. Based on the previous structural analysis these results suggest that the main contribution to the excitation spectrum of the sample doped with 0.5 mol% corresponds to $Nd^{3+}$ ions in β-$KLaF_4$ nanocrystals which are predominant for this concentration. The weak peaks at 801 and 871 nm, also observed for the other $Nd^{3+}$ concentrations, can be associated with $Nd^{3+}$ ions in the α-$KLaF_4$ nanocrystals.

In order to confirm if the features shown by the excitation spectra monitored at 1046 nm could be definitely related to the presence of $Nd^{3+}$ ions in the α-$KLaF_4$ and β-$KLaF_4$ NCs, site-selective steady-state emission spectra for the $^4F_{3/2} \rightarrow {}^4I_{11/2}$ transition were recorded by exciting at 792 and 801 nm in the $^4I_{9/2} \rightarrow {}^4F_{5/2}$ transition. Fig. 12 shows the normalized emission spectra at 9 K obtained under excitation at 792 and 801 nm for the GC01 and GC05 samples treated at 660 °C-66 h. The spectrum of GC01 (Fig. 12(a)) obtained under excitation at 792 nm shows a broadband similar to that of the glass sample. However, the spectrum of GC05 (Fig. 11(b)) shows a sharp peak at 1046 nm together with a structured band. This indicates that for the 792 nm excitation in GC05 we mainly excite $Nd^{3+}$ ions in the β-$KLaF_4$ crystalline phase. The spectral features of the emission obtained under excitation at 801 nm are similar for both concentrations. In both GC samples, the spectra show a narrow peak at around 1046.5 nm together with a broad band. As can be seen in Fig. 12(b), this narrow peak is slightly broader than the one observed under 792 nm excitation and can be attributed to $Nd^{3+}$ ions in α-$KLaF_4$ NCs. The spectral overlapping between the crystalline and

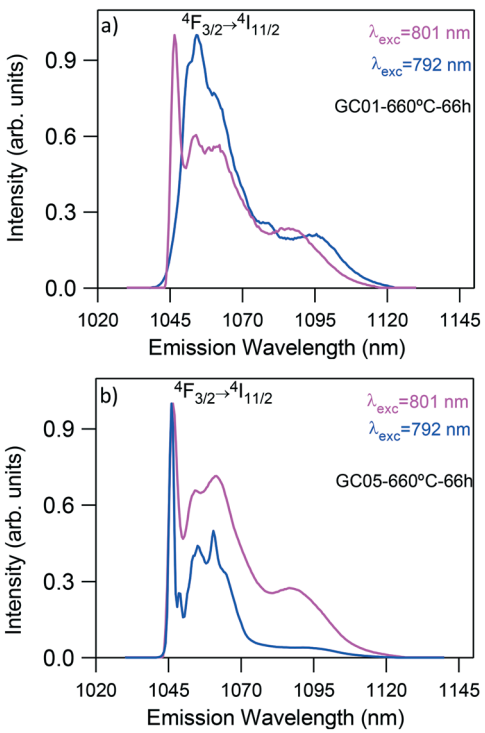


**Fig. 12** Low temperature normalized emission spectra of the $^4F_{3/2} \rightarrow {}^4I_{11/2}$ laser transition obtained under excitation at 792 and 801 nm for the (a) GC01 and (b) GC05 samples heat treated at 660 °C-66 h.

amorphous phases makes it difficult to isolate the emissions of $Nd^{3+}$ in the α-$KLaF_4$ and β-$KLaF_4$ crystalline phases.

The relative contribution of the emissions from $Nd^{3+}$ ions in the α-$KLaF_4$ and β-$KLaF_4$ crystalline phases for GC05 depends on the heat treatment. Assuming that the excitation peak at 792 nm corresponds to the $Nd^{3+}$ ions in the β-$KLaF_4$ crystalline phase and the one at 801 nm to those in the α-$KLaF_4$, the highest intensity for the emission of $Nd^{3+}$ in the β-$KLaF_4$ crystalline phase corresponds to the GC sample treated at 660 °C-66 h. Fig. 13 shows the relative intensities of the peaks at 792 and 801 nm for three different treatments at 590 °C-150 h, 660 °C-66 h, and 660 °C-150 h.

The excitation spectra obtained by collecting the luminescence at 1053 nm, around the peak of the broad band emission, also show a different behavior depending on the $NdF_3$ concentration. As observed in the spectrum of the sample doped with 0.1 mol% (Fig. 14(a)), the $^4I_{9/2} \rightarrow {}^4F_{5/2}$ band is composed of two narrow and well resolved peaks at around 798 and 804 nm in addition to a broad component. Moreover, the $^4I_{9/2} \rightarrow {}^4F_{3/2}$ transition shows at least four main bands instead of the one (cubic symmetry) or two (lower symmetry) expected Stark components of the $^4F_{3/2}$ level in a well-defined crystal field site. This behavior is similar to the one observed for the glass sample. However, the spectrum of GC05 shows the presence of the peaks at 792 nm and 863.5 nm corresponding to the β-$KLaF_4$ crystalline phase together with the peak at around 804 nm, also observed in the glass sample, which indicates that the emission at 1053 nm corresponds to $Nd^{3+}$ ions in the amorphous and β-$KLaF_4$ crystalline phases. For other $NdF_3$ concentrations, the emission is mainly due to $Nd^{3+}$ ions in the amorphous environment.

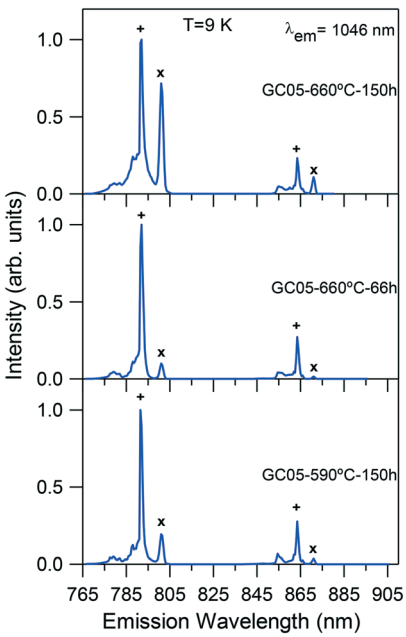


Fig. 13 Low temperature excitation spectra obtained by collecting the luminescence at 1046 nm for the GC05 sample heat treated at 590 °C-150 h, 660 °C-66 h, and 660 °C-150 h. Peak labels correspond to (x) α-$KLaF_4$ and (+) β-$KLaF_4$ crystalline phases.

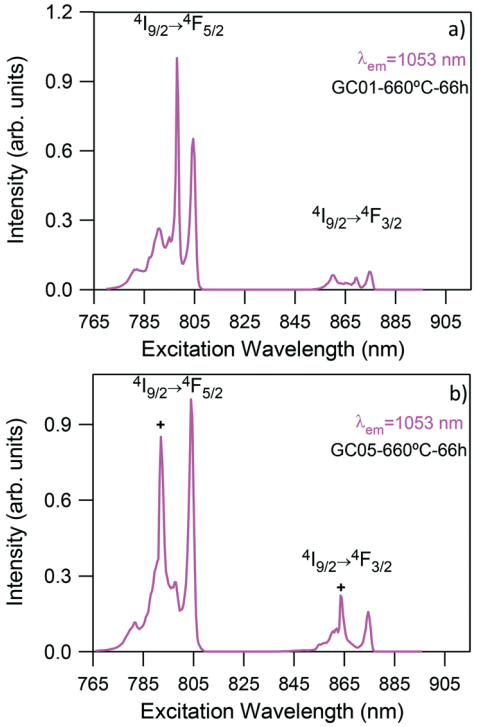


Fig. 14 Low temperature excitation spectra obtained by collecting the luminescence at 1053 nm for the (a) GC01 and (b) GC05 samples heat treated at 660 °C-66 h, peak labels (+) correspond to the β-$KLaF_4$ crystalline phase.

The emission spectra obtained under excitation at 804 nm are similar for all GCs and glass samples, which indicates that at this wavelength we mainly excite $Nd^{3+}$ ions in the amorphous phase.

The existence of different environments for $Nd^{3+}$ ions is also reflected by the lifetimes of the $^4F_{3/2}$ state. Lifetime measurements of the $^4F_{3/2}$ state were performed by exciting the samples at 792 and 801 nm and collecting the luminescence at different emission wavelengths in the $^4F_{3/2} \rightarrow {}^4I_{11/2}$ transition, corresponding to different sites observed in the emission and excitation spectra. If different environments for the $Nd^{3+}$ ions are present, the lifetime values should be dependent on the excitation and emission wavelengths. In this case, due to the spectral overlapping of the emission coming from $Nd^{3+}$ ions in amorphous and crystalline environments, it is somewhat difficult to give accurate values for the excited state lifetime of each site. In the case of the GC01 and GC05 samples, where the main crystalline phase is α-$KLaF_4$, the decay obtained at 9 K under excitation at 801 nm by collecting the luminescence at 1046 nm can be described by a single exponential function, with lifetime values of 494 μs and 423 μs for the glass-ceramics heat treated at 660 °C-60 h doped with 0.1 and 1 mol%, respectively. These lifetime values can be associated with $Nd^{3+}$ ions in the α-$KLaF_4$ crystalline phase. At other excitation wavelengths along the $^4F_{5/2}$ absorption band the decay results deviate from a single exponential function and the lifetime values range between 535 μs and 466 μs for the GC01 sample, whereas for the GC1 specimen, this

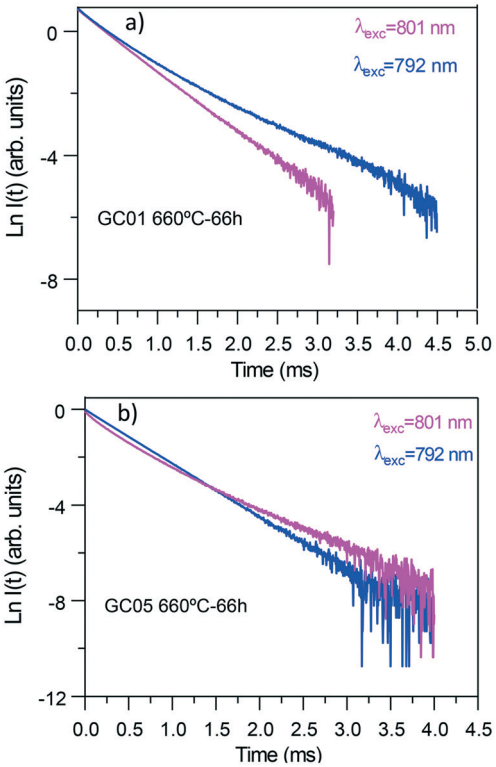


**Fig. 15** Experimental decay of the $^4F_{3/2}$ level obtained under excitation at 792 (blue) and 801 (pink) by collecting the luminescence at 1046 nm for the (a) GC01 and (b) GC05 samples heat-treated at 660 °C-66 h.

variation is from 429 μs to 335 μs depending on the excitation and emission wavelengths. As an example, Fig. 15(a) shows the decay results, obtained under 792 and 801 nm excitation by collecting the luminescence at 1046 nm, for GC01. In the case of GC05 (Fig. 15(b)) the decay can be described by a single exponential function with a lifetime of 440 μs only under excitation at 792 nm by collecting the luminescence at 1046 nm, whereas under 801 nm excitation it deviates from an exponential function due to the overlapping of the emission of $Nd^{3+}$ in the two crystalline phases. The lifetime value obtained from the single exponential decay (440 μs) in the case of the GC05 sample can be attributed to the lifetime of $Nd^{3+}$ ions in the β-$KLaF_4$ NCs.

## 4. Conclusions

The structural characterization of $Nd^{3+}$ doped $KLaF_4$ GCs showed the formation of NCs with sizes ranging from 9 to almost 40 nm depending on both $Nd^{3+}$ content and treatment conditions. α-$KLaF_4$ NCs were observed for all the studied compositions; however, by high resolution XRD, both α and β phases were identified, with the relative intensity of the β phase being very small in all cases except for the composition doped with 0.5 $Nd^{3+}$. The crystallization was proved to be diffusion-controlled leading to a constant crystal size after a viscous barrier enriched in $SiO_2$ was formed around the NCs. Site-selective laser spectroscopy in the $^4I_{9/2} \rightarrow {}^4F_{3/2}/{}^4F_{5/2}$ transitions of $Nd^{3+}$ performed in the GC samples confirmed that $Nd^{3+}$ is incorporated into both the crystalline and amorphous phases. The differences among the spectral features of the site-selective excitation and emission spectra of $Nd^{3+}$ in the studied glass and GC samples allowed distinguishing between crystalline and amorphous environments for $Nd^{3+}$ ions and correlation of the spectroscopic properties with structural properties. The presence of α-$KLaF_4$ and β-$KLaF_4$ crystalline phases can be unambiguously identified from the emission and excitation spectra as well as from the lifetime measurements of the $^4F_{3/2}$ state of $Nd^{3+}$ ions. Whereas $Nd^{3+}$ doped α-$KLaF_4$ NCs are present for all $Nd^{3+}$ concentrations, the incorporation of $Nd^{3+}$ into β-$KLaF_4$ NCs is only observed for GC05 samples.

## Conflicts of interest

There are no conflicts to declare.

## Acknowledgements

This work was supported by MINECO under projects MAT2013-48246-C2-1-P/-2-P and MAT2017-87035-C2-1-P/-2-P (AEI/FEDER, UE) and Basque Country University PPG17/07 and GIU17/014. We acknowledge the European Syncrothron Radiation Facility for the provision of synchrotron radiation facilities in using the beamline BM25-SpLine to perform the experiments MA-3350 and 25-01-1014. Aluisio A. Cabral and Jose Joaquín Velázquez also acknowledge CAPES (#BEX 2598/15-9) and MINECO for Grant FPDI-2013-16895, respectively.

## References

1 J. Fu, J. M. Parker, P. S. Flower and R. M. Brown, *Mater. Res. Bull.*, 2002, **37**, 1843–1849, DOI: 10.1016/S0025-5408(02)00862-0.
2 S. Tanabe, H. Hayashi, T. Hanada and N. Onodera, *Opt. Mater.*, 2002, **19**, 343–349, DOI: 10.1016/S0925-3467(01)00236-1.
3 M. Mortier, A. Monteville, G. Partiache, G. Mazé and F. Auzel, *Opt. Mater.*, 2001, **16**, 255–267, DOI: 10.1016/S0925-3467(00)00086-0.
4 M. J. Dejneka, *J. Non-Cryst. Solids*, 1998, **239**, 149–155, DOI: 10.1016/S0022-3093(98)00731-5.
5 Y. Wang and J. Ohwaki, *Appl. Phys. Lett.*, 1993, **63**, 3268–3270, DOI: 10.1063/1.110170.
6 J. S. Kim, M. Müller and W. Seeber, *Glass Sci. Technol.*, 2002, **75**, 330–333, DOI: 10.1364/OME.4.001574.
7 C. Rüssel, *Chem. Mater.*, 2005, **17**, 5843–5847, DOI: 10.1021/cm051430x.
8 C. Bocker and C. Rüssel, *J. Eur. Ceram. Soc.*, 2009, **29**, 1221–1225, DOI: 10.1016/j.jeurceramsoc.2008.08.005.
9 S. Bhattacharyya, C. Bocker, T. Heil, J. R. Jinschek, T. Höche, C. Rüssel and H. Kohl, *Nano Lett.*, 2009, **9**, 2493–2496, DOI: 10.1021/nl901283r.
10 M. Sroda, I. Wacławska, L. Stoch and M. Reben, *J. Therm. Anal. Calorim.*, 2004, **77**, 193–200, DOI: 10.1023/B:JTAN.0000033203.95251.d6.

 

11 S. Bhattacharyya, T. Höche, N. Hémono, M. J. Pascual and P. A. van Aken, *J. Cryst. Growth*, 2009, **311**, 4350–4355, DOI: 10.1016/j.jcrysgro.2009.07.027.
12 N. Hémono, G. Pierre, F. Munoz, A. de Pablos-Martín, M. J. Pascual and A. Durán, *J. Eur. Ceram. Soc.*, 2009, **29**, 2915–2920, DOI: 10.1016/j.jeurceramsoc.2009.05.013.
13 A. de Pablos-Martín, N. Hémono, G. C. Mather, S. Bhattacharyya, T. Höche, H. Bornhöft, J. Deubener, F. Muñoz, A. Durán and M. J. Pascual, *J. Am. Ceram. Soc.*, 2011, **94**, 2420–2428, DOI: 10.1111/j.1551-2916.2011.04547.x.
14 A. de Pablos-Martin, C. Patzig, T. Höche, A. Duran and M. J. Pascual, *CrystEngComm*, 2013, **15**, 6979–6985, DOI: 10.1039/c3ce40731d.
15 A. de Pablos-Martín, D. Ristic, S. Bhattacharyya, T. Höche, G. C. Mather, M. O. Ramírez, S. Soria, M. Ferrari, G. C. Righini, L. E. Bausá, A. Duran and M. J. Pascual, *J. Am. Ceram. Soc.*, 2013, **96**, 447–457, DOI: 10.1111/jace.12120.
16 G. Gorni, J. J. Velázquez, G. C. Mather, A. Durán, G. Chen, M. Sundararajan, R. Balda, J. Fernández and M. J. Pascual, *J. Eur. Ceram. Soc.*, 2017, **37**, 1695–1706, DOI: 10.1016/j.jeurceramsoc.2016.11.014.
17 G. Gorni, R. Balda, J. Fernández, I. Iparraguirre, J. J. Velázquez, Y. Castro, L. Pascual, G. Chen, M. Sundararajan, M. J. Pascual and A. Durán, *CrystEngComm*, 2017, **19**, 6620–6629, DOI: 10.1039/C7CE01380A.
18 A. de Pablos-Martín, G. C. Mather, F. Muñoz, S. Bhattacharyya, T. Höche, J. R. Jinschek, T. Heil, A. Durán and M. J. Pascual, *J. Non-Cryst. Solids*, 2010, **356**, 3071–3079, DOI: 10.1016/j.jnoncrysol.2010.04.057.
19 A. de Pablos-Martín, M. O. Ramírez, A. Durán, L. E. Bausá and M. J. Pascual, *Opt. Mater.*, 2010, **33**, 180–185, DOI: 10.1016/j.optmat.2010.08.004.
20 A. de Pablos-Martín, F. Muñoz, G. C. Mather, C. Patzig, S. Bhattacharyya, J. R. Jinschek, T. Höche, A. Durán and M. J. Pascual, *CrystEngComm*, 2013, **15**, 10323–10332, DOI: 10.1039/c3ce41345d.
21 A. de Pablos-Martín, D. Ristic, A. Durán, M. Ferrari and M. J. Pascual, *CrystEngComm*, 2017, **19**, 967–974, DOI: 10.1039/c6ce01845a.
22 L. Wang, P. Li and Y. Li, *Adv. Mater.*, 2007, **19**, 3304–3307, DOI: 10.1002/adma.200700144.
23 F. Liu, E. Ma, D. Chen, Y. Yu and Y. Wang, *J. Phys. Chem. B*, 2006, **110**, 20843–20846, DOI: 10.1021/jp063145m.
24 K. W. Krämer, D. Biner, G. Frei, H. U. Güdel, M. P. Hehlen and S. R. Lüthi, *Chem. Mater.*, 2004, **16**, 1244–1251, DOI: 10.1021/cm031124o.
25 P. Ptacek, H. Schäfer, O. Zerzouf, K. Kömpe and M. Haase, *Cryst. Growth Des.*, 2010, **10**, 2434–2438, DOI: 10.1021/cg100282w.
26 P. Ptacek, H. Schäfer, K. Kömpe and M. Haase, *Adv. Funct. Mater.*, 2007, **17**, 3843–3848, DOI: 10.1002/adfm.200600974.
27 A. Herrmann, M. Tylkowski, C. Bocker and C. Rüssel, *Chem. Mater.*, 2013, **25**, 2878–2884, DOI: 10.1021/cm401454y.
28 J. Zhang, C. Mi, H. Wu, H. Huang, C. Mao and S. Xu, *Anal. Biochem.*, 2012, **421**, 673–679, DOI: 10.1016/j.ab.2011.11.008.
29 J. C. Zhou, Z. L. Yang, W. Dong, R. J. Tang, L. D. Sun and C. H. Yan, *Biomaterials*, 2011, **32**, 9059–9067, DOI: 10.1016/j.biomaterials.2011.08.038.
30 R. E. Thoma, G. M. Hebert, H. Insley and C. F. Weaver, *Inorg. Chem.*, 1963, **2**, 1005–1012, DOI: 10.1021/ic50009a030.
31 S. Ahmad, G. V. Prakash and R. Nagarajan, *Inorg. Chem.*, 2012, **51**, 12748–12754, DOI: 10.1021/ic301566e.
32 N. Tyagi, A. A. Reddy and R. Nagarajan, *Opt. Mater.*, 2010, **33**, 42–47, DOI: 10.1016/j.optmat.2010.07.014.
33 C. P. Groen, A. Oskam and A. Kovacs, *Inorg. Chem.*, 2003, **42**, 851–858, DOI: 10.1021/ic0260973.
34 S. Das, A. Amarnath Reddy, S. Ahmad, R. Nagarajan and G. Vijaya Prakash, *Chem. Phys. Lett.*, 2011, **508**, 117–120, DOI: 10.1016/j.cplett.2011.04.029.
35 S. Ahmad, S. Das, R. Nagarajan and G. Vijaya Prakash, *Opt. Mater.*, 2013, **36**, 396–401, DOI: 10.1016/j.optmat.2013.09.031.
36 M. J. Weber, Science and technology of laser glass, *J. Non-Cryst. Solids*, 1990, **123**, 208–222, DOI: 10.1016/0022-3093(90)90786-L.
37 R. R. Jacobs and M. J. Weber, *IEEE J. Quantum Electron.*, 1976, **12**, 102–111, DOI: 10.1109/JQE.1976.1069101.
38 V. M. Fokin, A. A. Cabral, R. M. C. V. Reis, M. L. F. Nascimento and E. D. Zanotto, *J. Non-Cryst. Solids*, 2010, **356**, 358–367, DOI: 10.1016/j.jnoncrysol.2009.11.038.
39 H. Guo, *et al.*, *Opt. Express*, 2013, **21**, 24742–24752, DOI: 10.1364/OE.21.024742.
40 Y. Li, L. Zhao, Y. Fu, Y. Shi, X. Zhang and H. Yu, *AIP Adv.*, 2016, **6**, 025001–025007, DOI: 10.1063/1.4941442.
41 F. Wang, Y. Han, C. S. Lim, Y. H. Lu, J. Wang, J. Xu, H. Y. Chen, C. Zhang, M. H. Hong and X. G. Liu, *Nature*, 2010, **463**, 1061–1065, DOI: 10.1038/nature08777.
42 D. Q. Chen, Y. L. Yu, F. Huang, P. Huang, A. Yang and Y. Wang, *J. Am. Chem. Soc.*, 2010, **132**, 9976–9978, DOI: 10.1021/ja1036429.
43 X. Wang, Y. Bu, Y. Xiao, C. Kan, D. Lu and X. Yan, *J. Mater. Chem. C*, 2013, **1**, 3158–3166, DOI: 10.1039/C3TC00669G.

# *PAPER 7*

**Oxyfluoride glass-ceramic fibers doped with $Nd^{3+}$: structural and optical characterization.**

G. Gorni, R. Balda, J. Fernández, I. Iparraguirre, J.J. Velázquez, Y. Castro, L. Passcual, G. Chen, M. Sundararajan,, M.J. Pascual, A. Durán.

*CrystEngComm*. **19** (2017) 6620-6629. doi: 10.1039/C7CE01380A

CrystEngComm

PAPER

View Article Online
View Journal | View Issue





Cite this: *CrystEngComm*, 2017, **19**, 6620

# Oxyfluoride glass–ceramic fibers doped with $Nd^{3+}$: structural and optical characterization

G. Gorni, [a] R. Balda,[bc] J. Fernández,[bc] I. Iparraguirre,[b] J. J. Velázquez, [a] Y. Castro, [a] L. Pascual,[d] G. Chen,[e] M. Sundararajan,[e] M. J. Pascual *[a] and A. Durán [a]

Received 28th July 2017,
Accepted 26th September 2017

DOI: 10.1039/c7ce01380a

rsc.li/crystengcomm

Transparent oxyfluoride glass–ceramic fibers containing $LaF_3$ nanocrystals have been drawn using a single crucible method and crystallization after an appropriate heat treatment. Optical fibers have been obtained *a posteriori* through the deposition of $SiO_2$ cladding prepared by sol–gel and deposited by dip-coating. Detailed thermal and structural characterization performed by DTA, XRD, HRTEM and SAXS showed the good reproducibility of the technology. Phase separation, due to fluorine immiscibility in an oxide glass matrix, initiates the crystallization. The crystallization mechanism is a diffusion-controlled process and the local compositional changes of the glass matrix around the nanocrystals limit the crystal size to 10–20 nm depending on the treatment conditions. The optical characterization demonstrated the light propagation into the glass–ceramic core and the possibility to selectively excite $Nd^{3+}$ ions in the fluoride nanocrystals with a corresponding increase of the luminescence efficiency.

## Introduction

Many efforts have been made during the last few decades to study and develop new non-silica fibers with different applications, most of them as optical fibers,[1] in the field of photonics.[2] For example, tellurite glasses and fibers show advantages such as a wide transmittance window, chemical durability and high nonlinearity, being used in applications as broadband amplifiers or for continuum frequency generation;[3–9] phosphate optical fibers revealed good properties for application as high power fiber lasers and amplifiers[10–13] and also for medical applications due to the capability of phosphate glasses to be resorbed in aqueous media.[14,15] Fluoride glasses have also received attention because of their low phonon energy and mid-infrared transparency.[16] Therefore, these glasses are excellent candidates for fiber lasers in visible and mid-infrared regions where emissions are hardly obtained from silicate and phosphate fibers. Fluoride fibers have been studied for lasing actions due to their high suitable doping levels (up to 10 mol%), relatively high strength and low transmission loss ($<0.05$ dB $m^{-1}$).[17] These properties are attractive for photonic applications such as remote spectroscopy, thermometry, IR imaging and laser power delivery.[18] However, fluoride glasses have poor chemical durability as compared to oxide ones.

The growing interest in glass–ceramics (GCs), *i.e.* glasses that undergo controlled crystallization, has shown, in the last few decades, the potential of this new class of optical materials, whose properties, especially the optical ones, improve significantly due to the controlled crystallization of certain crystalline phases. Oxyfluoride glass–ceramics (OxFGCs) combining oxide matrices with low-phonon-energy fluoride crystals[19–23] showed the possibility to increase the optical efficiency of rare earth ions (REI), the most widely used active ions in the field of photonics, and allow a strong material in terms of thermal, mechanical and chemical resistance to be obtained at the same time.

Most of the studies on OxFGCs doped with REI are about their optical properties as bulk materials[24–37] and a few are about thin films.[38–41] However, very few works have been published about OxFGC fibers.[42–44] This is strictly correlated with the difficulty of preparing glass and GC fibers in standard labs because dedicated drawing towers and suitable core and cladding properties are required. In fact, even though light propagation occurs in the optical fiber core, the cladding plays a relevant role as well. The cladding refractive index has to be smaller than that of the glass core to ensure light propagation into the core; moreover, good matching of mechanical and thermal properties is also required for the drawing process as well as for the subsequent heat treatment to obtain optical fibers with a GC core.

The sol–gel method is an alternative route to obtain transparent glass with a low refractive index using low sintering

[a] *Instituto de Cerámica y Vidrio ICV-CSIC, Madrid, Spain. E-mail: mpascual@icv.csic.es*
[b] *Departamento de Física Aplicada I, Escuela Superior de Ingeniería, Universidad del País Vasco UPV-EHU, Bilbao, Spain*
[c] *Centro de Física de Materiales UPV/EHU-CSIC, San Sebastian, Spain*
[d] *Instituto de Catálisis y Petroleoquímica ICP-CSIC, Madrid, Spain*
[e] *Department of Physics and Astronomy, Ohio University, Athens, OH 45701, USA*

temperatures (<500 °C). Some papers report silica coatings obtained by the sol–gel method and used as optical fiber cladding.[45,46] Sol–gel starts with a liquid phase and coating deposition can be achieved by dip-coating or spin-coating methods. The main advantage of sol–gel cladding materials in the field of glass fibers is their possibility to be deposited *a posteriori* onto the glass core and, therefore, no thermal or mechanical matching conditions are required.

In this paper, we describe the crystallization, structural and optical properties of OxFGC fibers doped with $Nd^{3+}$ and coated by means of silica sol–gel cladding. The bulk glass–ceramics were previously studied in detail.[35] Both uncoated and coated $LaF_3$-GC optical fibers were prepared in our lab using a two-step process, which is easy to apply to a variety of glass compositions. Doping of $Nd^{3+}$ ions has been used considering the good optical results obtained for bulk GCs, thus making interesting the possibility to use these materials as integrated optical amplifiers or fiber lasers.

## Experimental section

### Materials preparation

**Uncoated fiber procedure.** Glass fibers were prepared starting from the undoped glass of composition (mol%) $55SiO_2$–$20Al_2O_3$–$15Na_2O$–$10LaF_3$ (55Si–10La). $Nd^{3+}$-doped fibers were also prepared from doped glasses of the same base composition with the addition of 0.1 and 2 mol% $NdF_3$. A full description of the doped bulk glasses is given in detail elsewhere.[35] Fibers were prepared using a single crucible method; the description of the equipment was given in a previous paper.[47] The glasses were heated and drawn in a wide temperature range from 1150 °C up to 1480 °C, corresponding to values of $\log\eta$ equal to 5.8 and 3.2 dPa s, respectively.[48]

Fibers with diameters in the range from 50 up to 500 μm were successfully prepared. Among these fibers, those with a diameter around 200 μm were selected and characterized in detail to study the crystallization mechanism. In the following, the undoped, 0.1 and 2 $Nd^{3+}$-doped fibers will be named GF0, GF0.1 and GF2, respectively, while their corresponding glass–ceramic samples will be named GCF*x*.

The GC fibers were obtained upon heat treatments of small fiber specimens 5–10 cm in length at 620 °C and 640 °C for 40 h, at 660 °C for 20, 40, and 90 h, and at 680 °C for 5, 20, 40, 90, and 120 h, using a heating rate of 10 °C $min^{-1}$.

**Cladding of optical fibers.** To obtain the cladding of the optical fibers, a silica coating was deposited onto the fibers using the sol–gel method.

The fibers were previously treated at 640 °C for 40 h to convert them into GC samples and then coated by dip-coating. In particular, only thicker fibers (core around 500 μm) with a length of 30 cm were coated using a silica sol prepared by mixing tetraethyl orthosilicate (TEOS), methyltriethoxysilane (MTES) and a colloidal silica suspension (Ludox-4S, Aldrich, aqueous suspension 40 wt%, particle size 20 nm, pH 9). Then, concentrated nitric acid ($HNO_3$) was added to induce hydrolysis and condensation reactions. The sol was diluted with absolute ethanol (EtOH, Panreac, 99.8%) to obtain a $SiO_2$ concentration of 170 g $L^{-1}$. The final molar ratio of the silica sol was 1(TEOS + MTES) : 0.5Ludox : 2.7EtOH.

The multilayer coatings were prepared by dip-coating at a withdrawal rate of 50 cm $min^{-1}$. After the first deposition, the fibers were dried at 300 °C for 5 minutes and coated again by a second deposition process. The coated fibers were annealed at 450 °C for 1 h to obtain dense $SiO_2$ cladding. The untreated glass fibers were also coated with the sol to compare their luminescence efficiency with that of the GC fibers. Photographs of the transverse and cross-section of the coated GC fibers were obtained using a ZEISS Axiophot microscope equipped with a Zeiss AxioCam MR 5 camera.

**Thermal and structural characterization.** DTA was performed on small fibers with a length of 3 cm and a diameter of 250 μm using an SDT Q600 (TA Instruments). The DTA curves were obtained with heating rates in the range of 10–80 °C $min^{-1}$. From the DTA data, the most relevant information on the glass transition temperature ($T_g$) and crystallization peak ($T_p$) was obtained.

The heat treated fibers were milled and sieved to a size less than 60 μm and the powders were analyzed by XRD using a Bruker D8 Advance diffractometer. The diffractograms were acquired in the range $10° \leq 2\theta \leq 70°$, with a step-size of 0.02° and an acquisition time of 1 s for each step. The crystal size was calculated using the generalized Scherrer equation:

$$D = \frac{0.94\lambda}{\cos\theta\sqrt{B_m^{\,2} - B_i^{\,2}}}$$

where $\lambda$ is the wavelength (1.54056 Å, CuK$\alpha$), $B_i$ is the instrumental broadening, $B_m$ is the full width at half maximum of the most intense diffraction peak and $\theta$ is its diffraction angle. The numerical constant 0.94 corresponds to spherical crystals, which is commonly assumed. The (111) diffraction peak, around 27.5°, was used to estimate the crystal size by pseudo-Voigt function fitting.

TEM analysis was performed on glasses and GC samples prepared starting from sieved powders of size <60 μm. An ethanol dispersion was prepared, and then one drop was deposited onto a nickel grid supporting a perforated carbon film. High resolution transmission electron microscopy (HRTEM) data as well as scanning transmission electron microscopy-high angle annular dark field (STEM-HAADF) images and energy dispersive X-ray spectra (EDXS) were recorded on a JEOL TEM/STEM2100F field emission gun transmission electron microscope operating at 200 kV equipped with an EDS spectrometer (Oxford INCA X-sight system). EDXS analysis was performed in a STEM mode with a beam size of 1 nm.

Small-angle X-ray scattering (SAXS) was used to measure the glasses and GC fibers, and the details of the experiment were described elsewhere.[35]

**Optical characterization.** Site-selective steady-state emission and excitation spectra were recorded by transversely exciting the fibers with a continuous wave (cw) Ti:sapphire ring laser (0.4 cm–1 linewidth) in the 770–920 nm spectral range. The fluorescence was analyzed with a 0.25 m monochromator, and the signal was detected with an extended IR Hamamatsu H10330A-75 photomultiplier and finally amplified using a standard lock-in technique.

Lifetime measurements were carried out by exciting the fibers with a Ti–sapphire laser pumped using a pulsed frequency-doubled Nd:YAG laser (9 ns pulse width) and detecting the emission with a Hamamatsu H10330A-75 photomultiplier. The data were processed using a Tektronix oscilloscope.

## Results and discussion

### Uncoated and coated fibers

The uncoated fibers drawn using the single crucible method were transparent and uniform in size and morphology. Different diameters, from 50 to 500 μm, were obtained by changing the drawing temperature.

After the coating process, transparent and very thin (3 μm) $SiO_2$ cladding was obtained. Previous tests were performed by depositing the sol onto soda-lime glass substrates which were then heat-treated at 450 °C for 1 h. Good coating adhesion was achieved. The film thickness, around 3 μm, was measured by ellipsometry using a Cauchy model.

Considering that the sintering temperature was only 450 °C, almost 150 °C less than $T_g$, no deformation or softening was observed and the fibers maintained their shape and transparency. An optical-microscopy image in the transverse direction of a coated fiber with a core thickness of around 500 μm is given in Fig. 1, and good fiber homogeneity is evident. A cross-section image of the coated GC fiber is given in Fig. 1b. A detailed image of the core/cladding is shown in Fig. 1c and no cracks are observed. In comparison with the scale, cladding with a thickness around 3 μm is observed.

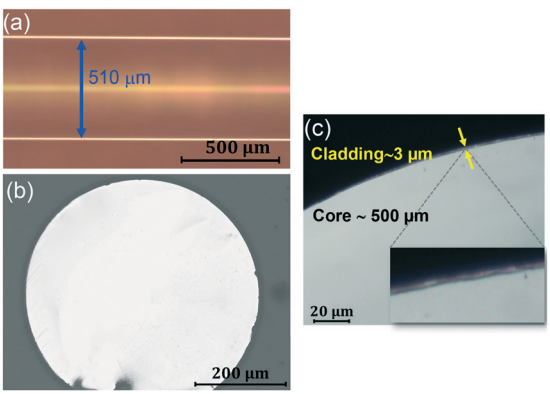


Fig. 1 (a) Photograph in the transverse direction of $SiO_2$-coated GCF0.1 treated at 640 °C for 40 h. The core is around 500 μm, as shown in detail in (b). (c) Details of glass–ceramic fiber cladding where a 3 μm coating is observed.

### DTA and crystallization mechanism

For the thermal characterization performed by DTA, Fig. 2a shows a weak exothermic peak corresponding to $LaF_3$ crystallization. The fiber crystallization trend is weaker than that of bulk samples, as shown in the comparison of their corresponding DTA curves (Fig. 2b). To obtain a more evident crystallization peak, fast heating rates up to 60–80 °C $min^{-1}$ were used, while for bulk samples with a heating rate of 10 or 20 °C $min^{-1}$, the crystallization peak can be perfectly recognized. The $T_g$ increases from bulk to fiber samples, passing from 590 °C to 605 °C, respectively, for a rate of 10 °C $min^{-1}$, the one used to obtain crystallized GC fibers. This result indicates that the fictive temperature depends on the cooling rate, as studied by Huang and Gupta for bulk and uncoated glass fibers,[49] this being generally higher during fiber drawing by the single crucible method. Moreover, no change of $T_g$ was observed passing from undoped to $Nd^{3+}$-doped fibers, the only difference being the crystallization stability parameter $\Delta T = T_p - T_g$, whose value decreased from 100 °C to 75 °C for the undoped and $Nd^{3+}$-doped samples, respectively. A similar behavior was observed for bulk samples.[35]

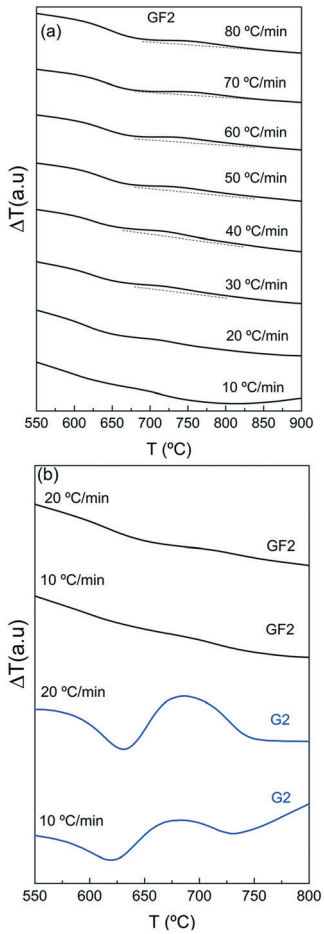


Fig. 2 (a) DTA curves of GF2 samples heated from 10 up to 80 °C $min^{-1}$. The dashed line is the baseline of the $LaF_3$ crystallization peak. (b) Comparison of DTA curves of bulk (G2) and fiber (GF2) samples of the same composition.

### XRD and crystal size

The crystallization behavior of GCs was firstly studied by XRD to compare with that of bulk samples. Fig. 3a and c show diffractograms where only $LaF_3$ diffraction peaks appear (JCPDS 00-032-0483).[50] The as-made glass fibers (untreated) were amorphous as can be seen in the diffractograms. When the temperature was increased to 620 °C and the treatment time to 40 h, the suitable conditions for $LaF_3$ precipitation in bulk samples, the fibers were still amorphous. To observe $LaF_3$ crystallization (not presented in Fig. 3), it was necessary to increase the treatment time up to 120 h.

Therefore, as compared to bulk samples, a clear delay in the crystallization was observed. This can be explained considering the fast thermal quenching during the drawing process using the crucible method. It affects the phase separation in the glass and causes a smaller nuclei density, as compared to bulk samples, with a subsequent delay in the crystallization process, as also observed in DTA. For undoped and $Nd^{3+}$-doped fibers, very similar results were obtained and the suitable heat treatment conditions were at 640 °C for 40 h. Higher temperatures cause $LaF_3$ crystallization but at temperatures as high as 660 °C, the glass softening produced notable fiber deformations. Hence, treatment temperatures higher than 640 °C are not useful for practical purposes. The $LaF_3$ crystal size is between 10–23 nm depending on the composition and the treatment temperature, as shown in Fig. 3b and c. Smaller crystals are formed for the $Nd^{3+}$-doped samples, as compared to the undoped ones. Moreover, while for undoped fibers treated at 660 °C from 20 h up to 90 h the crystal size changes from 14 to 19 nm, for $Nd^{3+}$-doped fibers, this change is smaller passing from almost 14 to 15 nm.

A different behavior is observed for heat treatments at 680 °C. In this case, the undoped fibers do not show any appreciable variation in the crystal size for 20 or 90 h of treatment, with the crystal size being around 23 nm. In contrast, in the $Nd^{3+}$-doped fibers, the crystals grow from 19 up to 22 nm. This indicates that the doping delays the crystallization kinetics. In fact, it is well known that in OxFGCs, where phase separation initiates crystallization, a viscous shell is formed around crystals due to a local change in the composition of the residual glass matrix. In particular, enrichment in a network former such as Si was observed for these GCs[35,36,51] and other oxyfluoride glass compositions.[52,53] This shell prevents further crystal growth because it inhibits atom diffusion and the final result is an asymptotic value for the crystal size at a certain treatment temperature. Higher temperatures speed up the process; therefore, crystals grow faster but also the viscous shell is formed earlier. This explains why for treatments of undoped fibers at 660 °C the crystal size still increases, while at 680 °C a viscous diffusion barrier is formed earlier and the asymptotic behavior is reached faster.

For $Nd^{3+}$-doped fibers at both treatment temperatures, the crystal size still increases due to a delay in the process kinetics; the constant value is obtained at 90 h of treatment.

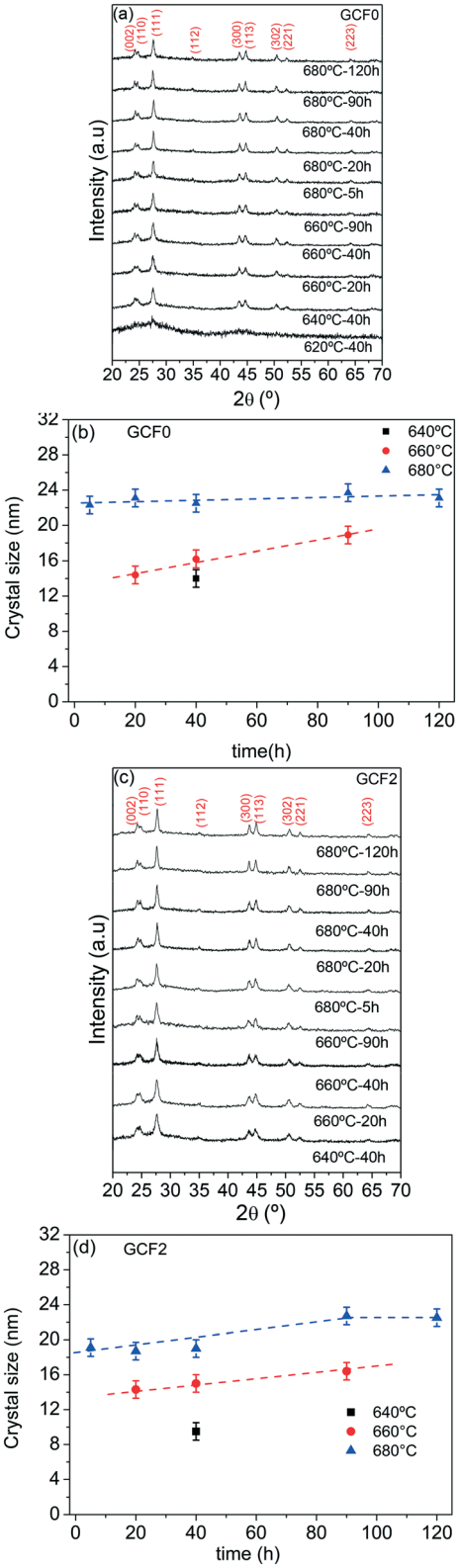


Fig. 3 (a)–(d) XRD patterns of GCF0 and GCF2 with the crystal size of the corresponding GC samples.

This delay could be associated with the increase of $T_g$ with increasing $Nd^{3+}$ content. In a previous paper, we have shown that Nd addition causes a delay in the crystallization process

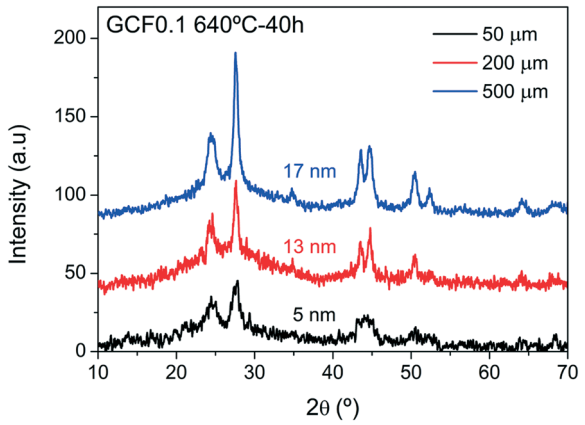


Fig. 4 XRD patterns of GCF0.1 640 °C–40 h fibers with diameters from 50 μm up to 500 μm. The corresponding crystal size is also given.

but allows a higher crystal fraction to be obtained.[35] On the other hand, it also acts as a nucleating agent promoting phase separation.

Fig. 4 shows XRD diffractograms of GCF0.1 fibers treated at 640 °C for 40 h whose size increases from 50 μm up to 500 μm. It is clear that, for thinner fibers, the crystallization process is delayed producing smaller crystals (5 nm) as compared to thicker fibers (17 nm), which also affects the crystal fraction (proportional to the peak area). This is a direct consequence of the higher cooling rate suffered by thin fibers during the drawing process, resulting in glass fibers with lower crystal size. For this reason, thick fibers (500 μm) where selected for the coating process.

## HRTEM and EDXS

The structural analysis was complemented with characterization performed by HRTEM and related techniques, STEM-HAADF along with EDXS analysis. Fig. 5 and 6 show the selected area electron diffraction patterns (SAED) and HRTEM micrographs of GF2 and GCF2 640 °C–40 h, respectively. The glass fibers obtained during the drawing process are amorphous, as confirmed by the absence of electron diffraction spots in the SAED pattern and HRTEM image in Fig. 5(a) and 6(a). For GC fibers, the $LaF_3$ crystals can be clearly detected in the SAED pattern with the diffraction spots corresponding to the $LaF_3$ phase (Fig. 5(b)), as well as in the HRTEM micrograph in Fig. 6(b).

In particular, a quite similar structure is observed for bulk samples.[35]

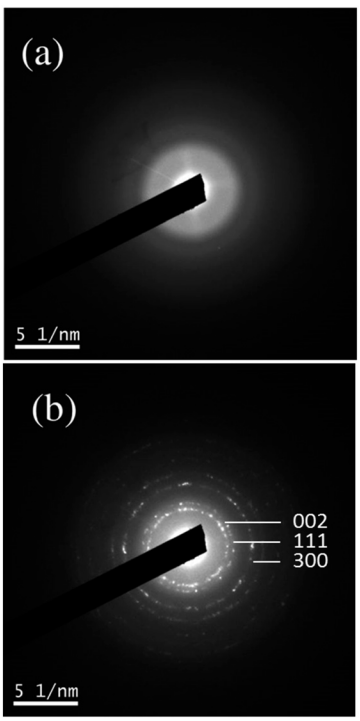


Fig. 5 Electron diffraction patterns of (a) GF2 and (b) GCF2 640 °C–40 h.

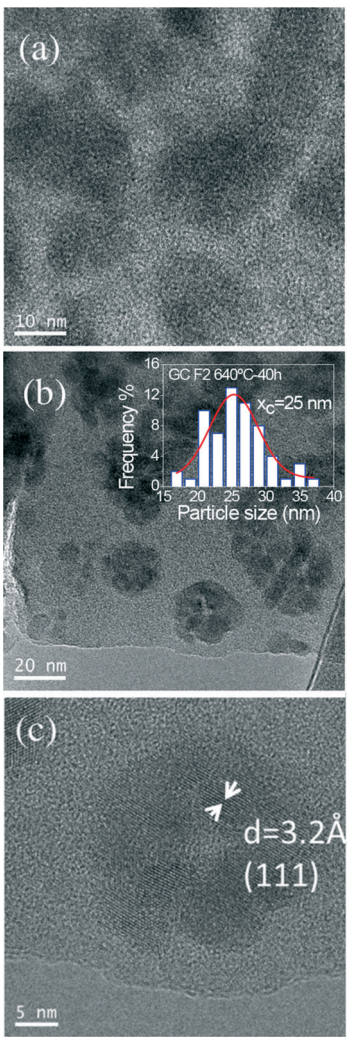


Fig. 6 HRTEM images of (a) GF2 and (b) GCF2 640 °C–40 h. (c) Details of a phase separation droplet with $LaF_3$ crystals inside.

The phase separation droplets are clearly visible with an average size of around 25 nm and a FWHM of 5 nm. Moreover, the multi-crystal formation observed inside the droplets is a relevant feature of the 55Si–10La composition. The crystal segregation inside the droplets is likely due to residual Si and Al diffusion that forms very thin shells of high viscosity that are not appreciable with the EDXS measurement. Fig. 6c shows a detailed view of a droplet where the lattice planes are clearly seen. The interplanar distance obtained is 3.2 Å, attributed to the (111) planes of the hexagonal $LaF_3$ crystalline phase, which is described in detail in the previous section through XRD analysis. Incorporation of $Nd^{3+}$ ions is confirmed by EDXS analysis across one crystallized phase separation droplet, as given in Fig. 7. A Si viscous shell is mainly formed just at the interphase with the crystals while a clear enrichment in La, Nd and F is observed inside the crystals.

By taking into account the results in previous sections and by comparing with bulk samples,[35] it can be concluded that the drawing process does not influence either the glass and GC structure or the crystallization mechanism. However, the crystallization depends on the drawing speed that determines the cooling rate. The higher the cooling velocity, the higher the treatment temperature needed to obtain a similar crystal size and crystal fraction.

## SAXS

Four main peaks can be identified from SAXS measurements (Fig. 8a) through deconvolution with Gaussian functions. The first one centered at 6 nm could be associated with the scattering of small phase separation droplets that further crystallize in the GC samples. The peaks around 17 and 20 nm (only for GCFs) could be related to bigger phase separation droplets with $LaF_3$ crystals inside, which precipitate with a size of around 11 nm (Fig. 3). A notable increase in the vol. particle distribution is obtained passing from GFs to GCFs, which means that crystallization occurred and the number of phase separation droplets increased. A similar behavior was observed for the GF2 and GCF2 640 °C–40 h samples, as shown in Fig. 8b. In this case, the particle distribution between 15–30 nm is associated with bigger phase separation droplets (Fig. 6b). By proper deconvolution, a further hidden peak centered at 9 nm is observed which is probably associated with crystal scattering, whose size is consistent with the one obtained by XRD as shown in Fig. 3b. Therefore, a rough agreement between HR-TEM, XRD and SAXS analyses was confirmed.

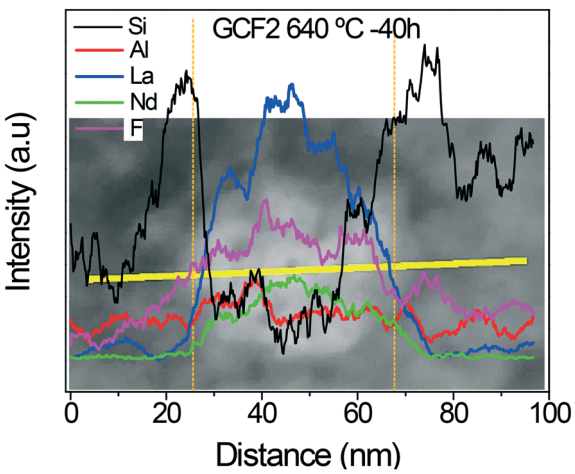


Fig. 7 EDXS analysis in STEM mode of a phase separation droplet (in the background) containing $LaF_3$ crystals in the GCF2 640 °C–40 h sample. The yellow line indicates the scanning line.

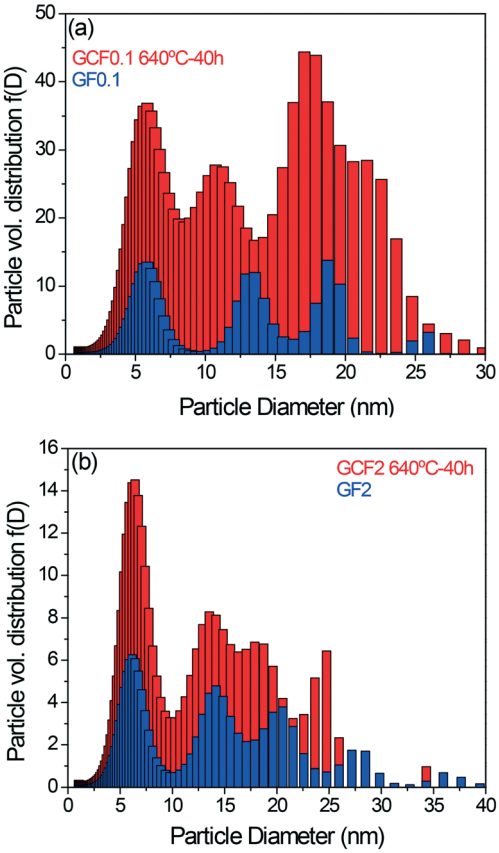


Fig. 8 Particle distribution obtained by SAXS for (a) GF0.1 and GCF0.1 640 °C–40 h and for (b) GF2 and GCF2 640 °C–40 h.

## Optical characterization

The transmission losses at 633 nm were determined by a conventional cut-back (or differential) method.[54] Fig. 9 shows a photo of the coated fiber and the experimental setup for measuring losses. The guided mode is also observed when projected onto a white screen. The input for the power was provided by a He–Ne laser and the transmitted power was measured using a Si detector. Then, the fiber is cut back and the transmitted power is measured again. The loss of the fiber in decibels per unit length is obtained from the measured transmitted power ratio of the two measurements. The obtained value for these multimode optical glass–ceramic fibers doped with 0.1% $NdF_3$ is about 20 dB $m^{-1}$.

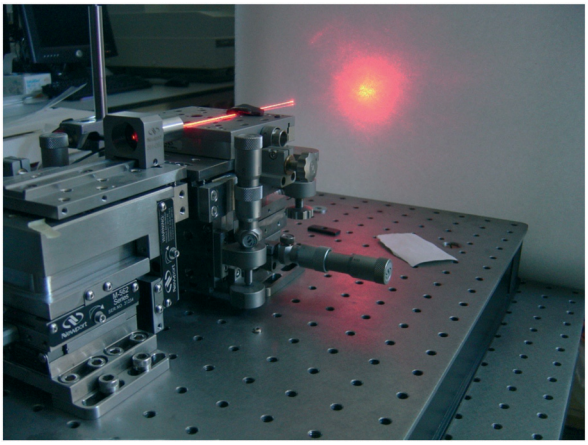

Fig. 9 GC fiber and experimental set-up for measuring fiber losses. The excitation source was obtained with a He–Ne laser and the guided mode is observed.

The emission and excitation spectra of coated fibers with a core thickness of around 500 μm untreated and treated at 640 °C for 40 h doped with 0.1 and 2% $NdF_3$ have been recorded at different excitation and emission wavelengths. Following the results obtained for the bulk samples, the emission spectra were obtained under excitation at 786 and 802 nm, the wavelengths at which it is possible to separate the contribution of $Nd^{3+}$ in the amorphous and crystalline phases.[35] Fig. 10(a) shows the normalized emission spectra obtained under excitation at 786 and 802 nm for the GC fiber doped with 0.1% $NdF_3$ and treated at 640 °C for 40 h. The spectra shows the same features as those obtained from the bulk samples.[35]

Although the crystal size may affect the luminescence properties of rare-earth ions, the obtained results are similar to those found in bulk glass–ceramic samples with relatively smaller $LaF_3$ NCs (between 9 and 12 nm), which indicates that the optical properties are not affected by the crystal size in both fiber and bulk samples.

The spectrum obtained under excitation at 786 nm corresponds to $Nd^{3+}$ ions in the $LaF_3$ NCs, whereas the one obtained under excitation at 802 nm shows an inhomogeneously broadened band similar to that of the glass sample (Fig. 10(b)). Moreover, the excitation spectra obtained by collecting the luminescence at 1039 and 1057 nm also show the presence of different environments for $Nd^{3+}$ ions. Fig. 11 shows the normalized excitation spectra for the same fiber doped with 0.1 mol% $NdF_3$. The spectrum monitored at 1039 nm presents narrower and well-resolved peaks corresponding to $Nd^{3+}$ ions in a crystalline environment.

As the concentration increases, the emission from $Nd^{3+}$ ions in the NCs decreases, and the spectra become broader with less resolved peaks. Fig. 12 shows the normalized emission and excitation spectra of the coated glass–ceramic fiber doped with 2 mol% $NdF_3$. As can be seen, the spectra are broader and less resolved than that of the fiber doped with 0.1 mol% $NdF_3$. This can be explained considering previous results of bulk materials where an estimation of the $Nd^{3+}$ concentration in the $LaF_3$ NCs was given.[35] Using Rietveld refinement and XANES analysis to calculate the crystal fraction and the $Nd^{3+}$ diffusion into the NCs, we concluded that doping the batch with a nominal concentration of 0.1 mol% $NdF_3$ results in an effective concentration of around 1 mol% in the NCs. As this value is close to the onset of concentration quenching, higher doping would cause a much higher

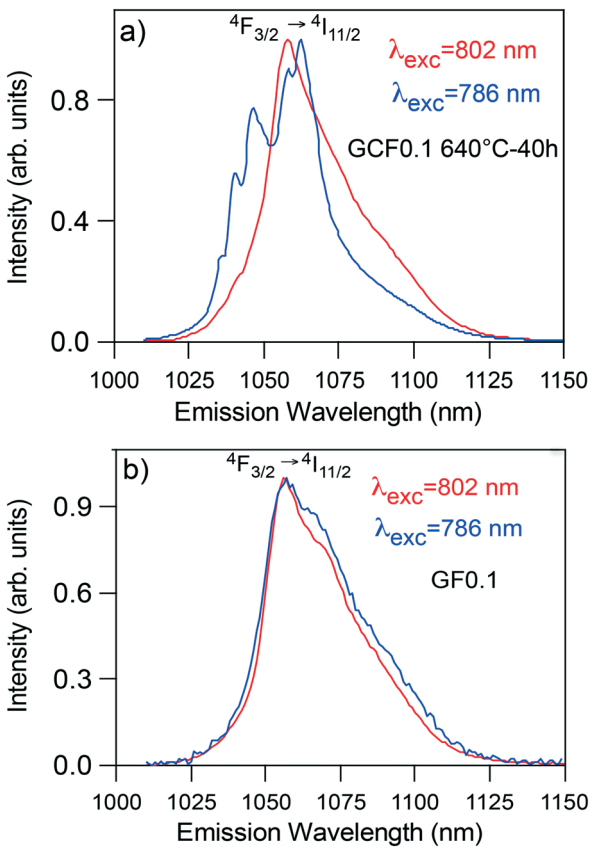


Fig. 10 Normalized emission spectra obtained under excitation at 786 and 802 nm for (a) GCF0.1 640 °C–40 h and (b) GF0.1.

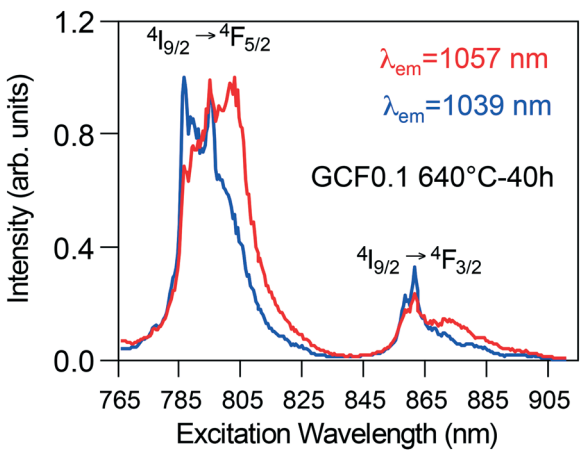


Fig. 11 Normalized excitation spectra of GCF0.1 640 °C–40 h obtained by collecting the luminescence at 1039 and 1057 nm.

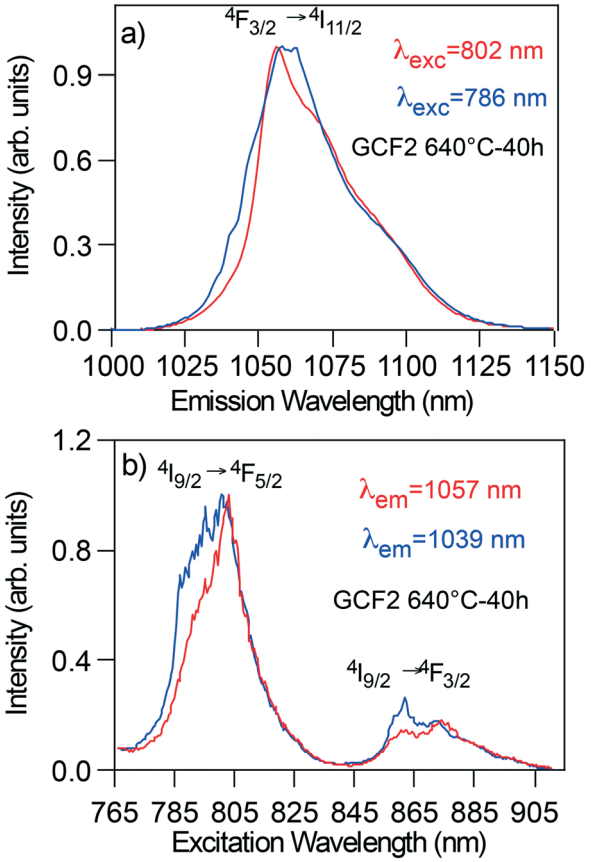


**Fig. 12** (a) Normalized emission spectra of GCF2 640 °C–40 h obtained under excitation at 786 and 802 nm. (b) Normalized excitation spectra of GCF2 640 °C–40 h obtained by collecting the luminescence at 1039 and 1057 nm.

$Nd^{3+}$ concentration in the NCs, with subsequent luminescence quenching.

Lifetime measurements of the $^4F_{3/2}$ state were performed by exciting the samples at 786 and 802 nm and collecting the luminescence at 1039 and 1057 nm, respectively. The decays of the GC fiber doped with 0.1 mol% $NdF_3$ can be described by single exponential functions to a good approximation for both excitation and emission wavelengths. However, the lifetime value is different depending on the excitation and emission wavelengths. Under excitation at 786 nm and by collecting the luminescence at 1039 nm, the lifetime value is 608 μs, whereas under excitation at 802 nm and by collecting the luminescence at 1057 nm, the lifetime is 374 μs. The longer lifetime corresponds to the $Nd^{3+}$ ions incorporated into the NCs. Fig. 13 shows the experimental decay curves of GCF0.1 treated at 640 °C for 40 h. As in the case of the bulk samples, the lifetime of $Nd^{3+}$ ions in the NCs is strongly reduced as the concentration increases, being 32 μs for the GC fibers doped with 2 mol%. This quenching is less relevant to the lifetime of $Nd^{3+}$ in the amorphous phase which is reduced from 374 μs to 159 μs as the concentration increases from 0.1% to 2 mol%. This behavior, also observed in the GC bulk samples, was explained by high diffusion and incorporation of $Nd^{3+}$ ions from the glass matrix to the $LaF_3$ NCs causing concentration quenching.[35] The same results were obtained for the uncoated fibers.

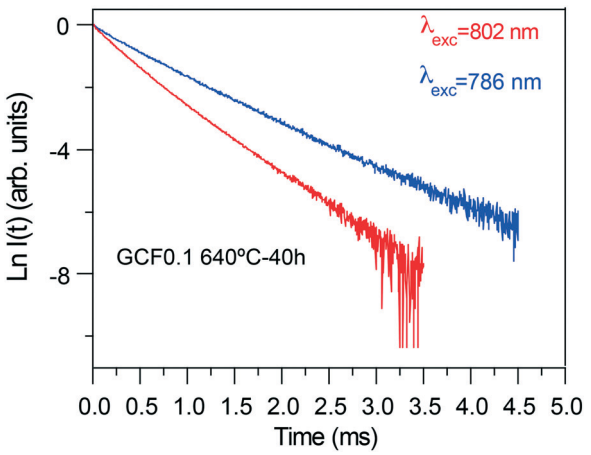


**Fig. 13** Logarithmic plot of the experimental decays from the $^4F_{3/2}$ state obtained under excitation at 786 nm (blue line) and 802 nm (red line) for GCF0.1 640 °C–40 h.

## Conclusions

Transparent OxFGC optical fibers doped with $Nd^{3+}$ were successfully prepared by a single crucible method and then covered with $SiO_2$ cladding using the sol–gel method. No differences were observed from the structural analysis, performed by HRTEM, SAXS, and XRD, as compared to the corresponding bulk GC materials. The crystallization mechanism is a diffusion-controlled process that starts from phase separation in the as-made fibers. However, by comparison with bulk materials of the same composition, a delay in the crystallization kinetics is observed due to the higher cooling rate during the drawing process. The higher the cooling velocity, the higher the treatment temperature needed to obtain a similar crystal size and crystal fraction.

The analysis of the luminescence properties confirms the incorporation of $Nd^{3+}$ ions into the NCs in the uncoated and coated GC fibers. Site-selective emission and excitation laser spectroscopy allows isolation of the emission of $Nd^{3+}$ ions in $LaF_3$ NCs. The lifetime values of $Nd^{3+}$ in the NCs show strong concentration quenching probably due to the redistribution of $Nd^{3+}$ ions from the glass matrix to the $LaF_3$ NCs. It is worth noting that these oxyfluoride glass fibers present the great advantage of maintaining the precursor crystalline phase during the drawing process, which allows thermal control of the size of the crystallites in the resulting glass–ceramic fibers and preservation of their optical guidance. Further improvements in the optical quality of the fibers are in progress in order to minimize the transmission losses to perform amplification experiments.

## Conflicts of interest

There are no conflicts to declare.

## Acknowledgements

This work was supported by MINECO under Project No. MAT2013-48246-C2-1-P and MAT2013-48246-C2-2-P and Basque Country University PPG17/07. J. J. Velázquez also acknowledges MINECO under Grant FPDI-2013-16895. G. Chen acknowledges the U.S. National Science Foundation for partial support under Grant #DMR-1507670. The authors wish to thank Aritz Iglesias for his support with the sol–gel cladding deposition and Prof. Dominik Dorosz (AGH University of Science and Technology) for his suggestions about the preparation of the samples.

## References

1 G. P. Agrawal, *Fiber-Optic communication systems*, Wiley, New Jersey, 4th edn, 2010.
2 G. Tao, H. Ebendorff-heidepriem, A. M. Stolyarov, S. Danto, J. V. Badding, Y. Fink, J. Ballato and A. F. Abouraddy, *Adv. Opt. Photonics*, 2015, **7**, 379–458.
3 J. S. Wang, E. M. Vogel and E. Snitzer, *Opt. Mater.*, 1994, **3**, 187–203.
4 V. V. Ravi Kantha Kumar, A. K. George, J. C. Knight and P. St. J. Russell, *Opt. Express*, 2003, **11**, 2641–2645.
5 I. Savelii, O. Mouawad, J. Fatome, B. Kibler, F. Désévédavy, G. Gadret, J.-C. Jules, P.-Y. Bony, H. Kawashima and W. Gao, *Opt. Express*, 2012, **20**, 2641–2645.
6 T. Cheng, L. Zhang, X. Xue, D. Deng and T. Suzuki, *Opt. Express*, 2015, **23**, 4125–4134.
7 Z. Jia, H. Li, X. Meng, L. Liu, G. Qin and W. Qin, *Opt. Lett.*, 2013, **3**, 1049–1051.
8 M. Kochanowicz, W. Mazerski, J. Żmojda, K. Czajkowski and D. Dorosz, *Photonics Lett. Pol.*, 2013, **5**, 35–37.
9 V. V. Atuchin, A. P. Yelisseyev, E. N. Galashov and M. S. Molokeev, *Mater. Chem. Phys.*, 2014, **147**, 1191–1194.
10 S. Jiang, T. Luo, B.-C. Hwang, F. Smekatala, K. Seneschala, J. Lucas and N. Peyghambariana, *J. Non-Cryst. Solids*, 2000, **263–264**, 364–368.
11 S. Xu, C. Li, W. Zhang, S. Mo, C. Yang, X. Wei, Z. Feng and Q. Qian, *Opt. Lett.*, 2013, **38**, 501–503.
12 P. Hofmann, C. Voigtländer, S. Nolte, N. Peyghambarian and A. Schülzgen, *J. Lightwave Technol.*, 2013, **31**, 756–760.
13 N. G. Boetti, G. C. Scarpignato, J. Lousteau, D. Pugliese, L. Bastard, J.-E. Broquin and D. Milanese, *J. Opt.*, 2015, **17**, 065705–065712.
14 C. Vitale-Brovarone, G. Novajra, D. Milanese, J. Lousteau and J. C. Knowles, *Mater. Sci. Eng., C*, 2011, **31**, 434–442.
15 E. Ceci-Ginistrelli, D. Pugliese, N. G. Boetti, G. Novajra, A. Ambrosone, J. Lousteau, C. Vitale-Brovarone, S. Abrate and D. Milanese, *Opt. Mater. Express*, 2016, **6**, 2040–2051.
16 J. Lucas, *Mater. Sci.*, 1989, **24**, 1–13.
17 Y. Miyajima, T. Komukai, T. Sugawa and T. Yamamoto, *Opt. Fiber Technol.*, 1994, **1**, 35–47.
18 V. Nazabal, M. Poulain, M. Olivier, P. Pirasteh, P. Camy, J.-L. Doualan, S. Guy, T. Djouama, A. Boutarfaia and J. L. Adam, *J. Fluorine Chem.*, 2012, **134**, 18–23.
19 Y. Wang and J. Ohwaki, *Appl. Phys. Lett.*, 1993, **63**, 3268–3270.
20 M. C. Gonçalves, L. F. Santos and R. M. Almeida, *C. R. Chim.*, 2002, **5**, 845–854.
21 A. de Pablos-Martín, A. Durán and M. J. Pascual, *Int. Mater. Rev.*, 2012, **57**, 165–186.
22 P. P. Fedorov, A. A. Luginina and A. I. Popov, *J. Fluorine Chem.*, 2015, **172**, 22–50.
23 A. de Pablos-Martín, M. Ferrari, M. J. Pascual and G. C. Righini, *La Rivista del Nuovo Cimento*, 2015, **38**, 311–369.
24 P. A. Tick, N. F. Borrelli, L. K. Cornelius and M. A. Newhouse, *J. Appl. Phys.*, 1995, **78**, 6367–6374.
25 M. J. Dejneka, *J. Non-Cryst. Solids*, 1998, **239**, 149–155.
26 S. Tanabe, H. Hayashi, T. Hanada and N. Onodera, *Opt. Mater.*, 2002, **19**, 343–349.
27 V. Lavín, I. Iparraguirre, J. Azkargorta, A. Mendioroz, A. Gonzalez-Platas, R. Balda and J. Fernández, *Opt. Mater.*, 2004, **25**, 201–208.
28 M. Mattarelli, M. Montagna, E. Moser, A. Chiasera, V. Tikhomirov, A. B. Seddon, S. Chaussedent, G. Nunzi Conti, S. Pelli and G. C. Righini, *J. Non-Cryst. Solids*, 2004, **345–346**, 354–358.
29 D. Chen, Y. Wang, Y. Yu and P. Huang, *Appl. Phys. Lett.*, 2007, **91**, 051920–051923.
30 S. Ye, B. Zhu, J. Luo, J. Chen, G. Lakshminarayana and J. Qiu, *Opt. Express*, 2008, **16**, 8989–8994.
31 D. Chen, Y. Wang, Y. Yu and P. Huang, *J. Phys. Chem. C*, 2008, **112**, 18943–18947.
32 Y. Xu, X. Zhang, S. Dai, B. Fan, H. Ma, J.-L. Adam, J.-L. Ren and G. Chen, *J. Phys. Chem. C*, 2011, **115**, 13056–13062.
33 A. de Pablos-Martín, M. Ramírez, S. Soria, M. Ferrari, G. C. Righini, L. E. Bausá, A. Durán and M. J. Pascual, *J. Am. Ceram. Soc.*, 2013, **96**, 447–457.
34 Z. Chen, G. Wu, H. Jia, K. Sharafudeen, W. Dai, X. Zhang, S. Zeng, J. Liu, R. Wei and S. Lv, *J. Phys. Chem. C*, 2015, **119**, 24056–24061.
35 G. Gorni, J. J. Velázquez, G. C. Mather, A. Durán, G. Chen, M. Sundararajan, R. Balda, J. Fernández and M. J. Pascual, *J. Eur. Ceram. Soc.*, 2017, **37**, 1695–1706.
36 G. Gorni, R. Balda, J. Fernández, L. Pascual, A. Durán and M. J. Pascual, *J. Lumin.*, 2017, DOI: 10.1016/j.jlumin.2017.05.063.
37 A. de Pablos-Martín, D. Ristic, A. Durán, M. Ferrari and M. J. Pascual, *CrystEngComm*, 2017, **19**, 967–974.
38 S. J. L. Ribeiro, C. C. Araújo, L. Bueno, R. R. Gonçalves and Y. Messaddeq, *J. Non-Cryst. Solids*, 2004, **348**, 180–184.
39 S. Fujihara, T. Kato and T. Kimura, *J. Sol-Gel Sci. Technol.*, 2003, **26**, 953–956.
40 S. Fujihara, S. Koji and T. Kimura, *J. Mater. Chem.*, 2004, **14**, 1331–1335.
41 L. Armelao, G. Bottaro, L. Bovo, C. Maccato, M. Pascolini, C. Sada, E. Soini and E. Tondello, *J. Phys. Chem. C*, 2009, **113**, 14429–14434.
42 E. Augustyn, M. Żelechower, D. Stróż and J. Chrapoński, *Opt. Mater.*, 2012, **34**, 944–950.
43 M. Reben, D. Dorosz, J. Wasylak, B. Burtan-Gwizdala, J. Jaglarz and J. Zontek, *Opt. Appl.*, 2012, **42**, 353–364.

 

44 K. V. Krishnaiah, Y. Ledemi, C. Genevois, E. Veron, X. Sauvage, S. Morency, E. Soares de Lima Filho, G. Nemova, M. Allix and Y. Messaddeq, *Opt. Mater. Express*, 2017, **7**, 1980–1994.
45 C. A. Browne, D. H. Tarrant, M. S. Olteanu, J. W. Mullens and E. L. Chronister, *Anal. Chem.*, 1996, **68**, 2289–2295.
46 G. Maxwell, B. Ponting, E. Gebremichael and R. Magana, WO2016153508A1, 2016.
47 A. de Pablos, A. Durán and M. I. Nieto, *Bol. Soc. Esp. Ceram. Vidrio*, 1997, **36**, 517–524.
48 A. de Pablos-Martín, N. Hémono, G. C. Mather, S. Bhattacharyya, T. Höche, H. Bornhöft, J. Deubener, F. Muñoz, A. Durán and M. J. Pascual, *J. Am. Ceram. Soc.*, 2013, **96**, 447–457.
49 J. Huang and P. K. Gupta, *J. Non-Cryst. Solids*, 1992, **151**, 175–181.
50 O. Greis, *PhD thesis*, University of Freiburg i Br, Germany, Private Communication, 1976.
51 G. Gorni, A. Cosci, S. Pelli, L. Pascual, A. Durán and M. J. Pascual, *Front. Mater.*, 2017, **3**, 58.
52 C. Rüssel, *Chem. Mater.*, 2005, **17**, 5843–5847.
53 S. Bhattacharyya, C. Bocker, T. Heil, J. R. Jinschek, T. Höche, C. Rüssel and H. Kohl, *Nano Lett.*, 2009, **9**, 2493–2496.
54 J. Wang, L. Reekie, W. S. Brocklesby, Y. T. Chow and D. N. Payne, *J. Non-Cryst. Solids*, 1995, **180**, 207–216.

# *PAPER 8*

**Crystallization mechanism in sol-gel oxyfluoride glass-ceramics.**

G. Gorni, M.J. Pascual, A. Caballero, J.J. Velázquez, J. Mosa, Y. Castro, A. Durán.

*J. Non-Cryst. Solids* 501 (2018) 145-152. doi:10.1016/j.jnoncrysol.2018

Journal of Non-Crystalline Solids 501 (2018) 145–152

Contents lists available at ScienceDirect

Journal of Non-Crystalline Solids

journal homepage: www.elsevier.com/locate/jnoncrysol

# Crystallization mechanism in sol-gel oxyfluoride glass-ceramics

G. Gorni*, M.J. Pascual, A. Caballero, J.J. Velázquez, J. Mosa, Y. Castro, A. Durán

*Instituto de Cerámica y Vidrio (CSIC), Madrid, Spain*

A B S T R A C T

The crystallization mechanism of $LaF_3$ in sol-gel oxyfluoride glass-ceramics in the system $SiO_2$-$LaF_3$ has been studied using DTA, XRD, FTIR, HRTEM and NMR. Based on classical calculations of non-isothermal DTA curves involving Ozawas's plots, a diffusion-controlled process should be responsible for the fluorides crystallization similarly to that obtained for melt-quenching oxyfluoride glass-ceramics. Therefore, an increase of the crystal size and fraction is expected when increasing the time and/or temperature of the treatment. Nevertheless, XRD, FIR, HRTEM and NMR demonstrated that neither bigger crystals nor higher crystal fraction are obtained for treatment times longer than 1 min at 550 °C. However, further heat treatment causes that the structural order of the crystals is lost. On the other hand, typical fluorides crystallization temperatures (~300 °C) in sol-gel materials are much lower than $T_g$ of the matrix (~1130 °C) thus being very different to what observed for oxyfluoride glasses prepared by melt-quenching. The proposed crystallization mechanism is a fast process that occurs when crystallization temperature is reached. This behavior is explained as a chemical reaction from the xerogels, followed by the fast precipitation of the nanocrystals without energy barrier. The nanocrystals are unstable in the surrounding $SiO_2$ matrix for aging at crystallization or higher temperatures. These treatments lead to a dissolution process, favored by the compositional gradient between matrix and crystals, which drive the material to reach the equilibrium.

## 1. Introduction

Oxyfluoride glass-ceramics have been deeply studied since the pioneering work in 1993 by Wang and Ohwaki [1] that opened the way to a new class of materials with improved active optical properties with respect to common glasses. Such materials combine the low phonon-energy of fluoride crystals with excellent mechanical, thermal and chemical stability of oxide glasses, especially the alumino-silicate ones, showing an improvement of linear and non-linear optical properties when active ions are embedded in the fluoride crystal phase. In fact, as compared to typical oxide glass matrices, the phonon energy of several fluoride crystals is in the range 250–450 $cm^{-1}$, being therefore 4–5 times smaller than those of oxide glass matrices [2]. Such low phonon energy values allow preventing or strongly reducing the non-radiative losses thus permitting higher emissions intensity and longer lifetimes.

Rare-earth (RE) ions are commonly used as active ions because they show emissions in a wide spectral range, from UV to NIR, and their use in telecom, lasers, lightening etc. makes them indispensable nowadays. Moreover, the screening of the outer electronic levels allows maintaining the emission energies centered near the same values in different hosts, making them suitable for applications where certain defined and fixed wavelengths are required.

For these reasons, a great number of publications about oxyfluoride glass-ceramics emerged in the last two decades and many different compositions have been prepared showing how the crystallization of fluorides doped with RE ions increases the optical properties with respect to glasses of the same composition [3–5].

Glasses are commonly prepared by melt-quenching and then heat treated in a controlled way for obtaining glass-ceramic samples. The heat treatment is generally performed at temperatures slightly higher than $T_g$ ($T_g$ + 20–100 °C) allowing the precipitation of nano-crystals. In fact, due to a big difference in the refractive index of fluoride crystals and oxide glasses, the Rayleigh scattering strongly reduces the final transparency if the crystal size exceeds 40–50 nm. In most cases, phase separation takes place during the cooling of the melt in which a fluorine rich phase is immersed in the oxide glass matrix. This phase separation acts as precursor for the subsequent crystallization of fluorides.

Several authors studied the crystallization mechanism for non-isothermal conditions using DTA or DSC analysis and the Avrami's theory or the modified Ozawa's, Matusita's and Kissinger's equations [6–13]. The results show that the crystallization mechanism for glass-ceramics produced by melt-quenching is a diffusion-controlled process that starts from a fixed number of nuclei with no further nuclei produced during the heating process. Crystalline structures are developed starting from

* Corresponding author.
*E-mail address:* ggorni@icv.csic.es (G. Gorni).

https://doi.org/10.1016/j.jnoncrysol.2018.01.031
Received 1 December 2017; Received in revised form 17 January 2018; Accepted 18 January 2018
Available online 13 June 2018

phase separation droplets already present in the precursor glass and the crystal growth is linear with the square root of time, thus confirming the diffusion-limited mechanism. Given that oxyfluoride compositions are non-isochemical systems, crystals and glass matrix do not have the same composition. The crystallization process produces a redistribution of elements and local compositional changes of the residual glass matrix, causing the increase of $T_g$ with the dwelling time [14]. A shell enriched in glass formers is built around the crystals acting as a diffusion barrier and slowing down the crystal growth [15–18]. Therefore, no increase of the crystal size is observed after such viscous barrier is formed and the only effect of longer heat treatments is to redistribute ions inside crystals or favor the phase transformation of polymorphous crystals [19–23].

However, glass-ceramics produced by melt-quenching present some drawbacks, most of them related to the high temperatures involved in the melting process that cause relevant fluorine losses, thus limiting the final content of crystal fraction that can be obtained. Furthermore, phase separation can affect the final optical quality of the samples making difficult obtaining highly homogeneous materials with suitable optical quality.

An alternative route to obtain materials with enhanced optical properties is offered by the sol-gel method. The synthesis typically involves the hydrolysis and polycondensation of metal salts or metal-organic precursors, such as tetraethyl orthosilicate (TEOS), in alcoholic medium. After hydrolysis and polycondensation reactions, a network polymers ("gel") is formed in liquid phase.

A two-step process is involved in the preparation of oxyfluoride materials by sol-gel [24]. First, a silica sol is prepared using alkoxide precursors and following the classical route. Second, a mixture of fluoride and RE ion precursors (acetates, nitrates, chlorides etc.) is prepared separately dissolving them in ethanol and/or acidic medium. The mixing of both solutions, followed by suitable thermal treatments, leads to the precipitation of fluoride crystals in the silica-glass matrix. By this method, much lower crystallization and sintering temperatures are used with respect to melt-quenching method, thus allowing a much higher fluorine content being added. Additionally, no phase separation is observed in oxyfluoride sol-gel samples, permitting obtaining nanomaterials with improved homogeneity and enhanced optical properties.

A great contribution in the preparation of sol-gel oxyfluoride glass-ceramics came from the first works of Fujihara et al. [24,25]. In particular, the use of trifluoarecetic acid (TFA) as fluorine precursor allowed preventing $La^{3+}$ ions to be incorporated into the $SiO_2$ matrix. Thanks to the screening action of $CF_3COO^-$ ions these ions are already coordinated to $La^{3+}$ in the silica sol, thus allowing the precipitation of $LaF_3$ crystals.

In spite of the sol-gel method has been extensively used since the end of nineties to prepare oxyfluoride glass-ceramics, materials with maximum $LaF_3$ amounts of only 10 mol% have been prepared. Moreover, the crystallization mechanism of fluorides in sol-gel glass ceramics is still unclear and has not been elucidated yet [26,27].

In this work, we studied the crystallization mechanism of $LaF_3$ crystals in $SiO_2$-$LaF_3$ materials prepared by sol-gel using DTA, XRD, HRTEM, FTIR and NMR. The paper compares the crystallization process that takes place in materials containing 20 mol% of $LaF_3$ with others obtained by melt-quenching previously developed by the authors.

## 2. Experimental

### 2.1. Materials preparation

$80SiO_2$-$20LaF_3$ (mol%) sols were prepared using tetraethylorthosilicate (TEOS, ABCR, 98%) as $SiO_2$ precursor, lanthanum acetate ($La(CH_3COO\text{-}nH_2O)_3$, Sigma-Aldrich, 99.9%) and TFA (Sigma-Aldrich, 99%) as fluorine source. The synthesis of the sol was performed by a two steps process. First, a $SiO_2$ sol, labelled as SOL-1, was prepared, mixing TEOS, absolute ethanol (EtOH) and $H_2O$ (0.1 M HCl) in a molar ratio 1TEOS:9.5EtOH:$2H_2O$ and stirred for 2 h at room temperature [28]. To start the hydrolysis process, $H_2O$ was added drop by drop under vigorous stirring. Then, a mixture, labelled as SOL-2, containing lanthanum acetate, TFA, absolute ethanol and distilled water was prepared separately stirring the mix at 40 °C during 2 h to ensure complete dissolution of the reagents. The molar ratio was fixed to 1La(ac):5TFA:5EtOH:$4H_2O$. The last step was mixing SOL-1 and SOL-2 to obtain the desired composition.

### 2.2. Thermal characterization and crystallization mechanism

Non-isothermal crystallization kinetics was studied by differential thermal analysis (DTA) and thermogravimetry (TG) (SDT Q600 – TA Instruments) using 20–30 mg of bulk specimens, grinded to a size of 1–1.25 mm and obtained after drying the sol at 80 °C. The measurements were performed between 25 and 850 °C using heating rates from 10 up to 40 °C/min. From these results the Avrami's parameter $n$ and crystal-growth dimensionality parameter $m$ were calculated from the Ozawa's equation [29] and the Matusita's equation [30] given by Eqs. (1) and (2), respectively:

$$\left(\frac{d[\ln[-\ln(1-x)]]}{d(\ln q)}\right)_T = -n \tag{1}$$

$$\ln\left(\frac{q^n}{T_p^2}\right) = -\frac{mE_a}{RT_p} + Const \tag{2}$$

In these equations, $x$ is the partial area of the crystallization peak calculated for a fixed temperature $T$ and $q$ is the heating rate; $T_p$ and $R$ are the crystallization peak temperature and the gas constant, respectively. The activation energy for crystallization, $E_a$, was calculated using the Kissinger's equation [31,32]:

$$\ln\left(\frac{q}{T_p^2}\right) = -\frac{E_a}{RT_p} + Const \tag{3}$$

### 2.3. Structural characterization and crystal growth

X-Ray-Diffraction (XRD) was performed on milled and sieved powders (< 60 μm) derived from heat-treated bulk specimens. Diffractograms were acquired in the range 10–70° using a step size of 0.02° and 1 s of integration time for each step. The crystal size was calculated using the Scherrer's equation [33]:

$$\varphi_x = \frac{0.94\lambda}{\cos\theta\sqrt{B_m^2 - B_i^2}} \tag{4}$$

where λ is the wavelength (1.54056 Å – $CuK_{\alpha 1}$), $B_m$ the full width half maximum of the $LaF_3$ peak (111) and $\theta$ the corresponding diffraction angle. The constant factor 0.94 corresponds to spherical crystals and is commonly used. Pseudo-Voigt function was used to fit diffraction-peak parameters. High resolution diffractograms were also acquired at the European Synchrotron Radiation Facility using a wavelength of 0.619 Å.

A JEOL 2100 field-emission gun transmission electron microscope operating at 200 kV with a point resolution of 0.19 nm was used to acquire high resolution transmission electron microscopy (HRTEM) images. Samples were prepared depositing, onto a copper grid carbon lacey, two drops of an ethanol suspension containing a small amount of powder sample. Then, the ethanol was removed by drying under a UV lamp, leaving small traces of sample on the copper grid.

Fourier Transform Infra-Red (FTIR) spectra in the range 4000–450 $cm^{-1}$ were obtained, with a resolution of 4 $cm^{-1}$, using a Perkin Elmer Spectrum 100 instrument. Transmission spectra were obtained using KBr pellets prepared mixing 2–3 mg of powder samples with 250 mg of KBr. Far Infra-Red spectroscopy (FIR) spectra were

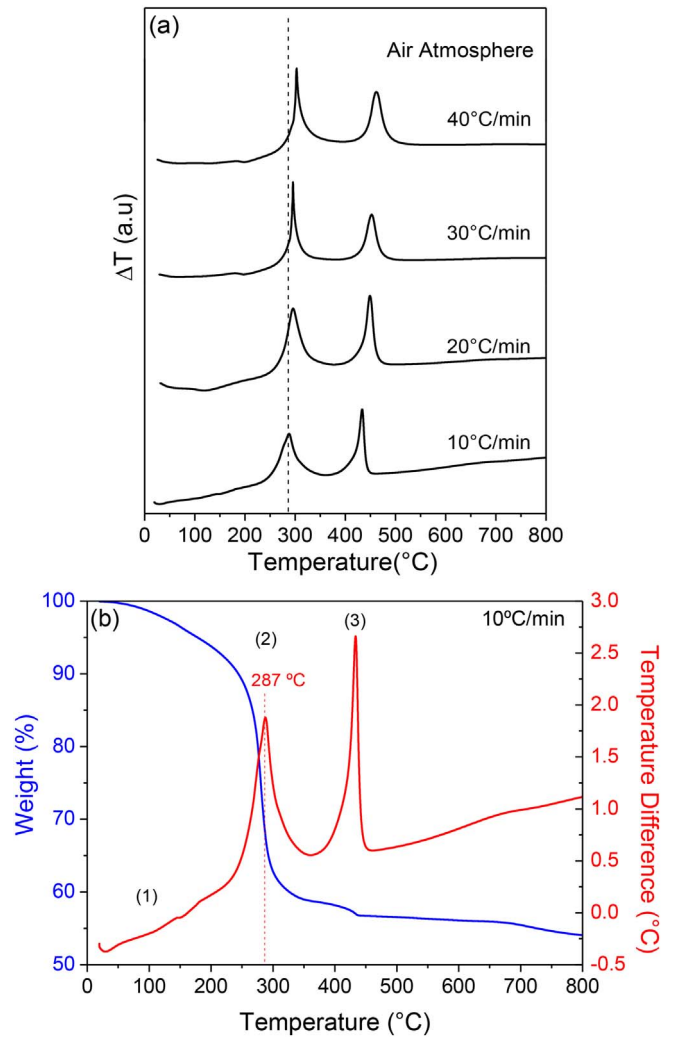


**Fig. 1.** (a) DTA of $80SiO_2$-$20LaF_3$ bulk samples treated in air from RT to 800 °C with heating rates 10–40 °C/min. (b) Detail of DTA (right axis) and TG (left axis) curves for the sample treated using a rate of 10 °C/min. The endothermic process (1) is assigned to solvent removal. The exothermic processes (2) and (3) are associated to $LaF_3$ crystallization and combustion process, respectively.

collected directly on the samples in ATR configuration in the range 600–175 $cm^{-1}$ with a resolution of 4 $cm^{-1}$ using a Nicolet 6700-Thermo Scientific.

$^{19}F$ magic-angle spinning nuclear magnetic resonance ($^{19}F$ MAS/NMR) spectra of xerogel and glass-ceramics were recorded using a NMR Spectrometer AVANCE II (BRUKER) equipped with a 9.4 Tesla magnet (400 MHz) and a 2.5 mm rotor spinning at 20 kHz.

## 3. Results

### 3.1. Thermal and morphological characterization

Transparent and crack-free $80SiO_2$-$20LaF_3$ bulk samples were obtained after drying the sol at 80 °C. After heating at 550–650 °C the transparency and homogeneity were preserved.

Fig. 1a shows the DTA curves of $80SiO_2$-$20LaF_3$ bulk samples performed in air using heating rates between 10 and 40 °C/min. In all cases, two exothermic (upward) peaks are identified. The first one appears at 285 °C and shifts toward higher temperatures, up to 302 °C, when the heating rate increases. The second peak appears around 440 °C and shifts to 464 °C for the fastest heating rate. The area of both peaks increases with the heating rate and the FWHM of the first peak narrows producing more intense and well defined peaks. This means that more crystals are produced in the same time interval because of faster heating. Fig. 1b shows a detail of the DTA together with the TG curve. A small weight loss, around 10 wt%, is observed between 100 and 250 °C and assigned to residual water and solvents elimination. The weight loss of around 30% in the range 250–380 °C is associated with the first exothermic peak. For temperatures higher than 400 °C only a

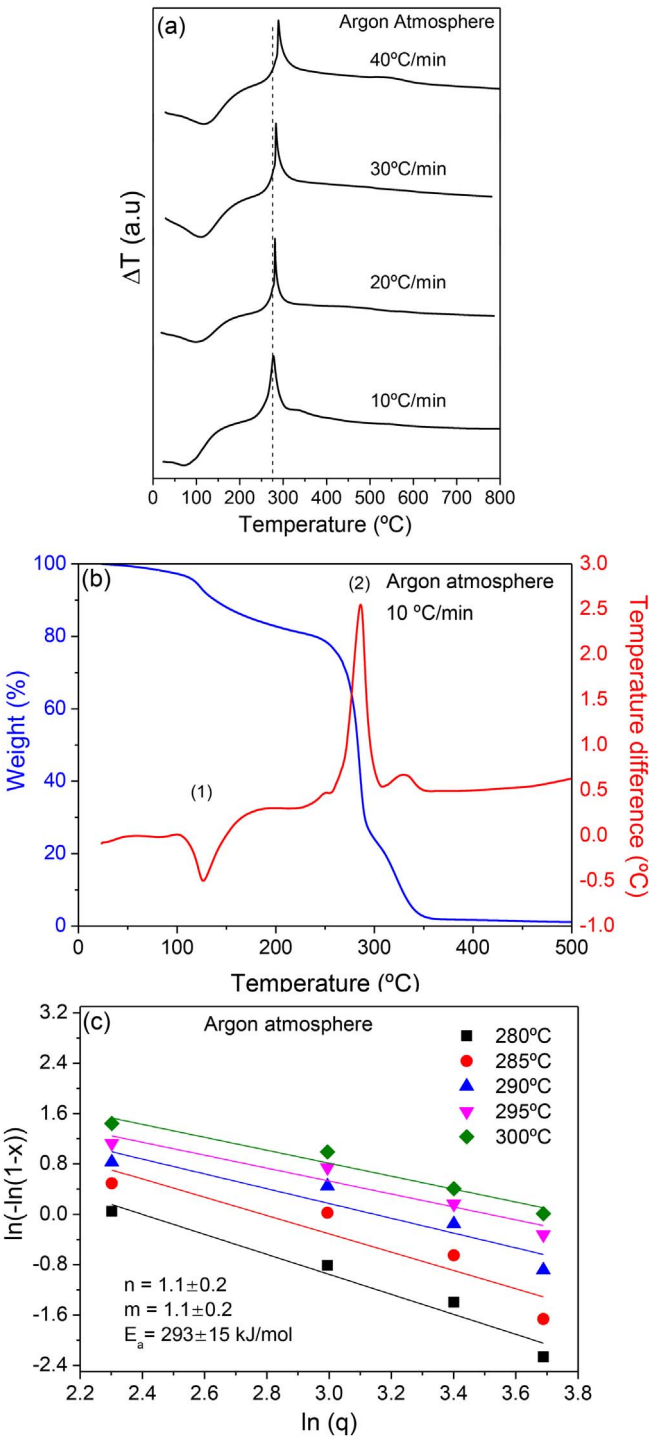


**Fig. 2.** (a) DTA of $80SiO_2$-$20LaF_3$ bulk samples treated in argon from RT to 800 °C with heating rates 10–40 °C/min. (b) DTA and TG of SOL-2 in argon atmosphere using a heating rate of 10 °C/min. The endothermic peak (1) corresponds to solvent removal and the exothermic peak (2) is assigned to $LaF_3$ crystallization. (c) Ozawa's plot for five different temperatures. In the bottom the n mean value together with the m parameter and the crystallization activation energy are also given.

small weight loss, about 3 wt%, appears, related with the combustion of residual organic compounds. The first exothermic peak is associated with the crystallization of fluoride crystals [24], in accordance with similar behaviors observed for other fluoride phases with DTA exothermic peaks between 280 and 350 °C [34–37]. It is worth nothing that such behavior is true only for sol-gel derived oxyfluoride glass-ceramics while for melt-quenching samples much higher crystallization temperatures are observed [11,12,22,38–40].

DTA curves were also measured in argon (inert gas) atmosphere to avoid oxidations processes, Fig. 2a. In this case, only the first exothermic peak appears at the same temperature of DTA curves performed in air. The second exothermic peak disappeared, indicating that it was related to some oxidation processes. Fig. 2b shows DTA and TG curves in argon atmosphere for SOL-2 dried at 80 °C, Fig. 2a. Once again, a first mass loss is observed around 125 °C related to water and solvents removal, and only an intense exothermic peak, at 286 °C, appears along a 80% mass loss. Therefore, the exothermic peak appearing around 300 °C (for heating rate of 10–40 °C/min) is assigned to $LaF_3$ crystallization process.

The crystallization process is not usually related to a mass loss, but only to an energy release. However, in the case of sol-gel materials, a chemical reaction [24,41] occurs previously and it is responsible for crystals formation and associated with the big mass loss:

$$La(CF_3COO)_3 \rightarrow LaF_3 + (CF_3CO)_2O + CO_2 + CO \quad (5)$$

By using the Eqs. (1)–(3), the crystallization mechanism was evaluated using the DTA in argon to avoid overlaps of other processes. Fig. 3c shows the Ozawas's plots for five different temperatures. In all cases, a straight line is obtained for each temperature and an $n$ mean value equal to 1 was calculated with the corresponding standard deviation. By applying Eq. (2) the $m$ crystal growth dimensionality parameter was also calculated, giving a value equal to 1. Considering these results, the use of the Kissinger's equation to calculate the crystallization activation energy is correct. The crystallization activation energy, around 293 kJ/mol, is smaller than that obtained for $LaF_3$ crystallization in melt-quenching derived glass-ceramics, around 340 kJ/mol [12,21]. From these results and according to Donald [42], the crystallization mechanism could be described as a diffusion-controlled process starting from a fix number of nuclei that occurs in the volume of the sample. This is the typical crystallization mechanism for $LaF_3$ or other fluoride phases in melt-quenching oxyfluoride glass-ceramics [12,21,22]. Indeed, some authors [34,35] reported similar results for sol-gel derived oxyfluoride glass-ceramics, concluding that a diffusion-controlled process is the main crystallization mechanism of fluorides in sol-gel materials.

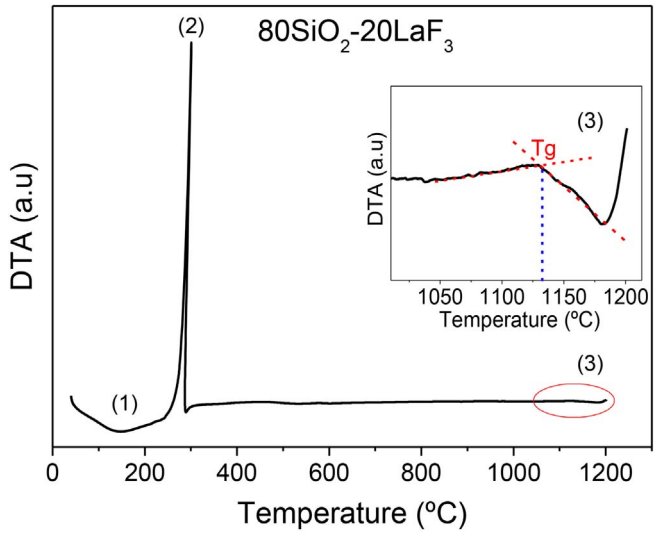


**Fig. 3.** High temperature DTA of $80SiO_2$-$20LaF_3$ bulk sample. The inset shows a detail of the encircled zone where the endothermic peak corresponding to $SiO_2$ $T_g$ appears at about 1130 °C. Endothermic processes (1) and (3) are due to solvent removal and glass transition, respectively. The exothermic peak (2) is assigned to $LaF_3$ crystallization.

Fig. 3 shows the DTA of $80SiO_2$-$20LaF_3$ sample recorded up to 1200 °C. The endothermic process appearing at 1175 °C allows estimating $T_g \sim 1130$ °C, along with the $LaF_3$ crystallization peak at ~280 °C.

### 3.2. Structural characterization and crystal growth

Fig. 4a shows XRD patterns for $80SiO_2$-$20LaF_3$ bulk samples treated at 550 °C from 1 min up to 80 h. As observed, after only 1 min of treatment $LaF_3$ crystals (JCPDS 00-032-0483) are detected with a size of 11 nm. The increment of treatment time to 1 h decreases the crystal size to 8 nm. This decrease is more evident when the treatment is maintained for 20 h, the crystal size reducing to 6.5 nm.

For a fixed temperature two effects are observed when treatment time increases: 1) the decrease of the crystal size, associated to broader and less resolved peaks, and 2) the decrease of the crystal fraction (related to the peak height). Fig. 4b shows the diffractograms of $80SiO_2$-$20LaF_3$ samples treated at 550 °C for 1 min and 1 h performed at the synchrotron ESRF BM25B beamline. In the inset of Fig. 4b, a detail of the most intense (111) diffraction peak is given for comparison confirming the broadening of the peak when increasing the treatment time. The calculated crystal sizes agree with those obtained from Fig. 4a. Moreover, as shown in Fig. 4c, if no thermal quenching is performed at crystallization temperature only small and not defined crystals are detected.

To further study the crystal growth, samples were treated at 650 °C. A comparison of samples treated at 550 °C and 650 °C for 1 h is given in Fig. 4d. The crystal size is quite similar for both samples being 8 and 7.5 nm, respectively, and no better crystallinity is observed even increasing the treatment temperature by 100 °C.

FIR spectra were also acquired to study the fluoride vibrations evolution with the heat treatment, considering that the main vibration band of La-F in $LaF_3$ crystals is around 350 $cm^{-1}$ [43]. The spectra, collected in the range 600–175 $cm^{-1}$, allow comparing the evolution of the bands with the treatment time and/or temperature. Fig. 5a shows FIR spectra of $80SiO_2$-$20LaF_3$ bulk xerogel and glass-ceramic samples treated at 550 °C from 1 min up to 80 h. The spectrum of pure silica glass was also measured together with pure $LaF_3$ crystalline powders. Silica glass spectrum shows a band around 460 $cm^{-1}$ associated to O—Si—O bending vibration [44–47], while $LaF_3$ reference sample shows three main bands centered at around 345, 250 and 190 $cm^{-1}$ [43]

The xerogel, obtained after drying the sol at 80 °C, does not show any band characteristic of $LaF_3$ thus confirming the absence of fluoride crystals; a weak band at ~270 $cm^{-1}$ is assigned to $CF_3$ rocking vibration in TFA derived compounds [48]. The vibration band at around 425 $cm^{-1}$ is associated to O—Si—O bending. This band broadens and shifts toward lower wavenumbers with respect to glass-ceramic samples, such behavior being related to the formation of $SiO_4$ units with larger inter-tetrahedra angles [49,50].

On the other side, the glass-ceramic sample treated at 550 °C for 1 min clearly shows the La-F vibrations of $LaF_3$ crystals, especially the higher frequency mode near 350 $cm^{-1}$ along with the O—Si—O bending vibration. A small band shift is observed as compared to the references likely related to ATR configuration that causes a peak shift depending on the refractive index/density difference of the samples. In particular, La-F vibrations diminish for increasing treatment times, almost disappearing for very long treatment times (80 h). The stronger La-F contribution is obtained for the fastest heat treatment although such bands are still appreciable up to 5 h (Fig. 5a).

Fig. 5b shows the effect of the treatment temperature for $80SiO_2$-$20LaF_3$ samples treated at 550 and 650 °C during 1 h. The O—Si—O bending band is still centered around 460 $cm^{-1}$, thus indicating that

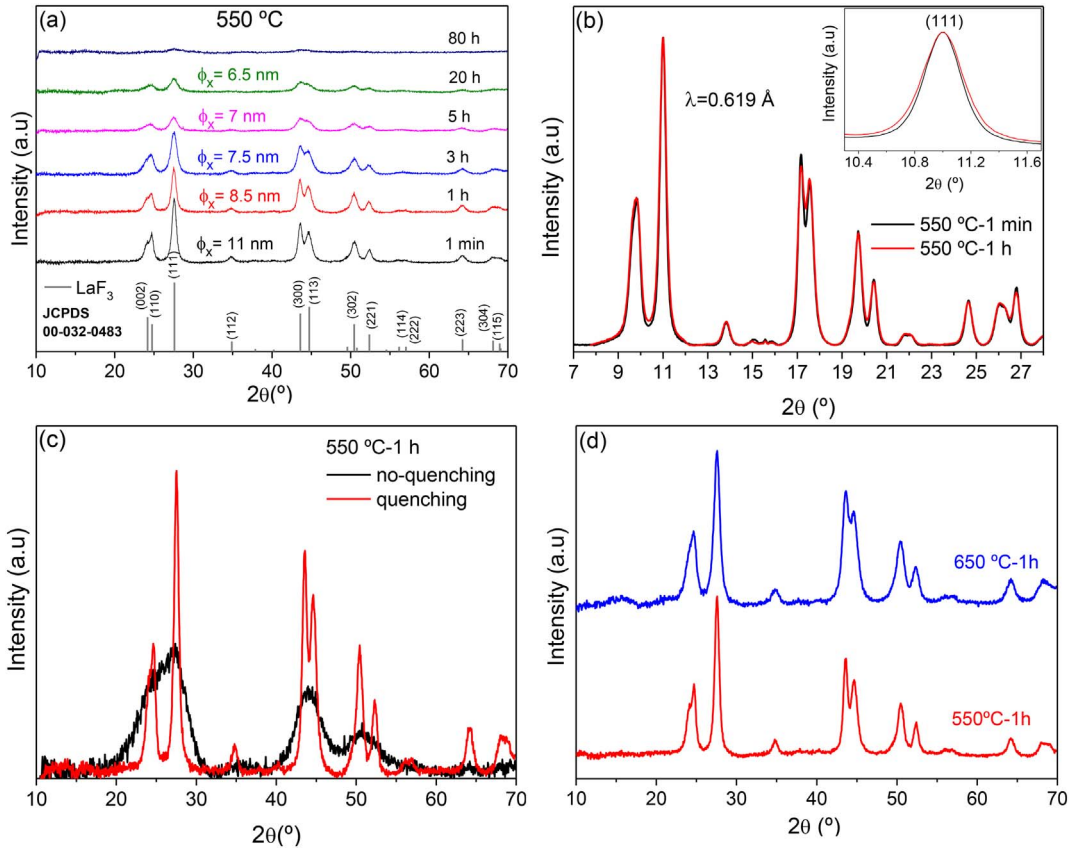


**Fig. 4.** (a) XRD of 80SiO2-20$LaF_3$ sol-gel glass-ceramics treated at 550 °C from 1 min up to 80 h. (b) Comparison of high resolution XRD, performed with synchrotron radiation at Spline of the ESRF, of 80$SiO_2$-20$LaF_3$ glass-ceramics treated at 550 °C during 1 min and 1 h. (c) 80$SiO_2$-20$LaF_3$ glass-ceramics treated at 550 °C during 1 h and followed or not by thermal quenching. (d) 80$SiO_2$-20$LaF_3$ glass-ceramics treated at 550 and 650 °C for 1 h.

the condensation of the silica network at 550 °C is not significantly altered by rising the temperature by 100 °C. The same effect is observed for the main La-F vibration at 350 $cm^{-1}$, meaning that no big differences exist with respect to the crystallization process. Vibration changes in the range 250–175 $cm^{-1}$ may be related to less resolution in the experiment. These results are in agreement with those shown in Fig. 4d where similar diffractograms and crystal size are obtained for these samples.

FTIR spectra of the 80$SiO_2$-20$LaF_3$ xerogel and glass-ceramic sample treated at 550 °C-1 min are shown in Fig. 6a. For the xerogel sample, a more complex spectrum is observed due to incomplete condensation of the glass-matrix and the presence of residual organic compounds. The bands centered at 1680 and 1650 $cm^{-1}$ are associated to C═O carboxyl acid dimer stretching [51,52] and H—O—H bending [53–55] vibrations, respectively. In the range 1500–1400 $cm^{-1}$ the vibrations associated with TFA or derived ions appear [24,48]: the $-COO^-$ groups have three main absorption bands while the C—F stretching band is identified between 1400 and 1000 $cm^{-1}$. For the glass-ceramic sample, the spectrum is simpler and the asymmetric stretching vibration of Si—O—Si is observed around 1060 $cm^{-1}$ together with the symmetric vibration around 800 $cm^{-1}$ [46,47,56]. The sharp band at 1279 $cm^{-1}$ is associated to unremoved organic compounds (C—O) [57,58] which disappears with increasing treatment times.

The structural characterization and the study of fluorine environment were completed by $^{19}F$ Magic angle spinning (MAS) NMR of 80$SiO_2$-20$LaF_3$ xerogel and glass-ceramic samples treated at 550 °C for 1 min, Fig. 6b. The signal is given as a function of the chemical shift of the nucleus whose resonance frequency is affected by the electron screening, thus making possible to identify the local environment of the atom. The $^{19}F$ NMR spectrum of pure $LaF_3$ powder is also shown. For the xerogel, a sharp band appears around −76 ppm associated to $^{19}F$ surrounding the precursor TFA acid [59]. Instead, after 1 min of heat treatment at 550 °C, all the appearing bands at −22, −18 and 26 ppm are associated to $^{19}F$ in $LaF_3$ crystals. In fact, due to the space group symmetry of $LaF_3$ crystals ($P\bar{3}c1$) three different fluorine sites are identified (see black spectrum of pure $LaF_3$ crystals). Only one peak at about −155 ppm is not assigned neither to $^{19}F$ in $LaF_3$ crystals nor to spinning side bands. It could be related to $^{19}F$ in four-coordinated Si-F species [60].

HRTEM of 80$SiO_2$-20$LaF_3$ samples treated at 550 °C during 1 min and 1 h, and at 650 °C for 1 h are given in Fig. 7a, b and c, respectively. Homogeneously dispersed $LaF_3$ crystals are clearly visible for each heat treatment, confirming XRD and FIR results. Fig. 6c also offers a detail of the [111] planes of $LaF_3$ obtained by the Fourier Transform of one of the crystals. The average crystal size was estimated by using several micrographs and measuring the size of around 100 crystals. The corresponding distributions are also compared in Fig. 7d. The average crystal sizes, obtained by Gaussian fitting, are in well agreement with those calculated by the Scherrer's equation given in Fig. 4a. After 1 min of heat treatment many $LaF_3$ crystals are observed with an average size of 10.5 nm.

## 4. Discussion

From DTA results some distinctive features of sol-gel samples can be derived. The $LaF_3$ crystallization peak is much sharper and more intense, appearing at much lower temperature than those obtained for melt-quenching samples. This suggests that the crystallization process in sol-gel is very fast and different from the diffusion-limited process of melt-quenching materials. On the other hand, melt-quenching glass-ceramics are treated at temperatures slightly higher than $T_g$ to promote and facilitate ions diffusion and to limit the crystal size to few tens of

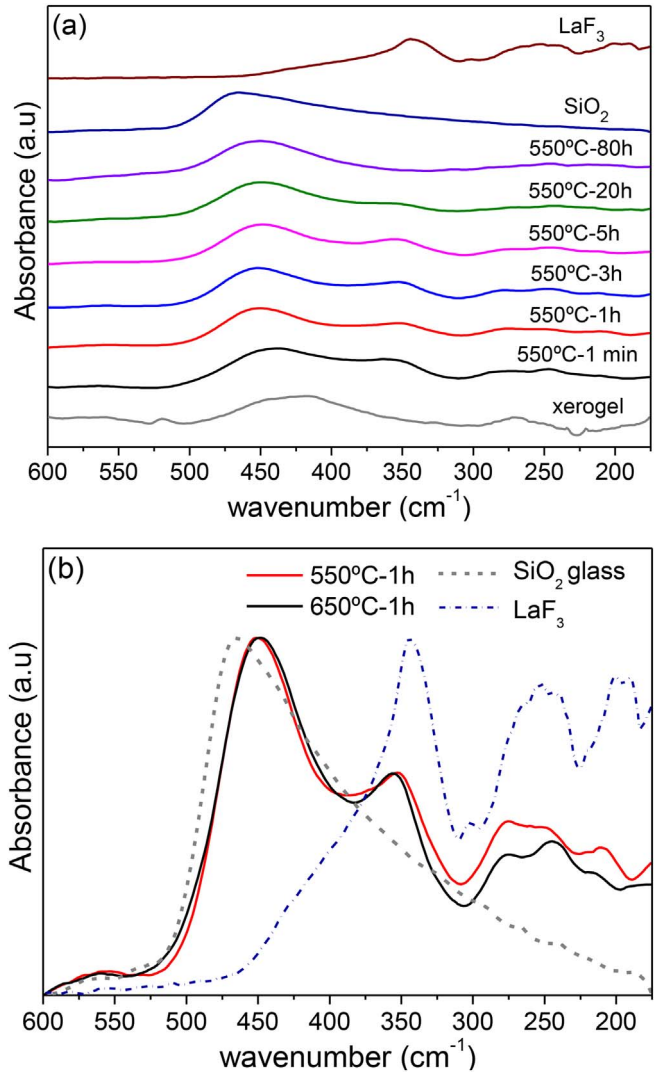


**Fig. 5.** (a) FIR spectra of $80SiO_2$-$20LaF_3$ xerogel and samples treated at 550 °C-from 1 min up to 80 h. Spectra of $SiO_2$ and $LaF_3$ reference materials are also given for comparison and their vibrations are highlighted by a vertical dashed line. (b) FIR spectra of $80SiO_2$-$20LaF_3$ samples treated at 550 and 650 °C during 1 h.

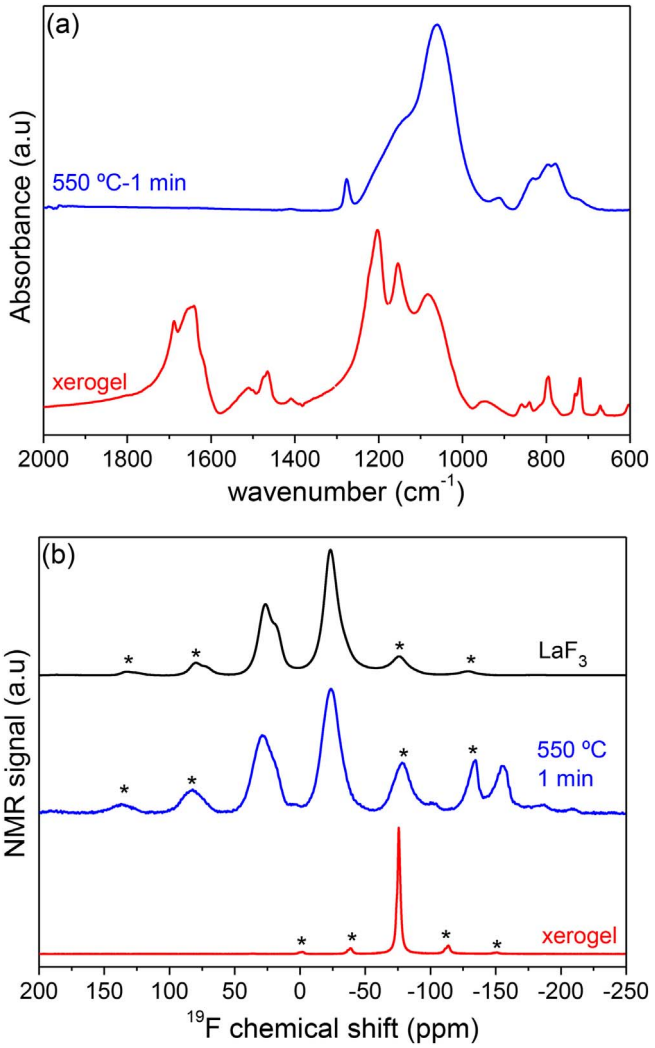


**Fig. 6.** (a) FTIR spectra of the $80SiO_2$-$20LaF_3$ xerogel and glass-ceramic sample treated at 550 °C-1 min. (b) $^{19}F$ MAS-NMR spectra of the $80SiO_2$-$20LaF_3$ xerogel and glass-ceramic sample treated at 550 °C-1 min. The spectrum of pure crystalline $LaF_3$ is also given for comparison. Stars indicate spinning side bands.

nm. According to the definition of glass-ceramics of Höland [61] "*Glass-ceramics are ceramic materials formed through the controlled nucleation and crystallization of glass*". But for sol-gel oxyfluoride materials a different situation appears, since fluoride crystallization is produced at much lower temperatures, far from $T_g$ (~1130 °C) as shown in Fig. 3.

Tohge et al. [62] demonstrated that materials produced by sol-gel are indistinguishable from conventional melted glasses when heated to $T_g$. However, structural features of silica glasses treated at 800 °C, hence far from $T_g$, are already identical to those of melted glasses. Furthermore, the properties of silica gels are also identical to those of melted silica in terms of density, refractive index, hardness, thermal expansion and modulus. So, dense glass with metastable structures can be obtained by sol-gel.

XRD experiments also showed that the crystallization behavior is very different from a nucleation and growing process that usually occurs for melt-quenching oxyfluoride glass-ceramics. In particular, for only 1 min of treatment at 550 °C a perfect crystallization is obtained and no better crystallinity is achieved for longer treatment times, while for diffusion-controlled processes, crystal size and fraction increase with the treatment time [12]. Therefore, in sol-gel materials, the fluoride crystallization is a very fast process that takes place once the crystallization temperature is reached. Longer treatment times produce the loss of crystal structure and/or partial or total dissolution of crystals in the glass matrix. Even increasing the treatment temperature by 100 °C no increase of crystal size and/or crystalline fraction is obtained. On the contrary, for melt-quenching derived oxyfluoride glass-ceramics, an increment of temperature of 20 or 40 °C causes notable effects on both crystal size and crystal fraction [12,21]. This conclusion is further supported by the FIR results of Fig. 5: 1) no relevant changes in the crystallization of fluoride crystals are observed with the increment of treatment temperature by 100 °C, and 2) the increase of the treatment time does not allow increasing the intensity of the bands associated with fluoride crystals but an opposite effect is observed.

HRTEM showed the presence of homogeneously dispersed $LaF_3$ crystals after a short heat treatment of 1 min at 550 °C, thus confirming that 1 min of heat treatment is enough to produce the perfect precipitation and crystallization of nano-fluoride crystals in the $SiO_2$ matrix. Such time (1 min) is much shorter than typical times required for diffusion processes in melt-quenching glasses that generally need from few hours (1 − 3 h) up to several days (72–120 h) to grow the crystals. It is known that a real diffusion process is controlled by the root square of time and the crystal growth, for non-isochemical compositions, generally shows an asymptotic behavior due to the formation of a viscous barrier enriched in glass formers that surround the crystals and prevents further crystal growth. In sol-gel materials, such behavior is not

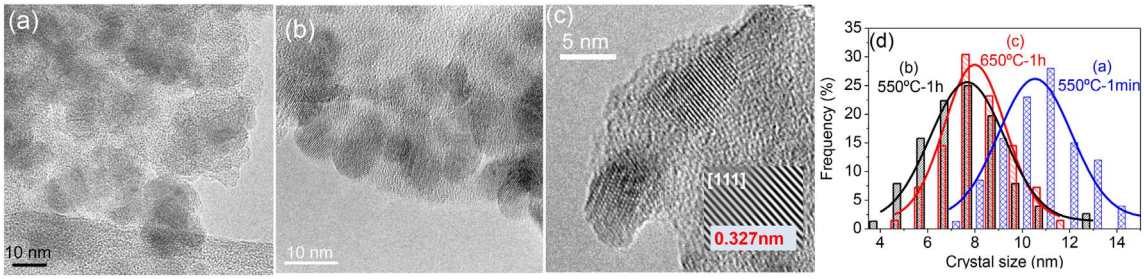


**Fig. 7.** HRTEM of $80SiO_2$-$20LaF_3$ samples treated at 550 °C for (a) 1 min, (b) 1 h and at (c) 650 °C for 1 h. (d) Crystal size distribution for samples shown in (a), (b) and (c).

observed.

Finally, $^{19}F$ NMR showed that no $^{19}F$ bonds of $LaF_3$ are present in the xerogel, the ions being bonded as in the precursor acid. On the other hand, a very fast heat treatment allows precipitating the $LaF_3$ nanocrystals, and almost all $^{19}F$ bonds of the glass-ceramic samples correspond to the $LaF_3$ phase.

Although the DTA analysis following Eqs. (1)–(3) indicates that crystallization is a diffusion-limited process with $n = m = 1$, similar to that appearing in melted oxyfluoride glass-ceramics, these calculations are demonstrated to be wrong. We think that this approach should only be used in the case that $T_x$ and $T_p$ are above $T_g$. Our proposal is that the crystallization mechanism of $LaF_3$ (and other fluorides) in oxyfluoride sol-gel materials consists on a chemical reaction followed by a fast crystals precipitation, the obtained crystals being unstable.

To further explain this behavior a thermodynamic analysis is necessary. Sol-gel glass-ceramics are obtained after the treatment of xerogels that consist of a continuous solid network surrounding a continuous liquid phase; condensation and shrinkage reducing the free energy of the system. It is well known that conventional glass systems may reside in a metastable equilibrium with a free energy higher than the equilibrium state. On the other side, gels have higher free energy than a melted glass of the same nominal composition. But xerogels are unstable, not metastable, because there is no energy barrier to prevent the gel from relaxing toward the glassy state. Aging generates structural changes leading to denser amorphous or crystalline state whenever mobility is increased by increasing the treatment temperature.

Structural techniques (NMR, FTIR, Raman) demonstrate that local bonding in gels is quite similar to that of melted glasses below $T_g$ [63]. The absence of energy barrier may explain that crystallization occurs as a precipitation process at quite low temperature and very short times not following the diffusion-limited crystallization processes of conventional melted glasses.

In addition, all the results show that the $SiO_2$ network evolves along with the fluoride crystallization, and the two systems, from a thermodynamic point of view, develop independently. As observed from DTA, $LaF_3$ crystallization occurs around 300 °C. Further heating or aging at crystallization or higher temperatures will lead to the decomposition of the crystals and their further dissolution in the matrix. Such dissolution process is favored due to the compositional gradient between matrix and crystals that will drive the material to reach the equilibrium of chemical potentials.

It remains as an open question the study of the fluorine content evolution from the sol, containing an excess of TFA, to the gel and the final glass-ceramic material. This point is under investigation by using XRD and $^{19}F$ NMR.

## 5. Conclusions

The crystallization mechanism of sol-gel oxyfluoride glass-ceramics, studied by non-isothermal DTA showed that $LaF_3$ crystallization is a diffusion-controlled process similar to that occurring for melt-quenching samples. However, from DTA curves narrow crystallization peaks are observed at temperatures (~300 °C) much lower than $SiO_2$ $T_g$ (~1130 °C), demonstrating a quite different crystallization process in sol-gel materials.

Sol-gel oxyfluoride glass-ceramics, studied by XRD, FTIR, FIR, HRTEM and $^{19}F$ NMR, behave differently from melt-quenching glass-ceramic materials. Neither increase of the crystallinity nor of crystal size were observed when increasing the treatment time. On the contrary, the best crystallization was obtained for very fast treatments (1 min) at temperatures much lower than $T_g$, thus confirming that crystallization process is very fast and only needs to reach the suitable energy.

Therefore, it is proposed that the crystallization process of $LaF_3$ in sol-gel materials is not a diffusion-controlled nucleation and growing process, but a chemical reaction followed by the fast precipitation of crystals. Given that such crystals are unstable, the aging at crystallization or higher temperatures will cause their dissolution trying to reach the equilibrium of chemical potentials.

Although non-isothermal DTA analysis indicates that crystallization is a diffusion-limited process, with $n = m = 1$, these calculations are demonstrated to be wrong. We think that this approach should only be used in the case that $T_x$ and $T_p$ are above $T_g$.

## Acknowledgements

This work was supported by MINECO under Project No.MAT2013-48246-C2-1-P and MAT2017-87035-C2-1-P/-2-P (AEI/FEDER, UE). J.J. Velázquez also acknowledges MINECO under Grant FPDI-2013-16895. The Spanish Beamline (SpLine) of the ESRF facilities in Grenoble is also acknowledged for the experiments MA-3350 and 25-01-1014. The authors thank Dr. Aitana Tamayo (ICV-CSIC) for her support with FIR measurements, and Dr. Francisco Muñoz (ICV-CSIC) for the fruitful discussion on NMR results.

## References

[1] Y. Wang, J. Ohwaki, New transparent vitroceramics codoped with $Er^{3+}$ and $Yb^{3+}$ for efficient frequency upconversion, Appl. Phys. Lett. 63 (1993) 3268–3270, http://dx.doi.org/10.1063/1.110170.
[2] F. Gan, L. Xu, Photonic Glasses, World Scientific Publishing, 2006, p. 28.
[3] A. de Pablos-Martín, A. Durán, M.J. Pascual, Nanocrystallisation in oxyfluoride systems: mechanisms of crystallisation and photonic properties, Int. Mater. Rev. 57 (2012) 165–186, http://dx.doi.org/10.1179/1743280411Y.0000000004.
[4] M. Ferrari, M.J. Pascual, G.C. Righini, Glass-ceramics: a class of nanostructured materials for, Photo-Dermatology 38 (2015) 311–369, http://dx.doi.org/10.1393/ncr/i2015-10114-0.
[5] P.P. Fedorov, A.A. Luginina, A.I. Popov, Transparent oxyfluoride glass ceramics, J. Fluor. Chem. 172 (2015) 22–50, http://dx.doi.org/10.1016/j.jfluchem.2015.01.009.
[6] Z. Hu, Y. Wang, F. Bao, W. Luo, Crystallization behavior and microstructure investigations on $LaF_3$ containing oxyfluoride glass ceramics, J. Non-Cryst. Solids 351 (2005) 722–728, http://dx.doi.org/10.1016/j.jnoncrysol.2005.01.075.
[7] D. Chen, Y. Wang, Y. Yu, Z. Hu, Crystallization and fluorescence properties of $Nd^{3+}$-doped transparent oxyfluoride glass ceramics, Mater. Sci. Eng. B 123 (2005) 1–6, http://dx.doi.org/10.1016/j.mseb.2005.06.008.
[8] Y. Yu, D. Chen, Y. Cheng, Y. Wang, Z. Hu, F. Bao, Investigation on crystallization and influence of $Nd^{3+}$ doping of transparent oxyfluoride glass-ceramics, J. Eur. Ceram. Soc. 26 (2006) 2761–2767, http://dx.doi.org/10.1016/j.jeurceramsoc.2005.05.002.
[9] D. Chen, Y. Wang, Y. Yu, E. Ma, Influence of $Yb^{3+}$ content on microstructure and fluorescence of oxyfluoride glass ceramics containing $LaF_3$ nano-crystals, Mater. Chem. Phys. 101 (2007) 464–469, http://dx.doi.org/10.1016/j.matchemphys.

2006.08.005.
[10] F. Liu, Y. Wang, D. Chen, Y. Yu, Investigation on crystallization kinetics and microstructure of novel transparent glass ceramics containing Nd:$NaYF_4$ nano-crystals, Mater. Sci. Eng. B 136 (2007) 106–110, http://dx.doi.org/10.1016/j.mseb.2006.09.012.
[11] A. de Pablos-Martín, F. Muñoz, G.C. Mather, C. Patzig, S. Bhattacharyya, J.R. Jinschek, T. Höche, A. Durán, M.J. Pascual, $KLaF_4$ nanocrystallisation in oxyfluoride glass-ceramics, CrystEngComm 15 (2013) 10323–10332, http://dx.doi.org/10.1039/c3ce41345d.
[12] A. de Pablos-Martín, N. Hémono, G.C. Mather, S. Bhattacharyya, T. Höche, H. Bornhöft, J. Deubener, F. Muñoz, A. Durán, M.J. Pascual, Crystallization kinetics of $LaF_3$ nanocrystals in an oxyfluoride glass, J. Am. Ceram. Soc. 94 (2011) 2420–2428, http://dx.doi.org/10.1111/j.1551-2916.2011.04547.x.
[13] A. de Pablos-Martín, D. Ristic, S. Bhattacharyya, T. Höche, G.C. Mather, M.O. Ramírez, S. Soria, M. Ferrari, G.C. Righini, L.E. Bausá, A. Durán, M.J. Pascual, Effects of $Tm^{3+}$ additions on the crystallization of $LaF_3$ nanocrystals in oxyfluoride glasses: optical characterization and up-conversion, J. Am. Ceram. Soc. 96 (2013) 447–457, http://dx.doi.org/10.1111/jace.12120.
[14] C. Rüssel, Nanocrystallization of $CaF_2$ from $Na_2O/K_2O/CaO/CaF_2/Al_2O_3/SiO_2$ glasses, Chem. Mater. 17 (2005) 5843–5847.
[15] N. Hémono, G. Pierre, F. Muñoz, A. de Pablos-Martín, M.J. Pascual, A. Durán, Processing of transparent glass-ceramics by nanocrystallisation of $LaF_3$, J. Eur. Ceram. Soc. 29 (2009) 2915–2920, http://dx.doi.org/10.1016/j.jeurceramsoc.2009.05.013.
[16] S. Bhattacharyya, T. Höche, N. Hémono, M.J. Pascual, P.A. van Aken, Nano-crystallization in $LaF_3$–$Na_2O$–$Al_2O_3$–$SiO_2$ glass, J. Cryst. Growth 311 (2009) 4350–4355, http://dx.doi.org/10.1016/j.jcrysgro.2009.07.027.
[17] C. Bocker, C. Rüssel, Self-organized nano-crystallisation of $BaF_2$ from $Na_2O/K_2O/BaF_2/Al_2O_3/SiO_2$ glasses, J. Eur. Ceram. Soc. 29 (2009) 1221–1225, http://dx.doi.org/10.1016/j.jeurceramsoc.2008.08.005.
[18] C. Bocker, C. Christian, I. Avramov, Transparent nano crystalline glass-ceramics by interface controlled crystallization, Int. J. Appl. Glas. Sci. 181 (2013) 174–181, http://dx.doi.org/10.1111/ijag.12033.
[19] M. Mortier, G. Patriarche, Structural characterisation of transparent oxyfluoride glass-ceramics, J. Mater. Sci. 35 (2000) 4849–4856, http://dx.doi.org/10.1023/A:1017512232431.
[20] A. de Pablos-Martín, G.C. Mather, F. Muñoz, S. Bhattacharyya, T. Höche, J.R. Jinschek, T. Heil, A. Durán, M.J. Pascual, Design of oxy-fluoride glass-ceramics containing $NaLaF_4$ nano-crystals, J. Non-Cryst. Solids 356 (2010) 3071–3079, http://dx.doi.org/10.1016/j.jnoncrysol.2010.04.057.
[21] G. Gorni, A. Cosci, S. Pelli, L. Pascual, A. Durán, M.J. Pascual, Transparent oxyfluoride nano-glass ceramics doped with $Pr^{3+}$ and $Pr^{3+}$–$Yb^{3+}$ for NIR emission, Front. Mater. 3 (2017) 58, http://dx.doi.org/10.3389/fmats.2016.00058.
[22] G. Gorni, J.J. Velázquez, G.C. Mather, A. Durán, G. Chen, M. Sundararajan, R. Balda, J. Fernández, M.J. Pascual, Selective excitation in transparent oxyfluoride glass-ceramics doped with $Nd^{3+}$, J. Eur. Ceram. Soc. 37 (2017) 1695–1706, http://dx.doi.org/10.1016/j.jeurceramsoc.2016.11.014.
[23] G. Gorni, R. Balda, J. Fernández, L. Pascual, A. Durán, M.J. Pascual, Effect of the heat treatment on the spectroscopic properties of $Er^{3+}$-$Yb^{3+}$-doped transparent oxyfluoride nano-glass-ceramics, J. Lumin. 193 (2018) 51–60, http://dx.doi.org/10.1016/j.jlumin.2017.05.063.
[24] S. Fujihara, C. Mochizuki, T. Kimura, Formation of $LaF_3$ microcrystals in sol-gel-silica, J. Non-Cryst. Solids 244 (1999) 267–274, http://dx.doi.org/10.1016/S0022-3093(99)00009-5.
[25] S. Fujihara, M. Tada, T. Kimura, Sol-gel processing of $LaF_3$ thin films, J. Ceram. Soc. Jpn. 106 (1998) 124–126, http://dx.doi.org/10.2109/jcersj.106.124.
[26] C.E. Secu, R.F. Negrea, M. Secu, $Eu^{3+}$ probe ion for rare-earth dopant site structure in sol–gel derived $LiYF_4$ oxyfluoride glass–ceramic, Opt. Mater. 35 (2013) 2456–2460, http://dx.doi.org/10.1016/j.optmat.2013.06.053.
[27] R.M. Almeida, M.C. Gonçalves, Crystallization of solgel-derived glasses, Int. J. Appl. Glas. Sci. 5 (2014) 114–125, http://dx.doi.org/10.1111/ijag.12075.
[28] G. Gorni, R. Balda, J. Fernández, J.J. Velázquez, L. Pascual, J. Mosa, A. Durán, Y. Castro, $80SiO_2$-$20LaF_3$ oxyfluoride glass ceramic coatings doped with $Nd^{3+}$ for optical applications, Int. J. Appl. Glas. Sci. 00 (2017) 1–10, http://dx.doi.org/10.1111/ijag.12338.
[29] T. Ozawa, Kinetics of non-isothermal crystallization, Polymer 12 (1971) 150–158, http://dx.doi.org/10.1016/0032-3861(71)90041-3.
[30] K. Matusita, T. Komatsu, R. Yokota, Kinetics of non-isothermal crystallization process and activation energy for crystal growth in amorphous materials, J. Mater. Sci. 19 (1984) 291–296, http://dx.doi.org/10.1007/BF02403137.
[31] H.E. Kissinger, Variation of peak temperature with heating rate in differential thermal analysis, J. Res. Natl. Bur. Stand. 57 (1956) 217–221, http://dx.doi.org/10.6028/jres.057.026.
[32] H.E. Kissinger, Reaction kinetics in differential thermal analysis, Anal. Chem. 29 (1957) 1702–1706, http://dx.doi.org/10.1021/ac60131a045.
[33] M. De Graef, M.E. McHenry, Structure of Materials: An Introduction to Crystallography, Diffraction and Symmetry, Cambridge University Press, 2012, pp. 532–534.
[34] W. Luo, Y. Wang, F. Bao, L. Zhou, X. Wang, Crystallization behavior of $PbF_2$–$SiO_2$ based bulk xerogels, J. Non-Cryst. Solids 347 (2004) 31–38, http://dx.doi.org/10.1016/j.jnoncrysol.2004.09.020.
[35] W. Luo, Y. Wang, Y. Cheng, F. Bao, L. Zhou, Crystallization and structural evolution of $YF_3$–$SiO_2$ xerogel, Mater. Sci. Eng. B 127 (2006) 218–223, http://dx.doi.org/10.1016/j.mseb.2005.10.034.
[36] C.E. Secu, C. Bartha, S. Polosan, M. Secu, Thermally activated conversion of a silicate gel to an oxyfluoride glass ceramic: optical study using $Eu^{3+}$ probe ion, J. Lumin. 146 (2014) 539–543, http://dx.doi.org/10.1016/j.jlumin.2013.10.013.
[37] B. Szpikowska-Srokaa, N. Pawlika, T. Goryczka, E. Pietrasik, M. Bańczyk, W.A. Pisarski, Lead fluoride β-$PbF_2$ nanocrystals containing $Eu^{3+}$ and $Tb^{3+}$ ions embedded in sol-gel materials: thermal, structural and optical investigations, Ceram. Int. 43 (2017) 8424–8432, http://dx.doi.org/10.1016/j.ceramint.2017.03.192.
[38] M.J. Dejneka, The luminescence and structure of novel transparent oxyfluoride glass-ceramics, J. Non-Cryst. Solids 239 (1998) 149–155, http://dx.doi.org/10.1016/S0022-3093(98)00731-5.
[39] D. Chen, Y. Yu, P. Huang, Y. Wang, Nanocrystallization of lanthanide trifluoride in an aluminosilicate glass matrix: dimorphism and rare earth partition, CrystEngComm 11 (2009) 1686–1690, http://dx.doi.org/10.1039/b904169a.
[40] M. Środa, K. Szlósarczyk, M. Rózanski, M. Sitarz, P. Jelen, Spectroscopic properties of transparent Er-doped oxyfluoride glass–ceramics with $GdF_3$, Spectrochim. Acta A 134 (2015) 631–637, http://dx.doi.org/10.1016/j.saa.2014.06.066.
[41] H. Eloussifi, J. Farjas, Pere Roura, J. Camps, M. Dammak, S. Ricart, T. Puig, X. Obradors, Evolution of yttrium trifluoroacetate during thermal decomposition, J. Therm. Anal. Calorim. 108 (2012) 589–596, http://dx.doi.org/10.1007/s10973-011-1899-5.
[42] I.W. Donald, Crystallization kinetics of a lithium zinc silicate glass studied by DTA and DSC, J. Non-Cryst. Solids 345&346 (2004) 120–126, http://dx.doi.org/10.1016/j.jnoncrysol.2004.08.007.
[43] E. Liarokapis, E. Anastassakis, G.A. Kourouklis, Raman study of phonon anharmonicity in $LaF_3$, Phys. Rev. B 32 (1985) 8346–8355, http://dx.doi.org/10.1103/PhysRevB.32.8346.
[44] M. Sitarz, W. Mozgawa, M. Handke, Vibrational spectra of complex ring silicate anions - method of recognition, J. Mol. Struct. 404 (1997) 193–197, http://dx.doi.org/10.1016/S0022-2860(96)09381-7.
[45] M. Handke, M. Sitarz, W. Mozgawa, Model of silicooxygen ring vibrations, J. Mol. Struct. 450 (1998) 229–238, http://dx.doi.org/10.1016/S0022-2860(98)00433-5.
[46] M. Lubas, M. Sitarz, Z. Fojud, S. Jurga, Structure of multicomponent $SiO_2$–$Al_2O_3$–$Fe_2O_3$–CaO–MgO glasses for the preparation of fibrous insulating materials, J. Mol. Struct. 744–747 (2005) 615–619, http://dx.doi.org/10.1016/j.molstruc.2004.12.011.
[47] R. Al-Oweini, H. El-Rassy, Synthesis and characterization by FTIR spectroscopy of silica aerogels prepared using several Si(OR)4 and R″Si(OR′)$_3$ precursors, J. Mol. Struct. 919 (2009) 140–145, http://dx.doi.org/10.1016/j.molstruc.2008.08.025.
[48] R.L. Redington, K.C. Len, Infrared spectra of trifluoroacetic acid and trifluoroacetic anhydride, Spectrochim. Acta A 27 (1971) 2445–2460, http://dx.doi.org/10.1016/0584-8539(71)80143-5.
[49] C. Kinowski, M. Bouazaoui, R. Bechara, L.L. Hench, J.M. Nedelec, S. Turrell, Kinetics of densification of porous silica gels: a structural and textural study, J. Non-Cryst. Solids 291 (2001) 143–152, http://dx.doi.org/10.1016/S0022-3093(01)00863-8.
[50] N. Rangelova, L. Radev, S. Nenkova, I.M. Miranda Salvado, M.H. Vas Fernandes, M. Herzog, Methylcellulose/$SiO_2$ hybrids: sol-gel preparation and characterization by XRD, FTIR and AFM, Cen, Eur. J. Chem. 9 (2011) 112–118, http://dx.doi.org/10.2478/s11532-010-0123-y.
[51] D. Lin-Vien, N.B. Colthup, W.G. Fateley, J.G. Grasselli, The Handbook of Infrared and Raman Characteristic Frequencies of Organic Molecules, Academic Press, London, 1991, pp. 137–140.
[52] C. Moreno-Castilla, M.V. Lo'pez-Ramo'n, F. Carrasco-Mar'ın, Changes in surface chemistry of activated carbons by wet oxidation, Carbon 38 (2000) (1995–2001), http://dx.doi.org/10.1016/S0008-6223(00)00048-8.
[53] M. Falk, The frequency of the H-O-H bending fundamental in solids and liquids, Spectrochim. Acta A 40 (1984) 43–48, http://dx.doi.org/10.1016/0584-8539(84)80027-6.
[54] R. Buzzoni, S. Bordiga, G. Ricchiardi, G. Spoto, A. Zecchina, Interaction of $H_2O$, $CH_3OH$, $(CH_3)_2O$, $CH_3CN$, and pyridine with the superacid perfluorosulfonic membrane Nafion: an IR and Raman study, J. Phys. Chem. 99 (1995) 11937–11951, http://dx.doi.org/10.1021/j100031a023.
[55] L. Kovács, K. Lengyel, Á. Péter, K. Polgár, A. Beran, IR absorption spectroscopy of water in $CsLiB_6O_{10}$ crystals, Opt. Mater. 24 (2003) 457–463, http://dx.doi.org/10.1016/S0925-3467(03)00028-4.
[56] M. Sitarz, The structure of simple silicate glasses in the light of Middle Infrared spectroscopy studies, J. Nol-Cryst. Solids 357 (2011) 1603–1608, http://dx.doi.org/10.1016/j.jnoncrysol.2011.01.007.
[57] R. Takahashi, T. Noguchi, Criteria for determining the hydrogen-bond structures of a tyrosine side chain by Fourier transform infrared spectroscopy: density functional theory analyses of model hydrogen-bonded complexes of p-cresol, J. Phys. Chem. B 111 (2007) 13833–13844, http://dx.doi.org/10.1021/jp0760556.
[58] B. Yan, B. Zhang, Analytical Methods in Combinatorial Chemistry, 2nd ed., CRC Press, Boca Raton, 2011, pp. 63–64.
[59] P. Shi, H. Wang, Z. Xi, C. Shi, Y. Xiong, C. Tian, Site-specific $^{19}F$ NMR chemical shift and side chain relaxation analysis of a membrane protein labeled with an unnatural amino acid, Protein Sci. 20 (2011) 224–228, http://dx.doi.org/10.1002/pro.545.
[60] Y. Liu, H. Nekvasil, Si-F bonding in aluminosilicate glasses: inferences from ab initio NMR calculations, Am. Mineral. 87 (2012) 339–346, http://dx.doi.org/10.2138/am-2002-2-17.
[61] W. Höland, G. Beall, Glass-ceramic Technology, 2nd ed., Wiley, Hoboken, 2012, pp. XV–XVII.
[62] N. Tohge, G.S. Moore, J.D. Mackenzie, Structural development during gel to glass transition, J. Non-Cryst. Solids 63 (1984) 95–103, http://dx.doi.org/10.1016/0022-3093(84)90389-2.
[63] C.J. Brinker, G.W. Scherrer, Sol-Gel Science. The Physics and Chemstry of Sol-Gel Processing, Academic Press, 1990, pp. 746–777.

## *PAPER 9*

**$80SiO_2$-$20LaF_3$ oxyfluoride glass ceramic coatings doped with $Nd^{3+}$ for optical applications.**

G. Gorni, R. Balda, J. Fernández, J.J. Velázquez, L. Pascual, J. Mosa, A. Durán, Y. Castro

*Int. J. Appl. Glass Sci*. **9** (2018) 208-217. doi:10.1111/ijag.12338

Received: 27 July 2017 | Accepted: 12 December 2017

DOI: 10.1111/ijag.12338

INTERNATIONAL JOURNAL OF
Applied Glass
SCIENCE

ORIGINAL ARTICLE

# $80SiO_2$-$20LaF_3$ oxyfluoride glass ceramic coatings doped with $Nd^{3+}$ for optical applications

**Giulio Gorni**[1] | **Rolindes Balda**[2,3] | **Joaquín Fernández**[2,3] | **Jose J. Velázquez**[1] | **Laura Pascual**[4] | **Jadra Mosa**[1] | **Alicia Durán**[1] | **Yolanda Castro**[1]

[1]Instituto de Cerámica y Vidrio (CSIC), Madrid, Spain

[2]Departamento de Física Aplicada I, Escuela Superior de Ingeniería, Universidad del País Vasco UPV-EHU, Bilbao, Spain

[3]Centro de Física de Materiales, UPV/EHU-CSIC, San Sebastian, Spain

[4]Insituto de Catalisis y PetroleoquÍmica (CSIC), Madrid, Spain

**Correspondence**
Giulio Gorni
Email: ggorni@icv.csic.es

**Funding information**
Ministerio de Economía y Competitividad, Grant/Award Number: FPDI-2013-16895; Consejo Superior de Investigaciones Científicas; Basque Country University, Grant/Award Number: PPG17/07

**Abstract**

Transparent glass ceramic (GC) films and self-supported layers of composition $80SiO_2$-$20LaF_3$ doped with $Nd^{3+}$ were prepared by sol-gel method for the first time. GC films were deposited by dip coating on different substrates and heat-treated between 350°C and 850°C for 1, 3, and 80 hours. The structural analysis of thin films was performed by GI-XRD and HR-TEM to check the $LaF_3$ nanocrystals precipitation in the $SiO_2$ matrix, revealing a crystal size lower than 5 nm. The emission and excitation spectra and lifetimes of the films have been obtained for different thermal treatments and $Nd^{3+}$ contents. The luminescence intensity of the $^4F_{3/2} \rightarrow {}^4I_{11/2}$ laser transition increases with the treatment temperature and $Nd^{3+}$ content, whereas a reduction for the luminescence lifetime is observed compared to those observed in bulk samples prepared by melting quenching.

**KEYWORDS**

coatings, glass ceramics, glass manufacturing, optical properties, oxyfluoride, photoluminesence, sol-gel

## 1 | INTRODUCTION

Rare-earth (RE)-doped materials have gained great interest in the last decade for their use in solid-state lasers, sensing, solar cells, etc.[1-7] Silicate glasses were commonly used for these applications due to their good mechanical and chemical properties compared to borate, phosphate, or chalcogenide glasses. However, oxide glasses, especially silicates, have quite high phonon energy (1200 $cm^{-1}$) that causes nonradiative relaxation with subsequent low optical efficiency.[8] Thereby, oxyfluoride GCs have been considered as promising host materials due to their high transparency, low phonon energy of fluoride crystals, and the possibility to effectively host RE ions inside the crystals.[9] Moreover, they present high chemical and mechanical stability typical of oxide glasses, in particular silicates and aluminasilicates.

Many oxyfluoride GCs have been prepared by the melting quenching (MQ) method[10,11] using several RE ions, as $Eu^{3+}$,[12] $Nd^{3+}$ for its use as laser material at 1.06 μm,[13-15] $Pr^{3+}$-$Yb^{3+}$ as down-converter materials,[16-18] and $Er^{3+}$-$Yb^{3+}$ for up-conversion.[19,20] But MQ method presents some limitations such as the high temperature of processing that causes fluorine loss by evaporation. Moreover, phase separation is commonly produced during the quenching, thus limiting the possibility to obtain homogenous materials with high optical quality. Therefore, many efforts were concentrated to prepare oxyfluoride materials by sol-gel method.[21-31] This process allows obtaining purer materials, and compositions impossible or extremely difficult to

obtain by MQ method using much lower temperatures. Furthermore, it is a very flexible and rather cheap method.

In the last years, different authors have reported the development of $SiO_2$-$LaF_3$/LaOF oxyfluoride glass ceramics by sol-gel, highlighting the works of Fujihara et al[21-23] and Ribeiro et al[24] Fujihara et al described the preparation of $90SiO_2$-$10LaF_3$/LaOF thin films doped with $Eu^{3+}$ and reported that the luminescence associated to $Eu^{3+}$ ions increased when the RE ions are introduced in a oxyfluoride GCs matrix compared to silica glass matrix. Anyway, at high temperature (600-900°C) LaOF crystals instead of $LaF_3$ are identified. On the other hand, Ribeiro et al prepared films with the same composition finding that for heat treatment between 600-900°C both $LaF_3$ and LaOF phases appeared. They used these films as planar waveguides at Vis (500-600 nm) and IR (1.44-1.46 μm) wavelengths obtaining losses of 1.8 dB/cm at 632.8 nm.

Different authors have reported the doping of GC materials with RE ions and demonstrated that these ions are preferably incorporated into the crystalline phase and not into the silica matrix, confirming that the sol-gel process is suitable for the synthesis of oxyfluoride GC materials with photonic applications. Biswas et al[25] prepared $95SiO_2$-$5LaF_3$ xerogels doped with $Er^{3+}$-$Yb^{3+}$ for up-conversion. Upon $Yb^{3+}$ excitation at 980 nm, $Er^{3+}$ emission from the $^4F_J$ levels (at 450 and 490 nm) was observed, suggesting that $Er^{3+}$ ions are present in a local environment of very low phonon energy. An $Er^{3+}$ emission $^4I_{13/2}$-$^4I_{15/2}$ quite broad compared to the emission of $Er^{3+}$ in the $LaF_3$ crystals was observed. The emission had two contributions: one produced by $Er^{3+}$ ions inside the $LaF_3$ crystals and the other associated with the ions near of crystals surface that feel the high phonons of the silica matrix. Velázquez et al[30,31] have also prepared $95SiO_2$-$5LaF_3$ xerogels doped with $Tb^{3+}$ and codoped with $Dy^{3+}$ to enhance the UV absorption band and shift this energy to the visible range. The precipitation of $LaF_3$ crystals inside the $SiO_2$ matrix was observed and the lifetimes reported show that around 75% of the RE ions are in the $LaF_3$ crystals. The same materials doped with $Pr^{3+}$-$Yb^{3+}$ ions for Vis UC upon $Yb^{3+}$ excitation at 980 nm were also studied.

Finally, a review of sol-gel monoliths with more than 200 references focused on the preparation of silica and silica-based materials, especially $SiO_2$-$LnF_3$ GCs, was reported by Kajihara.[32] However, in all of these works, typical $LaF_3$ concentration was between 5 and 10 mol%; furthermore, the same synthesis procedure was used without modifying the processing parameters. On the other hand, structural characterization of thin films together with optical properties have been poorly evaluated.

The aim of this work was the preparation of $80SiO_2$-$20LaF_3$ transparent GC films doped with $Nd^{3+}$ using the sol-gel method. The structural characterization was performed by GI-XRD and HR-TEM, whereas the optical properties were investigated using steady-state emission and excitation spectra and lifetimes. This work demonstrates the possibility to prepare completely transparent films with higher $LaF_3$ amount (20 mol%) compared to the materials reported up to now, and opens the door to new compositions with even higher $LaF_3$ content (30-40 mol%) and with promising optical properties of coating and self-supported sol-gel materials.

## 2 | EXPERIMENTAL

### 2.1 | Preparation of $80SiO_2$-$20LaF_3$ sols, coatings, and self-supported layers

The $80SiO_2$-$20LaF_3$ sol was prepared in alcoholic media using tetraethylorthosilicate (TEOS, ABCR, 98%) as precursor of silica, lanthanide acetate ($La(CH_3COO\text{-}nH_2O)_3$, Sigma-Aldrich, St. Louis, MO, 99.9%) and trifluoroacetic acid (TFA, Sigma-Aldrich, 99%) as lanthanide and fluorine sources, respectively. The synthesis of the sol was performed in two steps. First, SOL-1 was obtained mixing TEOS, absolute ethanol (EtOH) and $H_2O$ (0.1M HCl) in a molar ratio $1TEOS:9.5EtOH:2H_2O$ and maintained under stirring for 2 hours at room temperature. Water was added drop by drop, to start the hydrolysis process. Then, SOL-2 was prepared from lanthanum acetate (La(ac)), trifluoracetic acid (TFA), absolute ethanol, and distilled water. The molar ratio was fixed to $1La(ac):5TFA:5EtOH:4H_2O$. SOL-2 was stirred for 2 hours at 40°C to obtain a homogenous solution. Finally, SOL-1 and SOL-2 were mixed and maintained at room temperature before using.

Doped $80SiO_2$-$20LaF_3$ sols with 2 ad 3 mol% of $Nd^{3+}$ were also prepared by adding the corresponding molar ratio of neodymium acetate (Nd(ac)) ($Nd(CH_3CO_2)_3{\cdot}xH_2O$, Sigma-Aldrich, 99.9%) to SOL-2 and then, mixing with the SOL-1.

$SiO_2$ films doped with $3Nd^{3+}$ were also prepared using the same $TEOS:H_2O:EtOH$ ratio as for the $80SiO_2$-$20LaF_3$ composition but substituting Nd(ac) with $Nd(NO_3)_3$ (Sigma-Aldrich 99.9%) because the latter can be easily dissolved in $H_2O$ and EtOH without using TFA.

Doped and undoped $80SiO_2$-$20LaF_3$ films were deposited on silicon wafers and silica substrates by dip-coating method using a withdrawal rate of 30 cm/min. Films were sintered between 350 and 850°C during 1, 3, or 80 hours using a heating rate of 10°C/min. Two-layers films were also prepared on silica substrates using an intermediate heat treatment at 200°C for 20 minutes and a final heat treatment at 750°C for 3 and 80 hours. $SiO_2$-3Nd coatings were also prepared using the same withdrawal rate and varying the heat treatment between 350 and 850°C during 3 hours.

A similar synthesis with a different $H_2O$/EtOH ratio was used to prepared self-supported layers with composition $80SiO_2$-$20LaF_3$ doped with 0.5 and $3Nd^{3+}$ (mol%). A wet-gel was obtained by leaving the solution in a sealed container at 50°C for 2 days and then dried for 15 days at 50°C. Finally, the self-supported layers were heat-treated in air at 650°C for 3 hours with a rate of 1°C/min to obtain the precipitation of $LaF_3$ nanocrystals and giving rise to crack-free transparent GCs.

## 2.2 | Characterization of coatings and self-supported layers

Ellipsometry measurements were performed using a spectral Ellipsometer (M-2000UTM, J.A. Co., Woollam) to characterize the films deposited onto silica substrates. The spectra were taken between 250 and 1000 nm at two different incident angles: 50 and 60°. The data were fitted using the WVASE32 software with a Cauchy model. From the fitting data, the refractive index (n) (taken at $\lambda$ = 700 nm) and the thickness of the films were obtained.

Fourier transform infrared spectroscopy (FTIR) of doped and undoped $80SiO_2$-$20LaF_3$ films on Si-wafer substrates was performed in transmission mode, using a Perkin Elmer Spectrum 100 equipment, in the range 4000-400 $cm^{-1}$ with a resolution of 4 $cm^{-1}$.

The crystallization behavior was followed by Grazing Incidence X-ray diffraction (GI-XRD) of doped samples deposited on Si-wafers. GI-XRD spectra were obtained using a X'pert PRO Theta/2Theta diffratometer (Panalytical). The 2θ scanning angle was varied between 20 and 70° with a step of 0.05° and with a grazing angle of 0.5°.

After the heat treatment, the self-supported layers were milled and sieved to a particle size less than 60 μm to measure XRD. Diffractograms were acquired in the range 10-70° with a step size of 0.02° and 1 second of integration time using a D8 Advance diffractometer (Bruker, Billerica, MA).

Self-supported layers and coatings on silicon wafers were also characterized by high-resolution electron microscopy (HR-TEM), including scanning transmission electron microscopy-high angle annular dark field (STEM-HAADF). A JEOL 2100 field-emission gun transmission electron microscope operating at 200 kV with a point resolution of 0.19 nm was used. The samples were obtained by scratching the films and depositing the scaled fragments onto carbon-coated copper grids.

## 2.3 | Optical characterization

Luminescence measurements were performed at room temperature with a single grating monochromator (focal length 0.25 m), an extended IR Hamamatsu H10330A-75 photomultiplier, and amplified by a standard lock-in technique. The films were excited with a tunable Ti-sapphire ring laser (0.4 $cm^{-1}$ linewidth) in the 770-920 nm spectral range, and the incident beam formed a 25° angle with the sample normal. The emitted light was collected along the direction perpendicular to the films. For all the samples, the excitation power was 700 mW, except for the self-supported layers for which a power of 100 mW was used. Luminescence decay curves were obtained by exciting the samples with a Ti:sapphire laser pumped by a pulsed frequency-doubled Nd:YAG laser (9 ns pulse width), and detecting the emission with a Hamamatsu H10330A-75 photomultiplier. The sample temperature was varied between 9 and 300 K in a continuous-flow cryostat.

# 3 | RESULTS AND DISCUSSION

Transparent and stable sols were obtained after the synthesis process. The viscosity value was ~ 3 mPa.s and remained almost unchanged for at least 2 months. Figure 1 shows a picture of $80SiO_2$-$20LaF_3$-$3Nd^{3+}$ film treated at 750°C-80 hours. In the picture, the coating was marked with a yellow line. Homogeneous, transparent and crack-free doped and undoped coatings were obtained in all cases, and for all the sintering temperatures.

$80SiO_2$-$20LaF_3$-$3Nd^{3+}$ films deposited on silica substrates were characterized by ellipsometry to obtain the refractive index and thickness as a function of sintering temperature. Figure 2A shows the ellipsometry measurements with the corresponding Cauchy fits for single and double films on $SiO_2$ substrate treated at 750°C-3 hours. Very good agreement between the measurements and the fits is obtained, thus indicating the good film quality. The thickness and refractive index were obtained by measuring four films to obtain an n average ± standard deviation. Figure 2B shows the corresponding variation in the


**FIGURE 1** Photograph of $80SiO_2$-$20LaF_3$-$3Nd^{3+}$ thin film on silica substrate treated at 750°C during 80 h [Color figure can be viewed at wileyonlinelibrary.com]

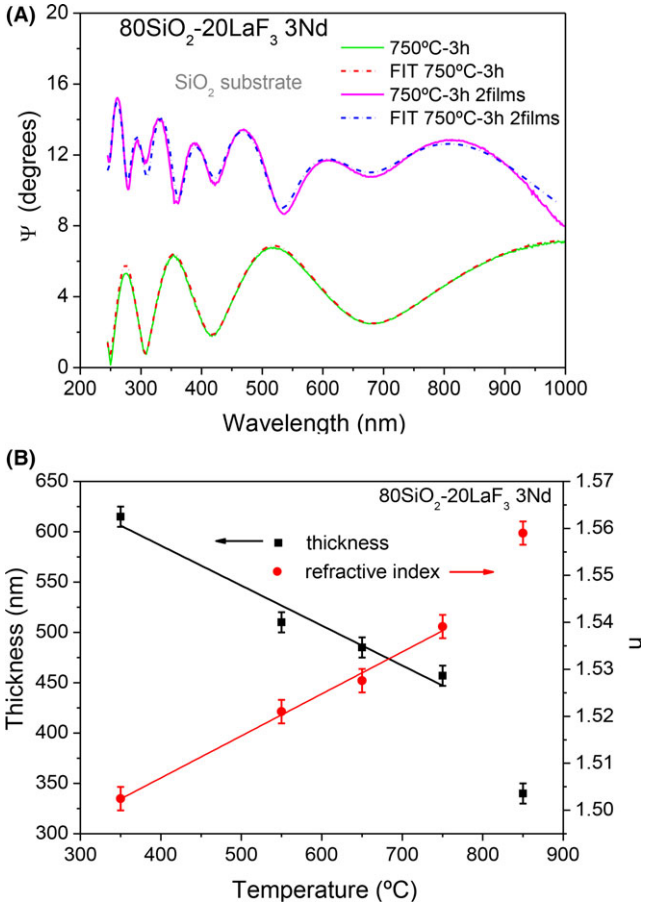


**FIGURE 2** Ellipsometric characterization of $80SiO_2$-$20LaF_3$-$3Nd^{3+}$ films. A, Fit of one and two film deposition using simple and double Cauchy layer model. B, Thickness and refractive index for films treated at 350-850°C during 3 h [Color figure can be viewed at wileyonlinelibrary.com]

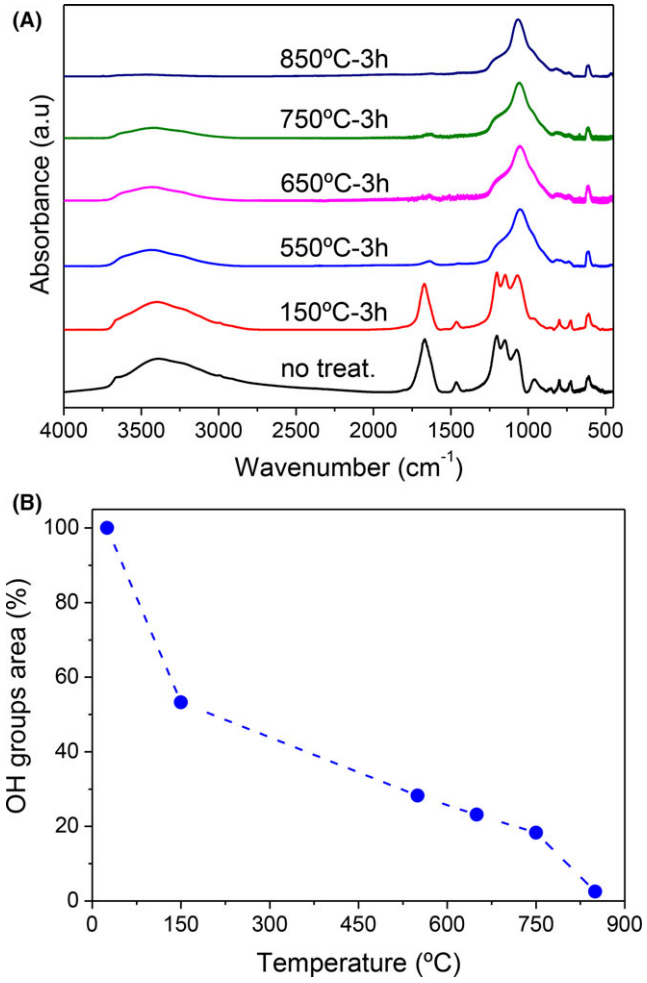


**FIGURE 3** A, FTIR spectra of $80SiO_2$-$20LaF_3$ films deposited on Si-wafer and treated between 150-850°C for 3 h. The FTIR for the untreated film is also shown. B, OH groups area of the films measured in (A) calculated in the range 3750-2850 $cm^{-1}$ [Color figure can be viewed at wileyonlinelibrary.com]

thickness and refractive index at $\lambda = 700$ nm for single film treated between 350 and 850°C during 3 hours. The thickness decreases linearly with temperature, from 625 nm at 350°C to 450 nm at 750°C with a slope of 0.4 nm/°C ($R^2$ = .96). Then, an important shrinkage of the coating is observed and the thickness decreases up to 325 nm at 850°C. In the case of refractive index, it increases with temperature. The increment of refractive index is associated with two effects: one with the condensation of the silica network and the corresponding elimination of the residual organic groups, and the other, with the increase in crystallization of $LaF_3$ with temperature. The refractive index increases linearly ($R^2$ = .998) from 1.50 at 350°C to 1.54 at 750°C, but from 750°C a faster increase is observed, the refractive index reaching the theoretical value of 1.56 at 850°C, closer to the $LaF_3$ refractive index (1.60 at $\lambda = 700$ nm).[33] To confirm the precipitation of $LaF_3$ crystals and the effect on the refractive index, $SiO_2$-3Nd doped samples were prepared and treated between 350 and 850°C for 3 hours. The $LaF_3$-free composition shows a refractive index value smaller than that of $80SiO_2$-$20LaF_3$-$3Nd^{3+}$ films and very close to silica coatings, around ~ 1.45. Moreover, very small change is observed passing from 350 to 550°C, the refractive index passing from 1.44 to 1.45, and for temperature higher than 550°C no change in the refractive index is observed. Instead, for 80SiO2-$20LaF_3$ coatings a remarkable change is obtained increasing the treatment temperature and this is associated to $LaF_3$ crystallization.

Film thicknesses from 450 to 910 nm were obtained for single and multilayer $80SiO_2$-$20LaF_3$ coatings, respectively, after heat treatment at 750°C during 3 hours (Figure 2).

Figure 3A shows the FTIR spectra of $80SiO_2$-$20LaF_3$-$3Nd^{3+}$ films treated at 150, 550, 650, 750, and 850°C during 3 hours together with the spectrum of the untreated film. FTIR bands associated to nontotally reacted precursors appear in the untreated film and in the one treated at 150°C with big bands related to molecular $H_2O$ and OH-Si

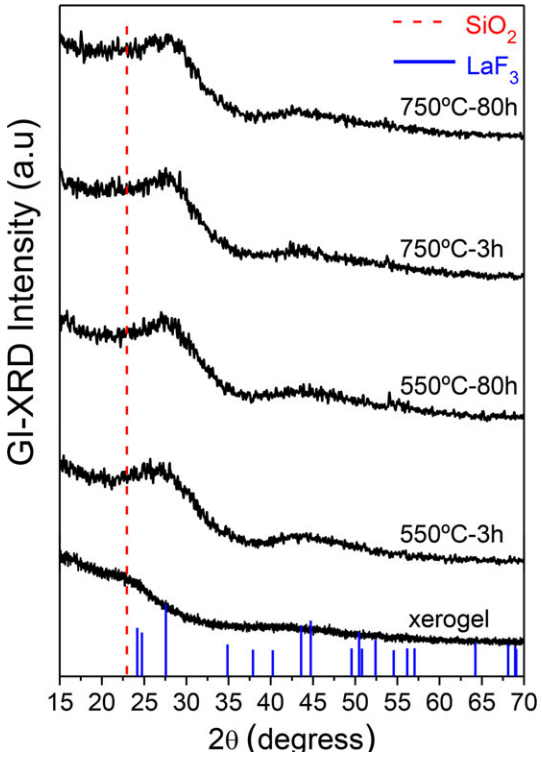


**FIGURE 4** GI-XRD of $80SiO_2$-$20LaF_3$ films deposited on Si-wafer treated at 550°C and 750°C for 3 and 80 h. The measurement for the untreated film is also shown for comparison [Color figure can be viewed at wileyonlinelibrary.com]

vibrations. Moreover, the absorption bands at 1460 and 1680 $cm^{-1}$ appear associated to C=O vibrations of organic compounds not completely removed. In the range 1350-1090 $cm^{-1}$ several sharp vibration bands appear related to $CF_2$ and $CF_3$ associated to TFA.[34] In the case of $80SiO_2$-$20LaF_3$-$3Nd^{3+}$ films treated at 550-850°C, a small band between at 845-780 $cm^{-1}$ corresponding to the symmetric stretching vibration of Si-O-Si is also identified. The spectra show a broad band ranging from 850-1250 $cm^{-1}$ ascribed to asymmetric stretching of Si-O-Si bonds. On the other hand, at 1640 $cm^{-1}$ the bending vibration of $H_2O$ molecules is identified together with a broad band centered around 3400 $cm^{-1}$ associated with the stretching vibrations of the -OH groups. The presence of -OH groups affects the optical properties, producing a quenching of the luminescence of RE ions due to the high vibration frequency of these groups (three times higher than the phonons of silicate glasses). In our case, these bands decrease with increasing the sintering temperature. Figure 3B shows the semiquantitative evolution of -OH groups as a function of temperature. The area was calculated considering a broad band (between 3750 and 2850 $cm^{-1}$) and assuming an area of 100% for the untreated coating. In general, a progressively decrease in the -OH groups is observed increasing the treatment temperature, reaching the 98% of elimination for sample treated at 850°C. However, this temperature is too high and other fluoride

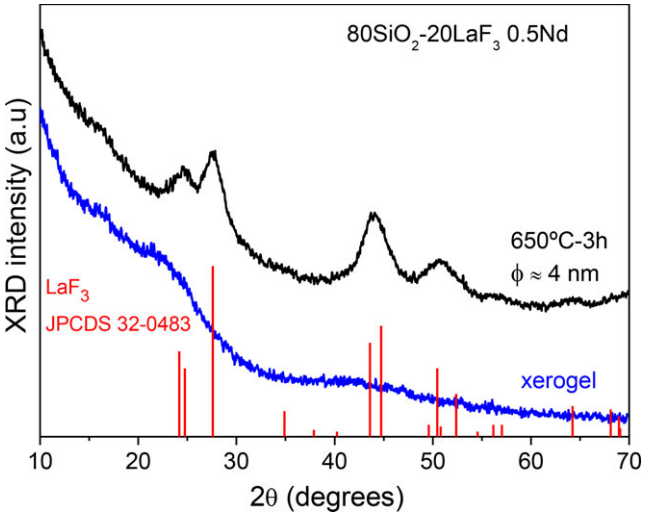


**FIGURE 5** XRD of $80SiO_2$-$20LaF_3$ self-supported layer treated at 650°C for 3 h. The measurement for the untreated (xerogel) sample is also shown for comparison [Color figure can be viewed at wileyonlinelibrary.com]

phase, such as LaOF, can appear.[24] Therefore, it is important to reach a compromise between sintering temperature, presence of hydroxyl groups and the precipitated crystal phase.

To identify the presence of crystalline phases, GI-XRD of $80SiO_2$-$20LaF_3$ thin films treated at 550°C and 750°C for 3 and 80 hours was performed (Figure 4). In all the diffractograms, two broad peaks are observed at $2\theta = 27.5°$ and 44°, corresponding to crystallization of $LaF_3$ in hexagonal form (JPCD 00-032-0483) and associated to the reflections of (111) and (300)-(113) planes, respectively. The diffraction peaks do not change with temperature probably associated with the small size of $LaF_3$ crystals. However, the nanocrystals sizes cannot be calculated using Scherrer's equation due to the broad width of the XRD peaks. No diffraction peaks appear in the untreated film.

Figure 5 shows XRD of $80SiO_2$-$20LaF_3$ self-supported layer treated at 650°C for 3 hours together with the untreated sample. The mean crystal size was evaluated by the Scherrer's equation,[35] using the full width at half maximum (FWHM) and position of the XRD peaks. From this equation, the mean size of the nanocrystals is ~ 4 nm.

HR-TEM images and electron diffraction patterns were obtained for $80SiO_2$-$20LaF_3$ coatings treated at 750°C for 80 hours to identify the presence of $LaF_3$ crystals (Figure 6). The micrograph clearly shows the presence of well distributed $LaF_3$ crystals with small nanocrystals size, between 3 and 5 nm, homogenously distributed in the glass matrix (Figure 6A). Similar results were obtained for $90SiO_2$-$10BaMgF_4$ films prepared by Fujihara et al[36] where 3 nm $BaMgF_4$ crystals were observed in thin films treated at 750°C. The small crystal size explains the difficulty of using GI-XRD to determine the crystal phase, since this size is close to the detection limit of the equipment. The

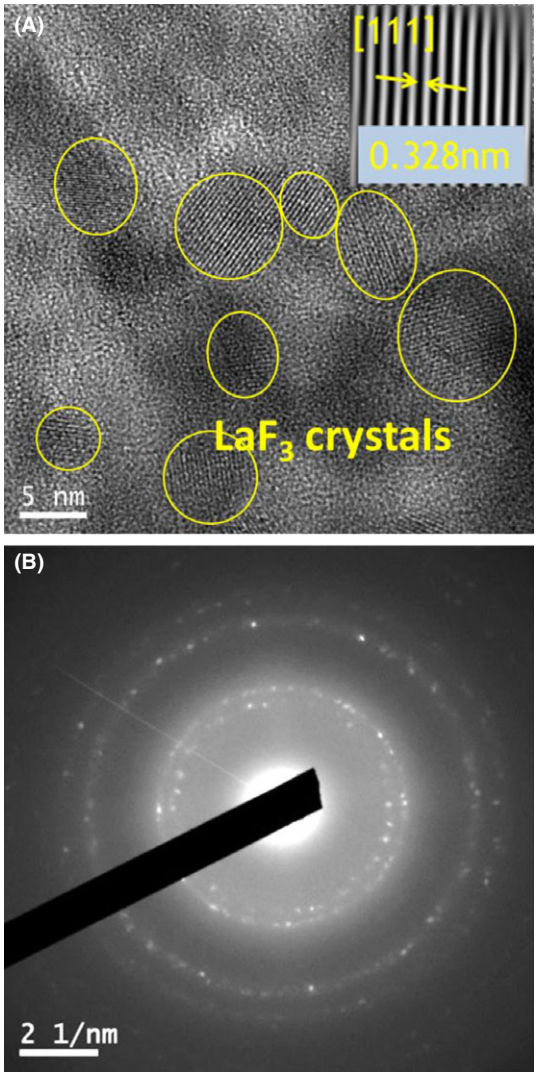


**FIGURE 6** HR-TEM micrographs (A) and electron diffraction (B) of $80SiO_2$-$20LaF_3$ film treated at 750°C for 80 h [Color figure can be viewed at wileyonlinelibrary.com]

inset in Figure 6A shows a magnified detail of the lattice structure. The distance between the adjacent lattice corresponds to the plane distance (111) of hexagonal $LaF_3$, the most intense diffraction peak (JPCD 00-032-0483), whose lattice spacing is $d_{111}$ = 0.328 nm.[15,29,37] No defects, such as planes mismatch, distortions etc, are observed from the analysis of the micrograph. The electron diffraction pattern (Figure 6B) shows diffraction rings and white spots that lay on the diffraction rings. The rings are attributed to certain lattice planes of $LaF_3$. For films treated at 750°C during 3 hours, crystals smaller than 3 nm were observed (not shown). The detection of $LaF_3$ crystals is complicated when the heat-treatment temperature is reduced because very small crystals are expected. Thus, an inhibition of the crystallization process could be associated with the presence of quite high internal stresses in the film that increase when the thickness decreases.

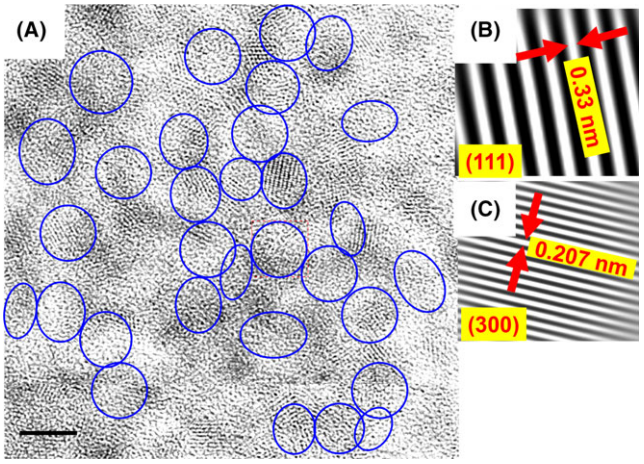


**FIGURE 7** HR-TEM micrographs A, and plane distance B, and C, of $80SiO_2$-$20LaF_3$ self-supported layer treated at 650°C for 3 h [Color figure can be viewed at wileyonlinelibrary.com]

Figure 7 shows HRTEM of the $80SiO_2$-$20LaF_3$ self-supported layer treated at 650°C-3 hours with nanocrystals homogeneously dispersed having a size around 4 nm, which is consistent with XRD results. Figure 7B and C show the corresponding Fast Fourier Transformation (FFT) image taken from two of the nanocrystals encircled in blue in the HRTEM image. The regular diffraction spots recorded along the zone axis unambiguously demonstrate that the nanocrystal has a single crystalline nature, which can be readily indexed as hexagonal $LaF_3$. The HRTEM interplanar distances are determined to be 0.33 nm and 0.207 nm corresponding to the (111) and (300) lattice planes, respectively, of the $LaF_3$ phase.

The emission spectra for untreated and heat-treated films with different $Nd^{3+}$ concentrations were obtained at room temperature by exciting at 806 nm in the $^4I_{9/2} \rightarrow {}^4F_{5/2}$ absorption band. A broad spectrum is observed for all the treated samples with a main peak at around 1060 nm corresponding to the $^4F_{3/2} \rightarrow {}^4I_{11/2}$ laser transition of $Nd^{3+}$ ions. As an example Figure 8 shows the room-temperature emission spectra of thin films doped with 3 mol% $Nd^{3+}$ untreated and treated between 350°C and 750°C for 3 hours. As can be seen, the luminescence of the untreated film is very weak, and increases as the heat-treatment temperature increases. However, the spectra show similar features for the different treatments indicating that no significant changes in the chemical surrounding of the $Nd^{3+}$ ions occur. These changes should affect the Stark splitting and the spectrum peak structure. The emission spectra for times longer than 3 hours show the same spectral features. The increase in the emission intensity is likely related to the reduction in -OH groups with temperature. Concerning to the peak position, the small red-shift observed as annealing temperature increases has been observed in oxyfluoride thin films and attributed to the

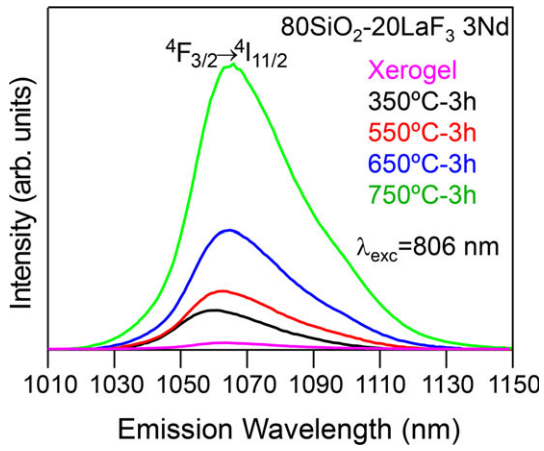


**FIGURE 8** Room-temperature emission spectra of $80SiO_2$-$20LaF_3$ thin films doped with 3 mol% $Nd^{3+}$ for different heat treatments. The emission spectrum of the untreated sample doped with 3% is also included [Color figure can be viewed at wileyonlinelibrary.com]

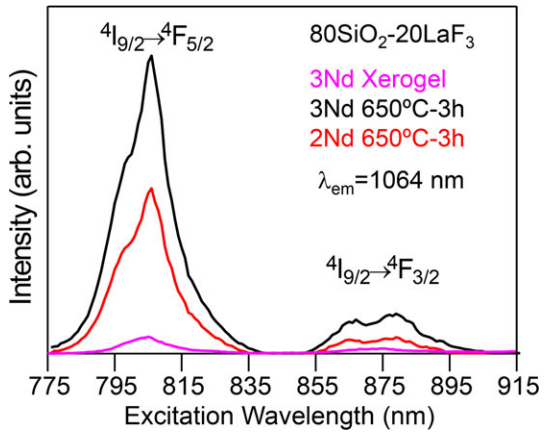


**FIGURE 9** Room-temperature excitation spectra of $80SiO_2$-$20LaF_3$ thin films doped with 2 and 3 mol% $Nd^{3+}$ heat-treated at 650°C-3 h. The excitation spectrum of the untreated sample doped with 3% is also included [Color figure can be viewed at wileyonlinelibrary.com]

formation of oxygen-rich phases at the expense of fluorine content which produces a small variation on the ligand field acting on the RE ions.[38]

Figure 9 shows the excitation spectra for the thin films doped with 2 and 3% $Nd^{3+}$ treated at 650°C-3 hours together with the excitation spectrum of the untreated film doped with 3% $Nd^{3+}$ for comparison. As the $Nd^{3+}$ concentration increases there is an increase in the emission intensity. On the other hand, the excitation spectra obtained between 775 and 915 nm by collecting the luminescence at 1064 nm show two broad bands corresponding to the $^4I_{9/2}\rightarrow{}^4F_{5/2}$ and $^4I_{9/2}\rightarrow{}^4F_{3/2}$ transitions. Similar excitation spectra are obtained for all heat treatments. The untreated sample shows similar spectral features with a very weak intensity.

**TABLE 1** Average lifetime of the $^4F_{3/2}$ state for the $80SiO_2$-$20LaF_3$ thin films doped with 2 and 3 mol% $Nd^{3+}$ for different temperatures. The experimental error is 3%

| Sample | <τ> (μs) |
|---|---|
| Nd 2% 350°C-3 h | 38 |
| Nd 2% 550°C-3 h | 40 |
| Nd 2% 650°C-3 h | 38 |
| Nd 2% 750°C-3 h | 45 |
| Nd 3% 350°C-3 h | 37 |
| Nd 3% 550°C-3 h | 40 |
| Nd 3% 650°C-3 h | 42 |
| Nd 3% 750°C-3 h | 41 |

Another important spectroscopic parameter to characterize the luminescent behavior of $Nd^{3+}$ ions in these films is the decay time of the emitting level. The lifetimes of the $^4F_{3/2}$ state were obtained by exciting at 806 nm and collecting the luminescence at 1064 nm. The decays deviate from a single exponential function and the lifetimes are unexpectedly short, around 40 μs. Table 1 shows the average lifetimes, calculated by $\langle\tau\rangle = \frac{\int_0^\infty tI(t)dt}{\int_0^\infty I(t)dt}$, where $I(t)$ represents the luminescence intensity at time $t$ corrected for the background for the samples doped with 2 and 3% for different thermal treatments. The lifetimes are nearly one order of magnitude shorter than those observed in bulk samples prepared by melting quenching.[15] The strong reduction in the lifetimes could be due to the formation of clusters leading to luminescence quenching[39,40] Moreover, the effective $RE^{3+}$ ions concentration into the nanocrystals is much different from the theoretical (or nominal) one, as shown in previous papers were an estimation of the effective $RE^{3+}$ ions diffusion and incorporation into the crystal phase was given.[15,41] The results showed that the effective concentration into the nanocrystals can be one order of magnitude higher than the nominal concentration.

In a previous work on Nd-doped GCs prepared by melting-quenching, the emission of $Nd^{3+}$ in $LaF_3$ nanocrystals has been isolated using site-selective laser spectroscopy.[15] It was observed that as the $Nd^{3+}$ concentration increases, a stronger quenching of lifetime occurs for $Nd^{3+}$ ions inside $LaF_3$ crystals with respect to those ions dispersed in the glass matrix. Moreover, by increasing $Nd^{3+}$ concentration the spectra become broader and less resolved. To clarify if the $Nd^{3+}$ ions are incorporated in the $LaF_3$ nanocrystals in the sol-gel coatings, the emission and excitation spectra and lifetime of a $80SiO_2$-$20LaF_3$ self-supported layers doped with 0.5 and 3%, and treated at 650°C for 3 hours were measured. The emission spectrum of this sample, obtained by exciting at 786 nm, is presented in Figure 10A, showing a more resolved structure which

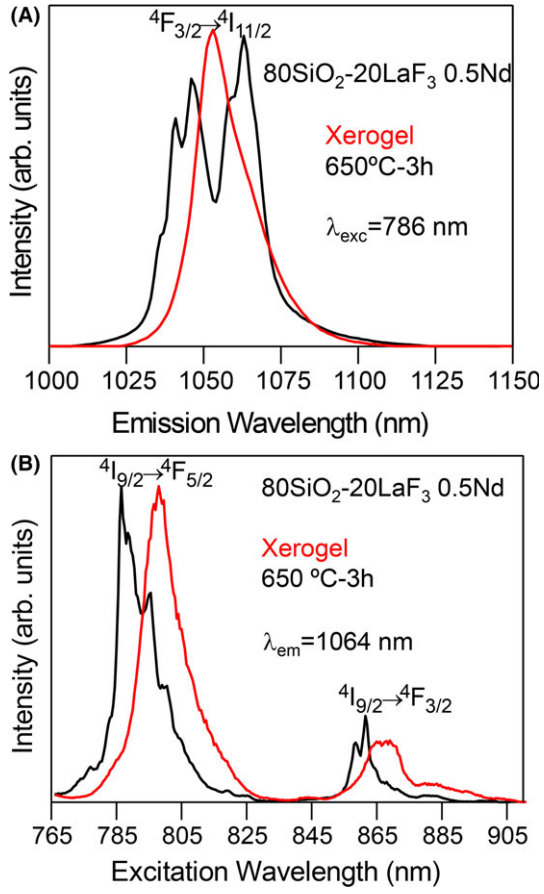


**FIGURE 10** Normalized room-temperature emission A, and excitation B, spectra of $Nd^{3+}$ in the $80SiO_2$-$20LaF_3$-$0.5Nd^{3+}$ sol-gel self-supported layer untreated (red line) and treated at 650°C-3 h (black line) [Color figure can be viewed at wileyonlinelibrary.com]

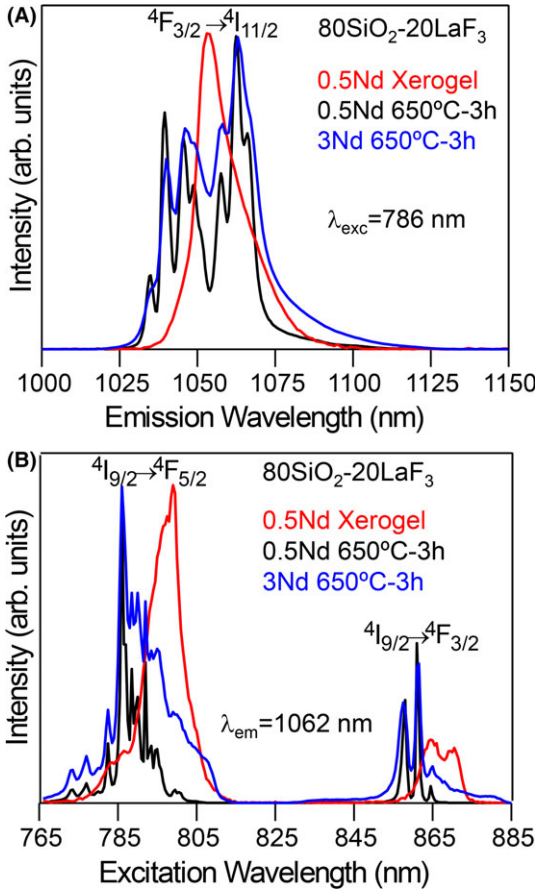


**FIGURE 11** Normalized emission A, and excitation B, spectra of $Nd^{3+}$ in the $80SiO_2$-$20LaF_3$ sol-gel self-supported layers treated at 650°C-3 h doped with 0.5% $Nd^{3+}$ (black line) and 3% $Nd^{3+}$ (blue line) together with the spectra of the untreated self-supported layer doped with 0.5% $Nd^{3+}$ (red line). Data correspond to 9 K [Color figure can be viewed at wileyonlinelibrary.com]

indicates a crystalline environment for $Nd^{3+}$ ions with similar features to those observed in $LaF_3$ crystals.[15,42] This is also confirmed by the excitation spectrum, Figure 10B, obtained by collecting the luminescence at 1064 nm. The spectrum presents narrow and well-resolved peaks corresponding to $Nd^{3+}$ ions in the nanocrystals. The normalized emission and excitation spectra of the untreated sample with the same $Nd^{3+}$ concentration are included in Figure 10 for comparison. It is worth noting that in the case of the untreated sample the spectral features of both spectra correspond to $Nd^{3+}$ ions in an amorphous environment. Moreover, the $Nd^{3+}$emission of the treated sample is around 100 times more intense than that of the untreated one. The decay from the $^4F_{3/2}$ level obtained under excitation at 786 nm collecting the luminescence at 1064 nm deviates from a single exponential function. The average lifetime decreases from 147 μs to 18 μs as $Nd^{3+}$ concentration increases from 0.5 to 3 mol%.

$Nd^{3+}$ incorporation into $LaF_3$ nanocrystals was unambiguously confirmed by measurements performed at low temperature. Figure 11A and B shows the emission and excitation spectra, respectively, obtained at 9 K for the samples doped with 0.5 and 3 mol% $Nd^{3+}$. The emission spectrum of the lowest concentrated sample shows sharp peaks which correspond to the emission of $Nd^{3+}$ in $LaF_3$ nanocrystals. As observed in the excitation spectrum, the low energy band corresponding to the $^4I_{9/2}\rightarrow{}^4F_{3/2}$ doublet narrows and defines into two single components as expected for a well-defined crystal field site. Moreover, the $^4I_{9/2}\rightarrow{}^4F_{5/2}$ band is composed of narrow and well-resolved peaks which indicate that the spectrum corresponds to $Nd^{3+}$ ions in the $LaF_3$ nanocrystals. These results confirm that in the self-supported layer treated at 650°C for 3 hours the $Nd^{3+}$ ions are mainly incorporated in the $LaF_3$ nanocrystals. However, the low-temperature emission and excitation spectra of the untreated sample doped with 0.5 mol% $Nd^{3+}$ show broad and structureless bands according with a predominant amorphous environment for $Nd^{3+}$ ions. Referring to the emission and excitation spectra of the treated sample doped with 3 mol% $Nd^{3+}$, although they show the peaks corresponding to $Nd^{3+}$ in $LaF_3$ nanocrystals they become broader and less resolved than those of the less concentrated sample

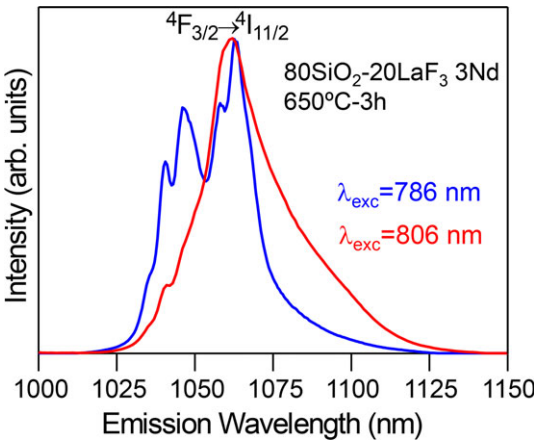


**FIGURE 12** Normalized emission spectra of $Nd^{3+}$ in the $80SiO_2$-$20LaF_3$ sol-gel self-supported layer treated at 650°C-3 h doped with 3% $Nd^{3+}$ obtained by exciting at 786 nm (blue line) and 806 nm (red line). Data correspond to 9 K [Color figure can be viewed at wileyonlinelibrary.com]

which indicates the presence of different $Nd^{3+}$environments. This is confirmed by the excitation wavelength dependence of the emission. Figure 12 shows the low temperature emission spectra corresponding to 786 and 806 nm excitations displaying the crystalline and amorphous $Nd^{3+}$ environments, respectively.

In summary, $Nd^{3+}$ incorporation into the $LaF_3$ nanocrystals was observed and by selective excitation spectra of pure $Nd^{3+}$:$LaF_3$ crystals were obtained for self-supported layers doped with 0.5$Nd^{3+}$ and 3%. For coatings similar lifetimes but broader spectra were observed doping with 2 and 3 mol%. This discrepancy could be attributed to a much higher $Nd^{3+}$ effective concentration into the $LaF_3$ nanocrystals. In fact, excessive $Nd^{3+}$ concentration may produce inhomogeneous spectral broadening giving rise to glassy-like luminescence emission. Similar behavior was observed in bulk samples prepared by MQ where it was observed that, increasing $Nd^{3+}$ content, spectra lost resolution and became similar to those of glass.[15]

## 4 | CONCLUSIONS

Transparent and crack-free $80SiO_2$-$20LaF_3$ GC films doped with 2 and 3 mol% $Nd^{3+}$ were successfully obtained by sol-gel. Self-supported GC layers of composition $80SiO_2$-$20LaF_3$ doped with 0.5 and 3$Nd^{3+}$ were also prepared to furtherly study the optical properties. By HRTEM it was shown the precipitation of $LaF_3$ nanocrystals with a size between 3 and 5 nm.

For self-supported layers the $Nd^{3+}$ incorporation into the nanocrystals allows reproducing spectra of pure $Nd^{3+}$:$LaF_3$ crystals, however, the lifetime is strongly quenched as compared to typical lifetime in oxyfluoride GCs. Optical properties of coatings show the increase in luminescence with the heat-treatment temperature due to an increase in the crystal fraction and removal of -OH groups. Much broader emission spectra were obtained as compared to self-supported layers likely due to extremely high $Nd^{3+}$ effective concentration. Further studies are in progress to optimize the RE concentration and glass matrix composition to obtain $Nd^{3+}$-doped films with optimal luminescence properties.

## ACKNOWLEDGMENTS

This work was supported by MINECO under Projects No.MAT2013-48246-C2-1-P and MAT2013-48246-C2-2-P and Basque Country University PPG17/07. J.J. Velázquez also acknowledges MINECO under Grant FPDI-2013-16895. The authors thank Aritz Iglesias for his support in coatings preparation.

## ORCID

*Giulio Gorni* http://orcid.org/0000-0001-8227-9022
*Jose J. Velázquez* http://orcid.org/0000-0001-7672-0539
*Jadra Mosa* http://orcid.org/0000-0001-9375-9531
*Alicia Durán* http://orcid.org/0000-0002-0067-1934
*Yolanda Castro* http://orcid.org/0000-0001-5747-2162

## REFERENCES

1. Mohageg M, Matsko AB, Maleki L. Lasing and up conversion from a nominally pure whispering gallery mode resonator. *Opt Express*. 2012;20:16704-16714.
2. Bettinelli M, Carlos L, Liu X. Lanthanide-doped upconversion nanoparticles. *Phys Today*. 2015;68:38-44.
3. Wang X, Wolfbeis OS, Meier RJ. Luminescent probes and sensors for temperature. *Chem Soc Rev*. 2013;42:7834-7869.
4. Qiu P, Zhou N, Chen H, et al. Recent advances in lanthanide-doped upconversion nanomaterials: synthesis, nanostructures and surface modification. *Nanoscale*. 2013;5:11512-11525.
5. Wang F, Han Y, Lim CS, et al. Simultaneous phase and size control of upconversion nanocrystals through lanthanide doping. *Nature*. 2010;463:1061-1065.
6. Jaque D, Vetrone F. Luminescence nanothermometry. *Nanoscale*. 2012;4:4301-4326.
7. Huang X, Han S, Huang W, et al. Enhancing solar cell efficiency: the search for luminescent materials as spectral converters. *Chem Soc Rev*. 2013;42:173-201.
8. Reisfeld R, Jùrgensen CK. Excited state phenomena in vitreous materials. In: Gschneidner KA Jr, Eyring L, eds. *Chapter 1 in Handbook on the Physics and Chemistry of Rare Earth* Vol. 9. North Holland, Amsterdam: Elsevier; 1987: 1-90.
9. Wang Y, Ohwaki J. New transparent vitroceramics codoped with $Er^{3+}$ and $Yb^{3+}$ for efficient frequency upconversion. *Appl Phys Lett*. 1993;63:3268-3270.

10. de Pablos-Martín A, Durán A, Pascual MJ. Nanocrystallisation in oxyfluoride systems: mechanisms of crystallisation and photonic properties. *Int Mater Rev*. 2012;57:165-186.
11. Fedorov P, Luginina AA, Popov AI. Transparent oxyfluoride glass ceramics. *J Fluorine Chem*. 2015;172:22-50.
12. Chen D, Wang Y, Yu Y. Structure and optical spectroscopy of Eu-doped glass ceramics containing $GdF_3$ nanocrystals. *J Phys Chem C*. 2008;112:18943-18947.
13. Lavín V, Iparraguirre I, Azkargorta J, et al. Stimulated and upconverted emissions of $Nd^{3+}$ in a transparent oxyfluoride glass-ceramic. *Opt Mater*. 2004;25:201-208.
14. Pisarska J, Ryba-Romanowski W, Dominiak-Dzik G. Nd-doped oxyfluoroborate glasses and glass-ceramics for NIR laser applications. *J Alloy Compds*. 2008;451:223-225.
15. Gorni G, Velázquez JJ, Mather GC, et al. Selective excitation in transparent oxyfluoride glass-ceramics doped with $Nd^{3+}$. *J Eur Ceram Soc*. 2017;37:1695-1706.
16. Xu Y, Zhang X, Dai S, et al. Efficient near-infrared down-conversion in $Pr^{3+}$-$Yb^{3+}$codoped glasses and glass ceramics containing $LaF_3$ nanocrystals. *J Phys Chem C*. 2011;115:13056-13062.
17. Chen QJ, Zhang WJ, Huang XY, et al. Efficient down- and up-conversion of $Pr^{3+}$–$Yb^{3+}$ co-doped transparent oxyfluoride glass ceramics. *J Alloy Compds*. 2012;513:139-144.
18. Gorni G, Cosci A, Pelli S, et al. Transparent oxyfluoride nano-glass ceramics doped with $Pr^{3+}$ and $Pr^{3+}$–$Yb^{3+}$ for NIR emission. *Front Mater*. 2017;3:58.
19. Hu Z, Wang Y, Ma E, et al. Microstructures and upconversion luminescence of $Er^{3+}$ doped and $Er^{3+}$/$Yb^{3+}$ co-doped oxyfluoride glass ceramics. *Mater Chem Phys*. 2007;101:234-237.
20. Gorni G, Balda R, Fernández J, et al. Effect of the heat treatment on the spectroscopic properties of $Er^{3+}$-$Yb^{3+}$- coped transparent oxyfluoride nano-glass-ceramics. *J Lumin*. 2018;193:51-60.
21. Fujihara S, Tada M, Kimura T. Sol-gel processing of $LaF_3$ thin films. *J Ceram Soc Jpn*. 1998;106:124-126.
22. Fujihara S, Kato T, Kimura T. Sol-Gel processing and luminescent properties of rare-earth oxyfluoride materials. *J Sol-Gel Sci Techn*. 2006;26:953-956.
23. Fujihara S, Kato T, Kimura T. Sol-Gel synthesis of silica-based oxyfluoride glass-ceramic thin films: incorporation of Eu3 + activators into crystallites. *J Am Ceram Soc*. 2001;84:2416-2418.
24. Ribeiro SJL, Araújo CC, Bueno LA, et al. Sol–gel $Eu^{3+}$/$Tm^{3+}$ doped transparent glass–ceramic waveguides. *J Non-Cryst Solids*. 2004;348:180-184.
25. Biswas A, Maciel GS, Friend CS, et al. Upconversion properties of a transparent $Er^{3+}$–$Yb^{3+}$ co-doped $LaF_3$–$SiO_2$ glass-ceramics prepared by sol–gel method. *J Non-Cryst Solids*. 2003;316:393-397.
26. Chen D, Wang Y, Yu Y, et al. Microstructure and luminescence of transparent glass ceramic containing $Er^{3+}$:$BaF_2$ nano-crystals. *J Solid State Chem*. 2006;179:532-537.
27. Luo W, Wang Y, Cheng Y, et al. Crystallization and structural evolution of $YF_3$–$SiO_2$ xerogel. *Mater Sci Eng, B*. 2006;127:218-223.
28. del-Castillo J, Mendez-Ramos J, Yanes AC, et al. Gain cross-section of 1.06 μm emission in $Nd^{3+}$-doped $SiO_2$-$LaF_3$ glass-ceramics prepared by sol-gel method. *J Non-Cryst Solids* 2007;354:2000-2003.
29. Yanes AC, del-Castillo J, Mendez-Ramos J, et al. Luminescence and structural characterization of transparent nanostructured $Eu^{3+}$-doped $LaF_3$-$SiO_2$ glass-ceramics prepared by sol-gel method. *Opt Mater* 2007;29:999-1003.
30. Velázquez JJ, Rodríguez VD, Yanes AC, et al. Increase in the $Tb^{3+}$ green emission in $SiO_2$–$LaF_3$ nano-glass-ceramics by codoping with $Dy^{3+}$ ions. *J Appl Phys*. 2010;108:113530-113535.
31. Velázquez JJ, Yanes AC, del-Castillo J, et al. Spectroscopic characterization and up-conversion in sol-gel derived $Yb^{3+}$-$Pr^{3+}$ co-doped $SiO_2$-$LaF_3$ nano-glass-ceramics. *J Non-Cryst Solids*. 2010;356:1349-1353.
32. Kajihara K. Recent advances in sol–gel synthesis of monolithic silica and silica-based glasses. *J Asian Cer Soc*. 2013;1:121-133.
33. Laiho R, Lakkisto M. Investigation of the refractive indices of $LaF_3$, $CeF_3$, $PrF_3$, and $NdF_3$. *Philos Mag B*. 1983;48:203-207.
34. Redington RL, Lin KC. Infrared spectra of trifluoroacetic acid and trifluoroacetic anhydride. *Spectrochim Acta*. 1971;27A:2445-2460.
35. Cullity BD. *Elements of X-ray Diffraction*. Massachusetts: Addison-Wesley; 1978.
36. Fujihara S, Kitta S, Kimura T. Porous phosphor thin films of oxyfluoride SiO2–BaMgF4: Eu2 + glass-ceramics prepared by Sol-Gel method. *Chem Lett*. 2003;32:928-929.
37. Zhao N, Nie W, Mao J, et al. A general synthesis of high-quality inorganic nanocrystals via a two-phase method. *Small*. 2010;6:2558-2565.
38. Armelao L, Bottaro G, Bovo L, et al. Luminescence properties of Eu-Doped lanthanum oxyfluoride Sol-gel thin films. *J Phys Chem C*. 2009;113:14429-14434.
39. Langlet M, Coutier C, Meffre W, et al. Microstructural and spectroscopic study of sol–gel derived Nd-doped silica glasses. *J Lumin*. 2002;96:295-309.
40. Sudarsan V, Sivakumar S, van Veggel FCJM, et al. General and convenient method for making highly luminescent sol-gel derived silica and alumina films by using $LaF_3$ nanoparticles doped with lanthanide ions ($Er^{3+}$, $Nd^{3+}$, and $Ho^{3+}$). *Chem Mater*. 2005;17:4736-4742.
41. de Pablos-Martín A, García MA, Muñoz-Noval A, et al. Analysis of the distribution of $Tm^{3+}$ ions in $LaF_3$ containing transparent glass-ceramics through X-ray absorption spectroscopy. *J Non-Cryst Solids* 2014;384:83-87.
42. Hong JQ, Zhang LH, Zhang PX, et al. Growth, optical characterization and evaluation of laser properties of Nd:$LaF_3$ crystal. *J Alloy Compd*. 2015;646:706-709.

**How to cite this article:** Gorni G, Balda R, Fernández J, et al. $80SiO_2$-$20LaF_3$ oxyfluoride glass ceramic coatings doped with $Nd^{3+}$ for optical applications. *Int J Appl Glass Sci*. 2018;9:208–217. https://doi.org/10.1111/ijag.12338

# *PAPER 10*

**Transparent sol-gel oxyfluoride glass-ceramics with high crystalline fraction and study of RE incorporation.**

G. Gorni, J.J. Velázquez, J. Mosa, G.C. Mather, M. Vila, A. Serrano, G R. Castro, D. Bravo, R. Balda, J. Fernández, A. Durán, Y. Castro.

*Draft*

# Transparent sol-gel oxyfluoride glass-ceramics with high crystalline fraction and study of RE incorporation

G. Gorni[1], J. J. Velázquez[1], J. Mosa[1], G.C. Mather[1], M. Vila[2], A. Serrano[1,2], G. R. Castro[2,3], D. Bravo[4], R. Balda[5,6], J. Fernández[7], A. Durán[1], Y. Castro[1*]

[1] *Instituto de Cerámica y Vidrio, CSIC, Madrid, Spain*

[2] *SpLine, Spanish CRG Beamline - European Synchrotron Radiation Facility (ESRF), France*

[3] *Instituto de Ciencia de Materiales de Madrid, CSIC, Spain*

[4] *Dept. Física de Materiales, Facultad de Ciencias, Universidad Autónoma de Madrid (UAM), Spain*

[5] *Departamento Física Aplica I, Escuela Superior de Ingeniería, Universidad del País Vasco (UPV-EHU), Spain*

[6] *Centro de Física de Materiales, (UPV/EHU-CSIC), Spain*

[7] *Donostia International Physics Center DIPC, 20018 San Sebastian, Spain*

castro@icv.csic.es

## 1. Introduction

Oxyfluoride glass-ceramics (OxGCs) have attracted great interest in the field of photonics since the pioneering work of Wang and Ohwaki [1]. OxGCs are polycrystalline materials containing fluoride nano-crystals (NCs) that crystallize in a glass matrix during a controlled heat treatment of the precursor glass. Alumina-silicate glass matrices are suitable due to their excellent mechanical, thermal and chemical properties compared to phosphate or fluoride glasses. In addition, OxGCs may host Rare-Earth (RE) ions in the low-phonon energy fluoride crystals (300-450 cm-1), thereby increasing the luminescence efficiency with respect to the corresponding oxide glasses [2–14]. The melt-quenching (MQ) method has been routinely used to prepare OxGCs that showed excellent optical properties and a significant enhancement of photoluminescence with respect to the precursor glasses. Moreover, the possibility to draw fibers and convert the core into a GC revealed the importance of this method for the preparation of novel devices with new or improved optical efficiencies [15–20]. However, the high melting temperatures (1400-1700 °C) greatly affect the fluoride content, limiting the crystal phase content to 10 wt% or less for some crystal phases, such as $LaF_3$ [7,9,10]. Furthermore, phase separation and spontaneous fluoride crystallization is usually present due to fluorine immiscibility at high temperature in oxide-glass matrices. For these reasons, this method still has to overcome some problems and efforts are required to improve the quality and processing of these materials. Another crucial point concerns the incorporation of dopants into the fluoride NCs. In fact, it is known that in melted glasses there is a portion of RE ions that remain outside

the fluoride NCs even after heat treatment for prolonged periods [10,12]. This phenomenon is explained considering the high glass viscosity at typical crystallization temperatures ($T_g$+20-100 °C) that limits ionic diffusion. Moreover, due to the depletion of crystal formers in the glass matrix, a viscous Si-enriched shell forms around the crystals, which further limits ionic diffusion. A challenging goal is to obtain homogeneous materials with much higher fluoride contents and with higher dopant incorporation in the NCs, thus improving the optical efficiency.

The sol-gel (SG) route appears to be a promising alternative to prepare OxGC films and bulk materials [21–34]. The SG process is a cheap and extremely flexible chemical method for obtaining pure and very homogenous materials, as well as offering a wide range of possible nano/micro-structures at relatively low sintering temperatures (100-600 °C). Synthesis classically involves the hydrolysis and polycondensation of metal salts or metal-organic precursors, such as tetraethyl orthosilicate (TEOS), in alcoholic media [35]. In the late nineties, Fujihara et al. prepared the first OxGC SG materials in a two-step process [21] involving preparation of silica sol using the classical route followed by mixing of fluoride and RE-ion precursors (acetates, nitrates, chlorides etc.) dissolved in ethanol or acidic medium. The mixing of both solutions, with subsequent controlled crystallization, leads to the precipitation of fluoride crystals in the silica-glass matrix. However, the literature mostly describes the preparation of OxGC materials with a nominal content of 5 mol% active crystal phase, and with the final crystal fraction not being estimated [36]. For example, Szpikowska-Sroka reported 3 wt% of crystallized phase for a nominal concentration of 5 mol% [34] Such concentrations are even lower than those obtained by MQ [2,10,12]. Other authors have attempted to increase the crystal content up to 15 mol% but opaque materials were obtained [21]. Moreover, high treatment temperatures (800-1000 °C) are used to obtain OxGCs from the amorphous precursors, even though the typical crystallization temperature of fluorides is between 280-350 °C. To date, the use of sol-gel to obtain OxGCs has not been widely investigated because no significant improvement in structural and optical properties has been achieved since the earliest papers. There is still much work to be performed on correlating the crystallization mechanism of these materials with the structure, dopant incorporation and optical properties.

In this work, novel OxGC materials with a much higher active crystal phase content and sintered at much lower temperature than previously reported have been prepared by taking advantage of the particular benefits of the SG process. In addition, it was demonstrated how this method leads to precipitation of RE-doped NCs using short heat treatment times. Moreover, it is shown how most RE ions are incorporated into the NCs during the crystallization process.

## 2. Materials and Methods

*Materials preparation*

Sols of composition (mol %) $80SiO_2$-$20LaF_3$ doped with 0.1 and $0.5Er^{3+}$ were prepared by partially replacing TEOS with methyl-trimethoxy-silane (MTES) as precursor with a TEOS/MTES molar ratio of 40/60. The synthesis was performed in two- step process starting from a silica sol with molar ratio: $0.4TEOS:0.6MTES:2.5EtOH:1H_2O(0.1HCl):0.2CH_3COOH$ stirred for 2 h at room temperature. Subsequently, $La(CH_3COO)_3$:$EtOH$:$H_2O$:TFA in the molar ratio 1:5:4:4 was stirred for 2 h at 40 °C and then mixed with the silica sol in the ratio 0.8(TEOS+MTES):0.2La

Thin films on silica and silicon wafers (111) were prepared by dip coating using withdrawal rates of 10-35 cm/min. Finally, the films were treated at 550 °C for 1 min and 1 h using a heating rate of 10 °C/min.

Moreover, self-supported layers (bulk-like monoliths 1-2 mm thick) were prepared using the molar ratio $0.4TEOS:0.6MTES:3EtOH:2H_2O(0.1HCl)$, respectively. An acetate dissolution, similar to that used for thin films, was prepared rising the $H_2O$ content to obtain a total molar ratio $1(TEOS+MTES):10H_2O$.

Then, the sol was deposited into Petri dishes, covered, sealed and kept at 50 °C for 1 week to obtain the xerogel samples. GC samples were obtained by heating the xerogels at 550 °C for 1 min up to 1 h, with an intermediate step at 150 °C to remove water and solvents.

*Characterization of coatings and self-supported layers*

Thin films deposited onto silica and silicon wafer were characterized by spectroscopic ellipsometry in the range 250-1000 nm using a M-2000UTM ellipsometer (J.A. Co., Woollam). The incident angles were set to 50 and 60 ° and the acquisition time to 10 s. The data were fitted using the CompleteEASE software representing the film as a Cauchy layer deposited onto the corresponding substrate.

Differential thermal analysis (DTA) and thermogravimetry (TG) of bulk xerogels were measured using the SDT Q600 instrument (TA Instruments). Around 20–30 mg of powder materials with a size of 1–1.25 mm, obtained after drying the sol at 50 °C, were measured in air and Argon using a heating rate of 10 °C/min.

X-Ray Diffraction (XRD) patterns of $80SiO_2$-$20LaF_3$-$0.5Er^{3+}$ self-supported layers and grazing incidence XRD (GI-XRD) of $80SiO_2$-$20LaF_3$ thin films were obtained at the BM25B-SpLine

beamline of the ESRF (European Synchrotron Radiation Facility, Grenoble, France) [37], using an X-ray wavelength of 0.619 Å. For G-XRD measurements, an incidence angle of 0.5 ° was used. The crystal size, D, was estimated using the Scherrer's equation:

$$D = \frac{0.94\lambda}{\cos\Theta\sqrt{B_m^2 - B_i^2}}$$

where λ is the wavelength, $B_m$ the full width half maximum of the peak and θ its diffraction angle. The instrumental broadening $B_i$ was also taken into account. The diffraction-peak parameters were fit using a pseudo Voigt function.

Rietveld Refinement was performed using the FullProf software [38] and the $LaF_3$ crystal fraction was estimated using NaF as internal weight standard in a similar manner to that described previously [12]. X-ray powder data were collected over the range $20 \leq 2\theta \leq 120$ ° in a step width of 0.0289° and a counting time of 4s per step employing a Bruker D8 high-resolution diffractometer equipped with a solid-state rapid LynxEye detector, and monochromatic Cu $K\alpha_1$ radiation.

High Resolution Transmission Electron Microscopy (HRTEM) was performed using a JEOL 2100 field emission gun operating at 200 kV with a point resolution of 0.19 nm. The samples were obtained by scratching the films or milling the self-supported layers and dispersing in EtOH. Then, one or two drops of suspensions were depositing on the scaled fragments onto carbon-coated copper grids. The solvent was removed after drying the copper grids under UV lamp.

$Er^{3+}$ $L_3$ edge X-Ray Absorption spectroscopy (XAS) were used to characterize the $80SiO_2$-$20LaF_3$ $0.5Er^{3+}$ films treated at 150 °C for 1 h (xerogel) and at 550 °C for 1 min (GC) employing the BM25A-SpLine beamline (ESRF). XAS measurements were collected in fluorescence mode using a 13 element Si (Li) solid-state detector with the sample surface placed at an angle of 45 ° to the incident beam. The spectra represent an average of at least six scans; the XAS data were processed using the software ATHENA [39]. Both $ErF_3$ and $Er_2O_3$ standards were also measured as references.

Electron Paramagnetic Resonance (EPR) spectra were obtained by a Bruker ESP 300E spectrometer working in the X-band with field modulation of 100 kHz. The temperature was controlled with a continuous-flow helium cryostat (Oxford Instruments ESR 900) and the calibration of the resonance magnetic fields and microwave frequencies measured with a NMR Gauss-meter (Bruker ER 035 M) and a frequency meter (Hewlett-Packard 5342A), respectively.

Self-supported layer samples (xerogel and GCs) doped with 0.1 and 0.5 $Er^{3+}$ were milled and rolled in Teflon tape to perform the measurements.

The steady-state emission spectra were performed by exciting the $80SiO_2$-$20LaF_3$ bulk samples and thin films doped with 0.1 and $0.5Er^{3+}$ with a tunable Ti-sapphire ring laser (0.4 $cm^{-1}$ linewidth) in the 770–920 nm spectral range. The fluorescence was analysed with a 0.25 m monochromator, and the signal was detected by an extended IR Hamamatsu H10330A-75 photomultiplier and finally amplified by a standard lock-in technique. The sample temperature was varied between 9 and 300 K in a continuous flow cryostat.

## 3. Results and Discussion

### *3.1. Self-supported layers and thin films*

Crack-free and homogeneous self-supported layers were obtained before and after heat treatment of the doped and undoped $80SiO_2$-$20LaF_3$ samples at 550 °C for 1min, Figure 1.

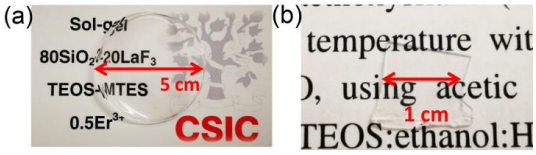


**Figure 1.** (a) Xerogel of composition $80SiO_2$-$20LaF_3$- $0.5Er^{3+}$ bulk sample obtained at 150 °C for 24 h. (b) GC of the same composition obtained at 550 °C for 1 min.

Homogeneous and transparent films with good adhesion were obtained for all the withdrawal rates used. The good agreement between measurement and fitted data, Figure 2a, demonstrated the good quality of the films. The corresponding thickness varies almost linearly with the withdrawal rate, up to a thickness of ~ 1.4 µm in a single deposition and using a withdrawal rate of 35 cm/min, Figure 2b. The addition of MTES allows the thickness of films to be increased, compared to when only TEOS is used. In particular, according to [40], the TEOS/MTES ratio 0.4/0.6 produces the highest critical thickness. Moreover, the addition of MTES improves the mechanical strength of self-supported layers. Such behavior is associated with the presence of $CH_3$ groups which allow the porosity to be increased in the silica network reducing the stress [40]. The amount of OH groups is also reduced when MTES is added to TEOS because the surfaces become more hydrophobic [40,41].

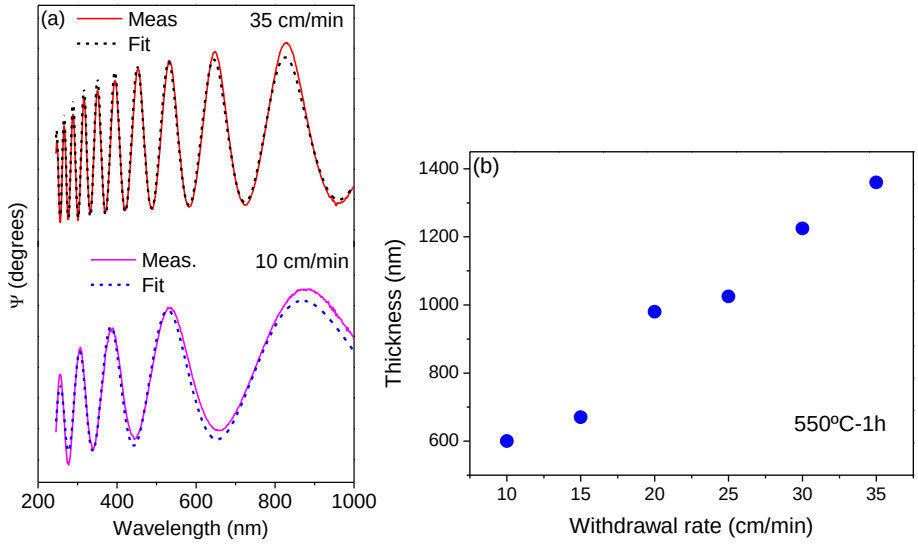


**Figure 2.** (a) Ellipsometric measurements and fit of $80SiO_2$-$20LaF_3$ $0.5Er^{3+}$ thin films treated at 550 °C for 1 deposited onto silica substrate using a withdrawal rate of 10 and 35 cm/min. (b) Variation of thickness with the withdrawal rate.

### *3.2. DTA and crystallization*

Figure 3 shows a DTA curve for self-supported layers measured in air with a heating rate of 10 °C/min. The endothermic process at ~ 100 °C corresponds to water and solvent removal. The first sharp exothermic peak at ~ 280 °C is associated to $LaF_3$ crystallization and the corresponding mass loss (~ 30 %) is due to decomposition reactions, as studied elsewhere [42]. The sharpness of the crystallization peak means that the process occurs very rapidly; in contrast, the $LaF_3$ crystallization peak in the melted glasses (MQ) is much broader and less intense [12]. Moreover, the $T_g$ of these samples is higher than 1000 °C, as reported in a previous paper [42], and the crystallization of SG OxGCs occurs at much lower temperature than the $T_g$. The crystallization mechanism is, thus, clearly different with respect to that of MQ OxGCs [43–47].

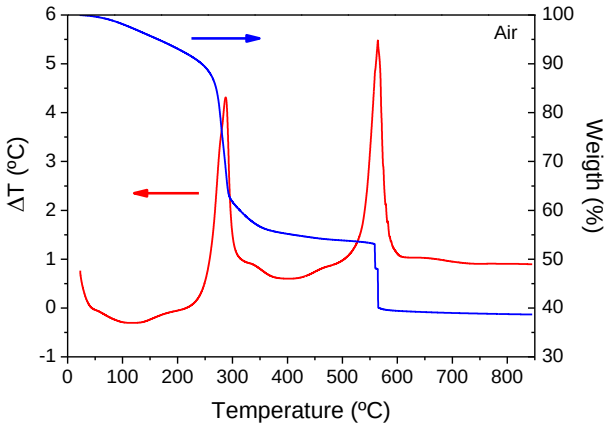


**Figure 3**. (a) DTA (red) and TG (blue) curves for $80SiO_2$-$20LaF_3$-$0.5Er^{3+}$ bulk sample treated in air with a heating rate of 10 °C/min.

The second exothermic process at ~ 575 °C, associated to oxidation of $CH_3$ groups with a further mass loss of around 10 %, does not appear in Ar atmosphere. Heat treatment at temperatures higher than that of $CH_3$ elimination causes a sudden shrink of films and self-supported layers, leading to crack of the samples.

*3.3. XRD, GI-XRD and crystal fraction*

The XRD patterns of self-supported layers exhibited well-defined peaks consistent with the crystallization of $LaF_3$ (JCPDS 00-032-0483) with a crystallite size of 9.0 ± 0.5 nm, demonstrating that only 1 min is sufficient to crystallize the phase, Figure 4. The crystallization mechanism of similar GCs was extensively studied in previous papers [42,48], demonstrating how the decomposition reaction of lanthanide fluoroacetates leads to precipitation of NCs once the crystallization temperature is reached. The crystallization mechanism of these materials is, therefore, completely different to that of oxyfluoride glasses by MQ in which the crystal growth is a diffusion-controlled process. Chemical bonds between fluorine and the glass matrix were observed using $^{19}F$ Nuclear Magnetic Resonance (NMR) [42]. Instead, for the xerogel samples, the fluorine environment is exactly the same as in the precursor TFA acid; almost all fluorine is then found in the form of $LaF_3$ after the crystallization process [42]. Furthermore, it was demonstrated that an increase of treatment time does not increase the crystal size or the crystal fraction of bulk samples; in contrast, crystal dissolution is observed for very long heat treatment times. Such results are clearly inconsistent with a diffusion-controlled process.

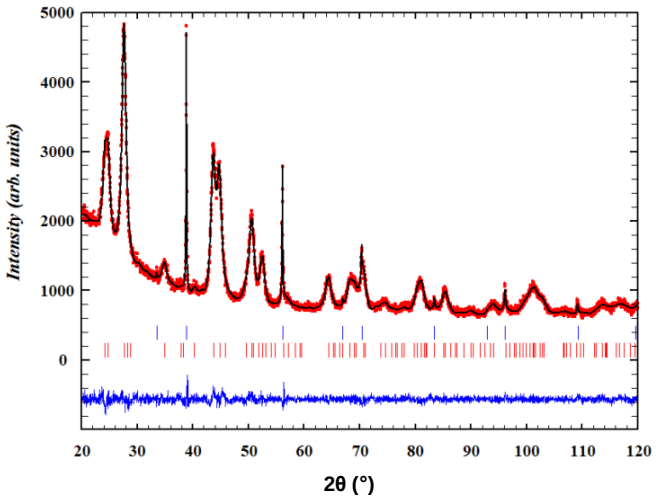


**Figure 4**. Observed (small red circles), calculated (continuous black line) and difference (continuous blue line at the bottom) XRD profiles of $80SiO_2$-$20LaF_3$-$0.5Er^{3+}$self-supported layer treated at 550 °C mixed with 9 wt.% NaF as internal standard. Bragg peaks of NaF and $LaF_3$ are indicated by blue and red vertical bars, respectively.

Quantitative Rietveld refinement of the $LaF_3$ crystalline fraction with NaF as internal standard was carried out for $80SiO_2$-$20LaF_3$ $0.5Er^{3+}$ bulk GC treated at 550 °C for 1 min [47]. The

observed diffraction pattern and the difference between observed and calculated diffraction patterns are shown in Figure 4. Weight fractions (wt%) of 17.8% and 82.2% were determined for the $LaF_3$ crystalline fraction and glassy phase, respectively. To our knowledge, this represents the highest crystal fraction reported in the literature for transparent OxGCs prepared by SG methods and it is the highest crystal fraction reported so far for $LaF_3$-OxGCs prepared by both MQ and SG [36]. A small shift of the diffraction peaks towards higher 2θ was also observed for the $Er^{3+}$-doped GC. This provides evidence of $Er^{3+}$ incorporation since the smaller $Er^{3+}$ ions (1.17 Å) on the sites of the larger $La^{3+}$ (1.31 Å) ion decrease the unit-cell volume (Table 1).

**Table 1.** Lattice constants of $80SiO_2$-$20LaF_3$-$0.5Er^{3+}$ GC bulk sample treated at 550°°C for 1 min

| **Sample** | **a(Å)** | **c(Å)** | **Unit Cell Volume ($Å^3$)** |
|---|---|---|---|
| Undoped $LaF_3$ [JCPDS][1] | 7.187 | 7.350 | 328 |
| $Er^{3+}$ doped GCs 550°C 1m | 7.16±0.01 | 7.32±0.01 | 325±1 |

[1] JCPDS cards no 00-032-0483. Ionic sizes in n-fold coordination for hexagonal phase: 1.31 Å for $La^{3+}$ and 1.17 Å for $Er^{3+}$ [49].

GI-XRD pattern of thin film was obtained at the BM25B-SpLine beamline of the ESRF [37] and is shown in Figure 5a. The XRD of bulk sample has also been acquired for comparison, Figure 5b. For the thin film, only a broad band, which could be deconvoluted into two peaks associated to $LaF_3$ crystals (Figure 5a). In this case, the crystallite size was much smaller, ~ 2.5 ± 0.5 nm. The difference in crystallite size between bulk and film samples, is likely to be related to the synthesis and sintering conditions since more diluted sols are necessary for film deposition with respect to bulk materials and during the sintering the coating densifies only by shrinkage normal to the substrate. Moreover, the fast evaporation of the solvent during the heat treatment may lead to the precipitation of such small NCs. This difference in crystal size between films and bulk-like materials has also been reported previously for similar systems but a clear explanation is still necessary [50]. For comparison, Figure 5b shows the XRD of bulk samples of the same composition treated under the same conditions.

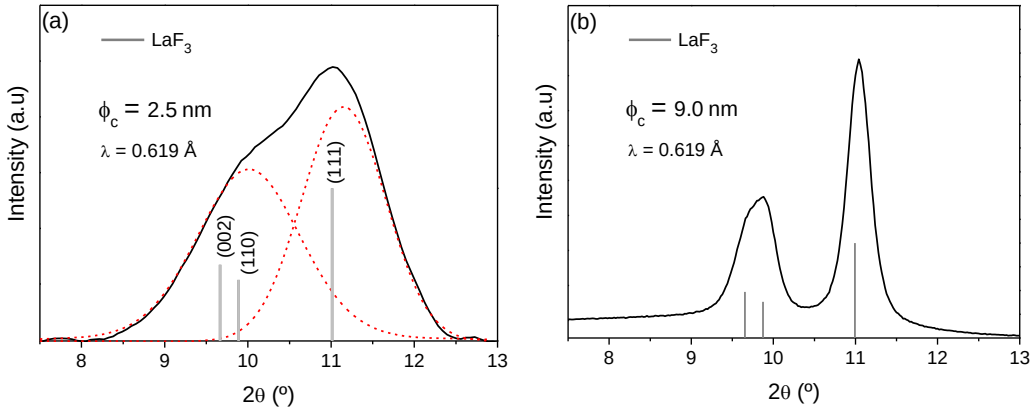


**Figure 5**. (a) GI-XRD of thin film and (b) XRD of bulk sample of composition $80SiO_2$-$20LaF_3$ $0.5Er^{3+}$ (TEOS-MTES) treated at 550 °C for 1 min. The crystal size is given together with the $LaF_3$ reference shown with vertical bars (JCPDS 00-032-0483).

### *3.4. HRTEM and nanostructure characterization*

HRTEM was used to reveal the lattice planes and crystal-size distribution of $LaF_3$ crystals in the thin films (Figure 6(a)-(c)) and self-supported layers ((d)-(f)) treated at 550 °C for 1 min. Small crystals are homogeneously distributed in the glass matrix. The crystal size is around 2.0 ± 0.5 nm and 8.0 ± 0.5 nm for films and self-supported layers, respectively, in agreement with the GI-XRD and XRD results. A similar structure is observed in both samples, consisting of separated crystals surrounded by the residual $SiO_2$ matrix. Fourier Transformation of the [111] crystal planes of the $LaF_3$ Tysonite phase was employed to estimate an interplanar distance of 0.33 nm [51]. These results demonstrate the absence of clusters even for such short heat treatment times and further support the hypothesis that the crystallization mechanism involves chemical decomposition followed by crystal precipitation.

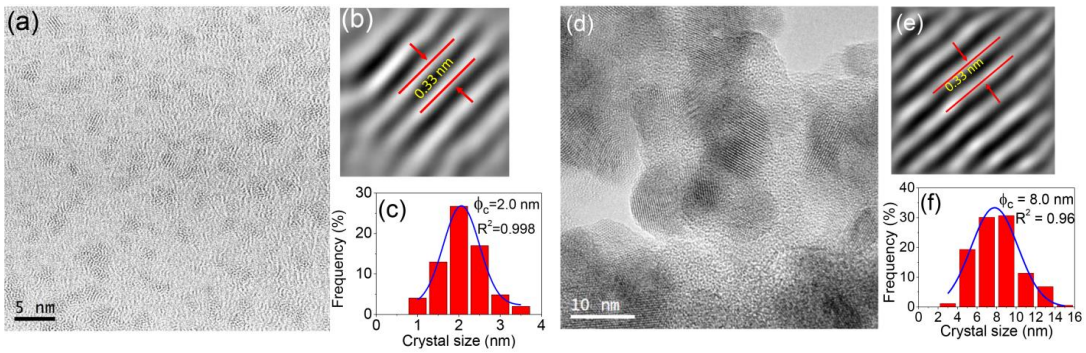


**Figure 6**. (a) HRTEM micrograph, (b) lattice distance and (c) crystal-size distribution of $80SiO_2$-$20LaF_3$ $0.5Er^{3+}$ thin film treated at 550 °C for 1 min. (d) HRTEM micrograph, (e) lattice distance and (f) crystal-size distribution of $80SiO_2$-$20LaF_3$ $0.5Er^{3+}$ self-supported layer treated at 550 °C for 1 min.

### *3.5. XAS, EPR and RE environment*

A crucial aspect of RE-doped OxGCs concerns distribution of dopants and the mechanism of incorporation into the fluoride NCs. In fact, RE ions are much more efficient when are embedded in low-phonon-energy fluoride crystals. Evidence of RE incorporation is often obtained by optical spectroscopy but sometimes only indirectly, unless specific selective excitation measurements are carried out. Here, the RE-ion environment and how it changes on transformation of the xerogel to the GCs have been studied in detail using the local structural techniques XAS and EPR.

XAS measurements of $Er_2O_3$ and $ErF_3$ were used as reference and compared to the results of thin films doped with $0.5Er^{3+}$, Figure 7. The presence of $Er^{3+}$ is clearly indicated by the absorption edge centred around 8370 eV. However, small shifts of the edge are produced by different ligand fields. In general, for the same RE ion, the edge energy increases passing from oxides to fluorides due to lesser hybridization of the chemical bonds in fluoride compounds attributable to a higher field strength [52–54]. In this case, the edge was obtained by the first derivative of the absorption spectrum and the edge shifts from 8356.6 to 8359 eV passing from $Er_2O_3$ to $ErF_3$. More insights are obtained by a comparison of the post-edge region that contains information about the local structure. In particular, the X-Ray Absorption Near Edge Structure (XANES) shown in Figure 7 as red and black spectra, for $ErF_3$ and $Er_2O_3$, respectively, show slight differences at the white line and at resonances of ~8375 and 8395 eV. The XANES spectra and derivative of the xerogel and OxGC thin film (bottom inset of Figure 7) exhibit an absorption edge centred at ~8359 eV, similar to pure $ErF_3$. Hence, a fluorine-rich environment is already observed in the xerogel. Nevertheless, differences in the XANES region (8370-8415 eV) are observed compared to $ErF_3$, which may indicate a change in the $Er^{3+}$ environment for the xerogel and the OxGC samples. Fourier-Transform calculations indicate a narrowing of the first shell as the xerogel transforms to the OxGC, which is consistent with the development of a higher symmetry environment corresponding to fluoride crystalline phase.

A linear combination of XANES spectra in the range 8325-8475 eV was performed for the OxGC sample using the standard $ErF_3$ and $Er_2O_3$ materials. Employing the crystal fraction of $LaF_3$ calculated by Rietveld refinement, approximate fractions of 91% and 9% were calculated for $Er^{3+}$ in $ErF_3$ and $Er_2O_3$-like environments, respectively. Thus, the $Er^{3+}$ ions are likely to be situated near fluoride ions in the xerogel state, precipitating in fluoride-rich crystals after the heat treatment at 550 °C for 1 min. These results are explained considering that, in the starting sol, the $La^{3+}$ and $Er^{3+}$ ions are surrounded by TFA cations that are screened and impeded from bonding with Si atoms. Hence, in the xerogel sample, fluorine is still coordinated as in TFA acid [42] and $Er^{3+}$ ions are principally coordinated by fluorine. During the heat treatment, decomposition promotes the precipitation of $LaF_3$ crystals in which $Er^{3+}$ ions become trapped.

Other techniques, such as Energy Dispersive X-Ray Spectroscopy (EDXS), demonstrated an Eu enrichment in $GdF_3$ NCs after just 1 min of treatment at 550 °C [48], further supporting the aforementioned conclusions.

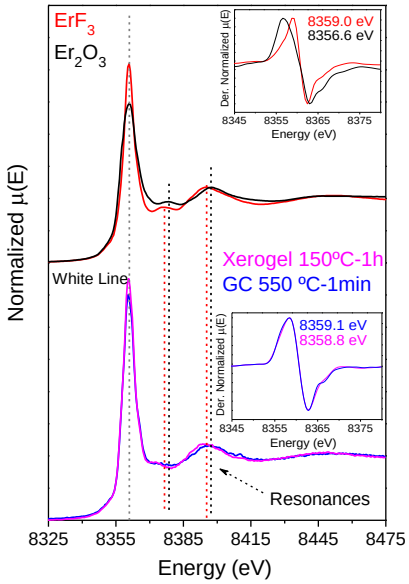


**Figure 7**.XAS spectra and derivatives (inset) of $Er_2O_3$ and $ErF_3$ references in black and red, respectively (top), and of XAS spectra and derivatives (inset) of $80SiO_2$-$20LaF_3$-$0.5Er^{3+}$ (TEOS-MTES) xerogel and GC thin film treated at 550 °C for 1 min, in pink and blue, respectively (bottom). The grey line indicates the white line and the red and black lines indicate resonance positions for $ErF_3$ and $Er_2O_3$, respectively.

Once the crystal fraction is obtained, an indication of the concentration of RE ions in $LaF_3$ crystals may be obtained. Supposing that 91 % of $Er^{3+}$ ions are embedded in the crystal phase and that the crystalline fraction is ~18 wt% (XRD), the effective concentration of $Er^{3+}$ ions in the crystal phase is around 6.5 mol%, representing an order of magnitude increase with respect to the nominal concentration (0.5 mol%). Similar values were obtained in previous studies of samples prepared by MQ, albeit with a lower fraction of RE ions incorporated in the crystal phase [55].

Further evidence supporting the mechanism for the incorporation RE ions is obtained by EPR of self-supported layers. Figure 8 shows the EPR spectra of xerogel samples doped with $0.5Er^{3+}$ (mol%) measured at 5 K. The EPR signal of a glass, prepared by MQ, containing $0.5Er^{3+}$ in an amorphous fluorine-rich environment is also shown for comparison. Several resonances are observed for the xerogel samples due to the presence of organic compounds which remain after heat treatment at 50 °C. $Er^{3+}$ resonances are associated with the broad signals appearing in the range 500-1000 G. Other authors reported EPR measurements of $Er^{3+}$ in oxyfluoride glasses showing the presence of broad signals at low magnetic fields (high g values) [56]. Moreover, such resonances disappear at RT and are only visible below 20 K, indicating that they are

associated with $Er^{3+}$ ions. Such broad signals are clearly related to an amorphous environment typical of glasses and liquids. The EPR signal of an oxyfluoride glass doped with $0.5Er^{3+}$ prepared by MQ is also shown for comparison. The signal around 2300 G, observed only in the xerogel, is attributed to the presence of organic compounds. Interesting results are obtained for the GC samples, which display resonances associated to paramagnetic species with effective spin *S'*=1/2 in rhombic or lower symmetry after just 1 min of heat treatment; the resonances appear at g values of $g_1$=11.2; $g_2$=4.9 and $g_3$=3.1. On comparison with the EPR results obtained for an $Er^{3+}$-doped $LaF_3$ single crystal [57,58], it can be unambiguously concluded that the resonances in the GC samples are those of $Er^{3+}$ in $LaF_3$ NCs. Broader signals are observed for the GC doped with $0.5Er^{3+}$ and associated to stronger relaxation processes due to a moderately high effective concentration.

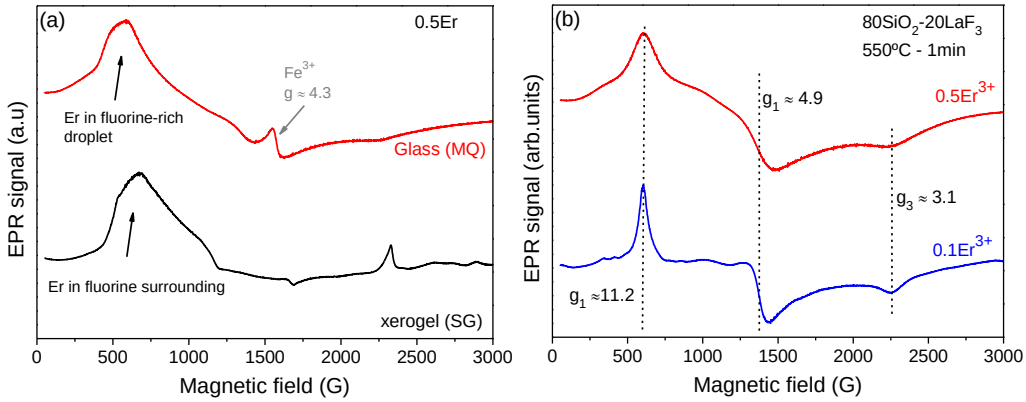


**Figure 8**. (a) EPR signals for the $80SiO_2$-$20LaF_3$-$0.5Er^{3+}$ xerogel and of a MQ glass doped with $0.5Er^{3+}$. (b) EPR signals of $80SiO_2$-$20LaF_3$ GCs doped with 0.1 and $0.5Er^{3+}$ (mol%) treated at 550 °C for 1 min.

For the composition with a lower concentration of dopant, the hyperfine structure is only partially resolved, due to the interaction of the electrons with nuclear spins. The low intensity of the hyperfine structure is due to the quantity of Er isotope nuclei with *I*=7/2 (~23%), while the remaining nuclei (77%) with *I*=0 do not produce any hyperfine interaction [56,59,60]. For the composition doped with $0.5Er^{3+}$, the hyperfine structure is too broad to be resolved but its presence may be discerned from the shape of the resonance at $g_1$=11.2 which presents broader sidebands. Another interesting result is the absence of any further $Er^{3+}$ resonance other than that of $Er^{3+}$ in the $LaF_3$ NCs.

These results, together with the previous discussion of XAS measurements, indicate that dopant incorporation occurs with crystal precipitation. In contrast, in melted glasses, residual contributions of RE ions in an amorphous environment are still observed even after the crystallization process, confirming that some RE ions remain in the glass matrix or in phase-separation droplets.

*3.6. Photoluminescence (PL)*

The near-infrared emission spectra corresponding to the $^4I_{13/2} \rightarrow {}^4I_{15/2}$ transition for $80SiO_2$-$20LaF_3$-$0.5Er^{3+}$ supported layer heat treated at 550 °C for 1 min were obtained at room temperature and at 9 K by exciting at 793 nm in the $^4I_{15/2} \rightarrow {}^4I_{9/2}$ absorption band. After excitation of this level, the next lower levels are populated by multiphonon relaxations. The room temperature emission spectrum (Figure 9a) shows a series of peaks with a maximum around 1540 nm. Figure 9b shows the excitation spectrum corresponding to the $^4I_{15/2} \rightarrow {}^4I_{9/2}$ transition obtained by collecting the luminescence spectrum at 1540 nm, revealing well defined peaks which suggest the partial incorporation of $Er^{3+}$ ions in the $LaF_3$ NCs.

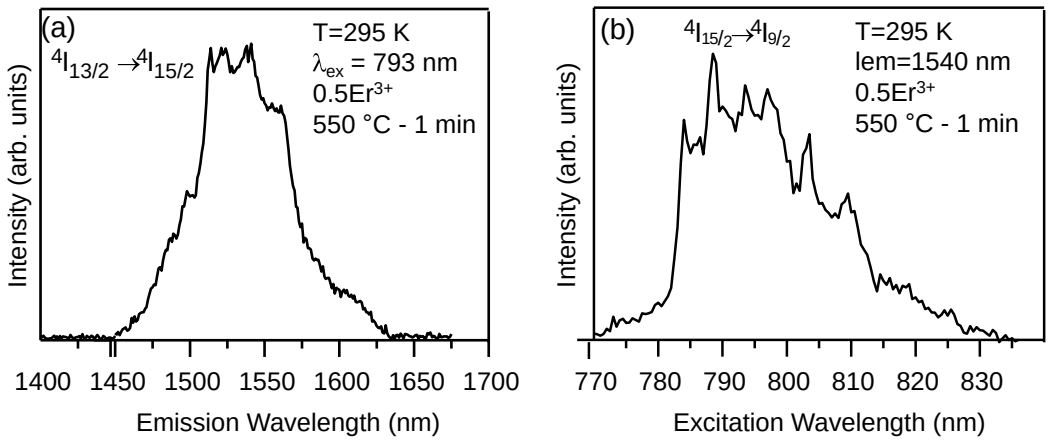


**Figure 9**. (a) Room temperature emission spectrum of $80SiO_2$-$20LaF_3$-$0.5Er^{3+}$ bulk sample heat treated at 550°C for 1h obtained on exciting at 793 nm. (b) Low-temperature excitation spectrum obtained at 1540 nm.

The incorporation of $Er^{3+}$ ions into $LaF_3$ NCs is unambiguously confirmed by measurements performed at low temperature. Figures 10a and b show the emission and excitation spectra, respectively, obtained at 9 K. The emission spectrum shows sharp peaks superimposed on a broad band. The excitation spectrum obtained by collecting the luminescence at the emission maximum also shows very well defined peaks. The features exhibited by the low-temperature spectra confirm the partial incorporation of $Er^{3+}$ ions in the NCs and provide evidence of the crystalline and amorphous $Er^{3+}$ environments.

Although, the emission and excitation spectra of the $80SiO_2$-$20LaF_3$-$0.5Er^3$ bulk sample show well-defined peaks, they are quite broad suggesting the presence of both crystalline and amorphous $Er^{3+}$ environments in the doped $80SiO_2$-$20LaF_3$-$0.5Er^{3+}$ GC sample.

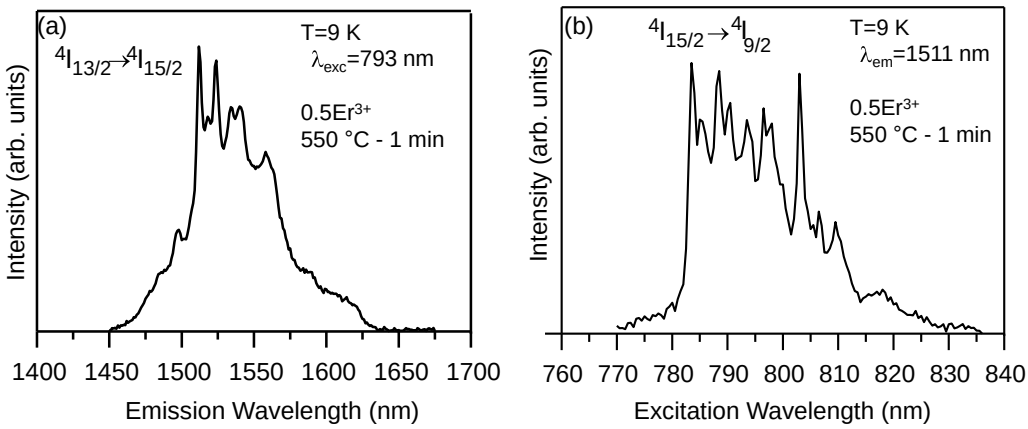


**Figure 10**. (a) Low temperature emission spectrum of $80SiO_2$-$20LaF_3$-$0.5Er^{3+}$ bulk sample heat treated at 550 °C for 1 min on exciting at 793 nm. (b) Low temperature luminescence spectrum obtained at 1511 nm.

The room temperature emission spectra of $80SiO_2$-$20LaF_3$ thin films doped with 0.1 and $0.5Er^{3+}$ heat treated at 550 °C for 1 h corresponding to the $^4I_{13/2}\rightarrow{}^4I_{15/2}$ transition obtained by exciting at 980 nm reveal a glass-like behaviour. Figure 11 shows the emission spectra for thin films doped with 0.1 and 0.5% $Er^{3+}$. In both samples the spectrum shows an unresolved structure with a maximum at around 1540 nm which indicates the absence of a crystalline environment for $Er^{3+}$ ions.

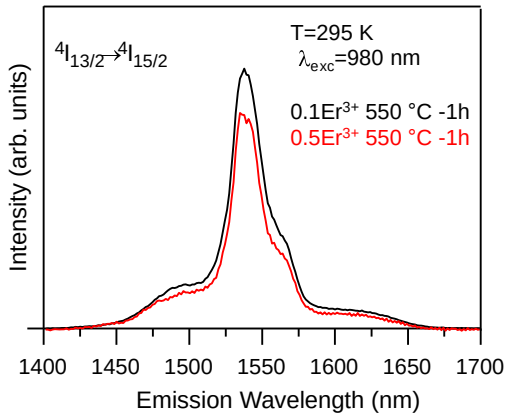


**Figure 11**. Room temperature emission spectrum of $80SiO_2$-$20LaF_3$ thin films doped with 0.1% (black line) and 0.5% (red line) $Er^{3+}$ heat treated at 550 °C for 1 h obtained on exciting at 980 nm.

## 4. Conclusions

For the first time the preparation of transparent oxyfluoride glass ceramics of composition $80SiO_2$-$20LaF_3$ containing $Er^{3+}$- dopant have been prepared by sol-gel using TEOS and MTES as silica precursors. XRD and HRTEM showed the precipitation of $LaF_3$ nanocrystals, with size of 9 and 3 nm, after heat treatment at 550 °C for 1 min for bulk and thin film, respectively.

Rietveld refinement indicated a $LaF_3$ crystal fraction of ~ 18 wt% for the bulk glass ceramic. To our knowledge, this represents the highest crystal fraction reported in the literature for transparent oxyfluoride glass ceramics prepared by both melt-quenching and sol-gel methods. XAS and EPR shown a fluorine-rich amorphous environment in the xerogel and confirmed the presence of $Er^{3+}$ in the $LaF_3$ nanocrystals after crystallization, with a concentration around one order of magnitude higher than the nominal value. No XAS and EPR results have previously been reported for RE-doped oxyfluoride glass-ceramics prepared by sol-gel. The incorporation of $Er^{3+}$ ions into $LaF_3$ nanocrystals was unambiguously confirmed by measurements performed at low temperature. A clear difference is found between the emission spectra of thin films and bulk samples, likely related to the different crystal size.

**Acknowledgments**

This work was supported by MINECO under projects MAT2013-48246-C2-1-P/-2-P and MAT2017-87035-C2-1-P/-2-P (AEI/FEDER, UE), and Basque Country University PPG17/07 and GIU17/014. We acknowledge The European Synchrotron (ESRF), MINECO, and CSIC for provision of synchrotron radiation facilities in using the BM25-SpLine beamline. We also thank the BM25-SpLine staff for the technical support beyond their duties. This presentation is a part of dissemination activities of project FunGlass. This project has received funding from the European Union´s Horizon 2020 research and innovation program under grant agreement No 739566. A.S. acknowledges the financial support from the Comunidad de Madrid for an "Atración de Talento Investigador" contract (No. 2017-t2/IND5395). D.B acknoweledges "Ministerio de Ciencia e Innovación" for the project MAT2016-75362-C3-1-R.

**REFERENCES**

[1] Wang, Y.; Ohwaki, J. New transparent vitroceramics codoped with $Er^{3+}$ and $Yb^{3+}$ for efficient frequency upconversion. *Appl. Phys. Lett*. **1993**, *63*, 3268–3270.

[2] Dejneka, M.J. The luminescence and structure of novel transparent oxyfluoride glass-ceramics. *J. Non-Cryst. Solids* **1998**, *239*, 149–155.

[3] Tanabe, S.; Hayashi, H.; Hanada, T.; Onodera, N. Fluorescence properties of $Er^{3+}$ ions in glass ceramics containing $LaF_3$ nanocrystals. *Opt. Mater.* **2002**, *19*, 343–349.

[4] Lavin, V.; Iparraguirre, I.; Azkargorta, J.; Mendioroz, A.; González-Plata, J.; Balda, R.; Fernández, J. Stimulated and upconverted emissions of $Nd^{3+}$ in a transparent oxyfluoride glass-ceramic. *Opt. Mater.* **2004**, *25*, 201–208.

[5] Mattarelli, M.; Tikhomirov, V.K.; Seddon, A.B.; Montagna, M.; Moser, E. $Tm^{3+}$-activated transparent oxy-fluoride glass–ceramics : structural and spectroscopic properties. *J. Non-Cryst. Solids* **2004**, *346*, 354–358.

[6] Chen, D.; Wang, Y.; Yu, Y.; Huang, P.; Weng, F. Near-infrared quantum cutting in $Ho^{3+}/Yb^{3+}$ codoped nanostructured glass ceramic. *Opt. Lett*. **2011**, *36*, 876–878.

[7] de Pablos-Martín, A.; Durán, A.; Pascual, M.J. Nanocrystallization in oxyfluoride systems: mechanisms of crystallization and photonic properties. *Int. Mater. Rev*. **2012**, *57*, 165–186.

[8] Wei, Y.; Li, J.; Yang, J.; Chi, X.; Guo, H. Enhanced green upconversion in $Tb^{3+}$-$Yb^{3+}$ co-doped oxyfluoride glass ceramics containing $LaF_3$ nanocrystals. *J. Lumin*. **2013**, *137*, 70–72.

[9] de Pablos-Martín, A.; Ferrari, M.; Pascual, M.J.; Righini, G.C. Glass-ceramics: A class of nanostructured materials for photonics. *Riv. Nuovo Cimento* **2015**, *38*, 311–369.

[10] Fedorov, P.P.; Luginina, A.A.; Popov, A.I. Transparent oxyfluoride glass ceramics. *J. Fluor. Chem.* **2015**, *172*, 22–50.

[11] Pascual, M.J.; Garrido, C.; Durán, A.; Pascual, L.; de Pablos-Martín, A.; Fernández, J.; Balda, R. Optical Properties of Transparent Glass–Ceramics Containing $Er^{3+}$-Doped Sodium Lutetium Fluoride Nanocrystals. *Int. J. Appl. Glass Sci*. **2016**, *40*, 27–40.

[12] Gorni, G.; Velázquez, J.J.; Mather, G.C.; Durán, A.; Chen, G.; Sundararajan, M.; Balda, R.; Fernández, J.; Pascual, M.J. Selective excitation in transparent oxyfluoride glass-ceramics doped with $Nd^{3+}$. *J. Eur. Ceram. Soc*. **2017**, *37*, 1695–1706.

[13] Gorni, G.; Balda, R.; Fernández, J.; Pascual, L.; Durán, A.; Pascual, M.J. Effect of the heat treatment on the spectroscopic properties of $Er^{3+}$-$Yb^{3+}$- doped transparent oxyfluoride nano-glass-ceramics. *J. Lumin*. **2018**, *193*, 51–60.

[14] Velázquez, J.J.; Balda, R.; Fernández, J.; Gorni, G.; Pascual, L.; Chen, G.; Sundararajan, M.; Durán, A.; Pascual, M.J. Transparent oxy fl uoride glass-ceramics with $NaGdF_4$ nanocrystals doped with $Pr^{3+}$ and $Pr^{3+}$-$Yb^{3+}$. *J. Lumin.* **2018**, *193*, 61–69.

[15] Samson, B.N.; Tick, P.A.; Borrelli, N.F. Efficient neodymium-doped glass-ceramic fiber laser and amplifier. *Opt. Lett***. 2001**, *26*, 145–147.

[16] Reben, M.; Jaglarz, J. $Nd^{3+}$-Doped Oxyfluoride Glass Ceramics Optical Fibre with $SrF_2$ Nanocrystals. *Opt. Appl*. **2012**, *42*, 353–364.

[17] Lisiecki, R.; Augustyn, E.; Ryba-romanowski, W.; Zelechower, M. Er-doped and Er, Yb co-doped oxyfluoride glasses and glass – ceramics, structural and optical properties. *Opt. Mater*. **2011**, *33*, 1630–1637.

[18] Kang, S.; Fang, Z.; Huang, X.; Chen, Z.; Yang, D.; Xiao, X.; Qiu, J.; Dong, G. Precisely controllable fabrication of $Er^{3+}$-doped glass ceramic fibers: novel mid-infrared fiber laser materials. *J. Mater. Chem. C* **2017**, *5*, 4549–4556.

[19] Gorni, G.; Balda, R.; Fernández, J.; Iparraguirre, I.; Velázquez, J.J.; Castro, Y.; Pascual, L.; Chen, G.; Sundararajan, M.; Pascual, M.J.; et al. Oxyfluoride glass–ceramic fibers doped with $Nd^{3+}$: structural and optical characterization. *CrystEngComm* **2017**, *19*, 6620–6629.

[20] Kang, S.; Yu, H.; Ouyang, T.; Chen, Q.; Huang, X.; Chen, Z.; Qiu, J.; Dong, G. Novel $Er^{3+}$/$Ho^{3+}$-codoped glass-ceramic fibers for broadband tunable mid-infrared fiber lasers. *J. Am. Ceram. Soc*. **2018**, *101*, 3956–3967.

[21] Fujihara, S.; Mochizuki, C.; Kimura, T. Formation of $LaF_3$ microcrystals in sol-gel silica. *J. Non-Cryst. Solids* **1999**, *244*, 267–274.

[22] Biswas, A.; Maciel, G.S.; Friend, C.S.; Prasad, P.N. Upconversion properties of a transparent $Er^{3+}$-$Yb^{3+}$ co-doped $LaF_3$-$SiO_2$ glass-ceramics prepared by sol-gel method. *J. Non- Cryst. Solids* **2003**, *316*, 393–397.

[23] Fujihara, S.; Koji, S.; Kimura, T. Structure and optical properties of (Gd,Eu)$F_3$-nanocrystallized sol–gel silica films. *J. Mater. Chem.* **2004**, *14*, 1331–1335.

[24] Ribeiro, S.J.L.; Araújo, C.C.; Bueno, L. A.; Gonçalves, R.R.; Messaddeq, Y. Sol-gel $Eu^{3+}$/$Tm^{3+}$ doped transparent glass-ceramic waveguides. *J. Non-Cryst. Solids* **2004**, *348*, 180–184.

[25] Luo, W.; Wang, Y.; Bao, F.; Zhou, L.; Wang, X. Crystallization behavior of PbF2-SiO2based bulk xerogels. *J. Non-Cryst. Solids* **2004**, *347*, 31–38.

[26] Zhou, L.; Chen, D.; Luo, W.; Wang, Y.; Yu, Y.; Liu, F. Transparent glass ceramic containing $Er^{3+}$: $CaF_2$ nano-crystals prepared by sol–gel method. *Mater. Lett.* **2007**, *61*, 3988–3990.

[27] Velázquez, J.J.; Yanes, A.C.; Del-Castillo, J.; Méndez-Ramos, J.; Rodríguez, V.D. Optical properties of $Ho^{3+}$-$Yb^{3+}$ co-doped nanostructured $SiO_2$-$LaF_3$ glass-ceramics prepared by sol-gel method. *Phys. Status Solidi* **2007**, *204*, 1762–1768.

[28] del-Castillo, J.; Yanes, A.C. Bright luminescence of $Gd^{3+}$ sensitized $RE^{3+}$-doped $SiO_2$-$BaGdF_5$ glass-ceramics for UV-LEDs colour conversion. *J. Alloys Compd.* **2017**, *695*, 3736–3743.

[29] Szpikowska-Sroka, B.; Pawlik, N.; Goryczka, T.; Pietrasik, E.; Bańczyk, M.; Pisarski, W.A. Lead fluoride β-$PbF_2$ nanocrystals containing $Eu^{3+}$ and $Tb^{3+}$ ions embedded in sol-gel materials: Thermal, structural and optical investigations. *Ceram. Int.* **2017**, *43*, 8424–8432.

[30] Szpikowska-Sroka, B.; Pawlik, N.; Goryczka, T.; Pisarski, W.A. Influence of silicate sol-gel host matrices and catalyst agents on the luminescent properties of $Eu^{3+}/Gd^{3+}$ under different excitation wavelengths. *RSC Adv*. **2015**, *5*, 98773–98782.

[31] Secu, C.E.; Bartha, C.; Polosan, S.; Secu, M. Thermally activated conversion of a silicate gel to an oxyfluoride glass ceramic: Optical study using $Eu^{3+}$ probe ion. *J. Lumin*. **2014**, *146*, 539–543.

[32] Secu, C.E.; Negrea, R.F.; Secu, M. $Eu^{3+}$ probe ion for rare-earth dopant site structure in sol–gel derived $LiYF_4$ oxyfluoride glass–ceramic. *Opt. Mater*. **2013**, *35*, 2456–2460.

[33] Santana-Alonso, A.; Méndez-Ramos, J.; Yanes, A.C.; Del-Castillo, J.; Rodríguez, V.D. Up-conversion in sol-gel derived nano-glass-ceramics comprising $NaYF_4$ nano-crystals doped with $Yb^{3+}$, $Ho^{3+}$ and $Tm^{3+}$. *Opt. Mater*. **2010**, *32*, 903–908.

[34] Szpikowska-Sroka, B.; Zur, L.; Czoik, R.; Goryczka, T.; Swinarew, A.S.; Zadlo, M.; Pisarski, W.A. Effect of fluoride ions on the optical properties of $Eu^{3+}$: $PbF_2$ nanocrystals embedded into sol-gel host materials. *Mater. Chem. Phys*. **2016**, *174*, 138–142

[35] Hench, L.L.; West, J.K. The sol-gel process. *Chem. Rev*. **1990**, *90*, 33–72.

[36] Gorni, G.; Velázquez, J.J.; Mosa, J.; Balda, R.; Fernández, J.; Durán, A.; Castro, Y. Transparent Glass-Ceramics Produced by Sol-Gel : A Suitable Alternative for Photonic Materials. *Materials* **2018**, *11*, 212.

[37] Rubio-zuazo, J.; Ferrer, P.; López, A.; Gutiérrez-León, A.; Silva, I.; Castro, G.R. Nuclear Instruments and Methods in Physics Research A The multipurpose X-ray diffraction end-station of the BM25B-SpLine synchrotron beamline at the ESRF. *Nucl. Inst. Methods Phys. Res. A* **2013**, *716*, 23–28.

[38] Rodríguez-Carvajal, J. Recent advances in magnetic structure determination by neutron powder diffraction. Phys. *B Condens. Matter* **1993**, *192*, 55–69.

[39] Ravel, B.; Newville, M. ATHENA, ARTEMIS, HEPHAESTUS: data analysis for X-ray absorption spectroscopy using IFEFFIT. *J. Synchrotron Radiat*. **2005**, *12*, 537–541.

[40] Innocenzi, P.; Abdirashid, M.O.; Guglielmi, M. Structure and properties of sol-gel coatings from methyltriethoxysilane and tetraethoxysilane. *J. Sol-Gel Sci. Technol.* **1994**, , 47–55.

[41] Ma, Y.; Lee, H.R.; Tsuru, T. Study on Preparation and Hydrophobicity of MTES Derived Silica Sol and Gel. *Adv. Mater. Res*. **2012**, *535–537*, 2563–2566.

[42] Gorni, G.; Pascual, M.J.; Caballero, A.; Velázquez, J.J.; Mosa, J.; Castro, Y.; Durán, A. Crystallization mechanism in sol-gel oxyfluoride glass-ceramics. *J. Non-Cryst. Solids* **2018**, *501*, 145–152.

[43] Yu, Y.; Chen, D.; Cheng, Y.; Wang, Y.; Hu, Z.; Bao, F. Investigation on crystallization and influence of $Nd^{3+}$ doping of transparent oxyfluoride glass-ceramics. *J. Eur. Ceram. Soc*. **2006**, *26*, 2761–2767.

[44] Bhattacharyya, S.; Bocker, C.; Heil, T.; Jinschek, R.; Höche, T.; Rüssel; Kohl, H.; Kohl, H. Experimental Evidence of Self-Limited Growth of Nanocrystals in Glass Experimental Evidence of Self-Limited Growth of Nanocrystals in Glass. *Nano Lett*. **2009**, *9*, 2493–2496.

[45] Bhattacharyya, S.; Höche, T.; Hemono, N.; Pascual, M.J.; van Aken, P.A. Nano-crystallization in $LaF_3$-$Na_2O$-$Al_2O_3$-$SiO_2$ glass. *J. Cryst. Growth* **2009**, *311*, 4350–4355.

[46] de Pablos-Martín, A.; Muñoz, F.; Mather, G.C.; Patzig, C.; Bhattacharyya, S.; Jinschek, J.R.; Höche, T.; Durán, A.; Pascual, M.J. $KLaF_4$ nanocrystallization in oxyfluoride glass-ceramics. *CrystEngComm* **2013**, *15*, 10323.

[47] de Pablos-Martín, A.; Hémono, N.; Mather, G.C.; Bhattacharyya, S.; Höche, T.; Bornhöft, H.; Deubener, J.; Muñoz, F.; Durán, A.; Pascual, M.J. Crystallization kinetics of $LaF_3$ nanocrystals in an oxyfluoride glass. *J. Am. Ceram. Soc*. **2011**, *94*, 2420–2428.

[48] Velázquez, J.J.; Mosa, J.; Gorni, G.; Balda, R.; Fernández, J.; Pascual, L.; Durán, A.; Castro, Y. Transparent $SiO_2$-$GdF_3$ sol–gel nano-glass ceramics for optical applications. *J. Sol-Gel Sci. Technol*. **2019**, *89*, 322–332.

[49] Jia, Y.Q. Crystal radii and effective ionic radii of the rare earth ions. *J. Solid State Chem*. 1991, 95, 184–187.

[50] Gorni, G.; Balda, R.; Fernández, J.; Velázquez, J.J.; Pascual, L.; Mosa, J.; Durán, A.; Castro, Y. $80SiO_2$ -$20LaF_3$ oxyfluoride glass ceramic coatings doped with $Nd^{3+}$ for optical applications. *Int. J. Appl. Glass Sci*. **2018**, *9*, 208–217.

[51] Li, F.; Li, C.; Liu, X.; Bai, T.; Dong, W.; Zhang, X.; Shi, Z.; Feng, S. Microwave-assisted synthesis and up–down conversion luminescent properties of multicolor hydrophilic $LaF_3$:$Ln^{3+}$ nanocrystals. *Dalt. Trans*. **2013**, *42*, 2015–2022.

[52] Agarwal, B.K.; Verma, L.P. A rule for chemical shifts of X-ray absorption edges. *J. Phys. C Solid State Phys.* **1970**, *3*, 535–537.

[53] Choi, Y.G. Covalence of chemical bonds and white-line intensity of an L3-edge X-ray absorption near-edge structure of rare earth elements embedded in glass. *Met. Mater. Int*. **2009**, *15*, 993–999.

[54] Figueroa, A.I.; van der Laan, G.; Harrison, S.E.; Cibin, G.; Hesjedal, T. Oxidation Effects in Rare Earth Doped Topological Insulator Thin Films. *Sci. Rep*. **2016**, *6*, 22935.

[55] de Pablos-Martín, A.; García, M. A.; Muñoz-Noval, A.; Castro, G.R.; Pascual, M.J.; Durán, A. Analysis of the distribution of $Tm^{3+}$ ions in $LaF_3$ containing transparent glass-ceramics through X-ray absorption spectroscopy. *J. Non-Cryst. Solids* **2014**, *384*, 83–87.

[56] Dantelle, G.; Mortier, M.; Vivien, D. EPR and optical studies of erbium-doped β-$PbF_2$ single-crystals and nanocrystals in transparent glass– ceramics. *Phys. Chem. Chem. Phys*. **2007**, *9*, 5591–5598.

[57] Baker, J.M.; Rubins, R.S. Electron Spin Resonance in Two Groups of Lanthanon Salts. *Proc. Phys. Soc*. **1961**, *78*, 1353–1360.

[58] Schulz, M.B.; Jefries, C.D. Spin-Lattice Relaxation of Rare-Earth Ions in $LaF_3$. Phys. Rev. 1966, 149, 270–288.

[59] Budoyo, R.P.; Kakuyanagi, K.; Toida, H.; Matsuzaki, Y.; Munro, W.J.; Yamaguchi, H.; Saito, S. Electron paramagnetic resonance spectroscopy of $Er^{3+}$:$Y_2SiO_5$ using a Josephson bifurcation amplifier: Observation of hyperfine and quadrupole structures. *Phys. Rev. Mater*. **2018**, *2*, 11403.

[60] Yang, S.; Evans, S.M.; Halliburton, L.E.; Slack, G.A.; Schujman, S.B.; Morgan, K.E.; Bondokov, R.T.; Mueller, G.; Yang, S.; Evans, S.M.; et al. Electron paramagnetic resonance of ions in aluminum nitride Electron paramagnetic resonance of $Er^{3+}$ ions in aluminum nitride. *J. Appl. Phys.* **2009**, *105*, 23714–5.

# *PAPER 11*

**Transparent $SiO_2$-$GdF_3$ sol-gel nano-glass ceramics for optical applications.**

J.J. Velázquez, J. Mosa, G. Gorni, R. Balda, J. Fernández, L. Pascual, A. Durán, Y. Castro.

*J. Sol-Gel Sci. Techn*ol. **89** (2019) 322-332. doi: 10.1007/s10971-018-4693-z

# *Transparent $SiO_2$-$GdF_3$ sol–gel nano-glass ceramics for optical applications*

**J. J. Velázquez, J. Mosa, G. Gorni, R. Balda, J. Fernández, L. Pascual, A. Durán & Y. Castro**

**Journal of Sol-Gel Science and Technology**

ISSN 0928-0707
Volume 89
Number 1

J Sol-Gel Sci Technol (2019) 89:322-332
DOI 10.1007/s10971-018-4693-z

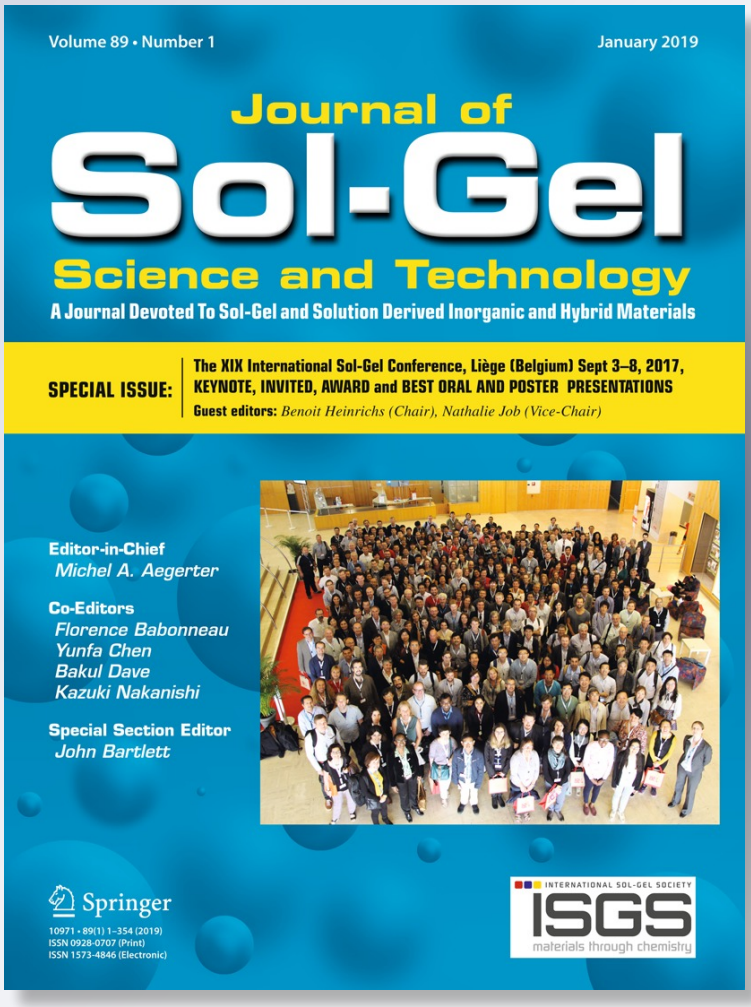


Springer

Journal of Sol-Gel Science and Technology (2019) 89:322–332
https://doi.org/10.1007/s10971-018-4693-z

ORIGINAL PAPER: SOL-GEL AND HYBRID MATERIALS FOR OPTICAL, PHOTONIC AND OPTOELECTRONIC APPLICATIONS

# Transparent $SiO_2$-$GdF_3$ sol–gel nano-glass ceramics for optical applications

J. J. Velázquez[1,2] · J. Mosa[1] · G. Gorni[1] · R. Balda[3,4] · J. Fernández[3,4] · L. Pascual[5] · A. Durán[1] · Y. Castro[1]

Received: 22 December 2017 / Accepted: 16 May 2018 / Published online: 1 June 2018


## Abstract

Transparent oxyfluoride nano-glass-ceramics (GCs) containing $GdF_3$ nanocrystals undoped and doped with 0.5 $Eu^{3+}$ (mol%) were obtained by a novel sol–gel method after sintering at temperatures such low as 550 °C. X-ray diffraction (XRD) and high-resolution transmission electron microscopy (HRTEM) show the precipitation of $GdF_3$ nanocrystals with size between 7 and 10 nm, depending on the crystalline phase (hexagonal or orthorhombic) and the heating time. Fourier transform infrared spectroscopy (FTIR) analysis allows following the system evolution during the heat treatment showing the decomposition of trifluoroacetic acid (TFA), used as fluorine precursor, together with the formation of fluoride lattice bonding. Energy dispersive X-ray (EDX) analysis confirms the incorporation of the RE ions in the fluoride nanocrystals in the GCs. The ions incorporation on the $GdF_3$ crystals is also supported by optical characterisation. Photoluminescence measurements result in a well resolved structure together with a narrowing of the $Eu^{3+}$ emission and excitation spectra in the GCs compared to the xerogel. Moreover, the asymmetry ratio between the electric dipole transition ($^5D_0 \rightarrow {}^7F_2$) to the magnetic dipole transition ($^5D_0 \rightarrow {}^7F_1$) is reduced in GCs, indicating that $Eu^{3+}$ ions are incorporated in the $GdF_3$ crystalline phases. Moreover, $Gd^{3+} \rightarrow Eu^{3+}$ energy transfer with enhancement of the energy transfer efficiency was observed in the GCs, further supported by fluorescence decay curves.

## Graphical Abstract

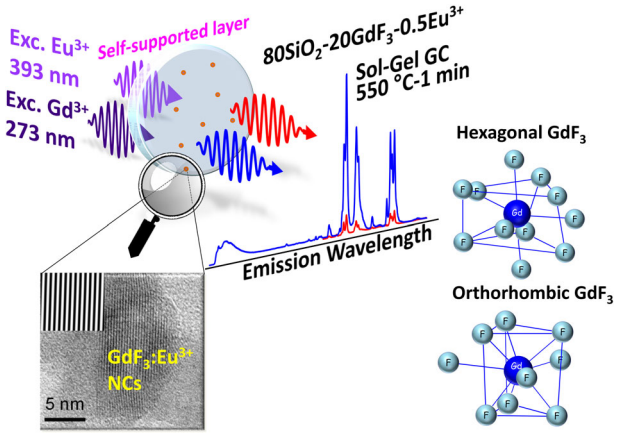


✉ Y. Castro
castro@icv.csic.es

[1] Grupo GlaSS, Instituto de Cerámica y Vidrio-CSIC, C/ Kelsen 5, 28049 Madrid, Spain

[2] FunGlass – Centre for Functional and Surface Functionalized Glass, Alexander Dubček University of Trenčín, Študentská 2, 911 50 Trenčín, Slovakia

[3] Applied Physic Department I, Superior school of Engineering, Pais Vasco University, Bilbao 48013, Spain

[4] Materials Physics Center CSIC-UPV/EHU, 20018 San Sebastián, Spain

[5] Instituto de Catálisis y Petroleoquímica-CSIC, 28049 Madrid, Spain

**Highlights**

- $Eu^{3+}$ doped $SiO_2$-$GdF_3$ GCs with 20 mol% of crystalline phase has been successfully obtained by sol–gel method.
- The use of methyl triethoxysilane allows obtaining crack-free GCs samples and reduces the hydroxyl groups.
- Energy transfer with enhancement of efficiency was observed from $Gd^{3+}$ to $Eu^{3+}$ in the nanocrystals.

**Keywords** Sol–gel · $GdF_3$ · Oxyfluoride nano-glass-ceramic · Luminescence · Energy transfer

## 1 Introduction

In recent years, the preparation of rare-earth (RE) doped transparent oxyfluoride glass-ceramic (OxFGCs) materials have attracted much attention due to their excellent mechanical, chemical, and optical properties along with wide photonic applications, such as infrared and tunable phosphors, bioimaging, photovoltaics, solid-state lasers, etc [1–3]. The most common process to prepare nano glass ceramic materials (nGCs) is the melt-quenching, based in the nucleation and growth of nanocrystals (NCs) from a glass matrix in a controlled process. Due to the small size of these NCs the Rayleigh scattering is very weak, and perfect transparency is maintained after the conversion from glass to GCs. Moreover, this technique allows obtaining materials in different shapes, such as bulks and fibers [4–6]. However, this technique has important limitations such as the evaporation of chemical components, due to the high temperatures (1400–1700 °C) required causing uncontrollable changes of the composition respecting to fluorine and rare earth, which affect the final crystal fraction achieved, with maximum around 10 wt% in $LaF_3$ GCs. This technique also requires long treatment times (10–80 h) to obtain nGCs [7–9].

With the aim of developing new materials, the sol–gel process (SG) appears as a suitable alternative to obtain OxFGCs with inherent advantages over conventional techniques, like the versatility for obtaining thin-films, powder and bulk materials; the high purity and homogeneity of the obtained materials, and the possibility to incorporate high quantities of fluorides into nGCs associated with low sintering temperatures [10–14]. Different papers report on the preparation of nGC materials by SG. In general, the authors use only tetraethyl orthosilicate (TEOS) as precursor of silica matrix and with a maximum theoretical content of fluoride of 10 mol% [15–17]. The intents to produce films and bulk samples containing up to 15 mol%, were not successful resulting without a loss of transparency [10]. On the other hand, most papers report the processing of GCs at treatments at high temperatures, from 700 to 1000 °C with the aim of eliminating the residual –OH groups that quench the luminescence properties [16, 18, 19]. Indeed, these treatment temperatures are much higher than the typical crystallization temperatures of fluoride NCs in MQ produced materials (550–700 °C) [6, 9].

Therefore, an improvement of the synthesis and processing is required to obtain high crystalline fraction and low –OH content using lower treatment temperatures. The incorporation of other silica precursors as methyl triethoxysilane (MTES) that presents an organic radical that remains in the final structure, improves the process, also enhancing the flexibility and avoiding the appearance of cracks in SG materials. This synthesis has been widely used in sol–gel coatings with the aim to increase the thin films thickness [20, 21].

$GdF_3$ is a well-known material, being a good RE ions host due to its low phonon energy (300–340 $cm^{-1}$) and the possibility to exchange $Gd^{3+}$ ions with other RE ions used as dopants. Furthermore, $Gd^{3+}$ ions can act as sensitizer transferring energy to several RE ions, such as $Eu^{3+}$, $Tb^{3+}$, and $Dy^{3+}$, thus allowing the conversion from UV to Vis light [1, 22–24]. For these reasons, there are several reports on the preparation of OxFGCs containing $GdF_3$ by melting-quenching process [1, 4, 25, 26]. However, only few papers about SG $GdF_3$ OxGCs have been published. Fujihara et al. [14] prepared thin films of $SiO_2$-$GdF_3$ doped with 1 mol% of $Eu^{3+}$ with nominal crystalline phase content lower than 10 mol%. They observed the precipitation of $GdF_3$ for heat treatments at 300 and 400 °C, but GdOF NCs was detected when the temperature increases above 500 °C. More recently, Szpikowska-Sroka reported $Eu^{3+}$-doped $SiO_2$-$GdF_3$ bulk GCs, with lowest concentration of $GdF_3$, around 3 mol%, following the Fuhijara synthesis. [19, 23, 27]. However, most of these articles are focused in the optical properties disregarding the details of synthesis process or structural characterisation.

$Eu^{3+}$ ion is frequently used as luminescent activator in a variety of host lattices for its abundant energy levels in a wide range of wavelengths giving rise to emission of reddish orange light. Moreover, this ion can act as spectroscopic probe of local structure, due to the electric dipole (ED) character of the $^5D_0 \rightarrow {}^7F_2$ hypersensitive transition of $Eu^{3+}$ ions. This transition exhibits a great dependence on the symmetry of the site occupied by these ions [18, 28]. The aforementioned properties, together with $Eu^{3+}$ intense absorption in the near UV or vacuum-ultraviolet (VUV) in combination with an efficient host, convert this ion, in a suitable candidate for potential applications in plasma display panels (PDPs) and mercury-free fluorescent lamps [29, 30].

In the present work, a novel synthesis of $Eu^{3+}$-doped $SiO_2$-$GdF_3$ transparent GC materials by sol–gel was explored. The effect of incorporating fluoride content up to 20 mol% in the GCs and the use of MTES as precursor of silica were studied and correlated with the structural and optical properties. The use of MTES in adequate combination with TEOS allows obtaining self-supporting layers, reducing the shrinkage during drying and facilitating the elimination of OH groups, also opening the way to obtain GCs at lower temperatures. The luminescence properties and energy transfer mechanism from the $GdF_3$ fluoride matrix to the $Eu^{3+}$ ions before and after heat treatment were also evaluated by steady state and time-resolved luminescence.

## 2 Experimental section

### 2.1 Synthesis of $SiO_2$-$GdF_3$ xerogel and glass-ceramics

Undoped and 0.5 $Eu^{3+}$ (mol%) doped $SiO_2$-$GdF_3$ sols containing 10 and 20 mol% of $GdF_3$ were prepared by a novel sol–gel method. First, the required amount of Gd $(CH_3COO)_3{\cdot}nH_2O$ and $Eu(CH_3COO)_3$ were dissolved in trifluoracetic acid ($CF_3COOH$), ethanol and acidulated $H_2O$ solution (0.1 N HCl). The molar ratio of $RE^{3+}$ ($La^{3+}$ and $Eu^{3+}$) to $CF_3COOH$ was 1:5. The solution was stirred vigorously for 24 h at 40 °C in a glycerin bath, in order to obtain a homogeneous solution of the precursors. Separately, tetraethyl ortosilicate (TEOS) and methyl triethoxysilane (MTES) were mixed with ethanol (EtOH), and prehydrolyzed adding acidulated $H_2O$ (0.1 N HCl) and acetic acid ($CH_3COOH$) as catalysts. The silica sol was stirred at room temperature during 3 h. The final molar ratio was fixed to 1 (TEOS + MTES):5 EtOH:10 $H_2O$:0.5 $CH_3COOH$ and to 40TEOS:60MTES. After that, corresponding amount of silica sol and lanthanide solution were slowly mixed to obtain the molar ratios $90SiO_2$-$10GdF_3$ and $80SiO_2$-$20GdF_3$. The resultant homogeneous solutions were stirred vigorously for 4 h at room temperature.

The final solution was filtered and deposited into Petri dishes, covered and maintained at 50 °C for 15 days to obtain the xerogel. Then, the samples were dried at 150 °C to eliminate the solvents and finally treated in air at 550 °C for different times (from 1 min up to 8 h) to obtain the transparent nGCs.

### 2.2 Thermal and structural characterization

The thermal evolution analysis of the xerogel was studied by thermogravimetry and differential thermal analysis (DTA/TG, SDT Q600—TA Instruments) using 20–30 mg of xerogel with particle size in the range 1–1.25 mm. DTA curves were obtained heating the samples from 20 to 950 °C with heating rates in the range of 10–50 °C/min.

Fourier-transform infrared (FTIR) spectroscopy of dried and heat treated samples was performed in ATR mode, with a Perkin Elmer Spectrum 100 spectrometer, in the range of 400–4000 $cm^{-1}$ with a resolution of 2 $cm^{-1}$.

X-ray diffraction (XRD) measurements were performed at the beamline BM25-B (SpLine) of the European Synchrotron Radiation Facility (ESRF) using an energy of 20 keV corresponding to an X-ray wavelength of 0.619 Å. The obtained patterns were converted in the range of $2\theta$ from 10° to 70° corresponding to standard lab measurements obtained using CuK$\alpha_1$ radiation ($\lambda = 1.54056$ Å).

The morphological, compositional, and crystallographic information of xerogel and GCs were evaluated by using a high resolution electron microscopy (HRTEM, JEOL 2100) operating at 200 kV and equipped with a scanning transmission microscopy-high angle annular dark field (STEM-HAADF) and X-ray energy dispersive spectroscopy (EDX, INCA X-Sight, Oxford Instruments), which allowed to achieve a point resolution of 0.19 nm. EDX analysis was performed in STEM mode, with a probe size of ca. 1 nm. Samples were prepared by dispersing the fine powder obtained by grinding the xerogel and GC pieces, in ethanol with ultrasonic agitation, and then, a droplet of the suspension was deposited onto a copper holey carbon grid.

### 2.3 Optical properties

Room temperature emission and excitation spectra as well as luminescence decays were recorded by using a FS5 fluorescence spectrometer (Edinburgh Instruments Ltd, UK) equipped with a 150 W Xenon lamp. The emission was detected by Hamamatsu R928P photomultiplier.

## 3 Results and discussion

Transparent and stable sols were obtained after the synthesis process, with viscosity around 4 mPa.s. Then, transparent and homogeneous (100-$x$)$SiO_2$-x$GdF_3$ materials undoped and doped with $Eu^{3+}$ were prepared: the xerogels after drying and treating at 150 °C and glass ceramics after sintering at 550 °C.

### 3.1 Thermal and structural characterization

Figure 1 shows the DTA/TG analysis of 0.5 $Eu^{3+}$-doped $90SiO_2$-$10GdF_3$ and $80SiO_2$-$20GdF_3$ xerogels at different heating rates. The analysis was performed in argon to avoid oxidation processes.

A first weight loss, corresponding to an endothermic band centred between 100 and 180 °C, due to desorption of

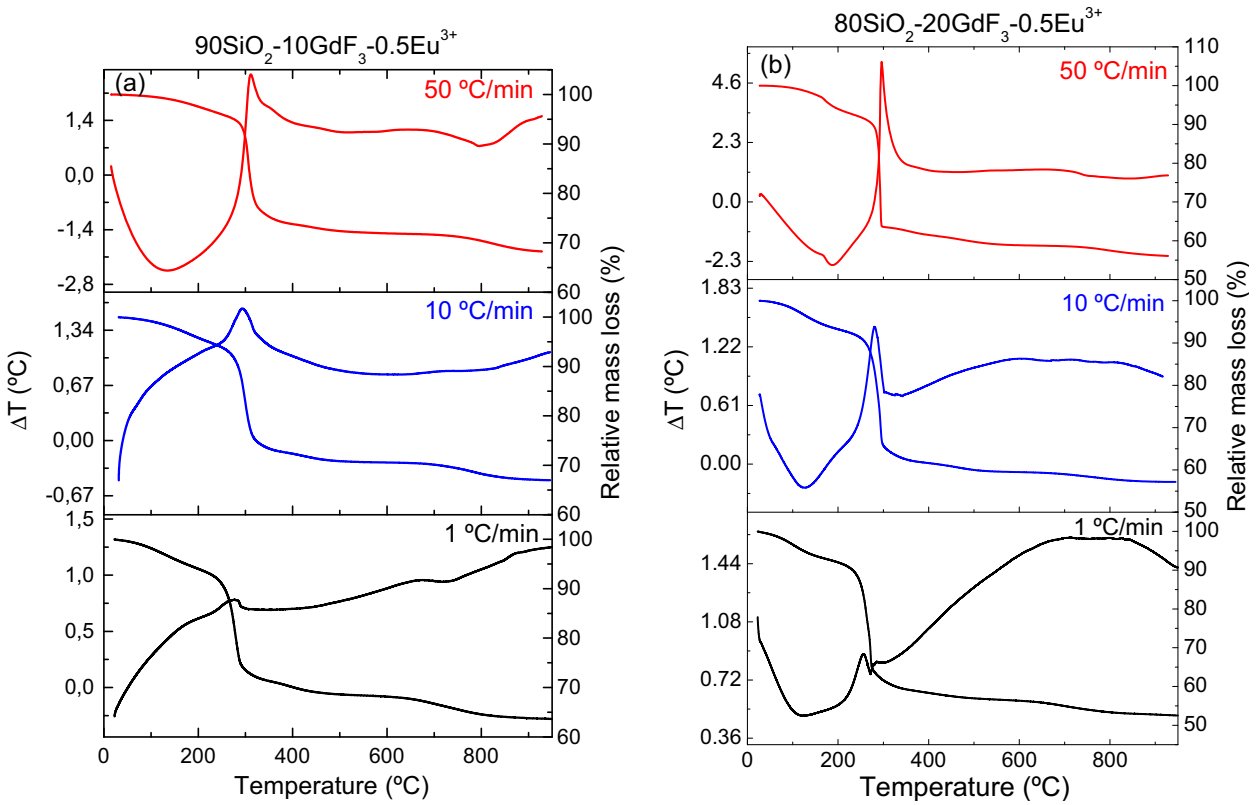


**Fig. 1** DTA and TG curves at different heating rates of 0.5 $Eu^{3+}$-doped $90SiO_2$-$10GdF_3$ **a** and 0.5 $Eu^{3+}$-doped $80SiO_2$-$20GdF_3$ **b** xerogels

the water and evaporation of the solvents is observed in both samples, with a mass loss around 3–5% for $90SiO_2$-$10GdF_3$ and 6–8% for $80SiO_2$-$20GdF_3$, for 1–50 °C/min heating rates, respectively. A following weight loss of about 30% is detected in the range of 250–325 °C for both samples, this being associated with the decomposition of Gd $(CH_3COO)_3{\cdot}nH_2O$, $Eu(CH_3COO)_3$ and TFA to obtain Gd $(CF_3COO)_3$ and $CH_3COOH$. The weight loss appears along with an exothermic peak, $T_p$, between 272 and 316 °C and is associated with the crystallization of $GdF_3$ phase. The peak is more intense and narrower with the increment of the heating rate and composition, indicating that crystallization increases. For $90SiO_2$-$10GdF_3$ composition, the $T_p$ position changes linearly by increasing the heating rate from 276 to 316 °C, while in the case of $80SiO_2$-$20GdF_3$ composition, the shift of $T_p$ deviates from linearity (272–296 °C).

Figure 2 shows the FTIR spectra obtained for 0.5 $Eu^{3+}$-doped $80SiO_2$-$20GdF_3$ xerogel and GC heat treated at 550 °C for 1 min. The bands around 3500–3400 $cm^{-1}$ and that at 1640 $cm^{-1}$ are assigned to stretching and bending vibrations of –OH and molecular water, respectively, both practically disappearing in the GCs. The bands appearing at 1100, 800, and 434 $cm^{-1}$ are associated to Si–O–Si stretching and bending vibrations. The bands appearing in the xerogel in the range 1750–1400 $cm^{-1}$ correspond with

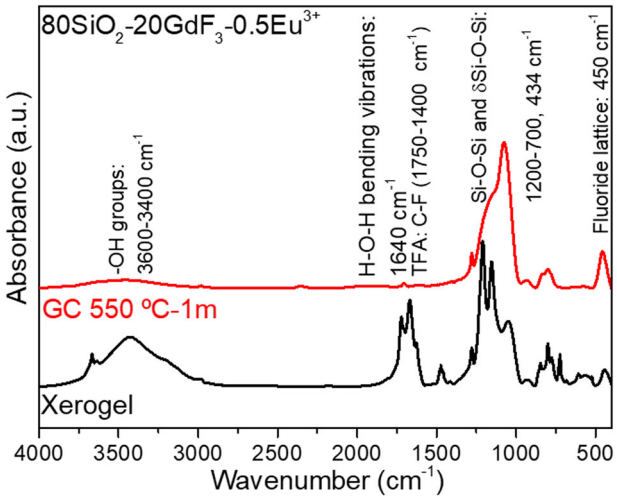


**Fig. 2** FTIR spectra of $Eu^{3+}$-doped $80SiO_2$-$20GdF_3$ xerogel and GC samples. Main absorption transitions are indicated

TFA and acetates precursors, all disappearing after the heat treatment [31, 32]. The band at 450 $cm^{-1}$ is only present in the treated sample and attributed to fluoride lattice, this confirming the formation of the fluoride nanocrystals [31].

The effect of sintering conditions on the crystallization of the $SiO_2$-$GdF_3$ materials was studied by XRD. Figure 3 shows the XRD patterns of $90SiO_2$-$10GdF_3$ and $80SiO_2$-

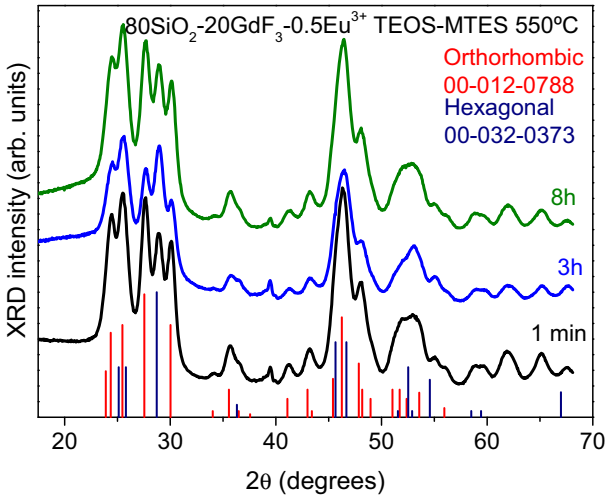


**Fig. 3** XRD of 0.5 $Eu^{3+}$-doped 0.5 $Eu^{3+}$-doped $80SiO_2$-$20GdF_3$ GCs heat treated at different times; PDF cards of hexagonal (32-0373) and orthorhombic (12-0788) phases have been included

$20GdF_3$ sol–gel GCs doped with 0.5 $Eu^{3+}$ heat treated at 550 °C at different sintering times (from 1 min to 8 h). Characteristics peaks of orthorhombic (PDF card 12-0788 card) $GdF_3$ structure were identified in both compositions and for all the heating times, whereas hexagonal phase was also indexed by using the PDF card of hexagonal $EuF_3$ phase (PDF card 32-0373), as made by Chen et al. [4] because of the corresponding $GdF_3$ hexagonal data have not been reported yet. The existence of the two phases in each composition for all the heating times, demonstrates that 1 min is enough time to obtain the total crystallization of $GF_3$.

The increase of heating time does not produce significant changes on the diffraction peaks, indicating that the nanocrystal size remains similar and independent of the heating time. The crystallite size was estimated by the Scherrer equation [33] using the full width at half maximum (FWHM) and the position of the XRD peaks at 28.9 and 41.2 degrees for hexagonal and orthorhombic crystalline phases, respectively. The values obtained for $80SiO_2$-$20GdF_3$ GCs are summarized in Table 1. The mean size of $GdF_3$ NCs is bigger for the orthorhombic phase respect to the hexagonal one. Moreover, NCs size slightly decreases for this phase with heating time, while remains near unchanged in hexagonal phase. This proves that crystallinity is not improving with dwelling time.

Additionally, the unit cell parameters and cell volume were estimated from the corresponding JCPDS files of both crystalline phases in $Eu^{3+}$-doped $80SiO_2$-$20GdF_3$ composition. Figure 4 shows the evolution of the unit cells parameters. These parameters diminish respecting to reference parameters but not changing significantly with dwelling time. For the hexagonal phase, the heating time increasing results in a large distortion of the "*c*" parameter and a slightly increases in the "*a*" parameter. As a result of the reduction of the unit cells parameters, the cell volume of hexagonal and orthorhombic crystalline phases slightly decreases in the doped samples from 294 to 284 $Å^3$ and from 202 to 198 $Å^3$, respectively.

**Table 1** Nanocrystal mean size of 0.5 $Eu^{3+}$-doped (100-*x*)$SiO_2$-x$GdF_3$ TEOS-MTES sol-gel glass ceramics heat treated at different temperatures and heating times

| Nanocrystal size (nm) | 550 °C 1 min | | 550 °C 3 h | | 550 °C 8 h | |
|---|---|---|---|---|---|---|
| | Hex. | Ort. | Hex. | Ort. | Hex. | Ort. |
| $80SiO_2$-$20GdF_3$ | 7.6 ± 0.5 | 9.0 ± 0.5 | 7.2 ± 0.5 | 8.4 ± 0.5 | 7.3 ± 0.5 | 7.7 ± 0.5 |

Figure 5 shows the structural characterization by HTREM of 0.5 mol% $Eu^{3+}$-doped $80SiO_2$-$20GdF_3$ GCs heat treated at 550 °C for 1 min. The micrograph (Fig. 5a, b) shows NCs dispersed in an amorphous silica matrix, with sizes around 7 nm, in agreement with XRD measurements for hexagonal phase. The amplification of the images and filtering using the fast Fourier transform (FFT) of the pattern (Fig. 5c, d) reveals the lattice planes with constant spacing of 3.2 Å (0.32 nm) attributed to (111) atomic plane of hexagonal phase and 2.9 Å (0.29 nm) to (210) atomic plane of orthorhombic structure [3, 26]. Figure 5f shows the EDX curves of the nanocrystal marked by yellow circle in Fig. 4d. The yellow line is the scanning line and the vertical dashed red lines limit the nanocrystal size. EDX analysis shows a clear enrichment in $Gd^{3+}$ and $F^-$ ions in the NCs. Furthermore, $Eu^{3+}$ ions are also detected inside the $GdF_3$ crystals evidencing that the dopant is incorporated in the nanocrystal.

From the previous results it is possible to discuss the crystallization mechanism; DTA results suggest that the crystallization process is very fast and different from the diffusion-limited process of melt-quenching materials. This assumption is also supported by XRD analysis, since after treatments at 550 °C for 1 min up to 8 h; no significant changes were observed in the NCs size. Indeed, after heat treatment at 550 °C for 1 min a perfect crystallization was achieved, thus confirming that this process cannot be described as a diffusion-limited one. These results are similar to those described by the authors in a previous work on $SiO_2$−$LaF_3$ GCs using TEOS as only alkoxide precursor [34]. We justified the crystallization process beginning with a chemical reaction followed by crystal precipitation. This was associated with a big mass loss [10, 35, 36] related to TFA and acetates decomposition, also observed in DTA and FTIR analysis, Figs. 1 and 2, respectively. The chemical reaction identified as responsible for the subsequent $GdF_3$ NCs precipitation is:

$$Gd(CF_3COO)_3 \rightarrow GdF_3 + (CF_3CO)_2O + O_2 + CO \quad (1)$$

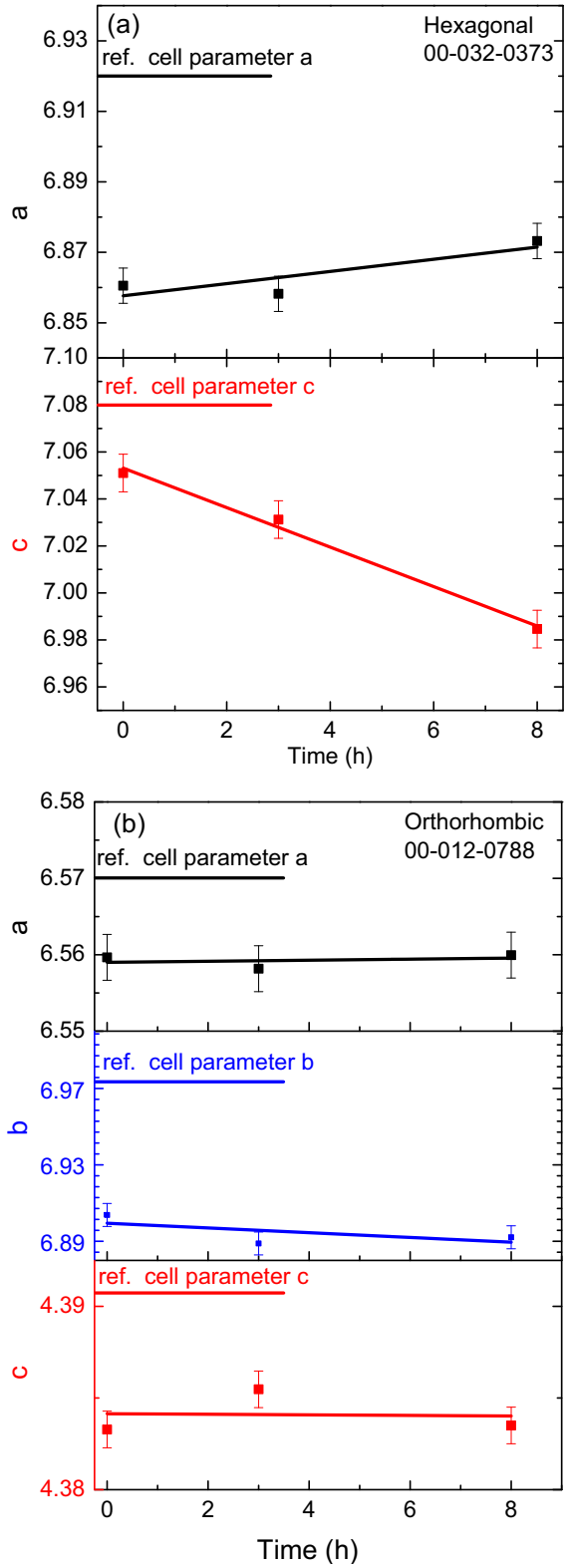


**Fig. 4** Unit cell parameters; a, b, and c of hexagonal **a** and orthorhombic phases **b** for $Eu^{3+}$-doped $80SiO_2$-$20GdF_3$ (TEOS-MTES) sol–gel glass ceramics

### 3.2 Optical properties

The emission spectra were obtained for all samples, in the 290–770 nm range, under excitation at 273 nm ($^8S_{7/2}\rightarrow{}^6I_J$ transition) for $Gd^{3+}$ and 393 nm ($^7F_0\rightarrow{}^5L_6$) for $Eu^{3+}$ ions. After 393 nm ($Eu^{3+}$) excitation, due to the small energy gap between $^5L_6$, $^5D_2$, $^5D_1$, and $^5D_0$ levels of $Eu^{3+}$ ions, the $^5D_0$ level is populated non-radiatively and the main emissions correspond to the $^5D_0\rightarrow{}^7F_{0,1,2,3,4}$ transitions. Excitation of $Gd^{3+}$ ions at 273 nm leads to the same emission bands of $Eu^{3+}$ together with the $Gd^{3+}$ emission at around 311 nm corresponding to the $^6P_J\rightarrow{}^8S_{7/2}$ transition. The presence of $Eu^{3+}$ emission after $Gd^{3+}$ excitation confirms the $Gd^{3+}\rightarrow Eu^{3+}$ energy transfer. According to the energy level diagram (Fig. 6) of $Gd^{3+}$ and $Eu^{3+}$ ions, after 273 nm excitation ($^8S_{7/2}\rightarrow{}^6I_J$ transition of $Gd^{3+}$), the $^6P_{7/2}$ level ($Gd^{3+}$) can be populated by multiphonon relaxation and the energy can be transferred to the $^5H_J$ levels of $Eu^{3+}$ from which the $^5D_0$ state is populated by non-radiatively transition. Another possibility is a direct transfer from levels $^6I_J$ of $Gd^{3+}$ to $^5F_J$ and/or $^5I_J$ levels of $Eu^{3+}$ from where the lower levels are populated non-radiatively until the lowest excited state $^5D_0$ is reached [30, 37].

Figure 7a shows the emission spectra of the untreated sample. The spectrum obtained under 273 nm excitation shows an intense peak corresponding to the $^6P_J\rightarrow{}^8S_{7/2}$ ($Gd^{3+}$) emission together with the $^5D_0\rightarrow{}^7F_{0,1,2,3,4}$ emissions of $Eu^{3+}$. When $Gd^{3+}$ ions are excited, the $Eu^{3+}$ emission band shows an intensity much higher, more than twice, than that obtained under direct excitation of $Eu^{3+}$ ions, thus indicating an efficient $Gd^{3+}\rightarrow Eu^{3+}$ energy transfer. In the case of the $Eu^{3+}$ emission, the highest intensity corresponds to the electric-dipole $^5D_0\rightarrow{}^7F_2$ transition. The intensity of this hyper-sensitive transition is strongly affected by the host and the influence of the local field on the emission spectra of $Eu^{3+}$ can be described by the asymmetry ratio, R, of the $^5D_0\rightarrow{}^7F_2$ and $^5D_0\rightarrow{}^7F_1$ emission intensities. It is known [38, 39] that in oxide glasses differences in this ratio are related to the Judd-Ofelt $\Omega_2$ parameter which depends on covalency and/or structural changes around $Eu^{3+}$ ions. In our case the obtained values, 2.86 and 2.77 for excitation at 273 and 393 nm, respectively, are closed to those found in Eu-oxide in silicate glasses [38] and indicate that $Eu^{3+}$ ions are located in a non-centrosymmetric site. The ratio is slightly higher under 273 nm excitation which could indicate that some weak contribution from the $^6G_J\rightarrow{}^6I_J$ emission lines of $Gd^{3+}$ in the orange/red (560–640 nm) spectral region overlaps with the $^5D_0\rightarrow{}^7F_{1,2}$ emissions of $Eu^{3+}$ [27]. The $^6G_J$ levels can be populated by excited state absorption from the metastable $^6P_{7/2}$ level. Measurements performed in the undoped sample under 273 nm excitation, show the presence of a weak $Gd^{3+}$ emission in the 565–650 nm spectral range (see inset in Fig. 7a). The emission from higher-lying

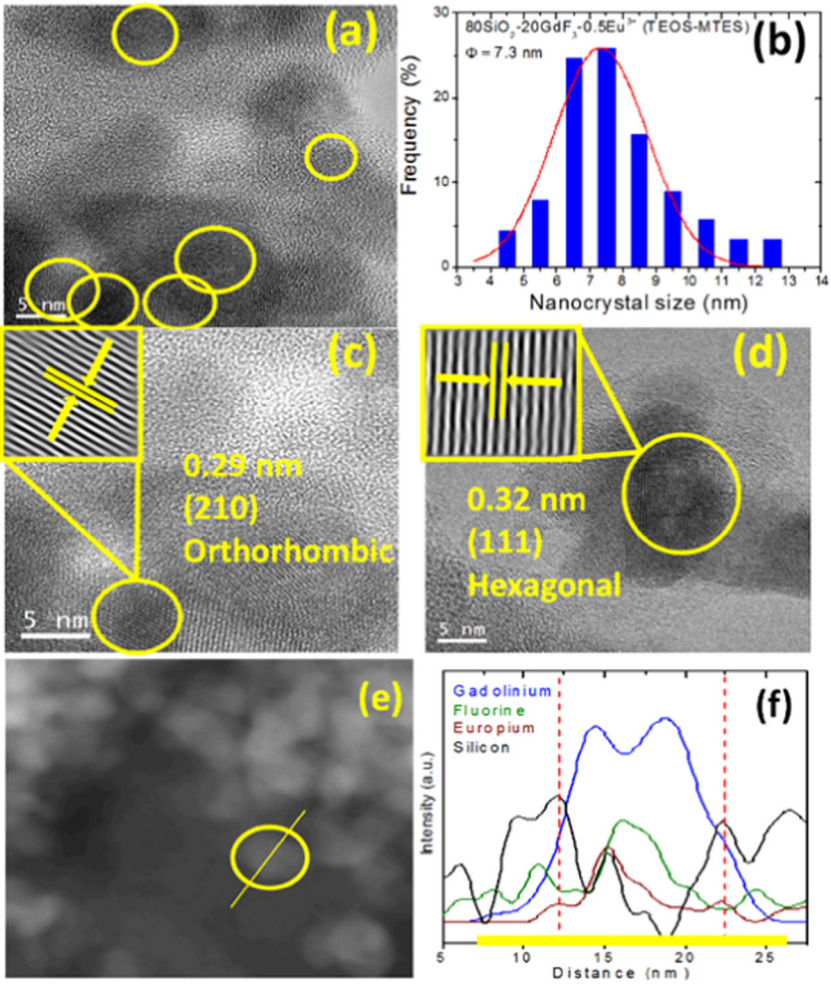


**Fig. 5** **a**, **c**, **d** HRTEM images of 0.5 $Eu^{3+}$-doped $80SiO_2$-$20GdF_3$ bulk heat treated at 550 °C for 1 min; **b** distribution of nanocrystals size; Inset in **c** and **d** crystalline structure with interplanar distances associated to the $GdF_3$ orthorhombic and hexagonal structure and corresponding selected area electron diffraction (SAED) pattern, respectively; **e** STEM image of 0.5 $Eu^{3+}$-doped $80SiO_2$-$20GdF_3$ heat treated at 550 °C 1 min used for the EDX measurement; **f** EDX of the corresponding NCs surrounded in **e** (yellow line indicates the scanning line)

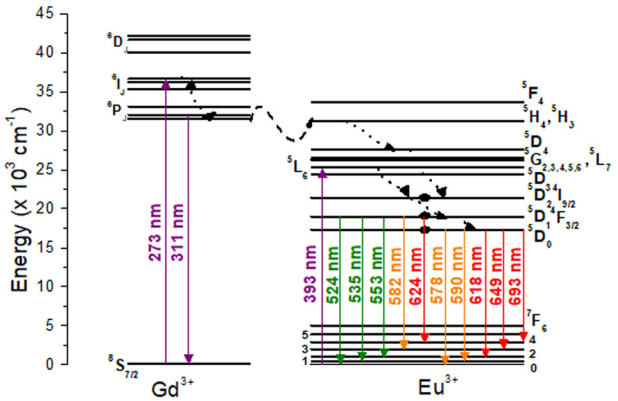


**Fig. 6** Energy level diagram of Gd3+ and Eu3+ ions

$^5D_1$ and $^5D_2$ levels of $Eu^{3+}$ is not observed in the xerogel sample due to nonradiative relaxation to the $^5D_0$ level.

The excitation spectra were recorded by monitoring the $^5D_0 \rightarrow {}^7F_2$ emission of $Eu^{3+}$ ions at 617 nm. The excitation spectrum of the untreated sample (Fig. 7b) consists of sharp peaks corresponding to the f–f transitions of the $Eu^{3+}$ and $Gd^{3+}$ ions. The peaks at 273 nm ($^8S_{7/2} \rightarrow {}^6I_J$), 298 nm ($^8S_{7/2} \rightarrow {}^6P_{3/2}$), 306 nm ($^8S_{7/2} \rightarrow {}^6P_{5/2}$), and 311 nm ($^8S_{7/2} \rightarrow {}^6P_{7/2}$), correspond to the f–f transitions of $Gd^{3+}$ (see energy level diagram in Fig. 6). The excitation peaks in the 350–330 nm spectral range are associated to the intra-configurational f–f transitions of $Eu^{3+}$ ions and attributed to $^7F_0 \rightarrow {}^5D_{4,3,2}$ at 361.5, 415, and 464.5 nm, respectively, to $^7F_0 \rightarrow {}^6L_7$ at 380 nm and to $^7F_0 \rightarrow {}^5L_6$ at 393 nm. The most intense excitation peaks correspond to $^8S_{7/2} \rightarrow {}^6I_J$ at 273 nm ($Gd^{3+}$) and $^7F_0 \rightarrow {}^5L_6$ at 393 nm ($Eu^{3+}$). On the other hand, the excitation peak at about 250 nm, corresponding to the $^8S_{7/2} \rightarrow {}^6D_J$ transition, has a very low intensity with respect to the excitation from $^8S_{7/2}$ to $^6I_J$ levels. The peaks at 250 and 273 nm are superimposed to a broad band that could be assigned to the $O^{2-} \rightarrow Eu^{3+}$ charge transfer [4] which means that $Eu^{3+}$ ions can also be excited through the charge transfer band. The same excitation spectrum is obtained by collecting the luminescence at 591 nm in the $^5D_0 \rightarrow {}^7F_1$ transition of $Eu^{3+}$ (not shown). The presence of $Gd^{3+}$ peaks in the excitation spectrum obtained monitoring the $Eu^{3+}$ emission further confirms the $Gd^{3+} \rightarrow Eu^{3+}$ energy transfer.

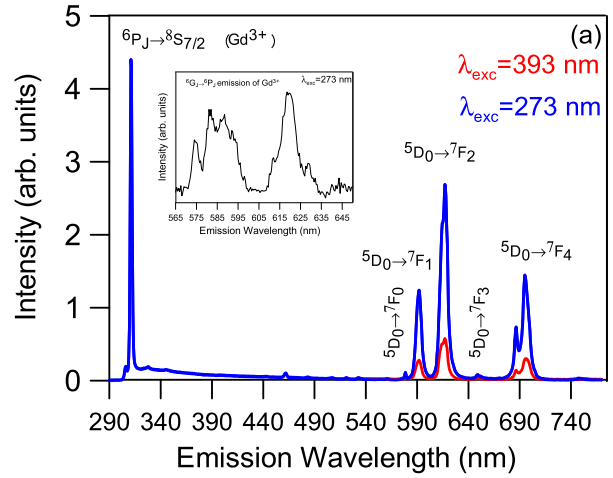


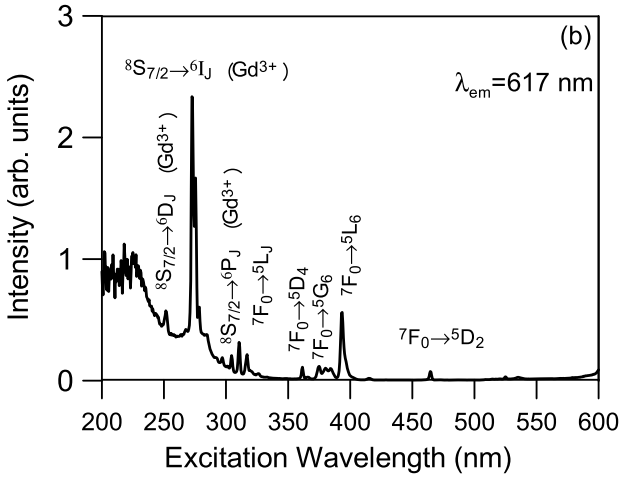


**Fig. 7** **a** Emission spectra of $Eu^{3+}$and $Gd^{3+}$ ions in sol–gel xerogel excited at 393 nm ($Eu^{3+}$) and 273 nm ($Gd^{3+}$). The inset shows the $Gd^{3+}$ emission of the undoped sample in the 565–650 nm spectral range; **b** Excitation spectrum of $Eu^{3+}$and $Gd^{3+}$ ions in sol–gel xerogel collecting the luminescence at 617 nm ($Eu^{3+}$)

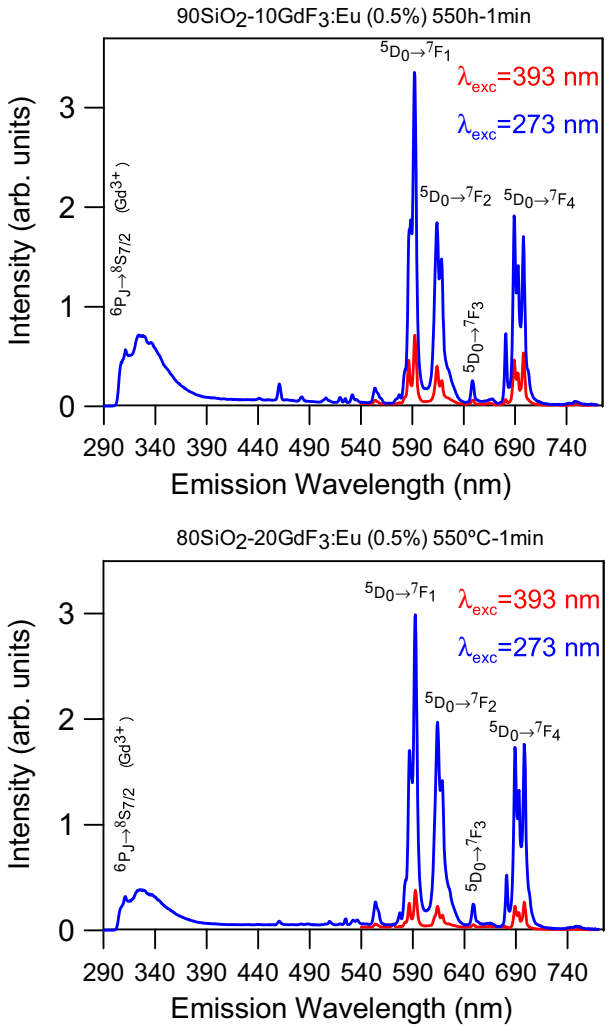


**Fig. 8** Emission spectra of $Eu^{3+}$ and $Gd^{3+}$ ions in sol–gel $90SiO_2$-$10GdF_3$ and $80SiO_2$-$20GdF_3$ treated at 550 °C for 1 min and excited at 393 nm ($Eu^{3+}$) and 273 nm ($Gd^{3+}$)

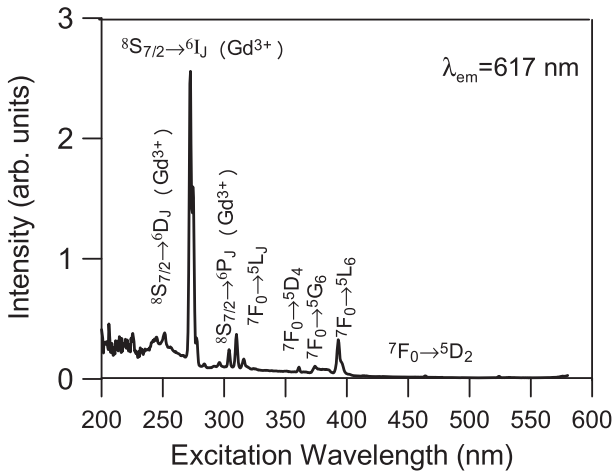


**Fig. 9** Excitation spectrum of $Eu^{3+}$ and $Gd^{3+}$ ions in sol–gel $80SiO_2$-$20GdF_3$ treated at 550 °C for 1 min collecting the luminescence at 617 nm

The emission spectra of the samples treated at 550 °C for 1 min show important different spectral features. As observed in Fig. 8, the intensity of the $^5D_0 \rightarrow {}^7F_1$ emission is higher than the $^5D_0 \rightarrow {}^7F_2$ one, which indicates a different surrounding of the $Eu^{3+}$ ions with respect to the xerogel sample. In addition, the emission bands are narrower and better resolved as compared to the untreated sample, thus confirming a crystalline environment for $Eu^{3+}$ ions. The *R* value for the $90SiO_2$-$10GdF_3$ GC sample, treated at 550 °C for 1 min, decreases from 0.74 to 0.66 exciting at 273 and 393 nm, respectively. A similar behaviour is obtained for the $80SiO_2$-$20GdF_3$ GC, which *R* value changes from 0.87 (273 nm) to 0.72 (393 nm). The small values of the *R* ratio suggest that, after the heat treatment, the ionic character of the bonds and the crystal field symmetry around $Eu^{3+}$ ions change according to the incorporation of $Eu^{3+}$ ions in the nanocrystals. The lower this ratio, the closer is the local

**Table 2** The $^5D_0 \rightarrow {}^7F_2/{}^5D_0 \rightarrow {}^7F_1$ ratio values and lifetimes of sol–gel samples before and after heat treatment at 550 °C during 1 min

| Sample | R $\lambda_{exc} = 273$ nm | R $\lambda_{exc} = 393$ nm | $\lambda_{exc} = 273$ nm lifetime $^5D_0$ (ms) | | $\lambda_{exc} = 393$ nm lifetime $^5D_0$ (ms) | |
|---|---|---|---|---|---|---|
| | | | $\lambda_{em} = 590$ nm | $\lambda_{em} = 614$ nm | $\lambda_{em} = 590$ nm | $\lambda_{em} = 614$ nm |
| Untreated | 2.86 | 2.77 | 0.38 | 2.5 | 0.22 | 2.3 |
| 550 °C for 1 min ($90SiO_2$-$10GdF_3$) | 0.74 | 0.66 | 1.57 | 8.3 | 1.18 | 7.6 |
| 550 °C for 1 min ($80SiO_2$-$20GdF_3$) | 0.87 | 0.72 | 1.64 | 8.7 | 0.86 | 8.7 |

symmetry to the one having an inversion center [38]. In these samples, the $^6P_J \rightarrow {}^8S_{7/2}$ ($Gd^{3+}$) intense peak is strongly reduced compared to untreated sample, which suggests a more efficient $Gd^{3+} \rightarrow Eu^{3+}$ energy transfer. This emission appears superimposed to a broad band centered around 326 nm associated to the matrix, since the $4f^6 5d\text{-}4f^7$ transition of $Eu^{2+}$ lies in the 360–420 nm range [40].

The excitation spectrum of the samples treated at 550 °C for 1 min shows the f–f transitions of the $Eu^{3+}$ and $Gd^{3+}$ ions with the most intense peak at 273 nm as in the case of the xerogel. However, in the heat treated samples, the broad band between 200 and 300 nm is much weaker than that of the xerogel probably due to the different environment of $Eu^{3+}$ ions. As an example, Fig. 9 shows the excitation spectrum for the $80SiO_2$-$20GdF_3$ sample doped with 0.5 mol% $Eu^{3+}$ and treated at 550 °C for 1 min.

The existence of different environments for $Eu^{3+}$ ions as well as the energy transfer from $Gd^{3+}$ ions should be reflected in the lifetimes of the $^5D_0$ state. The luminescence lifetimes of the $^5D_0$ level have been obtained for the xerogel and GC samples by exciting at 273 ($Gd^{3+}$) and 393 ($Eu^{3+}$) nm and collecting the luminescence at 591 and 614 nm, respectively. The decays can be described by two exponential functions which suggest the presence of different environments for $Eu^{3+}$ ions and the obtained lifetimes are given in Table 2. The lifetime values of the xerogel sample, 0.38 and 2.5 ms under 273 nm excitation, are longer than those obtained under 393 nm excitation (0.22 and 2.3 ms) confirming the energy transfer from $Gd^{3+}$ ions. Obtaining of longer lifetimes under $Gd^{3+}$ excitation at 273 nm compared with 393 nm is a common trend in all samples.

The GC samples treated at 550 °C $min^{-1}$ show lifetimes values more than twice longer than those of the xerogel sample, this behaviour agreeing with the lower *R* value of the GC. The longer lifetimes for $90SiO_2$-$10GdF_3$ and $80SiO_2$-$20GdF_3$ GCs are due to the incorporation of $Eu^{3+}$ ions in the low phonon energy fluoride NCs. These values are similar to those obtained for $LiGdF_4$:$Eu^{3+}$ NCs dispersed in a silica matrix [31]. Furthermore, the longer lifetimes obtained for GC samples are associated with the reduction of the hydroxyl groups, thus avoiding the luminescence quenching.

## 4 Conclusions

Europium doped and undoped GCs perfectly transparent with $(100-x)SiO_2$-$xGdF_3$ ($x = 10$ and 20 mol%) have been successfully obtained by a novel sol–gel method. MTES addition as silica precursor improves the mechanical properties avoiding the cracking even at high heating rates, around 10 °C/min. XRD peaks of the hexagonal and orthorhombic phases were shifted to larger $2\theta$ angles with the dwelling time indicating the incorporation of $Eu^{3+}$ ions into the nanocrystals. As a result, a contraction of the unit cell parameters and volume is observed. HRTEM and STEM-EDX confirm the results of XRD and the incorporation of $Eu^{3+}$ ions in the nanocrystals. Moreover, luminescence results also demonstrate that $Eu^{3+}$ ions are mainly incorporated in $GdF_3$ nanocrystals. Efficient energy transfer was observed from $Gd^{3+}$ to $Eu^{3+}$ in the nanocrystals, dismissing the $Gd^{3+}$ emission as well as increasing the $Eu^{3+}$ reddish visible emission. All these properties allow potential applications in Plasma Display Panels (PDPs) and mercury-free fluorescent lamps.

**Acknowledgements** This work was supported by MINECO under Projects N° MAT2013-48246-C2-1-P, MAT2013-48246-C2-2-P and Basque Country University PPG17/07 and GIU17/014. The authors thank the access to the Spanish Beamline (SpLine) at the ESRF facilities in Grenoble. J.J. Velázquez also acknowledges MINECO under Grant FPDI-2013-16895. This paper is also a part of dissemination activities of project FunGlass. This project has received funding from the European Union´s Horizon 2020 research and innovation programme under grant agreement No 739566.

### Compliance with ethical standards

**Conflict of interest** The authors declare that they have no conflict of interest.

## References

1. Shan Z, Chen D, Yu Y et al. (2010) Luminescence in rare earth-doped transparent glass ceramics containing $GdF_3$ nanocrystals for lighting applications. J Mater Sci 45:2775–2779. https://doi.org/10.1007/s10853-010-4266-1
2. Tikhomirov VK, Rodríguez VD, Méndez-Ramos J et al. (2012) Optimizing Er/Yb ratio and content in ErYb co-doped glass-ceramics for enhancement of the up- and down-conversion

luminescence. Sol Energy Mater Sol Cells 100:209–215. https://doi.org/10.1016/j.solmat.2012.01.019
3. Yin W, Zhao L, Zhou L et al. (2012) Enhanced red emission from $GdF_3$:$Yb^{3+}$,$Er^{3+}$ upconversion nanocrystals by $Li^+$ doping and their application for bioimaging. Chemistry 18:9239–9245. https://doi.org/10.1002/chem.201201053
4. Chen D, Wang Y, Yu Y, Huang P (2008) Structure and optical spectroscopy of Eu-doped glass ceramics containing $GdF_3$ nanocrystals. J Phys Chem C 112:18943–18947. https://doi.org/10.1021/jp808061x
5. Gorni G, Balda R, Fernández J et al. (2017) Oxyfluoride glass–ceramic fibers doped with $Nd^{3+}$: structural and optical characterization. CrystEngComm 19:6620–6629. https://doi.org/10.1039/C7CE01380A
6. Velázquez JJ, Balda R, Fernández J et al. (2018) Transparent oxyfluoride glass-ceramics with NaGdF4 nanocrystals doped with $Pr^{3+}$ and $Pr^{3+}$-$Yb^{3+}$. J Lumin 193:61–69. https://doi.org/10.1016/j.jlumin.2017.07.034
7. Fedorov PP, Luginina AA, Popov AI (2015) Transparent oxyfluoride glass ceramics. J Fluor Chem 172:22–50. https://doi.org/10.1016/j.jfluchem.2015.01.009
8. De Pablos-Martin A, Ferrari M, Pascual MJ, Righini GC (2015) Glass-ceramics: a class of nanostructured materials for photonics. Riv del Nuovo Cim. https://doi.org/10.1393/ncr/i2015-10114-0
9. de Pablos-Martín A, Durán A, Pascual MJ (2012) Nanocrystallisation in oxyfluoride systems: mechanisms of crystallisation and photonic properties. Int Mater Rev 57:165–186. https://doi.org/10.1179/1743280411Y.0000000004
10. Fujihara S, Mochizuki C, Kimura T (1999) Formation of $LaF_3$ microcrystals in sol-gel silica. J Non Cryst Solids 244:267–274. https://doi.org/10.1016/S0022-3093(99)00009-5
11. Velázquez JJ, Yanes AC, Del-Castillo J, et al. (2010) Spectroscopic characterization and up-conversion in sol-gel derived $Yb^{3+}$-$Pr^{3+}$ co-doped $SiO_2$-$LaF_3$ nano-glass-ceramics. J Non Cryst Solids. https://doi.org/10.1016/j.jnoncrysol.2010.03.001
12. Yanes AC, Velázquez JJ, Del-Castillo J, et al. (2008) Site-selective spectroscopy in $Sm^{3+}$-doped sol–gel-derived nano-glass-ceramics containing $SnO_2$ quantum dots. Nanotechnology. https://doi.org/10.1088/0957-4484/19/29/295707
13. Fujihara S, Tada M, Kimura T (1998) Sol–gel processing of $LaF_3$ thin films. Nippon Seramikkusu Kyokai Gakujutsu Ronbunshi/J Ceram Soc Jpn 106:124–126
14. Fujihara S, Koji S, Kimura T (2004) Structure and optical properties of (Gd,Eu)$F_3$ nanocrystallized sol–gel silica films. J Mater Chem 14:1331–1335. https://doi.org/10.1039/B313784H
15. Ribeiro SJL, Araújo CC, Bueno LA et al. (2004) Sol–gel $Eu^{3+}$/$Tm^{3+}$ doped transparent glass–ceramic waveguides. J Non Cryst Solids 348:180–184. https://doi.org/10.1016/j.jnoncrysol.2004.08.164
16. Biswas A, Maciel GS, Friend CS, Prasad PN (2003) Upconversion properties of a transparent $Er^{3+}$–$Yb^{3+}$ co-doped $LaF_3$–$SiO_2$ glass-ceramics prepared by sol–gel method. J Non Cryst Solids 316:393–397. https://doi.org/10.1016/S0022-3093(02)01951-8
17. Velázquez JJ, Rodríguez VD, Yanes AC et al. (2012) Down-shifting in $Ce^{3+}$–$Tb^{3+}$ co-doped $SiO_2$–$LaF_3$ nano-glass–ceramics for photon conversion in solar cells. Opt Mater 34:1994–1997. https://doi.org/10.1016/j.optmat.2011.12.020
18. Velázquez JJ, Rodríguez VD, Yanes AC et al. (2012) Photon down-shifting by energy transfer from $Sm^{3+}$ to $Eu^{3+}$ ions in sol–gel $SiO_2$-$LaF_3$ nano-glass-ceramics for photovoltaics. Appl Phys B 108:577–583. https://doi.org/10.1007/s00340-012-4950-8
19. Szpikowska-Sroka B, Pawlik N, Goryczka T, Pisarski WA (2015) Influence of silicate sol–gel host matrices and catalyst agents on the luminescent properties of $Eu^{3+}$/$Gd^{3+}$ under different excitation wavelengths. RSC Adv 5:98773–98782. https://doi.org/10.1039/C5RA15562B
20. Innocenzi P, Abdirashid MO, Guglielmi M (1994) Structure and properties of sol–gel coatings from methyltriethoxysilane and tetraethoxysilane. J Sol–Gel Sci Technol 3:47–55. https://doi.org/10.1007/BF00490148
21. Castro Y, Ferrari B, Moreno ADR (2010) Recubrimientos sol-gel obtenidos por deposición electroforética (EPD) sobre metales. Bol la Soc Esp Cerámica Y Vidr 39:705–710. https://doi.org/10.3989/cyv.082012
22. Grzyb T, Runowski M, Lis S (2014) Facile synthesis, structural and spectroscopic properties of $GdF_3$: $Ce^{3+}$, $Ln^{3+}$ ($Ln^{3+} = Sm^{3+}$, $Eu^{3+}$, $Tb^{3+}$, $Dy^{3+}$) nanocrystals with bright multicolor luminescence. J Lumin 154:479–486. https://doi.org/10.1016/j.jlumin.2014.05.020
23. Pawlik N, Szpikowska-Sroka B, Sołtys M, Pisarski WA (2016) Optical properties of silica sol-gel materials singly- and doubly-doped with $Eu^{3+}$and $Gd^{3+}$ ions. J Rare Earths 34:786–795. https://doi.org/10.1016/S1002-0721(16)60095-9
24. Pokhrel M, Mimun LC, Yust B et al. (2014) Stokes emission in $GdF_3$:$Nd^{3+}$ nanoparticles for bioimaging probes. Nanoscale 6:1667–1674. https://doi.org/10.1039/C3NR03317A
25. Lee G, Savage N, Wagner B et al. (2014) Synthesis and luminescence properties of transparent nanocrystalline $GdF_3$:Tb glass-ceramic scintillator. J Lumin 147:363–366. https://doi.org/10.1016/j.jlumin.2013.11.073
26. Liu S, Chen D, Wan Z et al. (2016) Phase structure control and optical spectroscopy of rare-earth activated $GdF_3$ nanocrystal embedded glass ceramics via alkaline-earth/alkali-metal doping. RSC Adv 6:71176–71187. https://doi.org/10.1039/C6RA17332B
27. Szpikowska-Sroka B, Żur L, Czoik R et al. (2014) Ultraviolet-to-visible downconversion luminescence in solgel oxyfluoride glass ceramics containing $Eu^{3+}$:$GdF_3$ nanocrystals. Opt Lett 39:3181. https://doi.org/10.1364/OL.39.003181
28. Bueno LA, Gouveia-Neto AS, da Costa EB et al. (2008) Structural and spectroscopic study of oxyfluoride glasses and glass-ceramics using europium ion as a structural probe. J Phys Condens Matter 20:145201
29. Zhong J, Liang H, Su Q et al. (2010) Luminescence properties of $NaGd(PO_3)_4$:$Eu^{3+}$ and energy transfer from $Gd^{3+}$ to $Eu^{3+}$. Appl Phys B 98:139–147. https://doi.org/10.1007/s00340-009-3673-y
30. Wegh R, Donker H, Oskam K, Meijerink A (1999) Visible quantum cutting in $Eu^{3+}$-doped gadolinium fluorides via down-conversion. J Lumin 82:93–104. https://doi.org/10.1016/S0022-2313(99)00042-3
31. Lepoutre S, Boyer D, Fujihara S, Mahiou R (2009) Structural and optical characterizations of sol–gel based composites constituted of $LiGdF_4$:$Eu^{3+}$ nanocrystallites dispersed into a silica matrix. J Mater Chem 19:2784. https://doi.org/10.1039/b819871c
32. Luo W, Wang Y, Cheng Y et al. (2006) Crystallization and structural evolution of $YF_3$-$SiO_2$ xerogel. Mater Sci Eng B Solid-State Mater Adv Technol 127:218–223. https://doi.org/10.1016/j.mseb.2005.10.034
33. Cullity BD (1978) Elements of X-ray diffraction, 2nd edition. Addison-Wesley Publ Co, Reading, MA 100-105-279. https://doi.org/10.1119/1.1934486
34. Gorni G, Pascual MJ, Caballero A, et al. (2018) Crystallization mechanism in sol-gel oxyfluoride glass-ceramics. J Non Cryst Solids. https://doi.org/10.1016/j.jnoncrysol.2018.01.031
35. Gorni G, Velázquez JJ, Mosa J, et al. (2018) Transparent glass-ceramics produced by sol-gel: a suitable alternative for photonic materials. Materials. https://doi.org/10.3390/ma11020212
36. Eloussifi H, Farjas J, Roura P et al. (2012) Evolution of yttrium trifluoroacetate during thermal decomposition. J Therm Anal Calorim 108:589–596. https://doi.org/10.1007/s10973-011-1899-5
37. Kondo Y, Tanaka K, Ota R et al. (2005) Time-resolved study of luminescence in soda-lime silicate glasses co-doped with $Gd^{3+}$

and $Eu^{3+}$. Opt Mater 27:1438–1444. https://doi.org/10.1016/j.optmat.2004.10.007

38. Reisfeld R, Zigansky E, Gaft M (2004) Europium probe for estimation of site symmetry in glass films, glasses and crystals. Mol Phys 102:1319–1330. https://doi.org/10.1080/00268970410001728609
39. EWJL Oomen, van Dongen AMA (1989) Europium (III) in oxide glasses: dependence of the emission spectrum upon glass composition. J Non Cryst Solids 111:205–213. https://doi.org/10.1016/0022-3093(89)90282-2
40. Karbowiak M, Mech A, Kępiński L et al. (2005) Effect of crystallite size on structural and luminescent properties of nanostructured $Eu^{3+}$:$KGdF_4$ synthesised by co-precipitation method. J Alloy Compd 400:67–75. https://doi.org/10.1016/j.jallcom.2005.01.058